IN-SILICO DESIGN, SYNTHESIS AND PHARMACEUTICAL ASSESSMENT OF SOME PHENOLIC COMPOUNDS

by

BASANTA SINGHA

Ph.D. REGN NO. PhD/CHE/00282

Submitted to

NAGALAND UNIVERSITY

In partial fulfillment of the requirements for the degree

of

DOCTOR OF PHILOSOPHY IN CHEMISTRY

DEPARTMENT OF CHEMISTRY

NAGALAND UNIVERSITY

LUMAMI-798627

NAGALAND, INDIA

2025

IN-SILICO DESIGN, SYNTHESIS AND PHARMACEUTICAL ASSESSMENT OF SOME PHENOLIC COMPOUNDS

by

BASANTA SINGHA

and

Prof. UPASANA BORA SINHA

(Supervisor)

Submitted

In partial fulfillment of the requirements for the degree

of

DOCTOR OF PHILOSOPHY IN CHEMISTRY

DEPARTMENT OF CHEMISTRY

NAGALAND UNIVERSITY

LUMAMI-798627

NAGALAND, INDIA

2025

Dedicated

to my

Dad (Basana Singha),

Mom (Leirang Singha)

and

Sister (Bijalata Singha).

नागालैण्ड विश्वविद्यालय
NAGALAND UNIVERSITY
(संसद द्वारा पारित अधिनियम 1989, क्रमांक 35 के अंतर्गत स्थापित केंद्रीय विश्वविद्यालय)
(A Central University established by an Act of Parliament No.35 of 1989)
मुख्यालय : लुमामी, जिला : जुन्हेबोटो (नागालैण्ड), पिनकोड – 798627
Hqrs : Lumami, Dist. Zunheboto (Nagaland), Pin Code – 798627
वेबसाइट / Website : www.nagalanduniversity.ac.in

DECLARATION

Nagaland University

2025

I, **Mr. Basanta Singha**, hereby declare that the subject matter of this Thesis is the record of work done by me, that the contents of this Thesis did not form basis of the award of any previous degree to me or to the best of my knowledge to anybody else, and that the thesis has not been submitted by me for any research degree in any other University/Institute.

This is being submitted to the Nagaland University for the degree of Doctor of Philosophy in Chemistry.

(Prof. Upasana Bora Sinha)
Supervisor

(Basanta Singha)

Head
Department of Chemistry
Nagaland University

नागालैण्ड विश्वविद्यालय
NAGALAND UNIVERSITY
(संसद द्वारा पारित अधिनियम 1989, क्रमांक 35 के अंतर्गत स्थापित केंद्रीय विश्वविद्यालय)
(A Central University established by an Act of Parliament No.35 of 1989)
मुख्यालय : लुमामी, जिला : जुन्हेबोटो (नागालैण्ड), पिनकोड – 798627
Hqrs : Lumami, Dist. Zunheboto (Nagaland), Pin Code – 798627
वेबसाइट / Website : www.nagalanduniversity.ac.in

Prof. Upasana Bora Sinha
upasanabsinha@gmail.com
Professor

DEPARTMENT OF CHEMISTRY

CERTIFICATE

This is to certify that the thesis entitled "***In-silico design, synthesis and pharmaceutical assessment of some phenolic compounds***" is a record of original research work carried out by **Mr. Basanta Singha** under my supervision. He is a registered research scholar, bearing the registration no. **PhD/CHE/00282** dated **31/08/2019** of the Department of Chemistry.

The candidate has fulfilled all the requirements of Ph.D. regulations of Nagaland University for the submission of thesis. The work is original and neither the thesis nor any part of it has been submitted elsewhere for the award of any degree or diploma. The thesis, therefore, forwarded for adjudication and consideration for the award of degree of Doctorate of Philosophy in Chemistry under Nagaland University.

I am highly impressed with his keen interest and hard work in completing the thesis and with best wishes for grand success in his future endeavor.

(Prof. Upasana Bora Sinha)
Supervisor

IN-SILICO DESIGN, SYNTHESIS AND PHARMACEUTICAL ASSESSMENT OF SOME PHENOLIC COMPOUNDS

by
BASANTA SINGHA
DEPARTMENT OF CHEMISTRY
NAGALAND UNIVERSITY

ABSTRACT

of

The thesis submitted in Fulfilment of the Requirement for the award of Degree of Doctor of Philosophy in Chemistry

To

NAGALAND UNIVERSITY
LUMAMI-798627, NAGALAND, INDIA

2025

ABSTRACT

In the vast landscape of scientific research, thousands of compounds are synthesized and analyzed every single day. While a handful advance for further development in their respective field of interest, countless others are sidelined, often shelved without deeper exploration. Many of these overlooked molecules may carry untapped potential, waiting to be uncovered. This work takes a different stance it does not view such compounds as failures, but as opportunities. By repurposing them with a purpose, the present thesis titled "***In silico* design, synthesis and pharmaceutical assessment of some phenolic compounds**" aims to breathe new life into some such underutilized compounds, applying innovative strategies to reveal latent potential and open new directions in drug discovery.

Chapter 1 sets the stage for the central theme of the research: the vast chemical space of compounds synthesized and characterized across laboratories and industries, many of which remain unused or "shelved." These overlooked molecules represent a hidden reservoir of potential therapeutic agents waiting to be explored. To unlock this latent value, the study integrates a suite of innovative strategies advanced computational methods to predict molecular interactions, quantum chemical analyses to probe electronic properties, green synthetic approaches for sustainable compound development, and *in vitro* assays to confirm biological relevance. Together, these methodologies form a cohesive and multidisciplinary framework, aimed at transforming underutilized compounds into viable candidates for therapeutic repurposing.

Chapter 2 investigated gentisyl alcohol derivatives modified through strategic halogenation (F, Br, Cl, I), revealing how substitution at specific positions markedly alters molecular reactivity, frontier orbital distributions, and ADME/T profiles. Among the analogues, 7F, 4F, 7Br, 1F, and 7I emerged as particularly promising, exhibiting superior docking interactions, favorable pharmacokinetics with high gastrointestinal absorption, low predicted toxicity, and strong stability in molecular dynamics simulations. These characteristics highlight their potential as hit candidates for therapeutic development targeting bacterial, viral, parasitic, and inflammatory

diseases. The chapter also emphasizes the significance of optimizing halogen substitution patterns as a forward-looking strategy to refine bioactivity and combat the growing challenge of resistant microbial strains.

Chapter 3 extends the investigation to fluorinated analogues of gentisyl alcohol, which exhibited notable outcome on molecular stability and binding affinity. Molecular dynamics simulations revealed that 1F, 4F, and 7F consistently adopt conformationally stable orientations across its respective targets along with favourable outcome through quantum analyses. Among these, 4F emerged as the most promising lead, with theoretical IC_{50} predictions strongly supporting its favorable bioactivity profile. This strategy sets the stage for subsequent *in vitro* and *in vivo* validation, aiming to confirm their broad-spectrum and multi-target therapeutic potential.

Chapter 4 brings into focus Terrestrol A (10), a quite underexplored natural derivative of gentisyl alcohol that emerges as a compound of remarkable interest. Demonstrating dual antiviral and antifungal potential, it holds particular significance in the context of SARS-CoV-2 and associated fungal co-infections. Computational insights from docking and molecular dynamics reveal not only strong and stable binding but also excellent drug-likeness and impressive bioactivity profiles. Its electronic structure suggests stable and reactive traits, while predicted pharmacological traits point toward real translational promise. Together, these findings position Terrestrol A(10) as a compelling therapeutic candidate.

Chapter 5 shifts attention to the structural essence of resveratrol, a polyphenol often described as a "double-edged sword" for its paradoxical effects. Building on this framework, the study highlights C144 (AZD7762), a molecule originally developed as a checkpoint kinase inhibitor that here emerges in a new light as a powerful nuclear receptor modulator of LXRα/β and FXR. These receptors though relatively underexplored in cancer research, open unconventional therapeutic pathways. Through extensive computational exploration, C144 demonstrated remarkable pharmacophore complementarity, systemic compatibility, and sustained stability within receptor complexes. Such features point toward its potential role in reshaping lipid metabolism, bile acid regulation, inflammatory responses, and oncogenic signaling. Re-envisioned through this lens, C144 (AZD7762) stands not merely as a

kinase inhibitor but as a versatile anticancer candidate with strong nuclear receptor affinity.

Chapter 6 explores the repurposing potential of some bromophenols, with 1-bromo-2-naphthol emerging as the lead candidate. Synthesized using the green reagent TBATB, the process reflects an eco-conscious “waste-to-wealth” approach in medicinal chemistry, where neglected synthetic intermediates are transformed into valuable therapeutic scaffolds. Remarkably, 1-bromo-2-naphthol displayed potent antibacterial, antifungal and antioxidant activities, findings reinforced by computational predictions and supported by preliminary experimental validation. Together, these results highlight the compound’s promise as a sustainable and multifunctional bioactive lead.

Taken together, this thesis converges on a multidisciplinary strategy, where an extensive suite of computational and quantum chemical analyses, green synthesis and experimental validations are integrated not as isolated methods but as complementary tools within a holistic discovery pipeline. The identified compounds halogenated and fluorinated gentisyl alcohol derivatives, Terrestrol A, C144 (AZD7762) and 1-bromo-2-naphthol emerge as potent leads with applications spanning antimicrobial resistance, viral and invasive fungal co-infections, cancer therapy and oxidative stress modulation.

नागालैण्ड विश्वविद्यालय
NAGALAND UNIVERSITY
(संसद द्वारा पारित अधिनियम 1989, क्रमांक 35 के अंतर्गत स्थापित केंद्रीय विश्वविद्यालय)
(A Central University established by an Act of Parliament No.35 of 1989)
मुख्यालय : लुमामी, जिला : जुन्हेबोटो (नागालैण्ड), पिनकोड – "9862"
Hqrs : Lumami, Dist. Zunheboto (Nagaland), Pin Code – "9862"
वेबसाइट / Website : www.nagalanduniversity.ac.in

CERTIFICATE

This is to Certify that **Mr. Basanta Singha**, a registered Research Scholar for Ph.D. degree in Chemistry under Nagaland University, bearing Ph.D. Registration No. **PhD/CHE/00282**, has satisfactorily completed all the courses offered in the Pre-Ph.D. Course Work Programme in the Department of Chemistry, Nagaland University, *Hqrs*. Lumami.

The Course Includes:

CHEM-601 Research Methodology
CHEM-602 Advance in Chemistry
CHEM-603 Literature Review, Report Writing and Presentation

Ambrish Singh

Head
Department of Chemistry
Nagaland University

Sl. No. : 19- 91079

NAGALAND UNIVERSITY

STATEMENT OF MARKS

Ph. D COURSE WORK EXAMINATION, 2020

DEPARTMENT OF CHEMISTRY

The following are the marks secured by **Basanta Singha**
Roll No. **19PhD01** *of Ph.D Course Work Examination held in* **2020**

Subject(s)/Paper(s)	Max. Marks	Minimun Qualifying Marks	Marks Secured
Paper No. Chem-601 Research Methodology	100	35	**72**
Paper No. Chem-602 Advance in Chemistry	100	35	**77**
Paper No. Chem-603 Literature Review, Report Writing and Presentation	100	35	**79**
Total Aggregate Marks			**228**
Average Pass Mark – 55 %			

Result	Division	Percentage
Passed	**I Division**	**76 %**

Marks compared by

COE/Dy. Reg. AR (Exams)
Assistant Registrar (Exams)
Nagaland University
Hqrs. Lumami

NAGALAND UNIVERSITY

HEAD QUARTERS : LUMAMI

Ph. D COURSE WORK EXAMINATION

This is to certify that Mr/Ms Basanta Singha

of Nagaland University bearing Roll No. 19 Ph.D. 01 *is qualified in the Ph.D Course Work Examination*

in the Department of Chemistry *Nagaland University held in the Year* 2020

Head of Department

Dean
School of Sciences

ACKNOWLEDGEMENTS

I have many people to thank, but words will probably fall short.

I express my heartfelt gratitude to my supervisor, ***Prof. Upasana Bora Sinha****, Department of Chemistry, Nagaland University, Headquarters – Lumami, for her unwavering support and inspiration in getting me at this stage of my research journey. Without her guidance in every aspects, this would not have been possible. Her constant encouragement and suggestions have helped me refine my research skills, shaping me into a contributor in my field of specialization.*

I am deeply grateful to all the faculty members of the Department of Chemistry, Nagaland University, Prof. Dipak Sinha (Pro Vice-Chancellor, SAS Campus), Prof. Ambrish Singh (Head of Department), Prof. M. Indira Devi, Dr. I. Tovishe Phucho, Dr. M. Prabhakar, Dr. Nurul Alam Choudhary, and Dr. Seram Dushila Devi, for their constant encouragement and support.

I would also like to extend my sincere thanks to Ms. Bhoomika Arora and Mr. Mohammad Abid from the Medicinal Chemistry Laboratory, Department of Biosciences, Jamia Millia Islamia, New Delhi – 110025, India, as well as to Dr. Benzir Ahmed and Dr. Bipul Bezbaruah from the Department of Applied Sciences, Gauhati University, for their valuable contributions and support in my work.

I would also like to thank Nagaland University for the UGC NON-NET Fellowship, which provided essential financial assistance.

My sincere appreciation also goes to Mr. S. Bendangtemsu, Mrs. Sunepjungla, Ms. Temsuienla Amer, Ms. Lovi, and Ms. Kally Kinimi for their invaluable support.

I wish to convey my special thanks to my research labmates: Dr. Kekholeho Richa, Dr. Naruti Longkumer, Dr. Ritupurna Karmaker, Dr. Apuchu Sangtam, Ms. Narola Imchen, Ms. Angunuo Kheiya, Mr. Partha Pratim Gogoi, Ms. Penlisola Longkumer, Mr. Nichan Baruah, Ms. Beware Dkhar, Ms. Ilavanalangki Lytan, and Mr. Mhasilhoutuo Pucho, for their immense love, encouragement, support, and friendship that made this journey memorable.

I would like to express my deepest gratitude to my family, whose unwavering support has been the foundation of my journey. To my mother and father, thank you for your endless encouragement, patience, and belief in my abilities even during the most challenging times. To my sister, your love, laughter, and understanding have been a constant source of motivation.

I am also profoundly grateful to my friends, mentors, colleagues, and well-wishers, whose words of encouragement, guidance, and companionship have enriched this journey and made the PhD experience far more meaningful. Your support, whether through thoughtful advice, shared laughter, or simply being there to listen, has been invaluable.

Above all, I bow in deepest gratitude to the Almighty God and my Lord Jesus Christ, whose boundless grace, unwavering presence, and infinite blessings have been my guiding light throughout this journey. It is by His wisdom that I found clarity in times of doubt, by His strength that I persevered through challenges, and by His mercy that this work has reached its completion. Every page of this thesis stands as a testament not only to human effort but to divine guidance, without which none of this would have been possible. To God be all the glory and honor, now and always.

TABLE OF CONTENTS

List of Figures i-xxiv

List of Tables xxv-xxxi

List of Abbreviations xxxii-xxxv

Chapter 1: Introduction 1-49

1.1. Revisiting shelved compounds (repurpose with a purpose)
1.2. Structural Modification as a Perspective in Drug Discovery and
1.3. Drug Repurposing: An Evolving Paradigm in Modern
1.4. Importance of phenolic compounds
1.4.1. Therapeutic and pharmaceutical applications of phenol
1.4.1.1. Phenolic compounds as anti-cancer agent
1.4.1.2. Phenolic compounds as anti-Inflammatory and
1.4.1.3. Phenolic compounds as anti-microbial
1.4.1.4. Phenolic Compounds: Structural Subcategory and
1.4.2. Halogenated phenolic compounds
1.4.3. Computer-Aided Drug Design (CADD)
1.4.3.1. Computational Screening and Profiling of Candidate
1.4.3.2. Quantum mechanical (QM) calculations
1.4.3.2.1. Methods in QM calculations
1.4.3.2.2. Gaussian
1.4.3.2.3. Visual Molecular Dynamics
1.4.3.2.4. Multiwfn
1.4.4. Green Synthetic Pathways and Eco-Friendly
1.4.5. In vitro antimicrobial
1.4.6. In vitro antioxidant
Scope and Objectives

Chapter 2: Design and Multi-Target Evaluation of Halogenated Gentisyl Alcohol Derivatives Using Docking, DFT, and ADMET Profiling 50-81

2.1. Introduction
2.2. Materials and methods
2.2.1. Compounds in focus
2.2.2. Target selection

2.2.3. Preparation of ligands
2.2.4. Docking
2.2.5. Density functional theory (DFT)
2.2.6. Drug likeness and ADME/T screening
2.3. Results and discussion
2.3.1. Docking
2.3.2. Interaction study of the docked compounds
2.3.3. Density functional theory (DFT)
2.3.4. Druglikeness and ADME/T screening
2.4. Conclusion
References

Chapter 3: An Extensive Suite of Computational Investigations on Halogenated Gentisyl Alcohol Derivatives for Multi-target Pharmacological Profiling

82-147

3.1. Introduction
3.2. Materials and methods
3.2.1. Molecular dynamics (MD)
3.2.2. Structural pharmacophore
3.2.3. Quantum studies
3.2.3.1. Mulliken charge analysis
3.2.3.2. Nonlinear Optical (NLO) properties analysis
3.2.3.3. Analysis of MEP, ESP and contour plots
3.2.3.4. Natural Bond Orbital (NBO) analysis
3.2.3.5. Analysis of LOL, contour and ELF plots
3.2.3.6. Analysis of NCI and VMD
3.2.4. Bond length, bond angle and dihedral angle calculation
3.2.5. Bioactivity score prediction
3.2.6. Reacting atom (RA)
3.2.7. PASS prediction
3.2.8. IC_{50} calculation
3.3. Result and discussion
3.3.1. Molecular dynamics
3.3.1.1. Root mean square deviation (RMSD)
3.3.1.2. Root mean square fluctuation (RMSF)
3.3.1.3. Radius of gyration (Rg)

3.3.1.4. Hydrogen bond
3.3.1.5. Binding free energy
3.3.2. Structural pharmacophore
3.3.3. Mulliken Charge Analysis
3.3.4. Natural Bond Orbital (NBO) analysis
3.3.5. Nonlinear Optical (NLO) Properties Analysis
3.3.6. Analysis of MEP, ESP and contour plots
3.3.7. Analysis of LOL, contour and ELF plot
3.3.8. Analysis of NCI and VMD
3.3.9. Bond length, bond angle and dihedral angle analysis
3.3.10. Bioactivity score prediction
3.3.11. PASS Prediction
3.3.12. IC_{50} calculation
3.4. Conclusion
References
Supporting information

Chapter 4: Dual Inhibitory Potential of Terrestrol A, a Gentisyl Alcohol Derivative, Against SARS-CoV-2 and Invasive Fungal Pathogens: A Computational and Pharmacoinformatic Investigation 148-264

4.1. Introduction
4.2. Material and method
4.2.1. Set of compounds and standards under study
4.2.2. Molecular docking simulation
4.2.2.1. Preparation of ligands
4.2.2.2. Selections of target of interest
4.2.2.3. Molecular docking
4.2.3. Druglikeness (physicochemical properties)
4.2.4. Pharmacokinetics (ADME) and toxicity prediction
4.2.5. Bioactivity prediction
4.2.6. PASS (prediction of activity spectra for substances)
4.2.7. Molecular dynamics
4.2.8. DFT (Density functional theory)
4.3. Results and discussion
4.3.1. Validation of docking analysis
4.3.2. Druglikeness (physicochemical properties)
4.3.3. Pharmacokinetics (ADME) and toxicity prediction

4.3.3.1. ADME (pharmacokinetics)
4.3.3.2. Toxicity prediction
4.3.4. Bioactivity prediction
4.3.5. PASS (prediction of activity spectra for substances)
4.3.6. DFT (Density functional theory)
4.3.7. Results and Analysis for MD Simulation
4.3.7.1. Root mean square deviation (RMSD)
4.3.7.2. Root mean square fluctuation (RMSF)
4.3.7.3. Radius of gyration (Rg)
4.3.7.4. Solvent Accessible Surface Area (SASA)
4.3.7.5. Dynamics of Hydrogen Bonding
4.4. Discussion
4.5. Conclusion
References
Supporting information

Chapter 5: Resveratrol-Inspired Structure-Guided Computational Profiling of AZD7762 as a Potent and Selective Modulator of LXRα, LXRβ, and FXR: A Targeted Analysis of the Underexplored Pathway in Cancer Therapeutics

265-562

5.1. Introduction
5.2. Materials and methods
5.2.1. Swiss- similarity based virtual screening
5.2.2. Druglikeness and toxicity-based screening
5.2.3. Target selection
5.2.4. Ligand selection
5.2.5. Docking *via* Molegro virtual docker
5.2.5.1. Ligand preparation
5.2.5.2. Docking
5.2.5.2.1. Scoring functions
5.2.5.3. Protein-Ligand Interaction Profiler (PLIP)
5.2.6. Electronic Reactivity Parameters *via* DFT
5.2.7. Statistical analysis

5.2.7.1. Correlation matrix

5.2.7.2. Principal component analysis

5.2.8. Docking *via* AutoDock

5.2.8.1. Docking

5.2.9. Protein-Ligand Interaction Profiler (PLIP)

5.2.10. Molecular Ligand-Protein Interaction Classifier (ML-PLIC)

5.2.11. Structural pharmacophore

5.2.12. Bioactivity prediction

5.2.13. Detailed quantum calculation

5.2.14. CLC-Pred

5.2.15. Reacting atom and Pharmacokinetics (ADME)

5.2.16. Molecular dynamics

5.2.16.1. Molecular dynamics simulation

5.2.16.2. Calculation of hydrogen bond existences or occupancies

5.2.16.3. Binding affinity calculations between the protein and ligand

5.2.17. Shermo online

5.3. Results and discussion

5.3.1. Swiss similarity based virtual screening

5.3.2. Druglikeness and toxicity-based screening

5.3.3. Molecular docking via Molegro virtual docker

5.3.3.1. Docking score

5.3.3.2. Ligand-protein interaction

5.3.3.3. Protein-Ligand Interaction Profiler (PLIP)

5.3.4. Electronic Reactivity Parameters *via* DFT

5.3.5. Statistical analysis

5.3.5.1. Correlation matrix

5.3.5.2. Principal component analysis

5.3.6. AutoDock

5.3.6.1. Docking score

5.3.6.2. Ligand-protein interaction

5.3.7. Protein-Ligand Interaction Profiler (PLIP)

5.3.8. ML-based protein-ligand interaction capturer (ML-PLIC)

5.3.9. Structural pharmacophore

5.3.10. Bioactivity prediction

5.3.11. Detailed quantum calculation

5.3.11.1. Molecular electrostatic potential analysis

5.3.11.1.1. Analysis of molecular electrostatic potentials (MEPs)

5.3.11.1.2. Analysis of Electrostatic potentials (ESPs)

5.3.11.2. Mulliken Charge (MC) analysis

5.3.11.3. Natural bond orbital (NBO) analysis

5.3.11.4. Becke surface analysis (BSA)

5.3.11.5. Hirshfield surface analysis

5.3.11.6. Visualizations of non-covalent interaction

5.3.11.6.1. NCI-RDG analysis

5.3.11.6.2. Topology analysis

5.3.11.6.2.1. Electron localization (LOL) and localized orbital locator (ELF) analysis

5.3.11.7. CLC-Pred

5.3.11.8. Reacting atom (Biotransformation) and Pharmacokinetics

5.3.11.9. Molecular dynamics

5.3.11.9.1. Energy minimization

5.3.11.9.2. Equilibration

5.3.11.9.2.1. Temperature distribution during NVT equilibration

5.3.11.9.2.2. Pressure distribution during NPT equilibration

5.3.11.9.2.3. Density of the system during NPT equilibration

5.3.11.9.3. Outcomes of the molecular dynamic simulation

5.3.11.9.3.1. Root mean square deviation of the protein in the complex

5.3.11.9.3.2. Root mean square deviation of the ligand in the complex

5.3.11.9.3.3. Root mean square fluctuation of the protein

5.3.11.9.3.4. Radius of Gyration

5.3.11.9.3.5. Hydrogen bonds numbers

5.3.11.9.3.6. Hydrogen bonds existences

5.3.11.9.3.7. PCA of 1UHL and ligand C144

5.3.11.9.3.8. MM/PBSA energy calculations

5.3.11.10. Shermo online

5.4. Conclusion

References

Supporting information

Chapter 6: Integrated Computational, Synthetic and *in vitro* Evaluation of Minimally Explored Laboratory Compounds 563-668

6.1. Introduction

6.2. Materials and methods

6.2.1. Molecular docking

6.2.1.1. Target selection

6.2.1.2. Compounds under investigation

6.2.1.3. Docking via MVD

6.2.1.4. Docking via AutoDock

6.2.2. Pharmacophore mapping

6.2.3. Synthesis

6.2.3.1. General chemistry

6.2.3.2. Synthetic procedure

6.2.4. *In vitro* antibacterial Studies
6.2.5. *In vitro* antifungal activity
6.2.6. Antioxidant activity
6.2.6.1. 2, 2-diphenyl-1-picryl hydrazyl (DPPH) free radical scavenging assay
6.2.6.2. FRAP (Ferric reducing antioxidant power) assay
6.2.6.3. Antioxidant Capacity via ABTS (2, 2-Azino-(3-ethyl) benzothiazoline)-6-sulfonic acid diammonium salt)
6.2.6.4. Quantum Assessment of Antioxidant Reactivity via BDE (Bond Dissociation Energy)
6.2.7. Extensive quantum calculations
6.2.7.1. Frontier Molecular Orbitals (FMOs) and global reactivity descriptors
6.2.7.2. Mulliken Charge (MC)
6.2.7.3. Natural Bond Orbital (NBO)
6.2.7.4. Non-Linear Optics (NLO)
6.2.7.5. Real-Space Analysis of Non-Covalent Interactions (NCI) and Electron Localization
6.3. Results
6.3.1. Molecular docking
6.3.1.1. Docking *via* MVD
6.3.1.2. Docking *via* AutoDock
6.3.2. Pharmacophore mapping
6.3.3. Synthesis
6.3.4. Antibacterial activity
6.3.5. Antifungal activity
6.3.6. Antioxidant activity
6.3.7. Extensive quantum mechanical calculations
6.3.7.1. Frontier Molecular Orbitals (FMOs) and global reactivity descriptors
6.3.7.2. Molecular Electrostatic Potential Analysis
6.3.7.3. Mulliken charge (MC) analysis
6.3.8. Natural Bond Orbital (NBO) analysis
6.3.9. Nonlinear Optical (NLO) Analysis
6.3.10. Non-covalent Interactions (NCI) studies
6.4. Conclusion
References
Supporting Information

APPENDIXES

Appendix 1	Plagiarism report
Appendix 2	Curriculum vitae
Appendix 3	List of publications
Appendix 4	List of patents
Appendix 5	Papers presented in conference/ symposium/ workshop/ conclave/ seminar

LIST OF FIGURES

Figure number	Legends
Figure 1.1	Examples of some phenolic compound
Figure 1.2	The structure of phenol
Figure 1.3	Chemical structures of polyphenols with anticancer properties
Figure 1.4	Structural depiction of some phenolic compounds possessing antimicrobial activity
Figure 1.5	Structural depiction of gentisyl alcohol
Figure 1.6	Structural depiction of some bromophenolic compounds
Figure 2.1	Mode of interaction between the ligand and the target (PDB ID: 7DQL)
Figure 2.2	Mode of interaction between the ligand and the target (PDB ID: 3O4M)
Figure 2.3	Mode of interaction between the ligand and the target (PDB ID: 4YRE)
Figure 2.4	Mode of interaction between the ligand and the target (PDB ID: 7NNY)
Figure 2.5	Molecular Interaction Between the ligand inhibitor and target PDB 7OFS
Figure 2.6	Cartoon illustration of the HOMO-LUMO gap of 1F, 4F, 7F, 7Br and 7I.
Figure 3.1	Compounds under investigation
Figure S3.2 (A-C)	Root Mean Square Deviation (RMSD) of backbone carbon atoms of protein-ligand complexes for the duration of 100 ns simulation time. A). 7F-7DQL, B). 4F-3O4M, and C). 1F- 4YRE respectively.
Figure S3.3 (A-C)	Root Mean Square Fluctuation (RMSF) of amino acid residues in proteins upon ligand binding for the duration of

	100 ns simulation time. A). 7F-7DQL, B). 4F-3O4M, and C). 1F- 4YRE, respectively.
Figure S3.4(A-C)	Radius of Gyration of protein-ligand complexes for the duration of 100 ns simulation time. A). 7F-7DQL, B). 4F-3O4M, and C). 1F- 4YRE, respectively
Figure S3.5(A-C)	The number of hydrogen bonds formed between protein-ligand complexes for the duration of 100 ns simulation time. A). 7F-7DQL, B). 4F-3O4M, and C). 1F- 4YRE, respectively.
Figure 3.6 (A)	Structural pharmacophore mapping of 7F against 7DQL
Figure S3.6 (B-C)	Structural pharmacophore of compounds B). GA and C). NL2 for target 7DQL
Figure 3.7 (A)	Structural pharmacophore mapping of 4F against 3O4M
Figure S3.7 (B-C)	Structural pharmacophore of compounds B). GA and C). NL5 for target 3O4M
Figure 3.8 (A)	Structural pharmacophore mapping of 1F against target 4YRE
Figure S3.8 (B-C)	Structural pharmacophore of compounds B). GA and C). NL5 for target 4YRE
Figure 3.9	Mulliken Charge distribution of the compounds understudy computed by DFT/LANL2DZ basis set
Figure 3.10	Mulliken Charge distribution of the compounds understudy computed by DFT/LANL2DZ basis set
Figure 3.11	(a) Molecular electrostatic potentials (MEP) plot of 1F, (b) contour map plot of ESP isosurface of 1F, (c) visualization of the ESP array plot for 1F
Figure 3.12	(a) Molecular electrostatic potentials (MEP) plot of 4F, (b) contour map plot of ESP isosurface of 4F, (c) visualization of the ESP array plot for 4F

Figure 3.13	(a) Molecular electrostatic potentials (MEP) plot of 7F, (b) contour map plot of ESP isosurface of 7F, (c) visualization of the ESP array plot for 7F
Figure S3.14	(a) Molecular electrostatic potentials (MEP) plot of GA, (b) contour map plot of ESP isosurface of GA, (c) visualization of the ESP array plot for GA
Figure S3.15	(a) Molecular electrostatic potentials (MEP) plot of NL1, (b) contour map plot of ESP isosurface of NL1, (c) visualization of the ESP array plot for NL1
Figure S3.16	(a) Molecular electrostatic potentials (MEP) plot of NL2, (b) contour map plot of ESP isosurface of NL2, (c) visualization of the ESP array plot for NL2
Figure S3.17	(a) Molecular electrostatic potentials (MEP) plot of NL5, (b) contour map plot of ESP isosurface of NL5, (c) visualization of the ESP array plot of NL5.
Figure 3.18 (A-C)	LOL, Contour and ELF plots of the A) 1F, B) 4F and C) 7F respectively
Figure 3.19	NCI and VMD plots of 1F, 4F and 7F
Figure 4.1	Visualisation and illustration of A). Terrestrol A (10) positioned at the active site of the target Non-structural protein 3 (PDB ID: 6VXS) exhibiting potential modes of interaction (The green dotted lines depict the mode of interaction between the target and the ligand, accompanied by distance annotations, while the yellow-coloured structure represents the ligand itself) B). Within the probable active pocket of the target
Figures S4.2	Visualisation and illustration of A). Nafamostat positioned at the active site of the target Non-structural protein 3 (PDB ID: 6VXS) exhibiting potential modes of interaction (The green dotted lines depict the mode of interaction between the target and the ligand, accompanied by distance

	annotations, while the yellow-coloured structure represents the ligand itself) B). Within the probable active pocket of target
Figures S4.3	Visualisation and illustration of A). Ribavirin, positioned at the probable site of the target Non-structural protein 3 (PDB ID: 6VXS) exhibiting potential modes of interaction (The green dotted lines depict the mode of interaction between the target and the ligand, accompanied by distance annotations, while the yellow-coloured structure represents the ligand itself) B). Within the probable active pocket of target
Figures S4.4	Visaulisation and illustration of A). Arbidol, positioned at the active site of the target Non-structural protein 3 (PDB ID: 6VXS) exhibiting potential modes of interaction (The green dotted lines depict the mode of interaction between the target and the ligand, accompanied by distance annotations, while the yellow-coloured structure represents the ligand itself) B). Within the probable active pocket of target
Figures S4.5	Visualisation and illustration of A). Chloroquine positioned at the active site of the target Non-structural protein 3 (PDB ID: 6VXS) exhibiting potential modes of interaction (The green dotted lines depict the mode of interaction between the target and the ligand, accompanied by distance annotations, while the yellow-coloured structure represents the ligand itself) B). Within the probable active pocket of target
Figures S4.6	Visualisation and illustration of A). Hydroxychloroquine positioned at the active site of the target Non-structural protein 3 (PDB ID: 6VXS) exhibiting potential modes of interaction (The green dotted lines depict the mode of

	interaction between the target and the ligand, accompanied by distance annotations, while the yellow-coloured structure represents the ligand itself) B). Within the probable active pocket of target
Figures S4.7	Visualisation and illustration of A). Dexamethasone positioned at the active site of the target Non-structural protein 3 (PDB ID: 6VXS) exhibiting potential modes of interaction (The green dotted lines depict the mode of interaction between the target and the ligand, accompanied by distance annotations, while the yellow-coloured structure represents the ligand itself) B). Within the probable active pocket of target
Figures S4.8	Visualisation and illustration of A). Favipiravir positioned at the active site of the target Non-structural protein 3 (PDB ID: 6VXS) exhibiting potential modes of interaction (The green dotted lines depict the mode of interaction between the target and the ligand, accompanied by distance annotations, while the yellow-coloured structure represents the ligand itself) B). Within the probable active pocket of target
Figure 4.9	Visualisation and illustration of A). Terrestrol A (10) positioned at the active site of the target Spike protein S1 (PDB ID: 6LZG) exhibiting potential modes of interaction (The green dotted lines depict the mode of interaction between the target and the ligand, accompanied by distance annotations, while the yellow-coloured structure represents the ligand itself) B). Within the probable active pocket of the target
Figures S4.10	Visualisation and illustration of A). Ribavirin positioned at the active site of the target Spike protein S1 (PDB ID: 6LZG) exhibiting potential modes of interaction (The

	green dotted lines depict the mode of interaction between the target and the ligand, accompanied by distance annotations, while the yellow-coloured structure represents the ligand itself) B). Within the probable active pocket of target.
Figures S4.11	Visualisation and illustration of A). Arbidol positioned at the active site of the target Spike protein S1 (PDB ID: 6LZG) exhibiting potential modes of interaction (The green dotted lines depict the mode of interaction between the target and the ligand, accompanied by distance annotations, while the yellow-coloured structure represents the ligand itself) B). Within the probable active pocket of target.
Figures S4.12	Visualisation and illustration of A). Nafamostat positioned at the active site of the target Spike protein S1 (PDB ID: 6LZG) exhibiting potential modes of interaction (The green dotted lines depict the mode of interaction between the target and the ligand, accompanied by distance annotations, while the yellow-coloured structure represents the ligand itself) B). Within the probable active pocket of target.
Figures S4.13	Visualisation and illustration of A). Hydroxychloroquine positioned at the active site of the protein Spike protein S1 (PDB ID: 6LZG) exhibiting potential modes of interaction (The green dotted lines depict the mode of interaction between the target and the ligand, accompanied by distance annotations, while the yellow-coloured structure represents the ligand itself) B). Within the probable active pocket of target.
Figures S4.14	Visualisation and illustration of A). Chloroquine positioned at the active site of the target Spike protein S1

	(PDB ID: 6LZG) exhibiting potential modes of interaction (The green dotted lines depict the mode of interaction between the target and the ligand, accompanied by distance annotations, while the yellow-coloured structure represents the ligand itself) B). Within the probable active pocket of target.
Figures S4.15	Visualisation and illustration of A). Dexamethasone positioned at the active site of the target Spike protein S1 (PDB ID: 6LZG) exhibiting potential modes of interaction (The green dotted lines depict the mode of interaction between the target and the ligand, accompanied by distance annotations, while the yellow-coloured structure represents the ligand itself) B). Within the probable active pocket of target.
Figures S4.16	Visualisation and illustration of A). Favipiravir positioned at the active site of the target Spike protein S1 (PDB ID: 6LZG) exhibiting potential modes of interaction (The green dotted lines depict the mode of interaction between the target and the ligand, accompanied by distance annotations, while the yellow-coloured structure represents the ligand itself) B). Within the probable active pocket of target.
Figure 4.17	Visualisation and illustration of A). Terrestrol A (10) positioned at the active site of the target Nucleoprotein (PDB ID: 7CR5) exhibiting potential modes of interaction (The green dotted lines depict the mode of interaction between the target and the ligand, accompanied by distance annotations, while the yellow-coloured structure represents the ligand itself) B). Within the probable active pocket of the target

Figures S4.18	Visualisation nd illustration of A). Nafamostat positioned at the active site of the target Nucleoprotein (PDB ID: 7CR5) exhibiting potential modes of interaction (The green dotted lines depict the mode of interaction between the target and the ligand, accompanied by distance annotations, while the yellow-coloured structure represents the ligand itself) B). Within the probable active pocket of target.
Figures S4.19	Visualisation and illustration of A). Hydroxychloroquine positioned at the active site of the target Nucleoprotein (PDB ID: 7CR5) exhibiting potential modes of interaction (The green dotted lines depict the mode of interaction between the target and the ligand, accompanied by distance annotations, while the yellow-coloured structure represents the ligand itself) B). Within the probable active pocket of target
Figures S4.20	Visualisation and illustration of A). Arbidol positioned at the active site of the target Nucleoprotein (PDB ID: 7CR5) exhibiting potential modes of interaction (The green dotted lines depict the mode of interaction between the target and the ligand, accompanied by distance annotations, while the yellow-coloured structure represents the ligand itself) B). Within the probable active pocket of target.
Figures S4.21	Visualisation and illustration of A). Chlororquine positioned at the active site of the target Nucleoprotein (PDB ID: 7CR5) exhibiting potential modes of interaction (The green dotted lines depict the mode of interaction between the target and the ligand, accompanied by distance annotations, while the yellow-coloured structure represents the ligand itself) B). Within the probable active pocket of target.

Figures S4.22	Visualisation and illustration of A). Ribavirin positioned at the active site of the target Nucleoprotein (PDB ID: 7CR5) exhibiting potential modes of interaction (The green dotted lines depict the mode of interaction between the target and the ligand, accompanied by distance annotations, while the yellow-coloured structure represents the ligand itself) B). Within the probable active pocket of target.
Figures S4.23	Visualisation and illustration of A). Dexamethasone positioned at the active site of the target Nucleoprotein (PDB ID: 7CR5) exhibiting potential modes of interaction (The green dotted lines depict the mode of interaction between the target and the ligand, accompanied by distance annotations, while the yellow-coloured structure represents the ligand itself) B). Within the probable active pocket of target
Figures S4.24	Visualisation and illustration of A). Favipiravir positioned at the active site of the target Nucleoprotein (PDB ID: 7CR5) exhibiting potential modes of interaction (The green dotted lines depict the mode of interaction between the target and the ligand, accompanied by distance annotations, while the yellow-coloured structure represents the ligand itself) B). Within the probable active pocket of target.
Figure 4.25	Visualisation and illustration of A). Terrestrol A (10) positioned at the active site of the target Extracellular metalloproteinase mep (PDB ID: 4K90) exhibiting potential modes of interaction (The green dotted lines depict the mode of interaction between the target and the ligand, accompanied by distance annotations, while the yellow-coloured structure represents the ligand itself) B). Within the probable active pocket of the target.

Figures S4.26	Visualisation and illustration of A). Isavuconazole positioned at the active site of the target Extracellular metalloproteinase mep (PDB ID: 4K90) exhibiting potential modes of interaction (The green dotted lines depict the mode of interaction between the target and the ligand, accompanied by distance annotations, while the yellow-coloured structure represents the ligand itself) B). Within the probable active pocket of target.
Figures S4.27	Visualisation and illustration of A). Posaconazole positioned at the active site of the target Extracellular metalloproteinase mep (PDB ID: 4K90) exhibiting potential modes of interaction (The green dotted lines depict the mode of interaction between the target and the ligand, accompanied by distance annotations, while the yellow-coloured structure represents the ligand itself) B). Within the probable active pocket of target.
Figures S4.28	Visualisation and illustration of A). Amphotericin B positioned at the active site of the target Extracellular metalloproteinase mep (PDB ID: 4K90) exhibiting potential modes of interaction (The green dotted lines depict the mode of interaction between the target and the ligand, accompanied by distance annotations, while the yellow-coloured structure represents the ligand itself) B). Within the probable active pocket of target.
Figures 4.29	Visualisation and illustration of A). Terrestrol A (10) positioned at the active site of the target Peptidylprolyl isomerase (PDB ID: 6VSI) exhibiting potential modes of interaction (The green dotted lines depict the mode of interaction between the target and the ligand, accompanied by distance annotations, while the yellow-coloured

	structure represents the ligand itself) B). Within the probable active pocket of the target
Figures S4.30	Visualisation and illustration of A). Isavuconazole positioned at the active site of the target Peptidylprolyl isomerase (PDB ID: 6VSI) exhibiting potential modes of interaction (The green dotted lines depict the mode of interaction between the target and the ligand, accompanied by distance annotations, while the yellow-coloured structure represents the ligand itself) B). Within the probable active pocket of target.
Figures S4.31	Visualisation and illustration of A). Posaconazole positioned at the active site of the target Peptidylprolyl isomerase (PDB ID: 6VSI) exhibiting potential modes of interaction (The green dotted lines depict the mode of interaction between the target and the ligand, accompanied by distance annotations, while the yellow-coloured structure represents the ligand itself) B). Within the probable active pocket of target.
Figures S4.32	Visualisation and illustration of A). Amphotericin B positioned at the active site of the target Peptidylprolyl isomerase (PDB ID: 6VSI) exhibiting potential modes of interaction (The green dotted lines depict the mode of interaction between the target and the ligand, accompanied by distance annotations, while the yellow-coloured structure represents the ligand itself) B). Within the probable active pocket of target
Figures S4.33	RMSD Plots of Terrestrol Ab (10) with PDB IDs 4K90, 6LZG, 6VSI, 6VXS and 7CR5 respectively along with their respective PDF plots.

Figure S4.34	RMSF Plots of Terrestrol A (10) with with PDB IDs 4K90, 6LZG, 6VSI, 6VXS and 7CR5 respectively along with their respective PDF plots.
Figure S4.35	Rg Plots of Terrestrol A (10) with with PDB IDs 4K90, 6LZG, 6VSI, 6VXS and 7CR5 respectively along with their respective PDF plots.
Figure S4.36	SASA Plots of Terrestrol A (10) with with PDB IDs 4K90, 6LZG, 6VSI, 6VXS and 7CR5 respectively along with their respective PDF plots.
Figure S4.37	Hydrogen Bond Plots of Terrestrol A (10) with PDB IDs 4K90, 6LZG, 6VSI, 6VXS and 7CR5 respectively along with their respective PDF plots.
Figure 5.1	Illustration of LXRs and FXR modulation in cancer therapy highlighting key role.
Figure 5.2	Overview of some LXRs and FXR modulators in cancer therapy in select preclinical and clinical studies
Figure 5.3	Structural representations of selected modulators of LXRs and FXR
Figure 5.4	Workflow of the comprehensive computational studies conducted.
Figure S5.5	Scatter plot showing Docking score of all the compounds understudy with respect to PDB ID: 1UHL
Figure S5.6	Scatter plot showing Docking score of all the compounds understudy with respect to PDB ID: 1UPV
Figure S5.7	Plot showing Docking score of all the compounds understudy with respect to PDB ID: 5ICK
Figure 5.8	Structure of (C144) AZD776 or 3-(carbamoylamino)-5-(3-fluorophenyl)-N-[(3S)-piperidin-3-yl]thiophene-2-carboxamide
Figure 5.9	Molecular interactions between PDB: 1UHL (active site is depicted as a green, globular envelope) and the ligands.

	The binding interactions of C144 (top left), Native T-0901317 (bottom left), Resveratrol (top right), and Withaferin A (bottom right) are depicted with the protein 1UHL. Each ligand's interaction is pinpointed to key amino acid residues in the active site.
Figure 5.10:	Molecular interactions between PDB: 1UPV (active site is depicted as a green, globular envelope) and the ligands. The binding interactions of C144 (top left), Native T-0901317 (bottom left), Resveratrol (top right), and Bergapten (bottom right) are depicted with the protein 1UPV. Each ligand's interaction is pin pointed to key amino acid residues in the active site.
Figure 5.11	Molecular interactions between PDB: 5ICK (active site is depicted as a green, globular envelope) and the ligands. The binding interactions of C144 (top left), Native feroline (bottom left), Resveratrol (top right), and Obeticholic acid (bottom right) are depicted with the protein 5ICK. Each ligand's interaction is pinpointed to key amino acid residues in the active site.
Figure S5.12	PLIP analysis of compound C144-1UHL, C144-1UPV and C144-5ICK COMPLEX (MVD).
Figure 5.13	HOMO-LUMO energy gap comparisons of Resveratrol, C144, Bergapten, Native Feroline, Withaferin A, Native (T-0901317), and Obeticholic acid derived from DFT calculations.
Figure S5.14	The plot displays a principal component analysis (PCA) where Component 1 (PC1) is plotted on the x-axis and Component 2 (PC2) on the y-axis.
Figure 5.15	This figure illustrates the molecular interactions between the target protein IUHL and the ligands: C144 (top left), Native T-0901317 (bottom left), Resveratrol (top right),

	and Withaferin A (bottom right). The central image depicts the IUHL protein structure, highlighted with a spherical yellow active site.
Figure 5.16	This figure illustrates the molecular interactions between the target protein IUPV and the ligands: C144 (top left), Native T-0901317 (bottom left), Resveratrol (top right), and Bergapten (bottom right). The central image depicts the IUPV protein structure, highlighted with a spherical yellow active site.
Figure 5.17	This figure illustrates the molecular interactions between the target protein 5ICK and the ligands: C144 (top left), Native feroline (bottom left), Resveratrol (top right), and Obeticholic acid (bottom right). The central image depicts the 1UPV protein structure, highlighted with a spherical yellow active site.
Figure S5.18	PLIP analysis of compound C144-1UHL, C144-1UPV and C144-5ICK complex (AutoDock).
Figure S5.19 (a-c)	Protein-ligand interactions of C144 with 1UHL, 1UPV, and 5ICK, respectively, as visualized through ML-PLIC
Figure 5.20	Comparative Binding Analysis of Native T-0901317, Compound C144, Withaferin A, and Resveratrol in the LXR Depict the native T-0901317's pharmacophore features, 3D conformation, and interaction map with the LXR α α Binding Site (PDB ID: 1UHL) Panels A–C: binding site. Panels D–F: Depict C144's pharmaco phore features, 3D conformation, and interaction network map with the LXR α conformation, and interaction network map with the LXR α binding site. Panels G–I: Illustrate Withaferin A's pharmacophore model, 3D binding site. Panels J–L: Present Resveratrol's pharmacophore model,

	3D conformation, and interaction network map with the LXR α binding site.
Figure 5.21	Comparative Binding Analysis of Native T-0901317, C144, Bergapten and Resveratrol in the LXR native T-0901317's pharmacophore features, 3D conformation, and interaction map with the LXR α α Binding Site (PDB ID: 1UPV) Panels A–C: Depict the binding site. Panels D–F: Depict C144's pharmacophore features, 3D conformation, and interaction network map with the LXR α interaction network map with the LXR α binding site. Panels G–I: Illustrate Bergapten's pharmacophore model, 3D conformation, and binding site. Panels J–L: Present Resveratrol's pharmacophore model, 3D conformation, and interaction network map with the LXR α binding site.
Figure 5.22	Comparative Binding Analysis of Native Feroline, C144, Obeticholic acid and Resveratrol in the LXR native feroline pharmacophore features, 3D conformation, and interaction map with the LXR α α Binding Site (PDB ID: 5ICK) Panels A–C: Depict the binding site. Panels D–F: Depict C144's pharmacophore features, 3D conformation, and interaction network map with the LXR interaction network map with the LXR α α binding site. Panels G–I: Illustrate Obeticholic acid pharmacophore model, 3D conformation, and binding site. Panels J–L: Present Resveratrol's pharmacophore model, 3D conformation, and interaction network map with the LXR α binding site.
Figure S5.23 (a-c)	Molecular electrostatic potentials (MEP) plot of native T-0901317 (1UPV/1UHL), b: contour map plot of ESP isosurface of native T-0901317 (1UPV/1UHL), c: visualization of the ESP array plot for native T-0901317 (1UPV/1UHL)

Figure S5.24 (a-c)	Molecular electrostatic potentials (MEP) plot of native feroline(5ICK), b: contour map plot of ESP isosurface of native Feroline (5ICK), c: visualization of the ESP array plot for native feroline (5ICK)
Figure 5.25 (a-c)	a) Molecular electrostatic potentials (MEP) plot of C144 b) Contour map plot of ESP isosurface of C144 c) Visualization of the ESP array plot for C144.
Figure S5.26 (a-c)	a: Molecular electrostatic potentials (MEP) plot of bergapten, b: contour map plot of ESP isosurface of bergapten, c: visualization of the ESP array plot for bergapten
Figure S5.27 (a-c)	a: Molecular electrostatic potentials (MEP) plot of obeticholic acid, b: contour map plot of ESP isosurface of obeticholic acid, c: visualization of the ESP array plot for obeticholic acid
Figure S5.28 (a-c)	a: Molecular electrostatic potentials (MEP) plot of resveratrol, b: contour map plot of ESP isosurface of resveratrol, c: visualization of the ESP array plot for resveratrol
Figure S5.29 (a-c)	a: Molecular electrostatic potentials (MEP) plot of withaferin A, b: contour map plot of ESP isosurface of withaferin A, c: visualization of the ESP array plot for withaferin A
Figure S5.30	Mulliken Charge distribution of the compounds computed by DFT/6-311++g(d,p) basis set
Figure 5.31 (a-c)	Becke surface analysis (BSA) diagrams of the C144 system.
Figure 5.32	The Hirshfeld surface of C144, mapped with dnorm
Figure 5.33.(a-g)	The comprehensive 2D fingerprint plot for (a). contributing 100 %, (b). H···H interactions with a 31.94 % contribution,(c). S···H interactions at 21.92 %

	contribution,(d). O···H interactions at 20.82 % contribution,(e). C···C interactions at 7.64 % contribution (f). H···C interactions 18.90 % contributionand (g). C···H interactions at 6.26 % of C144; X and Y axes correspond to di and de, respectively.
Figure 5.34. (a)	Non-covalent Interaction (NCI) plot of C144.
Figure S5.34b	Non-covalent Interaction (NCI) plot of other compounds understudy.
Figure 5.35 (a)	Visual molecular dynamics (VMD) model of the C144
Figure S5.35b	VMD plots of other compounds under study.
Figure 5.36	Electron localized function (ELF) plot of C144.
Figure S5.37	Energy minimization of 1UHL-C144, 1UPV-C144 and 5ICK complex system. Convergence occurring at approximately 6–7 ns for the 1UHL and 1UPV complexes, and at 5–6 ns for the 5ICK complex.
Figure S5.38	The temperature distribution during the NVT equilibration of 1UHL-C144, 1UPV-C144, and 5ICK-C144 complexes exhibited fluctuations around 310 K.
Figure S5.39	The pressure distribution during the NPT equilibration of all three complexes demonstrated substantial fluctuations around the reference value of 1 bar, which is characteristic of the expected behavior in NPT equilibration.
Figure S5.40	During the NPT equilibration of the 1UHL-C144, 1UPV-C144, and 5ICK-C144 complexes, the density values remained highly stable over time.
Figure 5.41	Analysis of the simulations from left to right, the RMSD of the protein in the 1UHL–C144 simulation shows consistent stabilization from 25 ns onwards. In the subsequent panels, the RMSD for the 1UPV–C144 simulation stabilizes from 30 ns onwards, which is

	mirrored in the 5ICK–C144 simulation, where stabilization is also observed from 30 ns onwards.
Figure 5.42	The root mean square deviation (RMSD) of the ligand C144 relative to the proteins 1UHL, 1UPV, and 5ICK (from left to right) exhibited a commendable degree of stability throughout the duration of the simulations
Figure S5.43	The left panel illustrates the residue root mean square fluctuations (RMSF) of the protein 1UHL, highlighting regions of localized flexibility with RMSF values exceeding 0.3 nm during the simulation. The right panel presents the residue RMSF of the protein 1UPV, showcasing localized flexibility in regions with RMSF values greater than 0.26 nm throughout the simulation. The bottom panel displays the residue RMSF of the protein 5ICK, indicating localized flexibility in regions where RMSF values surpass 0.2 nm during the simulation.
Figure 5.44	The left panel displays the radius of gyration of the protein 1UHL in complex with ligand C144, demonstrating significant stability from 40 ns onwards. The middle panel illustrates the radius of gyration of the protein 1UPV in complex with ligand C144, indicating notable stability from 30 ns onwards. The right panel shows the radius of gyration of the protein 5ICK in complex with ligand C144, reflecting substantial stability from 50 ns onwards.
Figure S5.45	The number of hydrogen bonds formed during the simulation for the three complexes is illustrated as follows: 1UHL (left panel), 1UPV (middle panel), and 5ICK (right panel).
Figure S5.46	To enhance clarity, the most persistent hydrogen bond donors (HBD) and acceptors (HBA) for the 1UHL-C144

	(left panel), 1UPV-C144 (right panel), and 5ICK-C144 (bottom panel) complexes are illustrated.
Figure S5.47 (a-d)	Principal Component Analysis (PCA) of 1UHL, 1UPV, and 5ICK in complex with ligand C144 during the simulations. (a) Over 30 eigenvectors derived from the covariance matrix of the backbone of 1UHL, 1UPV, and 5ICK demonstrate values exceeding zero. (b) Similarly, more than 30 eigenvectors from the covariance matrix of the heavy atoms of ligand C144 also exhibit values greater than zero. (c) The projection of the first principal component (PC1) onto the second principal component (PC2) within the essential subspace allows for the estimation of collective motions of 1UHL, 1UPV, and 5ICK. (d) The projection of PC1 onto PC2 within the essential subspace facilitates the assessment of collective motions of ligand C144.
Figure 5.47 (e-f)	Principal Component Analysis (PCA) of 1UHL, 1UPV, and 5ICK in complex with ligand C144 during the simulations. (e) The Gibbs free energy landscape, derived from the first and second eigenvectors of the backbone of 1UHL, 1UPV, and 5ICK, reveals a substantial nonuniform conformational basin. (f) Conversely, the Gibbs free energy landscape derived from the first and second eigenvectors of the heavy atoms of ligand C144 demonstrates a prominent.
Figure 5.48	Molecular mechanics potential energy evaluation in MMPBSA calculation for all protein-ligand complexes
Figure S5.49	Polar solvation energy between 1UHL-C144. 1UPV-C144 and 5ICK-C144 during the simulation.
Figure S5.50	Solvent accessible non-polar energy between protein (1UHL, 1UPV and 5ICK) and ligand during the simulation

Figure 5.51	Three-dimensional visualization of the ligand C144 interactions with 1UHL, 1UPV and 5ICK from averaged MMPBSA calculation.
Figure 5.52	Two-dimensional plot of the ligand C144 interacting with the nearby amino acid residues of the protein 1UHL, 1UPV and 5ICK. The complex structure was averaged from MMPBSA calculation.
Figure S5.53	Residue-wise contribution of Binding Free Energy or free energy of binding (ΔG_{Bind}) during the simulation of 1UHL–C144, 1UPV–C144 and 5ICK-C144 complexes.
Figure 5.54	Three-dimensional visualization of the ligand C144 interactions with 1UHL, 1UPV and 5ICK from averaged MMPBSA calculation.
Figure S5.55a	Variation of Internal Energy (U), Enthalpy (H), and Gibbs Free Energy (G) with Temperature.
Figure S5.55b	Graph depicting the relationship between entropy (S), heat capacity at constant volume (Cv), and heat capacity at constant pressure (Cp) as functions of temperature, ranging from 100 K to 310 K.
Figure 6.1	Illustration of mode of interaction of A). 1B2N B). Co-crystallized ligand C). Streptomycin with PDB ID 7DQL.
Figure S6.2	Illustration of mode of interaction of A). 1B2N B). Co-crystallized ligand C). Streptomycin with PDB ID1JII.
Figure S6.3	Illustration of mode of interaction of A). 1B2N B). Co-crystallized ligand C). Streptomycin with PDB ID 7Y8B.
Figure S6.4	Illustration of mode of interaction of A). 1B2N B). Co-crystallized ligand C). Streptomycin with PDB ID 7MYL.
Figure S6.5	Illustration of mode of interaction of A). 1B2N B). Co-crystallized ligand C). Fluconazole with PDB ID 1M78.
Figure S6.6	Illustration of mode of interaction of A). 1B2N B). Co-crystallized ligand C). Fluconazole with PDB ID 8BHH.

Figure S6.7	Illustration of mode of interaction of A). 1B2N B). Co-crystallized ligand C). Ascorbic acid D). Trolox with PDB ID 4IN4.
Figure S6.8	Illustration of mode of interaction of A). 1B2N B). Co-crystallized ligand C). Ascorbic acid D). Trolox with PDB ID 4ZZI.
Figure 6.9	Illustration of mode of interaction of A). 1B2N B). Co-crystallized ligand C). Streptomycin with PDB ID 7DQL.
Figure S6.10	Illustration of mode of interaction of A). 1B2N B). Co-crystallized ligand C). Streptomycin with PDB ID 1JII.
Figure S6.11	Illustration of mode of interaction of A). 1B2N B). Co-crystallized ligand C). Streptomycin with PDB ID 1JII.
Figure S6.12	Illustration of mode of interaction of A). 1B2N B). Co-crystallized ligand C). Streptomycin with PDB ID 7MYL.
Figure S6.13	Illustration of mode of interaction of A). 1B2N B). Co-crystallized ligand C). Streptomycin with PDB ID 1M78.
Figure S6.14	Illustration of mode of interaction of A). 1B2N B). Co-crystallized ligand C). Streptomycin with PDB ID 8BHH.
Figure S6.15	Illustration of mode of interaction of A). 1B2N B). Co-crystallized ligand C). Streptomycin with PDB ID 4IN4.
Figure S6.16	Illustration of mode of interaction of A). 1B2N B). Co-crystallized ligand C). Streptomycin with PDB ID 4ZZI
Figure 6.17	2D and 3D illustrated pharmacophoric features of A). 1B2N B). Co-crystallized ligand C). Streptomycin against PDB ID 7DQL
Figure S6.18	2D and 3D illustrated pharmacophoric features of A. 1B2N B. CL C. Streptomycin against PDB ID 1JII
Figure S6.19	2D and 3D illustrated pharmacophoric features of A. 1B2N B. CL C. Streptomycin against PDB ID 7Y8B
Figure S6.20	2D and 3D illustrated pharmacophoric features of A. 1B2N B. CL C. Streptomycin against PDB ID 7MYL

Figure S6.21	2D and 3D illustrated pharmacophoric features of A. 1B2N B. CL C. Fluconazole against PDB ID 1M78
Figure S.6.22	2D and 3D illustrated pharmacophoric features of A. 1B2N B. CL C. Fluconazole against PDB ID 8BHH
Figure S.6.23	2D and 3D illustrated pharmacophoric features of A. 1B2N B. CL D. ASCORBIC ACID E. TROLOX against PDB ID 4IN4
Figure S.6.24	2D and 3D illustrated pharmacophoric features of A. 1B2N B. CL D. ASCORBIC ACID E. TROLOX against PDB ID 4ZZI
Figure S6.25	Spectral data's A). Mass B). 1HNMR C). 13C NMR and D). IR of 1B2N.
Figure 6.26.	Antibacterial activity of 1-bromo-2-naphthol (1B2N) through well diffusion assay
Figure 6.27	Antioxidant activity by DPPH assay.
Figure 6.28	Scavenging activity by ABTS assay
Figure 6.29	Antioxidants activity by Ferric reducing power assay.
Figure 6.30	Depiction of the frontier molecular orbital (HOMO–LUMO) energy gaps of the investigated compounds
Figure 6.31	A). Molecular electrostatic potentials (MEP) plot of 1B2N, B). Contour map plot of ESP isosurface of 1B2N, C). Visualization of the ESP array plot for 1B2N
Figure S6.32	A). Molecular electrostatic potentials (MEP) plot of BDDE, B). Contour map plot of ESP isosurface of BDDE, C) Visualization of the ESP array plot for BDDE
Figure 6.33	A). Molecular electrostatic potentials (MEP) plot of Ascorbic acid, B). Contour map plot of ESP isosurface of Ascorbic acid, C). Visualization of the ESP array plot for Ascorbic acid
Figure S6.34	A). Molecular electrostatic potentials (MEP) plot of Fluconazole, b contour map plot of ESP isosurface of

	Fluconazole, c visualization of the ESP array plot for Fluconazole
Figure 6.35	A). Molecular electrostatic potentials (MEP) plot of Trolox, B). Contour map plot of ESP isosurface of Trolox, C). Visualization of the ESP array plot for Trolox
Figure S6.36	A). Molecular electrostatic potentials (MEP) plot of Streptomycin, B). Contour map plot of ESP isosurface of Streptomycin, C). Visualization of the ESP array plot for Streptomycin
Figure 6.37	A) MC distribution mapped on the optimized geometry of 1-Bromo-2-naphthol. Carbon atoms are shown in brown, oxygen in red, hydrogen in light green and bromine in dark green. The numerical values near each atom denote the respective Mulliken charges. Electron-rich regions (-O) are highlighted in red, indicating strong electron localization, while electron-deficient regions (-H) are depicted in green. B). MC distribution on the optimized molecular structure of BDDE. Bromine atom (dark green) and hydroxyl groups (red oxygens with adjacent positively charged hydrogens) lead to significant electronic polarization. The highly negative charge on C/O identifies key nucleophilic centers, while positively charged (H) reflects a polar O–H bond. This distribution confirms BDDE's strong charge delocalization and structural suitability for bioactivity.
Figure 6.38	Bar plot comparison of Mulliken charges for selected atoms in BDDE and 1-Bromo-2-naphthol. The graph highlights key differences in electron density across C, O, H, and Br atoms in both molecules.
Figure 6.39	NBO interaction plots of (A) BDDE and (B) 1B2N computed at the B3LYP/6-31G(d,p) level, illustrating key donor–acceptor interactions. BDDE shows prominent

	π→π and n→π* delocalizations, while 1B2Nexhibits strong σ→σ* and n→σ* charge transfers involving the phenolic –OH and bromine substituents.
Figure 6.40:	A). IRI vs. sign(λ_2)ρ scatter plot of BDDE, B). IRI isosurface representation of BDDE
Figure 6.41	3D isosurface and 2D contour plots of the Electron Localization Function (ELF), illustrating electron pairing distribution in the BDDE.
Figure 6.42	A). IRI vs. sign(λ_2)ρ scatter plot of 1-Bromo-2-Naphthol, B). IRI isosurface representation of 1-Bromo-2-Naphthol visualized using VMD
Figure 6.43	3D isosurface and 2D contour plots of the Electron Localization Function (ELF), illustrating electron pairing distribution in the 1-Bromo-2-Naphthol

LIST OF TABLES

Table Number	Legends
Table 2.1	List of compounds understudy and their compound code
Table 2.2	Native co-crystallized ligand with their PDB ID's
Table 2.3	Docking score of the compounds understudy against PDB ID 7DQL
Table 2.4	Docking score of the compounds understudy against PDB ID 3O4M
Table 2.5	Docking score of the compounds understudy against PDB ID 4YRE
Table 2.6	Docking score of the compounds understudy against PDB ID 7NNY
Table 2.7	Docking score of the compounds understudy against PDB ID 7OFS
Table 2.8	Calculated HOMO-LUMO energy gap *via* DFT
Table 2.9	Druglikness and ADME/ screening *via* SwissADME and StopTox
Table S3.1	Binding free energy of the three complexes.
Table S3.2	Computed Mulliken Charge distribution of the compounds understudy computed by DFT/LANL2DZ basis set
Table 3.3	The computed NBO analysis for of the compounds understudy (1F, 4F and 7F) highlights key interactions and their E^2 energies
Table 3.4	Calculated NLO values of the compounds under investigation
Table S3.5	Bond length, bond angle and dihedral angle of 1F
Table S3.6	Bond length, bond angle and dihedral angle of 4F
Table S3.7	Bond length, bond angle and dihedral angle of 7F
Table 3.8	Bioactivity prediction of 1F, 4F, 7F, NL1, NL2 AND NL5 *via* Molinspiration
Table 3.9	PASS prediction of 1F, 4F and 7F

Table 3.10	Descriptors used for calculating IC_{50}
Table 3.11	Calculated IC_{50} values of the compounds
Table 4.1	2D structure, CID (Compound Identifier) and SMILES of the investigated compounds
Table S4.2	List of established standards and their activities
Tables S4.3	Docking score of the ligands and standards under investigation with PDB ID: 6VXS
Tables S4.4	Docking score of the ligands and standards under investigation with PDB ID: 6LZG
Tables S4.5	Docking score of the ligands and standards under investigation with PDB ID: 7CR5
Tables S4.6	Docking score of the ligands and standards under investigation with PDB ID: 4K90
Tables S4.7	Docking score of the ligands and standards under investigation with PDB ID: 6VSI
Tables S4.8	Ligand- receptor interactions of Terrestrol A (10) and the standards at the probable active site of the target with PDB ID: 6VXS
Tables S4.9	Ligand- receptor interactions of Terrestrol A (10) and the standards at the probable active site of the target with PDB ID: 6LZG
Tables S4.10	Ligand- receptor interactions of Terrestrol A (10) and the standards at the probable active site of the target with PDB ID: 7CR5.
Tables S4.11	Ligand- receptor interactions of Terrestrol A (10) and the standards at the probable active site of the target with PDB ID: 4K90
Tables S4.12	Ligand- receptor interactions of Terrestrol A (10) and the standards at the probable active site of the target with PDB ID: 6VSI

Table S4.13	Druglikeness screening of TerrestrolA (10) and the standards via SwissADME.
Table S4.14	Pharmacokinetic (ADME) property assessment of Terrestrol A (10) and the standards via SwissADME and PreADMET
Table S4.15	Toxicity profiling of Terrestrol A (10) and the standards conducted via ProTOX-II
Table S4.16	Bioactivity score prediction of Terrestrol A (10) and the standards *via* molinspiration
Table S4.17	PASS (Prediction of Activity Spectra for Substances) prediction of Terrestrol A (10) and the standards with respect to SARS-CoV2 (antiviral related activity) via PASS Online
Table S4.18	PASS (Prediction of Activity Spectra for Substances) prediction of Terrestrol A (10) and the standards with respect to SARS-CoV2 (antifungal related activity) via PASS Online
Table S4.19	Optimized structures of Terrestrol A (10) and the standards using DFT/B3LYP with a 6-311G (d, p) basis set
Table S4.20	Calculated global reactivity descriptors of Terrestrol A (10) and the standards using DFT/B3LYP with a 6-311G (d, p) basis set
Table S4.21	Calculated frontier molecular orbitals (FMOs) energy values of the HOMO, LUMO and the resultant HOMO-LUMO energy gap using DFT/B3LYP with a 6-311G (d, p) basis set.
Table S4.22	Cartoon illustration and visualisation of the HOMO, LUMO and the resultant HOMO-LUMO energy gap using DFT/B3LYP with a 6-311G (d, p) basis set.
Table S5.1	Screened compounds from library 1
Table S5.2	Screened compounds from library 2
Table S5.3	Screened compounds from library 3
Table S5.4:	Druglikeness screening of compounds from Library 1.
Table S5.5	Druglikeness screening of compounds from Library 2.
Table S5.6	Druglikeness screening of compounds from Library 3.

Table S5.7	Toxicity screening of druglikeness complied compounds from Library 1
Table S5.8	Toxicity screening of druglikeness complied compounds from Library 2
Table S5.9	Toxicity screening of druglikeness complied compounds from Library 3
Table S5.10	Docking scores of the ligands with PDB ID 1UHL generated *via* MVD
Table S5.11	Docking scores of the ligands with PDB ID 1UPV generated *via* MVD
Table S5.12	Docking scores of the ligands with PDB ID 5ICK generated *via* MVD
Table S5.13	Ligand-protein (1UHL) interaction *via* MVD
Table S5.14	Ligand-protein(1UPV) interaction *via* MVD
Table S5.15	Ligand-protein (5ICK) interaction *via* MVD
Table S5.16	PLIP analysis of compound C144 with respect to 1UHL, 1UPV, and 5ICK (MVD).
Table S5.17	The calculated HOMO, LUMO and ΔE.
Table S5.18	The calculated global reactivity descriptors
Table S5.19	Correlation Matrix Analyzing the Relationship Between Molecular Docking Scores (MDS) and Electronic Reactivity Descriptors Derived from Density Functional Theory (DFT)
Table S5.20	Docking profile of 1UHL and the ligands *via* AutoDock
Table S5.21	Docking profile of 1UPV and the ligands *via* AutoDock
Table S5.22	Docking profile of 5ICK and the ligands *via* AutoDock
Table S5.23	PLIP analysis of compound C144 with respect to 1UHL, 1UPV, and 5ICK (AutoDock).
Table S5.24	Docking scores and Interaction profile of C144 with respective targets obtained through ML-PLIP analysis.
Table S5.25	Bioactivity score prediction *via* molinspiration.

Table S5.26	Computed Mulliken Charge (MC) distribution of the compounds computed by DFT/6-311++g (d,p) basis set
Table S5.27	Computed NBO analysis for the most prominent therapeutic compounds with E^2 energies
Table S5.28	CLC-Pred of C144 (AZD7762), Native Ligands, and Reference Standards Across Cell Lines
Table S5.29	Prediction of reacting atom (Biotransformation) of C144 (AZD7762), Native Ligands, and Reference Standards.
Table S5.30	ADME prediction of C144 (AZD7762), Native Ligands, and Reference Standards *via* SwissADME and molinspiration.
Table S5.31	Hydrogen bonding percentage existences between 1UHL and ligand C144 (UNK446)
Table S5.32	Hydrogen bonding percentage existences between 1UPV and ligand C144 (UNK462)
Table S5.33	Hydrogen bonding percentage existences between 5ICK and ligand C144 (LIGC144)
Table S5.34	Average energetic contributions of the 1UHL–C144complex during the simulation.
Table S5.35	Average energetic contributions of the 1UPV–C144complex during the simulation.
Table S5.36	Average energetic contributions of the 5ICK–C144complex during the simulation.
Table S5.37	Illustrating the thermodynamic properties of C144 at varying temperatures (100 K to 310 K) under constant pressure (1 atm).
Table S5.38	Displaying the thermodynamic properties of Compound 144 at various temperatures (100 K to 310 K) under constant pressure (1 atm).
Table S5.39	Overview summarizing the computational methods employed, along with their specific applications and limitations

Table S6.1	List of compounds under investigation
Table S6.2	Grid co-ordinates defining the binding sites of the targets.
Tables S6.3	Docking scores of ligands against PDB ID 7DQL obtained *via* MVD
Tables S6.4	Docking scores of ligands against PDB ID 1JII obtained *via* MVD
Tables S6.5	Docking scores of ligands against PDB ID 7Y8B obtained *via* MVD
Tables S6.6	Docking scores of ligands against PDB ID 7MYL obtained *via* MVD
Tables S6.7	Docking scores of ligands against PDB ID 1M78 obtained *via* MVD
Tables S6.8	Docking scores of ligands against PDB ID 8BHH obtained *via* MVD
Tables S6.9	Docking scores of ligands against PDB ID 4in4 obtained *via* MVD
Tables S6.10	Docking scores of ligands against PDB ID 4ZZI obtained *via* MVD
Table S6.11	Binding affinities and interaction modes of ligands docked against PDB ID 7DQL
Table S6.12	Table S6.12: Binding affinities and interaction modes of ligands docked against PDB ID 1JII
Table S6.13	Table S6.13: Binding affinities and interaction modes of ligands docked against PDB ID 1JII
Table S6.14	Table S6.14: Binding affinities and interaction modes of ligands docked against PDB ID 7MYL
Table S6.15	Table S6.15: Binding affinities and interaction modes of ligands docked against PDB ID 1M78
Table S6.16	Table S6.16: Binding affinities and interaction modes of ligands docked against PDB ID 8BHH

Table S6.17	Table S6.17: Binding affinities and interaction modes of ligands docked against PDB ID 4IN4
Table S6.18	Table S6.18: Binding affinities and interaction modes of ligands docked against PDB ID 4ZZI
Table S6.19	Antibacterial activity of 1-bromo-2-naphthol (1B2N) through well diffusion assay
Table 6.20	Antibacterial activity of 1-bromo-2-naphthol (1B2N)
Table 6.21	MIC Antibacterial activity of 1-bromo-2-naphthol (1B2N)
Table 6.22	Antifungal activity of 1-bromo-2-naphthol (1B2N)
Table S6.23	Antifungal activity of 1-bromo-2-naphthol (1B2N) through well diffusion assay
Table 6.24	MIC Antifungal activity of 1-bromo-2-naphthol (1B2N)
Table 6.25	Antioxidant activity
Table 6.26	Structures of ascorbic acid, Trolox, and 1B2N The numbering 1,2, 3 and 4 indicates the phenolic group where antioxidant activity is studied.
Table 6.27	BDE, IP, PDE, PA, and ETE values of different positions of ascorbic acid, Trolox, and 1B2N DMSO solvent medium. All the listed values are in kJ/mol
Table S6.28	The calculated HOMO, LUMO and Energy gap
Table S6.29	The calculated quantum chemical parameters
Table S6.30	Computed Mulliken Charge distribution of some agents computed by DFT/B3LYP basis set
Table 6.31	Second-order perturbation theory analysis of key donor–acceptor NBO interactions in BDDE and 1-Bromo-2-naphthol, showing stabilization energies (E^2, kcal/mol), energy gaps between orbitals (E(j)–E(i)), and Fock matrix elements F(i,j)

LIST OF ABBREVIATIONS

Abbreviation	Meaning
AMR	Antimicrobial Resistance
CLC-Pred	Cell Line Cytotoxicity Prediction
ADME	Absorption, Distribution, Metabolism, Excretion
ADMET	Absorption, Distribution, Metabolism, Excretion, Toxicity
PASS	Prediction of Activity Spectra for Substances
BBB	Blood–Brain Barrier
HIA	Human Intestinal Absorption
CYP	Cytochrome P450
P-gp	P-glycoprotein
logP	Partition Coefficient (lipophilicity)
VDss	Steady-State Volume of Distribution
Cl	Clearance
t1/2	Half-Life
LD50	Lethal Dose 50%
Caco-2	Human epithelial colorectal adenocarcinoma cells
MDCK	Madin-Darby Canine Kidney cells
Ki	Inhibition Constant
EC50	Effective Concentration 50%
RBD	Receptor Binding Domain
H-bonding	Hydrogen Bonding
VDW	Van der Waals
MM	Molecular Mechanics

PMF	Potential of Mean Force
QM/MM	Quantum Mechanics/Molecular Mechanics Hybrid
RMSFavg	Average Root Mean Square Fluctuation
TLC	Thin Layer Chromatography
LOD50	Limit of Detection 50%
ELISA	Enzyme-Linked Immunosorbent Assay
RBC	Red Blood Cell
DPPH	2,2-Diphenyl-1-picrylhydrazyl
ABTS	2,2’-Azino-bis(3-ethylbenzothiazoline-6-sulfonic acid)
FRAP	Ferric Reducing Antioxidant Power
ROS	Reactive Oxygen Species
GSH	Glutathione
PDBQT	Protein Data Bank, Q & T format
B3LYP	Becke, 3-parameter, Lee–Yang–Parr functional
HF	Hartree–Fock
MP2	Møller–Plesset Perturbation Theory, 2nd order
6-31G	Split-valence Gaussian-type basis set
6-31G*	Polarized split-valence basis set
6-31+G*	Diffuse polarized split-valence basis set
TZVP	Triple-Zeta Valence with Polarization
VMD	Visual Molecular Dynamics
Multiwfn	Wavefunction analysis software
AIM	Atoms in Molecules
NCI	Non-Covalent Interaction

RDG	Reduced Density Gradient
FMO	Frontier Molecular Orbital
NBO	Natural Bond Orbital
MEP	Molecular Electrostatic Potential
ELF	Electron Localization Function
LOL	Localized Orbital Locator
BSA	Binding Site Analysis
MM/PBSA	Molecular Mechanics Poisson–Boltzmann Surface Area
ML-PLIC	Machine Learning Protein-Ligand Interaction Clustering
RMSD	Root Mean Square Deviation
Rg	Radius of Gyration
PASS	Prediction of Activity Spectra for Substances
LXRα	Liver X Receptor alpha
LXRβ	Liver X Receptor beta
FXR	Farnesoid X Receptor
SARS-CoV-2	Severe Acute Respiratory Syndrome Coronavirus 2
VOC	Variant of Concern
GA	Gentisyl Alcohol
TBATB	Tetrabutylammonium Tribromide
Terrestrol A(10)	SARS-CoV-2 and antifungal candidate
C144	AZD7762
C144 (AZD7762)	CHK1 kinase inhibitor targeting LXR/FXR
IC50	Half-maximal inhibitory concentration
RMSF	Root Mean Square Fluctuation

H-bond	Hydrogen bond
ΔGbind	Binding Free Energy
SARS-CoV	Severe Acute Respiratory Syndrome Coronavirus
MD	Molecular Dynamics
MIC Minimum	Inhibitory Concentration
UV-Vis	Ultraviolet–Visible Spectroscopy
FTIR	Fourier Transform Infrared Spectroscopy
NMR	Nuclear Magnetic Resonance
QSAR	Quantitative Structure–Activity Relationship
SAR	Structure–Activity Relationship
MVD	Molegro Virtual Docker
AutoDock	Molecular docking software
CTMATB	Cetyltrimethylammonium Tribromide
TBATB	Tetrabutylammonium Tribromide
BDE	Bond Dissociation Energy
HAT	Hydrogen Atom Transfer
SET	Single Electron Transfer
SETPPT	Single Electron Transfer Proton Transfer
SEPTLET	Sequential Proton and Electron Transfer
RO5	Rule of Five

Chapter 1

INTRODUCTION

1.1.Revisiting shelved compounds (*repurpose with a purpose*)

WHAT EXACTLY IS A CHEMICAL COMPOUND? In chemistry, it refers to a substance created when atoms of different elements unite in a precise and fixed ratio, producing a new material with properties unlike those of the elements themselves. This transformation is more than a simple blending; it is the birth of an entirely new entity governed by chemical bonds. Take aspirin (acetylsalicylic acid, $C_9H_8O_4$) as an example. It is a compound deliberately designed by chemists to alleviate pain and inflammation. Neither carbon, hydrogen, nor oxygen alone could perform such a task, but once combined in the correct structure, they give rise to a molecule with profound therapeutic value. This demonstrates how human ingenuity can extend the natural diversity of compounds by crafting entirely new ones with desired functions [1].

NOW, WHY REVISIT SUCH A BASIC CONCEPT? As researchers, we are well aware that thousands of chemical compounds are synthesized or extracted every day across laboratories worldwide. But for what purpose? Each compound is created or studied with an intention whether it is to develop a new therapeutic agent, design an advanced material, improve agricultural productivity, or provide an environmentally sustainable alternative to existing chemicals. In essence, compounds are synthesized to solve a problem, fulfil a need, or unlock a potential application [2].

YET AN EQUALLY IMPORTANT QUESTION ARISES: **DO ALL COMPOUNDS SUCCEED IN ACCOMPLISHING THE PURPOSE THEY WERE DESIGNED FOR?** Yes, some compounds succeed in fulfilling their intended purpose, while others do not. In certain cases, compounds are synthesized or extracted mainly to document the process rather than the product itself, which makes the final compound less relevant. Moreover, while some compounds achieve significant milestones in their respective target pathways, others may fail to do so. However, even those that do not align with their original target pathway may still prove useful by fitting into alternative pathways. Some are set aside after initial screening, while others remain underexplored. These “unused” or “underutilized” compounds often accumulate in chemical libraries, publications or patents scientifically documented but practically overlooked [3].

WHAT HAPPENS TO THESE COMPOUNDS? SHOULD THEY BE FORGOTTEN, OR CAN THEY BE REPURPOSED, REVISITED, AND REIMAGINED FOR NEW DIRECTIONS? This question is crucial because even compounds that fail their original purpose may still harbor hidden potential. Yet, this so-called surplus is not meaningless. It represents a vast, hidden reservoir of chemical diversity that remains largely unrecognized and underutilized. What has traditionally been regarded as waste or redundancy could instead be reframed as an untapped library of possibilities, carrying within it the potential for future breakthroughs.

This idea is not confined to a small subset of molecules; it extends to countless compounds scattered across the chemical and pharmaceutical landscape. Many of these compounds, at the time of their discovery, appeared highly promising demonstrating significant biological activity, structural novelty, or desirable physicochemical characteristics. They seemed destined to advance further in the development pipeline and were initially perceived as strong candidates to meet therapeutic or industrial benchmarks. However, due to practical barriers such as low natural abundance, difficulties in cost-effective large-scale synthesis, or challenges in formulation, these molecules were abandoned despite their intrinsic potential [4]. At the same time, there exists another category of compounds that did progress successfully some even reaching advanced clinical stages or gaining commercial approval. These molecules once stood at the forefront of research and development, hailed as breakthroughs and widely studied, even reaching the highest levels of recognition in their respective fields, but later lost relevance. In such cases, the focus was often on their shortcomings rather than their adaptability, leading to a failure to recognize the value they might hold if redirected or repurposed [5].

The economic dimension cannot be overlooked. For small laboratories, resource-limited institutions, and emerging biotech startups, this strategy is not just cost-saving it is survival. From the ecological standpoint, the argument grows even stronger. Every chemical synthesis carries an environmental cost solvent consumed, energy expended, waste generated. If compounds are created but never used, these costs become unjustifiable. Redirecting these molecules toward new purposes directly aligns with

the principles of green chemistry: preventing waste at the source, maximizing efficiency, and minimizing ecological harm [6]. Humanity today faces an unprecedented burden of health challenges that extend far beyond the walls of laboratories. Drug-resistant pathogens, novel viral outbreaks, rapidly mutating diseases, and the rise of non-communicable conditions such as cancer, diabetes, and cardiovascular disorders are reshaping the global medical landscape [7]. These issues highlight a pressing truth: the pace of disease evolution often outstrips the pace of drug discovery and development. One of the most alarming concerns is antimicrobial resistance (AMR). Overuse and misuse of antibiotics in healthcare, agriculture, and livestock production have accelerated the emergence of resistant bacterial strains. World Health Organization has identified AMR as one of the top ten global health threats, underscoring the urgency of discovering novel antimicrobials or repurposing old ones that were previously set aside [8]. In parallel, viral pandemics and emerging pathogens pose equally daunting challenges. The COVID-19 crisis demonstrated how a novel virus can cripple healthcare systems and economies worldwide, but it also revealed gaps in our preparedness [9]. Beyond coronaviruses, other viral threats such as Ebola, Zika, Nipah, and potential influenza pandemics continue to loom, requiring swift responses in drug development, vaccine innovation, and diagnostic technologies [10]. Furthermore, cancer and rare diseases continue to demand attention. Many cancers develop resistance to chemotherapy or targeted agents, leading to treatment failure. Similarly, rare diseases though affecting smaller populations collectively impact millions of individuals worldwide [11]. Thus, drug development is often limited due to poor commercial viability, leaving patients with few or no therapeutic options. Chronic and lifestyle-related diseases are another dimension of the crisis. With changing lifestyles, urbanization, and dietary patterns, diseases like obesity, type-2 diabetes, hypertension, and neurodegenerative disorders (e.g., Alzheimer's, Parkinson's) are on a steep rise. These conditions require long-term therapeutic management, putting additional strain on healthcare systems and highlighting the need for safer, more effective drugs with fewer side effects [12]. Thus, re-evaluating existing compounds, lowering drug discovery costs, and fostering open science collaborations are not just strategies of innovation they are moral imperatives aimed

at ensuring that life-saving therapies reach those who need them the most. In this sense, archived compounds are not remnants of the past, but bridges to the future.

Revisiting shelved molecules with aid of advanced computational approaches opens a whole new avenue for sustainable and innovative discovery. Modern computer-aided drug design (CADD), *in silico* simulations, and artificial intelligence driven machine learning models allow researchers to rapidly predict binding affinities, biological targets, and physicochemical properties, reducing the need for exhaustive trial-and-error experimentation [13]. High-throughput virtual screening can screen through vast libraries of overlooked compounds, while quantum chemical calculations provide deeper insights into frontier orbital interactions, bond dissociation energies, and electronic distributions that guide rational modification. Within this framework, re-engineering emerges as a powerful strategy: by introducing targeted structural modifications such as functional group substitution, scaffold hopping, electronic tuning, or stereochemical optimization scientists can drastically alter solubility, metabolic stability, or target selectivity. Even slight redesigns, suggested by computational feedback, can repurpose an inactive molecule into a promising drug lead, a selective catalyst, or a robust material precursor [14]. Thus, the computational studies and structural re-engineering work in synergy, converting once-forgotten molecules into valuable candidates with modern relevance and reduced environmental cost.

1.2. Structural Modification as a Perspective in Drug Discovery and design

Structural modification represents one of the central strategies in modern medicinal chemistry, offering a way to reimagine and repurpose compounds that may otherwise remain underutilized. The rationale is simple: small changes at the molecular level can profoundly alter biological interactions, physicochemical behavior, and therapeutic value. From this perspective, re-engineering is not just a process of adding or removing atoms, it is the deliberate redesign of molecular scaffolds to optimize their performance, unlock hidden properties, or redirect them toward entirely new biological targets [15].

Functional group modification: One of the most direct strategies involves functional group modification, where key substituents are altered to modulate reactivity, polarity, or binding affinity. Introducing hydroxyl, amino, carboxyl, or methoxy groups, for example, can improve hydrogen bonding and solubility, while removing labile groups may enhance stability against metabolic degradation. This approach often breathes new life into abandoned molecules by balancing hydrophilicity and lipophilicity, critical for effective absorption and distribution [16].

Ring Modification and Scaffold Hopping: Re-engineering can also involve ring expansion, contraction, or replacement to adjust conformational flexibility and electronic distribution. This is closely related to scaffold hopping, where the core backbone of a molecule is replaced with a different scaffold while maintaining key pharmacophoric features. These modifications allow a compound to explore new conformational space and interact with alternative biological receptors, often leading to entirely new therapeutic indications [17].

Halogenation as a Central Strategy in Molecular Re-engineering: Among the numerous strategies in medicinal and synthetic chemistry**,** halogenation holds a uniquely transformative role. What may initially appear as a subtle modification often yields disproportionately large effects on the fate of a compound in drug discovery. Halogenation is capable of reshaping both physicochemical and biological properties. Introducing halogen atoms can modulate lipophilicity, polarity, and conformational rigidity, thereby influencing absorption, membrane permeability, and binding interactions [18]. Halogenation also serves as a defense against rapid metabolic degradation, where replacing labile hydrogens with fluorine at oxidative hotspots protects molecules from cytochrome P450-mediated breakdown, prolonging half-life and reducing toxic byproducts [19]. Beyond stability, halogens participate in van der Waals contacts and directional halogen bonding with nucleophilic residues in proteins, an effect widely exploited in the design of kinase inhibitors and receptor modulators to improve affinity and specificity [20]. Fluorine, present in nearly a quarter of marketed drugs, is often introduced to improve metabolic stability, lipophilicity, and membrane permeability, as exemplified by fluoroquinolone antibiotics such as ciprofloxacin, where fluorine substitution broadens antibacterial activity and enhances efficacy [21]. Chlorine atoms contribute additional lipophilicity and steric bulk,

thereby improving absorption and selectivity, as seen in the anticancer agent gefitinib, where chlorination plays a pivotal role in maintaining stability and therapeutic performance [22]. Bromination, on the other hand, exerts both steric and electronic influences, providing intermediates for bioactive molecules such as α-bromoacetophenone derivatives, with recent synthetic advances enabling safer and high-yielding bromination suitable for pharmaceutical applications [23]. Heavier halogens such as bromine and iodine also participate in halogen bonding, a noncovalent interaction that strengthens molecular recognition and binding affinity; this has been particularly evident in kinase inhibitors and in experimental studies on cathepsin L and MEK1 inhibitors, where substitution with larger halogens improved potency through favorable interactions with nucleophilic sites in target proteins [24]. For compounds once deemed unsuitable due to poor stability, weak binding, or low bioavailability, halogenation offers a second life**.** By introducing halogen atoms, an otherwise discarded molecule may acquire the stability to survive metabolic clearance, the lipophilicity to cross membranes, or the affinity to engage a previously elusive binding pocket. What was once categorized as a "waste" molecule can, through halogenation, be repositioned as a scaffold of therapeutic relevance.

1.3. Drug Repurposing: An Evolving Paradigm in Modern Therapeutics

Drug discovery is traditionally a lengthy and costly process, often requiring more than a decade and billions of dollars before a compound reaches the market [25]. However, drug repurposing also termed drug repositioning has emerged as a complementary strategy that seeks to identify new therapeutic uses for existing drugs, including those already approved, shelved after unsuccessful trials, or discontinued due to market-related limitations. Unlike de novo discovery, repurposing leverages pre-existing pharmacological, toxicological, and clinical data, thereby reducing both the financial burden and the timeline for therapeutic development [26]. Several strategies are employed in drug repurposing [27]:

Computational Approaches (computational methods): These are computer-based methods that predict new uses for existing drugs. Techniques such as molecular docking, network pharmacology, and machine learning analyze chemical structures,

protein targets, and disease signatures to identify potential matches. They are cost-effective and help narrow down candidates before experimental testing.

Experimental Approaches: Lab-based studies are used to confirm computational predictions. This includes cell culture assays, animal models, and high-throughput screening to test drug activity against new targets. Phenotypic screening, which looks at overall effects without needing prior knowledge of mechanisms, is also important. These approaches ensure the drug shows real biological effectiveness.

Clinical and Real-world Data Mining: This strategy relies on patient data to uncover unexpected drug benefits. Sources include electronic health records, clinical trial results, and pharmacovigilance databases. For example, a drug may show improvement in a condition even if it was prescribed for another disease. Since the drugs already have known safety profiles, translation into clinical use is faster.

- *Case Studies in Drug Repurposing*

In oncology, several well-known drugs have been repositioned, such as metformin, originally an antidiabetic agent, which activates AMPK and inhibits mTOR signaling to suppress tumor growth in breast, colon, and pancreatic cancers [28]; disulfiram, a treatment for alcohol dependence, which exerts anticancer activity *via* ALDH inhibition and copper-dependent proteasome inactivation [29]; thalidomide, once withdrawn for teratogenicity but later repurposed for multiple myeloma due to its immunomodulatory and anti-angiogenic properties and chloroquine or hydroxychloroquine, antimalarials that block autophagy and enhance chemosensitivity in tumors [30]. Beyond cancer, repurposing has advanced antimicrobial and antiviral therapy, with colchicine demonstrating antiviral activity through microtubule disruption in flaviviruses and coronaviruses, remdesivir transitioning from Ebola to COVID-19 as an RNA polymerase inhibitor [31], doxycycline extending its use to malaria and filariasis *via* anti-inflammatory and MMP-inhibitory effects [32]. Repurposing has also targeted oxidative stress and inflammation, with N-acetylcysteine acting as an antioxidant and glutathione precursor in conditions ranging from COPD to psychiatric disorders [33].

APPLYING THE CONCEPT OF "REPURPOSE WITH A PURPOSE" TO CHEMICAL COMPOUNDS RAISES AN IMPORTANT QUESTION: WHAT TYPES OF COMPOUNDS SHOULD BE REVISITED? Phenols and polyphenols, both synthetic and natural, have long been recognized for their wide-ranging applications, particularly within the biological domain. However, simple phenols are often overlooked. Yet, in the context of drug design, these basic scaffolds are crucial, as understanding more complex structures would not have been possible without them. Among them, certain simple phenolic molecules once attracted considerable attention for their potent bioactive roles. However, factors such as their low natural abundance and other limiting aspects led to their gradual neglect. Rather than allowing these promising candidates to remain overlooked, this work revisits and re-engineers them, along with related derivatives, to uncover their hidden potential and reinstate their relevance in modern applications. In addition, the study also considered a well-established phenolic compound often described as a "double-edged sword" because of its contrasting biological effects. By approaching it in an innovative way, the aim was to unlock new possibilities and discover alternative applications. Furthermore, the work adopts the use of green reaction methodologies, ensuring that the revisiting of these small phenolic compounds not only broadens their potential but also aligns with sustainable and environmentally friendly practices ultimately allowing these overlooked molecules to "shine" in new and meaningful ways.

1.4. Importance of phenolic compounds

Phenolic compounds have garnered significant interest due to their diverse biological activities, including antimicrobial, antioxidant, anticarcinogenic, antiaging, antidiabetic, antimutagenic, anti-inflammatory, antiviral, cardioprotective, hepatoprotective, neuroprotective and antiparasitic making them valuable candidates for therapeutic development across a wide spectrum of diseases [34,35]. Several phenol-based pharmaceuticals are widely used in clinical settings. For instance, drugs such as salbutamol, thymol, terbutaline, terbutaline, fenoterol, resveratrol, and catechin exhibit important pharmacological actions [36,37]**.** Phenols are characterized by the presence of one or more hydroxyl (-OH) groups directly attached to an aromatic

ring, such as a phenyl or naphthyl group [38]. **Figure 1** illustrates some simple phenols along with their systematic and common names. The carbon atoms in the aromatic ring are all sp^2 hybridized, resulting in a planar hexagonal structure with internal bond angles of approximately 120 degrees, and a delocalized π-electron system spread across the ring. The C–O bond in phenols arises from the overlap of an sp^2-hybridized carbon orbital with an sp^3-hybridized oxygen orbital, while the O–H bond is formed between an sp^3 orbital of oxygen and a 1s orbital of hydrogen. The remaining two sp^3 orbitals of the oxygen atom contain lone pairs, giving the hydroxyl group (C–O–H) a bent geometry that approximates the tetrahedral angle of 109.5 degrees, as shown in **Figure 2**. Due to the higher electronegativity of oxygen compared to carbon and hydrogen, both the C–O and O–H bonds exhibit polarity.

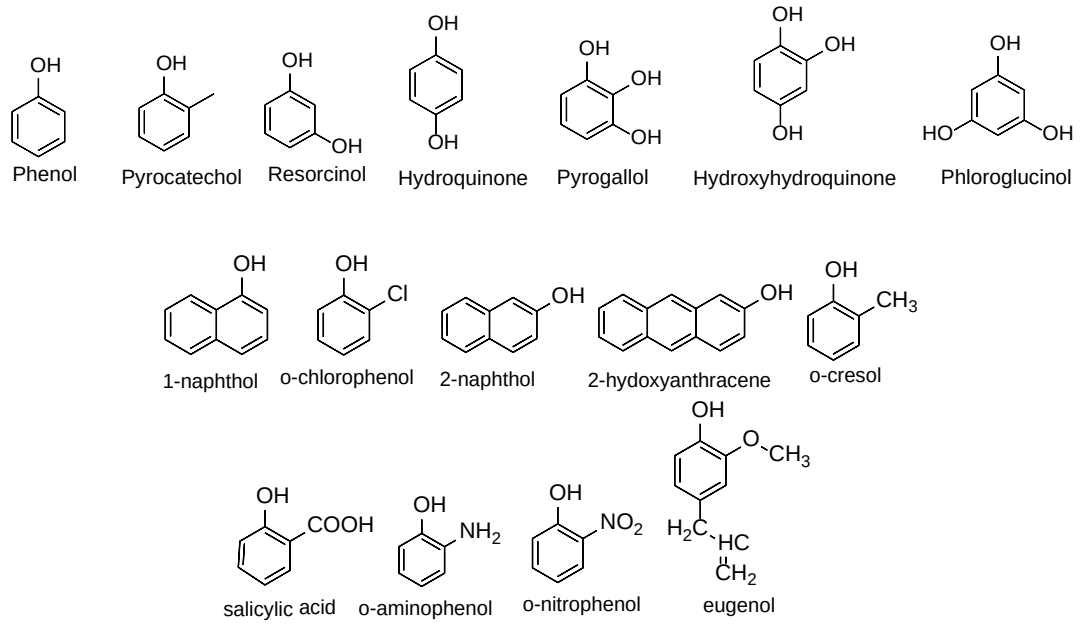

Figure 1: Examples of some phenolic compound

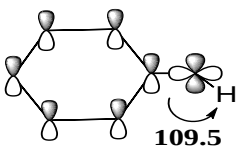

Figure 2: The structure of phenol

1.4.1. THERAPEUTIC AND PHARMACEUTICAL APPLICATIONS OF PHENOL SCAFFOLDS

1.4.1.1. Phenolic compounds as anti-cancer agent

Phenolic compounds have become highly relevant in anticancer research due to their antioxidant, anti-inflammatory, and pro-apoptotic activities. Their ability to modulate signaling pathways, suppress tumor-promoting factors, and enhance natural defense mechanisms makes them promising candidates for both cancer prevention and therapy. Cancer remains one of the major causes of death worldwide, yet its incidence can often be reduced through diet and lifestyle modifications. The cancer-protective effects of fruits and vegetables are strongly linked to their high polyphenol content [39]. As illustrated in **Figure 3**, several well-studied dietary phenolics such as resveratrol, gallic acid, caffeic acid, rosmarinic acid, sinapic acid, quercetin, genistein, epigallocatechin-3-gallate (EGCG), and curcumin have been shown to interfere with tumor progression through multiple mechanisms [40]. Resveratrol, commonly found in grapes and berries, inhibits tumor cell proliferation and induces apoptosis by targeting pathways such as NF-κB and PI3K/Akt. Gallic acid, present in teas and fruits, exerts pro-apoptotic effects and reduces metastatic potential by suppressing matrix metalloproteinases. Caffeic acid demonstrates strong radical-scavenging activity and inhibits angiogenesis, thereby restricting tumor blood supply. Rosmarinic and sinapic acids, found in herbs and seeds, contribute by reducing oxidative stress and modulating inflammatory mediators associated with tumor initiation. Quercetin, a flavonoid abundant in onions and apples, induces cell cycle arrest and promotes apoptosis in a variety of cancer cell lines. Genistein, a soy isoflavone, interferes with estrogen receptor signaling and inhibits tyrosine kinase activity, particularly relevant in hormone-dependent cancers. EGCG, the major catechin of green tea, suppresses tumor growth by blocking angiogenesis and reducing invasion and metastasis. Finally, curcumin, the yellow pigment in turmeric, has been extensively studied for its ability to inhibit multiple signaling pathways, including NF-κB, STAT3, and COX-2, leading to apoptosis induction and suppression of tumor growth. Together, these phenolic compounds demonstrate that dietary polyphenols can act at multiple molecular targets,

offering both chemopreventive and therapeutic benefits. Their presence in everyday foods highlights the potential of diet-based strategies in lowering cancer risk while also inspiring the design of novel anticancer drugs derived from natural scaffolds.

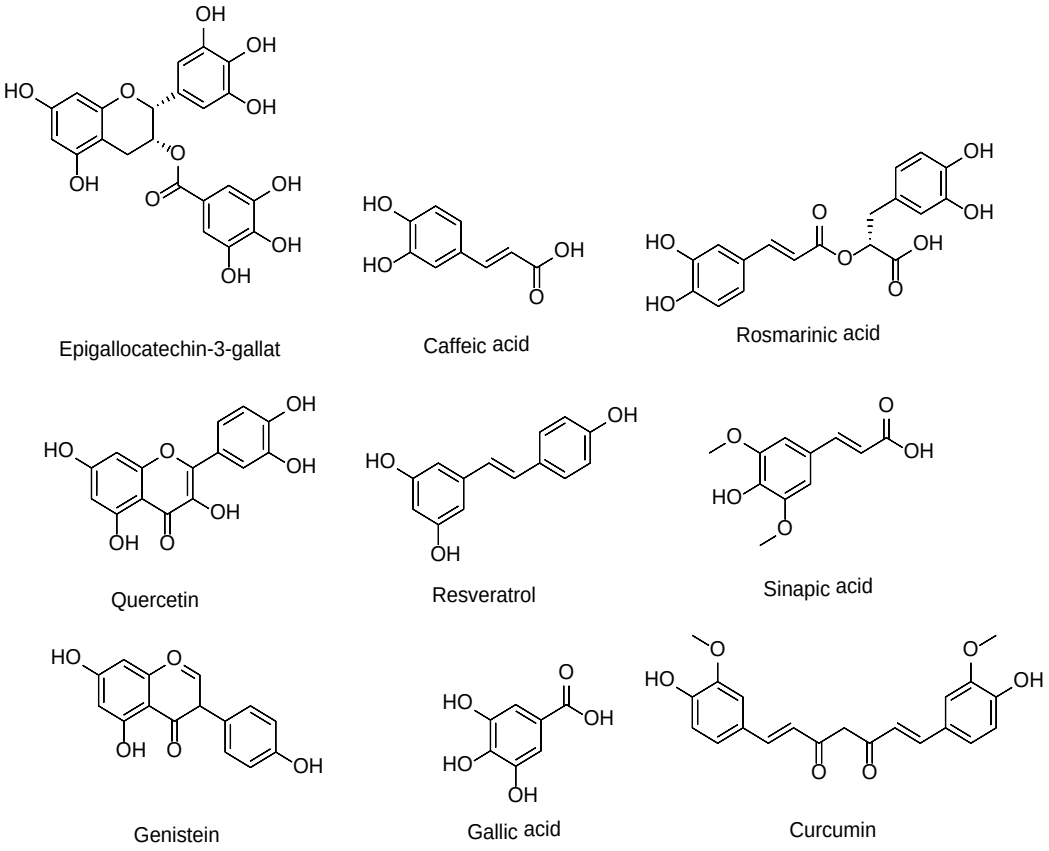

Figure 3: Chemical structures of polyphenols with anticancer properties

1.4.1.2. Phenolic compounds as anti-inflammatory and anti-oxidant Agents

Inflammation is a protective response to infections, injury, or toxins, but when sustained it contributes to chronic diseases such as arthritis, cardiovascular disorders, diabetes, and neurodegenerative conditions. Conventional anti-inflammatory drugs including NSAIDs, corticosteroids, and opioids are effective but often limited by long-term side effects such as ulcers, renal damage, or dependency [41]. Phenolic compounds offer a safer alternative due to their structural diversity and multitargeted actions. For example, resveratrol and curcumin as shown in **Figure 3** suppress NF-κB activation, reducing pro-inflammatory gene expression [42]. In addition, their strong antioxidant activity enables neutralization of reactive oxygen species (ROS), thereby

breaking the cycle of oxidative stress that perpetuates inflammation while also supporting neuroprotection and tissue healing [43]. They further modulate pain pathways by interacting with transient receptor potential (TRP) channels such as TRPV1 and TRPA1, reducing neuronal excitability and alleviating pain. Their therapeutic promise has been validated in disease models: quercetin as shown in **Figure 3** demonstrates significant anti-inflammatory and analgesic activity in arthritis, while curcumin shows efficacy in osteoarthritis, inflammatory bowel disease, and postoperative pain, often with fewer side effects than standard therapies. Importantly, phenolic compounds can also act synergistically with NSAIDs, enhancing efficacy and reducing required doses, thereby lowering toxicity risks [44].

Oxidative stress plays a central role in cellular aging and the progression of chronic diseases, and phenolic compounds are among the most effective natural agents in mitigating these effects. Some representative phenolic compounds, illustrated in **Figure 3**, are discussed here for their antioxidant potential. Resveratrol, commonly found in grapes and berries, supports cellular defense by both scavenging reactive oxygen species (ROS) and enhancing the activity of antioxidant enzymes. Curcumin, the yellow pigment of turmeric, is recognized for its strong ability to neutralize free radicals while also influencing molecular pathways that regulate inflammation and programmed cell death. Gallic acid, present in many fruits and teas, prevents oxidative injury by blocking lipid peroxidation and binding metal ions that trigger free radical reactions. Genistein, an isoflavone from soy, strengthens the body's antioxidant network by boosting internal defense mechanisms and reducing oxidative injury to DNA and lipids. Together, these compounds illustrate the multifaceted antioxidant strategies of phenolics combining direct radical elimination, enzyme activation, and metal ion regulation to protect cells and reduce the burden of oxidative stress-related disorders [45]. Collectively, these findings highlight phenolic compounds as versatile candidates for developing safer, more effective anti-inflammatory and anti-oxidant strategies.

1.4.1.3. Phenolic compounds as anti-microbial

Phenolic compounds represent a diverse arsenal of antimicrobial agents, each leveraging distinct mechanisms to combat pathogens. Some of these phenolic compounds are discussed here and illustrated in **Figure 4**, each demonstrating distinctive antimicrobial activities through varied mechanisms of action [46-50]. Salicylic acid, one of the simplest phenolic acids, compromises bacterial membranes and rapidly induces cell lysis, with encapsulated forms achieving MIC values as low as 4 mg/mL against *E. coli* and *S. aureus*. Cinnamic acid and its derivatives extend this membrane-targeting strategy to fungi, showing notable efficacy against *Candida* and *Aspergillus* species at low micromolar concentrations. Among polyphenols, epigallocatechin gallate (EGCG) from green tea stands out for its dual mechanism: hydrogen peroxide generation and membrane disruption, which collectively suppress the growth and biofilm development of Gram-positive pathogens such as *Staphylococcus aureus*. Sinapic acid broadens the antimicrobial scope, impairing both Gram-positive and Gram-negative bacteria, with MIC values ranging between 18 and 72 mg/mL, while flavones such as apigenin and baicalein provide additional modes of action. Apigenin exhibits measurable growth inhibition of *Pseudomonas aeruginosa*, *Salmonella typhimurium*, and *Proteus mirabilis*, whereas baicalein interferes with motility and biofilm integrity of *Aeromonas hydrophila*, demonstrating dose-dependent bactericidal potential. Phloretin, a dihydrochalcone, displays pronounced anti-biofilm activity against respiratory pathogens like *Haemophilus influenzae* and *Moraxella catarrhalis,* highlighting its therapeutic relevance in airway infections. Phenolic diterpenes from rosemary, including carnosic acid, carnosol, rosmanol, and epirosmanol, integrate antimicrobial and antioxidant properties, acting through reactive oxygen species (ROS) production and enzyme inhibition. Finally, myricetin, a flavonol, exerts multi-targeted effects by destabilizing bacterial membranes and modulating key enzymes, thereby showing activity against both *S. aureus* and *Listeria monocytogenes*. Together, these compounds illustrate how structurally diverse phenolics converge on a shared theme of microbial disruption, positioning them as valuable leads for developing next-generation antimicrobial therapies.

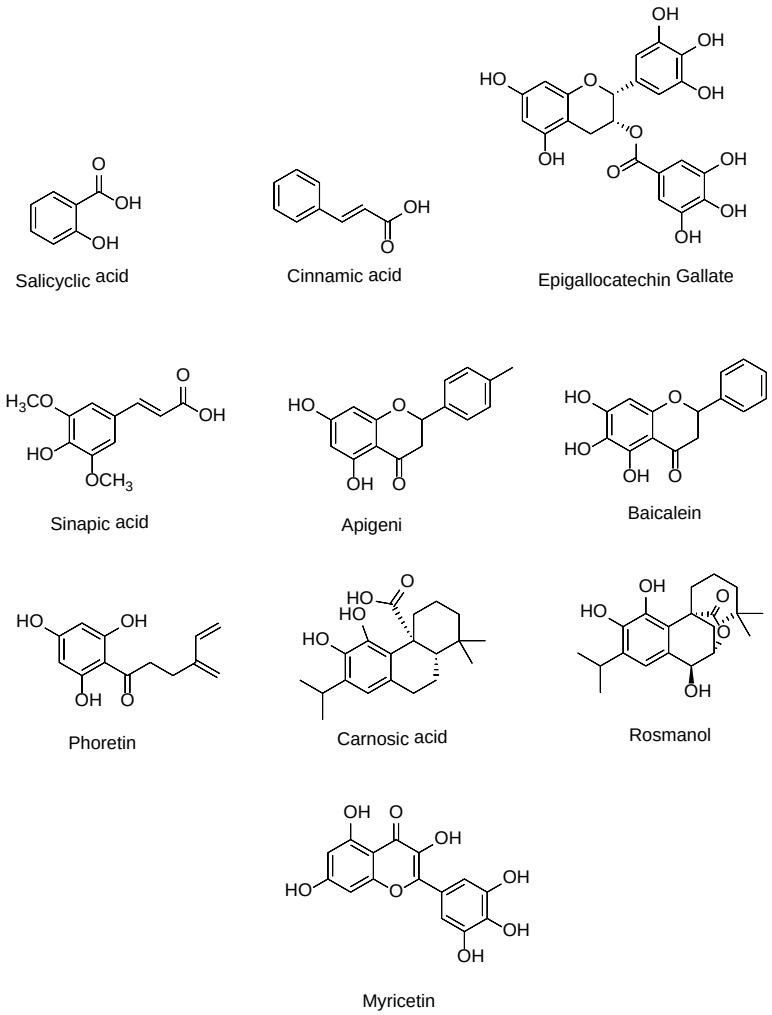

Figure 4: Structural depiction of some phenolic compounds possessing antimicrobial activity

1.4.1.4. Phenolic Compounds: Structural Subcategory and Biological Relevance

Within this broad category, numerous phenolic molecules and their derivatives have become valuable scaffolds in natural product chemistry and drug discovery. Gentisyl alcohol (2,5-dihydroxybenzyl alcohol) as shown in **Figure 5** is one such compound, representing a naturally occurring phenolic alcohol with significant biological relevance occurring naturally in fungi such as *Penicillium terrestre* and *Geosmithia langdonii* [51,52]. Its structure, containing hydroxyl and hydroxymethyl groups, allows it to neutralize reactive oxygen species and modulate cellular pathways, thereby exhibiting antioxidant, antineoplastic, antimicrobial, and cytoprotective effects. Derivatives of gentisyl alcohol display enhanced pharmacological activities. Notably,

dimeric derivatives known as terrestrol's A-H, isolated from *P. terrestre*, have shown cytotoxic activity against leukemia, liver, lung, and renal cancer cells, while also moderately inhibiting protein tyrosine kinases such as Src (proto-oncogene tyrosine-protein kinase Src) and KDR (kinase insert domain receptor, also known as VEGFR-2) [53,54]. These findings highlight the therapeutic relevance of gentisyl alcohol and its derivatives, which serve as valuable scaffolds in drug discovery and demonstrate potential applications ranging from oxidative stress protection to anticancer and antimicrobial therapies.

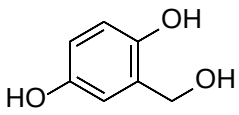

Gentisyl alcohol

Figure 5: Structural depiction of gentisyl alcohol

1.4.2. Halogenated phenolic compounds

Halogenated phenolic compounds are widely distributed in marine ecosystems, where their occurrence is closely associated with the abundance of halide ions, particularly chloride and bromide, in seawater. This halogen-rich environment drives marine organisms, such as algae and sponges, to biosynthesize a greater diversity of halogenated metabolites compared to their terrestrial counterparts. Many of these marine-derived halogenated phenolics have been extensively studied, with antibacterial and anticancer properties being among the most consistently reported biological activities [55]. By now, information is available on several dozen halogenated flavonoids, isoflavonoids, chromones, and depsides, isolated from bees, bacteria, fungi, algae, and lichens, as well as representatives of higher plants [56] Among the microbial sources of halogenated bioactive molecules, the genus *Streptomyces* holds particular importance due to its long-established role in pharmaceutical development. This group of actinobacteria synthesizes a wide variety of halogenated secondary metabolites, many of which have been transformed into clinically valuable antibiotics such as chloramphenicol, streptomycin, neomycin, bottromycin, and related derivatives. Chlorinated compounds are the most frequently encountered within this genus, while iodinated and fluorinated metabolites occur less

commonly but still contribute to the structural and functional diversity of the natural product repertoire [57,58]. Halogenated flavonoids and marine natural products such as bromophenols from red algae (e.g., 2,4-dibromophenol, brominated hydroquinones) have attracted increasing attention due to their potent anticancer, antibacterial, and antiviral activities [59]. Bromophenols are by far the most extensively studied subclass, largely because of the high abundance of bromide ions in seawater that facilitates their biosynthesis in marine organisms and they exhibit a wide spectrum of bioactivities of which some well-known bromophenolic compounds are shown in **Figure 6**. Thus, making them particularly promising as lead compounds for drug discovery and development [60]. One of the most extensively studied bromophenols is bis(2,3-dibromo-4,5-dihydroxybenzyl) ether (BDDE), isolated from *Rhodomela confervoides*. BDDE exhibits potent antioxidant [61], antibacterial [62], and anticancer activity through apoptosis induction in human cancer cells [63]. Another notable compound, bis(2,3,6-tribromo-4,5-dihydroxybenzyl) ether, has been reported to possess strong α-glucosidase inhibitory activity, making it a promising candidate for managing diabetes [64]. The simple bromophenol lanosol (2,3-dibromo-4,5-dihydroxybenzyl alcohol) is one of the earliest discovered bromophenols, exhibiting antimicrobial and cytotoxic properties [65,66]. Similarly, bis(2,3,6-tribromo-4,5-dihydroxyphenyl) methane has demonstrated strong cytotoxicity against tumor cell lines and other important bromophenols include 2,4,6-tribromophenol, a naturally occurring compound with potent antimicrobial and antifouling activity.

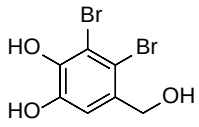

lanosol (2,3-dibromo-4,5-dihydroxybenzyl alcohol)

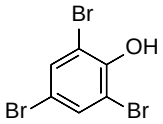

2,4,6-tribromophenol

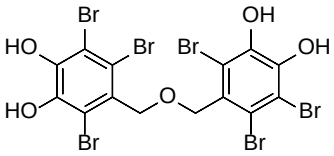

bis(2,3,6-tribromo-4,5-dihydroxybenzyl) ether

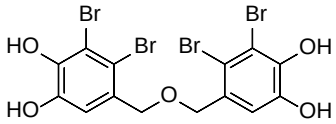

bis(2,3-dibromo-4,5-dihydroxybenzyl) ether

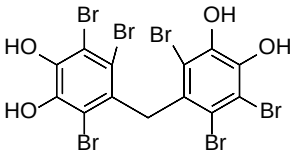

bis(2,3,6-tribromo-4,5-dihydroxyphenyl)methane

Figure 6: Structural depiction of some bromophenolic compounds

1.4.3. Computer-Aided Drug Design (CADD)

Computer-Aided Drug Design (CADD) has evolved into a pivotal strategy in pharmaceutical innovation, seamlessly integrating computational chemistry, structural biology, and artificial intelligence to transform how therapeutic agents are discovered and optimized. Unlike the conventional trial-and-error paradigm that often spans more than a decade, CADD accelerates the timeline by employing molecular docking, virtual screening, and predictive modeling, which collectively enable the rapid assessment of millions of molecules before wet-lab validation [67]. This computational pre-screening not only improves efficiency but also significantly reduces the staggering financial burden of drug discovery, which is estimated to cost between $1-3 billion per new chemical entity. By simulating ligand–receptor interactions *in silico*, molecular docking provides atomistic insights into hydrogen bonding, electrostatics, and hydrophobic complementarity, thereby prioritizing molecules with the highest predicted affinities [68]. Moreover, the ability to virtually screen massive chemical libraries allows the identification of both analogs of existing drugs and entirely novel scaffolds, as demonstrated in kinase inhibitor discovery for

oncology [69]. Structure-Based Drug Design (SBDD), relying on high-resolution macromolecular structures, has yielded breakthroughs such as HIV-1 protease inhibitors, which converted HIV into a manageable chronic disease, whereas Ligand-Based Drug Design (LBDD) continues to drive discovery where structural information is lacking, especially in GPCR-targeted research [70]. Importantly, CADD extends beyond binding affinity to early evaluation of pharmacokinetics and toxicity through ADMET prediction models, ensuring that compounds with suboptimal safety profiles are excluded before costly clinical trials [71]. Its value is also underscored in drug repurposing, where molecules like thalidomide and remdesivir were computationally redirected to new indications such as multiple myeloma and COVID-19, respectively [72]. More recently, the fusion of CADD with artificial intelligence and deep learning has given rise to automated drug generation pipelines capable of *de novo* design, optimization, and toxicity prediction with unprecedented accuracy [73]. These advances have been validated across therapeutic domains, from AI-generated antibiotics effective against multidrug-resistant MRSA and gonorrhea [74,75], to antiviral pipelines that designed inhibitors against HIV reverse transcriptase and SARS-CoV-2 proteins including the main protease, RNA-dependent RNA polymerase, and spike glycoprotein [70]. Collectively, CADD exemplifies how computational innovation not only expedites and economizes drug discovery but also broadens therapeutic horizons by enabling rational design, predictive safety assessment, and strategic repurposing across oncology, infectious diseases, inflammation, and beyond [69].

1.4.3.1.Computational Screening and Profiling of Candidate Molecules

The concept of *druglikeness* serves as a foundational filter in rational drug design, describing how closely a candidate molecule aligns with the physicochemical attributes of established therapeutics. Parameters such as molecular weight, lipophilicity, hydrogen bond capacity, and polarity classically codified in Lipinski's Rule of Five remain essential benchmarks for predicting solubility, membrane permeability, and oral bioavailability. Beyond these rules, more nuanced indicators, including ligand efficiency and lipophilic efficiency, provide valuable insights into

whether a compound can achieve sufficient potency while maintaining favorable absorption and systemic distribution profiles [76].

Once structural suitability is established, molecules undergo *ADMET (Absorption, Distribution, Metabolism, Excretion, and Toxicity) screening*, a critical step in ensuring that pharmacokinetic behavior aligns with therapeutic viability. Computational models and artificial intelligence frameworks have advanced to predict ADMET properties with remarkable precision, enabling early identification of liabilities such as poor oral availability, metabolic instability, cardiotoxicity from hERG channel blockade, or mutagenic potential. This early filtering process is indispensable, as pharmacokinetic or toxicological failures remain among the leading causes of attrition in clinical pipelines [77].

Complementing these filters, *bioactivity screening* evaluates whether candidate molecules engage biological targets in a therapeutically relevant manner. While high-throughput biochemical and microbial assays provide experimental confirmation, *in silico* bioactivity prediction models often using docking, QSAR, or machine learning allow researchers to estimate potency (e.g., IC_{50}, MIC values) against a spectrum of proteins and enzymes even before synthesis. Such approaches maximize efficiency by directing resources toward compounds with the highest predicted pharmacological relevance [78]. An additional layer of computational refinement is provided by *PASS (Prediction of Activity Spectra for Substances)*, which leverages large-scale structure–activity relationship datasets to forecast the probability of a molecule expressing diverse pharmacological activities. PASS outputs probability scores (Pa for likely activity, Pi for inactivity) across thousands of potential biological endpoints, making it a valuable tool for repurposing studies, activity clustering, and early prioritization of chemical libraries. Its widespread adoption in medicinal chemistry stems from its ability to integrate chemical space analysis with therapeutic potential, thereby accelerating hit-to-lead workflows [79]. Collectively, these computational strategies druglikeness assessment, ADMET filtering, bioactivity prediction, and PASS profiling function as an integrated pipeline that reduces experimental burden, mitigates late-stage attrition, and guides the rational progression of compounds from virtual design to preclinical evaluation. Widely accessible web-based platforms such

as SwissADME, ADMETlab, Molinspiration, and Way2Drug have democratized these methods, allowing researchers to perform comprehensive drug profiling with minimal resource investment, thus reshaping modern drug discovery into a more predictive and sustainable discipline.

Molecular docking, pharmacophore modeling, and molecular dynamics (MD) represent fundamental computational pillars in modern drug discovery, enabling the rational design and mechanistic understanding of therapeutic agents at the molecular level. These complementary techniques collectively provide a multi-scale framework: docking approximates binding events, pharmacophore modeling identifies the essential molecular determinants of activity, and MD simulates the temporal evolution of biomolecular systems to validate and refine predictions.

- **Molecular Docking** is designed to predict the binding orientation and affinity of small molecules within protein active sites, thereby guiding the identification of lead compounds. The process integrates search algorithms that explore conformational flexibility of ligands and, in certain approaches, receptor dynamics, coupled with scoring functions that approximate binding free energies. Beyond identifying the most favorable binding poses, docking allows exploration of binding-site plasticity and induced-fit effects. Widely adopted platforms include AutoDock Vina, AutoDock, DOCK, Glide (Schrödinger), Discovery Studio, and Molegro Virtual Docker (MVD), the latter offering robust cavity detection and user-friendly visualization that enhances both accuracy and interpretability of docking studies [80-83].
- **Pharmacophore Modeling** abstracts the critical spatial and electronic requirements that govern ligand–receptor interactions. By defining key pharmacophoric elements such as hydrogen bond donors, hydrogen bond acceptors, aromatic centers, hydrophobic groups, and charged moieties, this approach allows rapid screening of chemical libraries for molecules possessing the necessary three-dimensional features for activity. Importantly, pharmacophore hypotheses can be generated either from ligand-based datasets (common features among active compounds) or structure-based insights derived from protein-ligand complexes. Among the most widely used platforms are Molecular Operating

Environment (MOE), LigandScout, Discovery Studio, PharmaGist, and Catalyst, which collectively provide both predictive accuracy and high-throughput virtual screening capacity [84,85].

- **Molecular Dynamics (MD)** simulations extend the static approximations of docking and pharmacophore studies by incorporating temporal and thermodynamic dimensions. MD models the movement of atoms and molecules under defined force fields, thereby capturing protein flexibility, solvent interactions, and the stability of drug–target complexes under physiological conditions. It is particularly valuable for assessing binding free energy through methods such as MM-PBSA and MM-GBSA, as well as identifying allosteric mechanisms and dynamic conformational states. Widely established MD engines include GROMACS, AMBER, NAMD, CHARMM, and Desmond, each offering specialized strengths in terms of speed, scalability, and force-field implementations [86,87].

1.4.3.2.Quantum mechanical (QM) calculations

Quantum mechanical (QM) methods constitute the cornerstone of computational chemistry, providing profound insights into molecular behavior at the atomic scale. These approaches have significantly advanced our understanding of the structure and reactivity of small molecular systems. For example, QM-based techniques deliver structural parameters that closely correspond with experimental data, accurately predict reaction barrier heights, and yield chemically reliable interaction energies for hydrogen-bonded and dispersion-dominated systems [88]. Fundamentally, quantum mechanical methods are computational strategies grounded in the principles of quantum mechanics, employed to describe and predict the electronic structure, molecular geometry, and physicochemical properties of atoms, molecules, and solids. Since exact solutions to the Schrodinger equation are only feasible for simple systems such as the hydrogen atom [89], these methods rely on approximate solutions for many-electron systems. To address this complexity, a variety of approximation schemes and computational techniques have been developed.

1.4.3.2.1. Methods in QM calculations

Quantum mechanical methods solve the Schrödinger equation to study molecular systems. The main approaches include *ab initio* methods such as Hartree–Fock (HF) and post-HF methods, Density Functional Theory (DFT), and semi-empirical methods which are explained as follows:

- ***Ab initio methods***

Ab initio methods are quantum mechanical approaches that calculate molecular properties directly from first principles, without relying on experimental parameters. They are based on solving the Schrodinger equation using only fundamental constants, with the Hartree–Fock (HF) method as the starting point and more advanced post-HF methods (MP2, CI, CCSD, CASSCF) accounting for electron correlation [90]. These methods are used because they provide highly accurate, reliable, and systematically improvable results, making them essential for benchmarking and studying systems where experimental data is unavailable, though they are computationally expensive and mainly limited to small- and medium-sized molecules [91].

- ***Semi empirical methods***

Semiempirical (SE) methods can be obtained from either the Hartree–Fock or density functional theory framework through the application of systematic approximations, resulting in highly efficient computational schemes that are several orders of magnitude faster than *ab initio* calculations. This numerical efficiency, when combined with advances in computational resources and linear-scaling algorithms, allows the application of SE methods to very large molecular systems and extensive conformational sampling [92]. Well-established methods such as AM1, PM3, PM6, and MNDO are therefore extensively employed, as they allow the study of large molecular systems with minimal computational effort, making them especially valuable for preliminary geometry optimizations, high-throughput screening analysis, or cases where the highest level of accuracy is not critical [93].

- ***Density Functional Theory (DFT)***

Density functional theory (DFT) is a quantum-mechanical (QM) approach employed in chemistry and physics to determine the electronic structure of atoms, molecules, and solids. While it has been extensively utilized in computational solid-state physics since the 1970s, only advancements made during the 1990s rendered the method sufficiently accurate for quantum-chemical applications, leading to a rapid expansion of its use [94]. The fundamental principle of DFT is based on the concept that electron density serves as the primary variable governing the ground-state properties of a many-electron system. In contrast to wavefunction-based methods, which require solving for the complex many-electron wavefunction dependent on all electron coordinates simultaneously, DFT reformulates the problem in terms of electron density, a quantity dependent on only three spatial variables [95]. Owing to its favorable balance between computational efficiency and accuracy, DFT has become a versatile and powerful tool in chemistry, physics, and materials science for predicting molecular geometries, reaction mechanisms, and material properties.

- ***Basis sets***

Basis sets are defined as collections of mathematical functions employed to represent the shape and spatial distribution of atomic orbitals within a molecule. They act as fundamental building blocks for approximating both the molecular wavefunction and the electron density. The selection of a basis set critically influences the accuracy of the results as well as the overall computational cost of a DFT calculation [96]. The main types of basis sets are as follows:

- ***Minimal basis sets***

A minimal basis set uses the smallest possible number of functions, generally assigning a single basis function to each atomic orbital to describe the electron distribution. For instance, the STO-3G basis set is classified as minimal, wherein each atomic orbital is represented by a combination of three Gaussian functions designed to approximate a Slater-type orbital. Although minimal basis sets offer high computational efficiency, they yield only coarse approximations and lack the flexibility required to achieve accurate and reliable results [97].

- ***Split-Valence basis sets***

Split-valence basis sets represent a refinement over minimal basis sets by treating core and valence electrons differently. In this scheme, tightly bound core electrons are modeled with a single function, while the chemically active valence electrons are described using multiple functions of different widths. This layered representation provides additional flexibility in capturing variations in bonding and reactivity, which are primarily governed by valence orbitals. The method is particularly popular because it offers a practical compromise between computational cost and accuracy, yielding improved estimates of bond lengths, molecular geometries, and energies [98]. A common example is the 6-31G basis set, where core orbitals are expressed through six Gaussian primitives, while each valence orbital is split into a denser contraction of three Gaussians and a more diffuse single Gaussian.

- ***Polarization basis sets***

Polarization basis sets build upon split-valence models by introducing functions of higher angular momentum, which allow orbitals to deviate from their standard shapes during bonding. This added flexibility enables a more realistic description of molecular structure and electron distribution, particularly in cases involving lone pairs, multiple bonding, or heteroatoms. A representative example is the 6-31G* basis set, which augments heavy atoms with d-type polarization functions, thereby improving predictions of reactivity and intermolecular behavior. Such basis sets are widely used because they significantly enhance accuracy relative to split-valence sets, while maintaining a practical balance between reliability and computational cost [99,100].

- ***Diffuse basis sets***

Diffuse basis sets extend split-valence or polarized models by incorporating Gaussian functions with very small exponents, allowing electron density to occupy larger spatial regions. This modification is essential for accurately describing systems where electrons are weakly bound or highly delocalized, such as in anions, Rydberg excitations, and non-covalent interactions like hydrogen bonding or van der Waals forces. A well-known example is the 6-31+G* basis set, which applies diffuse

functions to heavy atoms, while the 6-31++G* version further includes them on hydrogen atoms. These additions make diffuse basis sets indispensable for capturing subtle electronic effects that standard basis sets often miss [101,102].

- ***Correlation consistent basis sets***

Correlation-consistent basis sets were specifically designed to improve the description of electron correlation in quantum chemical studies. They follow the general notation cc-pVXZ (where X = D, T, Q, etc.), with the zeta level reflecting the number of functions used to represent the valence orbitals. For instance, the cc-pVTZ set corresponds to a triple-zeta basis augmented with polarization functions, offering enhanced accuracy in electronic structure predictions. A key advantage of this family is that it provides a systematic pathway toward the complete basis set (CBS) limit, ensuring consistent and reliable convergence of molecular geometries, reaction energies, and other properties strongly influenced by electron correlation [103,104].

1.4.3.2.2. Gaussian

Gaussian is a widely used computational chemistry software package designed for quantum mechanical modeling of molecular systems. It incorporates multiple methodologies, including Hartree-Fock, density functional theory (DFT), and a variety of post-Hartree-Fock techniques, to accurately predict structural, thermodynamic, and spectroscopic properties. With capabilities ranging from molecular geometry optimization and vibrational frequency analysis to the exploration of reaction pathways and electronic spectra, Gaussian serves as a versatile tool for theoretical investigations. Its importance lies in offering a robust computational framework that complements experimental findings, facilitates rational molecular design, and enables the study of complex chemical processes with both accuracy and computational efficiency [105,106].

- ***Gaussview***

GaussView is a molecular modeling and visualization platform that functions as the graphical user interface for Gaussian. It simplifies computational workflows by allowing users to efficiently build molecular structures, generate input files, and

analyze output data. Beyond structure preparation, it provides advanced visualization tools for optimized geometries, molecular orbitals, electron density maps, vibrational modes, and electrostatic potential surfaces. By bridging user interaction with quantum chemical results, GaussView enhances the interpretability of complex calculations and significantly improves the accessibility and efficiency of theoretical studies [107].

1.4.3.2.3. Visual Molecular Dynamics

Visual Molecular Dynamics (VMD) is a versatile molecular modeling and visualization software widely applied in molecular dynamics and computational chemistry. It provides interactive 3D representations of molecular structures, enabling researchers to monitor conformational changes, dynamic processes, and interaction patterns within complex biological systems. Beyond visualization, VMD supports detailed analysis of non-covalent interactions, including hydrogen bonding and steric effects, thereby offering deeper insight into molecular behavior and facilitating interpretation of simulation data with high accuracy [108].

1.4.3.2.4. Multiwfn

Multiwfn is a versatile command-line program dedicated to the detailed analysis of electronic wavefunctions in quantum chemistry. It offers an extensive suite of functions, ranging from visualization of molecular orbitals and structural features to the calculation of real-space electronic properties on defined planes with corresponding contour or color-filled maps. The software supports advanced analyses such as Atoms in Molecules (AIM) theory, gradient path tracing, interbasin surface generation, and population analyses. These capabilities make Multiwfn particularly valuable for probing chemical bonding, electron density distribution, aromaticity, delocalization, and weak intra- and intermolecular interactions, thereby providing deep theoretical insights into molecular electronic structure [109].

1.4.4. Green Synthetic Pathways and Eco-Friendly Bromination

Green synthetic pathways represent a paradigm shift in chemical synthesis, focusing on environmentally responsible methodologies that reduce hazardous reagents, minimize waste streams, and enhance energy efficiency in accordance with the 12

principles of green chemistry [109]. These strategies include solvent-free transformations, adoption of greener solvents such as water, ionic liquids, and supercritical CO_2, as well as innovative enabling technologies like microwave-assisted reactions, mechanochemistry, and biocatalysis [110]. Together, these approaches enable safer and more sustainable processes for pharmaceutical, agrochemical, and fine chemical production.

Within this framework, green bromination has emerged as an important transformation, given the widespread utility of brominated intermediates in medicinal chemistry, polymer science, and materials engineering. Conventional bromination methods typically rely on molecular bromine (Br_2), which is volatile, corrosive, and hazardous to handle, often producing toxic by-products [111]. Modern sustainable approaches, however, mitigate these risks through safer reagent systems and in situ generation of bromine species. For instance, continuous-flow bromination enables on-demand generation of bromine from precursors such as hydrobromic acid and hydrogen peroxide, offering improved safety, scalability, and minimized environmental burden by avoiding the bulk handling of Br_2 [112].

Among various green bromination methods, ammonium tribromides such as tetrabutylammonium tribromide (TBATB) and cetyltrimethylammonium tribromide (CTMATB) represent environmentally friendly brominating reagents that provide controlled electrophilic bromination while reducing hazardous bromine usage. These tribromides can be synthesized *via* green protocols involving mild oxidants and aqueous media and are applied as selective brominating agents in one-pot, catalyst-free, or solvent-free procedures, often in green solvents such as polyethylene glycol (PEG). Their use exemplifies atom economy, operational simplicity, and minimal waste generation, fundamentally supporting the advancement of green synthetic pathways in pharmaceutical and fine chemical industries. The stability, thermal tolerance, and recyclability of TBATB and CTMATB further enhance their utility for sustainable bromination, aligning with goals of safer chemical manufacturing [113]

By integrating tribromide chemistry with other green synthetic tools, researchers achieve efficient halogenation processes that drastically reduce hazardous waste

generation and energy demands. These innovations highlight how green bromination strategies especially tribromide-based methodologies contribute to the broader agenda of sustainable synthesis, ensuring safer industrial applications while maintaining high synthetic efficiency and selectivity.

1.4.5. *In vitro* antimicrobial

In vitro antimicrobial assays represent essential preclinical methodologies for evaluating the activity of candidate antimicrobial compounds against a broad spectrum of microorganisms, including bacteria, fungi, and viruses. These assays offer a highly controlled experimental setting that enables the systematic assessment of growth inhibition, bactericidal effects, and the capacity of compounds to disrupt microbial survival strategies. Given the accelerating threat of antimicrobial resistance (AMR), such *in vitro* evaluations are critical to the early-stage discovery pipeline, allowing researchers to filter and prioritize natural products, synthetic derivatives, and repurposed drugs before moving into *in vivo* validation [114].

A variety of assay formats exist, each optimized for different experimental needs:

- *Disc Diffusion (Kirby-Bauer method):* A rapid and inexpensive qualitative approach where compound-impregnated paper discs are applied to agar seeded with microorganisms. The zone of inhibition surrounding the disc reflects antimicrobial potency.
- *Broth Microdilution and Macrodilution:* Considered the gold standard for quantitative antimicrobial testing, these methods determine minimum inhibitory concentration (MIC) and minimum bactericidal concentration (MBC) values by exposing microbes to serial dilutions of test compounds in liquid culture.
- *Agar Dilution:* A plate-based method in which antimicrobial agents are incorporated at defined concentrations into agar media, enabling parallel evaluation of multiple isolates to establish MIC endpoints.
- *Time-Kill Kinetics:* Provides dynamic information on microbial viability over time following drug exposure, offering insights into bactericidal versus bacteriostatic activity.

- *Bioautography:* Integrates thin-layer chromatography (TLC) with microbial growth detection directly on chromatographic plates, facilitating localization of active metabolites within complex mixtures.
- *Biofilm Assays:* Designed to evaluate the ability of compounds to inhibit biofilm development or disrupt preformed biofilms, thereby addressing one of the most clinically significant resistance mechanisms.

Together, these methodologies form a complementary toolkit that combines qualitative screening with quantitative kinetic and mechanistic insights. Their integration into antimicrobial discovery pipelines not only accelerates the identification of effective agents but also provides a foundation for understanding how candidate compounds may perform under physiologically relevant conditions [115-117].

1.4.6. *In vitro* antioxidant

In vitro antioxidant assays are indispensable tools in preclinical research, designed to evaluate the ability of natural or synthetic compounds to neutralize free radicals, reactive oxygen species (ROS), and other oxidative stress mediators. Since oxidative imbalance is implicated in aging, cancer, cardiovascular diseases, neurodegenerative disorders, and metabolic dysfunctions, reliable screening of antioxidant activity forms the foundation for therapeutic development and nutraceutical applications [118]. These assays are rapid, reproducible, and allow comparative evaluation of multiple compounds under standardized laboratory conditions before advancing to *in vivo* testing.

Several well-established *in vitro* methodologies are employed, each probing distinct mechanisms of antioxidant action:

- *DPPH Radical Scavenging Assay:* Based on the reduction of the stable purple-colored DPPH radical to a yellow product upon electron or hydrogen donation by antioxidants, quantified spectrophotometrically.

- *ABTS Radical Cation Decolorization Assay:* Measures the ability of antioxidants to quench the ABTS•+ radical cation, producing a decrease in absorbance proportional to scavenging potential.
- *Ferric Reducing Antioxidant Power (FRAP):* Assesses the electron-donating capacity of a sample by monitoring the reduction of Fe^{3+}–TPTZ complex to its ferrous form (Fe^{2+}–TPTZ), resulting in an intense blue coloration.
- *Oxygen Radical Absorbance Capacity (ORAC):* Quantifies the capacity of test compounds to scavenge peroxyl radicals through hydrogen atom transfer, using fluorescent decay kinetics.
- *Hydroxyl Radical and Superoxide Scavenging Assays:* Evaluate the capacity to neutralize highly reactive ROS species, which play critical roles in oxidative damage to biomolecules.
- *Lipid Peroxidation Inhibition Assays (TBARS, FTC, etc.):* Determine the ability of compounds to prevent oxidative degradation of lipids, a major process linked to membrane damage and cellular dysfunction.

Each of these assays provides complementary insights into different antioxidant mechanisms, ranging from radical scavenging and metal ion chelation to lipid peroxidation inhibition. By integrating multiple assay formats, a comprehensive antioxidant profile can be established, enabling prioritization of the most potent bioactive candidates for further pharmacological and therapeutic studies [119-121].

SCOPE AND OBJECTIVE

Chemical research is often accompanied by the accumulation of “unused” or “underutilized” compounds within laboratory chemical libraries, patents, and published reports. Although such molecules are scientifically documented, they frequently remain neglected due to scarcity, insufficient evaluation of their biological potential, or their “double-edged sword” characteristics, which make them less attractive. This paradox underscores a major limitation in contemporary research: vast numbers of potentially valuable chemical entities are effectively shelved as waste, despite their inherent promise. The present thesis seeks to address this challenge by

revisiting and repurposing such overlooked compounds, with a particular emphasis on phenolic derivatives.

The present thesis specifically focuses on compounds with high therapeutic potential but limited exploration, largely owing to their natural scarcity or restricted accessibility. Among these, gentisyl alcohol, a naturally occurring polyphenol reported to exhibit significant biological activities, emerges as a promising yet underutilized candidate. To bridge these gaps, the present work employs an integrated computational strategy comprising molecular docking, pharmacophore modeling, molecular dynamics simulations, and quantum chemical analyses to generate and evaluate analogs of such phenolic scaffolds. These approaches enable the prediction of their biological interactions, stability, and electronic features, thereby providing a rational framework for their repurposing and advancement as therapeutic leads.

The present work also incorporates resveratrol, a well-studied natural polyphenol frequently described as a *"double-edged sword."* This characterization stems from its dual pharmacological profile, as it can exert both beneficial and adverse biological effects depending on the dose and duration of exposure. Rather than diminishing its scientific value, this duality renders the resveratrol scaffold particularly compelling, since its structural framework provides a versatile platform for the design of improved derivatives. By leveraging the resveratrol backbone, the present study seeks to design and identify compounds with improved therapeutic windows. To achieve this, advanced computational methodologies including molecular docking, pharmacophore modeling, molecular dynamics simulations, and quantum mechanical calculations were employed to systematically explore their interaction landscapes and mechanistic possibilities. Importantly, the focus extended beyond classical therapeutic targets, with particular attention given to non-conventional and underexplored cancer-related pathways, thereby broadening the scope of resveratrol's pharmacological relevance. The thesis work also focuses exclusively on some small brominated phenolic compounds, a class of molecules previously synthesized in our laboratory but remained shelved. These compounds were systematically investigated using advanced computational approaches including molecular docking, pharmacophore modeling, molecular dynamics simulations, and quantum chemical analyses to elucidate their

structural and functional properties. Based on this screening, the most promising candidate was identified and subsequently re-synthesized through a sustainable green bromination strategy, ensuring both efficiency and environmental compliance. The re-synthesized compound was then subjected to *in vitro* assays, including antimicrobial and antioxidant evaluations, to experimentally validate the predicted bioactivities. By integrating computational modeling, green synthetic methodologies, and biological assessment, this study seeks to repurpose previously overlooked brominated phenolic compounds into valuable therapeutic leads, thereby transforming shelved laboratory products into meaningful pharmacological candidates.

Overall, the objective of this work is twofold: (i) to systematically explore and repurpose underutilized phenolic compounds as therapeutic candidates, and (ii) to showcase how a combined strategy of computational modeling, sustainable synthesis, and biological evaluation can transform overlooked chemical entities into meaningful contributors to drug discovery. The study bridges the gap between theoretical predictions offering a strong rational foundation and experimental validation. In doing so, it not only repurposes shelved laboratory compounds into viable drug leads but also illustrates how sustainable innovation can transform chemical “waste” into valuable pharmacological opportunities.

References

[1] Admin, "Acetylsalicylic acid (Aspirin)," *BYJUS*, Nov. 28, 2022. Available: https://byjus.com/chemistry/acetylsalicylic-acid/

[2] "Lesson 6.12: Project based lessons: Natural Resources & Synthetic Materials - American Chemical Society," *American Chemical Society*. Available: https://www.acs.org/middleschoolchemistry/lessonplans/chapter6/lesson12.html

[3] D. Sun, W. Gao, H. Hu, and S. Zhou, "Why 90% of clinical drug development fails and how to improve it?," *Acta Pharmaceutica Sinica B*, vol. 12, no. 7, pp. 3049–3062, Feb. 2022, doi: 10.1016/j.apsb.2022.02.002. Available: https://doi.org/10.1016/j.apsb.2022.02.002

[4] K. E. Van Oorschot, L. N. Van Wassenhove, M. Jahre, K. Selviaridis, and H. De Vries, "Drug shortages: A systems view of the current state," *Decision Sciences*, vol. 53, no. 6, pp. 969–984, Oct. 2022, doi: 10.1111/deci.12583. Available: https://doi.org/10.1111/deci.12583

[5] A. Garzón-Vico, J. Rosier, P. Gibbons, and P. McNamara, "The impact of failure and success experience on drug development," *Journal of Product Innovation Management*, vol. 37, no. 1, pp. 74–96, Oct. 2019, doi: 10.1111/jpim.12514. Available: https://doi.org/10.1111/jpim.12514

[6] S. Bhar, "Role of drug repurposing in sustainable drug discovery," in *IntechOpen eBooks*, 2023. doi: 10.5772/intechopen.110621. Available: https://doi.org/10.5772/intechopen.110621

[7] D. H. Howard, R. D. Scott, R. Packard, and D. Jones, "The global impact of drug resistance," *Clinical Infectious Diseases*, vol. 36, no. Supplement_1, pp. S4–S10, Jan. 2003, doi: 10.1086/344656. Available: https://doi.org/10.1086/344656

[8] M. Ferri, E. Ranucci, P. Romagnoli, and V. Giaccone, "Antimicrobial resistance: A global emerging threat to public health systems," *Critical Reviews in Food Science and Nutrition*, vol. 57, no. 13, pp. 2857–2876, Oct. 2015, doi: 10.1080/10408398.2015.1077192. Available: https://doi.org/10.1080/10408398.2015.1077192

[9] M. Ciotti, M. Ciccozzi, A. Terrinoni, W.-C. Jiang, C.-B. Wang, and S. Bernardini, "The COVID-19 pandemic," *Critical Reviews in Clinical Laboratory Sciences*, vol.

57, no. 6, pp. 365–388, Jul. 2020, doi: 10.1080/10408363.2020.1783198. Available: https://doi.org/10.1080/10408363.2020.1783198

[10] L. A. Reperant and A. D. M. E. Osterhaus, "AIDS, Avian flu, SARS, MERS, Ebola, Zika… what next?," *Vaccine*, vol. 35, no. 35, pp. 4470–4474, Jun. 2017, doi: 10.1016/j.vaccine.2017.04.082. Available: https://doi.org/10.1016/j.vaccine.2017.04.082

[11] C. Holohan, S. Van Schaeybroeck, D. B. Longley, and P. G. Johnston, "Cancer drug resistance: an evolving paradigm," *Nature Reviews. Cancer*, vol. 13, no. 10, pp. 714–726, Sep. 2013, doi: 10.1038/nrc3599. Available: https://doi.org/10.1038/nrc3599

[12] Y. Vodovotz *et al.*, "Prioritized research for the prevention, treatment, and reversal of Chronic disease: Recommendations from the Lifestyle Medicine Research Summit," *Frontiers in Medicine*, vol. 7, Dec. 2020, doi: 10.3389/fmed.2020.585744. Available: https://doi.org/10.3389/fmed.2020.585744

[13] S. Rawat *et al.*, "Drug repositioning using Computer-aided Drug design (CADD)," *Current Pharmaceutical Biotechnology*, vol. 25, no. 3, pp. 301–312, Aug. 2023, doi: 10.2174/1389201024666230821103601. Available: https://doi.org/10.2174/1389201024666230821103601

[14] P. W. Kenny and J. Sadowski, "Structure modification in chemical databases," *Methods and Principles in Medicinal Chemistry*, pp. 271–285, Jan. 2005, doi: 10.1002/3527603743.ch11. Available: https://doi.org/10.1002/3527603743.ch11

[15] H. Yao, J. Liu, S. Xu, Z. Zhu, and J. Xu, "The structural modification of natural products for novel drug discovery," *Expert Opinion on Drug Discovery*, vol. 12, no. 2, pp. 121–140, Dec. 2016, doi: 10.1080/17460441.2016.1272757. Available: https://doi.org/10.1080/17460441.2016.1272757

[16] P. Ertl, E. Altmann, and J. M. McKenna, "The Most Common Functional Groups in Bioactive Molecules and How Their Popularity Has Evolved over Time," *Journal of Medicinal Chemistry*, vol. 63, no. 15, pp. 8408–8418, Jul. 2020, doi: 10.1021/acs.jmedchem.0c00754. Available: https://doi.org/10.1021/acs.jmedchem.0c00754

[17] H. Sun, G. Tawa, and A. Wallqvist, "Classification of scaffold-hopping approaches," *Drug Discovery Today*, vol. 17, no. 7–8, pp. 310–324, Oct. 2011, doi:

10.1016/j.drudis.2011.10.024. Available: https://doi.org/10.1016/j.drudis.2011.10.024

[18] M. C. Ford and P. S. Ho, "Computational tools to model halogen bonds in medicinal chemistry," *Journal of Medicinal Chemistry*, vol. 59, no. 5, pp. 1655–1670, Oct. 2015, doi: 10.1021/acs.jmedchem.5b00997. Available: https://doi.org/10.1021/acs.jmedchem.5b00997

[19] Z. Xu, Z. Yang, Y. Liu, Y. Lu, K. Chen, and W. Zhu, "Halogen Bond: Its Role beyond Drug–Target Binding Affinity for Drug Discovery and Development," *Journal of Chemical Information and Modeling*, vol. 54, no. 1, pp. 69–78, Dec. 2013, doi: 10.1021/ci400539q. Available: https://doi.org/10.1021/ci400539q

[20] R. Cao *et al.*, "Enhanced bioactivity of natural products by halogenation: A database survey and quantum chemistry calculation study," *Journal of Medicinal Chemistry*, May 2025, doi: 10.1021/acs.jmedchem.5c00944. Available: https://doi.org/10.1021/acs.jmedchem.5c00944

[21] G. Chandra, D. V. Singh, G. K. Mahato, and S. Patel, "Fluorine-a small magic bullet atom in the drug development: perspective to FDA approved and COVID-19 recommended drugs," *Chemical Papers*, vol. 77, no. 8, pp. 4085–4106, Apr. 2023, doi: 10.1007/s11696-023-02804-5. Available: https://doi.org/10.1007/s11696-023-02804-5

[22] W.-Y. Fang *et al.*, "Synthetic approaches and pharmaceutical applications of chloro-containing molecules for drug discovery: A critical review," *European Journal of Medicinal Chemistry*, vol. 173, pp. 117–153, Apr. 2019, doi: 10.1016/j.ejmech.2019.03.063. Available: https://doi.org/10.1016/j.ejmech.2019.03.063

[23] Jitareanu, Tataringa, Zbancioc, and Trifan, "Bromination-A versatile tool for drugs optimization," *The Medical-Surgical Journal*, vol. 122, no. 3, pp. 614–626, 2018.

[24] R. Wilcken, M. O. Zimmermann, A. Lange, A. C. Joerger, and F. M. Boeckler, "Principles and applications of halogen bonding in medicinal chemistry and chemical biology," *Journal of Medicinal Chemistry*, vol. 56, no. 4, pp. 1363–1388, Nov. 2012, doi: 10.1021/jm3012068. Available: https://doi.org/10.1021/jm3012068

[25] J. A. DiMasi, H. G. Grabowski, and R. W. Hansen, “Innovation in the pharmaceutical industry: New estimates of R&D costs,” *Journal of Health Economics*, vol. 47, pp. 20–33, Feb. 2016, doi: 10.1016/j.jhealeco.2016.01.012. Available: https://doi.org/10.1016/j.jhealeco.2016.01.012

[26] S. Pushpakom *et al.*, “Drug repurposing: progress, challenges and recommendations,” *Nature Reviews Drug Discovery*, vol. 18, no. 1, pp. 41–58, Oct. 2018, doi: 10.1038/nrd.2018.168. Available: https://doi.org/10.1038/nrd.2018.168

[27] B. M. Sahoo, B. V. V. R. Kumar, J. Sruti, M. K. Mahapatra, B. K. Banik, and P. Borah, “Drug Repurposing Strategy (DRS): Emerging approach to identify potential therapeutics for treatment of novel coronavirus infection,” *Frontiers in Molecular Biosciences*, vol. 8, Feb. 2021, doi: 10.3389/fmolb.2021.628144. Available: https://doi.org/10.3389/fmolb.2021.628144

[28] B. M. Heckman-Stoddard, A. DeCensi, V. V. Sahasrabuddhe, and L. G. Ford, “Repurposing metformin for the prevention of cancer and cancer recurrence,” *Diabetologia*, vol. 60, no. 9, pp. 1639–1647, Aug. 2017, doi: 10.1007/s00125-017-4372-6. Available: https://doi.org/10.1007/s00125-017-4372-6

[29] Z. Skrott *et al.*, “Alcohol-abuse drug disulfiram targets cancer via p97 segregase adaptor NPL4,” *Nature*, vol. 552, no. 7684, pp. 194–199, Dec. 2017, doi: 10.1038/nature25016. Available: https://doi.org/10.1038/nature25016

[30] R. K. Amaravadi *et al.*, “Principles and Current Strategies for Targeting Autophagy for cancer treatment,” *Clinical Cancer Research*, vol. 17, no. 4, pp. 654–666, Feb. 2011, doi: 10.1158/1078-0432.ccr-10-2634. Available: https://doi.org/10.1158/1078-0432.ccr-10-2634

[31] S. G. Deftereos *et al.*, “Effect of Colchicine vs Standard Care on Cardiac and Inflammatory Biomarkers and Clinical Outcomes in Patients Hospitalized With Coronavirus Disease 2019,” *JAMA Network Open*, vol. 3, no. 6, p. e2013136, Jun. 2020, doi: 10.1001/jamanetworkopen.2020.13136. Available: https://doi.org/10.1001/jamanetworkopen.2020.13136

[32] W. R. Taylor *et al.*, “Chloroquine/doxycycline combination versus chloroquine alone, and doxycycline alone for the treatment of Plasmodium falciparum and Plasmodium vivax malaria in northeastern Irian Jaya, Indonesia.,” *American Journal of Tropical Medicine and Hygiene*, vol. 64, no. 5, pp. 223–228, May 2001,

doi: 10.4269/ajtmh.2001.64.223. Available: https://doi.org/10.4269/ajtmh.2001.64.223

[33] Y. Samuni, S. Goldstein, O. M. Dean, and M. Berk, "The chemistry and biological activities of N-acetylcysteine," *Biochimica Et Biophysica Acta (BBA) - General Subjects*, vol. 1830, no. 8, pp. 4117–4129, Apr. 2013, doi: 10.1016/j.bbagen.2013.04.016. Available: https://doi.org/10.1016/j.bbagen.2013.04.016

[34] W. Sun and M. H. Shahrajabian, "Therapeutic Potential of Phenolic Compounds in Medicinal Plants—Natural health products for human health," *Molecules*, vol. 28, no. 4, p. 1845, Feb. 2023, doi: 10.3390/molecules28041845. Available: https://doi.org/10.3390/molecules28041845

[35] F. F. D. Dongmo *et al.*, "Enhancing Health through Phenolic Compounds: A Comprehensive Review of Spices and Herbs Consumed in Cameroon Based on Global Research," *Applied Food Research*, p. 100837, Mar. 2025, doi: 10.1016/j.afres.2025.100837. Available: https://doi.org/10.1016/j.afres.2025.100837

[36] M. F. N. Meeran, H. Javed, H. A. Taee, S. Azimullah, and S. K. Ojha, "Pharmacological properties and molecular mechanisms of thymol: Prospects for its therapeutic potential and pharmaceutical development," *Frontiers in Pharmacology*, vol. 8, Jun. 2017, doi: 10.3389/fphar.2017.00380. Available: https://doi.org/10.3389/fphar.2017.00380

[37] S. Mori, A. H. Pang, N. T. Chandrika, S. Garneau-Tsodikova, and O. V. Tsodikov, "Unusual substrate and halide versatility of phenolic halogenase PltM," *Nature Communications*, vol. 10, no. 1, Mar. 2019, doi: 10.1038/s41467-019-09215-9. Available: https://doi.org/10.1038/s41467-019-09215-9

[38] A. Zeb, *Phenolic Antioxidants in Foods: Chemistry, Biochemistry and Analysis*. 2021. doi: 10.1007/978-3-030-74768-8. Available: https://doi.org/10.1007/978-3-030-74768-8

[39] R. Arrigoni *et al.*, "Another look at dietary polyphenols: Challenges in cancer prevention and treatment," *Current Medicinal Chemistry*, vol. 29, no. 6, pp. 1061–1082, Aug. 2021, doi: 10.2174/0929867328666210810154732. Available: https://doi.org/10.2174/0929867328666210810154732

[40] S. Bakrim, N. E. Omari, N. E. Hachlafi, Y. Bakri, L.-H. Lee, and A. Bouyahya, "Dietary phenolic compounds as anticancer natural drugs: recent update on molecular mechanisms and clinical trials," *Foods*, vol. 11, no. 21, p. 3323, Oct. 2022, doi: 10.3390/foods11213323. Available: https://doi.org/10.3390/foods11213323

[41] N. K. Panchal and E. P. Sabina, "Non-steroidal anti-inflammatory drugs (NSAIDs): A current insight into its molecular mechanism eliciting organ toxicities," *Food and Chemical Toxicology*, vol. 172, p. 113598, Jan. 2023, doi: 10.1016/j.fct.2022.113598. Available: https://doi.org/10.1016/j.fct.2022.113598

[42] M. Alipour *et al.*, "The antimicrobial, Antioxidative, and Anti-Inflammatory effects of Polycaprolactone/Gelatin scaffolds containing chrysin for regenerative endodontic purposes," *Stem Cells International*, vol. 2021, pp. 1–11, Sep. 2021, doi: 10.1155/2021/3828777. Available: https://doi.org/10.1155/2021/3828777

[43] P. Marrazzo and C. O'Leary, "Repositioning natural antioxidants for therapeutic applications in tissue engineering," *Bioengineering*, vol. 7, no. 3, p. 104, Sep. 2020, doi: 10.3390/bioengineering7030104. Available: https://doi.org/10.3390/bioengineering7030104

[44] R. Li, U. Goswami, M. King, J. Chen, T. C. Cesario, and P. M. Rentzepis, "In situ detection of live-to-dead bacteria ratio after inactivation by means of synchronous fluorescence and PCA," *Proceedings of the National Academy of Sciences*, vol. 115, no. 4, pp. 668–673, Jan. 2018, doi: 10.1073/pnas.1716514115. Available: https://doi.org/10.1073/pnas.1716514115

[45] T. Manso, M. Lores, and T. De Miguel, "Antimicrobial activity of polyphenols and natural polyphenolic extracts on clinical isolates," *Antibiotics*, vol. 11, no. 1, p. 46, Dec. 2021, doi: 10.3390/antibiotics11010046. Available: https://doi.org/10.3390/antibiotics11010046

[46] T. P. T. Cushnie and A. J. Lamb, "Recent advances in understanding the antibacterial properties of flavonoids," *International Journal of Antimicrobial Agents*, vol. 38, no. 2, pp. 99–107, Apr. 2011, doi: 10.1016/j.ijantimicag.2011.02.014. Available: https://doi.org/10.1016/j.ijantimicag.2011.02.014

[47] M. Daglia, "Polyphenols as antimicrobial agents," *Current Opinion in Biotechnology*, vol. 23, no. 2, pp. 174–181, Sep. 2011, doi: 10.1016/j.copbio.2011.08.007. Available: https://doi.org/10.1016/j.copbio.2011.08.007

[48] A. Borges, C. Ferreira, M. J. Saavedra, and M. Simões, "Antibacterial activity and mode of action of ferulic and gallic acids against pathogenic bacteria," *Microbial Drug Resistance*, vol. 19, no. 4, pp. 256–265, Mar. 2013, doi: 10.1089/mdr.2012.0244. Available: https://doi.org/10.1089/mdr.2012.0244

[49] F. Nazzaro, F. Fratianni, L. De Martino, R. Coppola, and V. De Feo, "Effect of essential oils on pathogenic bacteria," *Pharmaceuticals*, vol. 6, no. 12, pp. 1451–1474, Nov. 2013, doi: 10.3390/ph6121451. Available: https://doi.org/10.3390/ph6121451

[50] V. G. Luzhanin, A. K. Whaley, A. O. Ponkratova, V. V. Novikova, and E. A. Bezverkhniaia, "Antimicrobial activity of polyphenolic compounds," *Drug Development & Registration*, vol. 11, no. 2, pp. 65–72, May 2022, doi: 10.33380/2305-2066-2022-11-2-65-72. Available: https://doi.org/10.33380/2305-2066-2022-11-2-65-72

[51] J. Ham *et al.*, "Gentisyl alcohol inhibits proliferation and induces apoptosis via mitochondrial dysfunction and regulation of MAPK and PI3K/AKT pathways in epithelial ovarian cancer cells," *Marine Drugs*, vol. 17, no. 6, p. 331, Jun. 2019, doi: 10.3390/md17060331. Available: https://doi.org/10.3390/md17060331

[52] L. Chen, Y. Fang, T. Zhu, Q. Gu, and W. Zhu, "Gentisyl Alcohol Derivatives from the Marine-Derived Fungus Penicillium terrestre," *Journal of Natural Products*, vol. 71, no. 1, pp. 66–70, Dec. 2007, doi: 10.1021/np070421v. Available: https://doi.org/10.1021/np070421v

[53] D. Chung *et al.*, "In vitro and in vivo antimicrobial activity of the fungal metabolite toluquinol against phytopathogenic bacteria," *Frontiers in Microbiology*, vol. 14, Jul. 2023, doi: 10.3389/fmicb.2023.1221865. Available: https://doi.org/10.3389/fmicb.2023.1221865

[54] M. Zhang *et al.*, "New gentisyl alcohol derivatives from Aspergillus japonicas collected from the Arctic 6700-4 sea area," *Tetrahedron*, p. 134507, Jan. 2025, doi: 10.1016/j.tet.2025.134507. Available: https://doi.org/10.1016/j.tet.2025.134507

[55] N. Kasanah and T. Triyanto, "Bioactivities of Halometabolites from Marine Actinobacteria," *Biomolecules*, vol. 9, no. 6, p. 225, Jun. 2019, doi: 10.3390/biom9060225. Available: https://doi.org/10.3390/biom9060225

[56] T. Řezanka and J. Spížek, "Halogen-Containing antibiotics from streptomycetes," in *Studies in natural products chemistry*, 2003, pp. 309–353. doi: 10.1016/s1572-5995(03)80010-8. Available: https://doi.org/10.1016/s1572-5995(03)80010-8

[57] Kolomiets, "HALOGENATED PHENOLIC COMPOUNDS OF NATURAL ORIGIN CONSTITUTE A RARE MINOR GROUP OF SUBSTANCES (A REVIEW)," *Химия Растительного Сырья*, no. 4, pp. 24–31, 2024.

[58] C. Wang, W. Du, H. Lu, J. Lan, K. Liang, and S. Cao, "A Review: Halogenated Compounds from Marine Actinomycetes," *Molecules*, vol. 26, no. 9, p. 2754, May 2021, doi: 10.3390/molecules26092754. Available: https://doi.org/10.3390/molecules26092754

[59] A. Dudek *et al.*, "Structural investigation of interactions between halogenated flavonoids and the lipid membrane along with their role as cytotoxic agents," *Scientific Reports*, vol. 14, no. 1, May 2024, doi: 10.1038/s41598-024-61037-y. Available: https://doi.org/10.1038/s41598-024-61037-y

[60] M. Liu, P. E. Hansen, and X. Lin, "Bromophenols in marine algae and their bioactivities," *Marine Drugs*, vol. 9, no. 7, pp. 1273–1292, Jul. 2011, doi: 10.3390/md9071273. Available: https://doi.org/10.3390/md9071273

[61] K. Li, X.-M. Li, J. B. Gloer, and B.-G. Wang, "Isolation, Characterization, and Antioxidant Activity of Bromophenols of the Marine Red Alga Rhodomela confervoides," *Journal of Agricultural and Food Chemistry*, vol. 59, no. 18, pp. 9916–9921, Aug. 2011, doi: 10.1021/jf2022447. Available: https://doi.org/10.1021/jf2022447

[62] N. Xu, X. Fan, X. Yan, X. Li, R. Niu, and C. K. Tseng, "Antibacterial bromophenols from the marine red alga Rhodomela confervoides," *Phytochemistry*, vol. 62, no. 8, pp. 1221–1224, Mar. 2003, doi: 10.1016/s0031-9422(03)00004-9. Available: https://doi.org/10.1016/s0031-9422(03)00004-9

[63] X. Qi, G. Liu, L. Qiu, X. Lin, and M. Liu, "Marine bromophenol bis(2,3-dibromo-4,5-dihydroxybenzyl) ether, represses angiogenesis in HUVEC cells and in zebrafish embryos via inhibiting the VEGF signal systems," *Biomedicine &*

Pharmacotherapy, vol. 75, pp. 58–66, Sep. 2015, doi: 10.1016/j.biopha.2015.08.033. Available: https://doi.org/10.1016/j.biopha.2015.08.033

[64] M. Liu, W. Zhang, J. Wei, and X. Lin, "Synthesis and A-Glucosidase inhibitory mechanisms of BiS(2,3-dibromo-4,5-dihydroxybenzyl) ether, a potential marine bromophenol A-Glucosidase inhibitor," *Marine Drugs*, vol. 9, no. 9, pp. 1554–1565, Sep. 2011, doi: 10.3390/md9091554. Available: https://doi.org/10.3390/md9091554

[65] A. L. L. De Oliveira, D. B. Da Silva, N. P. Lopes, H. M. Debonsi, and N. S. Yokoya, "Chemical constituents from red algae Bostrychia radicans (Rhodomelaceae): new amides and phenolic compounds," *Química Nova*, vol. 35, no. 11, pp. 2186–2188, Jan. 2012, doi: 10.1590/s0100-40422012001100016. Available: https://doi.org/10.1590/s0100-40422012001100016

[66] A. Jesus, M. Correia-Da-Silva, C. Afonso, M. Pinto, and H. Cidade, "Isolation and Potential Biological Applications of Haloaryl Secondary Metabolites from Macroalgae," *Marine Drugs*, vol. 17, no. 2, p. 73, Jan. 2019, doi: 10.3390/md17020073. Available: https://doi.org/10.3390/md17020073

[67] L. G. Ferreira, R. N. D. Santos, G. Oliva, and A. D. Andricopulo, "Molecular Docking and Structure-Based drug design Strategies," *Molecules*, vol. 20, no. 7, pp. 13384–13421, Jul. 2015, doi: 10.3390/molecules200713384. Available: https://doi.org/10.3390/molecules200713384

[68] G. M. Morris and M. Lim-Wilby, "Molecular docking," *Methods in Molecular Biology*, pp. 365–382, Jan. 2008, doi: 10.1007/978-1-59745-177-2_19. Available: https://doi.org/10.1007/978-1-59745-177-2_19

[69] A. Lavecchia and C. Giovanni, "Virtual Screening Strategies in Drug Discovery: A Critical review," *Current Medicinal Chemistry*, vol. 20, no. 23, pp. 2839–2860, Jun. 2013, doi: 10.2174/09298673113209990001. Available: https://doi.org/10.2174/09298673113209990001

[70] A. Wlodawer and J. Vondrasek, "INHIBITORS OF HIV-1 PROTEASE: a major success of Structure-Assisted drug design," *Annual Review of Biophysics and Biomolecular Structure*, vol. 27, no. 1, pp. 249–284, Jun. 1998, doi:

10.1146/annurev.biophys.27.1.249. Available: https://doi.org/10.1146/annurev.biophys.27.1.249

[71] D. Schuster, C. Laggner, and T. Langer, "Why Drugs Fail - A study on side effects in new chemical entities," *Current Pharmaceutical Design*, vol. 11, no. 27, pp. 3545–3559, Oct. 2005, doi: 10.2174/138161205774414510. Available: https://doi.org/10.2174/138161205774414510

[72] D. E. V. Pires, T. L. Blundell, and D. B. Ascher, "PKCSM: Predicting Small-Molecule Pharmacokinetic and Toxicity Properties Using Graph-Based Signatures," *Journal of Medicinal Chemistry*, vol. 58, no. 9, pp. 4066–4072, Apr. 2015, doi: 10.1021/acs.jmedchem.5b00104. Available: https://doi.org/10.1021/acs.jmedchem.5b00104

[73] C. J. Gordon *et al.*, "Remdesivir is a direct-acting antiviral that inhibits RNA-dependent RNA polymerase from severe acute respiratory syndrome coronavirus 2 with high potency," *Journal of Biological Chemistry*, vol. 295, no. 20, pp. 6785–6797, Apr. 2020, doi: 10.1074/jbc.ra120.013679. Available: https://doi.org/10.1074/jbc.ra120.013679

[74] H. Chen, O. Engkvist, Y. Wang, M. Olivecrona, and T. Blaschke, "The rise of deep learning in drug discovery," *Drug Discovery Today*, vol. 23, no. 6, pp. 1241–1250, Jan. 2018, doi: 10.1016/j.drudis.2018.01.039. Available: https://doi.org/10.1016/j.drudis.2018.01.039

[75] M. Mongia, M. Guler, and H. Mohimani, "An interpretable machine learning approach to identify mechanism of action of antibiotics," *Scientific Reports*, vol. 12, no. 1, Jun. 2022, doi: 10.1038/s41598-022-14229-3. Available: https://doi.org/10.1038/s41598-022-14229-3

[76] A. Daina, O. Michielin, and V. Zoete, "SwissADME: a free web tool to evaluate pharmacokinetics, drug-likeness and medicinal chemistry friendliness of small molecules," *Scientific Reports*, vol. 7, no. 1, Mar. 2017, doi: 10.1038/srep42717. Available: https://doi.org/10.1038/srep42717

[77] L. Fu *et al.*, "ADMETlab 3.0: an updated comprehensive online ADMET prediction platform enhanced with broader coverage, improved performance, API functionality and decision support," *Nucleic Acids Research*, vol. 52, no. W1, pp.

W422–W431, Apr. 2024, doi: 10.1093/nar/gkae236. Available: https://doi.org/10.1093/nar/gkae236

[78] A. Lagunin, A. Stepanchikova, D. Filimonov, and V. Poroikov, "PASS: prediction of activity spectra for biologically active substances," *Bioinformatics*, vol. 16, no. 8, pp. 747–748, Aug. 2000, doi: 10.1093/bioinformatics/16.8.747. Available: https://doi.org/10.1093/bioinformatics/16.8.747

[79] "Molinspiration Cheminformatics." Available: https://www.molinspiration.com/

[80] P. C. Agu *et al.*, "Molecular docking as a tool for the discovery of molecular targets of nutraceuticals in diseases management," *Scientific Reports*, vol. 13, no. 1, Aug. 2023, doi: 10.1038/s41598-023-40160-2. Available: https://www.nature.com/articles/s41598-023-40160-2

[81] X.-Y. Meng, H.-X. Zhang, M. Mezei, and M. Cui, "Molecular Docking: a powerful approach for Structure-Based drug discovery," *Current Computer - Aided Drug Design*, vol. 7, no. 2, pp. 146–157, Jun. 2011, doi: 10.2174/157340911795677602. Available: https://pmc.ncbi.nlm.nih.gov/articles/PMC3151162/

[82] M. Chaudhary and K. Tyagi, "A REVIEW ON MOLECULAR DOCKING AND ITS APPLICATION," *International Journal of Advanced Research*, vol. 12, no. 03, pp. 1141–1153, Mar. 2024, doi: 10.21474/ijar01/18505. Available: https://doi.org/10.21474/ijar01/18505

[83] N. S. Pagadala, K. Syed, and J. Tuszynski, "Software for molecular docking: a review," *Biophysical Reviews*, vol. 9, no. 2, pp. 91–102, Jan. 2017, doi: 10.1007/s12551-016-0247-1. Available: https://doi.org/10.1007/s12551-016-0247-1

[84] Y. Kurogi and O. Guner, "Pharmacophore modeling and three-dimensional database searching for drug design using Catalyst," *Current Medicinal Chemistry*, vol. 8, no. 9, pp. 1035–1055, Jul. 2001, doi: 10.2174/0929867013372481. Available: https://doi.org/10.2174/0929867013372481

[85] G. Wolber and T. Langer, "LigandScout: 3-D Pharmacophores Derived from Protein-Bound Ligands and Their Use as Virtual Screening Filters," *Journal of Chemical Information and Modeling*, vol. 45, no. 1, pp. 160–169, Nov. 2004, doi: 10.1021/ci049885e. Available: https://doi.org/10.1021/ci049885e

[86] S. A. Hollingsworth and R. O. Dror, "Molecular dynamics simulation for all," *Neuron*, vol. 99, no. 6, pp. 1129–1143, Sep. 2018, doi: 10.1016/j.neuron.2018.08.011. Available: https://doi.org/10.1016/j.neuron.2018.08.011

[87] M. Karplus and J. A. McCammon, "Molecular dynamics simulations of biomolecules," *Nature Structural & Molecular Biology*, vol. 9, no. 9, pp. 646–652, Aug. 2002, doi: 10.1038/nsb0902-646. Available: https://doi.org/10.1038/nsb0902-646

[88] K. M. Merz, "Using quantum mechanical approaches to study biological systems," *Accounts of Chemical Research*, vol. 47, no. 9, pp. 2804–2811, Jun. 2014, doi: 10.1021/ar5001023. Available: https://doi.org/10.1021/ar5001023

[89] J. Gao, "Methods and applications of combined quantum mechanical and molecular mechanical potentials," *Reviews in Computational Chemistry*, pp. 119–185, Jan. 1996, doi: 10.1002/9780470125847.ch3. Available: https://doi.org/10.1002/9780470125847.ch3

[90] E. G. Lewars, "Ab initio calculations," in *Computational Chemistry*, 2024, pp. 199–432. doi: 10.1007/978-3-031-51443-2_5. Available: https://doi.org/10.1007/978-3-031-51443-2_5

[91] B. Huang and O. A. Von Lilienfeld, "AB Initio Machine Learning in Chemical Compound Space," *Chemical Reviews*, vol. 121, no. 16, pp. 10001–10036, Aug. 2021, doi: 10.1021/acs.chemrev.0c01303. Available: https://doi.org/10.1021/acs.chemrev.0c01303

[92] A. S. Christensen, T. Kubař, Q. Cui, and M. Elstner, "Semiempirical quantum mechanical methods for noncovalent interactions for chemical and biochemical applications," *Chemical Reviews*, vol. 116, no. 9, pp. 5301–5337, Apr. 2016, doi: 10.1021/acs.chemrev.5b00584. Available: https://doi.org/10.1021/acs.chemrev.5b00584

[93] J. J. P. Stewart and A. C. Stewart, "A semiempirical method optimized for modeling proteins," *Journal of Molecular Modeling*, vol. 29, no. 9, Aug. 2023, doi: 10.1007/s00894-023-05695-1. Available: https://doi.org/10.1007/s00894-023-05695-1

[94] T. Van Mourik, M. Bühl, and M.-P. Gaigeot, "Density functional theory across chemistry, physics and biology," *Philosophical Transactions of the Royal Society a Mathematical Physical and Engineering Sciences*, vol. 372, no. 2011, p. 20120488, Feb. 2014, doi: 10.1098/rsta.2012.0488. Available: https://doi.org/10.1098/rsta.2012.0488

[95] M. A. Radia and S. A. Saafan, "An overview for beginners on density functional theory in computational materials science and some of the related software packages," *Egyptian Journal of Solids*, vol. 47, no. 1, pp. 110–138, Mar. 2025, doi: 10.21608/ejs.2025.366425.1061. Available: https://doi.org/10.21608/ejs.2025.366425.1061

[96] A. E. A. Fouda and N. A. Besley, "Assessment of basis sets for density functional theory-based calculations of core-electron spectroscopies," *Theoretical Chemistry Accounts*, vol. 137, no. 1, Dec. 2017, doi: 10.1007/s00214-017-2181-0. Available: https://doi.org/10.1007/s00214-017-2181-0

[97] K. Kapusta, E. Voronkov, S. Okovytyy, V. Korobov, and J. Leszczynski, "Reconstruction of STO-3G family basis set for the accurate calculation of magnetic properties," *Russian Journal of Physical Chemistry A*, vol. 92, no. 13, pp. 2827–2834, Dec. 2018, doi: 10.1134/s0036024418130174. Available: https://doi.org/10.1134/s0036024418130174

[98] F. Jensen, "Atomic orbital basis sets," *Wiley Interdisciplinary Reviews Computational Molecular Science*, vol. 3, no. 3, pp. 273–295, Oct. 2012, doi: 10.1002/wcms.1123. Available: https://doi.org/10.1002/wcms.1123

[99] S. M. Bachrach, "Computational organic chemistry," *Annual Reports Section B (Organic Chemistry)*, vol. 104, p. 394, Jan. 2008, doi: 10.1039/b719311b. Available: https://doi.org/10.1039/b719311b

[100] V. A. Rassolov, M. A. Ratner, J. A. Pople, P. C. Redfern, and L. A. Curtiss, "6-31G* basis set for third-row atoms," *Journal of Computational Chemistry*, vol. 22, no. 9, pp. 976–984, Apr. 2001, doi: 10.1002/jcc.1058. Available: https://doi.org/10.1002/jcc.1058

[101] E. Papajak and D. G. Truhlar, "Efficient diffuse basis sets for density functional theory," *Journal of Chemical Theory and Computation*, vol. 6, no. 3, pp. 597–601, Feb. 2010, doi: 10.1021/ct900566x. Available: https://doi.org/10.1021/ct900566x

[102] A. V. Mitin, J. Baker, and P. Pulay, "An improved 6-31G* basis set for first-row transition metals," *The Journal of Chemical Physics*, vol. 118, no. 17, pp. 7775–7782, Apr. 2003, doi: 10.1063/1.1563619. Available: https://doi.org/10.1063/1.1563619

[103] Muller, "Basis Sets, Accuracy, and Calibration in Quantum Chemistry," in *Computational Nanoscience: Do It Yourself!*, 2006, pp. 19–43.

[104] E. Semidalas and J. M. L. Martin, "Canonical and DLPNO-Based Composite Wavefunction Methods Parametrized against Large and Chemically Diverse Training Sets. 2: Correlation-Consistent Basis Sets, Core–Valence Correlation, and F12 Alternatives," *Journal of Chemical Theory and Computation*, vol. 16, no. 12, pp. 7507–7524, Nov. 2020, doi: 10.1021/acs.jctc.0c01106. Available: https://doi.org/10.1021/acs.jctc.0c01106

[105] M. V. Malyshkina and A. S. Novikov, "Modern software for computer modeling in quantum chemistry and molecular dynamics," *Compounds*, vol. 1, no. 3, pp. 134–144, Nov. 2021, doi: 10.3390/compounds1030012. Available: https://doi.org/10.3390/compounds1030012

[106] J. G. Hill, "Gaussian basis sets for molecular applications," *International Journal of Quantum Chemistry*, vol. 113, no. 1, pp. 21–34, Oct. 2012, doi: 10.1002/qua.24355. Available: https://doi.org/10.1002/qua.24355

[107] A. Allouche, "Gabedit—A graphical user interface for computational chemistry softwares," *Journal of Computational Chemistry*, vol. 32, no. 1, pp. 174–182, Jul. 2010, doi: 10.1002/jcc.21600. Available: https://doi.org/10.1002/jcc.21600

[108] B. Silvi and A. Savin, "Classification of chemical bonds based on topological analysis of electron localization functions," *Nature*, vol. 371, no. 6499, pp. 683–686, Oct. 1994, doi: 10.1038/371683a0. Available: https://doi.org/10.1038/371683a0

[109] C.-J. Li and B. M. Trost, "Green chemistry for chemical synthesis," *Proceedings of the National Academy of Sciences*, vol. 105, no. 36, pp. 13197–13202, Sep. 2008, doi: 10.1073/pnas.0804348105. Available: https://doi.org/10.1073/pnas.0804348105

[110] G. Papanikolaou, G. Centi, S. Perathoner, and P. Lanzafame, "Green synthesis and sustainable processing routes," *Current Opinion in Green and Sustainable*

Chemistry, vol. 47, p. 100918, Mar. 2024, doi: 10.1016/j.cogsc.2024.100918. Available: https://doi.org/10.1016/j.cogsc.2024.100918

[111] Bhardwaj and Bhardwaj, "Development Of Green Synthetic Pathways For Organic Compounds," *International Journal of Creative Research Thoughts*, vol. 13, no. 3, pp. 434–440, Mar. 2025, Available: https://www.ijcrt.org/papers/IJCRT25A3311.pdf

[112] R. Van Kerrebroeck, P. Naert, T. S. A. Heugebaert, M. D'hooghe, and C. V. Stevens, "Electrophilic bromination in flow: a safe and sustainable alternative to the use of molecular bromine in batch," *Molecules*, vol. 24, no. 11, p. 2116, Jun. 2019, doi: 10.3390/molecules24112116. Available: https://doi.org/10.3390/molecules24112116

[113] N. Kuotsu, C. Pongen, T. Phucho, and U. Sinha, "Comparative degradation Kinetic studies of Tetrabutyl-ammonium tribromide (TBATB) and Cetyltrimethyl-ammonium Tribromide(CTMATB) - A route to reactivity Assessment for Solvent-Free Reactions," *Chemical Science Transactions*, Jan. 2015, doi: 10.7598/cst2015.972. Available: https://doi.org/10.7598/cst2015.972

[114] M. Balouiri, M. Sadiki, and S. K. Ibnsouda, "Methods for in vitro evaluating antimicrobial activity: A review," *Journal of Pharmaceutical Analysis*, vol. 6, no. 2, pp. 71–79, Dec. 2015, doi: 10.1016/j.jpha.2015.11.005. Available: https://doi.org/10.1016/j.jpha.2015.11.005

[115] T. J. Hossain, "Methods for screening and evaluation of antimicrobial activity: A review of protocols, advantages, and limitations," *European Journal of Microbiology and Immunology*, vol. 14, no. 2, pp. 97–115, Apr. 2024, doi: 10.1556/1886.2024.00035. Available: https://doi.org/10.1556/1886.2024.00035

[116] H. A. Mohamed, Y. A. Ammar, G. A. M. Elhagali, H. A. Eyada, D. S. Aboul-Magd, and A. Ragab, "In Vitro Antimicrobial Evaluation, Single-Point Resistance Study, and Radiosterilization of Novel Pyrazole Incorporating Thiazol-4-one/Thiophene Derivatives as Dual DNA Gyrase and DHFR Inhibitors against MDR Pathogens," *ACS Omega*, vol. 7, no. 6, pp. 4970–4990, Feb. 2022, doi: 10.1021/acsomega.1c05801. Available: https://doi.org/10.1021/acsomega.1c05801

[117] B. L. Zimmer PhD, “Clinical and Laboratory Standards Institute.” Available: https://clsi.org/shop/standards/m07/

[118] Md. N. Alam, N. J. Bristi, and Md. Rafiquzzaman, “Review on in vivo and in vitro methods evaluation of antioxidant activity,” *Saudi Pharmaceutical Journal*, vol. 21, no. 2, pp. 143–152, Jun. 2012, doi: 10.1016/j.jsps.2012.05.002. Available: https://doi.org/10.1016/j.jsps.2012.05.002

[119] I. D. Nwachukwu, R. A. Sarteshnizi, C. C. Udenigwe, and R. E. Aluko, “A concise review of current in vitro chemical and Cell-Based antioxidant assay methods,” *Molecules*, vol. 26, no. 16, p. 4865, Aug. 2021, doi: 10.3390/molecules26164865. Available: https://doi.org/10.3390/molecules26164865

[120] N. J. Miller and C. A. Rice-Evans, “Factors influencing the antioxidant activity determined by the ABTS•+Radical Cation assay,” *Free Radical Research*, vol. 26, no. 3, pp. 195–199, Jan. 1997, doi: 10.3109/10715769709097799. Available: https://doi.org/10.3109/10715769709097799

[121] S. Singh and R. P. Singh, “In VitroMethods of Assay of Antioxidants: An Overview,” *Food Reviews International*, vol. 24, no. 4, pp. 392–415, Sep. 2008, doi: 10.1080/87559120802304269. Available: https://doi.org/10.1080/87559120802304269

Chapter 2

Design and Multi-Target Evaluation of Halogenated Gentisyl Alcohol Derivatives Using Docking, DFT, and ADMET Profiling

A variety of phenolic compounds exhibits a wide spectrum of biological activities. Gentisyl alcohol, a phenolic secondary metabolite, possesses significant pharmacological potential but remains underutilized due to its limited natural abundance and low synthetic yield. Developing structural analogues offers a promising strategy to overcome these constraints and facilitate drug discovery. This chapter delves into the design of halogenated variants of gentisyl alcohol, with the objective of enhancing its physicochemical properties and inherent therapeutic potential through a multitargeted, therapeutic strategy. Computational approaches were utilized to provide a foundational assessment of its bioactivity and molecular interactions.

The text of this chapter has been published and patented as:

- Ein rechnergestütztes System zur Bewertung des Potenzials von halogenierten Gentisylalkoholderivaten als pharmazeutische Wirkstoffe *Basanta Singha, Nichan Boruah, Partha Pratim Gogoi, Penlisola Longkumer, Upasana Bora Sinha (Published on 27th June, 2024) (German Patent)*
- Singha, B., Gogoi, P. P., Longkumer, P., Boruah, N., & Sinha, U. B. (2024). Evaluation of Some Designed Halogenated Variants of Gentisyl Alcohol: Molecular Docking, DFT, Druglikeness, and ADMET Studies for Assessing Biological Properties. *Journal of Applicable Chemistry*, *13*(2), 98-113.

2.1. Introduction

According to the World Health Organization (WHO), infectious diseases stemming from bacteria, viruses, and parasites constitute a significant cause of human mortality, contributing to approximately 25% of all disease-related deaths [1]. The pace of antibiotic development has notably fallen behind the rapid emergence of bacterial drug resistance. Concurrently, since the onset of the 21st century, the world has witnessed the emergence of novel viral infections such as H1N1 influenza, Ebola, Zika, poliomyelitis, and COVID-19, leading to numerous Public Health Emergencies of International Concern [2]. Antimicrobial resistance (AMR) occurs when bacteria, viruses, fungi, or parasites evolve to withstand antimicrobial drugs, largely through genetic mutations driven by natural selection as well as misuse and overuse of antimicrobials. This undermines treatment efficacy, increasing disease transmission, severity, and mortality [3]. Drug resistance renders infections difficult or impossible to treat. Chronic inflammatory diseases such as ischemic heart disease, stroke, cancer, diabetes, chronic kidney disease, non-alcoholic fatty liver disease, and various autoimmune or neurodegenerative disorders are now the leading global cause of death, responsible for over 50% of fatalities [4, 5]. From this perspective, there is a clear and urgent need to explore and develop novel antimicrobial and anti-inflammatory agents through innovative strategies capable of generating potent leads with the potential to overcome drug resistance. Developing an effective drug costs between $900 million and $2 billion, with only one in 10,000 compounds reaching the market and just a third recovering its costs. This highlights the significant risk inherent in drug development [6]. Amid challenges, modern drug discovery utilizes innovative techniques like computer-aided drug design (CADD), including *in silico* methods, bioinformatics, cheminformatics, and quantum calculations. Advances in computational methods have accelerated this process, enabling cost-effective identification of promising candidates, reducing animal model use, facilitating rational drug design, and supporting drug repositioning [7, 8]. Phenolic compounds represent a rich source of bioactive molecules with immense potential in drug discovery. Research indicates that halogen substitution in phenolic compounds can markedly enhance their pharmacological potential. Such modifications have been associated with pronounced antibacterial, antifungal, antioxidant, and anticancer and may other activities making them valuable candidates in the design of

therapeutic agents aimed at the treatment and prevention of high-burden, socially significant diseases [9]. Novel halophenols have attracted increasing attention due to their diverse biological activities, including antioxidant, antimicrobial, antithrombotic, enzyme inhibitory, and cytotoxic effects, as well as anti-inflammatory properties and protective actions on the vascular endothelium [10-14]. These promising activities have motivated efforts to optimize their structures efficiently and to investigate the underlying mechanisms of their bioactivity.

Gentisyl alcohol is a phenolic alcohol naturally occurring in various fungi and has been investigated for its ability to exhibit a diverse spectrum of biological activities, including antimicrobial, antioxidant, and anti-inflammatory effects [15,16]. However, its broader pharmacological potential remains underexplored, primarily due to its limited natural abundance and the challenges associated with large-scale isolation or synthesis. This scarcity restricts comprehensive biological evaluation and hinders its integration into drug discovery pipelines, emphasizing the need for efficient production of its analog to fully realize its therapeutic promise. Furthermore, their structural framework allows for strategic chemical modifications, serving as pivotal intermediates in synthetic organic transformations [17]. Halogen bonding serves as a key non-covalent interaction in contemporary drug design, contributing to enhanced molecular recognition and binding specificity. Halogen atoms such as fluorine, chlorine, bromine, and iodine (collectively represented as X) are frequently incorporated into drug molecules as functional substituents to modulate their physicochemical properties and optimize therapeutic efficacy. They are prevalent in approximately half of all molecules screened through high-throughput methods and are found in about 40% of drugs either on the market or in clinical trials. Furthermore, around a quarter of medicinal chemistry literature and patents involve adding halogen atoms in later synthesis stages [18-21]. The intentional utilization of halogen bonding as a potent tool, akin to hydrogen bonding, holds promise for enhancing binding affinity and influencing binding selectivity. The rational design of potent drugs against therapeutic targets *via* halogen bonding remains an intriguing field, set to be further explored through a combination of experimental techniques and theoretical calculations in the future [20]. CADD and quantum-based studies have emerged as

invaluable assets in this domain, providing a wide array of advanced tools and techniques that substantially enhance both the efficiency and precision of the drug discovery process [22].

This study focuses on designing halogenated variants of gentisyl alcohol, a compound known for its diverse range of bioactivities, but which remains understudied, with only limited availability of its analogues in nature or synthetic libraries. By strategically incorporating bromine, fluorine, chlorine, and iodine atoms (=X) the aim is to markedly enhance its pharmacological potential. The primary objective is to evaluate these derivatives as potential antibacterial, anti-tubercular, antiviral, anti-parasitic, and anti-inflammatory agents, thereby addressing the growing threat of antimicrobial resistance (AMR) and identifying potent leads capable of countering inflammation and infectious disease related conditions. Computer-aided *in silico* methodologies will be implemented, given their high reliability, cost-effectiveness, and ability to explicate molecular modes of action in a time-efficient manner. In particular, molecular docking will be employed to assess binding energies against the respective biological targets using a redocking approach with native co-crystallized ligands as references. Compounds demonstrating the most favorable docking scores for each target will subsequently undergo Density Functional Theory (DFT) calculations to examine their electronic properties, reactivity, and stability. Furthermore, drug-likeness evaluation, pharmacokinetic profiling, and toxicity screening will be performed to assess their suitability as drug-like molecules and their potential as lead candidates.

2.2. Materials and methods

2.2.1. Compounds in focus

The compounds investigated, as shown below in **Table 2.1**, were designed from gentisyl alcohol, strategically incorporating bromine (Br), chlorine (Cl), and fluorine (F) substitutions at the unoccupied ortho and meta positions of the parent compound. This substitution strategy presents a versatile approach for modulating the chemical properties and reactivity of the resulting compounds, thereby broadening their potential applications across diverse scientific domains such as pharmaceutical research, materials science, and organic synthesis [23]. With the exception of

compound codes 1Br, 3Br, 1Cl, 2Cl, 3Cl, 2F, 1F, and the parent gentisyl alcohol, which are documented in the ChemSpider (http://www.chemspider.com) and PubChem (https://pubchem.ncbi.nlm.nih.gov) databases, the remaining compounds, were designed *via* halogen substitution.

Table 2.1: List of compounds understudy and their compound code

Sl. No	Compounds and their compound code	Sl. No	Compounds and their compound code	Sl. No	Compounds and their compound code	Sl. No	Compounds and their compound code
1	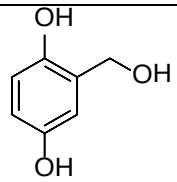 **Gentisyl alcohol (GA)**	**10**	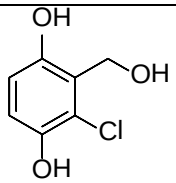 **2Cl**	**19**	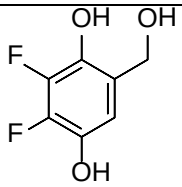 **4F**	**28**	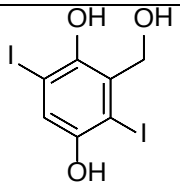 **6I**
2	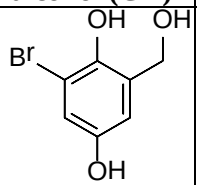 **1Br**	**11**	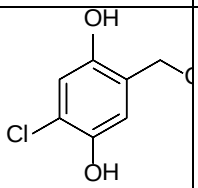 **3Cl**	**20**	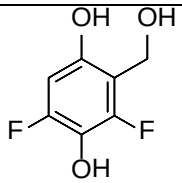 **5F**	**29**	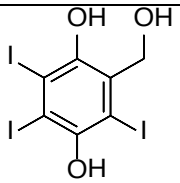 **7I**
3	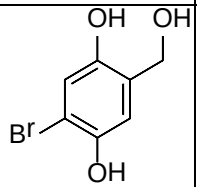 **2Br**	**12**	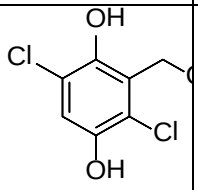 **4Cl**	**21**	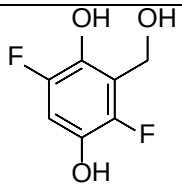 **6F**		
4	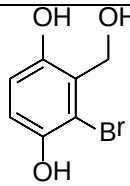 **3Br**	**13**	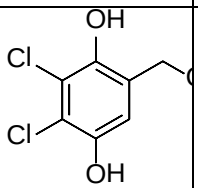 **5Cl**	**22**	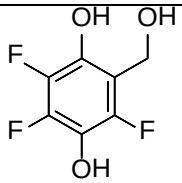 **7F**		
5	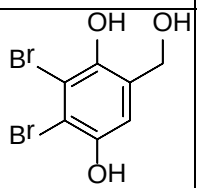 **4Br**	**14**	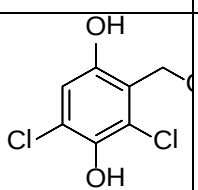 **6Cl**	**23**	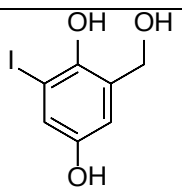 **1I**		

6	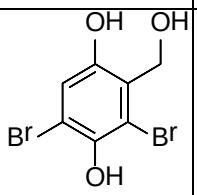 **5Br**	**15**	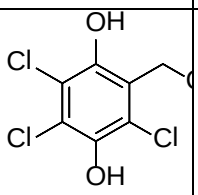 **7Cl**	**24**	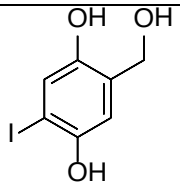 **2I**		
7	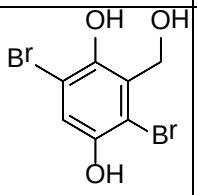 **6Br**	**16**	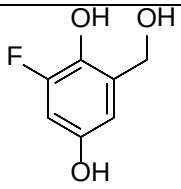 **1F**	**25**	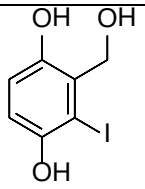 **3I**		
8	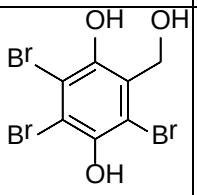 **7Br**	**17**	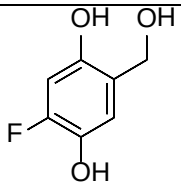 **2F**	**26**	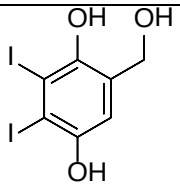 **4I**		
9	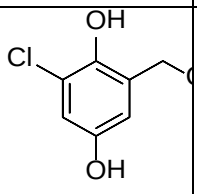 **1Cl**	**18**	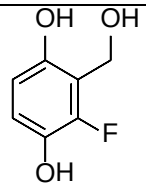 **3F**	**27**	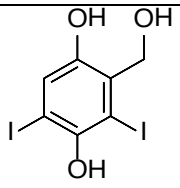 **5I**		

The compounds presented in **Table 2.2** correspond to the co-crystallized ligands resolved within their respective PDB entries. As these ligands are already deposited and annotated in the Protein Data Bank, their ability to induce or modulate their respective biological activities has been previously validated and reported with respect to their PDB ID's. Using the native-co-crystallized ligand as benchmark for comparing docking outcomes against these new ligands is crucial in computational docking studies for various reasons. Firstly, it serves as a validation tool for the docking methodology by assessing the accuracy in reproducing binding modes and affinities. Secondly, it aids in evaluating the binding site's suitability for different ligands, indicating its adaptability and consistency. Thirdly, it helps in identifying ligand similarities, facilitating ligand optimization and SAR studies. Additionally, it allows for the benchmarking of predicted affinities and provides context to the results

obtained for new ligands, thereby enhancing the reliability and interpretability of computational simulations for rational drug design and lead optimization [24].

Table 2.2: Native co-crystallized ligand with their PDB ID's

Sl. No	Compound code	Native Co-crystallized ligand	PDB ID
1	NL1	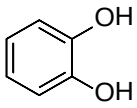 1,2-dihydroxybenzene	**3O4M**
2	NL2	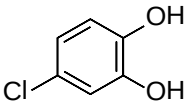 4-chlorobenzene-1,2-diol	**7DQL**
3	NL3	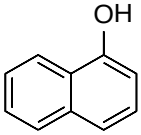 Naphthalen-1-ol	**7NNY**
4	NL4	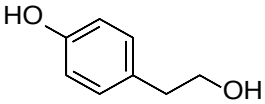 4-(2-hydroxyethyl)phenol	**7OFS**
5	NL5	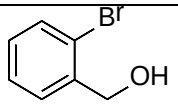 (2-bromophenyl)methanol)	**4YRE**

2.2.2. Target selection

To evaluate the compound's potential for interacting with diverse biological systems, five therapeutically relevant disease-associated targets were carefully selected, representing different pathways. DNA gyrase subunit B, the ATP-binding component of the DNA gyrase enzyme, is critical for bacterial DNA replication and transcription. Absent in humans, it introduces negative DNA supercoils essential for bacterial survival, making it a promising antibacterial drug target (PDB ID: 7DQL) [25].

Phospholipase A2 (PLA2) catalyzes the breakdown of membrane phospholipids, generating arachidonic acid and lysophospholipids, which serve as key precursors for inflammatory mediators. Blocking PLA2 activity can interrupt these pathways, presenting a promising strategy for managing inflammatory disorders (PDB ID: 3O4M) [26]. Histidyl-tRNA synthetase (HisRS) plays a crucial role in parasite viability by attaching histidine to its corresponding tRNA, an essential step in protein biosynthesis. Notably, its structural divergence from the human enzyme provides an opportunity to design selective inhibitors with minimal off-target effects (PDB ID: 4YRE) [27]. ArgF enzyme, part of the arginine biosynthesis pathway absent in humans, is vital for bacterial growth, rendering it an attractive target for selective anti-tuberculosis drug development (PDB ID: 7NNY) [28]. Furthermore, the SARS-CoV-2 papain-like protease (PLpro) is essential for viral polyprotein cleavage, replicase–transcriptase complex assembly, and suppression of host immune responses, making it an important antiviral target (PDB ID: 7OFS) [29].

2.2.3. Preparation of ligands

The 2D structures of the compounds under investigation, together with the native co-crystallized ligands were converted into their corresponding 3D conformations. These models were then subjected to energy minimization using the Molecular Mechanics 2 (MM2) force field implemented in ChemBio3D Ultra 12.0, ensuring optimal geometric stability. The refined 3D structures were subsequently exported in SYBYL MOL2 format, rendering them ready for molecular docking simulations.

2.2.4. Docking

Molegro Virtual Docker (MVD 6.0) was employed to perform the molecular docking studies [30], providing an integrated platform for predicting and visualizing the optimal binding poses of ligands within the active sites of their respective target proteins. The software's scoring functions, including MolDock and rerank scores, were utilized to estimate binding energies, while its interactive interface facilitated the analysis of ligand–receptor interactions and binding conformations. MVD utilizes an internal algorithm to identify potential binding sites within protein structures, typically generating multiple cavities based on concave regions capable of accommodating

ligands. Docking parameters were set with the MolDock score [GRID] and rerank score as the scoring function and a grid resolution of 0.30 Å. Binding site coordinates for each target were specified accordingly: PDB ID: 7DQL (Chain A) with a volume of 27.136 Å^3, centre X: 25.06, Y: 20.36, Z: 19.70, within a constraint of a radius of 12 Å; PDB ID: 3O4M (Chain A) having a volume of 120.32 Å^3, centre designated as X: 36.06, Y: -17.38, Z: 18.63 within a constraint of radius 12 Å; PDB ID: 4YRE (Chain A) having a volume of 345.088 Å^3, centre designated as X: 11.29, Y: -5.91, Z: 39.34 within a constraint of radius 12 Å; PDB ID: 7NNY (Chain A) having a volume of 210.94 Å^3, centre designated as X: -0.79, Y: -16.86, Z: -56.46 within a constraint of radius 12 Å; and PDB ID: 7OFS (Chain A) having a volume of 66.56 Å^3, centre designated as X: 42.59, Y: 6.76, Z: 35.50 within a constraint of radius 12 Å. The parameters were standardized across all PDB IDs, with a maximum iteration limit of 1,500 and a population size capped at 50. [31,32].

2.2.5. Density functional theory (DFT)

The top-ranking compounds from the docking study, together with the native co-crystallized ligands, were subsequently subjected to Density Functional Theory (DFT) calculations to evaluate their frontier molecular orbitals. The energies of the Highest Occupied Molecular Orbital (HOMO) and the Lowest Unoccupied Molecular Orbital (LUMO) were computed, as these parameters provide critical insights into the electronic distribution, chemical reactivity, and stability of the compounds. The Gaussian16 [33] suite of programs was employed to optimize the structures, and vibrational frequency analysis was performed to ensure that the structures were at their ground state and free from any imaginary frequency. LANL2DZ basis sets were utilized to optimize the structures. The CubeGen extension within GaussView6 [34] was employed to generate the HOMO and LUMO orbital's and other descriptors for all structures.

2.2.6. Drug likeness and ADME/T screening

The compounds further underwent drug-likeness screening *via* SwissADME [35] to ensure compliance with Lipinski, Veber, and Egan filters, which predict oral

bioavailability and pharmacokinetic suitability, and to verify that no PAINS (Pan-Assay Interference Compounds) alerts were present, reducing the likelihood of false-positive results in biological assays [36]. The ADME process involves absorption, distribution, metabolism, and excretion. In this phase, screening was conducted for skin permeation (log Kp), P-glycoprotein (P-gp) substrate, blood-brain barrier (BBB) permeability, and gastrointestinal (GI) absorption. SwissADME software was utilized for these screenings, employing standard values derived from validated experimental studies. Employing StopTox [37], which focuses on identifying hazard potentials from short exposure durations, compounds underwent toxicity screening. Canonical SMILES were used to generate the predictions across all the aforementioned software platforms.

2.3. Results and discussion

2.3.1. Docking

The docking results provided critical insights into the interaction between halogen-substituted compounds and their target proteins. Docking is a computational technique used to predict the binding mode and affinity of ligands (compounds) to their respective protein targets. The MolDock score serves as an initial scoring function to estimate the binding energy of ligands to proteins, whereas the rerank score provides a refined evaluation by re-scoring the best docking poses of the interaction. A higher negative MolDock score, in compliance with rerank score, indicates stronger binding between the ligand and the protein target. Compounds 7F, 4F, 1F, 7Br, and 7I exhibited MolDock and rerank scores against the target PDB IDs 7DQL, 3O4M, 4YRE, 7NNY, and 7OFS, respectively, as follows: 7F (−70.4628 kcal/mol MolDock; −65.6483 kcal/mol rerank), 4F (−71.4785 kcal/mol MolDock; −64.1709 kcal/mol rerank), 1F (−77.6122 kcal/mol MolDock; −66.2661 kcal/mol rerank), 7Br (−73.4757 kcal/mol MolDock; −61.6228 kcal/mol rerank), and 7I (−82.2235 kcal/mol MolDock; −68.1329 kcal/mol rerank) as shown in **Tables 2.3-2.7** respectively.

Table 2.3: Docking score of the compounds understudy against **PDB ID 7DQL**

Ligand	MolDock Score	[a]Rerank Score	[b]Interaction	[c]Internal	[d]HBond	[e]LE1	[f]LE3
7F	-70.4628	-65.6483	-93.4103	22.9476	-5.82177	-5.42021	-5.04987
5F	-72.5714	-65.6069	-90.3917	17.8203	-5.79773	-6.04762	-5.46724
5Cl	-74.6447	-63.7137	-86.9625	12.3178	-5.8212	-6.22039	-5.30947
6F	-70.519	-63.2919	-87.6199	17.1009	-1.28428	-5.87659	-5.27433
7Cl	-73.2493	-63.2623	-87.436	14.1867	-5.62176	-5.63456	-4.86633
3F	-72.7512	-62.9849	-84.0496	11.2984	-2.22558	-6.61375	-5.7259
1F	-73.0575	-62.7751	-84.7883	11.7309	-5.7945	-6.64159	-5.70683
4F	-70.4898	-62.7033	-87.7335	17.2437	-5.82175	-5.87415	-5.22527
6Cl	-70.9534	-62.5584	-84.3457	13.3923	-3.75978	-5.91279	-5.2132
6Br	-71.8858	-62.2944	-83.5337	11.6479	-3.77016	-5.99048	-5.1912
5Br	-74.4058	-62.1774	-84.8352	10.4294	-5.82015	-6.20049	-5.18145
6I	-73.8062	-62.1499	-82.6073	8.80105	-3.74881	-6.15052	-5.17916
3Cl	-71.9115	-61.7287	-81.9208	10.0093	-5.23017	-6.53741	-5.6117
2I	-71.0765	-60.8434	-81.2415	10.165	-3.96401	-6.4615	-5.53122
3Br	-71.6115	-60.6086	-81.1864	9.57486	-5.67337	-6.51014	-5.50988
3I	-71.1294	-59.9436	-79.8594	8.72994	-5.54653	-6.46631	-5.44942
7Br	-72.212	-59.9328	-85.4527	13.2406	-5.82151	-5.55477	-4.61022
1Cl	-68.4207	-59.6828	-79.8163	11.3955	-5.00679	-6.22007	-5.42571
1Br	-71.6571	-59.4586	-81.2776	9.62049	-5.82077	-6.51428	-5.40533
NL2	-67.3256	-59.2371	-76.4208	9.09519	-5.88406	-7.48063	-6.5819
Gentisyl alcohol (GA)	-66.8757	-59.1602	-74.1881	7.31239	-5.54791	-6.68757	-5.91602
2F	-66.0272	-58.6322	-81.2373	15.2102	-5.82168	-6.00247	-5.3302
7I	-72.0759	-58.5214	-81.5107	9.43479	-5.82197	-5.5443	-4.50164
4Br	-69.782	-58.2967	-81.3774	11.5953	-5.82134	-5.81517	-4.85806
1I	-70.0378	-57.8883	-79.6168	9.57899	-5.18438	-6.36707	-5.26257
2Cl	-66.7151	-57.5678	-79.1778	12.4627	-5.50462	-6.06501	-5.23344
4Cl	-68.8166	-57.3128	-82.8852	14.0685	-5.82159	-5.73472	-4.77607
4I	-69.0603	-57.1619	-77.968	8.90763	-5.74322	-5.75503	-4.76349

5I	-70.7795	-56.1653	-80.5975	9.81798	-5.61982	-5.89829	-4.68044
2Br	-65.59	-54.7224	-77.3757	11.7857	-5.8218	-5.96273	-4.97476

[a]The rerank score is a linear combination of E-inter (steric, Van der Waals, hydrogen bonding, electrostatic) between the ligand and the protein, and E-intra. (torsion, sp2-sp2, hydrogen bonding, Van der Waals, electrostatic) of the ligand weighted by pre-defined coefficients. [b]The total interaction energy between the pose and the protein (kJ/mol). [c]The internal energy of the pose. [d]Hydrogen bonding energy (kJ/mol). [e]Ligand efficiency 1: MolDock score divided by heavy atoms count. [f]Ligand efficiency 3: Rerank score divided by heavy atoms count.

Table 2.4: Docking score of the compounds understudy against **PDB ID 3O4M**

Ligand	**MolDock Score**	**[a]Rerank Score**	**[b]Interaction**	**[c]Internal**	**[d]HBond**	**[e]LE1**	**[f]LE3**
4F	-71.4785	-64.1709	-88.7104	17.2319	-8.83335	-5.95654	-5.34758
1F	-74.3025	-63.5966	-85.9808	11.6783	-9.37795	-6.75477	-5.78151
4Cl	-73.1747	-62.5083	-86.5354	13.3606	-9.15153	-6.09789	-5.20902
6I	-74.6296	-62.2742	-83.65	9.02039	-9.80542	-6.21913	-5.18952
1Cl	-73.6334	-62.12	-83.8841	10.2507	-9.13806	-6.69395	-5.64728
6Br	-71.8577	-61.8909	-83.7726	11.915	-10.3074	-5.98814	-5.15758
1Br	-73.5002	-61.7015	-83.1511	9.65095	-8.98585	-6.68184	-5.60923
1I	-73.042	-61.1701	-82.1135	9.07146	-10.5154	-6.64018	-5.56092
6Cl	-69.8085	-61.159	-83.3911	13.5827	-10.3157	-5.81737	-5.09659
4Br	-74.6667	-61.1359	-86.2614	11.5947	-10.2168	-6.22223	-5.09466
5I	-72.3453	-60.9883	-81.1236	8.77832	-9.04221	-6.02877	-5.08236
5Br	-70.9759	-60.9084	-80.9286	9.95271	-8.83748	-5.91466	-5.0757
5F	-69.2788	-60.8901	-86.7299	17.451	-9.65363	-5.77324	-5.07418
4I	-75.1495	-60.5237	-84.1262	8.97673	-10.1132	-6.26246	-5.04364
Gentisyl alcohol (GA)	-69.3514	-60.3189	-76.6234	7.27199	-9.80373	-6.93514	-6.03189
7F	-60.8021	-60.1955	-83.7583	22.9562	-10	-4.67709	-4.63042
7I	-71.4452	-59.2918	-79.8452	8.39995	-6.55376	-5.49579	-4.5609
7Br	-67.1677	-59.1331	-79.8604	12.6927	-7.33557	-5.16675	-4.5487
6F	-64.7639	-59.094	-82.0247	17.2609	-8.87449	-5.39699	-4.9245
3I	-69.1523	-58.7262	-77.9045	8.75227	-9.10798	-6.28657	-5.33875

5Cl	-72.1902	-58.5299	-84.1317	11.9415	-9.43259	-6.01585	-4.87749
3Br	-68.756	-58.3809	-77.876	9.11998	-6.06484	-6.25055	-5.30736
3Cl	-68.2285	-58.173	-77.6926	9.46415	-6.0461	-6.20259	-5.28846
7Cl	-65.391	-58.1658	-79.57	14.179	-10	-5.03008	-4.47429
3F	-66.0586	-57.7016	-77.4571	11.3984	-6.13598	-6.00533	-5.2456
2Cl	-65.2571	-57.4611	-77.6982	12.441	-7.38549	-5.93247	-5.22374
2Br	-67.0841	-57.3168	-78.3205	11.2364	-6.94903	-6.09856	-5.21062
2I	-66.792	-56.8794	-76.2332	9.44122	-7.67612	-6.072	-5.17086
2F	-64.6764	-55.3344	-80.5942	15.9178	-8.63567	-5.87968	-5.0304
NL1	-54.6871	-49.9012	-66.1336	11.4465	-6.57237	-6.83589	-6.23765

Table 2.5: Docking score of the compounds understudy against **PDB ID 4YRE**

Ligand	**MolDock Score**	**[a]Rerank Score**	**[b]Interaction**	**[c]Internal**	**[d]HBond**	**[e]LE1**	**[f]LE3**
1F	-77.6122	-66.2661	-89.0099	11.3978	-5.03434	-7.05565	-6.02419
2Cl	-78.2777	-66.1686	-90.8406	12.5629	-5.37026	-7.11616	-6.01533
7F	-71.7519	-65.7285	-94.6684	22.9165	-4.33829	-5.51938	-5.05604
2I	-77.6853	-65.3122	-87.3005	9.61515	-4.55721	-7.0623	-5.93747
6F	-72.4403	-65.2636	-91.695	19.2547	-5.13668	-6.03669	-5.43863
2Br	-75.8134	-64.9217	-87.215	11.4016	-4.54579	-6.89213	-5.90197
2F	-72.6898	-64.8635	-88.0412	15.3514	-4.48116	-6.60817	-5.89669
5F	-73.7169	-64.6726	-91.3466	17.6297	-4.44498	-6.14307	-5.38939
4Cl	-73.4337	-64.5737	-87.4786	14.0449	-5.07313	-6.11948	-5.38114
4F	-72.2288	-64.2278	-89.4661	17.2373	-4.94979	-6.01907	-5.35231
Gentisyl alcohol (GA)	-72.8163	-63.3134	-82.2533	9.43707	-3.92414	-7.28163	-6.33134
4Br	-73.1637	-63.1493	-84.6806	11.5169	-5.04334	-6.09698	-5.26244
5Cl	-75.9018	-62.8429	-87.8108	11.909	-5.24905	-6.32515	-5.23691
3F	-75.4836	-62.3833	-86.8031	11.3195	-5.2614	-6.86215	-5.67121
NL5	-72.8867	-61.6306	-80.7632	7.87651	-2.5	-8.09852	-6.84784
Cl1	-71.6956	-61.0823	-81.9332	10.2376	-4.46491	-6.51778	-5.55294
Cl6	-70.2211	-60.9664	-84.2217	14.0006	-5.07568	-5.85176	-5.08054
1I	-71.8691	-60.8673	-82.2845	10.4154	-7.4398	-6.53355	-5.53339

Cl3	-74.7331	-60.7047	-84.1731	9.44001	-5.35559	-6.79392	-5.51861
4I	-71.9176	-59.7697	-80.9195	9.00193	-6.96512	-5.99313	-4.98081
1Br	-70.4729	-59.6567	-80.0949	9.62201	-4.34495	-6.40663	-5.42334
5Br	-71.8011	-59.3654	-83.3061	11.505	-7.11429	-5.98342	-4.94712
6Br	-71.6027	-59.051	-83.0581	11.4554	-3.40566	-5.96689	-4.92091
7I	-69.8574	-58.3767	-78.2599	8.40244	-9.65896	-5.37365	-4.49051
5I	-73.9179	-58.1599	-82.6868	8.76887	-5.12291	-6.15983	-4.84665
Cl7	-66.8602	-58.0553	-84.3215	17.4614	-4.78077	-5.14309	-4.46579
7Br	-68.6993	-58.0458	-81.4227	12.7234	-11.188	-5.28456	-4.46506
3Br	-70.9891	-58.0013	-81.6089	10.6198	-6.9452	-6.45355	-5.27285
3I	-70.7326	-57.7763	-79.4703	8.73773	-3.74692	-6.43024	-5.25239
6I	-72.9806	-57.7031	-81.5924	8.61182	-3.4	-6.08172	-4.80859

Table 2.6: Docking score of the compounds understudy against **PDB ID 7NNY**

Ligand	**MolDock Score**	**[a]Rerank Score**	**[b]Interaction**	**[c]Internal**	**[d]HBond**	**[e]LE1**	**[f]LE3**
7Br	-73.4757	-61.6228	-86.9809	13.5052	-9.41049	-5.65198	-4.74021
NL3	-69.036	-61.5524	-82.3051	13.2691	-2.5	-6.276	-5.59567
7Cl	-72.2875	-60.5637	-86.6541	14.3666	-9.305	-5.56058	-4.65875
4F	-68.7423	-60.5387	-85.9525	17.2102	-9.17913	-5.72852	-5.04489
7F	-64.6036	-60.3864	-90.0297	25.4261	-8.65865	-4.96951	-4.6451
7I	-74.2003	-59.7522	-83.2668	9.0665	-8.98444	-5.70771	-4.59632
6F	-68.7985	-59.7145	-85.926	17.1275	-9.30967	-5.73321	-4.97621
Gentisyl alcohol (GA)	-67.5666	-59.2873	-74.8421	7.2755	-8.24933	-6.75666	-5.92873
4Cl	-70.1272	-59.2126	-83.4985	13.3713	-9.02367	-5.84393	-4.93438
5F	-65.4319	-58.9731	-82.9228	17.4909	-6.9353	-5.45266	-4.91443
1F	-67.8203	-58.4701	-79.4955	11.6753	-7.3217	-6.16548	-5.31546
2Br	-66.6925	-58.0626	-77.8897	11.1972	-9.09996	-6.06295	-5.27842
1Cl	-68.2937	-58.0237	-78.5227	10.229	-7.03368	-6.20852	-5.27488
Cl6	-69.05	-58.0089	-83.1496	14.0996	-9.29885	-5.75416	-4.83408
4I	-71.3	-57.9545	-79.7675	8.46751	-8.88519	-5.94167	-4.82954
6Br	-69.8278	-57.9283	-81.563	11.7352	-9.37385	-5.81898	-4.82736

1Br	-68.5094	-57.9051	-78.1439	9.63444	-6.96236	-6.22813	-5.2641
2I	-68.2615	-57.8421	-77.0867	8.82522	-8.83096	-6.20559	-5.25837
3F	-69.5895	-57.4601	-81.3371	11.7477	-9.28316	-6.32631	-5.22364
4Br	-68.5305	-57.3763	-80.4653	11.9348	-9.31339	-5.71087	-4.78136
5Br	-67.2605	-56.9265	-77.5072	10.2467	-7.71109	-5.60504	-4.74388
1I	-67.6619	-56.8633	-76.749	9.08711	-6.8827	-6.15108	-5.16939
2Cl	-64.8843	-56.6145	-77.8605	12.9762	-10.5972	-5.89858	-5.14677
3Cl	-70.244	-56.4473	-80.1207	9.87673	-9.28169	-6.38582	-5.13157
3Br	-69.5534	-55.9859	-79.0206	9.46721	-9.17558	-6.32303	-5.08963
2F	-63.7513	-55.6793	-78.9572	15.2059	-9.77021	-5.79557	-5.06175
5Cl	-65.4088	-55.0807	-77.6217	12.2128	-8.94345	-5.45074	-4.59006
6I	-67.9268	-54.6134	-75.9178	7.99101	-5.08904	-5.66057	-4.55112
5I	-66.0541	-53.8953	-75.1481	9.09401	-7.61317	-5.50451	-4.49127
3I	-63.4395	-52.4566	-74.7244	11.2849	-7.71831	-5.76723	-4.76878

Table 2.7: Docking score of the compounds understudy against **PDB ID 7OFS**

Ligand	**MolDock Score**	**[a]Rerank Score**	**[b]Interaction**	**[c]Internal**	**[d]HBond**	**[e]LE1**	**[f]LE3**
7 I	-82.2235	-68.1329	-91.7848	9.56132	-9.29862	-6.32489	-5.24099
NL4	-78.9391	-67.9609	-85.1029	6.16384	-4.85818	-7.89391	-6.79609
5Cl	-74.4179	-67.8277	-91.9548	17.5368	-10.0593	-6.20149	-5.6523
4F	-75.564	-67.7576	-92.7712	17.2071	-8.21206	-6.297	-5.64647
7Br	-78.6958	-67.4568	-91.6596	12.9639	-8.58233	-6.05352	-5.18898
7Cl	-77.4249	-66.8503	-91.579	14.154	-8.1243	-5.95576	-5.14233
5F	-72.7737	-66.8458	-90.4026	17.6289	-4.04249	-6.06448	-5.57049
4Br	-77.1484	-66.5823	-88.8715	11.7231	-10.2082	-6.42903	-5.54853
5Br	-78.2318	-66.3815	-88.2782	10.0464	-4.27472	-6.51932	-5.5318
6I	-80.4923	-66.1831	-88.4531	7.96071	-7.60343	-6.7077	-5.51526
4I	-80.0177	-66.1625	-88.2878	8.27009	-7.98051	-6.66815	-5.51354
7F	-68.5016	-65.7634	-91.8764	23.3748	-7.39549	-5.26935	-5.05872
6Br	-78.2992	-65.5591	-89.6193	11.32	-7.65224	-6.52494	-5.46326
1F	-76.5402	-65.2239	-88.2081	11.668	-8.47902	-6.9582	-5.92945

5I	-76.3179	-65.1968	-88.2919	11.974	-8.93125	-6.35982	-5.43306
1Cl	-76.5867	-64.4931	-86.8185	10.2318	-8.6776	-6.96243	-5.86301
4Cl	-73.3926	-64.0162	-86.6971	13.3046	-8.12743	-6.11605	-5.33469
2F	-70.5651	-63.7715	-85.8142	15.249	-4.91977	-6.41501	-5.79741
1Br	-76.0694	-63.7132	-85.6891	9.61969	-8.74588	-6.9154	-5.79211
6F	-73.4738	-63.5666	-90.5982	17.1244	-4.95443	-6.12282	-5.29721
3F	-73.5263	-63.3952	-85.2737	11.7474	-4.4313	-6.68421	-5.7632
6Cl	-72.3967	-63.2652	-85.7224	13.3257	-9.39264	-6.03306	-5.2721
Gentisyl alcohol (GA)	-72.0798	-63.2432	-79.3546	7.27477	-5.48439	-7.20798	-6.32432
3Cl	-73.9985	-62.8006	-83.9689	9.97043	-2.8086	-6.72713	-5.70915
3I	-73.6983	-62.7672	-83.7807	10.0823	-3.85488	-6.69985	-5.70611
3Br	-74.1524	-62.6513	-83.6095	9.45709	-3.97088	-6.74113	-5.69557
1I	-74.3596	-62.4431	-83.3816	9.022	-10.1454	-6.75996	-5.67664
2I	-74.7751	-62.2444	-83.5592	8.78404	-8.94574	-6.79774	-5.65858
2Br	-72.0048	-62.0882	-83.2212	11.2165	-5.16072	-6.54589	-5.64438
2Cl	-71.1398	-62.0512	-83.5597	12.4198	-5.15843	-6.46726	-5.64102

Emphasis was placed primarily on the rerank score, followed by the MolDock score, as these provide refined estimates of binding energy after identifying the optimal poses and re-scoring the interactions. The markedly negative rerank values observed for these compounds indicate highly stable docked conformations and a strong binding propensity toward their respective targets. This trend was observed for the aforementioned compounds against their designated targets of interest, thereby establishing them as the top candidates. Furthermore, upon comparative analysis with the parent compound gentisyl alcohol and the native co-crystallized ligand, these five compounds demonstrated notably enhanced MolDock and rerank scores. This highlights the importance of halogen substitutions in modulating the pharmacological properties of the compounds, potentially enhancing their therapeutic efficacy, suggesting that the halogenated derivatives of gentisyl alcohol, especially those bearing halogen substitutions, possess significant potential as antibacterial, anti-

inflammatory, anti-parasitic, anti-tubercular and antiviral agents, showcasing a broad spectrum of bioactivity.

2.3.2. Interaction study of the docked compounds

The analysis of interactions between the docked ligands and their respective targets offers valuable insights into the nature and specificity of molecular recognition. Such studies are essential on how ligands orient, position, and stabilize within the binding site and interact through forces such as hydrogen bonding. In the present work, the interaction analysis focused on determining whether the studied ligands share key residues and binding patterns with the native co-crystallized ligand, thereby suggesting potential similarities in binding mode and, consequently, biological activity.

Figure 2.1 (A-C) depicts the key interacting residues for PDB ID 7DQL, showing that compound 7F shares Asp73, Thr165, and Val71 with the native co-crystallized ligand (NL2). Asp73, an acidic polar residue, forms hydrogen bonds that facilitate stable polar interactions. Thr165, a polar uncharged residue, can establish directional hydrogen bonds through its hydroxyl side chain, thereby contributing to ligand stabilization within the binding site. Val71, although generally nonpolar, participates in hydrogen bonding via its backbone atoms, underscoring the role of main-chain groups in ligand recognition. Additionally, 7F shares Asp73 and Val71 with gentisyl alcohol (GA), highlighting conserved hydrogen-bonding contacts. This overlap suggests that 7F may adopt a binding orientation similar to both NL2 and GA, potentially conferring comparable or perhaps better stability and biological activity.

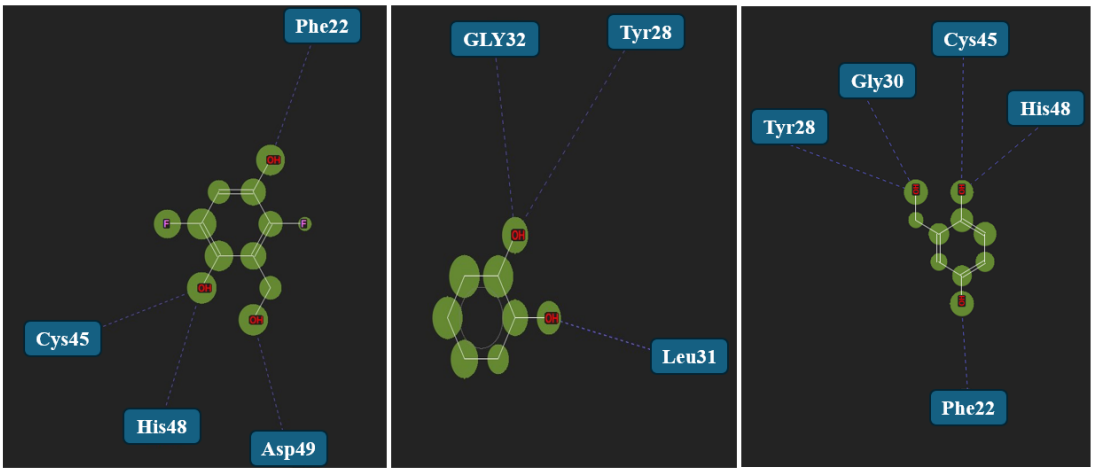

Figure 2.1: Mode of interaction between the ligand and the target (PDB ID: 7DQL)

Figure 2.2 (A-C) illustrates the interacting residues for PDB ID 3O4M, showing that compound 4F does not share any identical contacts with the native co-crystallized ligand (NL1). Instead, it forms four hydrogen bonds with residues such as Phe22, His48, and Cys45, which are also engaged with gentisyl alcohol (GA). Phe22 through hydrogen bonding aids ligand stabilization. His48, a polar residue with an imidazole side chain, can serve as both donor and acceptor, supporting flexible yet stable interactions. Cys45, containing a thiol group, further anchors the ligand *via* hydrogen bonding. These interactions depicted indicates that 4F adopts a distinct binding mode from NL1 but similar to the parent GA and achieving stability through its unique hydrogen-bonding network.

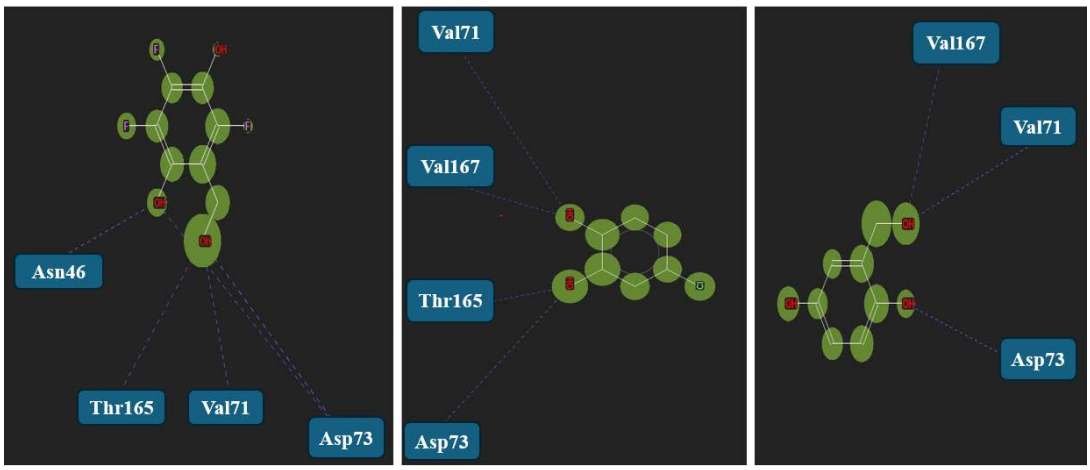

Figure 2.2: Mode of interaction between the ligand and the target (PDB ID: 3O4M)

Figure 2.3 (A-C), corresponding to PDB ID 4YRE, shows that 1F does not share any interacting residues with the native co-crystallized ligand (NL5). However, it forms a hydrogen bond with Trp155, an aromatic residue whose indole side chain can participate in hydrogen bonding, enhancing ligand stability within the binding site. This residue is also engaged by gentisyl alcohol (GA), suggesting a partial similarity in binding mode between 1F and GA, as illustrated.

Figure 2.3: Mode of interaction between the ligand and the target (PDB ID: 4YRE)

Figure 2.4 (A-C) presents the interacting residues for PDB ID 7NNY, where 7Br and the native co-crystallized ligand (NL3) share Gln231. Additionally, 7Br shares Asp156 and Asn160 with gentisyl alcohol (GA). Asp156, a negatively charged residue, and Asn160, a polar uncharged residue, both participate in hydrogen bonding, contributing to the ligand's stabilization within the binding pocket.

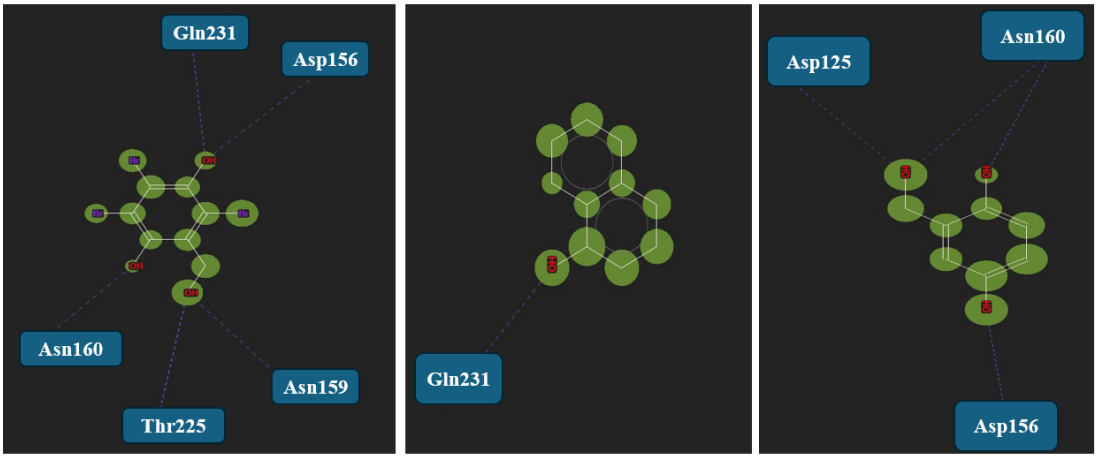

A (7Br) **A (NL3)** **C (GA)**

Figure 2.4: Mode of interaction between the ligand and the target (PDB ID: 7NNY)

Figure 2.5 (A-C) for PDB ID 7OFS shows that 7I and the native co-crystallized ligand (NL4) both interact with Asp76. Additionally, 7I shares Asp76 and Asn160 with gentisyl alcohol (GA). Asp76, a negatively charged residue, and Asn160, a polar uncharged residue capable of forming hydrogen bonds, which can enhance the stability and proper orientation of the ligand within the binding site, thereby contributing to its inhibitory effectiveness.

A(7I) **B(NL4)** **C(GA)**

Figure 2.5: Molecular Interaction Between the ligand inhibitor and target PDB 7OFS

Overall, from all the interactions observed in this study, it can be inferred that these intercations with key residues play a crucial role in stabilizing the ligand within the binding pocket. The overlap between the test ligands and other reference ligands (such as the co-crystallized ligands or GA) not only reinforces the structural importance of these residues but also suggests that ligands engaging them are more likely to exhibit comparable or even enhanced inhibitory effects due to similar modes of binding ensuring effective contact and likely to enhance the ligand's inhibitory potential which are key factors in drug design and optimization [38].

2.3.3. Density functional theory (DFT)

The HOMO–LUMO energy gap is a critical parameter in drug design and optimization. A smaller gap indicates higher molecular reactivity, which can be advantageous for facilitating strong target binding or rapid biological interaction. Conversely, a larger gap reflects greater molecular stability, which may help maintain therapeutic activity over extended periods and reduce susceptibility to degradation or metabolic breakdown [39].Specifically, as shown in Table 2.8 and illustrated in **Figure 2.6**, the order of the HOMO-LUMO energy gap (7I > 7Br > NL3 > 4F > 7F > 1F > NL4 > NL1 > NL2 > NL5) suggests that 7I may exhibit the highest reactivity and stability, while NL5, characterized by a larger HOMO-LUMO gap, could possess lower reactivity and stability compared to the other compounds. This finding is significant as it provides insights into the potential chemical reactivity and stability of the compounds. These findings offer valuable guidance for further exploration and optimization of the compounds for therapeutic use.

Table 2.8: Calculated HOMO-LUMO energy gap *via* DFT

COMPOUND	HOMO	LUMO	HOMO-LUMO (in H)	HOMO-LUMO (in eV)
NL 1	-0.22123	-0.01054	0.21069	5.733169866
NL 2	-0.23289	-0.02661	0.20628	5.613167592
NL 3	-0.20976	-0.04053	0.16923	4.604985222
NL 4	-0.22577	-0.01512	0.21065	5.73208141
NL 5	-0.25902	-0.03428	0.22474	6.115490036
1F	-0.22171	-0.01917	0.20254	5.511396956
4F	-0.23665	-0.04193	0.19472	5.298603808
7F	-0.24834	-0.04778	0.20056	5.457518384

7Br	-0.23711	-0.07139	0.16572	4.509473208
7I	-0.23048	-0.08919	0.14129	3.844698706

7I may be particularly well-suited for applications where rapid molecular interactions with the biological target are beneficial, potentially enhancing its inhibitory potency. 7Br, with a slightly larger gap than 7I, also shows a good balance between reactivity and stability, indicating it may combine strong binding potential with moderate resilience against unwanted side reactions.4F occupies a mid-range position, suggesting moderate reactivity and stability a balance that can be advantageous in sustaining activity over time without excessive degradation or off-target interactions. 7F, ranking just below 4F, exhibits slightly reduced reactivity, which could translate into greater molecular stability but may require stronger interaction-driving forces to achieve optimal inhibition. 1F, positioned lower in the reactivity ranking, may be the most stable among these five, which could be advantageous for long-term drug efficacy and lower side-effect risks, though possibly at the expense of slower target engagement.

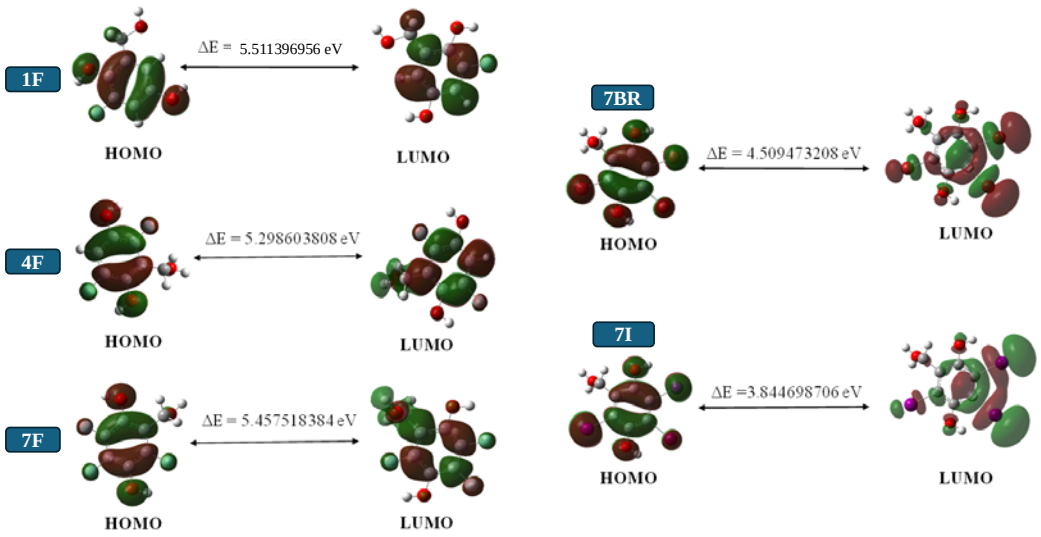

Figure 2.6: Cartoon illustration of the HOMO-LUMO gap of 1F, 4F, 7F, 7Br and 7I

Overall, the HOMO–LUMO analysis indicates that 7I and 7Br are potentially more reactive and suited for fast, potent inhibition, while 4F and 7F strike a balance between stability and activity, and 1F may lean more toward stability, making it suitable for applications where prolonged activity and minimal chemical degradation are critical.

These electronic properties, when combined with docking and interaction profile data, provide a more holistic view of each compound's suitability for further therapeutic development.

2.3.4. Druglikeness and ADME/T screening

According to the druglikeness rule of five, an orally active drug should not violate more than one of the implemented criteria. Upon druglikeness screening, it is evident that, except for the compound 7I, which exhibits one violation for the Lipinski rule, all other compounds under study demonstrate zero violations, indicating their druglike characteristics and are likely to have suitable pharmacokinetic profiles for oral administration. In ADME screening, all compounds exhibit high gastrointestinal absorption, a favourable trait. All the compounds are predicted to cross the blood-brain barrier, indicating limited penetration into the central nervous system. Furthermore, the absence of substrate activity for P-glycoprotein among these compounds may lower the risk of drug resistance and improve their therapeutic potential. Furthermore, their moderate skin permeability, reflected by log KP values between –5.51 and –7.45 cm/s, suggests suitability for transdermal absorption or balanced skin penetration. In toxicity screening, the top hit compounds 1F, 4F, 7F, 7I, and 7Br, along with the parent compound gentisyl alcohol, showed negative results for acute inhalation toxicity, eye irritation, and skin irritation. These findings suggest a favorable safety profile, indicating that these compounds are unlikely to cause immediate toxic or irritant effects upon exposure, which supports their potential for safe therapeutic use. In contrast, the native co-crystallized compounds display at least one toxic liability. Overall, the top hit compounds exhibit favorable drug-like properties, along with well-characterized pharmacokinetic and toxicity profiles, as demonstrated by the drug-likeness and ADME/T screening results summarized in **Table 2.9**.

Table 2.9: Druglikness and ADME/ screening *via* SwissADME and StopTox

Compound ID	ADME SCREENING				DRUGLIKENESS SCREENING				TOXICITY		
	GI absorption	BBB permeant	P-gp substrate	Log K_p (skin permeation) (cm/s)	Lipinski	Veber	Egan	Bioavailability Score	Acute Inhalation Toxicity	Eye Irritation and Corrosion	Skin Irritation and Corrosion
GA	High	No	No	-6.68	Yes; 0 violation	Yes	Yes	0.55	Non Toxic	Non Toxic	Negative
1F	High	Yes	No	-6.5	Yes; 0 violation	Yes	Yes	0.55	Non Toxic	Non Toxic	Negative
4F	High	Yes	No	-6.61	Yes; 0 violation	Yes	Yes	0.55	Non Toxic	Non Toxic	Negative
7F	High	Yes	No	-6.65	Yes; 0 violation	Yes	Yes	0.55	Non Toxic	Non Toxic	Negative
7I	High	Yes	No	-7.45	Yes; 1 violation: MW >500	Yes	Yes	0.55	Non Toxic	Non Toxic	Negative
7Br	High	Yes	No	-6.5	Yes; 0 violation	Yes	Yes	0.55	Non Toxic	Non Toxic	Negative
NL1	High	Yes	No	-6.35	Yes; 0 violation	Yes	Yes	0.55	Toxic	Toxic	Negative
NL2	High	Yes	No	-5.51	Yes; 0 violation	Yes	Yes	0.55	Toxic	Toxic	Negative
NL3	High	Yes	No	-5.16	Yes; 0 violation	Yes	Yes	0.55	Non Toxic	Toxic	Negative
NL4	High	Yes	No	-6.84	Yes; 0 violation	Yes	Yes	0.55	Non Toxic	Toxic	Positive

NL5	High	Yes	No	-6.57	Yes; 0 violation	Yes	Yes	0.55	Toxic	Toxic	Positive

2.4. Conclusion

- Halogenation is a valuable strategy in drug discovery, as the introduction of halogen atoms can enhance lipophilicity, membrane permeability, metabolic stability, and binding affinity, often leading to improved potency, selectivity, and broader biological activity. Genistyl alcohol, known for its diverse bioactivity, has low natural occurrence and limited synthetic availability, highlighting the need for new, more effective variants that may surpass the parent compound.
- The present study was designed to develop halogenated variants of gentisyl alcohol by incorporating F, Cl, Br, and I atoms, with the aim of exploring their antibacterial, anti-tubercular, antiviral, anti-parasitic, and anti-inflammatory potential through computational approaches, thereby assessing their feasibility and therapeutic prospects.
- Our analysis demonstrated that compounds 7Br, 7I, 1F, 4F and 7I exhibited superior docking scores compared to gentisyl alcohol and their respective co-crystallized ligands, indicating enhanced predicted binding energies toward the selected targets, suggestive of stronger inhibitory potential.

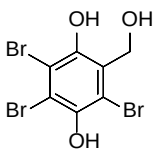

7Br

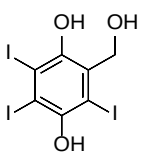

7I

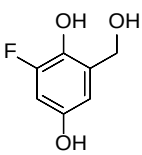

1F

4F

7F

- Furthermore, DFT analysis revealed that these compounds exhibited favorable stability and reactivity profiles compared to the native ligands, suggesting a balanced chemical and electronic responsiveness that could enhance their overall pharmacological potential. These compounds also exhibited favorable drug-like

properties, complying with Lipinski's Rule of Five and showing promising absorption, distribution, metabolism, excretion, and toxicity (ADME/T) profiles, further supporting their potential as viable therapeutic candidates.

- In summary, the identified compounds show promise for further exploration and optimization in therapeutic applications, providing a strong theoretical foundation for the rational design of next-generation drug entities. Continued investigation may yield novel therapeutic candidates with broad-spectrum clinical applicability, particularly in addressing antimicrobial resistance and inflammation-related disorders.

References

[1] "Global health estimates." Available: https://www.who.int/data/global-health-estimates/

[2] A. Wilder-Smith and S. Osman, "Public health emergencies of international concern: a historic overview," *Journal of Travel Medicine*, vol. 27, no. 8, Dec. 2020, doi: 10.1093/jtm/taaa227. Available: https://doi.org/10.1093/jtm/taaa227

[3] World Health Organization: WHO, "Antimicrobial resistance," Nov. 21, 2023. Available: https://www.who.int/news-room/fact-sheets/detail/antimicrobial-resistance

[4] D. Furman *et al.*, "Expression of specific inflammasome gene modules stratifies older individuals into two extreme clinical and immunological states," *Nature Medicine*, vol. 23, no. 2, pp. 174–184, Jan. 2017, doi: 10.1038/nm.4267. Available: https://doi.org/10.1038/nm.4267

[5] D. Furman *et al.*, "Chronic inflammation in the etiology of disease across the life span," *Nature Medicine*, vol. 25, no. 12, pp. 1822–1832, Dec. 2019, doi: 10.1038/s41591-019-0675-0. Available: https://doi.org/10.1038/s41591-019-0675-0

[6] R. J. Mumper, C. G. Smith, and J. T. O'Donnell, "The Process of New Drug Discovery and Development, 2nd edition," *Drug Development and Industrial Pharmacy*, vol. 34, no. 11, p. 1267, Jan. 2008, doi: 10.1080/03639040802071844. Available: https://doi.org/10.1080/03639040802071844

[7] T. Usha, D. Shanmugarajan, A. K. Goyal, C. S. Kumar, and S. K. Middha, "Recent updates on computer-aided drug discovery: Time for a paradigm shift," *Current Topics in Medicinal Chemistry*, vol. 17, no. 30, pp. 3296–3307, Jan. 2018, doi: 10.2174/1568026618666180101163651. Available: https://doi.org/10.2174/1568026618666180101163651

[8] N. Dhingra, "Computer-Aided Drug Design and Development: an Integrated approach," in *IntechOpen eBooks*, 2022. doi: 10.5772/intechopen.105003. Available: https://doi.org/10.5772/intechopen.105003

[9] N. E. Kolomiets, "HALOGENATED PHENOLIC COMPOUNDS OF NATURAL ORIGIN CONSTITUTE a RARE MINOR GROUP OF SUBSTANCES (A

REVIEW),” *Chemistry of Plant Raw Material*, no. 4, pp. 24–31, Nov. 2024, doi: 10.14258/jcprm.20240413424. Available: https://doi.org/10.14258/jcprm.20240413424

[10] W. Zhao, X. Feng, S. Ban, W. Lin, and Q. Li, “Synthesis and biological activity of halophenols as potent antioxidant and cytoprotective agents,” *Bioorganic & Medicinal Chemistry Letters*, vol. 20, no. 14, pp. 4132–4134, Jun. 2010, doi: 10.1016/j.bmcl.2010.05.068. Available: https://doi.org/10.1016/j.bmcl.2010.05.068

[11] F. Zheng, S. Ban, X. Feng, C. Zhao, G. Du, and Q. Li, “Synthesis and biological activities of new halophenols,” *Medicinal Chemistry*, vol. 9, no. 2, pp. 303–311, Jan. 2013, doi: 10.2174/1573406411309020013. Available: https://doi.org/10.2174/1573406411309020013

[12] N. Öztaşkın, Y. Çetinkaya, P. Taslimi, S. Göksu, and İ. Gülçin, “Antioxidant and acetylcholinesterase inhibition properties of novel bromophenol derivatives,” *Bioorganic Chemistry*, vol. 60, pp. 49–57, Apr. 2015, doi: 10.1016/j.bioorg.2015.04.006. Available: https://doi.org/10.1016/j.bioorg.2015.04.006

[13] B. P. Bandgar *et al.*, “Synthesis and biological evaluation of nitrogen-containing benzophenone analogues as TNF-α and IL-6 inhibitors with antioxidant activity,” *Bioorganic & Medicinal Chemistry Letters*, vol. 20, no. 7, pp. 2292–2296, Feb. 2010, doi: 10.1016/j.bmcl.2010.02.001. Available: https://doi.org/10.1016/j.bmcl.2010.02.001

[14] G. a. E. Shoubaky, M. M. Abdel-Daim, M. H. Mansour, and E. A. Salem, “Isolation and Identification of a Flavone Apigenin from Marine Red AlgaAcanthophora spiciferawith Antinociceptive and Anti-Inflammatory Activities,” *Journal of Experimental Neuroscience*, vol. 10, Jan. 2016, doi: 10.4137/jen.s25096. Available: https://doi.org/10.4137/jen.s25096

[15] L. Chen, Y. Fang, T. Zhu, Q. Gu, and W. Zhu, “Gentisyl Alcohol Derivatives from the Marine-Derived Fungus Penicillium terrestre,” *Journal of Natural Products*, vol. 71, no. 1, pp. 66–70, Dec. 2007, doi: 10.1021/np070421v. Available: https://doi.org/10.1021/np070421v

[16] S. Gupta, S. Kaul, B. Singh, R. A. Vishwakarma, and M. K. Dhar, "Production of Gentisyl Alcohol from Phoma herbarum Endophytic in Curcuma longa L. and Its Antagonistic Activity Towards Leaf Spot Pathogen Colletotrichum gloeosporioides," *Applied Biochemistry and Biotechnology*, vol. 180, no. 6, pp. 1093–1109, Jun. 2016, doi: 10.1007/s12010-016-2154-0. Available: https://doi.org/10.1007/s12010-016-2154-0

[17] H.-S. Wang, H.-J. Li, L.-F. Wang, Z.-L. Shen, and Y.-C. Wu, "Regioselective synthesis of gentisyl alcohol-type marine natural products," *Natural Product Research*, vol. 33, no. 13, pp. 1891–1896, May 2018, doi: 10.1080/14786419.2018.1478831. Available: https://doi.org/10.1080/14786419.2018.1478831

[18] M. Hernandes, S. M. Cavalcanti, D. R. Moreira, W. De Azevedo Junior, and A. C. Leite, "Halogen atoms in the Modern Medicinal Chemistry: Hints for the drug design," *Current Drug Targets*, vol. 11, no. 3, pp. 303–314, Feb. 2010, doi: 10.2174/138945010790711996. Available: https://doi.org/10.2174/138945010790711996

[19] Z. Xu, Z. Yang, Y. Liu, Y. Lu, K. Chen, and W. Zhu, "Halogen Bond: Its Role beyond Drug–Target Binding Affinity for Drug Discovery and Development," *Journal of Chemical Information and Modeling*, vol. 54, no. 1, pp. 69–78, Dec. 2013, doi: 10.1021/ci400539q. Available: https://doi.org/10.1021/ci400539q

[20] Y. Lu, Y. Liu, Z. Xu, H. Li, H. Liu, and W. Zhu, "Halogen bonding for rational drug design and new drug discovery," *Expert Opinion on Drug Discovery*, vol. 7, no. 5, pp. 375–383, Mar. 2012, doi: 10.1517/17460441.2012.678829. Available: https://doi.org/10.1517/17460441.2012.678829

[21] S. Jiang *et al.*, "The important role of halogen bond in substrate selectivity of enzymatic catalysis," *Scientific Reports*, vol. 6, no. 1, Oct. 2016, doi: 10.1038/srep34750. Available: https://doi.org/10.1038/srep34750

[22] M. C. Ford and P. S. Ho, "Computational tools to model halogen bonds in medicinal chemistry," *Journal of Medicinal Chemistry*, vol. 59, no. 5, pp. 1655–1670, Oct. 2015, doi: 10.1021/acs.jmedchem.5b00997. Available: https://doi.org/10.1021/acs.jmedchem.5b00997

[23] R. Wilcken, M. O. Zimmermann, A. Lange, A. C. Joerger, and F. M. Boeckler, "Principles and applications of halogen bonding in medicinal chemistry and chemical biology," *Journal of Medicinal Chemistry*, vol. 56, no. 4, pp. 1363–1388, Nov. 2012, doi: 10.1021/jm3012068. Available: https://doi.org/10.1021/jm3012068

[24] Z. U. Haq, R. Uddin, L. K. Wai, A. Wadood, and N. H. Lajis, "Docking and 3D-QSAR modeling of cyclin-dependent kinase 5/p25 inhibitors," *Journal of Molecular Modeling*, vol. 17, no. 5, pp. 1149–1161, Aug. 2010, doi: 10.1007/s00894-010-0817-2. Available: https://doi.org/10.1007/s00894-010-0817-2

[25] Y. Yu *et al.*, "Identification of new building blocks by fragment screening for discovering GyrB inhibitors," *Bioorganic Chemistry*, vol. 114, p. 105040, May 2021, doi: 10.1016/j.bioorg.2021.105040. Available: https://doi.org/10.1016/j.bioorg.2021.105040

[26] K. V. Dileep, I. Tintu, P. K. Mandal, P. Karthe, M. Haridas, and C. Sadasivan, "Binding to PLA2 may contribute to the Anti-Inflammatory activity of catechol," *Chemical Biology & Drug Design*, vol. 79, no. 1, pp. 143–147, Oct. 2011, doi: 10.1111/j.1747-0285.2011.01258.x. Available: https://doi.org/10.1111/j.1747-0285.2011.01258.x

[27] C. Y. Koh *et al.*, "A binding hotspot inTrypanosoma cruzihistidyl-tRNA synthetase revealed by fragment-based crystallographic cocktail screens," *Acta Crystallographica Section D Biological Crystallography*, vol. 71, no. 8, pp. 1684–1698, Jul. 2015, doi: 10.1107/s1399004715007683. Available: https://doi.org/10.1107/s1399004715007683

[28] P. Gupta *et al.*, "A fragment-based approach to assess the ligandability of ArgB, ArgC, ArgD and ArgF in the L-arginine biosynthetic pathway of Mycobacterium tuberculosis," *Computational and Structural Biotechnology Journal*, vol. 19, pp. 3491–3506, Jan. 2021, doi: 10.1016/j.csbj.2021.06.006. Available: https://doi.org/10.1016/j.csbj.2021.06.006

[29] V. Srinivasan *et al.*, "Antiviral activity of natural phenolic compounds in complex at an allosteric site of SARS-CoV-2 papain-like protease," *Communications*

Biology, vol. 5, no. 1, Aug. 2022, doi: 10.1038/s42003-022-03737-7. Available: https://doi.org/10.1038/s42003-022-03737-7

[30] *Docking screens for drug discovery*. 2019. doi: 10.1007/978-1-4939-9752-7. Available: https://doi.org/10.1007/978-1-4939-9752-7

[31] W. L. M. Alencar, T. Da Silva Arouche, A. F. G. Neto, T. De Castro Ramalho, R. N. De Carvalho Júnior, and A. M. De Jesus Chaves Neto, "Publisher Correction: Interactions of Co, Cu, and non-metal phthalocyanines with external structures of SARS-CoV-2 using docking and molecular dynamics," *Scientific Reports*, vol. 12, no. 1, Mar. 2022, doi: 10.1038/s41598-022-08312-y. Available: https://doi.org/10.1038/s41598-022-08312-y

[32] V. R. Shah, J. D. Bhaliya, and G. M. Patel, "In silico approach: docking study of oxindole derivatives against the main protease of COVID-19 and its comparison with existing therapeutic agents," *Journal of Basic and Clinical Physiology and Pharmacology*, vol. 32, no. 3, pp. 197–214, Feb. 2021, doi: 10.1515/jbcpp-2020-0262. Available: https://doi.org/10.1515/jbcpp-2020-0262

[33] M. J. Frisch, G. W. Trucks, H. B. Schlegel *et al.*, *Gaussian 16*, *Revision C.01*, Gaussian, Inc., Wallingford, CT, USA, 2016.

[34] Dennington, T. Keith, and J.Millam, "Semichem Inc," *Shawnee Mission KS*, *GaussView*, *Version*, vol. 5, 2009.

[35] A. Daina, O. Michielin, and V. Zoete, "SwissADME: a free web tool to evaluate pharmacokinetics, drug-likeness and medicinal chemistry friendliness of small molecules," *Scientific Reports*, vol. 7, no. 1, Mar. 2017, doi: 10.1038/srep42717. Available: https://doi.org/10.1038/srep42717

[36] C. A. Lipinski, F. Lombardo, B. W. Dominy, and P. J. Feeney, "Experimental and computational approaches to estimate solubility and permeability in drug discovery and development settings," *Advanced Drug Delivery Reviews*, vol. 23, no. 1–3, pp. 3–25, Jan. 1997, doi: 10.1016/s0169-409x(96)00423-1. Available: https://doi.org/10.1016/s0169-409x(96)00423-1

[37] J. V. B. Borba *et al.*, "STopTOX: an in silico alternative to animal testing for acute systemic and topical toxicity," *Environmental Health Perspectives*, vol. 130,

no. 2, Feb. 2022, doi: 10.1289/ehp9341. Available: https://doi.org/10.1289/ehp9341

[38] X.-Y. Meng, H.-X. Zhang, M. Mezei, and M. Cui, "Molecular Docking: a powerful approach for Structure-Based drug discovery," *Current Computer - Aided Drug Design*, vol. 7, no. 2, pp. 146–157, Jun. 2011, doi: 10.2174/157340911795677602. Available: https://doi.org/10.2174/157340911795677602

[39] Aicha, Belaidi, Dalal, Lanez, Sinha, and Prasad, "Investigations on Molecular Structure, Electronic Properties, NLO Properties, HOMO–LUMO Analysis and Comparison of Drug-likeness of Triazolothiadiazole Derivatives by Quantum methods and QSAR Analysis," *Reviews in Theoretical Science*, vol. 3, pp. 1–10, 2015

Chapter 3

An Extensive Suite of Computational Investigations on Halogenated Gentisyl Alcohol Derivatives for Multi-target Pharmacological Profiling

Halophenols are well-known for their diverse range of biological activities. Building on this foundation, the present work explores halogenated derivatives of gentisyl alcohol. In our earlier investigation, five halogenated derivatives were highlighted as bioactive hits; however, only three analogs 1F, 4F, and 7F demonstrated convergence in molecular dynamics simulations. The present study conducts an in-depth evaluation of these fluorinated derivatives using a combination of computational approaches and quantum chemical analyses thereby expanding the chemical diversity of halophenolic scaffolds and potentially providing a strong foundation for rational drug design and development.

The text of this chapter has been patent published as:

- *Halogenated Gentsiyl Alcohol Derivatives for Multi-target Pharmacological Profiling, Indian Patent Application No. 202531050810 A, filed May 27, 2025, published June 6, 2025. Inventors: Basanta Singha, Penilosa Longkumer, Nichan Boruah, Partha Pratim Gogoi, Benzir Ahmed, Bijpul Bezbaruah, Konda Mani Saravanan, Upasana Bora Sinha, Giridharan Bupesh. Assignee: Nagaland University*

3.1. Introduction

Halophenols, a class of phenolic compounds containing halogen substituents, are frequently isolated from biologically active natural sources such as marine algae, ascidians, and sponges. Their unique structural features, often characterized by varying halogen types and substitution patterns, contribute to a remarkable diversity of biological activities. These compounds exhibit PTP1B inhibition, antioxidant, broad-spectrum antimicrobial, anti-inflammatory, enzyme inhibitory, and cytotoxic activities, highlighting their value as versatile leads for drug discovery across diverse therapeutic areas. [1,2]. Natural products based on the gentisyl alcohol and its derivatives are recognized for their pharmacological relevance. Notably, chlorogentisyl alcohol was the first compound derived from marine fungi to demonstrate potent activity against both macrofouling and microfouling organisms, with minimal or negligible toxicity highlighting its promise as a non-toxic antifouling agent [3]. The limited natural abundance of gentisyl alcohol-type compounds has posed obstacle to their comprehensive pharmacological investigation and therapeutic development. This scarcity necessitates the implementation of alternative strategies to ensure a sustainable and scalable supply [4]. Halogenation or pharmacophore conjugation can enhance bioavailability, specificity, and potency. In medicinal chemistry, halogenation is used to modulate a molecule's electronics, size, lipophilicity, and interactions, often improving affinity, selectivity, stability, and membrane permeability critical for progressing hits to viable drug candidates [5-7]. Gentisyl alcohol provides a compact, synthetically tractable phenolic scaffold with existing biological activity, making it an excellent starting point for systematic halogenation to generate optimized derivatives. [8-10]. In our previous work, we systematically modified gentisyl alcohol by introducing halogen substituents fluorine, chlorine, bromine, and iodine at various positions on the aromatic ring. This design strategy led to the generation of a focused library comprising 28 halogenated derivatives. Preliminary screening identified compounds 7F, 4F, 1F, 7B and 7I as promising candidates [11]. The initial investigation served primarily as an exploratory effort and was inherently preliminary in scope, necessitating more in-depth analysis to substantiate the observed findings.

In response, the current study performed a comprehensive assessment of the previously identified hit compounds, with the objective of delineating their therapeutic potential and validating their biological significance. Among the five hits, only the fluorinated analogues namely 1F, 4F and 7F demonstrated favorable structural and computational convergence. Strategic halogenation often blocks sites of metabolic oxidation (e.g., by cytochrome P450), increasing metabolic half-life. Fluorine is especially effective at blocking metabolic hotspots and modulating membrane permeability. Therefore, these three fluorinated compounds were selected for advanced analyses, alongside the parent compound, gentisyl alcohol (GA), and the co-crystallized ligand (NL1, NL2 and NL5) employed in certain selected studies, as illustrated in **Figure 3.1**. This integrated computational–structural approach, applied to fluorinated gentisyl alcohol variants, will yield a comprehensive understanding of the relationship between fluorination and biological effects in these compounds. Bridging this gap will provide mechanistic insights into how targeted fluorination can be harnessed to develop next-generation therapeutic leads with enhanced affinity, selectivity, and pharmacokinetic profiles. The present study employs an integrative computational approach that includes molecular dynamics simulations and structural pharmacophore mapping to predict receptor interactions and binding affinity. In addition, quantum chemical investigations were conducted, encompassing Mulliken charge distribution, Natural Bond Orbital (NBO) analysis, and Nonlinear Optical (NLO) property evaluation to assess electronic behavior and charge delocalization. Electrostatic properties were further characterized through Molecular Electrostatic Potential (MEP) and Electrostatic Potential (ESP) contour mapping, as well as through analysis of Localized Orbital Locator (LOL) and Electron Localization Function (ELF) plots. To gain insights into intramolecular and intermolecular interactions, Non-Covalent Interaction (NCI) analysis was performed using tools such as the Visual Molecular Dynamics (VMD) platform. The study also includes prediction of bioactivity scores, assessment of reactive atomic sites (RA analysis), and biological activity forecasting using the PASS (Prediction of Activity Spectra for Substances) model. Finally, IC_{50} values were theoretically estimated using reference-based computational methods to evaluate the inhibitory potential of the compounds. Collectively, this multi-tiered computational workflow provides a framework for the

rational assessment and future development of these fluorinated gentisyl alcohol derivatives as pharmacologically relevant agents.

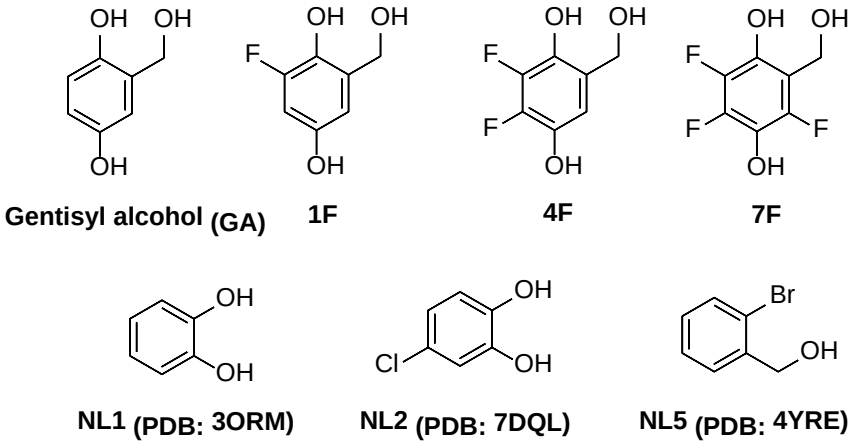

Figure 3.1: Compounds under investigation

3.2. Materials and methods

3.2.1. Molecular dynamics (MD)

Molecular dynamics (MD) simulations were performed using the GROMACS software package with the AMBER-99SB force field [12]. Among the five protein–ligand complexes evaluated, two did not achieve convergence. The remaining three complexes—1F–4YRE, 4F–3O4M, and 7F–7DQL successfully converged and were subsequently selected for extended simulations. Ligand structural and electrostatic parameters were generated using the ACPYPE tool. [13]. A dodecahedron box was fabricated, with the structural complex positioned at its middle location. The simulation environment was hydrated using TIP3P water molecules to solvate the system. To prevent boundary artifacts, a minimum separation of 1 nanometer was maintained between the protein and the edges of the simulation box. The Gromacs software application incorporated counter-ions to achieve charge neutrality. A distance threshold of 14 Å was employed to ascertain non-covalent van der Waals interactions. Geometric constraints were applied to hydrogen-containing covalent bonds using the LINCS algorithm. The process of energy minimization was carried out using a step size of 0.001 nanoseconds. Afterwards, a simulation lasting 100 picoseconds was performed using an isothermal–isovolumetric ensemble (NVT).

Subsequently, a 10-nanosecond simulation was conducted utilizing an isothermal–isobaric ensemble (NPT) to attain equilibrium for the water system. A molecular dynamics simulation was conducted using a non-polarizable tight-binding model. Molecular dynamics run was carried out for a duration of 100 nanoseconds. A time integration step of 2 femtoseconds was applied throughout the simulation. Thermodynamic conditions were maintained at 300 K and 1 atm through the application of a modified Berendsen thermostat for temperature coupling and the Parrinello–Rahman barostat for pressure regulation [14-18]. The Gromacs software 2023.1 tools were used to calculate the root-mean-square deviation (RMSD) of the trajectory.

- ***Binding Free Energy Calculations***

The Molecular Mechanics Poisson–Boltzmann Surface Area (MMPBSA) method was employed to estimate the binding free energies of the three complexes by analyzing their MD trajectories [19]. The binding free energy for each of the three complexes was estimated using the Molecular Mechanics Poisson–Boltzmann Surface Area (MM/PBSA) approach, implemented *via* the *g_mmpbsa* computational tool [20]. To ascertain the binding free energy, we examined the final 20 nanoseconds of the trajectory, extracting 20 frames from each nanosecond. The trajectory utilized in this study was generated by a comprehensive 40-nanosecond NPT molecular dynamics simulation. Binding free energy was determined using the following expression [21] as shown in equation 1.

$$\Delta G_{bind} = E_{complex}(minimized) - E_{ligand}(minimized) - E_{receptor}(minimized) \ldots. (1)$$

3.2.2. Structural pharmacophore

Pharmacophore mapping was performed using LigandScout 4.2 software [22] to identify shared structural and functional features critical for biological activity. This computational approach generates three-dimensional pharmacophore models by detecting and aligning key molecular features involved in target recognition and binding affinity. Typical structural characteristics encompass regions capable of participating in hydrogen bonding both as donors and acceptors as well as hydrophobic domains and other functional motifs critical for molecular recognition and interaction with biological targets [23]. In this study, compounds 1F, 4F, 7F, the co-crystallized

ligands with respect to PDB entries 4YRE (NL5), 3O4M (NL1), and 7DQL (NL2), and the parent compound gentisyl alcohol (GA) were analyzed to identify their pharmacophoric features. The corresponding PDB structures were retrieved and preprocessed by removing non-essential components, such as water molecules, while retaining the co-crystallized ligands. Co-crystallized ligands were energy-minimized using the MMFF94 force field, well-suited for organic molecule optimization in drug design. Ligands were aligned within their respective binding sites by superimposing them onto the co-crystallized ligands, and their geometries were subsequently refined using the same force field parameters. Structural superimposition with the Co-crystallized ligands ensured accurate spatial alignment, facilitating the generation of reliable pharmacophoric features.

3.2.3. Quantum studies

Quantum analyses of the selected compounds were performed using the Gaussian 16W software suite [24]. Molecular structures were visualized and analyzed with GaussView 6.0 [25]. All calculations employed Density Functional Theory (DFT) in the gas phase, utilizing the hybrid B3LYP functional. Geometry optimizations and electronic property evaluations were carried out using the LANL2DZ basis set in conjunction with the 6-311++G(d,p) basis set.

3.2.3.1.Mulliken Charge Analysis

Mulliken charge analysis is a fundamental method for evaluating the electron density distribution across a molecule. It is used to analyze chemical reactions and reactivity, as well as to predict the molecular properties such as dipole moments and bond orders. It provides insights into electron-rich or deficient atoms, helping us to understand molecular behavior in chemical and biological contexts [26]. The present study evaluates these properties in compounds 1F, 4F, 7F, GA, NL1, NL2, and NL5. In compounds containing hydrogen, carbon, oxygen, and halogens, Mulliken charges reveal important electronic features. Hydrogen atoms consistently show partial positive charges, marking them as electrophilic centers, while carbon atoms often appear electron-rich and stabilize electrophilic interactions. Oxygen atoms, with their

strong negative charges, play crucial roles in hydrogen bonding and stabilizing nearby positive centers. Negatively charged halogens exert strong electron-withdrawing effects, influencing the molecule's polarity and binding capacity. The spatial distribution of charge influences the molecular stability, chemical reactivity, and potential for biological interaction [27].

3.2.3.2.Nonlinear Optical (NLO) Properties Analysis

Nonlinear optical (NLO) property analysis examines how materials respond to intense electromagnetic fields, where the induced polarization is no longer linearly proportional to the field strength. This nonlinearity gives rise to phenomena such as frequency mixing, optical limiting and refractive index modulation. Density Functional Theory (DFT) provides valuable insights into the molecular-level mechanisms governing NLO behavior by analyzing factors such as electron distribution, electronic structure and intermolecular interactions [28]. To explore the correlation between molecular architecture and nonlinear optical behavior, the mean polarizability and first mean hyperpolarizability of the investigated complexes were computed at the B3LYP/LANL2DZ level of theory. Urea, a well-studied organic compound, serves as a benchmark for assessing NLO properties because of its moderate and well-documented nonlinear optical response. This study evaluates the NLO properties of the compounds 1F, 4F, 7F, GA, NL1, NL2 and NL5 by analyzing their static dipole moments (μ), mean polarizabilities (⟨α⟩) and first mean hyperpolarizabilities (⟨β⟩). The results are compared against urea, which has a first hyperpolarizability value of 0.3728×10^{-30} esu. Herein, the total static dipole moment (μ), the mean polarizability (⟨α⟩) and the first mean hyperpolarizability (⟨β⟩) were computed using the x, y, and z components, based on the following equations 1-7 [29]:

$$\mu = (\mu_X^2 + \mu_Y^2 + \mu_Z^2)^{1/2} \quad (1)$$

$$\alpha = \frac{(\alpha_{XX} + \alpha_{YY} + \alpha_{ZZ})}{3} \quad (2)$$

$$\Delta\alpha = ((\alpha_{xx} - \alpha_{yy})^2 + (\alpha_{yy} - \alpha_{zz})^2 + (\alpha_{zz} - \alpha_{xx})^2/2)^{1/2} \quad (3)$$

$$\langle\beta\rangle = (\beta_x^2 + \beta_y^2 + \beta_z^2)^{1/2} \quad (4)$$

Where,

$$\beta_x = \beta_{xxx} + \beta_{xyy} + \beta_{xzz} \quad (5)$$

$$\beta_y = \beta_{yyy} + \beta_{xxy} + \beta_{yzz} \quad (6)$$

$$\beta_z = \beta_{zzz} + \beta_{xxz} + \beta_{yyz} \quad (7)$$

3.2.3.3. Analysis of MEP, ESP and contour plots

Molecular Electrostatic Potential (MEP) and Electrostatic Potential (ESP) surface plots were employed to assess the spatial distribution of electron density across the molecular surface, providing insights into molecular polarity, distribution of charge density and identification of regions susceptible to electrophilic or nucleophilic interactions. These plots visually represent the electrostatic potential mapped onto the electron density isosurface, where regions of negative potential (typically colored red) correspond to electron-rich areas likely to attract electrophiles, and regions of positive potential (typically blue) indicate electron-deficient areas prone to nucleophilic attack [30]. The Molecular Electrostatic Potential (MEP) and Electrostatic Potential (ESP) analyses were performed for compounds 1F, 4F, 7F, NL1, NL2, NL5, and GA.

3.2.3.4.Natural Bond Orbital (NBO) analysis

Natural Bond Orbital (NBO) analysis is a powerful computational tool used to gain deeper insights into the electronic structure and bonding characteristics of molecules [31]. NBO analysis was performed for 1F, 4F, and 7F, it provides a clear picture of electron distribution, bond polarization and delocalization effects within a molecule by focusing on chemically intuitive atomic and bonding interactions. NBO analysis decomposes the molecular wave function into localized bonding units, such as lone pairs, bonding and anti-bonding which are referred to as natural bond orbitals. This method is highly effective for studying intra-molecular and inter-molecular charge transfer, resonance structures and stability of the molecular systems [32].

3.2.3.5. Analysis of LOL, contour and ELF plots

The Localized Orbital Locator (LOL), contour plots, and Electron Localization Function (ELF) diagrams collectively provide valuable insights into the electronic structure of these molecules. Specifically, these visualizations highlight regions of localized electron density, elucidate the nature and strength of covalent bonding, and reveal patterns of electron pairing. These collective analyses were performed for compounds 1F, 4F, and 7F. The LOL and ELF functions serve as key descriptors for identifying areas of strong electron localization, such as lone pairs and bonding interactions, thereby enabling a deeper understanding of the electronic distribution and reactivity within the molecular frameworks [33].

3.2.3.6. Analysis of NCI and VMD

Non-Covalent Interaction (NCI) analysis is a powerful computational method used to visualize weak intermolecular forces such as hydrogen bonding, π–π stacking and van der Waals interactions by analyzing the reduced density gradient over electron density. This helps reveal the spatial distribution and strength of non-covalent interactions within and between molecules. Visual Molecular Dynamics (VMD) (https://www.ks.uiuc.edu/Research/vmd/) [34] complements NCI by providing detailed 3D visualization of these interactions, enabling dynamic observation of molecular systems. Together, NCI and VMD offer critical insights into molecular stability, binding affinity, and structural organization, supporting rational design in drug discovery and materials science [35]. These analyses were performed for compounds 1F, 4F, and 7F.

3.2.4. Bond length, bond angle and dihedral angle calculation

The DFT-optimized geometries of the three selected compounds were employed to analyze their structural parameters, including bond lengths, bond angles, and dihedral angles. These geometrical descriptors were visualized and quantitatively extracted using ChemDraw Professional version 16, facilitating a detailed conformational assessment of each molecule based on its optimized structure [36].

3.2.5. Bioactivity score prediction

Molinspiration (https://www.molinspiration.com), a widely recognized cheminformatics platform, was employed in the present study to predict the bioactivity profiles of compounds 1F, 4F, 7F, NL1, NL2, NL5, and GA. This tool enables the computational estimation of biological activity scores against key drug targets such as GPCR ligands, ion channel modulators, kinase inhibitors, nuclear receptors, protease inhibitors, and enzyme targets [37]. The analysis provides valuable insight into the potential pharmacological behavior of these molecules, facilitating their prioritization for further drug development and experimental validation.

3.2.6. Reacting atom (RA)

To predict potential sites of metabolic transformation and understand the likely biotransformation routes of the selected compound, reacting atom identification was performed using the Way2Drug RA (*Reacting Atom*) prediction tool (available at: http://www.way2drug.com/RA).

3.2.7. PASS Prediction

To evaluate their potential bioactivity, the Prediction of Activity Spectra for Substances (PASS) online tool was employed to estimate the probability of each compound being pharmacologically active or inactive. The PASS prediction platform, accessible at http://www.way2drug.com/PASSOnline, utilizes structure–activity relationship models to forecast a wide range of biological activities based on the compounds' structural features.

3.2.8. IC_{50} calculation

To further evaluate the inhibitory efficacy of the selected compounds against their designated biological targets, a theoretical computation of their half-maximal inhibitory concentration (IC_{50}) was conducted [38]. Although QSAR-based techniques and quantum chemical approaches [39-41] are widely recognized for predicting IC_{50} values with minimal computational demands, certain physicochemical parameters involved can be computationally intensive due to their reliance on external variables.

Therefore, this study adopted the methodology proposed by Bag [42], which enables the prediction of IC_{50} for novel compounds using a single known IC_{50} value from a structurally related reference compound. This approach requires the dipole moment (μ) and the electrophilicity index (ω) both fundamental electronic descriptors of the test and reference molecules. The molecular descriptors were obtained through density functional theory (DFT) computations conducted using the Gaussian16 software suite. The estimated IC_{50} of each candidate inhibitor was calculated using the established relationship between these descriptors and the known IC_{50} of the reference compound, allowing for a computationally efficient yet reliable approximation of inhibitory potency.

3.3.Result and discussion

3.3.1. Molecular dynamics

3.3.1.1. Root mean square deviation (RMSD)

RMSD is a key indicator of binding stability, where lower values reflect a stable ligand–receptor complex, and higher values may signal partial or full dissociation or transient intermediate states [43]. RMSD of the complexes is shown in **Figure S3.2 (A–C) (supporting information)** indicating conformational changes over the simulation period. Thus, the RMSD values for complex 7F-7DQL increase from approximately 3 Å at 0 ns to around 6 Å at 100 ns, indicating a structural alteration in the system. This signifies that the system's structure or variety in complex 7F-7DQL evolves with time and gets more pronounced during the simulation. The incremental rise in RMSD is clearly evident in systems that are progressively diverging from their initial conformation but have not yet achieved stabilization. The complex 4F-3O4M illustrates a progressive increase in RMSD values, commencing at approximately 4 Å and exceeding 6 Å at 100 ns. It exhibits irregularity and minimal fluctuation in the RMSD values over time. These alterations indicate that the system is probably experiencing more significant conformational transitions and perhaps ephemeral structural states that lack longevity. The RMSD figure illustrated in complex 1F-4YRE indicates a progressive increase in the RMSD value over time, starting at approximately 3 Å and reaching nearly 5 Å at 100 ns. The curve in plot (C) is less

pronounced and steadier than those in (A) and (B), suggesting that the system in plot (C) undergoes fewer structural variations and may have achieved a relatively stable conformation early in the simulation. The result reveals the temporal structural changes of systems or models and their stability, as seen by the plots depicting varying degrees of structural alteration.

3.3.1.2. Root Mean Square Fluctuation (RMSF)

RMSF analysis of the three complexes (7F-7DQL, 4F-3O4M and1F-4YRE) corresponding to the residues in the analyzed protein or molecular system is depicted in **Figure S3.3 (A-C) (supporting information)**. RMSF is determined as the mean distance between the initial and final positions of individual residues in a protein during molecular dynamics simulations. All graphs depict the RMSF values plotted against the residue numbers for various portions of the protein. Figure 3A illustrates the RMSF values of residues, numbering from 35 to 205. The graph indicates several changes, particularly at the 70, 105, 140, 175, and 205 residue positions, suggesting that this portion of the protein has greater flexibility. The peaks suggest that these locations may be related with protein dynamics or other molecular interactions, as elevated RMS fluctuation values correlate with active sites or flexible links within protein structures. Figure 3B pertains to residues ranging from 20 to 120. High peak values around approximately residues 40, 80, and 100 may indicate significant flexibility, maybe representing a loop region or another flexible domain critical to the protein's function. The elevated baseline RMSF mean in this plot compared to other segments indicates that this portion of the protein is normally more flexible. Figure 3C exhibits a far broader range of residues, spanning from around 100 to 500. The subsequent graph indicates that the RMSF of this section is considerably lower, signifying that the structure of this segment is comparatively stiffer. Nonetheless, significant fluctuations persist (notably around residues 300 and 400), which may be crucial for the protein's architecture or functionality, potentially indicating flexibility at these sites or serving as interaction spots within the predominantly inflexible structure. The analysis of RMSF reveals the dynamic behavior of the protein at the residue level and indicates residues that exhibit sufficient flexibility to potentially

participate in the protein's function, interactions with other compounds, or stability. This information is vital for drug design applications, as the binding efficiency of compounds is often governed by the dynamic flexibility of specific regions within the target protein [44].

3.3.1.3.Radius of gyration (Rg)

The radius of gyration is a crucial measure used to assess the compactness of a protein or molecular system, as well as the protein's folding characteristics and conformational changes. As illustrated in **Figure S3.4A** (**supporting information**), the Rg value of 7F-7DQL complex commences at roughly 22 Å and exhibits minimal variation over the entire 100 ns simulation. This indicates that the system always remains compact, suggesting that the protein or molecule's structure does not undergo significant folding or unfolding. The lack of such oscillations suggests that the system may have reached a steady state early in the simulation, with the structures remaining stable throughout the duration. Figure **S3.4B** (**supporting information**) indicates that the initial value of Rg is around 17 Å, and this value remains rather constant throughout the simulation time. This indicates that 4F-3O4M complex possesses a greater density than that of Ligand 7F-7DQL, suggesting that 4F-3O4M may exhibit a more compact structural fold or represent a smaller protein. The Rg values exhibit notable consistency, suggesting that the structure does not experience significant conformational alterations or size fluctuations over the simulation. The stable state of the Rg curve indicates that the protein is neither unfolding nor collapsing; instead, it maintains a compact shape. In **Figure S3.4C (supporting information)**, Rg initiates at approximately 24 Å and progressively rises, with some fluctuations, ultimately attaining 26 Å at the conclusion of the study. This indicates a system that may be experiencing structural modifications, either through expansion or relaxation, during the simulation. The modest increase in Rg indicates that the molecule is undergoing partial unfolding or exposing flexible regions of its structure. The oscillations indicate that the system has not attained equilibrium or is undergoing structural conformational changes [45].

3.3.1.4. Hydrogen bond

Hydrogen bonding plays a crucial role in maintaining the structural stability and specificity of protein–ligand interactions during molecular dynamics simulations [46]. In this study, the temporal evolution of hydrogen bond (H-bond) formation was analyzed to evaluate the stability and interaction strength within the complex system as illustrated in **Figure S3.5 (A-C)** (**supporting information**). The number of hydrogen bonds formed within a defined cutoff distance of 0.35 nm was calculated throughout the simulation. The results show that hydrogen bond formation fluctuates over time, reflecting the dynamic nature of the complex. While certain intervals exhibit stable and persistent hydrogen bonding, others show increased or transient bonding activity, likely corresponding to conformational shifts observed in the RMSD plot. These fluctuations provide insights into the adaptive behavior of the system and the evolving nature of molecular interactions under simulated physiological conditions. Overall, our analysis offers a comprehensive understanding of both the structural integrity and flexibility of the complex, as well as the stabilizing role of hydrogen-bonded interactions observed during the simulation,

3.3.1.5. Binding Free Energy

Ligand-protein binding energy components were analyzed for three complexes: 7F-7DQL, 4F-3O4M, and 1F-4YRE. 7F-7DQL complex exhibits moderate negative electrostatic energy (-2.694 kJ/mol), Inefficient polar solvation energy (36.894 kJ/mol), moderate hydrophobic SASA energy (-4.767 kJ/mol), and favorable negative van der Waals energy (-49.681 kJ/mol). These energy components contribute to the overall binding profile, as detailed in **Table S3.1** (**supporting information**)**.** Nonetheless, its overall binding energy (-20.249 kJ/mol) is rather variable due to fluctuations in van der Waals forces. 4F-3O4M complex exhibits modest electrostatic interactions (-2.365 kJ/mol), significant hydrophobic effects (-12.179 kJ/mol), and extremely advantageous van der Waals interactions (-122.606 kJ/mol), resulting in a favorable binding energy (-97.205 kJ/mol) accompanied with considerable variations. 1F-4YRE exhibits the lowest electrostatic (0.119 kJ/mol) and polar solvation energy (17.098 kJ/mol), with the highest hydrophobic (-9.991 kJ/mol) and van der Waals (-

99.060 kJ/mol) energy, resulting in the most favorable and stable binding energy (-91.833 kJ/mol) [47]. Among the three, 1F-4YRE has the superior binding profile and demonstrates greater stability than 3F-3BQL and 7F-7DQL.

3.3.2. Structural pharmacophore

Structural pharmacophore mapping was carried out for compounds 1F, 4F, and 7F to determine whether these compounds shared any critical features that replicate the key interaction patterns of the co-crystallized ligands with their respective targets (PDB IDs: 4YRE, 3O4M, and 7DQL). Such mapping can reveal the presence of conserved hydrogen bond donors/acceptors, hydrophobic regions, aromatic centres, or charged groups aligned in three-dimensional space similar to the native ligands. This similarity suggests that the compounds may adopt a comparable binding orientation within the binding site, potentially resulting in a similar mechanism of action and, by extension, analogous biological activity [48].

- *For target **7DQL**:*

Compound 7F engages a triad of polar residues ASP73A, VAL71A and THR165A through hydrogen bonding, as shown in **Figure 3.6 (A)**. Surrounding these are hydrophobic residues (VAL43A, ILE78A, ALA47A, VAL167A, ILE94A, VAL120A) that provide shape complementarity and support binding. Notably, VAL43A, ILE78A, and ALA47A are positioned near the fluorinated aromatic ring, enhancing ligand snugness through hydrophobic interactions. This balance of polar and nonpolar contacts underpins the ligand's strong and selective binding. For GA, hydrogen bonds with polar residues (ASP73A, VAL71A, and THR165A) stabilize the ligand's position, as shown in **Figure S3.6 (B) (supporting information)**. A surrounding hydrophobic cluster (VAL43A, ALA47A, ILE78A, and VAL167A) contributes to shape complementarity and nonpolar interactions, particularly near the fluorinated aromatic ring. This combination of polar and nonpolar interactions ensures stable and selective ligand binding. The co-crystallized ligand (NL2) interacts through a combination of hydrogen bonds and nonpolar hydrophobic interactions, as shown in **Figure S3.6 (C) (supporting information)**. A triad of polar residues (ASP73A,

VAL71A, THR165A) forms hydrogen bonds with the ligand's hydroxyl groups, anchoring it in the binding pocket. Surrounding this core, hydrophobic residues (VAL43A, ALA47A, ILE78A, VAL167A, ILE94A, VAL120A) contribute to a tight fit. Additionally, the chlorine atom on the aromatic ring forms halogen interactions with VAL167A, ILE78A, ALA47A, and VAL43A, enhancing ligand orientation and binding affinity. This synergy ensures strong, specific, and stable ligand binding.

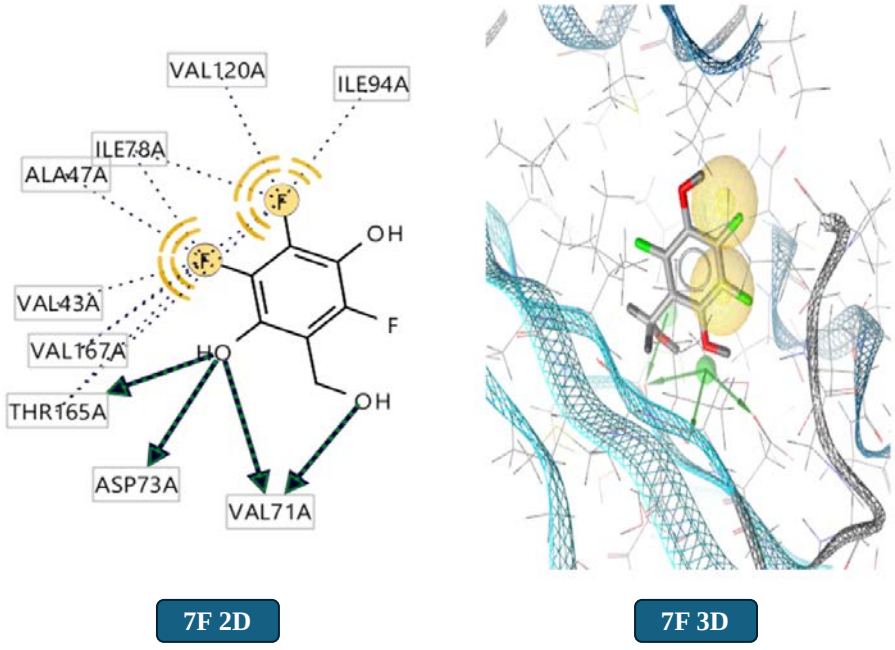

A

Figure 3.6 (A): Structural pharmacophore mapping of 7F against 7DQL

Collectively, compounds 7F, GA and the co-crystallized ligand all share interactions with the same set of key residues, including the polar triad ASP73A, VAL71A, and THR165A which form crucial hydrogen bonds that stabilize the ligand. Additionally, they are all surrounded by a common hydrophobic cluster composed of VAL43A, ALA47A, ILE78A, VAL167A, ILE94A, and VAL120A. Among them, 7F replicates these interactions most comprehensively, highlighting its strong structural alignment and favorable binding characteristics

- *For target **3O4M:***

Compound 4F interacts with three residues PHE22A, GLY30A, and LEU2A within the binding site, as shown in **Figure 3.7 (A)**. PHE22A, an aromatic residue, stabilizes and orients 4F through a hydrogen bond. GLY30A, with its flexibility, aids in ligand stabilization while allowing conformational adaptability. LEU2A, a hydrophobic residue, helps define the binding pocket's spatial and chemical characteristics, contributing to ligand positioning. Together, these residues create a balanced environment that supports effective binding of 4F. GA also interacts with the same three residues as 4F PHE22A, GLY30A, and LEU2A, as shown in **Figure S3.7 (B) (supporting information)**. PHE22A forms a hydrogen bond with GA's hydroxyl group, anchoring and orienting the ligand. GLY30A, through its flexibility, stabilizes GA while maintaining binding site adaptability. LEU2A, near GA’s aromatic ring, contributes to the nonpolar character of the pocket, aiding ligand positioning without hydrogen bonding. These residues collectively provide a balanced environment that supports GA binding. The co-crystallized ligand NL1 interestingly also forms contacts with PHE22A, GLY30A, and LEU2A, as shown in **Figure S3.7(C) (supporting information)**. PHE22A forms a hydrogen bond with the ligand’s hydroxyl group, stabilizing and orienting it in the active site. GLY30A, due to its small size and flexibility, also forms a hydrogen bond, enhancing stability while maintaining site adaptability. LEU2A, a hydrophobic residue, helps maintain the nonpolar environment and influences ligand positioning. Together, these residues provide a stable and compatible binding environment for NL1.

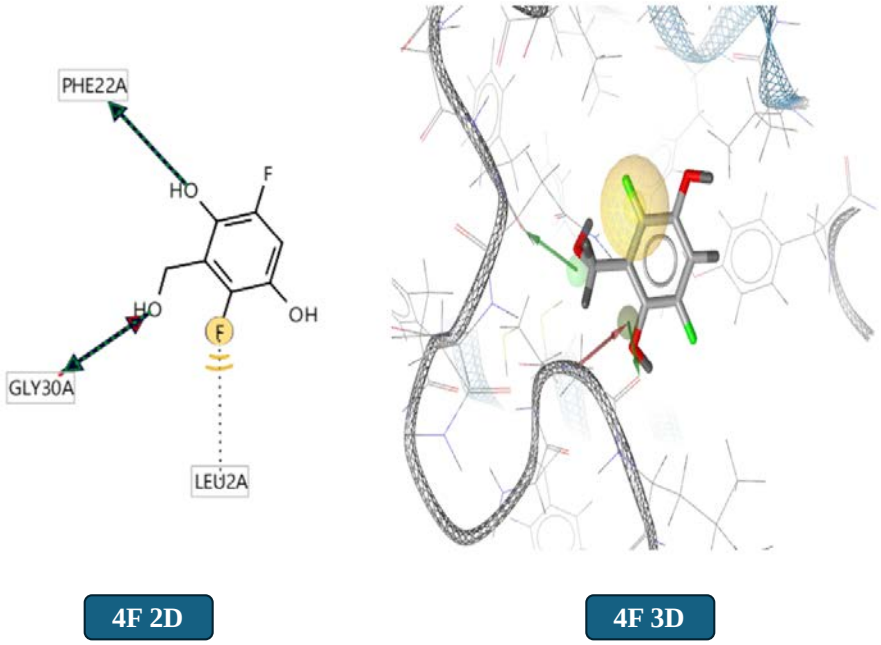

A

Figure 3.7 (A): Structural pharmacophore mapping of 4F against 3O4M

Collectively, compounds 4F, GA, and the co-crystallized ligand all interact with the same three conserved residues PHE22A, GLY30A, and LEU2A within the protein's binding pocket. This implies that its binding profile aligns well with that of the co-crystallized ligand. 4F**,** maintains these key contacts effectively, suggesting strong structural compatibility with the binding site and reinforcing its potential as a viable therapeutic candidate.

- *For target **4YRE:***

The interacting pharmacophoric features of compound 1F, illustrated in **Figure 3.8 (A)**, involves four key residues GLU167A, HIS168A, ARG156A, and ILE106A each contributing to ligand stabilization through distinct compound-specific roles. GLU167A forms a hydrogen bond with a hydroxyl group on the ligand, anchoring it *via* polar interactions. HIS168A, positioned near the ligand's aromatic ring, may enhance binding specificity through subtle electronic effects. ARG156A, though not

directly bonded, likely influences the local electrostatic environment near the fluorinated moiety. ILE106A provides hydrophobic support and steric complementarity. The interaction of compound GA, shown in **Figure S3.8 (B) (supporting information)**, involves the same residues GLU167A, HIS168A, ARG156A, and ILE106A each contributing to ligand stabilization within the active site. GLU167A forms a hydrogen bond with a hydroxyl group on GA, anchoring the ligand via polar interactions. HIS168A, though not directly bonded, may assist in ligand positioning through local polar effects. ARG156A, near GA's aromatic core, likely supports spatial orientation *via* electrostatic interactions. ILE106A enhances ligand stability through hydrophobic contacts and steric complementarity. The co-crystallized ligand NL5 also interacts with the same residues GLU167A, HIS168A, ARG156A, and ILE106A forming a complementary binding environment, as shown in **Figure S3.8 (C) (supporting information).** GLU167A anchors the ligand *via* a hydrogen bond with its hydroxyl group, stabilizing its orientation through polar interactions. HIS168A, positioned near the aromatic core, may aid in ligand alignment and pocket stabilization. ARG156A, adjacent to the ring system, likely contributes electrostatic support. ILE106A, near the bromine substituent, reinforces ligand stability through hydrophobic and steric effects. Together, these residues enable a stable and well-oriented binding pose for NL5 within the site.

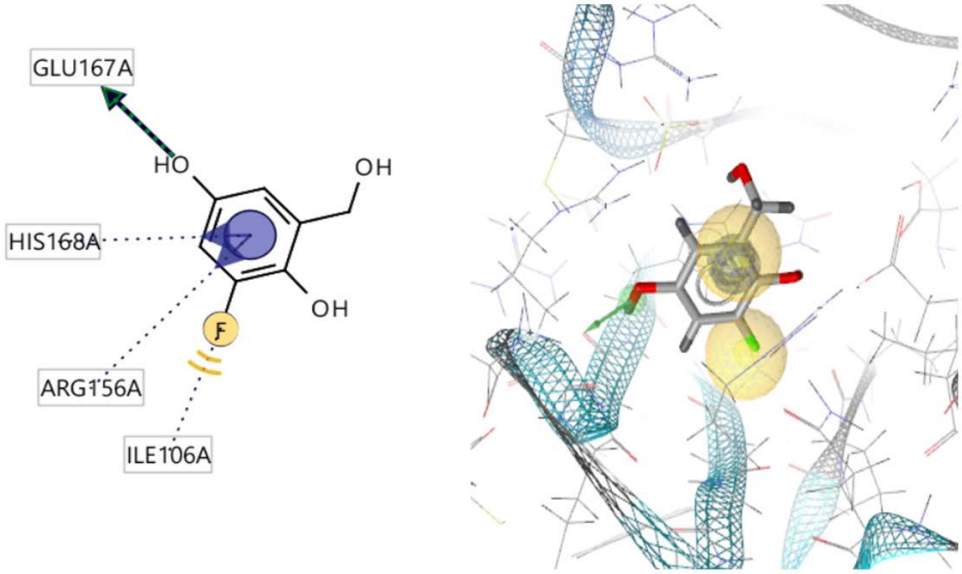

A

Figure 3.8 (A): Structural pharmacophore mapping of 1F against target 4YRE

Collectively, compound 1F, GA, and the co-crystallized ligand NL5 all interact with the same four key residues GLU167A, HIS168A, ARG156A, and ILE106A within the active site, indicating a conserved binding pattern. It implies that 1F exhibits a structurally and functionally compatible interaction profile**,** reinforcing its potential as a strong lead compound due to its ability to replicate critical molecular interactions essential for effective binding.

3.3.3. Mulliken Charge Analysis

The analysis of the charge distribution in different compounds reveals significant variations illustrated in **Figure 3.9** where the charge distribution between Carbon and Oxygen atoms are shown for all the compounds. Mulliken charge analysis reveals the electron distribution across a molecule, pinpointing reactive centres. Positively charged atoms, such as carbon, often act as electrophilic sites, while negatively charged atoms, like oxygen, can stabilize cations and engage in hydrogen bonding,

influencing molecular interaction [49]. The Mulliken charge (MC) analysis of the seven compounds such as 1F, 4F, 7F, GA, NL1, NL2 and NL5 offers crucial insights into their electronic environments and charge distributions across hydrogen (H), oxygen (O), carbon (C) and halogens. This section discusses the observed charge trends, with a particular focus on 1F, 4F and 7F as compounds that exhibit moderate stability coupled with enhanced electronic strength. The -H atoms consistently show positive Mulliken charges across all compounds, highlighting their role as electron-deficient centres. The values range from 0.342 in GA to 0.379 in NL2; with 1F, 4F and 7F showing moderate values of 0.360, 0.365 and 0.358, respectively as depicted in **Table S3.2 (supporting information)**. This suggests a balanced polarization and electron-withdrawing effect in these compounds. In contrast, 7F shows a slightly lower hydrogen charge of 0.358, reflecting balanced electron density withdrawal in its molecular framework. The -O atoms, characterized by high electronegativity, consistently carry negative charges across all compounds, ranging from -0.469 in NL5 to -0.524 in NL1 as shown in Table 2 and Figure16. The compounds containing 1F, 4F and 7F demonstrate -O charges of -0.511, -0.485 and -0.485, respectively. These values indicate moderate polarization, with 1F exhibiting slightly higher electron density on oxygen, which enhances its reactivity potential while maintaining structural stability. The -C atoms across all compounds show negative Mulliken charges, varying from -0.298 in NL2 to -0.379 in 7F. Among the highlighted compounds, 1F and 4F exhibit carbon charges of -0.347 and -0.378, respectively, indicating strong electron density localization due to halogen substituents. Whereas 7F with the most negative carbon charge (-0.379), demonstrates enhanced electronic strength, suggesting a significant role of fluorine in withdrawing electron density and increasing polarity. Halogens present in 1F, 4F, 7F and NL5, exhibit negative charges due to their high electronegativity. The Mulliken charges for halogens range from -0.051 in NL5 to -0.261 in 1F as shown in **Figure 3.10 & Table S3.2 (supporting information)**. Notably, 1F shows the most negative halogen charge (-0.261), reflecting a strong electron-withdrawing effect that redistributes charge within the molecule, enhancing its electronic strength. 4F and 7F exhibit halogen charges of -0.252 and -0.221, respectively, which contribute to a balanced charge distribution, making these compounds electronically stable.

Mulliken charge analysis indicates that 1F, 4F, and 7F possess moderate thermodynamic stability accompanied by notable electronic resilience. These molecules display a well-balanced interplay of charge polarization and electron withdrawal, which enhances their structural integrity. For instance, 1F shows moderate polarization with oxygen (-0.511), carbon (-0.347) and halogen (-0.261) charges, supporting its reactivity and stability. Similarly, 4F exhibits slightly less negative oxygen (-0.485) and carbon (-0.378) values, along with a halogen charge of -0.252, indicating a stable electronic configuration. 7F, with the most polarized carbon (-0.379), maintains a solid framework through balanced oxygen (-0.485) and halogen (-0.221) charges. In contrast, GA and NL5 are the most stable compounds due to their minimal charge polarization. GA shows the least polarized values for hydrogen (0.342), oxygen (-0.476) and carbon (-0.364), while NL5 presents low halogen (-0.051), oxygen (-0.469) and carbon (-0.375) charges, reflecting strong molecular stability. On the other hand, NL1 and NL2 appear least stable; NL1 shows highly negative oxygen (-0.524), indicating high reactivity and NL2 has the least negative carbon (-0.298), suggesting poor charge balance. Overall, 1F, 4F and 7F effectively balance reactivity and structural strength, making them promising candidates for applications demanding stable yet electronically active molecules. The MC analysis reinforces the significance of charge distribution and substituent effects in governing molecular behavior and stability.

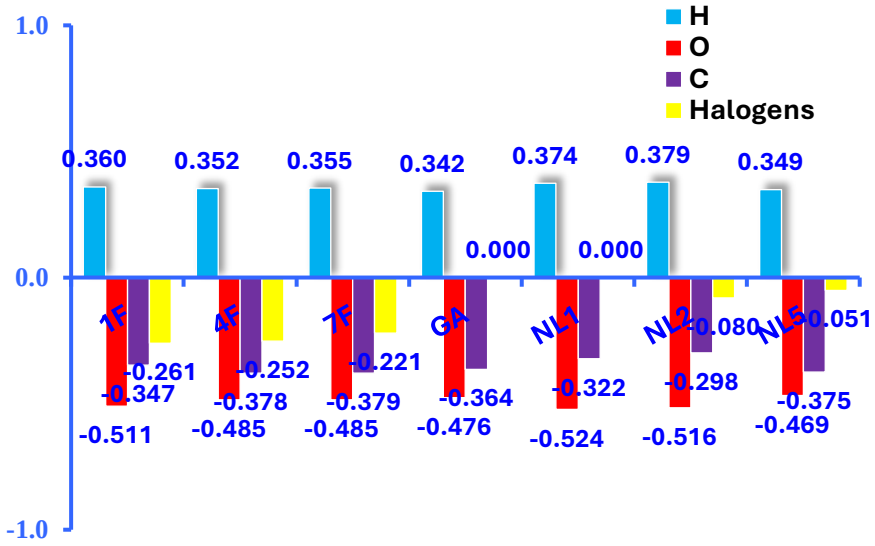

Figure 3.9: Mulliken Charge distribution of the compounds understudy computed by DFT/LANL2DZ basis set

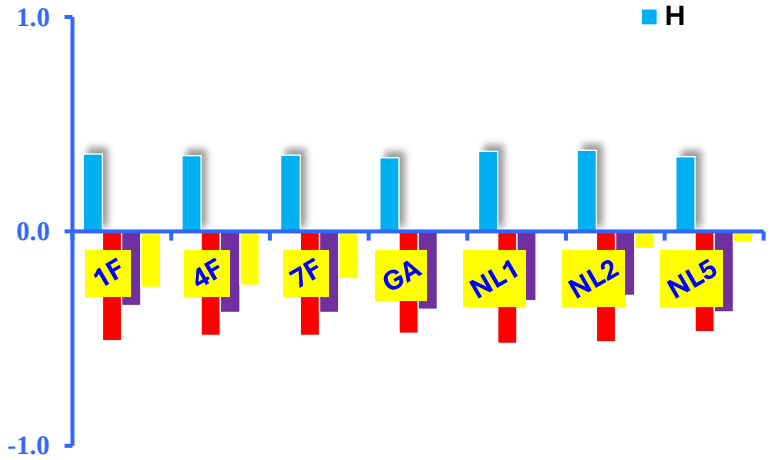

Figure 3.10: Mulliken Charge distribution of the compounds understudy computed by DFT/LANL2DZ basis set

3.3.4. Natural Bond Orbital (NBO) analysis:

The NBO analysis of the compounds 1F, 4F and 7F, in conjunction with Natural Population Analysis (NPA), provides a detailed understanding of the electronic interactions and stabilization effects within their molecular frameworks. This analysis

highlights the importance of donor-acceptor interactions, particularly π-π* delocalization and lone pair (LP) contributions, in determining their electronic structure and reactivity [50]. For compound 1F, the most significant interaction is $\pi C_7–C_9 \rightarrow \pi^*C_3–C_6$ with a stabilization energy (E^2) of 136.53 kcal/mol, reflecting effective π-electron delocalization that contributes strongly to the molecule's stability. An additional $\pi C_2–C_{10} \rightarrow \pi^*C_3–C_6$ interaction further enhances this effect with E^2 value of 109.37 kcal/mol. A lone pair donation from LP2 of oxygen (O_8) to $\pi^*C_7–O_9$ yields the energy value of 25.40 kcal/mol, indicating an important non-bonding interaction. The NPA results show a strongly negative charge on O_8, validating its role as a potent electron donor. In case of compound 4F, it demonstrates even more pronounced delocalization. The $\pi C_2–C_{11} \rightarrow \pi^*C_3–C_6$ interaction exhibits the highest E^2 value among all studied compounds at 232.61 kcal/mol, indicating extensive charge transfer and resonance stabilization. Another strong interaction, $\pi C_8–C_{10} \rightarrow \pi^*C_3–C_6$, contributes 208.08 kcal/mol, reinforcing the robust delocalization network. The lone pair on O_9 interacts with $\pi^*C_8–O_{10}$ with E^2 value of 26.00 kcal/mol as shown in **Table 3.3**. The NPA values for O9 reveal a highly negative charge, consistent with its ability to act as a strong donor. The high stabilization energies in 4F indicate superior charge transfer efficiency and greater resonance stabilization compared to 1F and 7F.

Again, for 7F, the interaction $\pi C_2–C_{12} \rightarrow \pi^*C_3–C_6$ contributes an E^2 energy of 182.87 kcal/mol, demonstrating significant π-electron delocalization. Additionally, $\pi C_8–C_{10} \rightarrow \pi^*C_3–C_6$ provides stabilization with an E^2 of 133.21 kcal/mol [**Table 3.3**]. The lone pair of O_9 interacts with $\pi^*C_8–O_{10}$, exhibiting an E^2 of 27.67 kcal/mol, which is the highest among all lone pair interactions observed across the compounds, further supporting the presence of strong donor–acceptor interactions. The NPA analysis consistently aligns with these findings, with negatively charged oxygen atoms acting as dominant electron donors, reinforcing the observed stabilization patterns. Therefore, the NBO and NPA analyses collectively emphasize the critical role of π-π* delocalization and lone pair contributions in stabilizing these therapeutic agents. Compound 4F stands out for its superior electronic stabilization, likely making it the most reactive and potentially effective among the studied molecules. These insights

provide a valuable framework for understanding molecular interactions and tailoring therapeutic agents for enhanced performance.

Table 3.3: The computed NBO analysis for of the compounds understudy (1F, 4F and 7F) highlights key interactions and their E^2 energies

Compounds	**Donor NBO (i) → Acceptor NBO (j)**	**E^2 kcal/mol**	**E(j)-E(i) a.u.**	**F(i,j) a.u.**
1F	$\pi^*C_7 - C_9 \rightarrow \pi^*C_3 - C_6$	136.53	0.02	0.084
	$\pi^*C_2 - C_{10} \rightarrow \pi^*C_3 - C_6$	109.37	0.03	0.084
	$LP_2\ O_8 \rightarrow \pi^*C_7 - O_9$	25.40	0.33	0.089
4F	$\pi^*C_2 - C_{11} \rightarrow \pi^*C_3 - C_6$	232.61	0.02	0.085
	$\pi^*C_8 - C_{10} \rightarrow \pi^*C_3 - C_6$	208.08	0.02	0.082
	$LP_2\ O_9 \rightarrow \pi^*C_8 - O_{10}$	26.00	0.32	0.089
7F	$\pi^*C_2 - C_{12} \rightarrow \pi^*C_3 - C_6$	182.87	0.02	0.086
	$\pi^*C_8 - C_{10} \rightarrow \pi^*C_3 - C_6$	133.21	0.03	0.083
	$LP_2\ O_9 \rightarrow \pi^*C_8 - O_{10}$	27.67	0.31	0.091

3.3.5. Nonlinear Optical (NLO) Properties Analysis

The static dipole moment (μ) is a critical indicator of the charge distribution asymmetry in a molecule and plays a vital role in determining NLO efficiency [51]. Among the studied compounds, 1F has a moderate static dipole moment of 0.44 Debye, while 4F displays a significantly higher value of 1.01 Debye, indicating greater charge separation. Similarly, 7F and NL5 have dipole moments of 0.83 Debye and 0.60 Debye, respectively. GA exhibits the highest dipole moment of 2.15 Debye, surpassing all other compounds. NL1, with a dipole moment of 0.45 Debye, shows the

least asymmetry, whereas NL2 demonstrates an elevated value of 1.61 Debye, reflecting a higher asymmetry as shown in **Table 3.4** compared to urea (as reported in literature). The average polarizability (⟨α⟩) quantifies the extent to which a molecule's electron cloud can be displaced under the influence of an external electric field. Compounds such as 1F and GA exhibit moderate polarizabilities of 100.23 a.u. and 95.97 a.u., respectively. In comparison, 4F and 7F show higher values of 105.62 a.u. and 106.23 a.u., indicating an improved optical response. While NL1 and NL2 demonstrate values of 86.47 a.u. and 112.99 a.u., respectively, NL5 stands out with the highest polarizability of 103.05 a.u., underscoring its potential for strong interaction with incident electromagnetic fields (**Table 3.4**). The first mean hyperpolarizability (⟨β⟩) is a fundamental parameter for evaluating a compound's NLO efficiency. Compound 1F exhibits a relatively low hyperpolarizability of 0.3642 × 10^{-30} esu, slightly below urea, reflecting its limited NLO potential. On the other hand, 4F demonstrates a substantial increase to 63.57 × 10^{-30} esu, highlighting its significant NLO efficiency. Compound 7F achieves the highest hyperpolarizability among the studied compounds, with a value of 147.58 × 10^{-30} esu, positioning it as a superior NLO candidate. GA and NL1 exhibit moderate hyperpolarizabilities of 110.96 × 10^{-30} esu and 152.89 × 10^{-30} esu, respectively, with NL1 outperforming urea and several other compounds. Furthermore, NL2 and NL5 exhibit enhanced hyperpolarizabilities of 158.07 × 10^{-30} esu and 125.63 × 10^{-30} esu, respectively, confirming their promising NLO behavior.

Table 3.4: Calculated NLO values of the compounds under investigation

Compound	**Static Dipole Moment (μ, Debye)**	**Polarizability (⟨α⟩, a.u.)**	**Hyperpolarizability (⟨β⟩, ×10^{-30} esu)**
1F	0.44	100.23	0.3642
4F	1.01	105.62	63.57
7F	0.83	106.23	147.58
GA	2.15	95.97	110.96
NL1	0.45	86.47	152.89

NL2	1.61	112.99	158.07
NL5	0.60	103.05	125.63

This comparative analysis of the studied compounds against urea demonstrates that 4F, 7F and NL2 exhibit significantly enhanced NLO properties. Therefore, among all the compounds, 7F with its superior polarizability and hyperpolarizability, emerges as the most promising candidate for NLO applications. These findings underscore the potential of these compounds in advancing photonic and optoelectronic technologies. Future experimental validations and computational studies could provide deeper insights into their practical applicability in real-world scenarios.

3.3.6. Analysis of MEP, ESP and contour plots

To investigate the electron density distribution, molecular polarity, and probable sites of electrophilic or nucleophilic attack, Molecular Electrostatic Potential (MEP), Electrostatic Potential (ESP), and contour mapping analyses were conducted for 1F, 4F, 7F, GA, NL1, NL2, and NL5 as shown in **Figures 3.11-3.13 and Figures S3.14-3.17** (**supporting information**). MEP surface plots use color gradients to depict electrostatic potential, with red indicating regions of highest negative potential, blue representing the most positive areas, and green showing neutral zones [52].

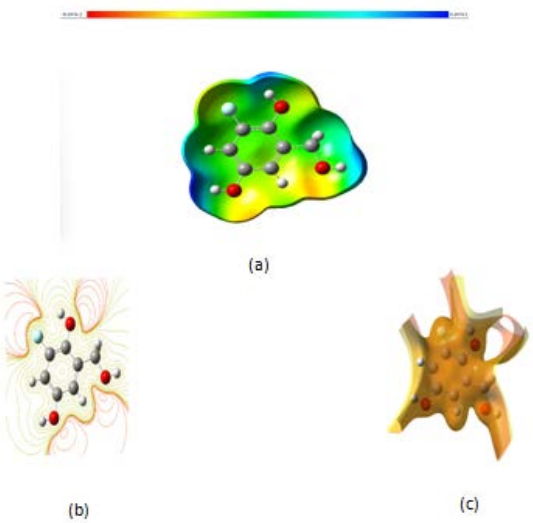

Figure 3.11: (a) Molecular electrostatic potentials (MEP) plot of 1F, (b) contour map plot of ESP isosurface of 1F, (c) visualization of the ESP array plot for 1F

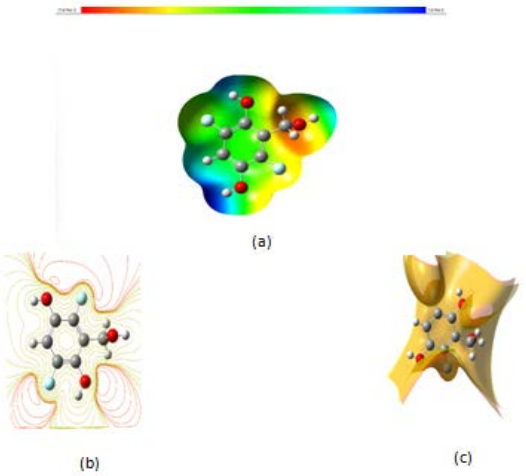

Figure 3.12: (a) Molecular electrostatic potentials (MEP) plot of 4F, (b) contour map plot of ESP isosurface of 4F, (c) visualization of the ESP array plot for 4F

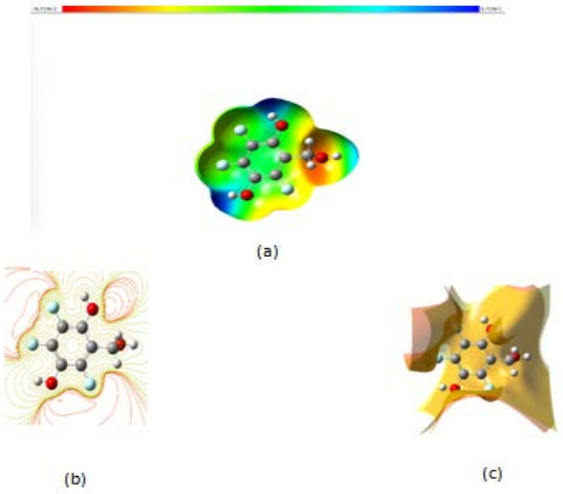

Figure 3.13: (a) Molecular electrostatic potentials (MEP) plot of 7F, (b) contour map plot of ESP isosurface of 7F, (c) visualization of the ESP array plot for 7F

In ESP visualizations, light red regions correspond to zones of high electron concentration, indicating favorable sites for proton affinity and increased vulnerability to electrophilic attack [53]. In 1F, fluorine substitution increased the negative potential, particularly near the substituted sites, as evidenced by deeper red MEP regions and more compact ESP contours. This enhancement suggests increased nucleophilic reactivity and polarity relative to GA. Again, 4F exhibited even greater electron localization, with intense MEP red zones and denser ESP contours around multiple fluorine atoms. The ESP array revealed clearly demarcated electron-rich zones, suggesting enhanced reactivity compared to 1F. In case of 7F, displayed the highest degree of electron localization, with extensive and deep red zones in the MEP map and tightly packed ESP contours, marking it as the most polar and nucleophilic of the fluorinated series. For GA, the MEP surface showed a moderately uniform electron distribution, with negative potentials localized primarily at hydroxyl groups, indicative of moderate nucleophilicity. ESP contour and surface plots affirmed the results, displaying a consistent electrostatic potential transition and uniformly dispersed molecular polarity. In contrast, the NL series demonstrated more moderate electrostatic behavior. NL1 showed a relatively uniform MEP surface with mild negative potentials near oxygen atoms, reflecting low reactivity. NL2 displayed slightly enhanced polarity, with increased electron density near functional groups. NL5, however, revealed significant electron localization with vivid MEP red regions and sharper ESP contours, indicating higher polarity and reactivity than NL1 and NL2. Comparatively, fluorination leads to a marked increase in polarity and nucleophilicity in the order GA < 1F < 4F < 7F, with 7F emerging as the most reactive species. The NL derivatives follow a subtler trend (NL1 < NL2 < NL5), with NL5 approaching the electron localization observed in fluorinated analogues. Overall, while functional group substitutions in the NL molecules improve reactivity to a degree, extensive fluorination has a more profound impact on increasing electron density localization and thus molecular reactivity.

3.3.7. Analysis of LOL, contour and ELF plots:

LOL, ELF, and contour plots were employed to examine electron localization in 1F, 4F, and 7F as shown in **Figure 3.18 (A-C)** collectively provide valuable insights into the electronic structure of these molecules. The Electron Localization Function (ELF) and Localized Orbital Locator (LOL) are topological descriptors used to analyze chemical bonding and electron distribution within molecules. Both are derived from kinetic-energy density (τ), capturing the quantum kinetic energy reduction associated with orbital sharing a key mechanism underlying covalent bond formation [53]. For compound 1F, the Localized Orbital Locator (LOL) plot shows a high degree of electron localization between bonded atoms, particularly around the carbon-fluorine bonds. The LOL values are strongly peaked along the bonding regions, indicating the dominance of classical covalent interactions and minimal electron delocalization. The contour diagram further corroborates this observation, revealing dense and tightly packed electron density contours surrounding the σ-bonds and fluorine atom. The electron density is symmetrically distributed with minimal spread, reflecting a highly localized electronic environment. In the 2D Electron Localization Function (ELF) plot, there is significant electron localization in bonding areas, as indicated by ELF values approaching unity (1.0). Distinct high ELF regions are observed between bonded pairs, confirming strong covalent character and well-defined electron pairing without notable π-delocalization. For compound 4F, the LOL distribution remains localized along the bonding framework but exhibits slightly broadened regions near the fluorinated sites compared to 1F. This suggests that while covalent bonding is dominant, there is some extension of electron density toward adjacent areas, hinting at weak delocalization effects possibly due to lone-pair interactions from fluorine. The contour plot reveals moderately diffuse electron density, especially surrounding the fluorine atom, indicating extended electron cloud delocalization beyond the bonded framework. The contour lines remain dense near bonds but start to smooth out as one moves away from the nuclei, indicating a slight loosening of electron localization. In the 2D ELF plot, strong localization persists between bonded atoms, but additional regions of high ELF values are evident around the fluorine atom, corresponding to non-bonded electron pairs. The broader ELF basins suggest a contribution from lone-

pair density to the overall electronic architecture of the molecule. In case of compound 7F, the LOL plot reveals a noticeable departure from strict localization seen in 1F and 4F. Here, broader and more diffused regions of moderate localization appear, especially across the conjugated aromatic system, indicating extensive π-delocalization. The LOL values suggest that electron density is not solely confined to individual bonds but rather distributed across the conjugated framework, consistent with resonance stabilization. The contour diagram supports this interpretation by displaying widely spaced and overlapping electron density contours across the aromatic rings and multiple bond systems. The contours are less concentrated around individual bonds and instead flow across larger molecular areas, illustrating a delocalized π-electron cloud. In the 2D ELF plot, a more uniform spread of moderate ELF values is observed across the conjugated skeleton. Unlike 1F and 4F, where distinct ELF basins are tightly localized, 7F shows interconnected ELF regions, highlighting delocalized bonding patterns typical of aromatic systems and confirming the presence of extensive π-electron sharing. A systematic trend is evident across the three compounds. Compound 1F exhibits highly localized, classical covalent bonding with negligible delocalization. Compound 4F maintains strong covalent bonds but introduces modest electron cloud spreading due to lone-pair effects from the fluorine substituent. In compound 7F, a significant degree of electron delocalization is observed across the π-conjugated system, leading to enhanced aromatic stabilization and dynamic electronic behavior. Together, the LOL, contour, and ELF analyses illustrate the critical influence of molecular structure and substitution on electron distribution patterns and potential chemical reactivity.

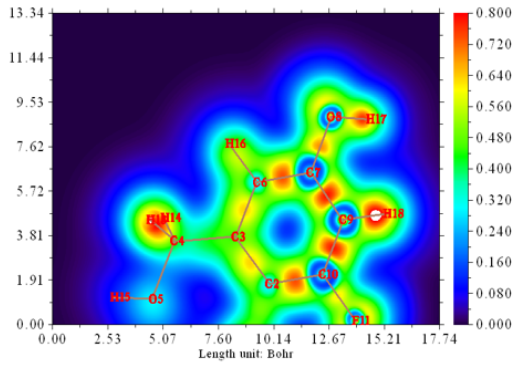

1F-LOL

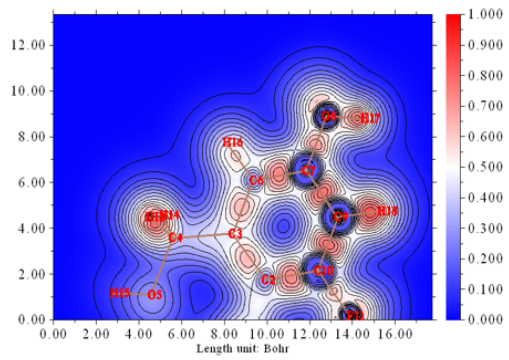

1F-Contour

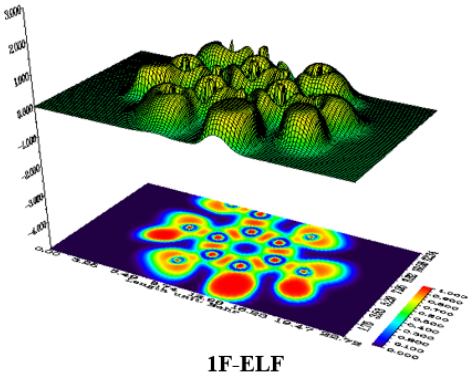

1F-ELF

A. LOL, Contour and ELF of compound 1F.

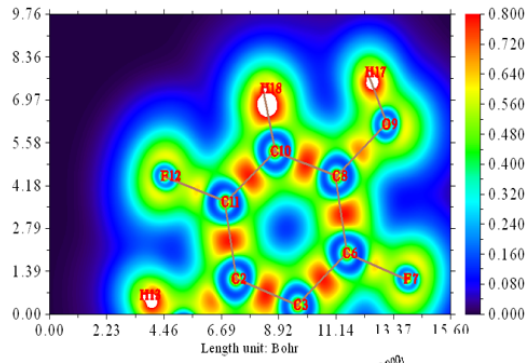

4F-LOL

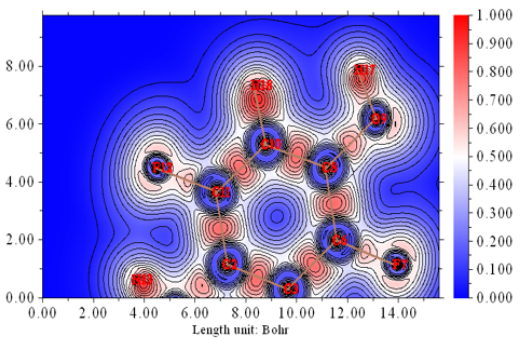

4F-Contour

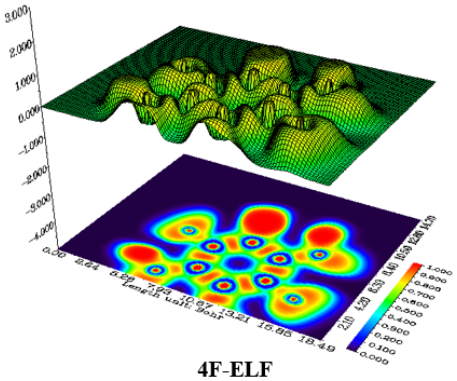

4F-ELF

B. LOL, Contour and ELF of compound 4F.

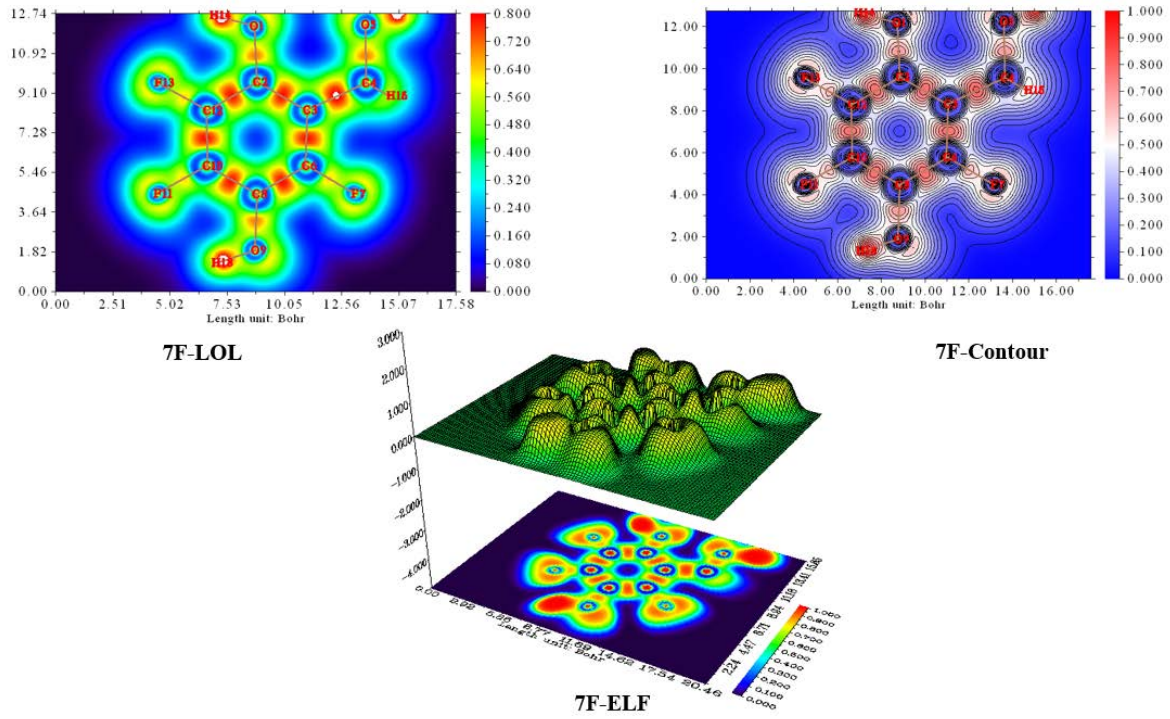

C. LOL, Contour and ELF of compound 7F.

Figure 3.18 (A-C): LOL, Contour and ELF plots of the A) 1F, B) 4F and C) 7F respectively

3.3.8. Analysis of NCI and VMD

The NCI and VMD plots are depicted in **Figure 3.19**. For compound 1F, the NCI plot reveals distinct regions corresponding to low reduced density gradient (RDG) values near zero, which are indicative of weak van der Waals interactions. Slightly negative values of sign(λ_2) ρ further suggest the presence of electrostatically driven hydrogen bonding interactions. The corresponding VMD surface map exhibits green-colored isosurface localized in non-bonded regions, substantiating the predominance of dispersive interactions that maintain the structural integrity of the molecule [55]. In compound 4F, the NCI plot features a more pronounced peak in the negative sign(λ_2)ρ

range, reflective of comparatively stronger attractive interactions. These observations imply the participation of hydrogen bonding interactions, potentially enhanced by the electron-withdrawing nature of the fluorine substituent. The corresponding VMD visualization exhibits both green and blue isosurfaces, the latter highlighting localized strong interactions near the fluorine atom and adjacent hydrogen-bearing sites, suggesting the presence of non-classical hydrogen bonding (C–H···F) interactions that contribute to molecular rigidity. For compound 7F, the NCI plot demonstrates a wider distribution of interaction intensities, encompassing both weak van der Waals and stronger attractive interactions. The VMD plot reveals a complex landscape of green and blue surfaces, particularly in the vicinity of the fluorine atoms and conjugated ring systems, indicating a rich network of dispersion forces and potential π···π or C–H···F interactions. This intricate interplay of weak forces suggests a potentially higher degree of conformational stability and enhanced interaction potential with biological targets. In summary, compound 1F is predominantly stabilized by van der Waals interactions; compound 4F exhibits stronger non-covalent features including fluorine-associated hydrogen bonding; and compound 7F displays a diverse and synergistic interaction profile with significant contributions from dispersive, hydrogen bonding, and possibly π-stacking interactions. These non-covalent features are integral to understanding the conformational behavior and bioactive potential of these fluorinated compounds.

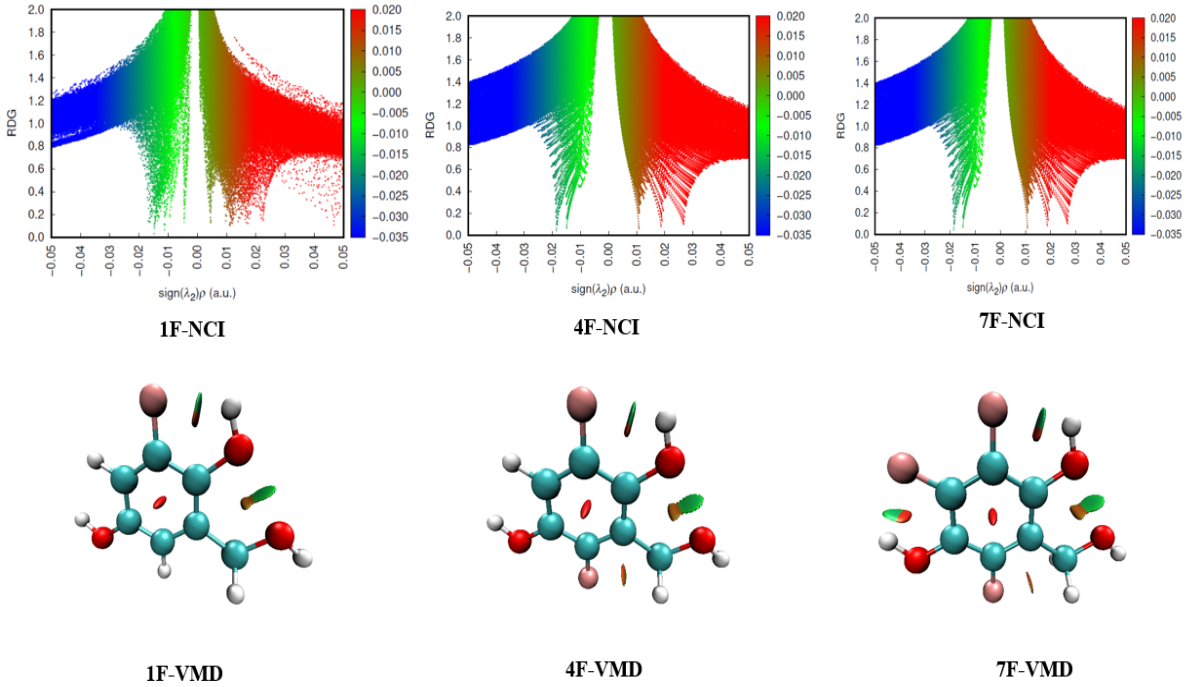

Figure 3.19: NCI and VMD plots of 1F, 4F and 7F

3.3.9. Bond length, bond angle and dihedral angle analysis

For 1F as shown in **Table S3.5 (supporting information)**, the bond lengths in the structure range from 0.9785 Å to 1.5127 Å, with the shortest bonds observed for O–H (~0.98 Å) and the longest for a C–C bond (~1.51 Å), indicating standard single bond character without abnormal elongation or compression. The C–F bond length (F(13)–C(4)) is 1.4127 Å, slightly longer than typical C–C bonds in the system, which reflects the larger atomic radius of fluorine and the polar nature of the C–F bond. Bond angles vary between 108.3° and 123.6°, with most C–C–C angles clustering around 120°, suggesting that the carbon centers maintain a near-planar, trigonal geometry; the angles involving fluorine (F(13)–C(4)–C(3)) are slightly contracted (116.4°), consistent with fluorine's high electronegativity exerting a pulling effect. The dihedral angles are predominantly near 0° or ±180°, confirming that the molecular framework is largely planar or anti-periplanar with negligible torsional strain. From the bond lengths, it can be concluded that the bonds retain typical single bond dimensions, with C–F slightly extending due to polar character; from the bond angles, it can be

concluded that the structure is predominantly planar with local compression around fluorinated carbons; and from the dihedral angles, it can be concluded that the molecule overall adopts a flat conformation with minimal twisting. For 4F as shown in **Table S3.6 (supporting information)**, the bond lengths in this structure range from 0.9806 Å to 1.5069 Å, with the shortest bonds occurring between O–H atoms (~0.98 Å) and the longest between C–C atoms (~1.51 Å), indicating that all bond distances fall within normal expected ranges for organic molecules. The C–F bonds (F(12)–C(2) and F(13)–C(5)) are measured at approximately 1.410 Å, slightly longer than the C–C aromatic bonds (~1.39–1.40 Å), consistent with the larger atomic size and polar character of fluorine. Bond angles vary from 107.04° to 123.89°, with most internal C–C–C and C–C–O angles clustering close to 120°, suggesting predominant sp^2 hybridization and a near-planar geometry, whereas smaller angles at C–O–C and C–O–H centers reflect local strain or tetrahedral distortions. Specifically, bond angles involving fluorine atoms (116.04° and 116.34°) are slightly contracted, reflecting the strong electronegativity of fluorine pulling bonding electrons toward itself. Dihedral angles are mostly close to 0°, ±120°, or ±180°, indicating a largely planar structure with minor twisting. A notable exception is observed at the O(15)–C(14) bond (−95.58°), indicating a significant torsion and non-planarity around that site, likely due to steric or electronic effects associated with the oxygen substituent. Thus, from bond lengths, it can be concluded that the molecular bonds are structurally normal with C–F bonds slightly longer; from bond angles, the structure is generally planar but shows slight compressions near highly electronegative atoms; and from dihedral angles, it is concluded that the majority of the molecule remains planar with localized torsional strain around the oxygenated side chain.

For 7F as shown in **Table S3.7 (supporting information)**, the bond lengths within the molecule indicate a relatively stable aromatic system, with C(2)-C(1) at 1.404 Å and C(3)-C(2) at 1.3959 Å, typical for conjugated C–C bonds. The bond angles are moderately distorted from the ideal 120°, suggesting slight electronic or steric effects; notably, C(3)-C(2)-C(1) measures 122.1291°, and C(4)-C(3)-C(2) at 119.861°. Dihedral angles are close to zero, such as C(4)-C(3)-C(2)-C(1) (0.6017°), showing planarity of the aromatic core. The oxygen atoms O(7)-C(1) and O(9)-C(4) exhibit

bond lengths of 1.39 Å and 1.3853 Å respectively, with bond angles around 121.4349° and 119.6171°, consistent with C–O bonding in aromatic systems. The fluorine substituents F(11), F(12), and F(13) demonstrate C–F bond lengths of 1.4003 Å, 1.3821 Å, and 1.4071 Å respectively, fitting well within typical aromatic C–F bonds. Fluorine atoms exert slight electron-withdrawing effects, which may explain the small deviations in nearby bond angles (e.g., F(11)-C(2)-C(1) at 117.6626° and F(13)-C(5)-C(4) at 115.229°), slightly compressing adjacent angles. C(14)-C(6) displays a bond length of 1.5069 Å, suggesting an sp^3-hybridized carbon connection. The oxygen atom attached to C(14) (O(15)) shows a C–O bond length of 1.472 Å and an associated bond angle O(15)-C(14)-C(6) of 106.9287°, characteristic of alcohol or ether linkages. Hydrogen atoms attached to oxygen exhibit expected bond lengths around 0.980–0.981 Å and maintain typical bond angles (approximately 111°), with dihedral angles suggesting relatively planar arrangements for O–H groups except minor deviations (e.g., H(8)-O(7)-C(1)-C(2) at -3.029°). Overall, the structure preserves aromatic planarity while minor angle compressions and elongations around fluorinated centers reflect localized electronic influences of the fluorine atoms.

3.3.10. Bioactivity score prediction

The bioactivity prediction of compounds 1F, 4F, and 7F was conducted using to evaluate their likelihood of interacting with key biological targets as shown in **Table 3.8**. Descriptors such as GPCR ligand, ion channel modulator, kinase inhibitor, nuclear receptor ligand, protease inhibitor, and general enzyme inhibitor were analyzed. These descriptors reflect the compounds' potential roles in modulating signal transduction, enzymatic pathways, gene regulation, and cellular communication highlighting their promise as multi-target therapeutic agents. A compound is generally classified as biologically active if its bioactivity score exceeds 0. Scores falling between −0.50 and 0.00 suggest moderate activity, whereas values below −0.50 typically indicate biological inactivity [56]. Among the compounds, 7F demonstrated the most favorable overall bioactivity profile, exhibiting the highest (i.e., least negative) average score across all evaluated descriptors, thereby indicating strong predicted bioactivity. 4F and 1F also displayed relatively high scores, suggesting moderate bioactivity potential. In

contrast, GA, the parent compound showed notably weaker predicted bioactivity, underscoring the enhanced pharmacological relevance of its derivatives. Furthermore, the native co-crystallized ligands from protein structures 7DQL, 3O4M, and 4YRE yielded significantly lower scores, reflecting inferior predicted bioactivity compared to the studied compounds. These results imply that compounds 1F, 4F, and 7F, particularly 7F, represent structurally optimized derivatives with good bioactivity potential, highlighting their promise as lead candidates for further pharmacological development.

Table 3.8: Bioactivity prediction of 1F, 4F, 7F, NL1, NL2 AND NL5 *via* Molinspiration

Compound	GPCR Ligand	Ion Channel Modulator	Kinase Inhibitor	Nuclear Receptor Ligand	Protease Inhibitor	Enzyme Inhibitor
1F	-0.55	-0.15	-0.68	-0.44	-0.88	-0.14
4F	-0.47	-0.11	-0.5	-0.25	-0.7	-0.05
7F	-0.46	-0.01	-0.38	-0.19	-0.37	0.18
GA	-0.88	-0.26	-0.97	-0.67	-0.98	-0.27
NL2	-2.14	-1.5	-2.33	-2.17	-2.52	-1.71
NL1	-3.04	-2.51	-3.1	-2.98	-3.24	-2.67
NL5	-2.39	-1.54	-2.38	-2.38	-2.36	-1.67

3.3.11. PASS Prediction

In PASS (Prediction of Activity Spectra for Substances), a higher Pa than Pi suggests that the compound is more likely to show the corresponding biological activity. This method is widely used in early-stage drug discovery to prioritize compounds with promising pharmacological potential [57]. The PASS prediction results indicate that all three compounds, 7F, 4F, and 1F, exhibit the likelihood of possible activities and is depicted in **Table 3.9**. Compound 7F shows antibacterial potential with a Pa of 0.183 and Pi of 0.134, suggesting moderate activity. Compound 4F demonstrates the highest

anti-inflammatory potential, with a Pa of 0.311 and Pi of 0.151, indicating strong anti-inflammatory activity. Compound 1F shows anti-protozoal activity, with a Pa of 0.243 and Pi of 0.075, reflecting a favourable likelihood of activity. Among these, **4F** stands out as the best candidate for anti-inflammatory activity, due to its superior Pa value, followed closely by 1F for anti-protozoal effects and 7F for antibacterial activity.

Table 3.9: PASS prediction of 1F, 4F and 7F

Compound	Activity	Pa (Probability of being Active)	Pi (Probability of being Inactive)
1F	Anti-protozoal	0.243	0.075
4F	Anti-inflammatory	0.311	0.151
7F	Anti-bacterial	0.183	0.134

3.3.12. IC_{50} calculation

The IC_{50} value of the investigated compound was estimated using a computational approach, as described in equation 1 below:

$$(IC_{50})_{inhibitor} = (IC_{50})_{substrate} \frac{\omega_{inhibitor}}{\omega_{substrate}} e^{(\mu_{substrate} - \mu_{inhibitor})} \quad (1)$$

In this context, $(IC_{50})_{substrate}$ denotes the inhibitory concentration of the reference compound. The dipole moment (μ) and electrophilicity index (ω), which serve as molecular reactivity descriptors, were calculated according to the equation 2-4 provided below [58]. The descriptors employed for IC_{50} estimation are summarized in **Table 3.10.**

$$\omega = \chi^2/2\eta \quad (2)$$

$$\chi = \{E_{LUMO} + E_{HOMO}\}/2 \text{ and} \quad (3)$$

$$\eta = \{E_{LUMO} - E_{HOMO}\}. E_{LUMO} \quad (4)$$

The IC_{50} values for the three test compounds were estimated in relation to their reported anti-protozoal, anti-inflammatory, and antibacterial activities. To evaluate the reliability of the computational approach, established phenolic inhibitors namely vestitol [59], genistein [60], and piceatannol [61] were employed as reference standards. This comparative analysis aimed to assess whether the predicted IC_{50} values are influenced by the selection of the reference compound. Computed results is presented in **Table 3.11**. The predicted IC_{50} for 1F is 50.2 µM, which is nearly ten times higher than the experimental IC_{50} of vestitol (5.2 µM). This suggests that fluorination at the 1-position may have adversely affected the compound's bioactivity, possibly due to unfavorable electronic or steric interactions diminishing its affinity for the biological target. With a predicted IC_{50} of 1.5 µM, 4F is significantly more potent than genistein (5.75 µM). This enhanced potency suggests that fluorine substitution at the 4-position likely enhances binding affinity or bioavailability, possibly through increased hydrophobicity or conformational rigidity. The predicted IC_{50} of 12.6 µM is slightly lower than piceatannol's experimental IC_{50} (14 µM), indicating a modest increase in activity. This could be attributed to minor improvements in molecular interactions, although the enhancement is not dramatic. Overall, **4F** emerges as the most promising derivative, showing markedly improved potency relative to its parent compound. These results underscore the importance of regioselective fluorine substitution in modulating bioactivity, highlighting compound 4F as a potentially superior lead candidate for further experimental validation.

Table 3.10: Descriptors used for calculating IC_{50}

Compound	E_{HOMO} (eV)	E_{LUMO} (eV)	Hardness (η)	Electrophilicity (ω)	Electronegativity (χ)	Dipole Moment (µ)
1F	6.033	0.5216	2.7557	1.9489	3.2773	2.9204
4F	6.4396	1.141	2.6493	2.7113	3.7903	2.0513
7F	6.7577	1.3002	2.7288	2.9743	4.0289	3.8805
Genistein	6.1043	2.2107	1.9468	4.4392	4.1575	1.2451
Piceatannol	5.5922	1.6308	1.9807	3.2925	3.6115	4.7036

Vestitol	5.7373	0.4645	2.6364	1.8236	3.1009	5.1219

Table 3.11: Calculated IC_{50} values of the compounds

Compound	IC_{50} (Experimental)	IC_{50} (Calculated Relative to Reference Compound)
1F	NA	50.2 µM (*via* Vestitol)
4F	NA	1.5 µM (*via* Genistein)
7F	NA	12.6 µM (*via* Piceatannol)
Piceatannol	14 µM	NA
Vestitol	5.2 µM	NA
Genistein	5.75 µM	NA

3.4.Conclusion

- This integrated computational–structural strategy, applied to fluorinated gentisyl alcohol derivatives, aims to elucidate the fluorination–activity relationship for this scaffold. Addressing this gap will yield mechanistic insights into how targeted fluorination can be leveraged to design next-generation therapeutic leads with improved affinity, selectivity, and pharmacokinetic behavior. Notably, fluorine substitution is known to block metabolic hotspots and modulate membrane permeability, further enhancing drug-like properties.
- Molecular dynamics simulations were initially conducted for the five variants, but only three achieved convergences. Analyses of RMSD, RMSF, Rg, hydrogen bonding, and MM/PBSA revealed moderate structural stability, noticeable conformational fluctuations, and variable binding energetics, indicating the need for further optimization.
- Extensive quantum analyses revealed the compounds' electronic structure, charge distribution, non-linear optical properties, electrostatic potential, electron localization, and non-covalent interactions. These findings

highlighted their reactivity patterns, stability, and intermolecular interaction profiles, indicating their potential as promising lead candidates.

- Bioactivity score predictions and PASS suggested a strong potential for diverse biological activities, indicating that the compounds are likely to interact effectively with relevant biological targets. These results provide preliminary evidence supporting their suitability for further pharmacological evaluation and optimization.
- Finally, theoretical IC_{50} calculations identified 4F as the most potent derivative, exhibiting greater activity than the parent compound and establishing it as a leading candidate for further investigation.

These findings lay a strong foundation for further rational development, including targeted synthesis, and *in vitro* and *in vivo* evaluations to validate their efficacy and pharmacological relevance.

References

1. Feng, X. E., Zhao, W. Y., Ban, S. R., Zhao, C. X., Li, Q. S., & Lin, W. H. (2011). Structure–Activity relationship of halophenols as a new class of protein tyrosine kinase inhibitors. *International Journal of Molecular Sciences*, *12*(9), 6104-6115.
2. Zhao, W., Feng, X., Ban, S., Lin, W., & Li, Q. (2010). Synthesis and biological activity of halophenols as potent antioxidant and cytoprotective agents. *Bioorganic & medicinal chemistry letters*, *20*(14), 4132-4134.
3. Chen, L., Fang, Y., Zhu, T., Gu, Q., & Zhu, W. (2008). Gentisyl alcohol derivatives from the marine-derived fungus Penicillium terrestre. *Journal of Natural Products*, *71*(1), 66-70.
4. Shen, X., Wang, J., Gall, B. K., Ferreira, E. M., Yuan, Q., & Yan, Y. (2018). Establishment of novel biosynthetic pathways for the production of salicyl alcohol and gentisyl alcohol in engineered Escherichia coli. *ACS synthetic biology*, *7*(4), 1012-1017.
5. Xu, Z., Yang, Z., Liu, Y., Lu, Y., Chen, K., & Zhu, W. (2014). Halogen bond: its role beyond drug–target binding affinity for drug discovery and development. *Journal of chemical information and modeling*, *54*(1), 69-78.
6. Gattu, R., Ramesh, S. S., Nadigar, S., & Ramesh, S. (2023). Conjugation as a tool in therapeutics: Role of amino acids/peptides-bioactive (including Heterocycles) hybrid molecules in treating infectious diseases. *Antibiotics*, *12*(3), 532.
7. Pal, S., Kumar, V., Kundu, B., Bhattacharya, D., Preethy, N., Reddy, M. P., & Talukdar, A. (2019). Ligand-based pharmacophore modeling, virtual screening and molecular docking studies for discovery of potential topoisomerase I inhibitors. *Computational and structural biotechnology journal*, *17*, 291-310.
8. Lu, Y., Liu, Y., Xu, Z., Li, H., Liu, H., & Zhu, W. (2012). Halogen bonding for rational drug design and new drug discovery. *Expert opinion on drug discovery*, *7*(5), 375-383.

9. Costa, P. J., Nunes, R., & Vila-Viçosa, D. (2019). Halogen bonding in halocarbon-protein complexes and computational tools for rational drug design. *Expert Opinion on Drug Discovery*, *14*(8), 805-820.
10. Davidsen, A. B., Mardal, M., & Linnet, K. (2019). In vitro metabolism and hepatic intrinsic clearance of the synthetic cannabinoid receptor agonist JWH-122 and its four ω-halogenated analogues. *The AAPS Journal*, *21*, 1-9.
11. Singha, B., Gogoi, P. P., Longkumer, P., Boruah, N., & Sinha, U. B. (2024). Evaluation of Some Designed Halogenated Variants of Gentisyl Alcohol: Molecular Docking, DFT, Druglikeness, and ADMET Studies for Assessing Biological Properties. *Journal of Applicable Chemistry*, *13*(2), 98-113.
12. Lindorff-Larsen, K., Piana, S., Palmo, K., Maragakis, P., Klepeis, J. L., Dror, R. O., & Shaw, D. E. (2010). Improved side-chain torsion potentials for the Amber ff99SB protein force field. *Proteins: Structure, Function, and Bioinformatics*, *78*(8), 1950-1958.
13. Sousa da Silva, A. W., & Vranken, W. F. (2012). ACPYPE-Antechamber python parser interface. *BMC research notes*, *5*, 1-8.
14. Berendsen, H. J., van der Spoel, D., & van Drunen, R. (1995). GROMACS: A message-passing parallel molecular dynamics implementation. *Computer physics communications*, *91*(1-3), 43-56.
15. Lindahl, E., Hess, B., & Van Der Spoel, D. (2001). GROMACS 3.0: a package for molecular simulation and trajectory analysis. *Molecular modeling annual*, *7*, 306-317.
16. Van Der Spoel, D., Lindahl, E., Hess, B., Groenhof, G., Mark, A. E., & Berendsen, H. J. (2005). GROMACS: fast, flexible, and free. *Journal of computational chemistry*, *26*(16), 1701-1718.

17. Hess, B., Kutzner, C., Van Der Spoel, D., & Lindahl, E. (2008). GROMACS 4: algorithms for highly efficient, load-balanced, and scalable molecular simulation. *Journal of chemical theory and computation*, *4*(3), 435-447.

18. Abraham, M. J., Murtola, T., Schulz, R., Páll, S., Smith, J. C., Hess, B., & Lindahl, E. (2015). GROMACS: High performance molecular simulations through multi-level parallelism from laptops to supercomputers. *SoftwareX*, *1*, 19-25.

19. Wang, C., Greene, D. A., Xiao, L., Qi, R., & Luo, R. (2018). Recent developments and applications of the MMPBSA method. *Frontiers in molecular biosciences*, *4*, 87.

20. Kumar, N., Mandal, P., Kumar, B., Rani, P., & Singh, D. V. (2025). Applications of Molecular Dynamics Simulation and MM-PBSA Methods in Discovery of Veterinary Drugs. In *Bioinformatics in Veterinary Science: Vetinformatics* (pp. 325-366). Singapore: Springer Nature Singapore.

21. Wu, Y., Lou, L., & Xie, Z. R. (2020). A pilot study of all-computational drug design protocol–from structure prediction to interaction analysis. *Frontiers in chemistry*, *8*, 81.

22. Wolber, G., & Langer, T. (2005). LigandScout: 3-D pharmacophores derived from protein-bound ligands and their use as virtual screening filters. *Journal of chemical information and modeling*, *45*(1), 160-169.

23. Choudhury, C., & Narahari Sastry, G. (2019). Pharmacophore modelling and screening: concepts, recent developments and applications in rational drug design. *Structural bioinformatics: applications in preclinical drug discovery process*, 25-53.

24. M. J. Frisch, G. W. Trucks, H. B. Schlegel, G. E. Scuseria, M. A. Robb, J. R. Cheeseman, G. Scalmani, V. Barone, G. A. Petersson, H. Nakatsuji, X. Li, M. Caricato, A. V. Marenich, J. Bloino, B. G. Janesko, R. Gomperts, B. Mennucci, H. P. Hratchian, J. V. Ortiz, A. F. Izmaylov, J. L. Sonnenberg, D. Williams-Young, F. Ding, F. Lipparini, F. Egidi, J. Goings, B. Peng, A.

Petrone, T. Henderson, D. Ranasinghe, V. G. Zakrzewski, J. Gao, N. Rega, G. Zheng, W. Liang, M. Hada, M. Ehara, K. Toyota, R. Fukuda, J. Hasegawa, M. Ishida,T. Nakajima, Y. Honda, O. Kitao, H. Nakai, T. Vreven, K. Throssell, J. A. Montgomery, Jr., J. E. Peralta, F. Ogliaro, M. J. Bearpark, J. J. Heyd, E. N. Brothers, K. N. Kudin, V. N. Staroverov, T. A. Keith, R. Kobayashi, J. Normand, K. Raghavachari, A. P. Rendell, J. C. Burant, S. S. Iyengar, J. Tomasi, M. Cossi, J. M. Millam, M. Klene, C. Adamo, R. Cammi, J. W. Ochterski, R. L. Martin, K. Morokuma, O. Farkas, J. B. Foresman, and D. J. Fox, Gaussian, Inc., Wallingford CT, 2016, Gaussian 16, Revision C.01, https://gaussian.com/gaussian16/

25. R.Dennington, T. Keith, and J.Millam, Semichem Inc, Shawnee Mission KS, GaussView, Version, 2009, 5, https://gaussian.com/gaussview6/

26. Ahmed, B., Barukial, P., & Bezbaruah, B. (2023). Some halogenated anticancer agents, role of halide (-X) and their interaction mechanism with AT/GC base pairs: a computational study. *Journal of the Indian Chemical Society*, *100*(7), 101027.

27. Carneiro, S. S., Lima, A. R., Marinho, M. M., & Marinho, E. S. (2016). In silico Study Of The Therapeutic Agent In The Treatment Of Non-Hodgkin's Lymphomas, Peripheral T-Cell Belinostat, A Semi-Empirical Approach. *Imp. J. Interdiscip. Res*, *2*(8), 1645-1648.

28. Patil, P. S., & Sekar, N. (2024). Nonlinear optical properties of natural hydroxyanthraquinones studied using density functional theory (DFT) technique. *Journal of Photochemistry and Photobiology A: Chemistry*, *446*, 115151.

29. Abdel-Rahman, L. H., Abu-Dief, A. M., Moustafa, H., & Abdel-Mawgoud, A. A. H. (2020). Design and nonlinear optical properties (NLO) using DFT approach of new Cr (III), VO (II), and Ni (II) chelates incorporating tri-dentate imine ligand for DNA interaction, antimicrobial, anticancer activities and molecular docking studies. *Arabian Journal of Chemistry*, *13*(1), 649-670.

30. Singh, J. S., Khan, M. S., & Uddin, S. (2023). A DFT study of vibrational spectra of 5-chlorouracil with molecular structure, HOMO–LUMO, MEPs/ESPs and thermodynamic properties. *Polymer Bulletin*, *80*(3), 3055-3083.

31. Glendening, E. D., Landis, C. R., & Weinhold, F. (2013). NBO 6.0: Natural bond orbital analysis program. *Journal of computational chemistry*, *34*(16), 1429-1437.

32. Ahmed, B., Barukial, P., Singha, B., Bora Sinha, U., & Bezbaruah, B. (2024). Some pyridyl moiety based metal complexes (viz., Mn+ 2, Co+ 2 and Zn+ 2) as potential anticancer agents and DNA nucleobase interaction: A DFT approach

33. Arulaabaranam, K., Muthu, S., Mani, G., & Geoffrey, A. B. (2021). Speculative assessment, molecular composition, PDOS, topology exploration (ELF, LOL, RDG), ligand-protein interactions, on 5-bromo-3-nitropyridine-2-carbonitrile. *Heliyon*, *7*(5).

34. Humphrey, W., Dalke, A., & Schulten, K. (1996). VMD: visual molecular dynamics. *Journal of molecular graphics*, *14*(1), 33-38.

35. Jezierska, A., Błaziak, K., Klahm, S., Lüchow, A., & Panek, J. J. (2021). Non-Covalent Forces in Naphthazarin—Cooperativity or Competition in the Light of Theoretical Approaches. *International Journal of Molecular Sciences*, *22*(15), 8033.

36. Moorthi, P. P., Gunasekaran, S., & Ramkumaar, G. R. (2014). Vibrational spectroscopic studies of Isoleucine by quantum chemical calculations. *Spectrochimica Acta Part A: Molecular and Biomolecular Spectroscopy*, *124*, 365-374.

37. Mkhayar, K., Elkhattabi, K., Elkhalabi, R., Haloui, R., Daoui, O., Edache, E. I., ... & Elkhattabi, S. (2023). Evaluation of dimedone-derived compounds as inhibitors against human colon cancer: Insights from 2D-QSAR, ADMET prediction, Osiris, Molinspiration, and molecular modeling. *Chinese Journal of Analytical Chemistry*, *51*(11), 100330.

38. Lotha, Tsenbeni N., Kikoleho Richa, Viphrezolie Sorhie, Ketiyala, Vevosa Nakro, Imkongyanger, Vimha Ritse, Lemzila Rudithongru, Nima D. Namsa, and Latonglila Jamir. "Environmentally benign synthesis of unsymmetrical ureas and their evaluation as potential HIV-1 protease inhibitors via a computational approach." *Molecular Diversity* 28, no. 2 (2024): 749-763.

39. Bag, A., & Ghorai, P. K. (2016). Development of quantum chemical method to calculate half maximal inhibitory concentration (IC50). *Molecular informatics*, *35*(5), 199-206.

40. Abu-Dief, A. M., El-Khatib, R. M., Aljohani, F. S., Al-Abdulkarim, H. A., Alzahrani, S., El-Sarrag, G., & Ismael, M. (2022). Synthesis, structural elucidation, DFT calculation, biological studies and DNA interaction of some aryl hydrazone Cr3+, Fe3+, and Cu2+ chelates. *Computational Biology and Chemistry*, *97*, 107643.

41. Alatawi, N. M., Alsharief, H. H., Alharbi, A., Alhasani, M., Attar, R. M., Khalifa, M. E., ... & El-Metwaly, N. M. (2022). Simulation for the behavior of new Fe (III) and Cr (III)-thiophenyl complexes towards DNA polymerase: synthesis, characterization, eukaryotic DNA and Hartree–Fock computation. *Chemical Papers*, *76*(6), 3919-3935.

42. Bag, A. (2021). Dft based computational methodology of ic50 prediction. *Current computer-aided drug design*, *17*(2), 244-253.

43. Vant, J. W., Sarkar, D., Streitwieser, E., Fiorin, G., Skeel, R., Vermaas, J. V., & Singharoy, A. (2020). Data-guided Multi-Map variables for ensemble refinement of molecular movies. *The Journal of Chemical Physics*, *153*(21).

44. Bagewadi, Z. K., Khan, T. Y., Gangadharappa, B., Kamalapurkar, A., Shamsudeen, S. M., & Yaraguppi, D. A. (2023). Molecular dynamics and simulation analysis against superoxide dismutase (SOD) target of Micrococcus luteus with secondary metabolites from Bacillus licheniformis recognized by genome mining approach. *Saudi Journal of Biological Sciences*, *30*(9), 103753.

45. Dey, J., Mahapatra, S. R., Raj, T. K., Misra, N., & Suar, M. (2023). Identification of potential flavonoid compounds as antibacterial therapeutics against Klebsiella pneumoniae infection using structure-based virtual screening and molecular dynamics simulation. *Molecular Diversity*, 1-18.
46. Chen, D., Oezguen, N., Urvil, P., Ferguson, C., Dann, S. M., & Savidge, T. C. (2016). Regulation of protein-ligand binding affinity by hydrogen bond pairing. *Science advances*, *2*(3), e1501240.
47. Wang, E., Sun, H., Wang, J., Wang, Z., Liu, H., Zhang, J. Z., & Hou, T. (2019). End-point binding free energy calculation with MM/PBSA and MM/GBSA: strategies and applications in drug design. *Chemical reviews*, *119*(16), 9478-9508.
48. Jack, K. S., Asaruddin, M. R. B., & Bhawani, S. A. (2022). Pharmacophore study, molecular docking and molecular dynamic simulation of virgin coconut oil derivatives as anti-inflammatory agent against COX-2. *Chemical and biological technologies in agriculture*, *9*(1), 73.
49. Govindasamy, P., Gunasekaran, S., & Srinivasan, S. (2014). Molecular geometry, conformational, vibrational spectroscopic, molecular orbital and Mulliken charge analysis of 2-acetoxybenzoic acid. *Spectrochimica Acta Part A: Molecular and Biomolecular Spectroscopy*, *130*, 329-336.
50. Steffy, A. D., Dhas, D. A., Joe, I. H., & Balachandran, S. (2024). Theoretical investigations on structural, spectral, NBO, NLO and topology exploration (AIM, ELF, LOL, RDG) of piperazine-2, 5-dione oxalic acid monohydrate. *Journal of Molecular Structure*, *1295*, 136653.
51. Shivaleela, B., Shivraj, G. G., & Hanagodimath, S. M. (2023). Estimation of dipole moments by Solvatochromic shift method, spectroscopic analysis of UV–Visible, HOMO-LUMO, ESP map, Mulliken atomic charges, NBO and NLO properties of benzofuran derivative. *Results in Chemistry*, *6*, 101046.
52. Murray, J. S., & Politzer, P. (2002). Electrostatic potentials: chemical applications. *Encyclopedia of computational chemistry*, *2*.

53. Luque, F. J., López, J. M., & Orozco, M. (2000). Perspective on "Electrostatic interactions of a solute with a continuum. A direct utilization of ab initio molecular potentials for the prevision of solvent effects" Miertus S, Scrocco E, Tomasi J (1981) Chem Phys 55: 117. *Theoretical Chemistry Accounts*, *103*(3), 343-345.

54. Sheeba, B. Q., Michael Mary, M. S., Amalanathan, M., & Job, C. B. (2021). Structural and vibrational spectral investigation on the identification of Non-Linear Optical properties and wave function analyses (electrostatic potential, electron localisation function, localised orbital locator) of 3-Ethoxy Salicilaldehyde. *Molecular Simulation*, *47*(15), 1217-1233.
55. Silvi, B., & Savin, A. (1994). Classification of chemical bonds based on topological analysis of electron localization functions. *Nature*, *371*(6499), 683-686.
56. Khan, T., Dixit, S., Ahmad, R., Raza, S., Azad, I., Joshi, S., & Khan, A. R. (2017). Molecular docking, PASS analysis, bioactivity score prediction, synthesis, characterization and biological activity evaluation of a functionalized 2-butanone thiosemicarbazone ligand and its complexes. *Journal of chemical biology*, *10*, 91-104.
57. Lagunin, A., Filimonov, D., & Poroikov, V. (2010). Multi-targeted natural products evaluation based on biological activity prediction with PASS. *Current Pharmaceutical Design*, *16*(15), 1703-1717.
58. Bhatia, M. (2024). An overview of conceptual-DFT based insights into global chemical reactivity of volatile sulfur compounds (VSCs). *Computational Toxicology*, *29*, 100295.
59. Sousa, L. R. D., Amparo, T. R., Souza, G. H. B. D., Ferraz, A. T., Fonseca, K. D. S., Azevedo, A. S. D., ... & Santos, V. M. R. D. (2023). Anti-Trypanosoma cruzi potential of vestitol isolated from lyophilized red propolis. *Molecules*, *28*(23), 7812.
60. Dharmappa, K. K., Mohamed, R., Shivaprasad, H. V., & Vishwanath, B. S. (2010). Genistein, a potent inhibitor of secretory phospholipase A 2: a new

insight in down regulation of inflammation. *Inflammopharmacology*, *18*, 25-31.

61. Dadi, P. K., Ahmad, M., & Ahmad, Z. (2009). Inhibition of ATPase activity of Escherichia coli ATP synthase by polyphenols. *International Journal of Biological Macromolecules*, *45*(1), 72-7

SUPPORTING INFORMATION

3.3. Result and discussion

3.3.1. Molecular dynamics

3.3.1.1. Root mean square deviation (RMSD)

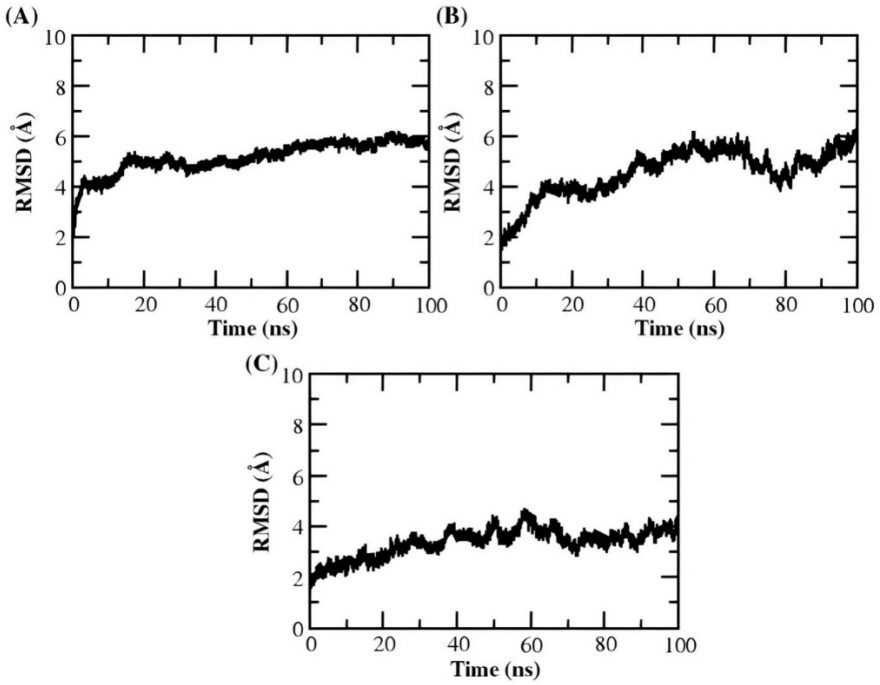

Figure S3.2 (A-C): Root Mean Square Deviation (RMSD) of backbone carbon atoms of protein-ligand complexes for the duration of 100 ns simulation time. A). 7F-7DQL, B). 4F-3O4M, and C). 1F- 4YRE respectively.

3.3.1.2.Root Mean Square Fluctuation (RMSF)

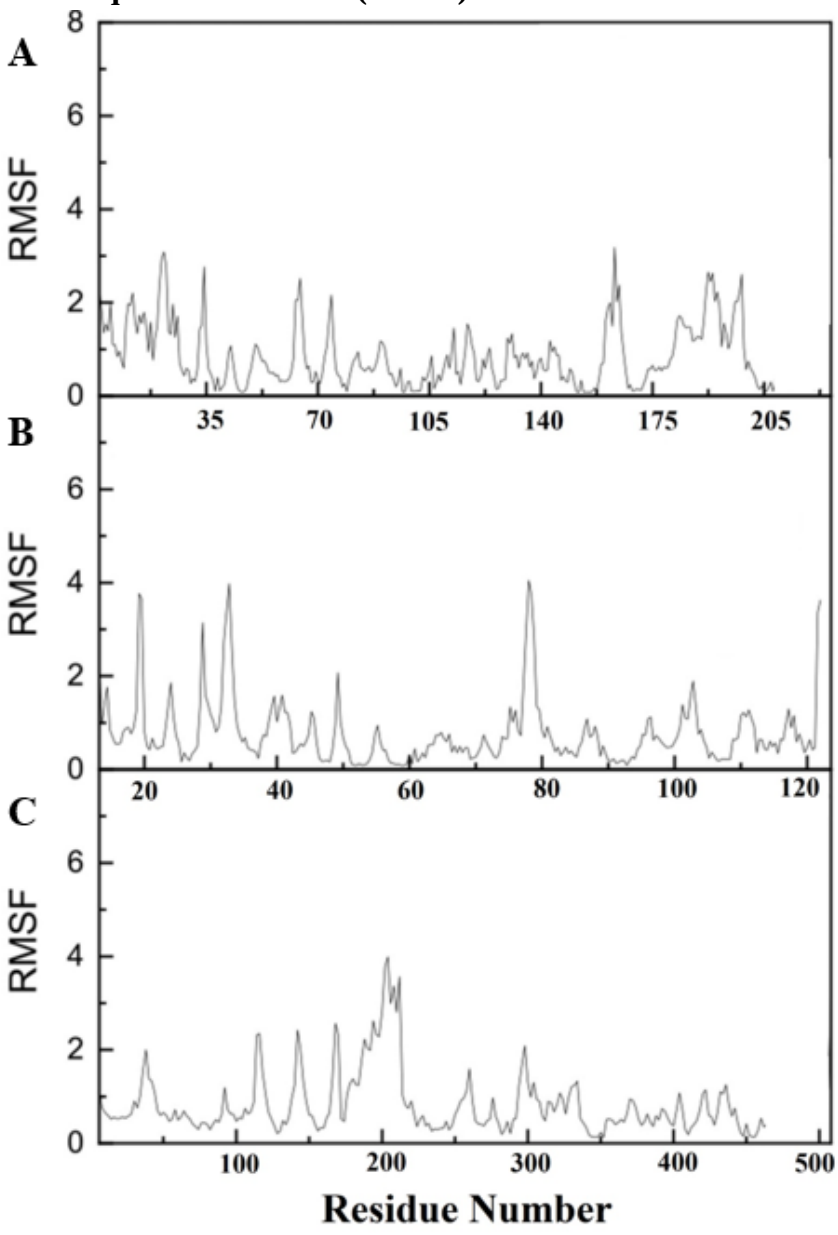

Figure S3.3 (A-C): Root Mean Square Fluctuation (RMSF) of amino acid residues in proteins upon ligand binding for the duration of 100 ns simulation time. **A).** 7F-7DQL, **B).** 4F-3O4M, and **C).** 1F- 4YRE, respectively.

3.3.1.3.Radius of gyration (Rg)

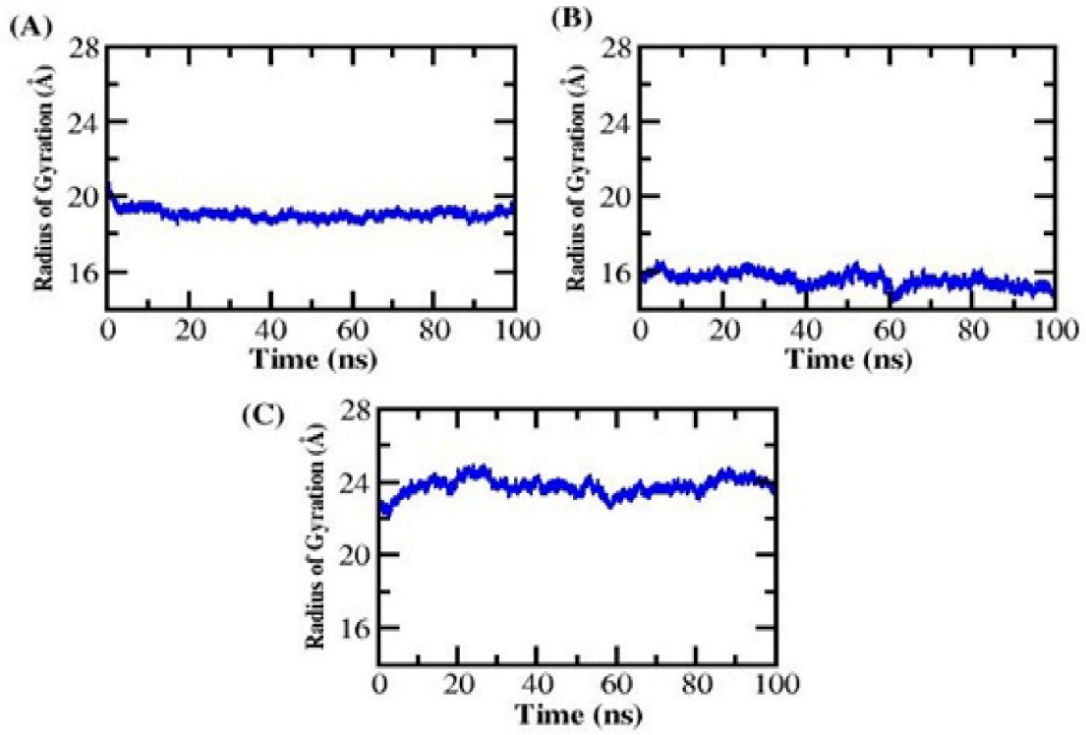

Figure S3.4 (A-C): Radius of Gyration of protein-ligand complexes for the duration of 100 ns simulation time. **A).** 7F-7DQL, **B).** 4F-3O4M, and **C).** 1F- 4YRE, respectively.

3.3.1.4.Hydrogen bond

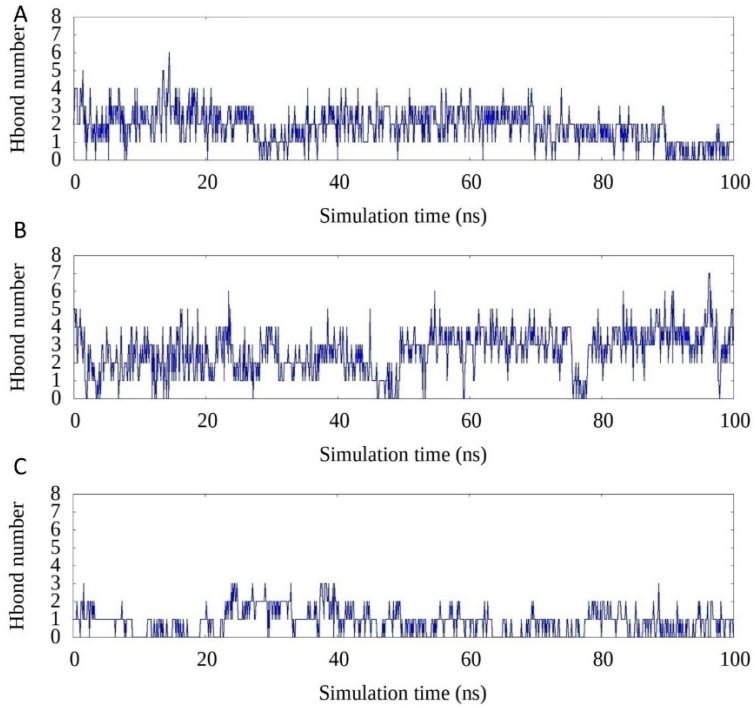

Figure S3.5(A-C): The number of hydrogen bonds formed between protein-ligand complexes for the duration of 100 ns simulation time. **A).** 7F-7DQL, **B).** 4F-3O4M, and **C).** 1F- 4YRE, respectively.

3.3.1.5.Binding Free Energy

Table S3.1: Binding free energy of the three complexes.

Complex	**Electrostatic energy (kJ/mol)**	**Polar solvation energy (kJ/mol)**	**SASA energy (kJ/mol)**	**Van der Waal energy (kJ/mol)**	**Binding energy (kJ/mol)**
7F-7DQL	-2.694 +/- 4.166	36.894 +/- 31.357	-4.767 +/- 7.154	-49.681 +/- 73.568	-20.249 +/- 78.547
4F-3O4M	-2.365 +/- 1.950	39.945 +/- 32.417	-12.179 +/- 6.445	-122.606 +/- 60.849	-97.205 +/- 40.589

1F-4YRE	0.119 +/- 0.745	17.098 +/- 11.360	-9.991 +/- 2.251	-99.060 +/- 21.772	-91.833 +/- 14.386

3.3.2. Structural pharmacophore

- *For target **7DQL**:*

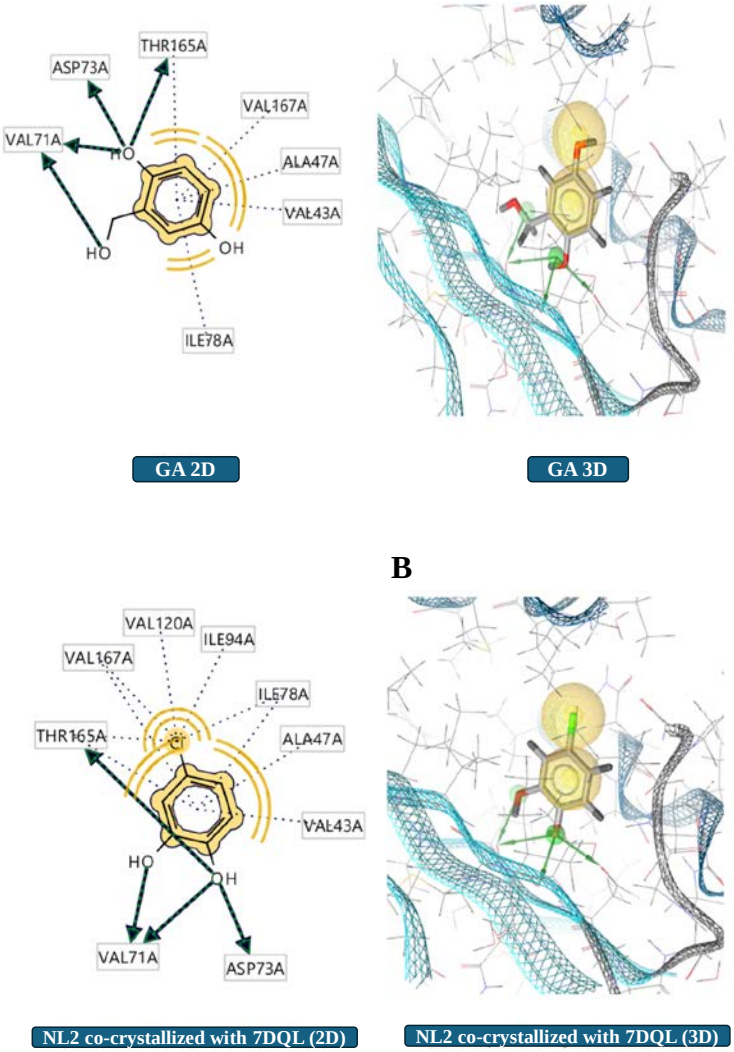

Figure S3.6 (B-C): Structural pharmacophore of compounds **B)**. GA and **C).** NL2 for target 7DQL

- *For target **3O4M:***

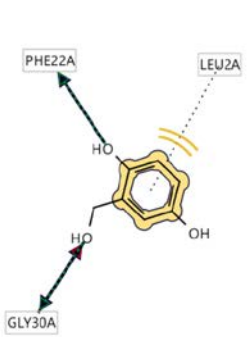

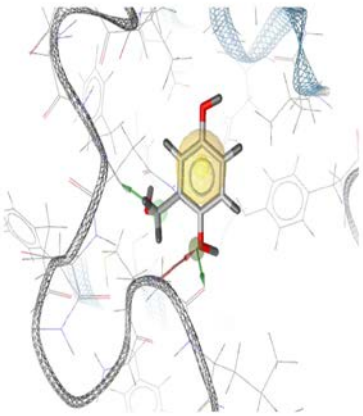

GA 2D GA 3D

B

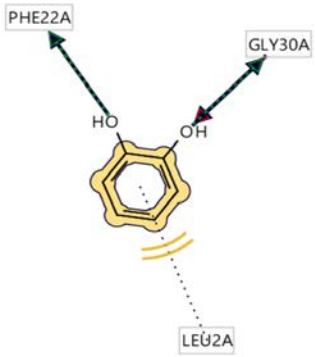

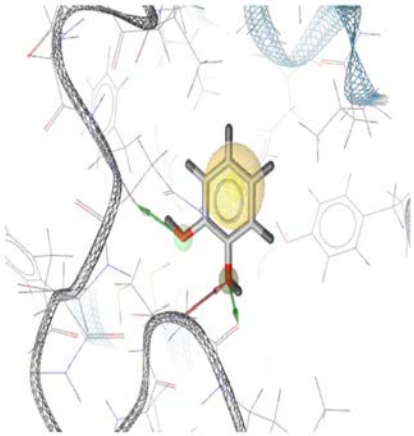

NL1 co-crystallized with 3O4M (2D) NL1 co-crystallized with 3O4M (3D)

C

Figure S3.7 (B-C): Structural pharmacophore of compounds B). GA and C). NL5 for target 3O4M

- *For target **4YRE:***

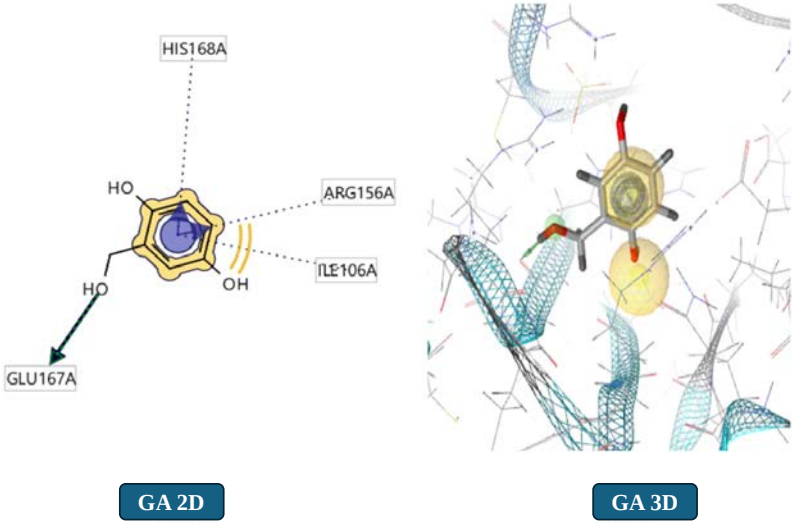

B

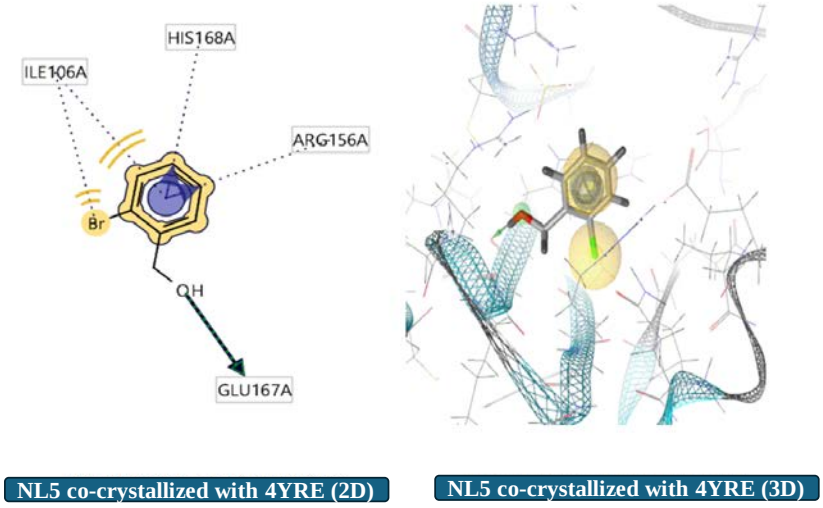

C

Figure S3.8 (B-C): Structural pharmacophore of compounds **B).** GA and **C).** NL5 for target 4YRE

3.3.3. Mulliken Charge Analysis

Table S3.2: Computed Mulliken Charge distribution of the compounds understudy computed by DFT/LANL2DZ basis set

SL NO.	COMPOUNDS	Atoms			
		H	O	C	Halogens
1	1F	0.360	-0.511	-0.347	-0.261
2	4F	0.352	-0.485	-0.378	-0.252
3	7F	0.355	-0.485	-0.379	-0.221
4	GA	0.342	-0.476	-0.364	----
5	NL1	0.374	-0.524	-0.322	----
6	NL2	0.379	-0.516	-0.298	-0.080
7	NL5	0.349	-0.469	-0.375	-0.051

3.3.6. Analysis of MEP, ESP and contour plots

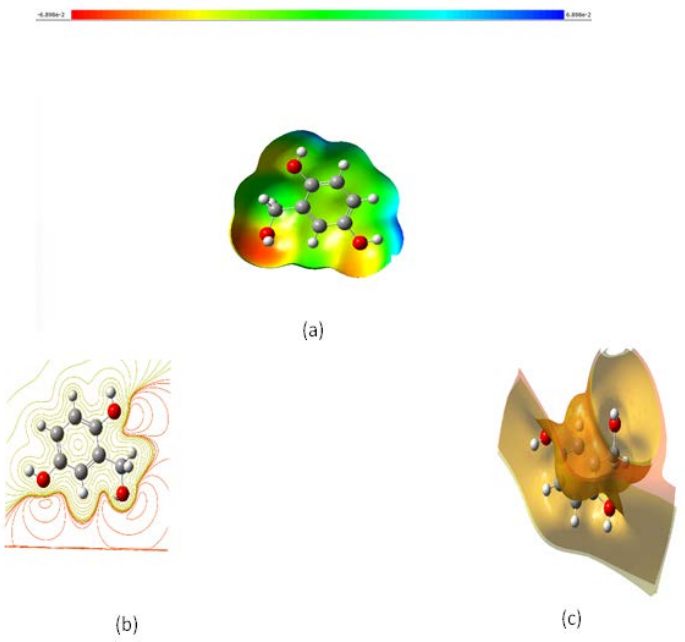

Figure S3.14: **(a)** Molecular electrostatic potentials (MEP) plot of GA, **(b)** contour map plot of ESP isosurface of GA, **(c)** visualization of the ESP array plot for GA

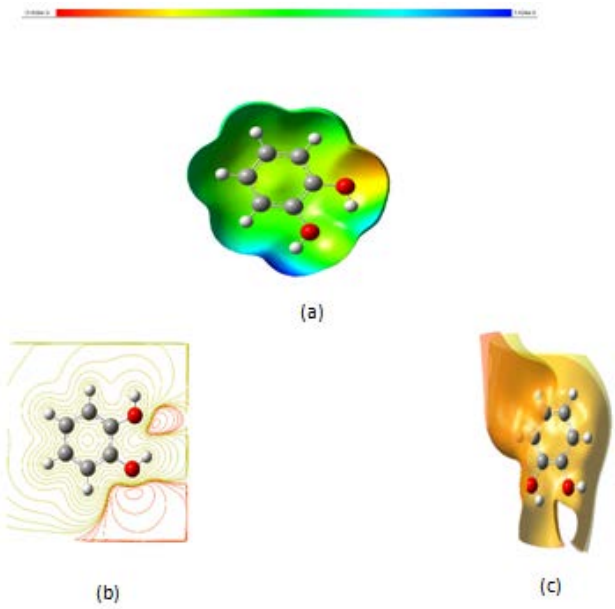

Figure S3.15: **(a)** Molecular electrostatic potentials (MEP) plot of NL1, **(b)** contour map plot of ESP isosurface of NL1, **(c)** visualization of the ESP array plot for NL1

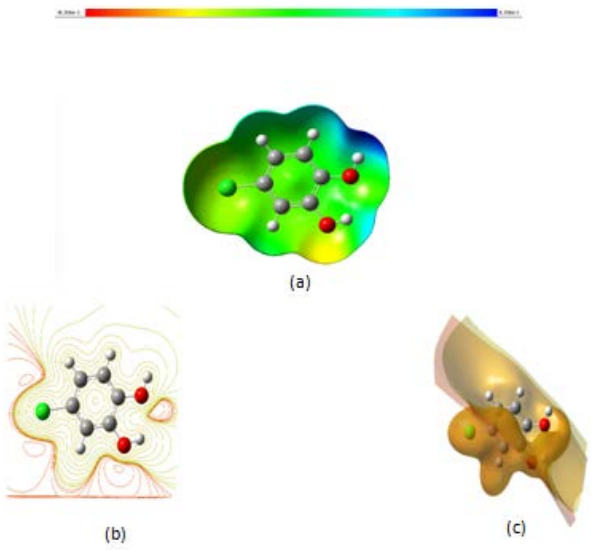

Figure S3.16: **(a)** Molecular electrostatic potentials (MEP) plot of NL2, **(b)** contour map plot of ESP isosurface of NL2, **(c)** visualization of the ESP array plot for NL2

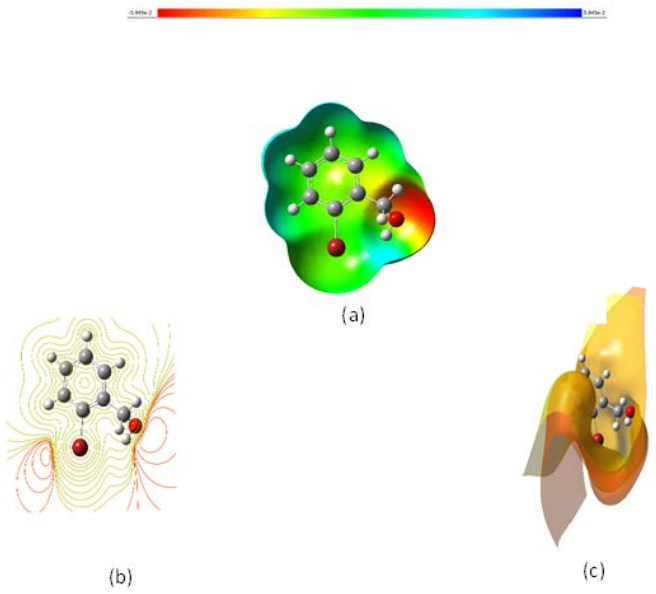

Figure S3.17: (a) Molecular electrostatic potentials (MEP) plot of NL5, **(b)** contour map plot of ESP isosurface of NL5, **(c)** visualization of the ESP array plot of NL5.

3.3.9. Bond length, bond angle and dihedral angle analysis

Table S3.5: Bond length, bond angle and dihedral angle of 1F

Bond length (Unit)		**Bond angle (Unit)**		**Dihedral angle**		
C(1)		C(1)		C(1)		
C(2)-C(1)	1.4059	C(2)-C(1)		C(2)-C(1)		
C(3)-C(2)	1.4071	C(3)-C(2)-C(1)	119.2551	C(3)-C(2)-C(1)		
C(4)-C(3)	1.4015	C(4)-C(3)-C(2)	118.5614	C(4)-C(3)-C(2)-C(1)	0.004	Dihedral
C(5)-C(4)	1.3909	C(5)-C(4)-C(3)	123.6177	C(5)-C(4)-C(3)-C(2)	-0.0014	Dihedral

C(6)-C(1)	1.4085	C(6)-C(1)-C(2)	120.4953	C(6)-C(1)-C(2)-C(3)	-0.004	Dihedral
H(7)-C(1)	1.0859	H(7)-C(1)-C(2)	117.8541	H(7)-C(1)-C(2)C(6)	121.6506	Pro-R
H(8)-C(5)	1.0837	H(8)-C(5)-C(4)	121.7083	H(8)-C(5)-C(4)-C(6)	121.1944	Pro-S
O(9)-C(3)	1.4013	O(9)-C(3)-C(2)	118.8018	O(9)-C(3)-C(2)-C(4)	122.6368	Pro-R
O(11)-C(6)	1.4012	O(11)-C(6)-C(1)	122.5516	O(11)-C(6)-C(1)-C(5)	116.4752	Pro-S
F(13)-C(4)	1.4127	F(13)-C(4)-C(3)	116.3877	F(13)-C(4)-C(3)-C(5)	119.9946	Pro-S
C(14)-C(2)	1.5127	C(14)-C(2)-C(1)	122.022	C(14)-C(2)C-(1)-C(3)	118.7229	Pro-R
O(15)-C(14)	1.4601	O(15)-C(14)-C(2)	108.3044	O(15)-C(14)-C(2)-C(1)	-0.0172	Dihedral
H(17)-C(14)	1.101	H(17)-C(14)-C(2)	109.5022	H(17)-C(14)-C(2)-O(15)	111.03	Pro-R
H(18)-C(14)	1.101	H(18)-C(14)-C(2)	109.4973	H(18)-C(14)-C(2)-O(15)	111.0235	Pro-S
H(10)-O(9)	0.9803	H(10)-O(9)-C(3)	111.2604	H(10)-O(9)-C(3)-C(2)	-179.975	Dihedral
H(12)-O(11)	0.9787	H(12)-O(11)-C(6)	111.8403	H(12)-O(11)-C(6)-C(1)	0.0377	Dihedral
H(16)-O(15)	0.9785	H(16)-O(15)-C(14)	110.6596	H(16)-O(15)-C(14)-C(2)	-179.894	Dihedral

Table S3.6: Bond length, bond angle and dihedral angle of 4F

Bond length (Unit)		**Bond angle (Unit)**		**Dihedral angle**		
C(1)		C(1)		C(1)		
C(2)-C(1)	1.4052	C(2)-C(1)		C(2)-C(1)		
C(3)-C(2)	1.3913	C(3)-C(2)-C(1)	123.8917	C(3)-C(2)-C(1)		
C(4)-C(3)	1.4034	C(4)-C(3)-C(2)	117.7624	C(4)-C(3)-C(2)-C(1)	0.4719	Dihedral
C(5)-C(4)	1.4048	C(5)-C(4)-C(3)	118.3237	C(5)-C(4)-C(3)-C(2)	-0.1855	Dihedral
C(6)-C(1)	1.4101	C(6)-C(1)-C(2)	118.85	C(6)-C(1)-C(2)-C(3)	-0.0719	Dihedral
H(7)-C(3)	1.0836	H(7)-C(3)-C(2)	121.5914	H(7)-C(3)-C(2)-C(4)	120.646	Pro-S
O(8)-C(1)-	1.3926	O(8)-C(1)-C(2)	121.9876	O(8)-C(1)-C(2)-C(6)	119.16	Pro-R
O(10)-C(4)	1.3912	O(10)-C(4)-C(3)	119.1069	O(10)-C(4)-C(3)-C(5)	122.5691	Pro-S
F(12)-C(2)	1.4103	F(12)-C(2)-C(1)	116.3468	F(12)-C(2)-C(1)-C(3)	119.7613	Pro-R
F(13)-C(5)	1.4101	F(13)-C(5)-C(4)	116.0375	F(13)-C(5)-C(4)-C(6)	119.5492	Pro-S
C(14)-C(6)	1.5069	C(14)-C(6)-C(1)	121.4497	C(14)-C(6)-C(1)-C(5)	121.7798	Pro-S
O(15)-C(14)	1.4729	O(15)-C(14)-C(6)	107.0365	O(15)-C(14)-C(6)-C(1)	-95.5758	Dihedral

H(17)-C(14)	1.0964	H(17)-C(14)-C(6)	109.2966	H(17)-C(14)-C(6)-O(15)	110.5674	Pro-S
H(18)-C(14)	1.0985	H(18)-C(14)-C(6)	110.0562	H(18)-C(14)-C(6)-O(15)	109.9853	Pro-R
H(9)-O(8)	0.9806	H(9)-O(8)-C(1)	111.4441	H(9)-O(8)-C(1)-C(2)	-2.6531	Dihedral
H(11)-O(10)	0.9808	H(11)-O(10)-C(4)	111.5571	H(11)-O(10)-C(4)-C(3)	178.0941	Dihedral
H(16)-O(15)	0.9814	H(16)-O(15)-C(14)	109.936	H(16)-O(15)-C(14)-C(6)	174.7838	Dihedral

Table S3.7: Bond length, bond angle and dihedral angle of 7F

Bond length (Unit)		**Bond angle (Unit)**		**Dihedral angle**		
C(1)		C(1)		C(1)		
C(2)-C(1)	1.404	C(2)-C(1)		C(2)-C(1)		
C(3)-C(2)	1.3959	C(3)-C(2)-C(1)	122.1291	C(3)-C(2)-C(1)		
C(4)-C(3)	1.4035	C(4)-C(3)-C(2)	119.861	C(4)-C(3)-C(2)-C(1)	0.6017	Dihedral
C(5)-C(4)	1.4053	C(5)-C(4)-C(3)	116.6551	C(5)-C(4)-C(3)-C(2)	-0.272	Dihedral
C(6)-C(1)	1.4102	C(6)-C(1)-C(2)	119.5567	C(6)-C(1)-C(2)-C(3)	-0.2556	Dihedral
O(7)-C(1)	1.39	O(7)-C(1)-C(2)	121.4349	O(7)-C(1)-C(2)-C(6)	119.0042	Pro-R
O(9)-C(4)	1.3853	O(9)-C(4)-C(3)	119.6171	O(9)-C(4)-C(3)-C(5)	123.7275	Pro-S

F(11)-C(2)	1.4003	F(11)-C(2)-C(1)	117.6626	F(11)-C(2)-C(1)-C(3)	120.2078	Pro-R
F(12)-C(3)	1.3821	F(12)-C(3)-C(2)	119.8612	F(12)-C(3)-C(2)-C(4)	120.2773	Pro-S
F(13)-C(5)	1.4071	F(13)-C(5)-C(4)	115.229	F(13)-C(5)-C(4)-C(6)	119.5963	Pro-S
C(14)-C(6)	1.5069	C(14)-C(6)-C(1)	121.5061	C(14)-C(6)-C(1)-C(5)	121.849	Pro-S
O(15)-C(14)	1.472	O(15)-C(14)-C(6)	106.9287	O(15)-C(14)-C(6)-C(1)	-95.0031	Dihedral
H(17)-C(14)	1.0963	H(17)-C(14)-C(6)	109.3195	H(17)-C(14)-C(6)-O(15)	110.6125	Pro-S
H(18)-C(14)	1.0984	H(18)-C(14)-C(6)	110.0614	H(18)-C(14)-C(6)-O(15)	110.0561	Pro-R
H(8)-O(7)	0.9808	H(8)-O(7)-C(1)	111.9794	H(8)-O(7)-C(1)-C(2)	-3.029	Dihedral
H(10)-O(9)	0.9811	H(10)-O(9)-C(4)	111.3835	H(10)-O(9)-C(4)-C(3)	177.8434	Dihedral
H(16)-O(15)	0.9814	H(16)-O(15)-C(14)	110.0409	H(16)-O(15)-C(14)-C(6)	175.2294	Dihedral

Chapter 4

Dual Inhibitory Potential of Terrestrol A, a Gentisyl Alcohol Derivative, Against SARS-CoV-2 and Invasive Fungal Pathogens: A Computational and Pharmacoinformatic Investigation

This chapter explores naturally occurring derivatives of gentisyl alcohol, an underexplored class of bioactive compounds with a particular focus on their potential as therapeutic agents against some of the most alarming global health threats of recent times. The emergence of SARS-CoV-2 and co-infection caused by invasive fungal pathogens (Candida auris and Aspergillus fumigatus) created a critical clinical challenge, especially due to their high mortality rates, drug resistance, and aggressive pathogenicity. In light of the urgent need for effective dual-action therapeutics, this study employs advanced computational strategies to evaluate the inhibitory potential of gentisyl alcohol derivatives, which exhibits promising structural and pharmacological features that may contribute to the disruption of both viral and fungal pathogenic mechanisms.

The text of this chapter has been published as:

- *Singha, B., Arora, B., Karmaker, R., Richa, K., Longkumer, N., Thaer Abdulhameed, H., ... & Bora Sinha, U. (2024). Evaluating Terrestrol A as an Inhibitor Against SARS-CoV-2 and Invasive Fungal Pathogens: A Comprehensive Computational Analysis. ChemistrySelect, 9(14), e202304761.*

4.1. Introduction

In late December 2019, clusters of unexplained pneumonia cases emerged, drawing worldwide concern due to their rapid spread and severity. What began as a localized health issue quickly escalated into a global alarm, prompting urgent investigations to identify the causative agent and implement measures to contain the outbreak [1]. After further research, it was found that this outbreak was caused by the severe acute respiratory syndrome coronavirus 2 (SARS-CoV-2). Despite severe containment efforts, the virus quickly spread globally, leading the World Health Organisation (WHO) to declare it a pandemic in March 2020. Countless lives were lost worldwide as a result of this catastrophe [2,3]. The global scientific community and researchers worldwide made substantial efforts to advance the development of vaccines and enhance antiviral medications, which resulted in saving innumerable lives [4]. However, the emergence of multiple variants of concern is an alarming trend of COVID-19 reinfection, whereby individuals are getting infected by distinct variants of SARS-CoV-2 despite possessing prior immunity [5]. These instances of reinfection have even been documented in vaccinated individuals, emphasising their continued susceptibility to severe consequences [6]. Furthermore, SARS-CoV-2 infection weakens the immune system, creating a favourable environment for various pathogens to cause severe health complications. Patients with SARS-CoV-2 infection have been reported to develop fungal diseases such as *mucormycosis*, COVID-19-associated invasive pulmonary *aspergillosis* (CAPA), invasive *candidiasis*, etc. Fungal infections that occurred with COVID-19 heightened the pathogenicity and virulence of the infection, leading to additional challenges in treatment [7].

Amidst the extensive repercussions induced by the COVID-19 pandemic, a concurrent outbreak emerged during the subsequent surge of COVID-19 in the summer of 2021. Multiple reports documented COVID-19 patients experiencing invasive fungal infections, including *invasive pulmonary*, *aspergillosis*, *candidemia*, and *mucormycosis* [8-10]. There are substantial difficulties in diagnosing, managing, and treating these fungal infections, which can lead to complications and higher rates of mortality. The exact mechanisms underlying the association between SARS-CoV-2

and fungal infections are not yet fully understood. However, it is believed that factors such as dysregulated immune responses, prolonged hospitalisation, utilisation of immunosuppressive therapies, and disruption of the normal microbiota due to COVID-19 and its treatments contribute to the development of a conducive environment for fungal colonisation and infection [9,10]. However, further research is necessary to unravel the precise mechanisms involved in the relationship between SARS-CoV-2 and fungal infections. Despite the demonstrated efficacy and effectiveness of vaccines and antiviral therapies in managing and preventing SARS-CoV-2 transmission, the emergence of multiple variants of concern with varying degrees of transmissibility and pathogenicity has raised significant health concerns and evoked a sense of apprehension in many nations [11,12]. As though matters weren't already complex enough, the possibility of drug resistance to current treatments makes the search for new and effective therapeutic agents all the more pressing [13]. Additionally, antifungal drug resistance has become a growing problem, particularly among immune-compromised patients, leading to limited treatment options for fungal pathogens such as *Aspergillus fumigatus* and *Candida auris* [14]. This highlights the imperative requirement for the development of novel and efficacious therapeutic interventions to mitigate and resolve this matter [15,16]. Nature has historically served as a valuable reservoir for drug discovery, providing an extensive array of compounds possessing potent pharmacological activities encompassing antitumor, antiviral, antioxidant, antimicrobial, and anticoagulant properties, among others [17-21]. The comprehensive investigation of diverse sources, including terrestrial plants and microorganisms, marine organisms, as well as terrestrial vertebrates and invertebrates has yielded a rich repertoire of natural product candidates with promising medicinal potential.

To streamline the process of identifying promising compounds, recent advancements in bioinformatics and *in silico* tools have played a pivotal role. These innovative tools and techniques allow efficient screening and analysis of the vast datasets associated with natural products, aiding in the discovery of bioactive compounds with therapeutic potential. By integrating these approaches into the exploration of natural sources, researchers can expedite the identification of valuable molecules and enhance the

development of novel and effective therapeutics, reducing lead times, understanding and predicting druggability and toxicity, thereby enabling early-stage drug discovery [22-24]. Amidst the backdrop of the COVID-19 pandemic, the amalgamation of *in silico* investigations, bioinformatics, and computational methodologies assumed a pivotal role in deciphering the intricate biological facets of SARS-CoV-2. These methodologies have facilitated the exploration of preventive strategies such as vaccine development and the assessment of therapeutic efficacy for both natural and synthetic discoveries of novel therapeutic agents [25-28]. Similarly, the utilisation of these methods in the pursuit of effective antifungal drugs against invasive fungal pathogens emerged as a valuable approach, yielding a number of promising lead compounds that demonstrated efficacy in preclinical models and presenting new avenues for the advancement of antifungal therapies [29,30]. Phenolic and polyphenolic compounds derived from various sources have garnered significant attention due to their recognised broad-spectrum pharmacological properties, including antiviral and antifungal [31-34]. These inherent characteristics position them as highly appealing natural substances that can significantly enhance the existing array of therapeutic options and also making them potential inhibitors of both SARS-CoV-2 and invasive fungal pathogens.

Gentisyl alcohol, a phenolic compound, is acknowledged as a bioactive compound possessing a diverse spectrum of pharmacological properties. It possesses promising potential for a multitude of therapeutic applications [35]. Notably, antioxidative and radical scavenging activity, promotes neovascularization, inhibits etoposide-induced apoptosis, demonstrates antibacterial activity against multi-drug-resistant *Staphylococcus aureus* and antifungal activity against *Colletotrichum gloeosporioides* [36-40]. Studies conducted on the derivatives of gentisyl alcohol also revealed a multitude of biological activities, including antibacterial, antifungal, antioxidant, cytotoxic, anti-inflammatory, and antiproliferative activities. These derivatives have predominantly been obtained through isolation from fungi, plants, and bacteria [41-53]. The accumulating scientific evidence strongly supports their substantial potential as a rich source for the exploration and development of pioneering medications and therapies [54]. Therefore, the objective of the present study was to assess the potential

of gentisyl alcohol and its derivatives as dual inhibitors targeting SARS-CoV-2 and invasive fungal pathogens (*Aspergillus fumigatus* and *Candida auris)* using *in silico* methodologies. In pursuit of compounds capable of modulating multiple pathways, given the high mutation rates of drug targets, a multi-targeted molecular docking simulation was conducted. This involved examining the compounds of interest alongside three standards relevant to fungal targets and seven standards pertinent to SARS-CoV-2. Subsequently, the most promising compound was subjected to comprehensive evaluations encompassing druglikeness screening, ADME assessment (absorption, distribution, metabolism, and excretion), toxicity prediction, bioactivity score, and PASS prediction (prediction of activity spectra for substances). To gain further insights into the stability of the ligand-receptor complex, molecular dynamics simulations were conducted. Additionally, quantitative evaluation of the electronic structure and reactivity potential were obtained through the utilization of density functional theory analysis.

4.2. Material and method

4.2.1. Set of compounds and standards under study

The 2D structures of the investigated compounds were obtained in SDF file format from the PubChem database (https://pubchem.ncbi.nlm.nih.gov), along with their corresponding compound identification numbers (CIDs) and canonical SMILES, as presented in **Table 4.1**. However, compound No. 18 was generated using ChemDraw Ultra 12.0 software. To facilitate comparative analysis, a selection of relevant standards was made from DrugBank [55], listed in **Table S4.2** (**supporting information**). The selection of multiple standards was based on the intention of capturing a broad spectrum of compounds with diverse chemical structures and potential activities, allowing for a more thorough exploration of their properties and potential activities. This broader analysis contributes to a comprehensive understanding of the compound's characteristics and their suitability for the intended purpose.

Table 4.1: 2D structure, CID (Compound Identifier) and SMILES of the investigated compounds.

Sl. No	Structure	Pubchem CID	Canonical smiles
1	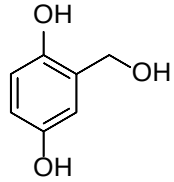 *Gentisyl alcohol*	188287	C1=CC(=C(C=C1O)CO)O
2	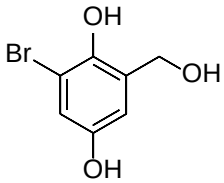 *2-Bromo-6-(hydroxymethyl)hydroquinone*	132606958	C1=C(C=C(C(=C1CO)O)Br)O
3	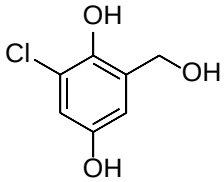 *2-chloro-6-(hydroxymethyl)benzene-1,4-diol*	593615	C1=C(C=C(C(=C1CO)O)Cl)O
4	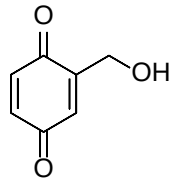 *Gentisyl quinone*	197730	C1=CC(=O)C(=CC1=O)CO
5	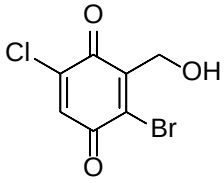 *Bromochlorogentisylquinone A*	46210723	C1=C(C(=O)C(=C(C1=O)Br)CO)Cl

6	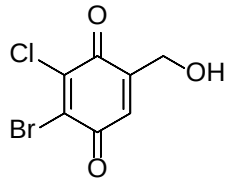 *Bromochlorogentisylquinone B*	46210724	C1=C(C(=O)C(=C(C1=O)Br)Cl)CO
7	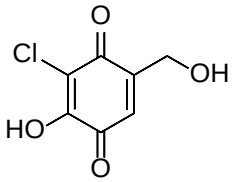 *Hydroxychlorogentisylquinone*	145960751	C1=C(C(=C(C(=O)C1=O)Cl)O)CO
8	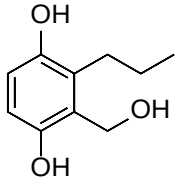 *Mirandamycin*	71593662	CCCC1=C(C=CC(=C1CO)O)O
9	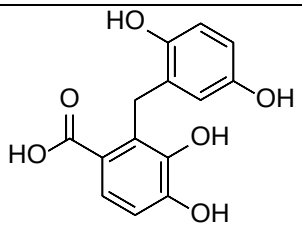 *Gentisyl-protocatacheuic acid*	91444309	C1=CC(=C(C=C1O)CC2=C(C=CC(=C2O)O)C(=O)O)O
10	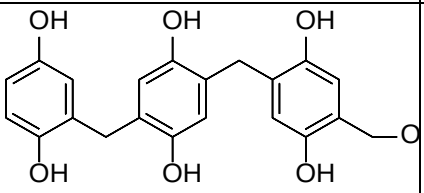 *Terrestrol A*	24770577	COCC1=C(C=C(C(=C1)O)CC2=C(C=C(C(=C2)O)CC3=C(C=CC(=C3)O)O)O)O
11	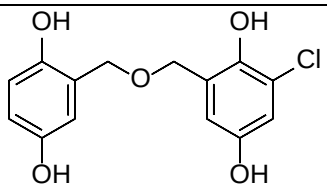 *Terrestrol B*	24770502	C1=CC(=C(C=C1O)COCC2=C(C(=CC(=C2)O)Cl)O)O

12	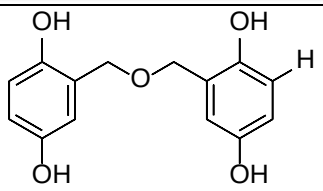 *Terrestrol C*	24770503	C1=CC(=C(C=C1O)COCC2=C(C=CC(=C2)O)O)O
13	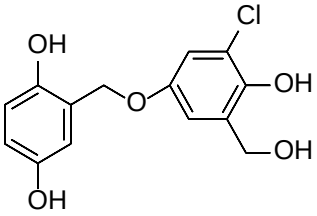 *Terrestrol D*	24770504	C1=CC(=C(C=C1O)COC2=CC(=C(C(=C2)Cl)O)CO)O
14	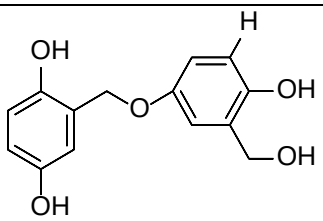 *Terrestrol E*	24770505	C1=CC(=C(C=C1O)COC2=CC(=C(C=C2)O)CO)O
15	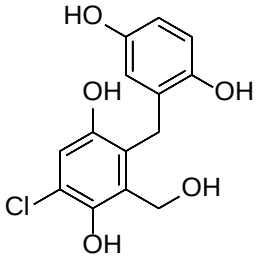 *Terrestrol F*	24770506	C1=CC(=C(C=C1O)CC2=C(C(=C(C=C2O)Cl)O)CO)O
16	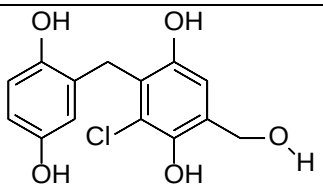 *Terrestrol G*	2476**10**35	C1=CC(=C(C=C1O)CC2=C(C=C(C(=C2Cl)O)CO)O)O
17	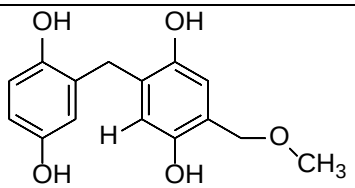	24770576	COCC1=C(C=C(C(=C1)O)CC2=C(C=CC(=C2)O)O)O

	Terrestrol H		
18	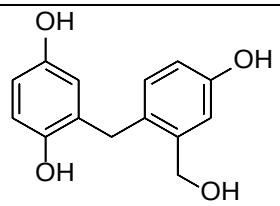 *Terrestrol I*	NA	OC1=CC(CC2=C(CO)C=C(O)C=C2)=C(O)C=C1
19	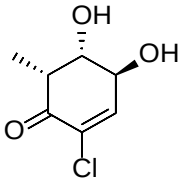 *Terrestrol K*	54772160	CC1C(C(C=C(C1=O)Cl)O)O
20	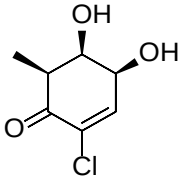 *Terrestrol L*	54772161	CC1C(C(C=C(C1=O)Cl)O)O

4.2.2. Molecular docking simulation

4.2.2.1. Preparation of ligands

The 2D structures of all the compounds and standards listed in **Table 4.1** and **Table S4.2** (**supporting information**) were acquired in SDF file format from the PubChem database (https://pubchem.ncbi.nlm.nih.gov). These structures were then transformed into 3D representations using molecular transformation techniques in ChemBio3D Ultra 12.0. The resulting 3D structures were then subjected to energy minimization utilising the molecular mechanics2 (MM2) force field within ChemBio3D Ultra 12.0. Following energy minimization, the optimised 3D structures were saved in SYBYL MOL2 file format, facilitating the subsequent docking simulations.

4.2.2.2. Selection of targets of interest

To gain insights into the structure-function relationships of the targets and their interactions with the investigated compounds, we obtained the crystal structures of all targets from the Research Collaboratory for Structural Bioinformatics (RCSB) Protein Data Bank (PDB) (http://www.rcsb.org/). Firstly, the target of interest with respect to SARS-CoV-2 comprised the *crystal structure of ADP ribose phosphatase of NSP3 from SARS-CoV-2* (PDB ID: 6VXS) [56]. NSP3, a multifunctional protein crucial for SARS-CoV-2 replication and pathogenesis, manipulates post-translational modifications through its ADP ribose phosphatase activity, facilitating viral replication and immune evasion. Targeting this enzyme holds potential to inhibit viral replication and combat SARS-CoV-2 [57]. Secondly, the *structure of the novel coronavirus spike receptor-binding domain complexed with its receptor ACE2* (PDB ID: 6LZG chain-B) [58] was analyzed. Inhibiting the spike protein is pivotal in therapeutic development against COVID-19, as this protein plays a critical role in facilitating virus recognition and binding to the host cell. Thus, targeting the interaction between the virus and the host membrane, as well as preventing viral particle entry into the host cell, represents a crucial therapeutic strategy [59]. Thirdly, the *complex structure of a human monoclonal antibody with SARS-CoV-2 nucleocapsid protein NTD* (PDB ID: 7CR5 chain A) [60] was examined. The nucleoprotein (NP) is pivotal in SARS-CoV-2 genome replication and assembly, justifying its selection as a target. NP facilitates the formation of the viral ribonucleoprotein complex by interacting with viral RNA, crucial for RNA synthesis and packaging. Hence, targeting NP offers a logical foundation for developing potential antiviral strategies against SARS-CoV-2 [61].

In targeting invasive fungal pathogens, this investigation focuses on fungal virulence factors, which play a significant role in disease progression and drug resistance emergence, particularly in individuals with underlying primary immunodeficiencies [62]. The targets of interest include firstly the *extracellular metalloproteinase from Aspergillus* (PDB ID: 4K90) [63]. Metalloproteinases are enzymatic proteins crucial for the degradation and remodelling of extracellular matrix components. They enable the invasive behaviour of *Aspergillus fungus*, facilitating tissue invasion and infection establishment. Targeting *metalloproteinase from Aspergillus* offers an opportunity to

disrupt its enzymatic activity, hindering fungal pathogenicity, and potentially enhancing antifungal treatment efficacy [64-66]. Secondly, the *crystal structure of FKBP12 of Candida auris* (PDB ID:6VSI) was considered [67]. Inhibiting *FKBP12* can impede fungal growth and survival, thereby reducing its pathogenicity. *FKBP12* is recognized as a promising antifungal drug target in various fungal species, highlighting its importance for innovative therapeutic approaches against *Candida auris* [68].

4.2.2.3. Molecular docking

Molecular docking studies was performed employing Molegro Virtual Docker (MVD 4.0) [69], a comprehensive platform for the prediction of protein-ligand interactions. In Molegro Virtual Docker the ligand can explore different conformations and orientations while the protein remains in a fixed or rigid state. This approach considers the ligand's flexibility and its ability to adapt to the target binding site, aiming to identify the optimal binding pose and interactions. Molegro Virtual Docker uses an algorithm for finding internal cavities to enable detection of possible binding sites inside a protein structure. By default, MVD generates multiple cavities, typically five, based on the analysis of the protein structure. This algorithm detects regions characterized by concave shapes suitable for accommodating ligand molecules. The evaluation of these cavities is based on their surface area, prioritising larger cavities that provide more space for ligand binding. The presence of native ligands in Protein Data Bank (PDB) structures linked to the target protein frequently influences the choice of cavities that enclose the ligand binding sites. Once the target (PDB ID) is imported into the MVD, *via* the protein preparation wizard, water molecules, co-factors, and native ligands attached to the target protein or enzymes can be eliminated and any errors rectified. The necessary docking parameters for the present study were configured with the MolDock score [GRID] as the scoring function and a grid resolution of 0.30 Å. The binding site coordinates for each target of interest were set as follows:

- PDB ID: 6VXS (Chain A: *Non-structural protein 3*) with a volume of 121.3 Å^3, center X: 8.90, Y: -0.57, Z: 2.02, within a constraint of a radius of 12 Å.

- PDB ID: 6LZG (Chain B: *Spike protein S1*) having a volume of 26.11 Å^3, centre designated as X: -25.87, Y: 31.99, Z: 32.28 within a constraint of radius 12 Å.
- PDB ID: 7CR5 (Chain A: *Nucleoprotein*) having a volume of 34.81 Å^3, centre designated as X: -29.92, Y: 10.82, Z: -4.93 within a constraint of radius 12 Å.
- PDB ID:4K90 (Chain A: *Extracellular metalloproteinase mep*) having a volume of 64 Å^3, centre designated as X: 44.23, Y: 0.29, Z: -8.43 within a constraint of radius 12 Å.
- PDB ID: 6VSI (Chain A: *Peptidylprolyl isomerase*) having a volume of 18.43 Å^3, centre designated as X: 31.58, Y: 4.57, Z: 4.29 within a constraint of radius 12 Å.

The maximum number of iterations for all PDB IDs mentioned above was established at 1,500 and the maximum population size was set to 50. Subsequently, 30 independent instantaneous runs were executed for each ligand to enhance the docking accuracy. Further analysis was conducted to assess the docking scores and interactions between the ligands and the receptors [70-74].

4.2.3. Druglikeness (physicochemical properties)

Chemical structures possess molecular attributes that influence physicochemical properties when interacting with the environment [75]. Druglikeness assessment like Lipinski's Rule of Five (Ro5) [76], Veber Rule [77], Egan [78], and Ghose filter [79] utilizes these properties to differentiate drugs from non-drugs. Lipinski's rule suggests that compounds with ClogP ≤ 5, MW ≤ 500 g/mol, HBA ≤ 10, HBD ≤ 5, nRotb≤ 10 and PSA < 140 Å2 are likely to exhibit good oral bioavailability, given that a compound should not violate any more than one of the criteria [80]. The Veber rule considers RBC < 10 and PSA < 140 Å2. Egan rule specifies TPSA > 131.6 Å or log P > 5.88 and -1 ≥ logP ≤ 6, with tPSA ≤ 132 Å2. Ghose filter defines cutoff values for MW (160-480), number of atoms (20-70), PSA ≤ 140, molar refractivity (40-130) and log P (-0.4 to 5.6). The top hit compound, namely Terrestrol A (**10**), identified through docking simulation, underwent further evaluation to assess its drug-like characteristics alongside ten other standards to facilitate a comparative analysis enabling the

evaluation of the relative efficacy of Terrestrol A (**10**). The canonical SMILES of the structures were retrieved and subjected to the SwissADME web server [81] to generate the predicted results.

4.2.4. Pharmacokinetics (ADME) and toxicity prediction

Pharmacokinetics, also referred as ADME (absorption, distribution, metabolism, and excretion), is a scientific concept that encompasses the processes through which a drug gains access to its target site, maintains its pharmacological effects over a defined period, and is eventually converted into harmless metabolites and eliminated at an appropriate rate [82]. Multiple studies have indicated that drug failures are frequently attributed to unfavourable ADME properties. Predicting the pharmacokinetic properties of chemical compounds using conventional methods like *in vitro* and *in vivo* is a laborious, expensive, and time-consuming process [83,84]. As a result, *in silico* ADME assessment of Terrestrol A(**10**) and the standards was performed using SwissADME and PreADMET (https://preadmet.bmdrc.kr) web tools in order to minimise failures and achieve a better success rate. Canonical SMILES of the structures were retrieved and inserted into the respective web tools, generating the predicted results.

Another pivotal consideration is the safety profile of the compounds, necessitating a thorough assessment for any potential toxic features or side effects. Therefore, toxicity screening assumes paramount importance in the evaluation process. Moreover, regulations governing the toxicity of any compounds prior to *in vitro* and *in vivo* are increasingly being integrated with computational predictions [85]. Toxicity prediction of Terrestrol A(**10**) along with the standards, was determined by employing the ProToxII web server (http://tox.charite.de/protox_II) [86], which assessed various toxicity endpoints, including organ toxicity (hepatotoxicity), immunotoxicity , genetic toxicity (cytotoxicity), mutagenicity and carcinogenicity, to generate a safe toxicity profile.

4.2.5. Bioactivity prediction

The Molinspiration web tool (https://www.molinspiration.com) was used to compute the bioactivity scores of Terrestrol A (**10**) and the standards with respect to several human receptors such as G protein-coupled receptors (GPCR), ion channel modulator (ICM), kinase inhibitor (KI), nuclear receptor ligand (NRL), protease inhibitor (PI), and enzyme inhibitor (EI) [87,88].

4.2.6. PASS (*prediction of activity spectra for substances*)

To predict the activity spectra of Terrestrol A (**10**) and the standards, the PASS (Prediction of Activity Spectra for Substances) method was utilised *via* the PASS Online web server [89]. This method employs structure-activity relationships (SAR) to assess a compound's potential for various pharmacological properties. The anticipated activity is represented by the disparity between the probabilities of being active (Pa) and inactive (Pi). Pa must exceed Pi (Pa > Pi) to indicate that experimental outcomes are more inclined to validate a compound's biological activity [90]. For potential antiviral activity, the activity spectra endpoints consisted of *picornavirus, influenza, adenovirus, herpes, cytomegalovirus (CMV)* and *3C-like protease (Human coronavirus).* In terms of potential antifungal activity, the activity spectra endpoints encompassed *Aspergillus nuclease S1, Aspergillopepsin I and II, yeast ribonuclease, antifungal enhancer, Pneumocystis, Lanosterol 14 alpha demethylase, Mucorpepsin, rhizopuspepsin*and *ADP-ribosylarginine hydrolase inhibitors* [91,92].

4.2.7. Molecular dynamics

To investigate the stability of the ligand-receptor complexes and the underlying interactions at a molecular level, molecular dynamics (MD) simulations were carried out on the highest-ranking ligand forming complexes with the respective targets. For the present study, molecular dynamics simulations were performed using GROMACS 2022 software [93]. Simulations were conducted for targets with PDB IDs 6VXS (*Non-structural protein 3*), 6LZG (*spike protein S1*), 7CR5 (*nucleoprotein*), 4K90 (*extracellular metalloproteinase mep*) and 6VS1 (*peptidylprolyl isomerase*), both in

their native form and in complex with the ligand Terrestrol A (**10**) for a duration of 50 nanoseconds *(ns)*. The topology file for the ligand was generated using the PRODRG server [94]. At the start of the simulation, force fields were chosen for both the native and complex systems. Specifically, the GROMOS53A5 force field (which includes 2001 dihedral parameters for amino acids) was used for all five ligand-receptor complexes, while the OPLS-AA/L all-atom force field was employed for the native target protein systems. Solvation of the systems was performed by placing them within a cubic box containing a specific number of water molecules, which were 21544, 19887, 10249, 9732, and 16771 for the targets 4K90, 6LZG, 6VSI, 6VXS, and 7CR5 respectively. To neutralise the native charge on the targets, an equal number of counterions were replaced with solvent molecules in the same cubic box. The energy minimization of the systems was performed using the steepest descent method, with parameters such as constant volume, pressure (1*atm*) and temperature (300 *K*) set during the process. After the simulation was completed, the resulting trajectories were analysed to generate graphs and figures using the XMGRACE software (Turner PJ. XMGRACE, Version 5.1.19. Center for Coastal and Land-Margin Research, Oregon Graduate Institute of Science and Technology, Beaverton, OR; 2005).

4.2.8. DFT (Density functional theory)

To facilitate comparative analysis, Terrestrol A (**10**) and the standards were further explored through the utilisation of density functional theory. This encompassed the computation of global reactivity descriptors, including ionization potential (IP), electron affinity (EA), chemical potential (μ), chemical hardness (η), electronegativity (χ), electrophilicity index (ω), and dipole moment, enabling a comprehensive investigation of their respective reactivity profiles [95,96]. The GaussView6 [97] graphical user interface was used to construct and visualise the structures before and after optimisation. No implicit solvent model was used for these calculations in order to achieve an optimum result. The Gaussian16 [98] suite of programmes was used to optimise the structures and vibrational frequency analysis was performed to ensure that the structures were in their ground state and free from any imaginary frequency. B3LYP hybrid functional along with 6-311G++ (d,p) was used to optimise the structures without imposing any symmetry constraints [99]. The CubeGen extension

within GaussView6 was used to generate the HOMO and LUMO orbitals and other descriptors for all structures.

4.3. Results and discussion

4.3.1. Validation of docking analysis

From the comprehensive multitargeted docking simulation carried out, the yielded dock scores are presented in **Tables S4.3-S4.7** (**supporting information**). The findings indicated that ligand Terrestrol A (**10**) exhibited the most consistent and favourable binding as it achieved the highest negative MolDock score of -129.018, -117.964, -133.184, -136.756, and -111.152 kcal/mol when docked against targets with PDB ID's (SARS-CoV2): 6VXS, 6LZG, 7CR5 and against 4K90 (*Aspergillus fumigatus)* and 6VSI (*Candida auris)* respectively. The most suitable targets were identified as PDB ID 4K90 (*extracellular metalloproteinase from Aspergillus*) and PDB ID 7CR5 (*complex structure of a human monoclonal antibody with SARS-CoV2 nucleocapsid protein NTD*) based on the scores. Docking scores quantify the energy contribution of the ligand-receptor interactions, wherein a more negative score signifies a stronger binding affinity between the ligand and the receptor. This output serves as an indicator of the compound's activity and offers promising evidence for its potential effectiveness [100]. Overall results shows that Terrestrol A (**10**) displayed significant potential as dual inhibitor of both SARS-CoV-2 and invasive fungal pathogens (*Aspergillus fumigatus* and *Candida auris*). Additional assessment was done to gain a better understanding of the interaction between the ligands and the receptor [101].

- ***Interaction study of the ligand and the receptor***

Given that Terrestrol A (**10**) exhibited fair potential and consistent high scores, a comparative interaction study was performed for Terrestrol A (**10**) along with the respective standards to understand the possible mode of interaction established. This was done to elucidate the mechanisms of biological regulation and provide greater insight into the study. Such interaction studies are crucial for understanding the

manner in which ligands interact with the target at its active pocket. The resulting data are presented in **Tables S4.8-S4.12** (**supporting information**).

- **Table S4.8 (supporting information)** presents the interaction between the ligands and the residues at the probable active pocket of the target with PDB ID: 6VXS. **Figure 4.1** below shows the 3D illustration for the interaction of Terrestrol A (**10**) with the receptor. While 3D illustrations for the interaction of ligands Nafamostat, Ribavirin, Arbidol, Chlororquine, Hydroxychloroquine, Dexamethasone and Favipiravir with the receptor (residues) showing possible modes of interaction are shown in **Figures S4.2-S4.8** (**supporting information**). The presented data demonstrates that Terrestrol A (**10**) interacts with several residues, including IIe23, Ala154, Ala129, IIe131, Leu126, Gly47, Ala38, and Ala50. Common residues shared between Terrestrol A(**10**) and other standards were IIe23 and Ala129 for Nafamostat; Ala129, Gly47, Ala38, and Ala50 for Ribavirin; Ala129 for Arbidol; Ala154 for Chloroquine; Ala129 and IIe23 for Hydroxychloroquine; IIe23, Leu126, and Ala129 for Dexamethasone and lastly Ala129 and Gly47 for Favipiravir. Overall, it can be observed that Terrestrol A(**10**) shares one or more common residues with all the standards, suggesting that a possible mode of interaction has been established.

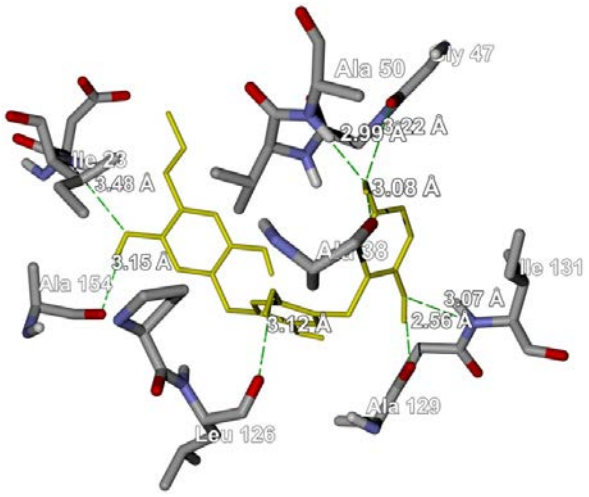

A

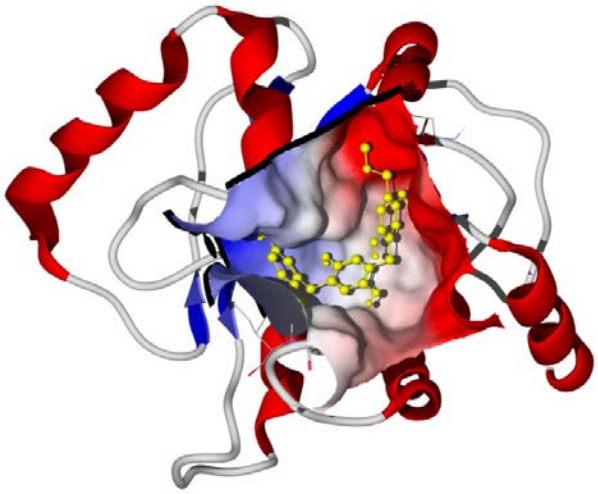

B

Figure 4.1: Visualisation and illustration of **A).** Terrestrol A (**10**) positioned at the active site of the target Non-structural protein 3 (PDB ID: 6VXS) exhibiting potential modes of interaction (The green dotted lines depict the mode of interaction between the target and the ligand, accompanied by distance annotations, while the yellow-coloured structure represents the ligand itself) **B).** Within the probable active pocket of the target.

- **Table S4.9 (supporting information)** presents the interaction between the ligands and the residues at the probable active pocket of the target with PDB ID: 6LZG. **Figure 4.9** below shows the 3D illustration for the interaction of Terrestrol A (**10**) with the receptor. While 3D illustrations for the interaction of ligands Ribavirin, Arbidol, Nafamostat, Hydroxychloroquine, Chlororquine, Dexamethasone, and Favipiravir with the receptor (residue) showing possible modes of interaction are given in **Figures S4.10-S4.16 (supporting information)**. The presented data demonstrates that Terrestrol A (**10**) was found to interact with residues namely Asp428, Glu516, Pro463, Arg355, Ser514, Phe515 and Thr430. Common residues shared between Terrestrol A (**10**) and other standards were Asp428, Glu516, Arg355 and Thr430 for Ribavirin; Asp428, Glu516, Arg355, Ser514 for Nafamostat; Arg355 and Thr430 for Hydroxychloroquine; Phe515 for Chloroquine; Thr430, Ser514 and Arg355 for Dexamethasone and Ser514 and Thr430 for Favipiravir. The results indicate that except for arbidol, Terrestrol A (**10**) shares at least one or more common residue

with all the other standards, providing insights into the possible mode of interaction.

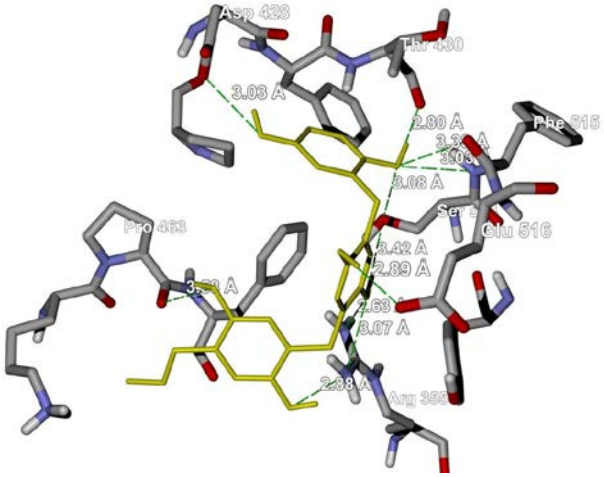

A

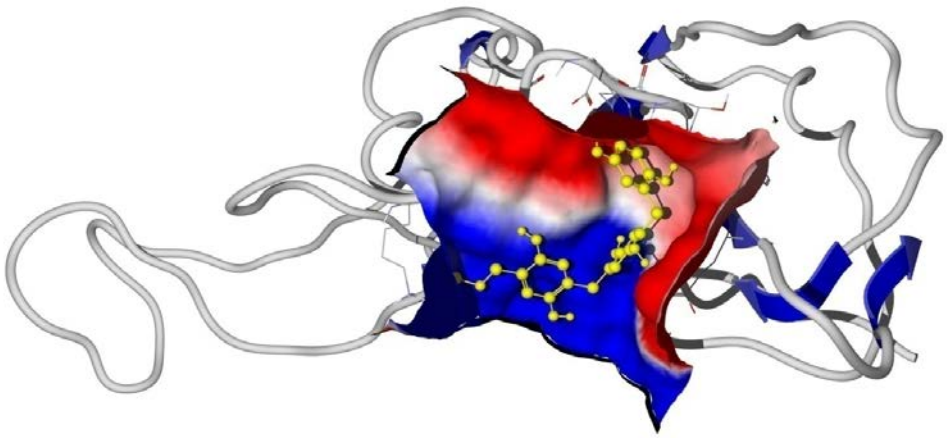

B

Figure 4.9: Visualisation and illustration of **A).** Terrestrol A (10) positioned at the active site of the target Spike protein S1 (PDB ID: 6LZG) exhibiting potential modes of interaction (The green dotted lines depict the mode of interaction between the target and the ligand, accompanied by distance annotations, while the yellow-coloured structure represents the ligand itself) **B).** Within the probable active pocket of the target.

- **Table S4.10 (supporting information)** presents the interaction between the ligands and the residues at the probable active pocket of the target protein PDB ID: 7CR5. **Figure 4.17** below shows the 3D illustration for the interaction of Terrestrol A (**10**) with the receptor. While the 3D illustration for the interaction of ligands Nafamostat, Hydroxychloroquine, Arbidol, Chlororquine, Ribavirin, Dexamethasone and Favipiravir with the receptor (residue) showing possible modes of interaction are given in **Figures S4.18-S4.24 (supporting information)**. The presented data demonstrates that Terrestrol A (**10**) binds to Glu136, Gly137, Ala138, Asn140, Tyr123, Glu136, Gln70and Ala134 residues. Common residues shared between Terrestrol A (**10**) and other standards were Glu136, Gly137, Ala134 and Tyr123 for Nafamostat; Ala134 for Hydroxychloroquine; Tyr123 for Arbidol; Glu136, Gln70 and Tyr123 for Ribavirin; Ala134 and Tyr123 for Dexamethasone and lastly Tyr123, Ala134 and Gln70 for Favipiravir. Thus, Terrestrol A(**10**) exhibits a possible mode of interaction with all the standards by sharing one or more common binding residues with the target.

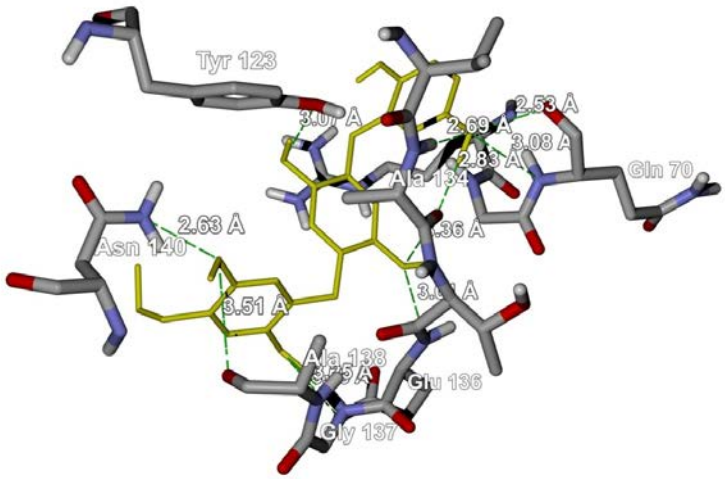

A

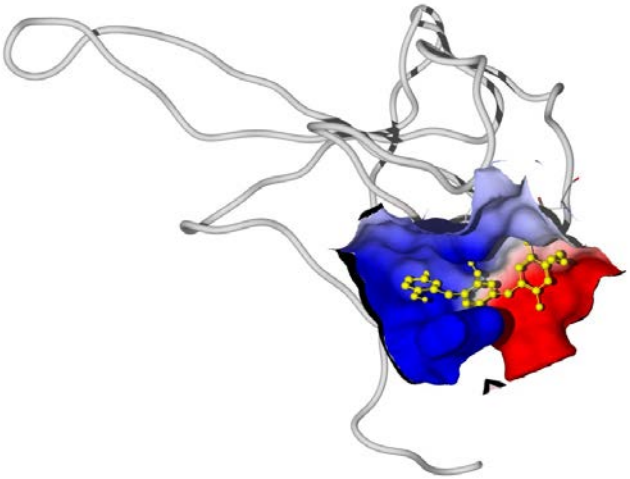

B

Figure 4.17: Visualisation and illustration of **A).** Terrestrol A (**10**) positioned at the active site of the target Nucleoprotein (PDB ID: 7CR5) exhibiting potential modes of interaction (The green dotted lines depict the mode of interaction between the target and the ligand, accompanied by distance annotations, while the yellow-coloured structure represents the ligand itself) **B).** Within the probable active pocket of the target.

- **Table S4.11 (see supplementary material)** presents the interaction between the ligands and the residues at the probable active pocket of the target with PDB ID: 4K90. **Figure 4.25** below shows the 3D illustration for the interaction of Terrestrol A(**10**) with the receptor. While the 3D Ilustration for the interaction of ligands Isavuconazole, Posaconazole and Amphotericin B with the receptor (residue) showing possible modes of interaction are given in **Figures S4.26-S4.28 (supporting information).** The presented data demonstrates that Terrestrol A (**10**) interacts with His520, Glu430, Arg490, Asp463, Asn392, Gly484, Asn391and Trp411 residues. While common residues shared between Terrestrol A (**10**) and other standards were Glu430 for Isavuconazole; Arg490 for Posaconazole and lastly Asn391 and Asn392 for Amphotericin B.

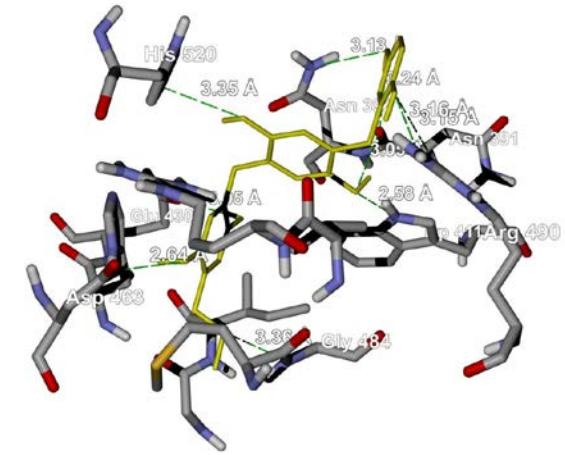

A

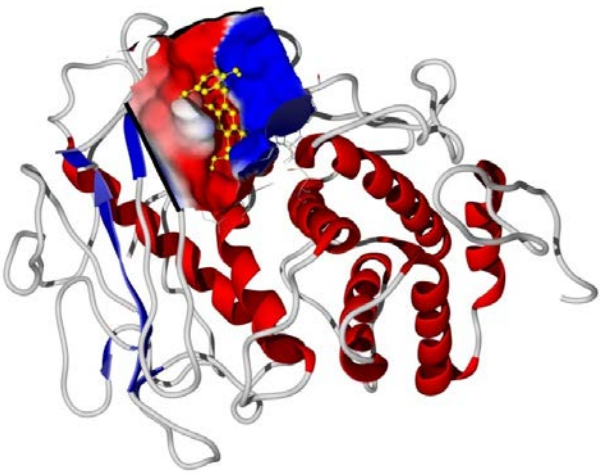

B

Figure 4.25: Visualisation and illustration of **A).** Terrestrol A (**10**) positioned at the active site of the target Extracellular metalloproteinase *mep* (PDB ID: 4K90) exhibiting potential modes of interaction (The green dotted lines depict the mode of interaction between the target and the ligand, accompanied by distance annotations, while the yellow-coloured structure represents the ligand itself) **B).** Within the probable active pocket of the target.

- **Table S4.12 (supporting information)** presents the interaction of the ligands and the residues at the probable active pocket of the target with PDB ID: 6VSI. **Figure 4.29** below shows the 3D illustration for the interaction of Terrestrol A (**10**) with the receptor. While the 3D Illustration for the interaction of ligands

Isavuconazole, Posaconazole and Amphotericin B with the receptor (residue) showing possible modes of interaction are given in **Figures S4.30-S4.32 (supporting information).** The presented data demonstrates that Terrestrol A (**10**) interacts with His58, Asp41 and Tyr30 residues. Posaconazole and Terrestrol A (**10**) share Asp41 as the common residue while Amphotericin B and Isavuconazole share Asp41 and Tyr30 with Terrestrol A (**10**) as the common residue. In general, Terrestrol A (**10**) establishes possible modes of interaction with all the standards by sharing one or more common binding residues with them.

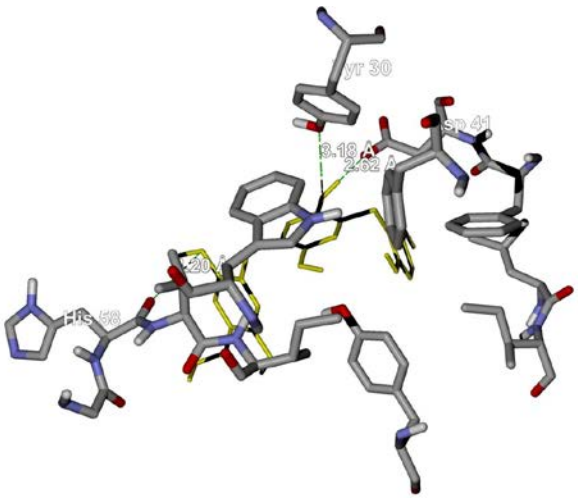

A

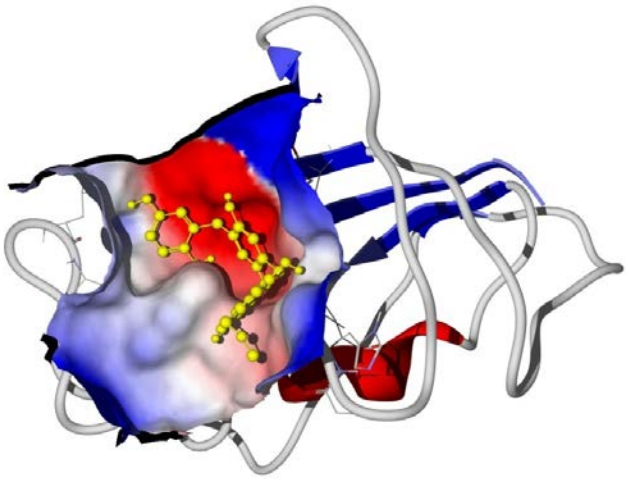

B

Figure 4.29: Visualisation and illustration of **A).** Terrestrol A (**10**) positioned at the active site of the target Peptidylprolyl isomerase (PDB ID: 6VSI) exhibiting potential modes of interaction (The green dotted lines depict the mode of interaction between the target and the ligand, accompanied by distance annotations, while the yellow-coloured structure represents the ligand itself) **B).** Within the probable active pocket of the target

4.3.2. Druglikeness (physicochemical properties)

As demonstrated by the data generated *via* Swiss ADME shown in **Table S4.13 (supporting information)** arbidol, dexamethasone, hydroxychloroquine, chloroquine, and isavuconazole meet the druglikeness criteria with zero violations. Generally, an orally active drug should not exceed one violation of Lipinski's Rule of Five (RO5) criteria. In the case of Terrestrol A (**10**), it adheres to this rule by having no more than one RO5 violation. However, the remaining standards failed to comply and violated at least one parameter implemented. As a result, they may exhibit inadequate oral bioavailability and permeability based solely on the screening technique employed.

4.3.3. Pharmacokinetics (ADME) and toxicity prediction

4.3.3.1.ADME (pharmacokinetics)

The ADME properties of Terrestrol A (**10**) and the standards were evaluated using SwissADME and PreADMET and the results are shown in **Table S4.14** (**supporting information**). SwissADME was used to test the permeability of the blood-brain barrier (BBB), the permeability of the skin (LogKp), and the possibility of being a substrate of P-glycoprotein (P-gp). Compounds intended for central nervous system (CNS) use should possess good BBB permeability, whereas non-CNS compounds should have low BBB permeability to avoid potential side effects [102]. Among the standards, chloroquine and hydroxychloroquine exhibited favourable BBB permeability while the remaining standards including Terrestrol A (**10**) did not demonstrate significant permeability. Skin permeability (LogKp) is a crucial factor in assessing transdermal delivery [103]. The prediction revealed LogKp values ranging from -4.96 cm/s to -11.94 cm/s for the standards, while Terrestrol A (**10**) displayed a

value of -6.40 cm/s, indicating moderate to good skin permeability. P-glycoprotein (P-gp) is a protein involved in drug resistance [104]. Among the standards, namely Dexamethasone, Isavuconazole, Posaconazole, and Amphotericin B displayed a propensity to act as P-glycoprotein (P-gp) substrates. The remaining standards and Terrestrol A (**10**) did not exhibit such characteristics.

PreADMET generated endpoints consisted of Caco-2 permeability, human intestinal absorption (HIA) and MDCK (Madin-Darby canine kidney). The Caco-2 cell line, derived from human colorectal cancer is a suitable model for studying the characteristics of the intestinal epithelial cell barrier due to its resemblance to *in vivo* morphology and functions [105]. In terms of permeability in Caco-2 cells, Ribavirin was classified as having low permeability (permeability value <4), while the other standards, including Terrestrol A (**10**) exhibited moderate permeability within the range of 4 to 70%. If a compound possesses a good human intestinal absorption (HIA) value, it can be assimilated through the human intestine. The HIA values predicted Amphotericin B to have lower absorption (0-20%), ribavirin fell within the moderate range (20-70%), and the remaining compounds, including Terrestrol A (**10**), exhibited higher HIA values (70-100%). These HIA percentage values reflect the combined impact of bioavailability and absorption, which are influenced by factors such as excretion ratio and cumulative excretion in urine, bile, and feces [106]. The MDCK (Madin-Darby canine kidney) permeability values predicted for the compounds showed weak to moderate diffusion in cell membranes, indicating their potential as a tool for rapid permeability assessment due to the shorter growth period of MDCK cells compared to Caco-2 cells [107]. Hydroxychloroquine demonstrated a moderate permeability value of 45.1085, falling under the range of 25-500%, while the remaining compounds exhibited weak permeability values (< 25%). Overall, the pharmacokinetic properties of Terrestrol A (**10**) were determined to be quite favourable, indicating its potential for further investigation.

4.3.3.2.Toxicity prediction

The toxicity profile of Terrestrol A (**10**) and the standards were evaluated utilising the Protox-2 webserver, and the corresponding results are presented in **Table S4.15**

(**supporting information**). The analysis classified Nafamostat, Ribavirin, and Dexamethasone into the Class-5 category. Arbidol, Favipiravir, Hydroxychloroquine, Chloroquine, Isavuconazole, Posaconazole, and Terrestrol A (**10**) falling into the Class-4 category. However, amphotericin B fell into Class-3, indicating a higher risk of toxicity. Overall, only Arbidol and Terrestrol A (**10**) exhibited favourable toxicity profiles, showing no indications of hepatotoxicity, carcinogenicity, immunotoxicity, mutagenicity, or cytotoxicity. These findings suggest that Arbidol and Terrestrol A (**10**) may possess the desirable attributes of a promising drug candidate.

4.3.4. Bioactivity prediction

Bioactivity score analysis was conducted for Terrestrol A (**10**) and the standards. Compounds with scores >0.00 are indicative of substantial biological activities, while those ranging from -0.50 to 0.00 are expected to exhibit moderate activity. Scores below -0.50 are considered inert. It can be noted that the key compound Terrestrol A (**10**) exhibited scores of 0.00 or >0.00 across all endpoints. In contrast, each standard obtained one or more negative scores calculated for different receptors as shown in **Table S4.16** (**supporting information**).

4.3.5. PASS (*prediction of activity spectra for substances*).

Terrestrol A (10) and the standards underwent PASS prediction using PASS Online to assess their potential activities. The screening focused on virus related endpoints [*Picornavirus, Influenza, Adenovirus, Herpes, Cytomegalovirus (CMV)* and *3C-like protease (Human coronavirus)*] and the results as presented in **Table S4.17 (supporting information)** revealed that Terrestrol A (**10**) displayed Pa > Pi values across all endpoints. The Pa values ranged from 0.237 to 0.356, while the Pi values ranged from 0.050 to 0.193. Notably, certain standards such as Nafamostat, Arbidol and Ribavirin exhibited excellent activity (Pa) on specific endpoints. In contrast, dexamethasone, hydroxychloroquine, and chloroquine were predicted to be inactive (Nil) across all endpoints. Based on these findings, it is reasonable to suggest that Terrestrol A (**10**) holds potential as a potent antiviral agent.

The antifungal activity of TerrestrolA(**10**), Isavuconazole, Posaconazole and Amphotericin-B was evaluated by implementing various endpoints associated with fungal infections, namely *Aspergillus nuclease S1, Aspergillopepsin I and II, yeast ribonuclease, antifungal enhancer, Pneumocystis, Lanosterol 14 alpha demethylase, Mucorpepsin, Rhizopuspepsin,* and *ADP-ribosylarginine hydrolase inhibitors*. The results of the PASS prediction, as depicted in **Table S4.18 (supporting information)** revealed notable activities for isavuconazole and posaconazole. Both standards demonstrated remarkable activity against the *antifungal* endpoint and acted as potent inhibitors of *lanosterol 14 alpha demethylase*. Additionally, Posaconazole exhibited modest activity as a *mucorpepsin inhibitor*. Amphotericin B displayed robust *antifungal* activity and showed mild activity as an *antifungal enhancer*. In contrast, Terrestrol A (**10**) demonstrated Pa > Pi values across all endpoints, indicating its potential as a candidate antifungal agent. The Pa values ranged from 0.097 to 0.387, while the Pi values ranged from 0.004 to 0.134. These findings suggest that Terrestrol A (**10**) holds promise as a potential antifungal agent worthy of further investigation.

4.3.6. DFT (Density functional theory)

Attempts have been made to understand the reactivity of Terrestrol A (**10**) using density functional theory. DFT calculations can be employed to evaluate key reactivity descriptors, derived from the energies of the highest occupied molecular orbital (HOMO) and the lowest unoccupied molecular orbital (LUMO), which might give indications towards the biological potency of compounds [108,109]. The optimised structures include Terrestrol A (**10**) and all the other standards presented in **Table S4.19** (**supporting information**). Calculated global reactivity descriptors are shown in **Table S4.20** (**supporting information**), while **Tables S4.21** and **S4.22**(**supporting information**) present comprehensive details and graphical representations elucidating the energies associated with the highest occupied molecular orbital (HOMO) and lowest unoccupied molecular orbital (LUMO), respectively. The study findings indicates that in terms of dipole moment, Amphotericin B exhibits a higher potential as a pharmacological agent compared to the others investigated. Further analysis of the chemical hardness reveals that Terrestrol A (**10**) may possess superior reactivity in comparison to ribavirin, given that the chemical hardness of ribavirin surpasses that

of Terrestrol A (**10**). Terrestrol A (**10**) demonstrated a more negative chemical potential, indicating a greater capacity for gaining an electron compared to posaconazole. It also exhibits a higher electrophilicity, suggesting a better ability to accept a pair of electrons in comparison to Posaconazole. Additionally, the higher electronegativity value of Terrestrol A (**10**) implies a stronger reactivity, as it signifies an enhanced capability to attract shared electrons during chemical bonding formation, further emphasizing its potential for favorable chemical interactions. The results, as reflected by the HOMO–LUMO energy gap, are arranged in the following order: **Posaconazole > Nafamostat > Arbidol > Favipiravir > Chloroquine > Isavuconazole > Dexamethasone > Hydroxychloroquine > Amphotericin B > Terrestrol A (10) > Ribavirin**, illustrating a progressive variation in orbital energy that aligns with differences in electronic stability and intrinsic chemical reactivity among these compounds, revealing that Posaconazole might be the most reactive while Ribavirin with a large HOMO-LUMO gap might be having lower reactivity than the rest. Overall, Terrestrol A (**10**) demonstrated promising reactivity supported by its chemical hardness, potential, electrophilicity, and electronegativity, while exhibiting a better HOMO-LUMO energy gap compared to Ribavirin. These findings offer valuable insights for further exploration and optimisation of these compounds in therapeutic applications.

4.3.7. Results and Analysis for MD Simulation

Molecular dynamics simulations play a crucial role in evaluating biochemical processes and protein folding dynamics, both in the absence and presence of ligand binding at the atomic level. A simulation was conducted for a duration of 50 nanoseconds (*ns*) to assess the stability of conformation, interactions, and efficacy of the ligand with the targets under study [110].

4.3.7.1.Root mean square deviation (RMSD)

This analysis allows the examination of the deviation of Cα atoms from their mean positions and provides insights into conformational perturbations induced by the binding of the compound, Terrestrol A (**10**), in the conducted simulation [111]. As

can be seen in **Figure S4.33** (**supporting information**), Terrestrol A (**10**) significantly induces alterations in the RMSD of 4K90 (*extracellular metalloproteinase mep*), 6LZG (*spike protein S1*), 6VXS (*non-structural protein 3*), and 6VSI (*peptidylprolyl isomerase*) such that the average RMSD is increased upon binding of the ligand molecule. The plot depicts an equilibrated system and stabilised RMSD throughout the duration of the simulation, implying that it is ideal for analysis by other parameters as well. The probability distribution function (PDF) of the RMSD of the target also shows the increased RMSD. The average RMSD value of the target 4K90 alone was 2.314 nm, whereas the RMSD of the target with the ligand increased to 3.310 nm. Similarly, the average RMSD value of all increased from 2.602 nm to 3.782 nm, 1.503 nm to 2.634 nm, 1.810 nm to 4.006 nm, and 4.770 to 5.615 for 6LZG, 6VXS, 6VSI, and 7CR5.

4.3.7.2. Root mean square fluctuation (RMSF)

RMSF is the displacement of either a particular atom or group of atoms measured relatively from the reference structure that is averaged over the number of atoms. RMSF is the fluctuation of the structure of interest around a stable average conformation, and computing these fluctuations of each subset of the structure relative to the average structure of the simulation gives the value of RMSF [112]. These values of RMSD and RMSF highlight structural flexibility during the course of MD simulation. As seen in **Figure S4.34** (**supporting information**), fluctuation in residues of target 4K90 was decreased, indicating stability of structure in the presence of ligand Terrestrol A (**10**) as evident by the average value of RMSF of the target alone being 9.893 nm, whereas that of target along with the ligand was 1.650 nm. Similarly, for targets 6VXS and 7CR5, there was a decrease in fluctuation in the binding of Terrestrol A(**10**) from 8.727 nm to 1.539 nm and 2.59 nm to 1.735 nm, respectively. Whereas the RMSF of 6LZG and 6VSI increased in the presence of ligand from 1.482 nm to 2.066 nm and 1.036 nm to 1.892 nm, respectively. The PDF plot also validates the data for all the respective targets.

4.3.7.3.Radius of gyration (Rg)

The radius of gyration (Rg) is a parameter that talks about conformational change in the protein on binding of the ligand molecule. It helps in monitoring the compactness of the targets and thereby it's folding and unfolding as well. It denotes the distance between the point where the target is rotating to the point where the transfer of energy has the maximum effect [113]. As seen in **Figure S4.35** (**supporting information**) the average Rg of targets 4K90, 6LZG, 6VSI, 6VXS AND 7CR5 before binding of Terrestrol A (**10**) was 2.061nm, 1.840 nm, 1.348 nm, 1.513 nm and 1.52 nm that increased to 2.095 nm, 1.849 nm, 1.351 nm, 1.524 nm and 1.578 nm after binding of ligand, respectively. The minimal increase in Rg of all the targets denotes mild unfolding an opening of the target. PDF analysis of the complexes also shows the increase in Rg on binding of Terrestrol A (**10**).

4.3.7.4.Solvent Accessible Surface Area (SASA)

During the course of simulation, changes in the accessibility of the targets to the solvent, i.e. water molecules, is studied by measuring SASA. This also provides an idea of conformational changes, including the folding and unfolding of the target when interacting with the ligand. As seen in **Figure S4.36** (**supporting information**) it was observed that SASA values also increased for all the targets on binding of the ligand molecule. The average SASA values increased from 1.563 nm^2, 1.087 nm^2, 6.633 nm^2, 8.349 nm^2, 8.105 nm^2 to 1.694 nm^2, 1.121 nm^2 ,6.727 nm^2, 8.695 nm^2, 8.643 nm^2 for 4K90, 6LZG, 6VSI, 6VXS, and 7CR5.

4.3.7.5. Dynamics of Hydrogen Bonding

The analysis of the intramolecular hydrogen bonding of the targets does not show much variation before or after the binding of Terrestrol A (**10**). As can be seen in **Figure S4.37** (**supporting information**) there is either none or very minimal decrease (in case of 4K90, 6VSI and 7CR5) in intramolecular hydrogen bonding in complexes over the period of 50ns. The PDF analysis also suggests constancy and does not show any significant change in intramolecular hydrogen bonding [114].

Overall, the MD simulations that were conducted revealed that the RMSD and RMSF values of the protein-ligand complexes indicated structural deviations and flexibility during the simulation. Despite an initial increase in RMSD upon binding with Terrestrol A (**10**), the complex remained stable throughout the entire simulation, rendering it an ideal system for further analysis. The fluctuations of residues varied among the different proteins, with some showing decreased fluctuations and others showing increased fluctuations. Notably, conformational changes were observed, as evidenced by increased Rg values, suggesting expansion, as well as alterations in SASA and hydrogen bonding dynamics, indicating a slight unfolding of the protein upon binding with Terrestrol A (**10**). Overall, the findings highlight the significant interactions of Terrestrol A (**10**) with the targets and provide insights into the stability and conformational changes of the complexes. These results indicate the potential for Terrestrol A (**10**) as a valuable compound for further investigations and drug development.

4.4. Discussion

Despite stringent global efforts to control SARS-CoV-2 transmission, it continues to pose a formidable threat to human health due to the recurrent emergence of novel variants. While numerous vaccines and therapeutic modalities are presently accessible, their sustained efficacy in the face of emerging novel variants awaits comprehensive evaluation. Additionally, certain SARS-CoV-2 variants can evade the neutralising antibodies produced by vaccines, exacerbating the situation. The COVID-19 pandemic further complicates matters, as this viral respiratory disease predisposes patients to secondary life-threatening fungal infections, notably *aspergillosis*, *candidiasis*, and *mucormycosis*, among others. COVID-19's immunosuppressive effects, combined with treatments like steroids and other drugs, render individuals susceptible to fungal infections by compromising their natural defences thus making an accurate diagnosis more challenging. Hence, there is a pressing and vital need for therapeutics capable of effectively managing these illnesses. This underscores the immediate necessity for treatments to alleviate symptoms, manage complications, and potentially prevent adverse outcomes linked with these diseases. Over the past century,

the emergence of *in silico* tools has greatly elevated the quality of healthcare research, providing precise predictions with exceptional accuracy. *In silico* methodologies have proved immensely valuable in exploring molecular architectures, categorizing infection-related datasets *via* AI and deep learning, scrutinising interactions between potential inhibitors and viral targets, and devising innovative and efficacious therapeutic agents.

Consequently, this study aims to evaluate the effectiveness of Gentisyl alcohol and its derivatives as dual inhibitors, possessing the ability to target both SARS-CoV-2 and invasive fungal pathogens (*Aspergillus fumigatus* and *Candida auris*) *via in silico* approaches. In drug discovery, targeting a diverse array of targets allows for an extensive exploration of drug-protein interactions, leading to the identification of innovative drug candidates. This approach, known as polypharmacology, facilitates the design of drugs capable of interacting with multiple targets, resulting in broader therapeutic effects. The diverse targeting strategy aids in the discovery of compounds that exhibit reduced susceptibility to resistance caused by mutations in drug targets. Furthermore, it enhances our understanding of intricate disease networks, providing valuable insights for effective therapeutic interventions. Thus, initially, a multitargeted molecular docking analysis was conducted on a test set comprising twenty compounds and a reference set of ten standards. Notably, Terrestrol A (**10**) demonstrated the highest negative MolDock score among all targets, particularly exhibiting a score of -136 against PDB ID 4K90 (*Extracellular metalloproteinase from Aspergillus*) and a score of -133 against PDB ID 7CR5 (*Complex structure of a human monoclonal antibody with SARS-CoV2 nucleocapsid protein NTD*). The interaction study further revealed that Terrestrol A (**10**) has the potential to bind to the same or structurally similar regions on the target site as the reference standards, which are acknowledged for their therapeutic effects. The shared binding residues between Terrestrol A (**10**) and the standards imply that it may possess comparable or potentially superior pharmacological properties, leading to significant biological activities. Further investigation was directed towards Terrestrol A (**10**) and ten chosen standards (commercially employed) to facilitate a comparative evaluation of the efficacy of Terrestrol A (**10**). The druglikeness screening indicated that Terrestrol A (**10**)

possessed favourable druggable characteristics, making it suitable for further development as a potential drug candidate. The ADME assessment of Terrestrol A (**10**) and the included standards yielded important findings, ADME studies are of paramount importance in assessing the pharmacokinetic profile of drugs, providing crucial insights to inform drug development strategies, ensure drug safety, and ultimately enhance patient outcomes. Chloroquine and hydroxychloroquine demonstrated favourable blood-brain barrier permeability, while Terrestrol A (**10**) and other standards did not exhibit significant permeability, suggesting that they may encounter challenges in crossing the blood-brain barrier if intended to exert their effects on the central nervous system. Terrestrol A (**10**) did not act as a substrate for P-glycoprotein, which could reduce the development of resistance. It exhibited moderate to good skin permeability, suggesting suitability for transdermal use. Terrestrol A (**10**) and certain standards demonstrated moderate permeability in Caco-2 cells, suggesting their ability to pass through intestinal epithelial cells for systemic absorption. Terrestrol A (**10**) and some standards exhibited high intestinal absorption, indicating efficient assimilation through the human intestine. However, Amphotericin B showed lower absorption, and Ribavirin displayed moderate absorption. Hydroxychloroquine demonstrated moderate permeability in MDCK cells, while the remaining compounds exhibited weak permeability. Overall, the pharmacokinetic characteristics of Terrestrol A (**10**) share similarities with certain standards, indicating similar traits to the known standards. This attribute increases the likelihood of a successful drug development and pave the way for further investigation and potential therapeutics. Toxicity screening results showed that only Terrestrol A (**10**) and Arbidol exhibited no signs of any toxicity traits. These two compounds showed no evidence of exhibiting harmful effects on the liver, did not possess properties that could potentially induce the development of cancer and showed no signs of negatively impacting the immune system or causing genetic mutations. The absence of hepatotoxicity, carcinogenicity, immunotoxicity, mutagenicity, and cytotoxicity in Terrestrol A (**10**) and Arbidol suggests that these compounds have favourable toxicity profiles. This is an encouraging finding as it enhances their potential as safe and well-tolerated drug candidates.

The bioactivity predictions conducted using Molinspiration consistently indicated that Terrestrol A (**10**) exhibited favorable interactions with all drug target receptors. It demonstrated noteworthy scores of 0.00 or >0.00 across all evaluated endpoints. Terrestrol A (**10**) exhibited a higher Pa (probable of being active) compared to Pi (probable of being inactive) across all endpoints. This indicates a strong likelihood of Terrestrol A (**10**) displaying effective activity against fungal and viral targets. The analysis of the structural dynamics of Terrestrol A (**10**) revealed a minor unfolding of the protein. Despite this, the complex formed by Terrestrol A (**10**) and the protein remained stable throughout the simulation. This stability indicates that the interaction between Terrestrol A (**10**) and the protein was sufficiently strong to preserve the overall integrity and structural coherence of the complex. Such stability is vital, as it ensures that the complex retains its functional properties and potential effectiveness as a therapeutic agent. The findings from the density functional theory (DFT) study shed light on the potential of Terrestrol A (**10**). It demonstrates promising reactivity when compared to ribavirin, as evidenced by its chemical hardness, chemical potential, electrophilicity, and electronegativity. Analysis of the HOMO-LUMO energy gap suggests that Posaconazole exhibits the highest reactivity among the compounds investigated, while Ribavirin exhibits lower reactivity. However, Terrestrol A (**10**) demonstrates good reactivity, surpassing Ribavirin. These findings indicate that Terrestrol A (**10**) shares similar traits with established standards or even slightly better reactivity compared to certain standards underscoring its potential as a promising compound.

4.5. Conclusion

The COVID-19 pandemic has exposed critical weaknesses in global healthcare systems, with deadly coinfections especially invasive fungal infections like aspergillosis and candidiasis further escalating the crisis. These opportunistic pathogens have significantly increased patient mortality, underscoring the urgent need for potent, broad-spectrum therapeutics to combat this dual threat and protect public health. The present study thus investigated Gentisyl alcohol and its derivatives as dual inhibitors targeting both SARS-CoV-2 and invasive fungal pathogens (*Aspergillus fumigatus* and *Candida auris*).

- Multi-targeted docking simulations highlighted the remarkable potential of Terrestrol A (10), which consistently achieved high MolDock scores across all targets, three SARS-CoV-2 proteins and two pathogenic fungal targets.

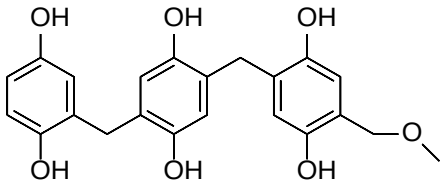

Terrestrol A

- Comprehensive evaluation of its drug-likeness, ADME properties, toxicity profile, bioactivity scores, and PASS predictions further affirmed its strong therapeutic potential.
- Molecular dynamics simulations revealed minor protein unfolding upon binding; however, the overall complex remained stable, preserving structural integrity.
- Additionally, DFT (Density Functional Theory) analysis demonstrated favorable electronic reactivity, with Terrestrol A (10) outperforming certain benchmark compounds.

Collectively, these findings establish Terrestrol A (10) as a highly promising lead molecule, warranting further validation through *in vitro* and *in vivo* studies to assess its therapeutic efficacy and clinical relevance.

References

[1] F. Jiang, L. Deng, L. Zhang, Y. Cai, C. W. Cheung, and Z. Xia, "Review of the Clinical Characteristics of Coronavirus Disease 2019 (COVID-19)," *Journal of General Internal Medicine*, vol. 35, no. 5, pp. 1545–1549, Mar. 2020, doi: 10.1007/s11606-020-05762-w. Available: https://doi.org/10.1007/s11606-020-05762-w

[2] N. Zhu *et al.*, "A Novel Coronavirus from Patients with Pneumonia in China, 2019," *New England Journal of Medicine*, vol. 382, no. 8, pp. 727–733, Jan. 2020, doi: 10.1056/nejmoa2001017. Available: https://doi.org/10.1056/nejmoa2001017

[3] A. Sharma, S. Tiwari, M. K. Deb, and J. L. Marty, "Severe acute respiratory syndrome coronavirus-2 (SARS-CoV-2): a global pandemic and treatment strategies," *International Journal of Antimicrobial Agents*, vol. 56, no. 2, p. 106054, Jun. 2020, doi: 10.1016/j.ijantimicag.2020.106054. Available: https://doi.org/10.1016/j.ijantimicag.2020.106054

[4] R. Agarwal and P. Gaule, "What drives innovation? Lessons from COVID-19 R&D," *Journal of Health Economics*, vol. 82, p. 102591, Jan. 2022, doi: 10.1016/j.jhealeco.2022.102591. Available: https://doi.org/10.1016/j.jhealeco.2022.102591

[5] M. Galanti and J. Shaman, "Direct observation of repeated infections with endemic coronaviruses," *The Journal of Infectious Diseases*, vol. 223, no. 3, pp. 409–415, Jul. 2020, doi: 10.1093/infdis/jiaa392. Available: https://doi.org/10.1093/infdis/jiaa392

[6] M. L. Page, "The risks from covid-19 reinfection," *The New Scientist*, vol. 255, no. 3394, p. 21, Jul. 2022, doi: 10.1016/s0262-4079(22)01208-8. Available: https://doi.org/10.1016/s0262-4079(22)01208-8

[7] N. Baten, S. Wajed, A. Talukder, Md. H. U. Masum, and Md. M. Rahman, "Coinfection of fungi with SARS-CoV-2 is a detrimental health risk for COVID-19 patients," *Beni-Suef University Journal of Basic and Applied Sciences*, vol. 11, no. 1, May 2022, doi: 10.1186/s43088-022-00245-9. Available: https://doi.org/10.1186/s43088-022-00245-9

[8] A. R. Bizri, H. H. Khachfe, M. Y. Fares, and U. Musharrafieh, "COVID-19 pandemic: An insult over injury for Lebanon," *Journal of Community Health*, vol. 46, no. 3, pp. 487–493, Jul. 2020, doi: 10.1007/s10900-020-00884-y. Available: https://doi.org/10.1007/s10900-020-00884-y

[9] P. Koehler *et al.*, "Defining and managing COVID-19-associated pulmonary aspergillosis: the 2020 ECMM/ISHAM consensus criteria for research and clinical guidance," *The Lancet Infectious Diseases*, vol. 21, no. 6, pp. e149–e162, Dec. 2020, doi: 10.1016/s1473-3099(20)30847-1. Available: https://doi.org/10.1016/s1473-3099(20)30847-1

[10] P. E. Verweij *et al.*, "Review of influenza-associated pulmonary aspergillosis in ICU patients and proposal for a case definition: an expert opinion," *Intensive Care Medicine*, vol. 46, no. 8, pp. 1524–1535, Jun. 2020, doi: 10.1007/s00134-020-06091-6. Available: https://doi.org/10.1007/s00134-020-06091-6

[11] C. Fenton and S. J. Keam, "Emerging small molecule antivirals may fit neatly into COVID-19 treatment," *Drugs & Therapy Perspectives*, vol. 38, no. 3, pp. 112–126, Feb. 2022, doi: 10.1007/s40267-022-00897-8. Available: https://doi.org/10.1007/s40267-022-00897-8

[12] M. Laws *et al.*, "Current Trends and Future Approaches in Small-Molecule therapeutics for COVID-19," *Current Medicinal Chemistry*, vol. 28, no. 19, pp. 3803–3824, Jul. 2020, doi: 10.2174/0929867327666200721161840. Available: https://doi.org/10.2174/0929867327666200721161840

[13] R. Khandia *et al.*, "Emergence of SARS-CoV-2 Omicron (B.1.1.529) variant, salient features, high global health concerns and strategies to counter it amid ongoing COVID-19 pandemic," *Environmental Research*, vol. 209, p. 112816, Jan. 2022, doi: 10.1016/j.envres.2022.112816. Available: https://doi.org/10.1016/j.envres.2022.112816

[14] M. C. Fisher, N. J. Hawkins, D. Sanglard, and S. J. Gurr, "Worldwide emergence of resistance to antifungal drugs challenges human health and food security," *Science*, vol. 360, no. 6390, pp. 739–742, May 2018, doi: 10.1126/science.aap7999. Available: https://doi.org/10.1126/science.aap7999

[15] P. E. Verweij *et al.*, "The one health problem of azole resistance in Aspergillus fumigatus: current insights and future research agenda," *Fungal Biology Reviews*, vol. 34, no. 4, pp. 202–214, Nov. 2020, doi: 10.1016/j.fbr.2020.10.003. Available: https://doi.org/10.1016/j.fbr.2020.10.003

[16] J. Rhodes and M. C. Fisher, "Global epidemiology of emerging Candida auris," *Current Opinion in Microbiology*, vol. 52, pp. 84–89, Jul. 2019, doi: 10.1016/j.mib.2019.05.008. Available: https://doi.org/10.1016/j.mib.2019.05.008

[17] D. J. Newman, G. M. Cragg, and K. M. Snader, "The influence of natural products upon drug discovery (Antiquity to late 1999)," *Natural Product Reports*, vol. 17, no. 3, pp. 215–234, Jan. 2000, doi: 10.1039/a902202c. Available: https://doi.org/10.1039/a902202c

[18] D. A. Dias, S. Urban, and U. Roessner, "A historical overview of natural products in drug discovery," *Metabolites*, vol. 2, no. 2, pp. 303–336, Apr. 2012, doi: 10.3390/metabo2020303. Available: https://doi.org/10.3390/metabo2020303

[19] A. Bhatt, P. Arora, and S. K. Prajapati, "Can algal derived bioactive metabolites serve as potential therapeutics for the treatment of SARS-COV-2 like viral infection?," *Frontiers in Microbiology*, vol. 11, Nov. 2020, doi: 10.3389/fmicb.2020.596374. Available: https://doi.org/10.3389/fmicb.2020.596374

[20] M. Yi, S. Lin, B. Zhang, H. Jin, and L. Ding, "Antiviral potential of natural products from marine microbes," *European Journal of Medicinal Chemistry*, vol. 207, p. 112790, Aug. 2020, doi: 10.1016/j.ejmech.2020.112790. Available: https://doi.org/10.1016/j.ejmech.2020.112790

[21] J. Berman and D. J. Krysan, "Drug resistance and tolerance in fungi," *Nature Reviews Microbiology*, vol. 18, no. 6, pp. 319–331, Feb. 2020, doi: 10.1038/s41579-019-0322-2. Available: https://doi.org/10.1038/s41579-019-0322-2

[22] V. S. Rao and K. Srinivas, "Modern drug discovery process: An in silico approach," *Journal of Bioinformatics and Sequence Analysis*, vol. 3, no. 5, pp. 89–94, Jun. 2011, doi: 10.5897/jbsa.9000016. Available:

https://academicjournals.org/journal/JBSA/article-full-text-pdf/6368F575575.pdf

[23] J. D. Romano and N. P. Tatonetti, "Informatics and Computational Methods in Natural Product Drug Discovery: A review and Perspectives," *Frontiers in Genetics*, vol. 10, Apr. 2019, doi: 10.3389/fgene.2019.00368. Available: https://doi.org/10.3389/fgene.2019.00368

[24] O. S. Chukwudozie, V. C. Duru, C. C. Ndiribe, A. T. Aborode, V. O. Oyebanji, and B. O. Emikpe, "The relevance of bioinformatics applications in the discovery of vaccine candidates and potential drugs for COVID-19 treatment," *Bioinformatics and Biology Insights*, vol. 15, Jan. 2021, doi: 10.1177/11779322211002168. Available: https://doi.org/10.1177/11779322211002168

[25] A. Alimadadi, S. Aryal, I. Manandhar, P. B. Munroe, B. Joe, and X. Cheng, "Artificial intelligence and machine learning to fight COVID-19," *Physiological Genomics*, vol. 52, no. 4, pp. 200–202, Mar. 2020, doi: 10.1152/physiolgenomics.00029.2020. Available: https://doi.org/10.1152/physiolgenomics.00029.2020

[26] F. Hufsky *et al.*, "Computational strategies to combat COVID-19: useful tools to accelerate SARS-CoV-2 and coronavirus research," *Briefings in Bioinformatics*, vol. 22, no. 2, pp. 642–663, Oct. 2020, doi: 10.1093/bib/bbaa232. Available: https://doi.org/10.1093/bib/bbaa232

[27] I. A. Guedes *et al.*, "Drug design and repurposing with DockThor-VS web server focusing on SARS-CoV-2 therapeutic targets and their non-synonym variants," *Scientific Reports*, vol. 11, no. 1, Mar. 2021, doi: 10.1038/s41598-021-84700-0. Available: https://doi.org/10.1038/s41598-021-84700-0

[28] M. Moradi, R. Golmohammadi, A. Najafi, M. M. Moghaddam, M. Fasihi-Ramandi, and R. Mirnejad, "A contemporary review on the important role of in silico approaches for managing different aspects of COVID-19 crisis," *Informatics in Medicine Unlocked*, vol. 28, p. 100862, Jan. 2022, doi: 10.1016/j.imu.2022.100862. Available: https://doi.org/10.1016/j.imu.2022.100862

[29] K. Wadhwa, H. Kaur, N. Kapoor, and S. Brogi, "Identification of Sesamin from Sesamum indicum as a Potent Antifungal Agent Using an Integrated in Silico and Biological Screening Platform," *Molecules*, vol. 28, no. 12, p. 4658, Jun. 2023, doi: 10.3390/molecules28124658. Available: https://doi.org/10.3390/molecules28124658

[30] I. Sama-Ae, N. C. Pattaranggoon, and A. Tedasen, "In silico prediction of Antifungal compounds from Natural sources towards Lanosterol 14-alpha demethylase (CYP51) using Molecular docking and Molecular dynamic simulation," *Journal of Molecular Graphics and Modelling*, vol. 121, p. 108435, Feb. 2023, doi: 10.1016/j.jmgm.2023.108435. Available: https://doi.org/10.1016/j.jmgm.2023.108435

[31] A. Tresserra-Rimbau, R. M. Lamuela-Raventos, and J. J. Moreno, "Polyphenols, food and pharma. Current knowledge and directions for future research," *Biochemical Pharmacology*, vol. 156, pp. 186–195, Aug. 2018, doi: 10.1016/j.bcp.2018.07.050. Available: https://doi.org/10.1016/j.bcp.2018.07.050

[32] J. O. Oladele *et al.*, "A systematic review on COVID-19 pandemic with special emphasis on curative potentials of Nigeria based medicinal plants," *Heliyon*, vol. 6, no. 9, p. e04897, Sep. 2020, doi: 10.1016/j.heliyon.2020.e04897. Available: https://doi.org/10.1016/j.heliyon.2020.e04897

[33] S. Shoaib *et al.*, "An Attention towards the Prophylactic and Therapeutic Options of Phytochemicals for SARS-CoV-2: A Molecular Insight," *Molecules*, vol. 28, no. 2, p. 795, Jan. 2023, doi: 10.3390/molecules28020795. Available: https://doi.org/10.3390/molecules28020795

[34] R. Abiri *et al.*, "A brief overview of potential treatments for viral diseases using natural plant compounds: the case of SARS-COV," *Molecules*, vol. 26, no. 13, p. 3868, Jun. 2021, doi: 10.3390/molecules26133868. Available: https://doi.org/10.3390/molecules26133868

[35] H.-S. Wang, H.-J. Li, L.-F. Wang, Z.-L. Shen, and Y.-C. Wu, "Regioselective synthesis of gentisyl alcohol-type marine natural products," *Natural Product Research*, vol. 33, no. 13, pp. 1891–1896, May 2018, doi:

10.1080/14786419.2018.1478831. Available: https://doi.org/10.1080/14786419.2018.1478831

[36] İ. Gülçin, Z. Huyut, M. Elmastaş, and H. Y. Aboul-Enein, "Radical scavenging and antioxidant activity of tannic acid," *Arabian Journal of Chemistry*, vol. 3, no. 1, pp. 43–53, Dec. 2009, doi: 10.1016/j.arabjc.2009.12.008. Available: https://doi.org/10.1016/j.arabjc.2009.12.008

[37] H. Ye, Q. Wang, F. Zhu, G. Feng, C. Yan, and J. Zhang, "Antifungal Activity of Alpha-Mangostin against Colletotrichum gloeosporioides In Vitro and In Vivo," *Molecules*, vol. 25, no. 22, p. 5335, Nov. 2020, doi: 10.3390/molecules25225335. Available: https://doi.org/10.3390/molecules25225335

[38] Kim, Kim, Kim, Kwon, Oh, and Lee, "Gentisyl alcohol inhibits apoptosis by suppressing caspase activity induced by etoposide," *Journal of Microbiology and Biotechnology*, vol. 15, no. 3, pp. 532–536, 2005.

[39] L. D. Abbott, J. D. Smith, and J. D. Reid, "Antibacterial activity of gentisyl alcohol and homogentisic acid," *Experimental Biology and Medicine*, vol. 69, no. 2, pp. 201–202, Nov. 1948, doi: 10.3181/00379727-69-16668. Available: https://doi.org/10.3181/00379727-69-16668

[40] S. Gupta, S. Kaul, B. Singh, R. A. Vishwakarma, and M. K. Dhar, "Production of Gentisyl Alcohol from Phoma herbarum Endophytic in Curcuma longa L. and Its Antagonistic Activity Towards Leaf Spot Pathogen Colletotrichum gloeosporioides," *Applied Biochemistry and Biotechnology*, vol. 180, no. 6, pp. 1093–1109, Jun. 2016, doi: 10.1007/s12010-016-2154-0. Available: https://doi.org/10.1007/s12010-016-2154-0

[41] L. Chen, Y. Fang, T. Zhu, Q. Gu, and W. Zhu, "Gentisyl Alcohol Derivatives from the Marine-Derived Fungus Penicillium terrestre," *Journal of Natural Products*, vol. 71, no. 1, pp. 66–70, Dec. 2007, doi: 10.1021/np070421v. Available: https://doi.org/10.1021/np070421v

[42] Miao *et al.*, "Identification and secondary metabolites of endophytic fungus PR20 from Paeonia delavayi," *Nat. Prod. Res. Dev*, vol. 24, no. 10, pp. 1339–1342, 2012.

[43] T. Ali, M. Inagaki, H.-B. Chai, T. Wieboldt, C. Rapplye, and L. H. Rakotondraibe, "Halogenated Compounds from Directed Fermentation of Penicillium concentricum, an Endophytic Fungus of the Liverwort Trichocolea tomentella," *Journal of Natural Products*, vol. 80, no. 5, pp. 1397–1403, Apr. 2017, doi: 10.1021/acs.jnatprod.6b01069. Available: https://doi.org/10.1021/acs.jnatprod.6b01069

[44] P. Maisuthisakul and M. H. Gordon, "Antioxidant and tyrosinase inhibitory activity of mango seed kernel by product," *Food Chemistry*, vol. 117, no. 2, pp. 332–341, Apr. 2009, doi: 10.1016/j.foodchem.2009.04.010. Available: https://doi.org/10.1016/j.foodchem.2009.04.010

[45] V. N. Nenkep, K. Yun, Y. Li, H. D. Choi, J. S. Kang, and B. W. Son, "New production of haloquinones, bromochlorogentisylquinones A and B, by a halide salt from a marine isolate of the fungus Phoma herbarum," *The Journal of Antibiotics*, vol. 63, no. 4, pp. 199–201, Mar. 2010, doi: 10.1038/ja.2010.15. Available: https://doi.org/10.1038/ja.2010.15

[46] R. Uchida, H. Tomoda, M. Arai, and S. Omura, "Chlorogentisylquinone, a new neutral sphingomyelinase inhibitor, produced by a marine fungus.," *The Journal of Antibiotics*, vol. 54, no. 11, pp. 882–889, Jan. 2001, doi: 10.7164/antibiotics.54.882. Available: https://doi.org/10.7164/antibiotics.54.882

[47] P. Ymele-Leki *et al.*, "A High-Throughput Screen Identifies a New Natural Product with Broad-Spectrum Antibacterial Activity," *PLoS ONE*, vol. 7, no. 2, p. e31307, Feb. 2012, doi: 10.1371/journal.pone.0031307. Available: https://doi.org/10.1371/journal.pone.0031307

[48] M. E. Rateb and R. Ebel, "Secondary metabolites of fungi from marine habitats," *Natural Product Reports*, vol. 28, no. 2, p. 290, Jan. 2011, doi: 10.1039/c0np00061b. Available: https://doi.org/10.1039/c0np00061b

[49] L. Chen, T. Zhu, Y. Ding, I. A. Khan, Q. Gu, and D. Li, "Sorbiterrin A, a novel sorbicillin derivative with cholinesterase inhibition activity from the marine-derived fungus Penicillium terrestre," *Tetrahedron Letters*, vol. 53, no. 3, pp.

325–328, Nov. 2011, doi: 10.1016/j.tetlet.2011.11.038. Available: https://doi.org/10.1016/j.tetlet.2011.11.038

[50] W. Liu, Q. Gu, W. Zhu, C. Cui, and G. Fan, "Dihydrotrichodimerol and Tetrahydrotrichodimerol, Two New Bisorbicillinoids, from a Marine-derived Penicillium terrestre," *The Journal of Antibiotics*, vol. 58, no. 10, pp. 621–624, Oct. 2005, doi: 10.1038/ja.2005.85. Available: https://doi.org/10.1038/ja.2005.85

[51] W. Liu, Q. Gu, W. Zhu, C. Cui, and G. Fan, "Two New Benzoquinone Derivatives and Two New Bisorbicillinoids were Isolated from a Marine-derived Fungus Penicillium terrestre," *The Journal of Antibiotics*, vol. 58, no. 7, pp. 441–446, Jul. 2005, doi: 10.1038/ja.2005.57. Available: https://doi.org/10.1038/ja.2005.57

[52] W. Liu *et al.*, "Penicillones A and B, two novel polyketides with tricyclo [5.3.1.03,8] undecane skeleton, from a marine-derived fungus Penicillium terrestre," *Tetrahedron Letters*, vol. 46, no. 30, pp. 4993–4996, Jun. 2005, doi: 10.1016/j.tetlet.2005.05.087. Available: https://doi.org/10.1016/j.tetlet.2005.05.087

[53] D. Li *et al.*, "Chloctanspirones A and B, novel chlorinated polyketides with an unprecedented skeleton, from marine sediment derived fungus Penicillium terrestre," *Tetrahedron*, vol. 67, no. 41, pp. 7913–7918, Aug. 2011, doi: 10.1016/j.tet.2011.08.037. Available: https://doi.org/10.1016/j.tet.2011.08.037

[54] S. Mathur and C. Hoskins, "Drug development: Lessons from nature," *Biomedical Reports*, vol. 6, no. 6, pp. 612–614, May 2017, doi: 10.3892/br.2017.909. Available: https://doi.org/10.3892/br.2017.909

[55] D. S. Wishart *et al.*, "DrugBank 5.0: a major update to the DrugBank database for 2018," *Nucleic Acids Research*, vol. 46, no. D1, pp. D1074–D1082, Nov. 2017, doi: 10.1093/nar/gkx1037. Available: https://doi.org/10.1093/nar/gkx1037

[56] K. Michalska *et al.*, "Crystal structures of SARS-CoV-2 ADP-ribose phosphatase: from the apo form to ligand complexes," *IUCrJ*, vol. 7, no. 5, pp.

814–824, Jul. 2020, doi: 10.1107/s2052252520009653. Available: https://doi.org/10.1107/s2052252520009653

[57] Q. Wang *et al.*, "Structural basis for RNA replication by the SARS-COV-2 polymerase," *Cell*, vol. 182, no. 2, pp. 417-428.e13, May 2020, doi: 10.1016/j.cell.2020.05.034. Available: https://doi.org/10.1016/j.cell.2020.05.034

[58] Q. Wang *et al.*, "Structural and functional basis of SARS-COV-2 entry by using human ACE2," *Cell*, vol. 181, no. 4, pp. 894-904.e9, Apr. 2020, doi: 10.1016/j.cell.2020.03.045. Available: https://doi.org/10.1016/j.cell.2020.03.045

[59] V. Choudhary, A. Gupta, R. Sharma, and H. S. Parmar, "Therapeutically effective covalent spike protein inhibitors in treatment of SARS-CoV-2," *Journal of Proteins and Proteomics*, vol. 12, no. 4, pp. 257–270, Sep. 2021, doi: 10.1007/s42485-021-00074-x. Available: https://doi.org/10.1007/s42485-021-00074-x

[60] S. Kang *et al.*, "A SARS-CoV-2 antibody curbs viral nucleocapsid protein-induced complement hyperactivation," *Nature Communications*, vol. 12, no. 1, May 2021, doi: 10.1038/s41467-021-23036-9. Available: https://doi.org/10.1038/s41467-021-23036-9

[61] Cong, Ulasli, Schepers, and Mauthe, "Nucleocapsid protein recruitment to replication-transcription complexes plays a crucial role in coronaviral life cycle," *J. Virol.*, vol. 94, pp. e01925-e19, 2020.

[62] S. Brunke, S. Mogavero, L. Kasper, and B. Hube, "Virulence factors in fungal pathogens of man," *Current Opinion in Microbiology*, vol. 32, pp. 89–95, Jun. 2016, doi: 10.1016/j.mib.2016.05.010. Available: https://doi.org/10.1016/j.mib.2016.05.010

[63] D. Fernández, S. Russi, J. Vendrell, M. Monod, and I. Pallarès, "A functional and structural study of the major metalloprotease secreted by the pathogenic fungusAspergillus fumigatus," *Acta Crystallographica Section D Biological Crystallography*, vol. 69, no. 10, pp. 1946–1957, Sep. 2013, doi:

10.1107/s0907444913017642. Available: https://doi.org/10.1107/s0907444913017642

[64] M. Monod, S. Capoccia, B. Léchenne, C. Zaugg, M. Holdom, and O. Jousson, "Secreted proteases from pathogenic fungi," *International Journal of Medical Microbiology*, vol. 292, no. 5–6, pp. 405–419, Jan. 2002, doi: 10.1078/1438-4221-00223. Available: https://doi.org/10.1078/1438-4221-00223

[65] J. a. G. Ferreira *et al.*, "Inhibition of Aspergillus fumigatus and Its Biofilm by Pseudomonas aeruginosa Is Dependent on the Source, Phenotype and Growth Conditions of the Bacterium," *PLoS ONE*, vol. 10, no. 8, p. e0134692, Aug. 2015, doi: 10.1371/journal.pone.0134692. Available: https://doi.org/10.1371/journal.pone.0134692

[66] L. Pan, S. Wen, J. Yu, L. Lu, X. Zhu, and Z. Zhang, "Genome-Wide Identification of M35 Family Metalloproteases in Rhizoctonia cerealis and Functional Analysis of RcMEP2 as a Virulence Factor during the Fungal Infection to Wheat," *International Journal of Molecular Sciences*, vol. 21, no. 8, p. 2984, Apr. 2020, doi: 10.3390/ijms21082984. Available: https://doi.org/10.3390/ijms21082984

[67] Q. Bashir, Z. Li, H. Li, D. M. LeMaster, and G. Hernández, "Crystal structure and transient dimerization for the FKBP12 protein from the pathogenic fungus Candida auris," *Biochemical and Biophysical Research Communications*, vol. 525, no. 4, pp. 1103–1108, Mar. 2020, doi: 10.1016/j.bbrc.2020.03.059. Available: https://doi.org/10.1016/j.bbrc.2020.03.059

[68] P. R. Juvvadi *et al.*, "Harnessing calcineurin-FK506-FKBP12 crystal structures from invasive fungal pathogens to develop antifungal agents," *Nature Communications*, vol. 10, no. 1, Sep. 2019, doi: 10.1038/s41467-019-12199-1. Available: https://doi.org/10.1038/s41467-019-12199-1

[69] G. Bitencourt-Ferreira and W. F. De Azevedo, "Molegro virtual docker for docking," *Methods in Molecular Biology*, pp. 149–167, Jan. 2019, doi: 10.1007/978-1-4939-9752-7_10. Available: https://doi.org/10.1007/978-1-4939-9752-7_10

[70] R. Thomsen and M. H. Christensen, "MolDock: a new technique for High-Accuracy Molecular Docking," *Journal of Medicinal Chemistry*, vol. 49, no. 11, pp. 3315–3321, Apr. 2006, doi: 10.1021/jm051197e. Available: https://doi.org/10.1021/jm051197e

[71] Ranjbar, Jamshidi, and Torabi, "Molecular modelling of the antiviral action of Resveratrol derivatives against the activity of two novel SARS CoV-2 and 2019-nCoV receptors," *Eur. Rev. Med. Pharmacol. Sci*, vol. 24, no. 14, pp. 7834–7844, 2019.

[72] W. L. M. Alencar, T. Da Silva Arouche, A. F. G. Neto, T. De Castro Ramalho, R. N. De Carvalho Júnior, and A. M. De Jesus Chaves Neto, "Interactions of Co, Cu, and non-metal phthalocyanines with external structures of SARS-CoV-2 using docking and molecular dynamics," *Scientific Reports*, vol. 12, no. 1, Feb. 2022, doi: 10.1038/s41598-022-07396-w. Available: https://doi.org/10.1038/s41598-022-07396-w

[73] V. R. Shah, J. D. Bhaliya, and G. M. Patel, "In silico approach: docking study of oxindole derivatives against the main protease of COVID-19 and its comparison with existing therapeutic agents," *Journal of Basic and Clinical Physiology and Pharmacology*, vol. 32, no. 3, pp. 197–214, Feb. 2021, doi: 10.1515/jbcpp-2020-0262. Available: https://doi.org/10.1515/jbcpp-2020-0262

[74] Z. Y. Ibrahim, A. Uzairu, G. Shallangwa, and S. Abechi, "Molecular docking studies, drug-likeness and in-silico ADMET prediction of some novel β-Amino alcohol grafted 1,4,5-trisubstituted 1,2,3-triazoles derivatives as elevators of p53 protein levels," *Scientific African*, vol. 10, p. e00570, Sep. 2020, doi: 10.1016/j.sciaf.2020.e00570. Available: https://doi.org/10.1016/j.sciaf.2020.e00570

[75] G. R. Bickerton, G. V. Paolini, J. Besnard, S. Muresan, and A. L. Hopkins, "Quantifying the chemical beauty of drugs," *Nature Chemistry*, vol. 4, no. 2, pp. 90–98, Jan. 2012, doi: 10.1038/nchem.1243. Available: https://doi.org/10.1038/nchem.1243

[76] C. A. Lipinski, "Drug-like properties and the causes of poor solubility and poor permeability," *Journal of Pharmacological and Toxicological Methods*, vol. 44,

no. 1, pp. 235–249, Jul. 2000, doi: 10.1016/s1056-8719(00)00107-6. Available: https://doi.org/10.1016/s1056-8719(00)00107-6

[77] D. F. Veber, S. R. Johnson, H.-Y. Cheng, B. R. Smith, K. W. Ward, and K. D. Kopple, "Molecular properties that influence the oral bioavailability of drug candidates," *Journal of Medicinal Chemistry*, vol. 45, no. 12, pp. 2615–2623, May 2002, doi: 10.1021/jm020017n. Available: https://doi.org/10.1021/jm020017n

[78] W. J. Egan, K. M. Merz, and J. J. Baldwin, "Prediction of drug absorption using multivariate statistics," *Journal of Medicinal Chemistry*, vol. 43, no. 21, pp. 3867–3877, Sep. 2000, doi: 10.1021/jm000292e. Available: https://doi.org/10.1021/jm000292e

[79] A. K. Ghose, V. N. Viswanadhan, and J. J. Wendoloski, "A Knowledge-Based Approach in designing combinatorial or medicinal chemistry libraries for drug discovery. 1. A qualitative and quantitative characterization of known drug databases," *Journal of Combinatorial Chemistry*, vol. 1, no. 1, pp. 55–68, Dec. 1998, doi: 10.1021/cc9800071. Available: https://doi.org/10.1021/cc9800071

[80] C. A. Lipinski, F. Lombardo, B. W. Dominy, and P. J. Feeney, "Experimental and computational approaches to estimate solubility and permeability in drug discovery and development settings," *Advanced Drug Delivery Reviews*, vol. 23, no. 1–3, pp. 3–25, Jan. 1997, doi: 10.1016/s0169-409x(96)00423-1. Available: https://doi.org/10.1016/s0169-409x(96)00423-1

[81] Daina, Michielin, and Zoete, "SwissADME: a free web tool to evaluate pharmacokinetics, drug-likeness and medicinal chemistry friendliness of small molecules," *Sci. Rep.*, vol. 7, no. 1, p. 42717, 2017.

[82] H. L. Forbes and T. M. Polasek, "Potential drug–drug interactions with direct oral anticoagulants in elderly hospitalized patients," *Therapeutic Advances in Drug Safety*, vol. 8, no. 10, pp. 319–328, Jul. 2017, doi: 10.1177/2042098617719815. Available: https://doi.org/10.1177/2042098617719815

[83] Wang and Urban, "he impact of early ADME profiling on drug discovery and development strategy," *DDW Drug Discovery World*, vol. 5, no. 4, pp. 73–86, 2004.

[84] J. A. DiMasi, R. W. Hansen, and H. G. Grabowski, "The price of innovation: new estimates of drug development costs," *Journal of Health Economics*, vol. 22, no. 2, pp. 151–185, Feb. 2003, doi: 10.1016/s0167-6296(02)00126-1. Available: https://doi.org/10.1016/s0167-6296(02)00126-1

[85] K.-T. Rim, "Adverse outcome pathways for chemical toxicity and their applications to workers' health: a literature review," *Toxicology and Environmental Health Sciences*, vol. 12, no. 2, pp. 99–108, Mar. 2020, doi: 10.1007/s13530-020-00053-7. Available: https://doi.org/10.1007/s13530-020-00053-7

[86] P. Banerjee, A. O. Eckert, A. K. Schrey, and R. Preissner, "ProTox-II: a webserver for the prediction of toxicity of chemicals," *Nucleic Acids Research*, vol. 46, no. W1, pp. W257–W263, Apr. 2018, doi: 10.1093/nar/gky318. Available: https://doi.org/10.1093/nar/gky318

[87] I. Azad, T. Khan, A. K. Maurya, Mohd. I. Azad, N. Mishra, and A. M. Alanazi, "Identification of Severe Acute Respiratory Syndrome Coronavirus-2 inhibitors through in silico structure-based virtual screening and molecular interaction studies," *Journal of Molecular Recognition*, vol. 34, no. 10, Jun. 2021, doi: 10.1002/jmr.2918. Available: https://doi.org/10.1002/jmr.2918

[88] P. Madanagopal, N. Ramprabhu, and R. Jagadeesan, "In silico prediction and structure-based multitargeted molecular docking analysis of selected bioactive compounds against mucormycosis," *Bulletin of the National Research Centre/Bulletin of the National Research Center*, vol. 46, no. 1, Jan. 2022, doi: 10.1186/s42269-022-00704-4. Available: https://doi.org/10.1186/s42269-022-00704-4

[89] D. A. Filimonov *et al.*, "Prediction of the biological activity spectra of organic compounds using the PASS online web resource," *Chemistry of Heterocyclic Compounds*, vol. 50, no. 3, pp. 444–457, May 2014, doi: 10.1007/s10593-014-1496-1. Available: https://doi.org/10.1007/s10593-014-1496-1

[90] R. K. Goel, D. Singh, A. Lagunin, and V. Poroikov, "PASS-assisted exploration of new therapeutic potential of natural products," *Medicinal Chemistry Research*,

vol. 20, no. 9, pp. 1509–1514, Aug. 2010, doi: 10.1007/s00044-010-9398-y. Available: https://doi.org/10.1007/s00044-010-9398-y

[91] A. Gupta *et al.*, "Exploration of novel lichen compounds as inhibitors of SARS-COV-2 MPRO: Ligand-Based Design, Molecular Dynamics, and ADMET analyses," *Applied Biochemistry and Biotechnology*, vol. 194, no. 12, pp. 6386–6406, Aug. 2022, doi: 10.1007/s12010-022-04103-3. Available: https://doi.org/10.1007/s12010-022-04103-3

[92] O. Pokharkar, H. Lakshmanan, G. Zyryanov, and M. Tsurkan, "In Silico Evaluation of Antifungal Compounds from Marine Sponges against COVID-19-Associated Mucormycosis," *Marine Drugs*, vol. 20, no. 3, p. 215, Mar. 2022, doi: 10.3390/md20030215. Available: https://doi.org/10.3390/md20030215

[93] A. W. Schüttelkopf and D. M. F. Van Aalten, "PRODRG: a tool for high-throughput crystallography of protein–ligand complexes," *Acta Crystallographica Section D Biological Crystallography*, vol. 60, no. 8, pp. 1355–1363, Jul. 2004, doi: 10.1107/s0907444904011679. Available: https://doi.org/10.1107/s0907444904011679

[94] Abraham, Van Der Spoel, Lindahl, and Hess, "The GROMACS development team," *GROMACS User Manual Version*, vol. 5, no. 4, 2016.

[95] S. Lakhera, K. Devlal, A. Ghosh, P. Chowdhury, and M. Rana, "Modelling the DFT structural and reactivity study of feverfew and evaluation of its potential antiviral activity against COVID-19 using molecular docking and MD simulations," *Chemical Papers*, vol. 76, no. 5, pp. 2759–2776, Jan. 2022, doi: 10.1007/s11696-022-02067-6. Available: https://doi.org/10.1007/s11696-022-02067-6

[96] V. Choudhary, A. Bhatt, D. Dash, and N. Sharma, "DFT calculations on molecular structures, HOMO–LUMO study, reactivity descriptors and spectral analyses of newly synthesized diorganotin(IV) 2-chloridophenylacetohydroxamate complexes," *Journal of Computational Chemistry*, vol. 40, no. 27, pp. 2354–2363, Jun. 2019, doi: 10.1002/jcc.26012. Available: https://doi.org/10.1002/jcc.26012

[97] Dennington, T. Keith, and J.Millam, "Semichem Inc," *Shawnee Mission KS, GaussView, Version*, vol. 5, 2009.

[98] M. J. Frisch, G. W. Trucks, H. B. Schlegel *et al.*, *Gaussian 16, Revision C.01*, Gaussian, Inc., Wallingford, CT, USA, 2016.

[99] M. Kadela-Tomanek, M. Jastrzębska, K. Marciniec, E. Bębenek, E. Chrobak, and S. Boryczka, "Spectroscopic investigations, computational analysis and molecular docking to SAR-COV-2 targets studies of 5,8-Quinolinedione attached to betulin derivatives," *Crystals*, vol. 11, no. 1, p. 76, Jan. 2021, doi: 10.3390/cryst11010076. Available: https://doi.org/10.3390/cryst11010076

[100] W. De Azevedo Jr, "MolDock applied to Structure-Based virtual screening," *Current Drug Targets*, vol. 11, no. 3, pp. 327–334, Feb. 2010, doi: 10.2174/138945010790711941. Available: https://doi.org/10.2174/138945010790711941

[101] Moh. F. Rahman, N. Aulanni'am, N. Masruri, A. Sabarudin, S. M. Ulfa, and F. M. Zubair, "Metabolites profiling of ethyl acetate extract of sponge Halichondriidae sp from Kangean Islands and their in silico activity as coronavirus drugs," *AIP Conference Proceedings*, vol. 2911, p. 080004, Jan. 2023, doi: 10.1063/5.0136600. Available: https://doi.org/10.1063/5.0136600

[102] X.-L. Ma, C. Chen, and J. Yang, "Predictive model of blood-brain barrier penetration of organic compounds1," *Acta Pharmacologica Sinica*, vol. 26, no. 4, pp. 500–512, Apr. 2005, doi: 10.1111/j.1745-7254.2005.00068.x. Available: https://doi.org/10.1111/j.1745-7254.2005.00068.x

[103] C.-P. Chen *et al.*, "Efficacy of predictive modeling as a scientific criterion in dermal hazard identification for assignment of skin notations," *Regulatory Toxicology and Pharmacology*, vol. 61, no. 1, pp. 63–72, Jun. 2011, doi: 10.1016/j.yrtph.2011.05.013. Available: https://doi.org/10.1016/j.yrtph.2011.05.013

[104] R. Callaghan, F. Luk, and M. Bebawy, "Inhibition of the multidrug resistance P-Glycoprotein: Time for a change of strategy?," *Drug Metabolism and Disposition*, vol. 42, no. 4, pp. 623–631, Feb. 2014, doi: 10.1124/dmd.113.056176. Available: https://doi.org/10.1124/dmd.113.056176

[105] T. J. Hou, W. Zhang, K. Xia, X. B. Qiao, and X. J. Xu, "ADME Evaluation in Drug Discovery. 5. Correlation of Caco-2 Permeation with Simple Molecular Properties," *Journal of Chemical Information and Computer Sciences*, vol. 44, no. 5, pp. 1585–1600, Jul. 2004, doi: 10.1021/ci049884m. Available: https://doi.org/10.1021/ci049884m

[106] Y. H. Zhao *et al.*, "Evaluation of human intestinal absorption data and subsequent derivation of a quantitative structure–activity relationship (QSAR) with the Abraham descriptors," *Journal of Pharmaceutical Sciences*, vol. 90, no. 6, pp. 749–784, Jun. 2001, doi: 10.1002/jps.1031. Available: https://doi.org/10.1002/jps.1031

[107] J. D. Irvine *et al.*, "MDCK (Madin-Darby Canine Kidney) Cells: a tool for membrane permeability screening," *Journal of Pharmaceutical Sciences*, vol. 88, no. 1, pp. 28–33, Jan. 1999, doi: 10.1021/js9803205. Available: https://doi.org/10.1021/js9803205

[108] K. Richa *et al.*, "Synthesis,In VitroEvaluation, molecular docking and DFT studies of some phenyl isothiocyanates as anticancer agents," *Anti-Cancer Agents in Medicinal Chemistry*, vol. 19, no. 18, pp. 2211–2222, Sep. 2019, doi: 10.2174/1871520619666190930122137. Available: https://doi.org/10.2174/1871520619666190930122137

[109] S. Singhal, P. Khanna, and L. Khanna, "Synthesis, DFT studies, molecular docking, antimicrobial screening and UV fluorescence studies on ct-DNA for novel Schiff bases of 2-(1-aminobenzyl) benzimidazole," *Heliyon*, vol. 5, no. 10, p. e02596, Oct. 2019, doi: 10.1016/j.heliyon.2019.e02596. Available: https://doi.org/10.1016/j.heliyon.2019.e02596

[110] K. Azeem *et al.*, "A multi-spectroscopic and computational simulations study to delineate the interaction between antimalarial drug hydroxychloroquine and human serum albumin," *Journal of Biomolecular Structure and Dynamics*, vol. 41, no. 13, pp. 6377–6393, Aug. 2022, doi: 10.1080/07391102.2022.2107077. Available: https://doi.org/10.1080/07391102.2022.2107077

[111] A. Kuzmanic and B. Zagrovic, "Determination of Ensemble-Average Pairwise Root Mean-Square Deviation from Experimental B-Factors," *Biophysical*

Journal, vol. 98, no. 5, pp. 861–871, Feb. 2010, doi: 10.1016/j.bpj.2009.11.011. Available: https://doi.org/10.1016/j.bpj.2009.11.011

[112] L. Martínez, "Automatic identification of mobile and rigid substructures in molecular dynamics simulations and fractional structural fluctuation analysis," *PLoS ONE*, vol. 10, no. 3, p. e0119264, Mar. 2015, doi: 10.1371/journal.pone.0119264. Available: https://doi.org/10.1371/journal.pone.0119264

[113] H. Tanwar, P. Sneha, D. T. Kumar, R. Siva, C. E. J. Walter, and C. G. P. Doss, "A computational approach to identify the biophysical and structural aspects of methylenetetrahydrofolate reductase (MTHFR) mutations (A222V, E429A, and R594Q) leading to schizophrenia," *Advances in Protein Chemistry and Structural Biology*, pp. 105–125, Jan. 2017, doi: 10.1016/bs.apcsb.2017.01.007. Available: https://doi.org/10.1016/bs.apcsb.2017.01.007

[114] A. Uddin *et al.*, "Target-Based virtual screening of natural compounds identifies a potent antimalarial with selective falcipain-2 inhibitory activity," *Frontiers in Pharmacology*, vol. 13, Apr. 2022, doi: 10.3389/fphar.2022.850176. Available: https://doi.org/10.3389/fphar.2022.850176

SUPPORTING INFORMATION

4.2. Material and method

4.2.1. Set of compounds and standards under study

Table S4.2: List of established standards and their activities.

Sl.no	STANDARDS	ACTIVITY
1	Nafamostat	Serine protease inhibitor
2	Arbidol	Antiviral
3	Ribavirin	Broad-spectrum antiviral
4	Favipiravir	Antiviral
5	Dexamethasone	Immune modulator/steroid/ antiinflammatory
6	Hydroxychloroquine	Antimalaria
7	Chloroquine	Antimalarial
8	Posaconazole	Antifungal
9	Isavuconazole	Broad spectrum Antifungal
10	Amphotericin.B	Antifungal

4.3.Result and discussion

4.3.1. Validation of docking analysis

Table 4.3: Docking score of the ligands and standards under investigation with PDB ID: 6VXS

Ligand	MolDock Score kcal/mol	[a]Rerank Score	[b]Interaction	[c]Internal	[d]HBond	[e]LE1	[f]LE3
Terrestrol A (10)	-129.018	-102.731	-150.866	21.8477	-13.7041	-4.4489	-3.54245
Nafamostat	-126.878	-101.272	-149.126	22.2485	-4.0528	-4.87991	-3.89509
Ribavirin	-108.756	-93.9921	-116.03	7.27386	-13.2618	-6.39743	-5.52894
Arbidol (Umifenovir)	-124.725	-89.1753	-136.481	11.756	-1.53662	-4.30088	-3.07501
Chloroquine	-104.972	-82.2317	-122.663	17.6911	-2.255	-4.77145	-3.73781
17	-99.7726	-81.0648	-120.192	20.4191	-10	-4.98863	-4.05324
Hydroxychloroquine	-106.869	-81.0073	-123.488	16.6192	-5.08265	-4.64647	-3.52206
12	-101.885	-79.7771	-116.494	14.6091	-7.40469	-5.36237	-4.19879
Dexamethasone	-82.0804	-79.7324	-119.573	37.4927	-9.14814	-2.93144	-2.84759
16	-95.6994	-79.7214	-115.089	19.39	-12.1473	-4.78497	-3.98607
9	-94.0418	-78.736	-108.996	14.9543	-5.23618	-4.70209	-3.9368
13	-94.9734	-78.2526	-118.442	23.4691	-10.1359	-4.74867	-3.91263

11	-94.4181	-77.564	-115.536	21.1181	-6.01746	-4.72091	-3.8782
14	-89.4951	-75.7658	-107.528	18.0326	-8.02023	-4.71027	-3.98767
15	-89.3834	-73.0045	-111.19	21.8069	-11.8563	-4.46917	-3.65022
18	-93.8459	-71.6159	-106.64	12.7942	-10.669	-5.21366	-3.97866
7	-64.0909	-61.0195	-83.504	19.4131	-14.2119	-5.34091	-5.08495
8	-70.6069	-59.504	-83.6959	13.089	-9.23535	-5.4313	-4.57723
Favipiravir	-59.1151	-53.2374	-71.7061	12.5911	-5.7192	-5.3741	-4.83977
3	-62.7574	-52.8355	-73.1098	10.3524	-11.0004	-5.70522	-4.80323
19	-57.3378	-52.4269	-68.4112	11.0734	-10.1585	-5.21253	-4.76608
1	-61.0474	-52.2782	-70.6035	9.55612	-11.2049	-6.10474	-5.22782
2	-62.5299	-51.9852	-72.4127	9.88277	-10.5269	-5.68454	-4.72592
6	-54.9701	-51.3399	-70.4262	15.4561	-9.36461	-4.58084	-4.27832
4	-55.0642	-50.3323	-68.9211	13.8569	-9.45053	-5.50642	-5.03323
5	-57.0274	-48.851	-69.921	12.8936	-4.80411	-4.75228	-4.07092
20	-44.7788	-46.921	-63.5677	18.7888	-3.97792	-4.0708	-4.26554

[a]Thererank score is a linear combination of E-inter (steric, Van der Waals, hydrogen bonding, electrostatic) between the ligand and the protein, and E-intra. (torsion, sp2-sp2, hydrogen bonding, Van der Waals, electrostatic) of the ligand weighted by pre-defined coefficients. [b]The total interaction energy between the pose and the protein (kJ/mol). [c]The internal energy of the pose. [d]Hydrogen bonding energy (kJ/mol). [e]Ligand efficiency 1: MolDock score divided by heavy atoms count. [f]Ligand efficiency 3: Rerank score divided by heavy atoms count.

Table S4.4: Docking score of the ligands and standards under investigation with PDB ID: 6LZG.

Ligand	**MolDock Score kcal/mol**	**[a]Rerank Score**	**[b]Interaction**	**[c]Internal**	**[d]HBond**	**[e]LE1**	**[f]LE3**
Terrestrol A (10)	-117.964	-83.2034	-141.401	23.4364	-9.47482	-4.06774	-2.86908
Ribavirin	-94.82	-81.2796	-101.083	6.26337	-12.4355	-5.57765	-4.78115
Arbidol (Umifenovir)	-116.994	-80.1414	-118.94	1.94548	-0.689743	-4.03428	-2.7635
9	-90.4759	-74.8069	-105.996	15.5201	-10.6348	-4.52379	-3.74034
Nafamostat	-97.7132	-74.6955	-115.984	18.2707	-5.75096	-3.7582	-2.8729
14	-96.0173	-73.6773	-111.067	15.0494	-9.15974	-5.05354	-3.87775
15	-87.6806	-72.5265	-108.468	20.7878	-11.6544	-4.38403	-3.62632

13	-93.6188	-71.2112	-105.132	11.5135	-7.93551	-4.68094	-3.56056
18	-91.2187	-69.0828	-104.311	13.092	-9.64899	-5.06771	-3.83793
16	-83.0475	-68.6101	-101.702	18.6542	-10.2792	-4.15238	-3.43051
11	-86.0022	-68.4916	-102.848	16.8458	-5.55612	-4.30011	-3.42458
Hydroxychloroquine	-99.2201	-68.3221	-114.42	15.1998	-4.08788	-4.31392	-2.97053
17	-93.301	-67.6933	-106.956	13.6555	-10.3052	-4.66505	-3.38467
12	-91.5344	-67.6371	-107.552	16.018	-7.13515	-4.8176	-3.55985
Chloroquine	-98.7785	-67.3507	-103.618	4.83988	-1.44028	-4.48993	-3.0614
Dexamethasone	-58.9691	-61.9835	-92.7676	33.7985	-2.59758	-2.10604	-2.2137
8	-66.8168	-56.4898	-77.9757	11.1589	-3.60171	-5.13975	-4.34537
Favipiravir	-58.9212	-53.132	-71.67	12.7489	-2.04769	-5.35647	-4.83018
2	-56.4881	-47.5332	-65.6742	9.18614	-4.73357	-5.13528	-4.3212
1	-55.102	-47.3415	-64.54	9.438	-7.54367	-5.5102	-4.73415
3	-55.7276	-47.3189	-65.5796	9.85205	-4.73153	-5.06614	-4.30172
7	-49.8177	-47.0109	-66.3709	16.5532	-4.9285	-4.15147	-3.91758
5	-53.6147	-46.3376	-66.2012	12.5865	-3.30636	-4.46789	-3.86146
4	-51.9243	-45.5188	-62.7735	10.8492	-3.16382	-5.19243	-4.55188
19	-47.9157	-45.1824	-58.9891	11.0734	-3.61926	-4.35597	-4.10749

20	-42.1117	-45.0992	-60.9005	18.7888	-3.40313	-3.82833	-4.09993
6	-51.0498	-44.2871	-63.3135	12.2637	0	-4.25415	-3.69059

Table S4.5: Docking score of the ligands and standards under investigation with PDB ID: 7CR5.

Ligand	**MolDock Score kcal/mol**	[a]**Rerank Score**	[b]**Interaction**	[c]**Internal**	[d]**HBond**	[e]**LE1**	[f]**LE3**
Terrestrol A (10)	-133.184	-104.028	-160.285	27.1009	-9.16425	-4.59256	-3.58716
Nafamostat	-124.022	-106.687	-154.545	30.523	-3.00859	-4.77007	-4.10333
Hydroxychloroquine	-127.395	-97.1746	-145.361	17.9655	-4.00658	-5.53891	-4.22498
Arbidol (Umifenovir)	-124.829	-95.0687	-135.592	10.7627	-2.83959	-4.30445	-3.27823
Chloroquine	-119.888	-92.0121	-133.76	13.8718	-2.47819	-5.44945	-4.18237
17	-111.481	-90.7584	-127.569	16.0883	-8.28505	-5.57404	-4.53792
14	-105.721	-90.2326	-128.176	22.455	-11.8096	-5.56426	-4.74909
Ribavirin	-103.176	-88.7415	-109.062	5.8852	-13.4833	-6.0692	-5.22009
11	-107.53	-88.0466	-130.903	23.3733	-11.4639	-5.37648	-4.40233
13	-104.441	-87.5316	-124.68	20.239	-14.7559	-5.22205	-4.37658
12	-105.036	-87.3608	-120.612	15.5759	-7.78506	-5.52821	-4.59793
9	-100.889	-81.8908	-116.344	15.4553	-8.92285	-5.04444	-4.09454
Dexamethasone	-78.1634	-79.0327	-109.519	31.3552	-5.08533	-2.79155	-2.8226
18	-99.9136	-78.59	-114.132	14.2183	-3.59266	-5.55076	-4.36611
16	-96.7903	-76.7486	-112.847	16.0565	-14.1298	-4.83952	-3.83743
15	-94.981	-73.4685	-112.749	17.7677	-15.8888	-4.74905	-3.67342
8	-76.9911	-66.3483	-88.3468	11.3557	-7.76249	-5.92239	-5.10372
3	-68.087	-58.3901	-77.9253	9.83832	-7.52204	-6.18973	-5.30819
Favipiravir	-64.6615	-58.3604	-77.2553	12.5938	-5.94227	-5.87832	-5.30549
6	-66.0276	-57.9874	-78.2021	12.1745	-5.50767	-5.5023	-4.83228
7	-60.1682	-55.7312	-76.6122	16.4439	-6.86015	-5.01402	-4.64427
2	-65.4783	-55.449	-74.6577	9.17935	-7.1218	-5.95258	-5.04081
5	-64.0484	-55.1699	-76.5664	12.518	-4.88576	-5.33737	-4.59749
1	-64.6146	-55.1228	-74.0448	9.43024	-8.32647	-6.46146	-5.51228
19	-61.0628	-54.8545	-72.1362	11.0734	-7.65788	-5.55116	-4.98678

20	-53.3894	-53.7397	-72.1782	18.7889	-5	-4.85358	-4.88543
4	-58.419	-51.2213	-69.3055	10.8865	-5.29797	-5.8419	-5.12213

Table S4.6: Docking score of the ligands and standards under investigation with PDB ID: 4K90

Ligand	MolDock Score kcal/mol	[a]Rerank Score	[b]Interaction	[c]Internal	[d]HBond	[e]LE1	[f]LE3
Terrestrol A (10)	-136.756	-102.831	-156.351	19.5946	-16.8171	-4.71574	-3.5459
Isavuconazole	-134.629	-101.827	-155.561	20.9313	1.60113	-4.34288	-3.28473
Posaconazole	-135.126	-95.9875	-164.797	29.6718	-4.41747	-2.64952	-1.88211
17	-117.493	-93.9365	-131.631	14.1376	-11.1771	-5.87465	-4.69683
9	-114.46	-92.285	-124.642	10.1818	-13.7811	-5.72302	-4.61425
11	-112.462	-90.2826	-130.52	18.0579	-9.75267	-5.62308	-4.51413
13	-119.966	-90.1375	-134.837	14.8715	-7.4276	-5.99829	-4.50688
14	-118.669	-89.917	-133.249	14.5799	-7.10966	-6.24572	-4.73247
16	-109.654	-88.6368	-129.029	19.3749	-8.14945	-5.48269	-4.43184
12	-112.928	-87.5941	-126.023	13.0954	-9.19022	-5.94358	-4.61022
15	-107.933	-86.0855	-125.796	17.8635	-9.0396	-5.39664	-4.30427
18	-99.9434	-79.2332	-115.255	15.3117	-8.17536	-5.55241	-4.40184
8	-87.8628	-71.4445	-101.04	13.1775	-9.17674	-6.75868	-5.49573

6	-69.9712	-60.5458	-82.1622	12.191	-5.51077	-5.83093	-5.04548
5	-71.6991	-60.2773	-84.0672	12.3681	-3.88493	-5.97492	-5.0231
19	-66.0672	-60.1348	-77.1406	11.0734	-7.90604	-6.0061	-5.4668
7	-62.9379	-59.2115	-79.619	16.6811	-7.95995	-5.24483	-4.93429
3	-69.2508	-57.8188	-79.1959	9.94507	-5.7944	-6.29553	-5.25625
1	-67.225	-57.4737	-76.7556	9.53058	-6.72336	-6.7225	-5.74737
20	-57.5243	-57.146	-76.3132	18.7889	-3.99239	-5.22948	-5.19509
2	-69.0482	-57.0622	-78.3425	9.29436	-5.3035	-6.27711	-5.18747
4	-61.349	-55.9082	-75.3719	14.0228	-2.69261	-6.1349	-5.59082
Amphotericin B	197.835	1686.92	180.382	17.4532	5.55282	3.04361	25.9526

Table S4.7: Docking score of the ligands and standards under investigation with PDB ID: 6VSI.

Ligand	**MolDock Score kcal/mol**	**[a]Rerank Score**	**[b]Interaction**	**[c]Internal**	**[d]HBond**	**[e]LE1**	**[f]LE3**
Terrestrol A (10)	-111.152	-79.6163	-134.039	22.8867	-4.92036	-3.83282	-2.74539
Isavuconazole	-99.9374	-80.9226	-118.859	18.9216	-3.61043	-3.22379	-2.61041
12	-100.665	-79.3054	-116.872	16.2066	-9.8719	-5.29817	-4.17397

11	-94.8298	-76.637	-112.794	17.9646	-5.98259	-4.74149	-3.83185
13	-92.3966	-74.1394	-110.311	17.9142	-5.16518	-4.61983	-3.70697
17	-89.8315	-71.6536	-105.452	15.6201	-4.22346	-4.49158	-3.58268
14	-85.7599	-71.385	-103.639	17.8787	-6.10033	-4.51368	-3.75711
9	-86.4947	-71.2784	-102.02	15.5254	-5.63146	-4.32473	-3.56392
16	-82.7259	-69.1359	-101.583	18.8569	-6.18555	-4.1363	-3.45679
18	-88.911	-68.6759	-102.226	13.3153	-6.56358	-4.9395	-3.81533
15	-80.8825	-67.1233	-99.7123	18.8298	-7.35393	-4.04412	-3.35616
8	-74.4412	-63.7069	-85.4777	11.0365	-7.02516	-5.72625	-4.90053
5	-66.6923	-57.3206	-79.2957	12.6034	-5	-5.55769	-4.77672
7	-59.6399	-54.5134	-77.6116	17.9717	-6.56848	-4.96999	-4.54278
20	-55.64	-54.4952	-74.4288	18.7888	-8.35068	-5.05818	-4.95411

3	-63.6697	-54.2796	-73.5614	9.8917 8	-7.649 08	-5.788 15	-4.934 51
2	-63.4435	-53.8052	-72.6773	9.2338 7	-7.228 59	-5.767 59	-4.891 38
4	-61.5029	-53.3168	-72.3702	10.867 3	-5	-6.150 29	-5.331 68
1	-62.8214	-53.3047	-71.8022	8.9807 9	-8.152 93	-6.282 14	-5.330 47
6	-59.212	-51.352	-71.4335	12.221 6	-2.107 34	-4.934 33	-4.279 34
19	-55.3813	-49.4073	-66.4546	11.073 3	-3.216 46	-5.034 66	-4.491 57
Posaconazol e	-82.6141	-24.4897	-107.926	25.311 8	-2.701 33	-1.619 88	-0.480 19
Amphotericin b	-82.2127	68.1021	-105.577	23.364 2	-16.51 92	-1.264 81	1.047 72

Table S4.8: Ligand- receptor interactions of Terrestrol A(**10**) and the standards at the probable active site of the target with PDB ID: 6VXS.

Ligand	**Interaction(P----L)**	**Interaction distance**	**Interaction Energy**	**Hybridization protein**	**Hybridization ligand**
Terrestrol A(10)	IIe23(N)----O(25)	3.48 Å	-0.3615	Sp2 donor	Sp3 both
	Ala154(O)----O(25)	3.15 Å	-2.26	Sp2 Acceptor	Sp3 both
	Ala129(O)----O(7)	2.56 Å	-2.192	Sp2 Acceptor	Sp3 both
	IIe131(N)----(O)	3.07 Å	-2.208	Sp2 donor	Sp3 both
	Leu126(O)----O(23)	3.12 Å	-2.417	Sp2 Acceptor	Sp3 both
	Gly47(O)----O(6)	3.22 Å	-1.893	Sp2 Acceptor	Sp3 both

	Ala38(O)----O(6)	3.08 Å	-2.5	Sp2 Acceptor	Sp3 both
	Ala50(N)----O(6)	2.99 Å	-2.5	Sp2 donor	Sp3 both
Nafamostat	Phe156(N)----O(1)	2.67 Å	-2.5	Sp2 donor	Sp2 Acceptor
	Ala129(O)----N(2)	2.76 Å	-2.5	Sp2 Acceptor	Sp2 donor
	Asp22(OD1)----N(6)	2.67 Å	-2.5	Sp3 Acceptor	Sp2 donor
	Asp22(OD1)----N(5)	2.81 Å	-0.268	Sp3 Acceptor	Sp2 donor
	IIe23(N)----N(4)	3.43 Å	-0.851	Sp2 donor	Sp2 Acceptor
Ribavirin	Gly47(O)----O(3)	2.77 Å	-2.5	Sp2 Acceptor	Sp3 both
	Val49(N)----O(1)	2.94 Å	-2.5	Sp2 donor	Sp3 both
	Val49(N)----O(2)	2.80 Å	-0.435	Sp2 donor	Sp3 both
	Ala50(N)----O(2)	2.73 Å	-2.5	Sp2 donor	Sp3 both
	Ala38(O)----O(2)	3.44 Å	-0.779	Sp2 Acceptor	Sp3 both
	Gly47(O)----O(2)	2.85 Å	-2.5	Sp2 Acceptor	Sp3 both
	Ala39(O)----N(8)	3.20 Å	-1.979	Sp2 Acceptor	Sp2 donor
	Val95(O)----N(8)	3.14 Å	-2.313	Sp2 Acceptor	Sp2 donor
	Ser128(OG)----O(4)	3.47 Å	-0.635	Sp3 both	Sp2 Acceptor
	Ser128(N)----O(4)	2.69 Å	-0.313	Sp2 donor	Sp2 Acceptor
	Ala129(N)----N(7)	3.39 Å	-0.382	Sp2 donor	Sp2 Acceptor
	Ser128(N)----N(7)	2.51 Å	-0.902	Sp2 donor	Sp2 Acceptor
Arbidol	Ser128(N)----O(3)	3.24 Å	-0.531	Sp2 donor	Sp3 Acceptor
	Ala129(N)----O(3)	3.27 Å	-1.005	Sp2 donor	Sp3 Acceptor
Chloroquine	Ala154(O)----N(2)	2.57 Å	-2.255	Sp2 Acceptor	Sp2 donor
Hydroxychloroquine	Ala129(O)----N(3)	3.09 Å	-1.371	Sp2 Acceptor	Sp2 Donor
	IIe23(N)----O(1)	3.08 Å	-2.206	Sp2 donor	Sp3 both

	Ala21(O)----O(1)	3.23 Å	-1.842	Sp2 Acceptor	Sp3 both
	IIe23(N)----O(5)	2.83 Å	-2.5	Sp2 donor	Sp2 Acceptor
	Leu126(O)---O(2)	3.27 Å	-1.669	Sp2 Acceptor	Sp3 both
	Leu126(O)---O(2)	2.82 Å	-1.663	Sp2 donor	Sp3 both
	Ser128(N)----O(4)	3.30 Å	-1.416	Sp2 donor	Sp3 both
	Ser128(N)----O(3)	3.01 Å	-0.143	Sp2 donor	Sp2 Acceptor
Dexamethasone	Ala129(N)---O(3)	2.78 Å	-1.902	Sp2 donor	Sp2 Acceptor
	Ala129(N)---N(5)	3.13 Å	-2.338	Sp2 Acceptor	Sp2 donor
	Gly47(O)----N(3)	3.06 Å	-0.888	Sp2 Acceptor	Sp2 donor
Favipiravir	Val49(N)----O(1)	2.82 Å	-2.492	Sp2 donor	Sp2 Acceptor

Table S4.9: Ligand- receptor interactions of Terrestrol A (**10**) and the standards at the probable active site of the target with PDB ID: 6LZG.

Ligand	Interaction(P---L)	Interaction distance	Interaction Energy	Hybridization protein	Hybridization ligand
	Asp428(OD1)---O(6)	3.03 Å	-2.5	Sp3 Acceptor	Sp3 Both
	Glu516(OE1)---O(23)	2.89 Å	-2.5	Sp2 Acceptor	Sp3 Both
	Pro463(O)----O(25)	3.58 Å	-0.108	Sp2 Acceptor	Sp3 Both
	Arg355(NH1)---O(24)	2.88 Å	-2.5	Sp2 Donor	Sp3 Both
	Arg355(NH1)---O(22)	3.07 Å	-2.5	Sp2 Donor	Sp3 Both
	Arg355(NH2)---O(22)	2.63 Å	-0.558	Sp2 Donor	Sp3 Both
	Ser514(OG)---O(22)	3.42 Å	-0.877	Sp3 Both	Sp3 Both
	Ser514(OG)---O(7)	3.08 Å	-2.5	Sp3 Both	Sp3 Both
	Phe515(N)----O(7)	3.03 Å	-1.25	Sp2 Donor	Sp3 Both
	Phe515(O)----O(7)	3.38 Å	-0.521	Sp2 Acceptor	Sp3 Both
Terrestrol A(10)	Thr430(O)----O(7)	2.80 Å	-2.5	Sp2 Acceptor	Sp3 Both
Ribavirin	Glu516(OE1)---N(8)	3.11 Å	-2.43	Sp2 Acceptor	Sp2 Donor

	Arg355(NH2)----O(4)	3.17 Å	-0.974	Sp2 Donor	Sp2 Acceptor
	Arg355(NH1)----O(4)	2.70 Å	-2.5	Sp2 Donor	Sp2 Acceptor
	Asp428(O)----N(8)	2.96 Å	-2.5	Sp2 Acceptor	Sp2 Donor
	Asp428(O)----O(2)	3.36 Å	-0.44	Sp2 Acceptor	Sp3 Both
	Thr430(O)----O(1)	2.60 Å	-2.5	Sp2 Acceptor	Sp3 Both
	Thr430(N)----O(2)	3.21 Å	-1.52	Sp2 Donor	Sp3 Both
	Thr430(N)----O(1)	2.77 Å	-2.05	Sp2 Donor	Sp3 Both
Arbidol	Leu517(O)----O(2)	2.49 Å	-1.56	Sp2 Acceptor	Sp3 Both
	Asp428(OD2)----N(2)	2.89 Å	-2.5	Sp2 Acceptor	Sp2 Acceptor
	Glu516(OE1)----N(6)	2.62 Å	-2.5	Sp2 Acceptor	Sp2 Donor
	Ser514(OG)----O(1)	3.20 Å	-1.02	Sp3 Both	Sp2 Acceptor
	Arg355(NH2)----O(1)	2.58 Å	-0.98	Sp2 Donor	Sp2 Acceptor
	Ser514(OG)----O(0)	2.95 Å	-2.5	Sp3 Both	Sp3 Acceptor
Nafamostat	Arg355(NH1)----O(1)	3.29 Å	-1.57	Sp2 Donor	Sp2 Acceptor
	Arg355(NH1)-----N(2)	2.97 Å	-2.5	Sp3 Acceptor	Sp2 Donor
Hydroxychloroquine	Thr430(N)----N(4)	3.22 Å	-1.89	Sp2 Donor	Sp2 Acceptor
Chloroquine	Phe515(O)----N(2)	2.97 Å	-1.44	Sp2 Acceptor	Sp2 Donor
	Thr430(N)----O(5)	3.05 Å	-2	Sp2 Donor	Sp2 Acceptor
	Ser514(OG)----O(2)	3.42 Å	-0.61	Sp3 Both	Sp3 Both
Dexamethasone	Arg355(NH10----O(3)	2.62 Å	-2.5	Sp2 Donor	Sp2 Acceptor
	Ser514(OG)----N(4)	2.81 Å	-2.5	Sp3 Both	Sp2 Acceptor
	Ser514(OG)----N(5)	2.89 Å	-1.7	Sp3 Both	Sp2 Donor
	Thr430(O)----N(5)	2.56 Å	-2.17	Sp2 Acceptor	Sp2 Donor
Favipiravir	Thr430(N)----O(2)	3.43 Å	-0.84	Sp2 Donor	Sp2 Acceptor

Table S4.10: Ligand- receptor interactions of Terrestrol A (**10**) and the standards at the probable active site of the target with PDB ID: 7CR5.

Ligand	Interaction(P----L)	Interaction distance	Interaction Energy	Hybridization protein	Hybridization ligand
Terrestrol A(10)	Glu136(OE2)----O(24)	3.53 Å	-0.34	Sp3 Acceptor	Sp3 Both
	Gly137(N)----O(24)	3.25 Å	-1.04	Sp2 Donor	Sp3 Both
	Ala138(O)----O(25)	3.51 Å	-0.43	Sp2 Acceptor	Sp3 Both
	Asn140(ND2)----O(25)	2.63 Å	-1.66	Sp2 Donor	Sp3 Both
	Tyr123(OH)----O(23)	3.07 Å	-2.5	Sp3 Both	Sp3 Both
	Glu136(N)----O(22)	3.01 Å	-0.11	Sp2 Donor	Sp3 Both
	Ala134(O)----O(22)	3.36 Å	-1.22	Sp2 Acceptor	Sp3 Both
	Gln70(O)----O(6)	2.53 Å	-1.88	Sp2 Acceptor	Sp3 Both
	Gln70(N)----O(6)	3.08 Å	-0.06	Sp2 Donor	Sp3 Both
	Ala134(N)----O(6)	2.69 Å	-2.12	Sp2 Donor	Sp3 Both
	Ala134(O)----O(6)	2.83 Å	-2.5	Sp2 Acceptor	Sp3 Both
Nafamostat	Glu136(OE2)----N(5)	3.05 Å	-2.5	Sp3 Acceptor	Sp2 Donor
	Glu136(OE1)----N(6)	3.01 Å	-0.25	Sp2 Acceptor	Sp2 Donor
	Phe66(O)----N(3)	3.20 Å	-0.534	Sp2 Acceptor	Sp2 Donor
	Gly137(N)----N(4)	3.39 Å	-0.98	Sp2 Donor	Sp2 Donor
	Leu64(O)----N(2)	3.56 Å	-0.2	Sp2 Acceptor	Sp2 Donor
	Gly69(N)----O(1)	3.06 Å	-0.17	Sp2 Donor	Sp2 Acceptor
	Ala134(N)----O(0)	3.09 Å	-0.935	Sp2 Donor	Sp3 Acceptor
	Tyr123(OH)----O(0)	3.10 Å	-2.4	Sp3 Both	Sp3 Acceptor
Hydroxychloroquine	Ala134(O)----N(3)	2.73 Å	-1.98	Sp2 Acceptor	Sp3 Donor
	Phe66(N)----O(1)	3.05 Å	-2.02	Sp2 Donor	Sp3 Both
Arbidol	Arg68(NE)----O(3)	2.72 Å	-2.06	Sp2 Donor	Sp3 Acceptor
	Arg68(NH2)----O(3)	3.31 Å	-0.77	Sp2 Donor	Sp3 Acceptor
	Tyr123(OH)----N(5)	3.28 Å	-1.61	Sp3 Both	Sp2 Acceptor
Chloroquine	Tyr123(OH)----N(2)	2.98 Å	-2.4	Sp3 Both	Sp2 Donor
Ribavirin	Glu136(OE1)----N(8)	2.82 Å	-2.5	Sp2 Acceptor	Sp2 Donor

	Glu136(N)----O(4)	3.01 Å	-0.74	Sp2 Donor	Sp2 Acceptor
	Phe66(O)----O(3)	3.22 Å	-1.88	Sp2 Acceptor	Sp3 Both
	Pro67(O)----O(3)	2.80 Å	-2.5	Sp2 Acceptor	Sp3 Both
	Gln70(O)----O(3)	3.06 Å	-2.5	Sp2 Acceptor	Sp3 Both
	Tyr123(OH)----O(2)	2.75 Å	-2.5	Sp3 Both	Sp3 Both
	Trp132(O)----O(2)	2.82 Å	-2.5	Sp2 Acceptor	Sp3 Both
	Arg68(NE)----N(6)	2.99 Å	-1.16	Sp2 Donor	Sp2 Acceptor
	Arg68(NE)----N(5)	3.27 Å	-0.23	Sp2 Donor	Sp2 Acceptor
	Gly69(N)----O(0)	2.59 Å	-2.4	Sp2 Donor	Sp3 Acceptor
	Gly69(N)----N(5)	3.24 Å	-0.93	Sp2 Donor	Sp2 Acceptor
	Gly69(N)----N(6)	2.85 Å	-0.14	Sp2 Donor	Sp2 Acceptor
	Arg68(NH1)----O(4)	3.02 Å	-2.5	Sp2 Donor	Sp3 Both
	Gly69(N)----O(3)	2.88 Å	-2.35	Sp2 Donor	Sp2 Acceptor
	Ala134(N)----O(1)	3.29 Å	-0.381	Sp2 Donor	Sp3 Both
	Trp132(O)----O(1)	3.00 Å	-2.5	Sp2 Acceptor	Sp3 Both
Dexamethasone	Tyr123(OH)----O(1)	2.50 Å	-1.64	Sp3 Both	Sp3 Both
	Tyr123(OH)----N(5)	2.73 Å	-2.5	Sp3 Both	Sp2 Donor
	Ala134(N)----O(1)	2.85 Å	-2.5	Sp2 Donor	Sp2 Acceptor
	Gln70(O)----N(3)	2.59 Å	-2.4	Sp2 Acceptor	Sp2 Donor
Favipiravir	Gln70(N)----O(1)	3.17 Å	-0.08	Sp2 Donor	Sp2 Acceptor

Table S4.11: Ligand- receptor interactions of Terrestrol A (**10**) and the standards at the probable active site of the target with PDB ID: 4K90

Ligand	**Interaction(P----L)**	**Interaction distance**	**Interaction Energy**	**Hybridization protein**	**Hybridization ligand**
	His520(NE2)----O(22)	3.35 Å	-1.24	Sp2 Acceptor	Sp3 Both
	Glu430(OE2)----O(24)	3.05 Å	-2.5	Sp3 Acceptor	Sp3 Both
Terrestrol A(10)	Arg490(NH2)----O(7)	3.16 Å	-1.72	Sp2 Donor	Sp3 Both

	Arg490(NH1)---O(7)	3.15 Å	-1.79	Sp2 Donor	Sp3 Both
	Asp463(OD1)---O(25)	2.64 Å	-2.5	Sp3 Acceptor	Sp3 Both
	Asn392(ND2)---O(6)	3.13 Å	-2.15	Sp2 Donor	Sp3 Both
	Gly484(N)----O(27)	3.36 Å	-0.324	Sp2 Donor	Sp3 Acceptor
	Asn391(O)----O(6)	3.24 Å	-1.81	Sp2 Acceptor	Sp3 Both
	Asn391(O)----O(23)	3.05 Å	-2.5	Sp2 Acceptor	Sp3 Both
	Trp411(NE1)---O(23)	2.58 Å	-2.32	Sp2 Donor	Sp3 Both
Isavuconazole	Ala393(O)----O(3)	3.18 Å	-2.12	Sp2 Acceptor	Sp3 Both
	Glu430(OE2)---O(3)	1.87 Å	3.72	Sp3 Acceptor	Sp3 Both
Posaconazole	Glu413(OE2)---O(4)	3.01 Å	-1.83	Sp3 Acceptor	Sp3 Both
	Arg490(NH1)---N(11)	3.10 Å	-0.63	Sp2 Donor	Sp2 Acceptor
	Arg490(NH1)---N(13)	2.57 Å	-0.29	Sp2 Donor	Sp2 Acceptor
	Arg490(NH1)---N(12)	3.17 Å	-1.74	Sp2 Donor	Sp2 Acceptor
Amphotericin B	Arg407(NH2)---O(10)	2.80 Å	-0.59	Sp2 Donor	Sp3 Both
	Asn394(ND2)---O(10)	3.06 Å	-2.5	Sp2 Donor	Sp3 Both
	Tyr409(OH)---O(10)	2.59 Å	-2.43	Sp3 Both	Sp3 Both
	Asn394(ND2)---O(4)	3.27 Å	-1.63	Sp2 Donor	Sp3 Acceptor
	Asn391(O)----O(8)	3.47 Å	-0.62	Sp2 Acceptor	Sp3 Both
	Asn392(ND2)---O(8)	3.31 Å	-1.44	Sp2 Donor	Sp3 Both
	Asn392(ND2)---O(5)	2.24 Å	0.5	Sp2 Donor	Sp3 Both
	Gly425(N)----O(14)	3.38 Å	-0.03	Sp2 Donor	Sp3 Acceptor
	Asn256(ND2)---O(14)	3.03 Å	-2.5	Sp2 Donor	Sp3 Acceptor
	lle426(N)----O(16)	2.01 Å	2.53	Sp2 Donor	Sp2 Acceptor
	Arg470(NH1)---O(15)	2.46 Å	-1.33	Sp2 Donor	Sp3 Both
	Thr482(O)----O(15)	1.22 Å	9.41	Sp2 Acceptor	Sp3 Both

Table S4.12: Ligand- receptor interactions of Terrestrol A (**10**) and the standards at the probable active site of the target with PDB ID: 6VSI

Ligand	Interaction(P----L)	Interaction distance	Interaction Energy	Hybridization protein	Hybridization ligand
Terrestrol A(10)	His58(O)----O(24)	3.20 Å	-1.99	Sp2 Acceptor	Sp3 Both
	Asp41(OD2)----O(23)	2.62 Å	-2.5	Sp2 Acceptor	Sp3 Both
	Tyr30(OH)----O(23)	3.18 Å	-2.08	Sp3 Both	Sp3 Both
Posaconazole	Tyr86(OH)----N(9)	3.39 Å	-1.04	Sp3 Both	Sp3 Acceptor
	Asp41(OD2)----N(9)	3.17 Å	-2.13	Sp3 Acceptor	Sp3 Acceptor
	Phe40(O)----O(4)	3.10 Å	-2.5	Sp2 Acceptor	Sp3 Both
Amphotericin B	Ala85(O)----O(13)	3.54 Å	-0.3	Sp2 Acceptor	Sp3 Both
	Tyr86(OH)----O(12)	2.62 Å	-2.5	Sp3 Both	Sp3 Both
	Phe40(O)----O(9)	2.75 Å	-2.5	Sp2 Acceptor	Sp3 Both
	Asp45(OD2)----O(10)	3.28 Å	-1.62	Sp2 Acceptor	Sp3 Both
	Asp41(OD2)----O(8)	3.16 Å	-2.18	Sp2 Acceptor	Sp3 Both
	Asp41(OD2)----O(5)	3.05 Å	-2.5	Sp2 Acceptor	Sp3 Both
	Tyr30(OH)----O(8)	3.43 Å	-0.82	Sp3 Both	Sp3 Both
	Tyr30(OH)----O(5)	3.29 Å	-1.56	Sp3 Both	Sp3 Both
	Arg46(NH1)----O(0)	2.66 Å	-2.5	Sp2 Donor	Sp3 Acceptor
	Arg46(NH1)----O(4)	3.04 Å	-2.5	Sp2 Donor	Sp3 Acceptor
	Ser42(N)----O(10)	2.94 Å	0	Sp2 Donor	Sp3 Both
	Ser42(N)----O(4)	2.97 Å	-2.5	Sp2 Donor	Sp3 Acceptor
	Gly57(O)----O(15)	2.60 Å	-2.46	Sp2 Acceptor	Sp3 Both
Isavuconazole	Tyr86(OH)----N(5)	3.20 Å	-1.98	Sp3 Both	Sp2 Acceptor
	Asp41(OD2)----O(3)	2.71 Å	-2.5	Sp2 Acceptor	Sp3 Both
	Tyr30(OH)----O(3)	2.90 Å	-2.5	Sp3 Both	Sp3 Both

	Tyr30(OH)----N(4)	3.06 Å	-2.5	Sp3 Both	Sp2 Acceptor
	Tyr30(OH)----N(6)	2.40 Å	-0.83	Sp3 Both	Sp2 Acceptor
	Arg46(NH2)----N(6)	3.22 Å	-0.73	Sp2 Donor	Sp2 Acceptor

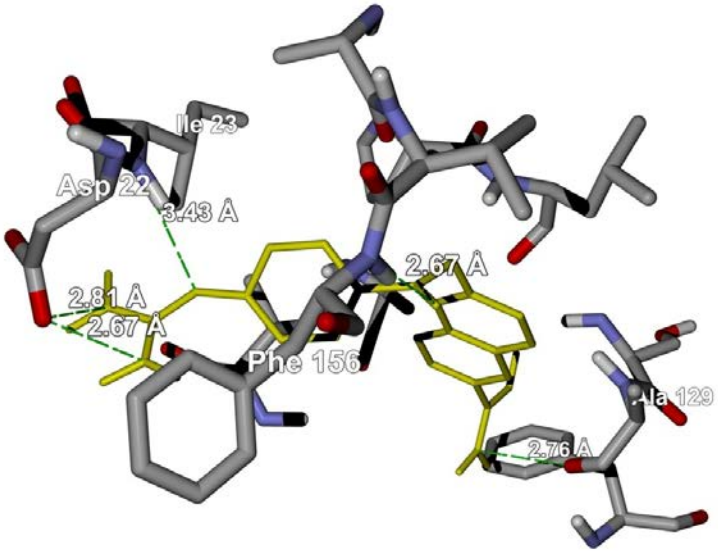

A

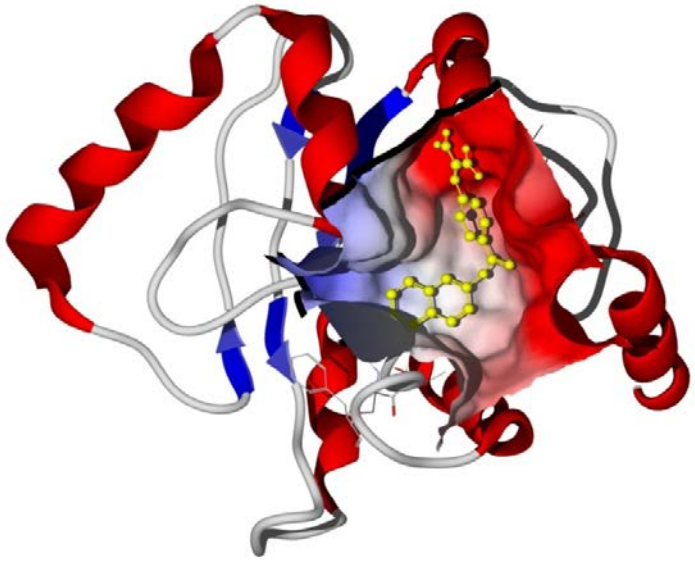

B

Figure S.4.2: Visualisation and illustration of **A).** Nafamostat positioned at the active site of the target Non-structural protein 3 (PDB ID: 6VXS) exhibiting potential modes of interaction (The green dotted lines depicts the mode of interaction between the target and the ligand, accompanied by distance annotations, while the yellow-coloured structure represents the ligand itself) **B).** Within the probable active pocket of target.

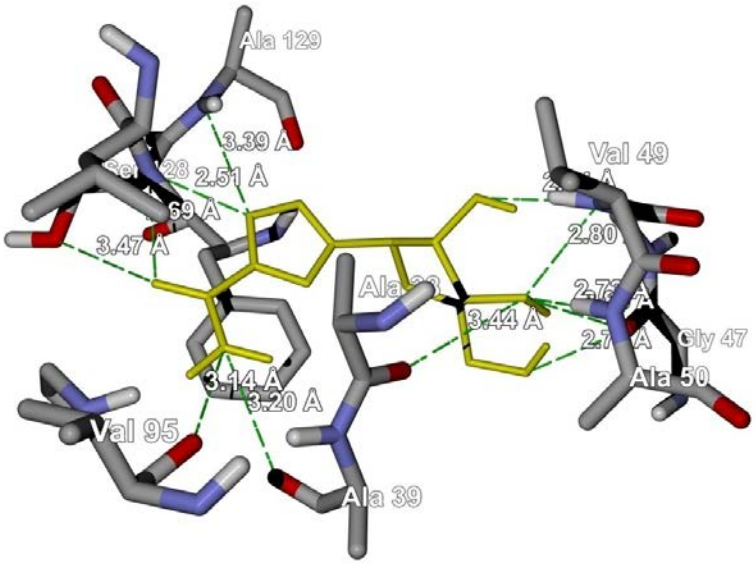

A

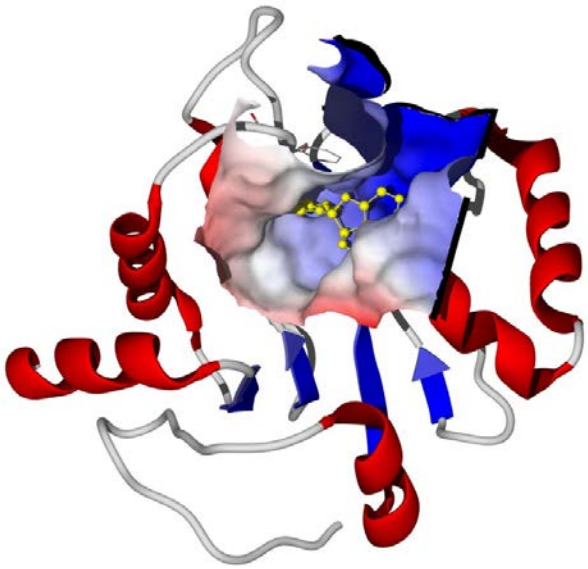

B

Figure S4.3: Visualisation and illustration of **A).** Ribavirin, positioned at the probable site of the target Non-structural protein 3 (PDB ID: 6VXS) exhibiting potential modes of interaction (The green dotted lines depict the mode of interaction between the target and the ligand, accompanied by distance annotations, while the yellow-coloured structure represents the ligand itself) **B).** Within the probable active pocket of target.

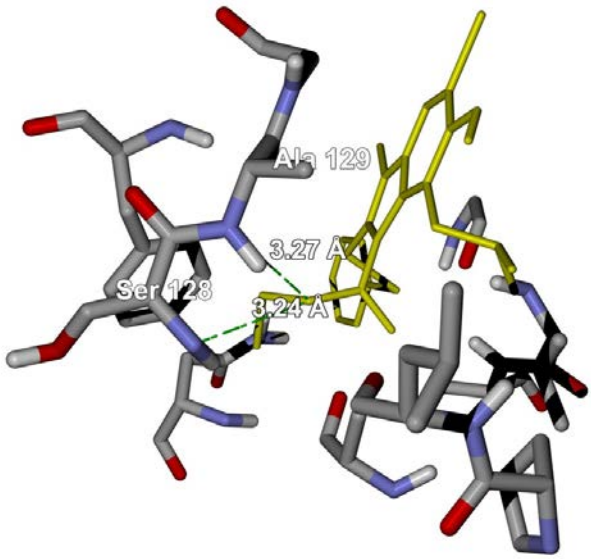

A

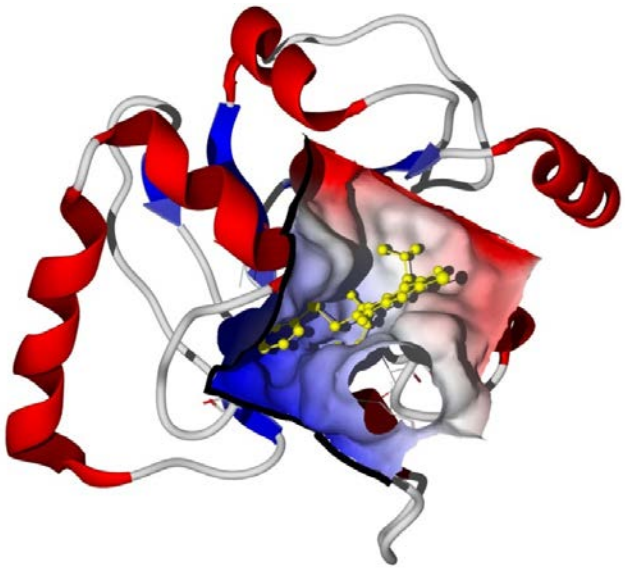

B

Figure S4.4: Visaulisation and illustration of **A).** Arbidol, positioned at the active site of the target Non-structural protein 3 (PDB ID: 6VXS) exhibiting potential modes of interaction (The green dotted lines depict the mode of interaction between the target and the ligand, accompanied by distance annotations, while the yellow-coloured structure represents the ligand itself) B**).** Within the probable active pocket of target.

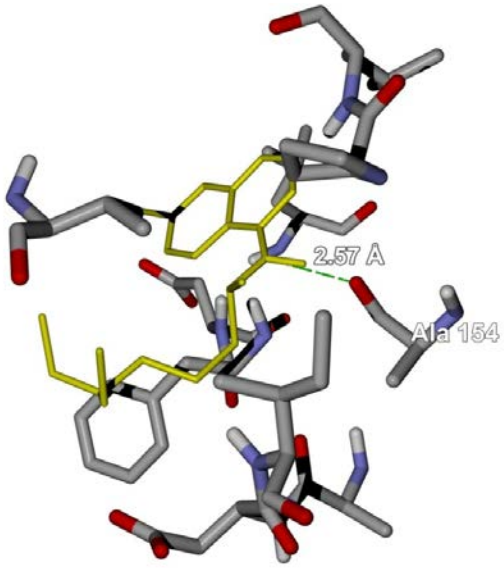

A

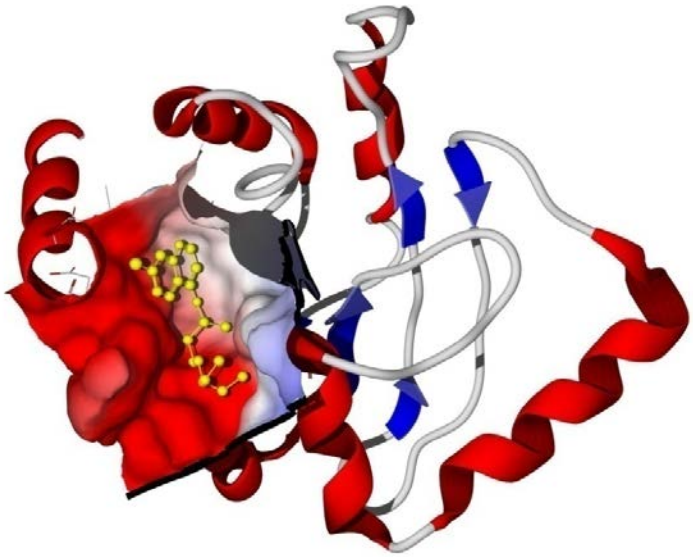

B

Figure S4.5: Visualisation and illustration of **A).** Chloroquine positioned at the active site of the target Non-structural protein 3 (PDB ID: 6VXS) exhibiting potential modes of interaction (The green dotted lines depicts the mode of interaction between the target and the ligand, accompanied by distance annotations, while the yellow-coloured structure represents the ligand itself) **B).** Within the probable active pocket of target.

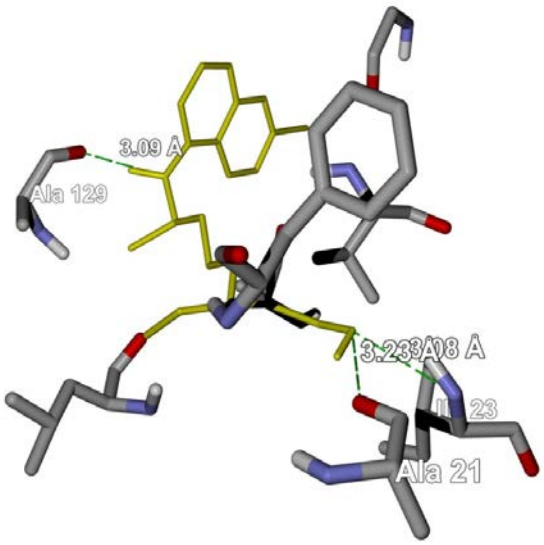

A

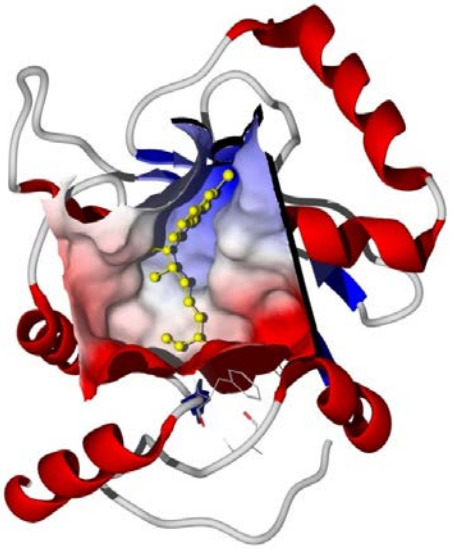

B

Figure 4.6: Visualisation and illustration of **A).** Hydroxychloroquine positioned at the active site of the target Non-structural protein 3 (PDB ID: 6VXS) exhibiting potential modes of interaction (The green dotted lines depict the mode of interaction between the target and the ligand, accompanied by distance annotations, while the yellow-coloured structure represents the ligand itself) **B).** Within the probable active pocket of target.

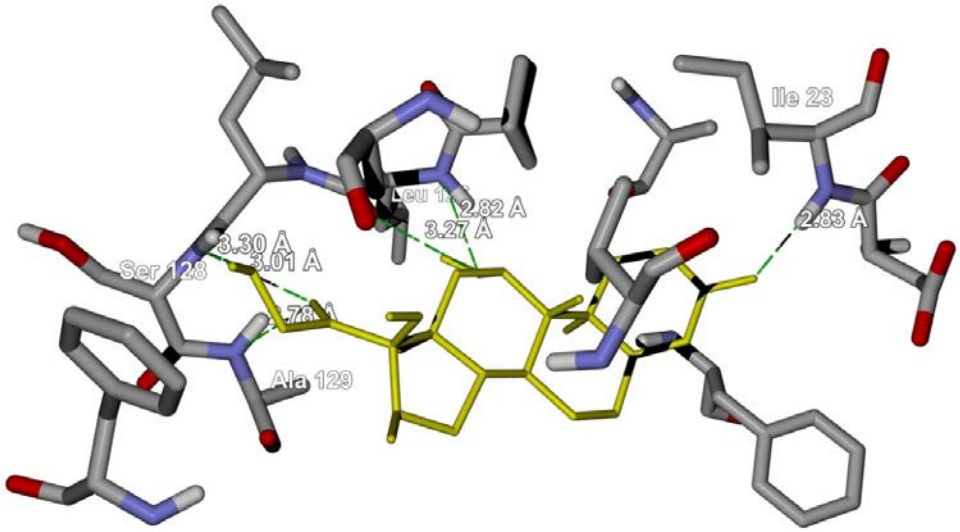

A

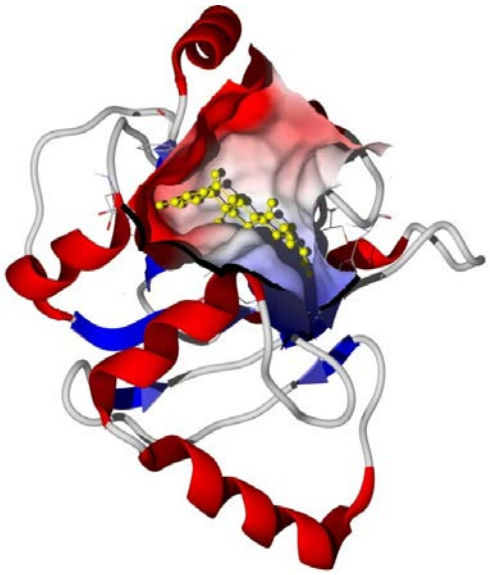

B

Figure 4.7: Visualisation and illustration of **A).** Dexamethasone positioned at the active site of the target Non-structural protein 3 (PDB ID: 6VXS) exhibiting potential modes of interaction (The green dotted lines depicts the mode of interaction between the target and the ligand, accompanied by distance annotations, while the yellow-coloured structure represents the ligand itself) B**).** Within the probable active pocket of target.

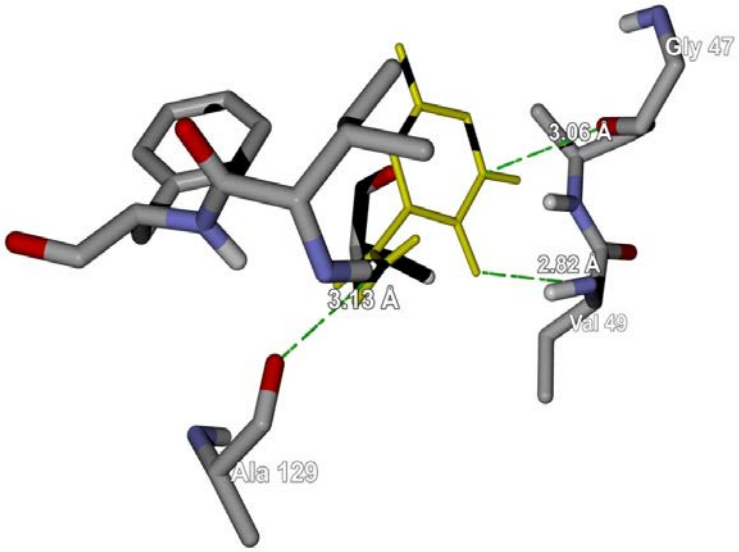

A

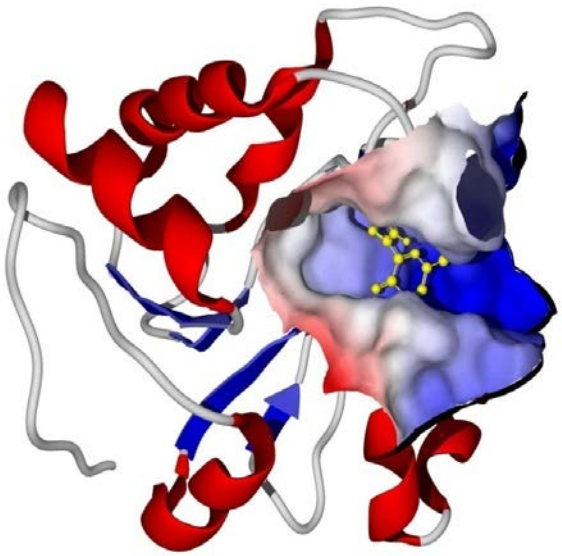

B

Figure 4.8: Visualisation and illustration of **A).** Favipiravir positioned at the active site of the target Non-structural protein 3 (PDB ID: 6VXS) exhibiting potential modes of interaction (The green dotted lines depicts the mode of interaction between the target and the ligand, accompanied by distance annotations, while the yellow-coloured structure represents the ligand itself) B**).** Within the probable active pocket of target.

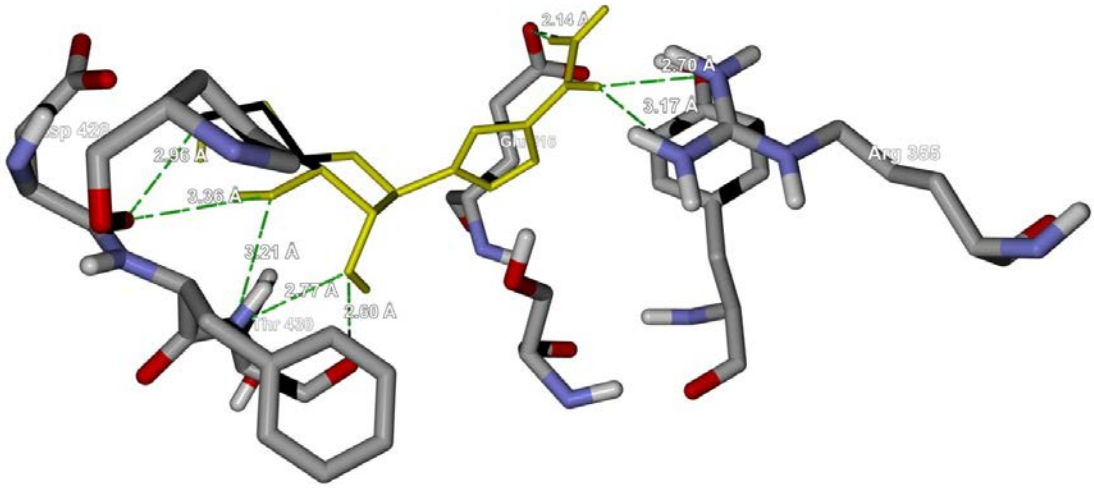

A

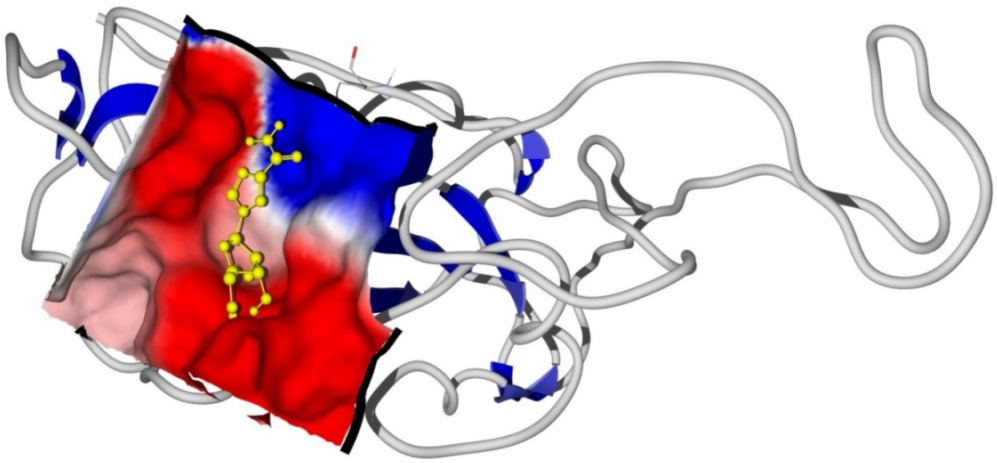

B

Figure S4.10: Visualisation and illustration of **A).** Ribavirin positioned at the active site of the target Spike protein S1 (PDB ID: 6LZG) exhibiting potential modes of interaction (The green dotted lines depicts the mode of interaction between the target and the ligand, accompanied by distance annotations, while the yellow-coloured structure represents the ligand itself) B**).** Within the probable active pocket of target.

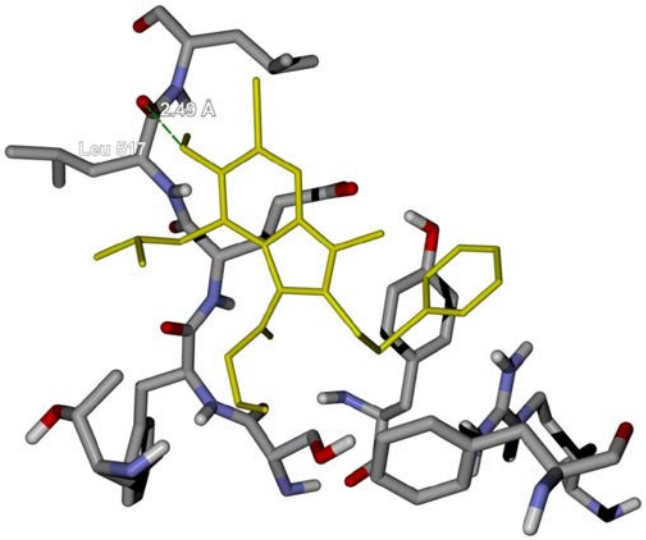

A

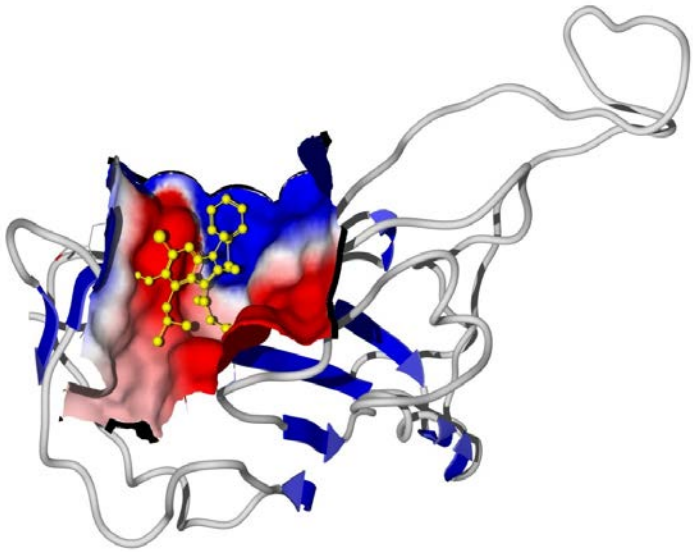

B

Figure S4.11: Visualisation and illustration of **A).** Arbidol positioned at the active site of the target Spike protein S1 (PDB ID: 6LZG) exhibiting potential modes of interaction (The green dotted lines depict the mode of interaction between the target and the ligand, accompanied by distance annotations, while the yellow-coloured structure represents the ligand itself) **B).** Within the probable active pocket of target.

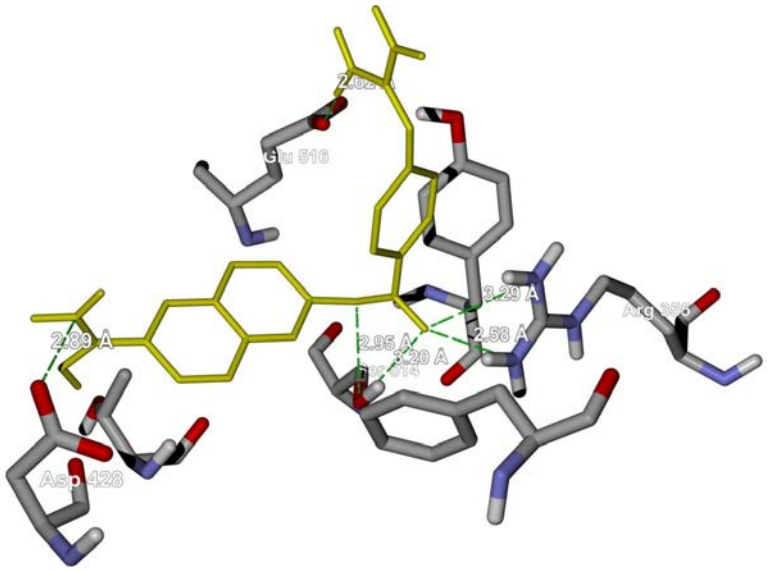

A

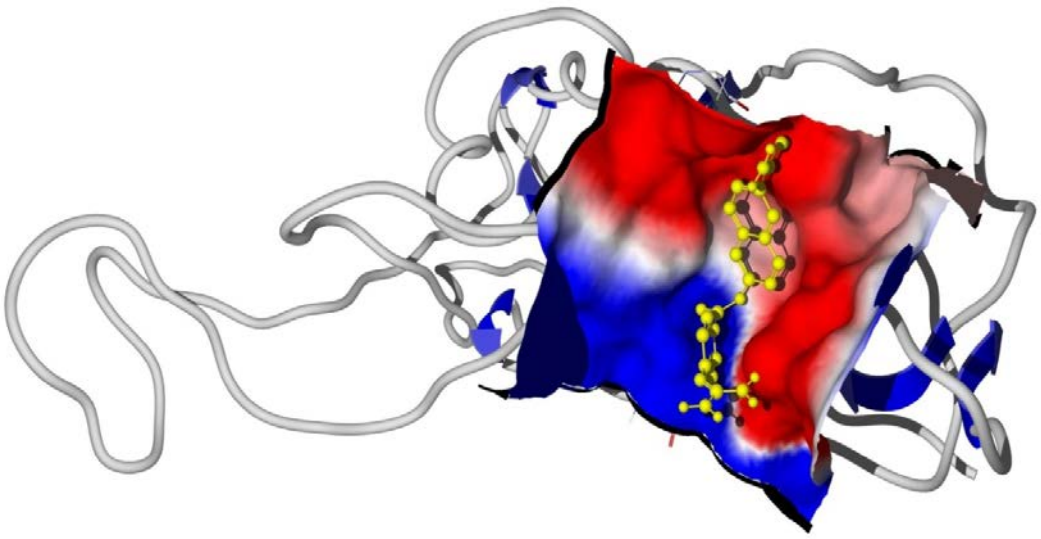

B

Figure S4.12: Visualisation and illustration of **A).** Nafamostat positioned at the active site of the target Spike protein S1 (PDB ID: 6LZG) exhibiting potential modes of interaction (The green dotted lines depict the mode of interaction between the target and the ligand, accompanied by distance annotations, while the yellow-coloured structure represents the ligand itself) **B).** Within the probable active pocket of target.

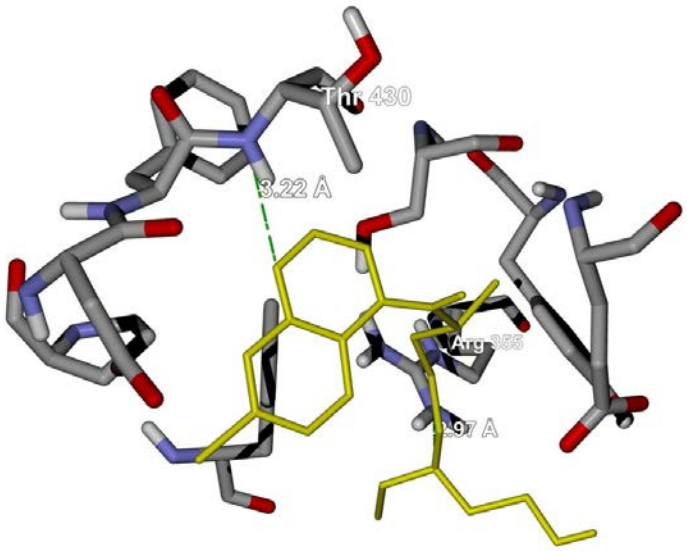

A

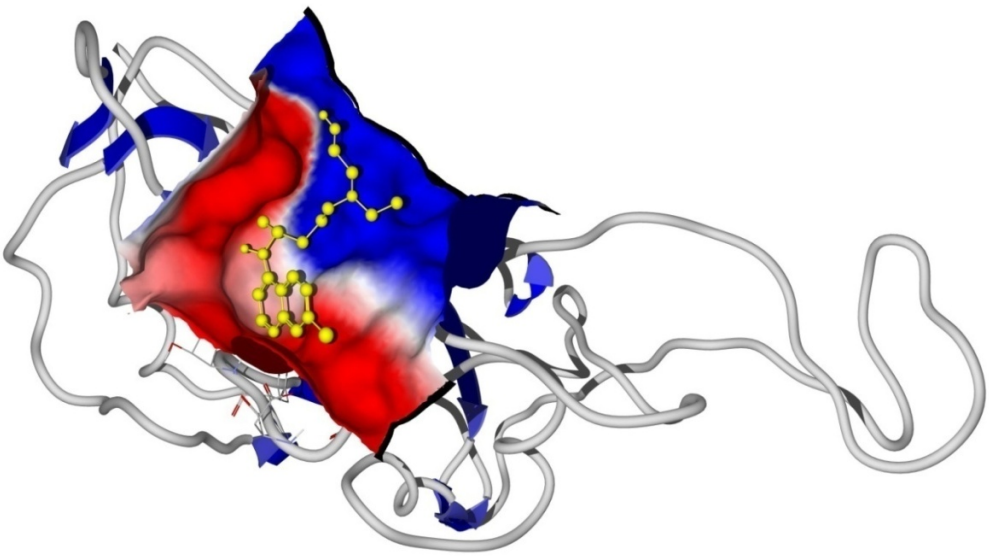

B

Figure S4.13: Visualisation and illustration of **A).** Hydroxychloroquine positioned at the active site of the protein Spike protein S1 (PDB ID: 6LZG) exhibiting potential modes of interaction (The green dotted lines depicts the mode of interaction between the target and the ligand, accompanied by distance annotations, while the yellow-coloured structure represents the ligand itself) **B).** Within the probable active pocket of target.

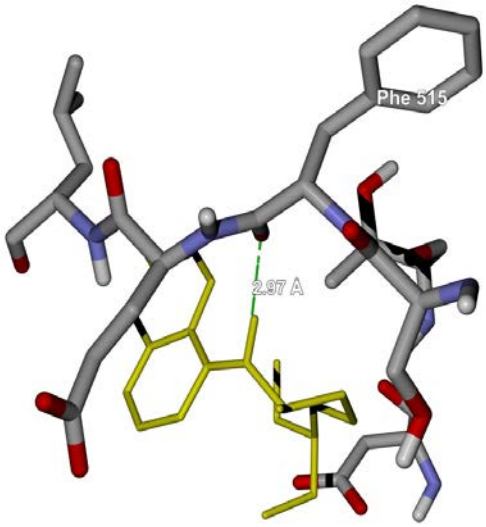

A

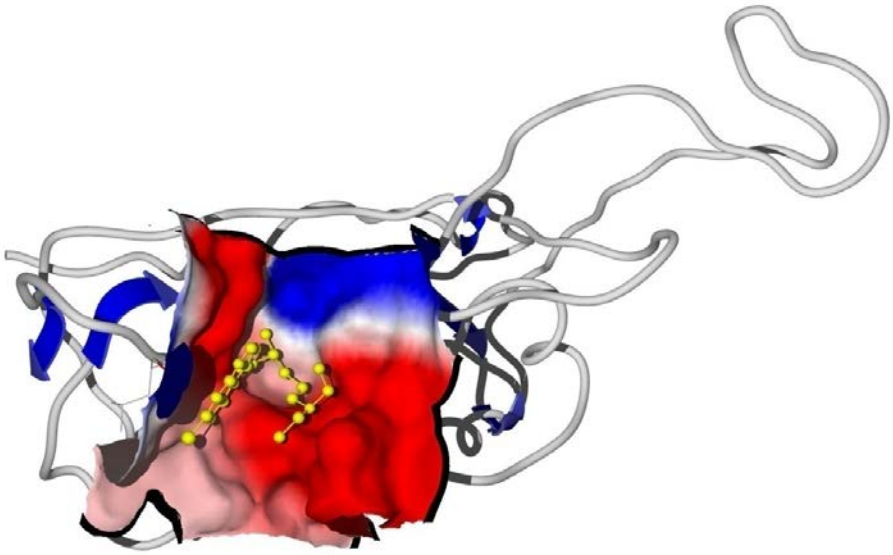

B

Figure S4.14: Visualisation and illustration of **A).** Chloroquine positioned at the active site of the target Spike protein S1 (PDB ID: 6LZG) exhibiting potential modes of interaction (The green dotted lines depicts the mode of interaction between the target and the ligand, accompanied by distance annotations, while the yellow-coloured structure represents the ligand itself) **B).** Within the probable active pocket of target.

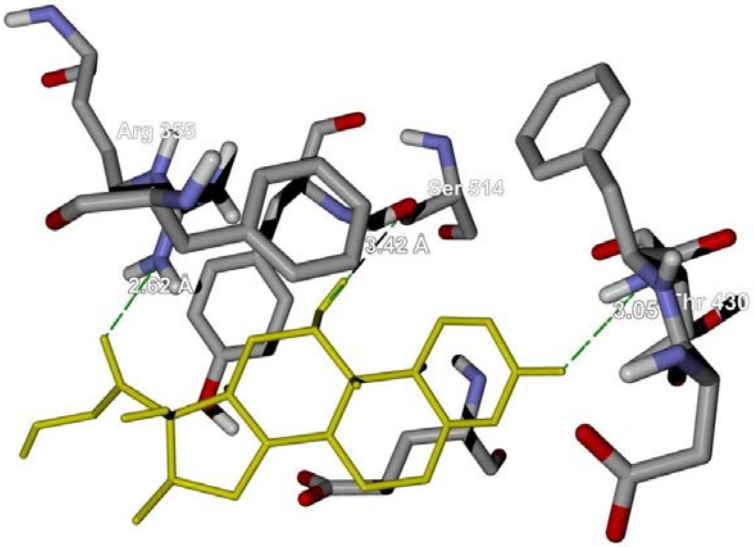

A

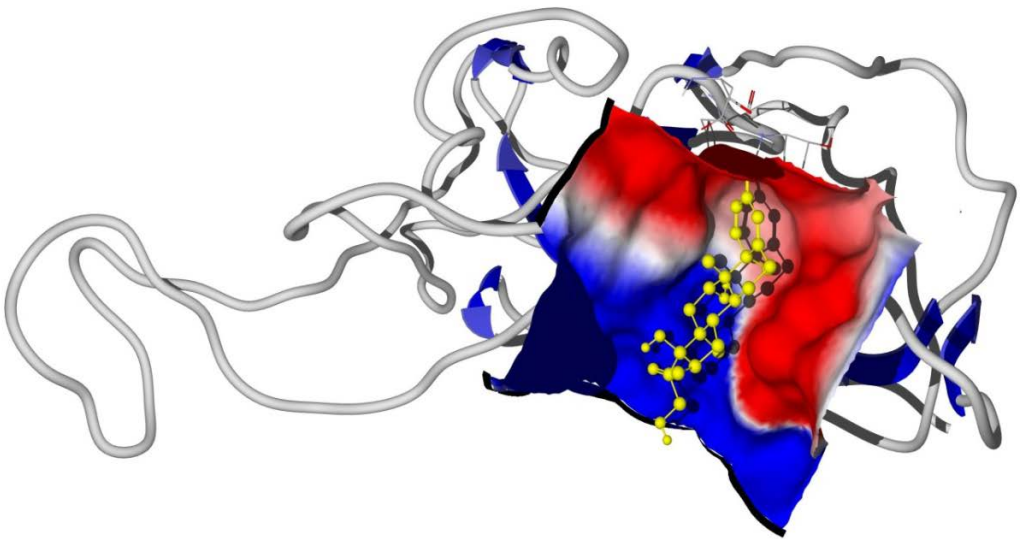

B

Figure S4.15: Visualisation and illustration of **A).** Dexamethasone positioned at the active site of the target Spike protein S1 (PDB ID: 6LZG) exhibiting potential modes of interaction (The green dotted lines depicts the mode of interaction between the target and the ligand, accompanied by distance annotations, while the yellow-coloured structure represents the ligand itself) B**).** Within the probable active pocket of target.

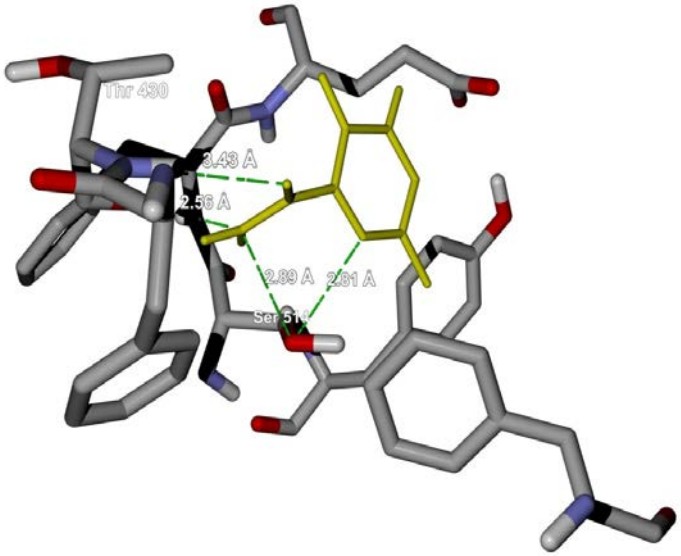

A

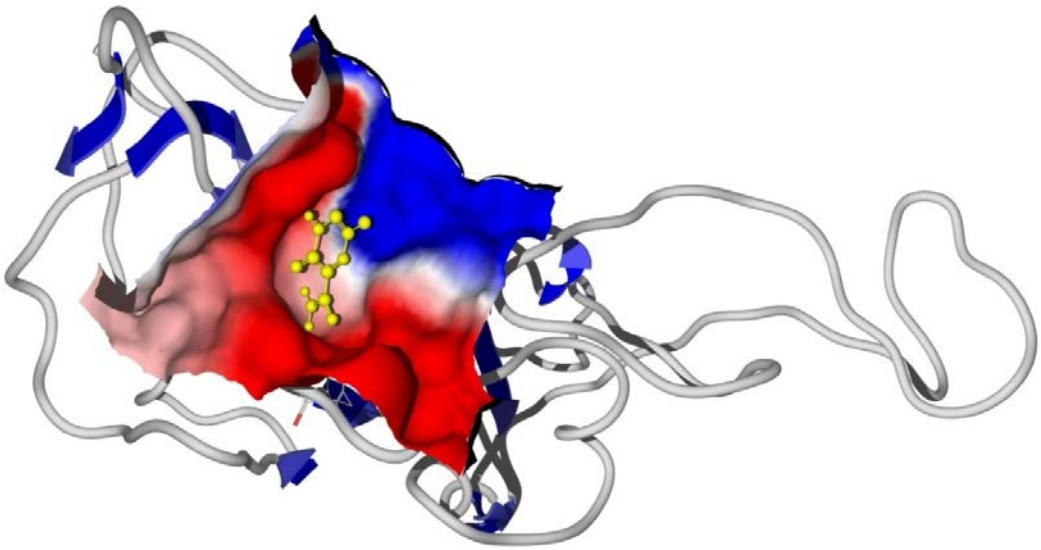

B

Figure S4.16: Visualisation and illustration of **A).** Favipiravir positioned at the active site of the target Spike protein S1 (PDB ID: 6LZG) exhibiting potential modes of interaction (The green dotted lines depicts the mode of interaction between the target and the ligand, accompanied by distance annotations, while the yellow-coloured structure represents the ligand itself) **B).** Within the probable active pocket of target.

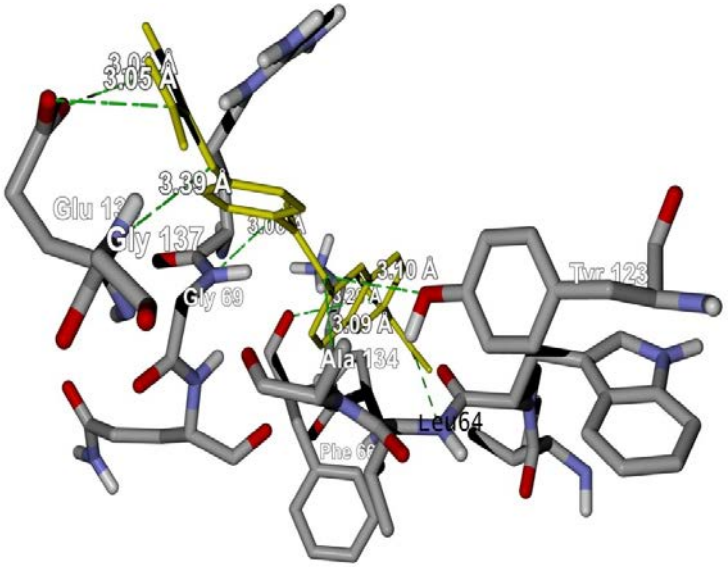

A

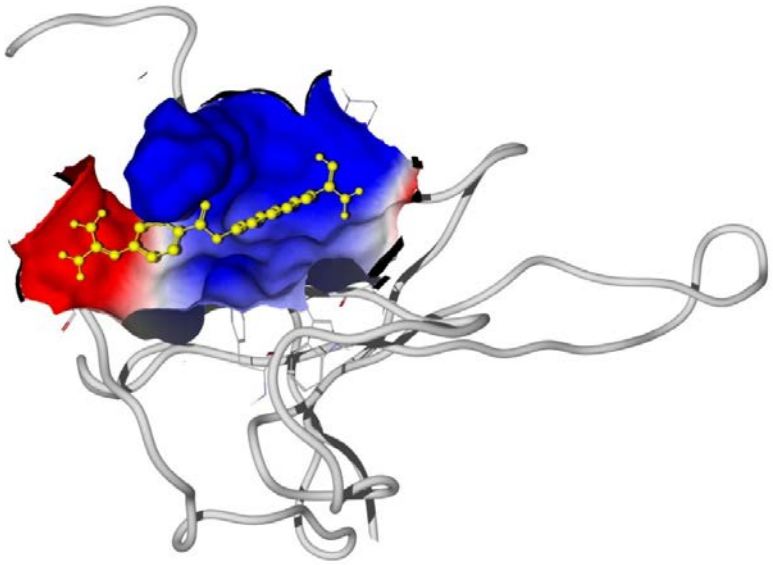

B

Figure S4.18: Visualisation and illustration of **A).** Nafamostat positioned at the active site of the target Nucleoprotein (PDB ID: 7CR5) exhibiting potential modes of interaction (The green dotted lines depict the mode of interaction between the target and the ligand, accompanied by distance annotations, while the yellow-coloured structure represents the ligand itself) **B).** Within the probable active pocket of target.

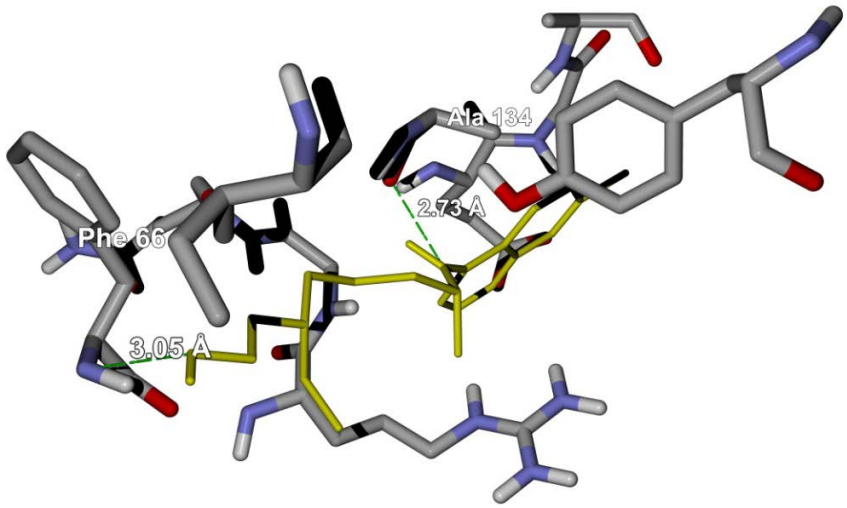

A

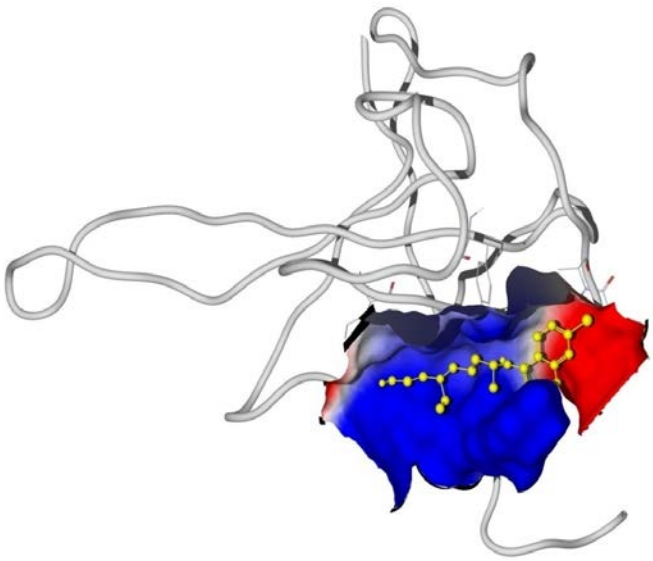

B

Figure S4.19: Visualisation and illustration of **A).** Hydroxychloroquine positioned at the active site of the target Nucleoprotein (PDB ID: 7CR5) exhibiting potential modes of interaction (The green dotted lines depicts the mode of interaction between the target and the ligand, accompanied by distance annotations, while the yellow-coloured structure represents the ligand itself) **B).** Within the probable active pocket of target.

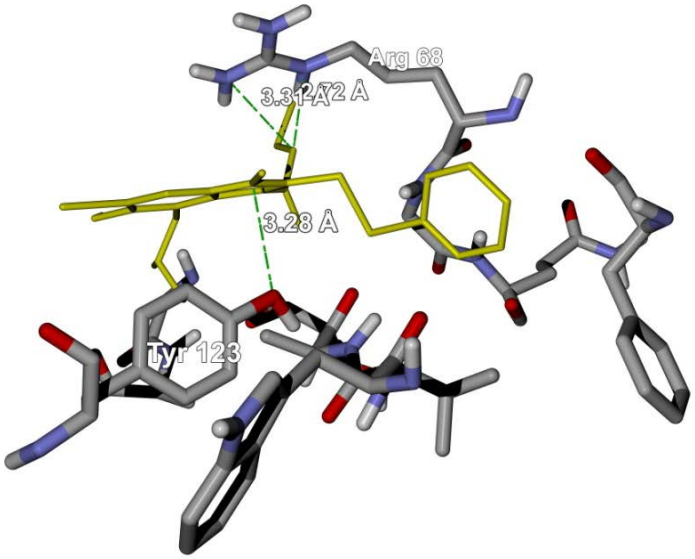

A

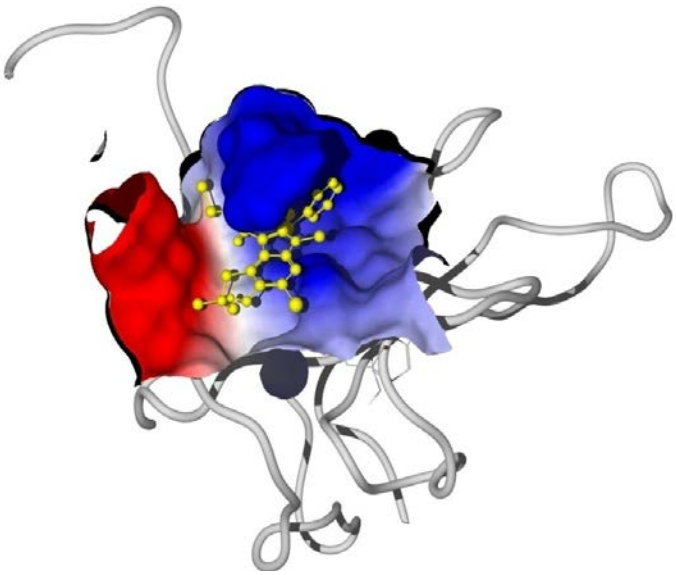

B

Figure S4.20: Visualisation and illustration of **A).** Arbidol positioned at the active site of the target Nucleoprotein (PDB ID: 7CR5) exhibiting potential modes of interaction (The green dotted lines depict the mode of interaction between the target and the ligand, accompanied by distance annotations, while the yellow-coloured structure represents the ligand itself) **B).** Within the probable active pocket of target.

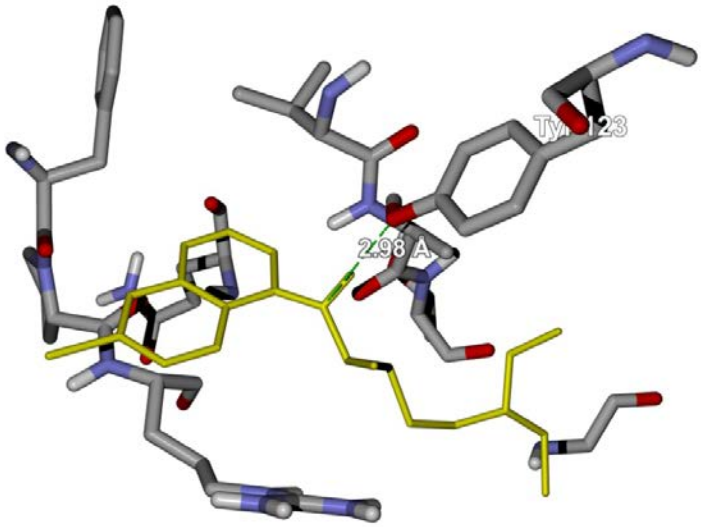

A

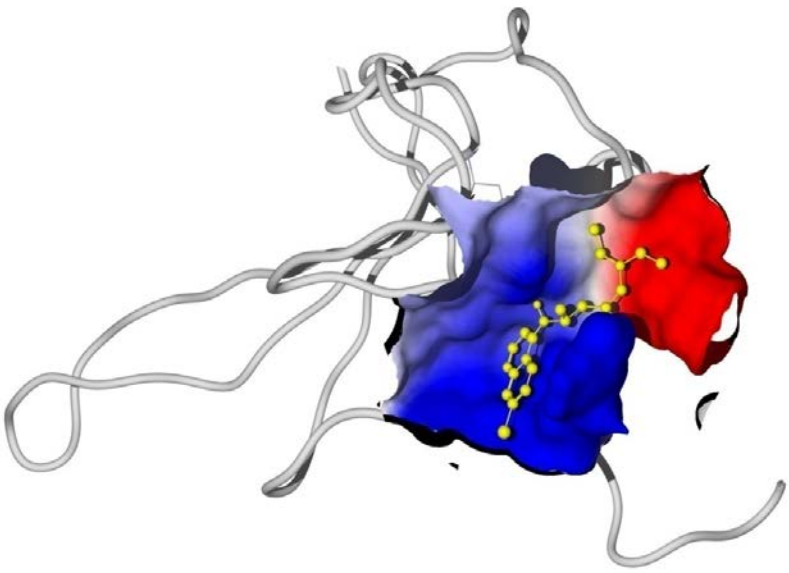

B

FigureS4. 21: Visualisation and illustration of **A).** Chlororquine positioned at the active site of the target Nucleoprotein (PDB ID: 7CR5) exhibiting potential modes of interaction (The green dotted lines depict the mode of interaction between the target and the ligand, accompanied by distance annotations, while the yellow-coloured structure represents the ligand itself) **B)**. Within the probable active pocket of target.

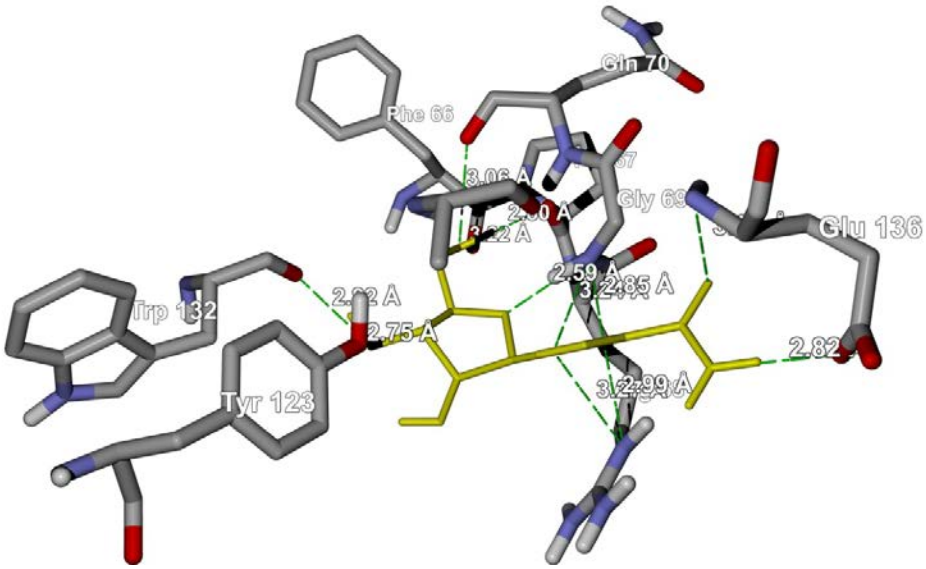

A

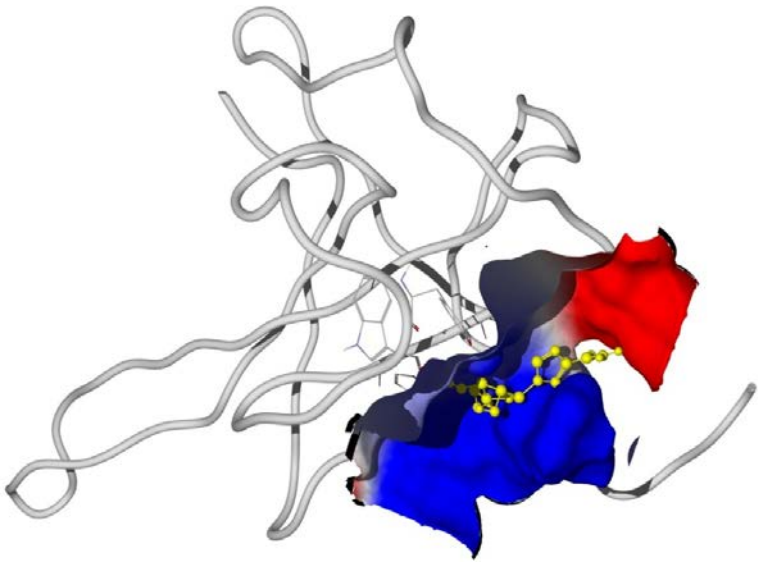

B

Figure S4.22: Visualisation and illustration of **A)**. Ribavirin positioned at the active site of the target Nucleoprotein (PDB ID: 7CR5) exhibiting potential modes of interaction (The green dotted lines depicts the mode of interaction between the target and the ligand, accompanied by distance annotations, while the yellow-coloured structure represents the ligand itself) **B)**. Within the probable active pocket of target.

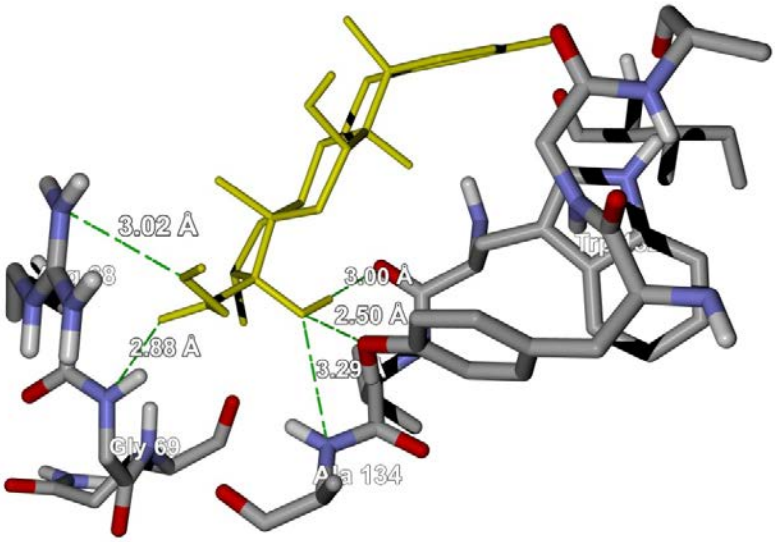

A

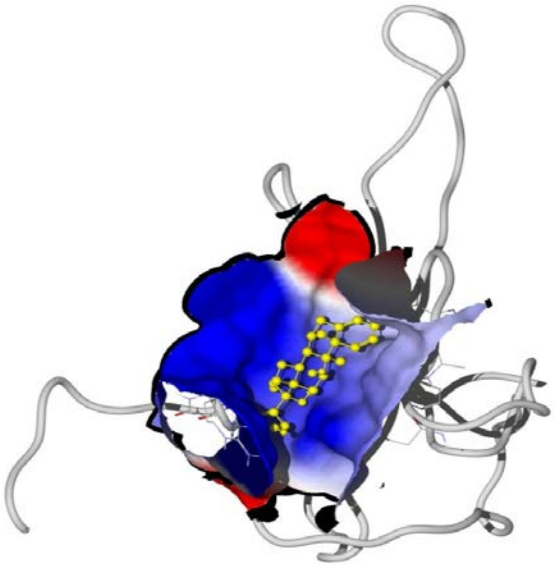

B

Figure S4.23: Visualisation and illustration of **A).** Dexamethasone positioned at the active site of the target Nucleoprotein (PDB ID: 7CR5) exhibiting potential modes of interaction (The green dotted lines depicts the mode of interaction between the target and the ligand, accompanied by distance annotations, while the yellow-coloured structure represents the ligand itself) **B).** Within the probable active pocket of target.

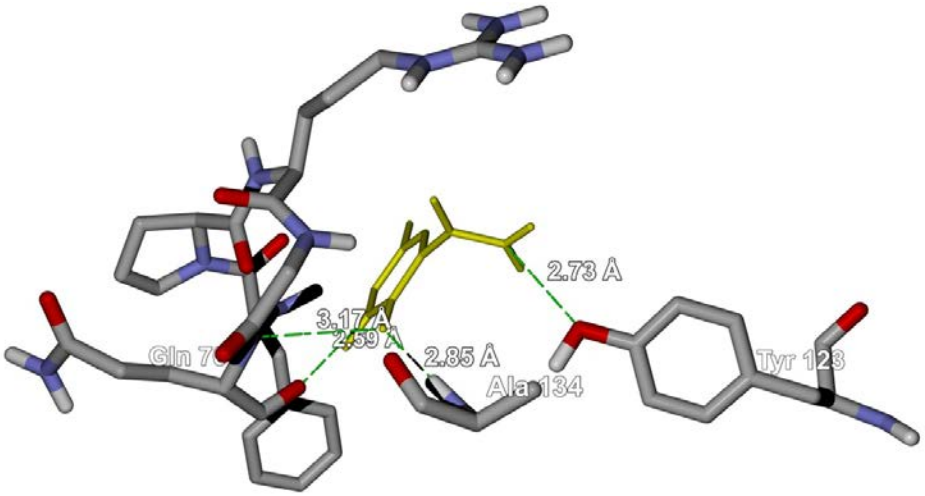

A

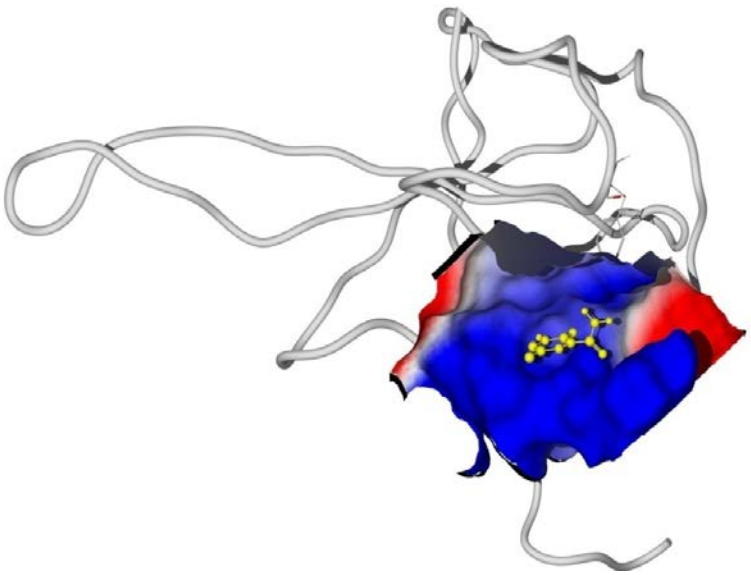

B

Figure S4.24: Visualisation and illustration of **A).** Favipiravir positioned at the active site of the target Nucleoprotein (PDB ID: 7CR5) exhibiting potential modes of interaction (The green dotted lines depicts the mode of interaction between the target and the ligand, accompanied by distance annotations, while the yellow-coloured structure represents the ligand itself) **B).** Within the probable active pocket of target.

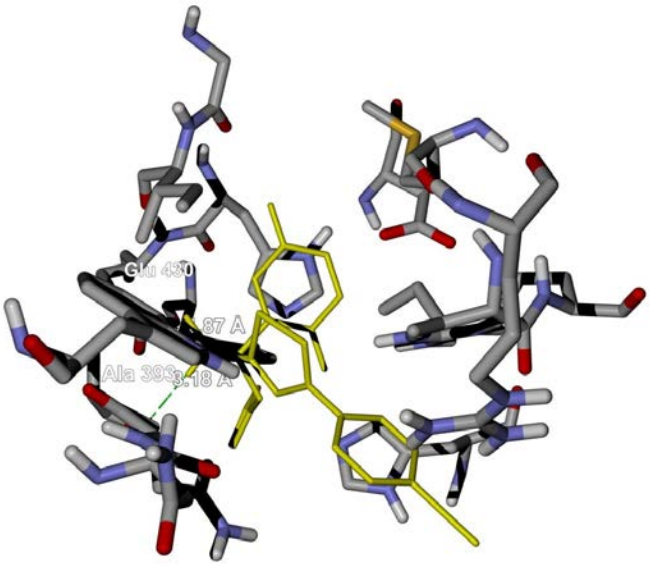

A

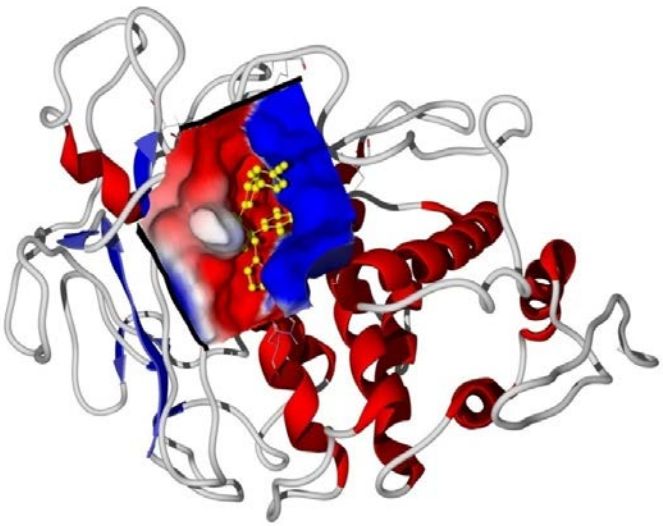

B

Figure S4.26: Visualisation and illustration of **A).** Isavuconazole positioned at the active site of the target Extracellular metalloproteinase mep (PDB ID: 4K90) exhibiting potential modes of interaction (The green dotted lines depicts the mode of interaction between the target and the ligand, accompanied by distance annotations, while the yellow-coloured structure represents the ligand itself) **B).** Within the probable active pocket of target.

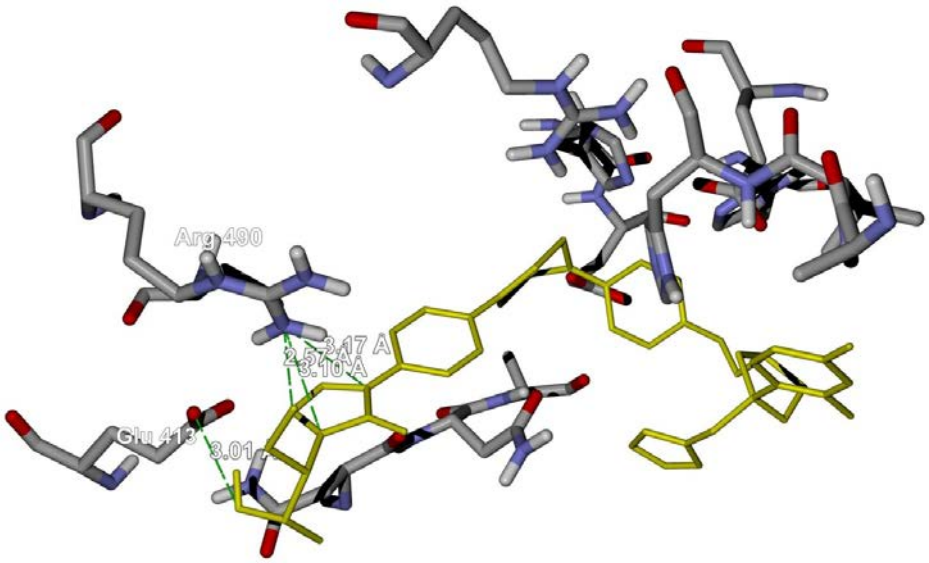

A

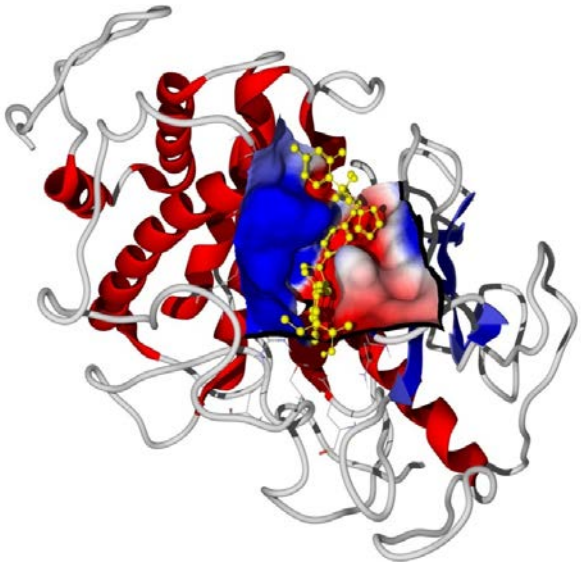

B

Figure S4.27: Visualisation and illustration of **A).** Posaconazole positioned at the active site of the target Extracellular metalloproteinase mep (PDB ID: 4K90) exhibiting potential modes of interaction (The green dotted lines depict the mode of interaction between the target and the ligand, accompanied by distance annotations, while the yellow-coloured structure represents the ligand itself) **B).** Within the probable active pocket of target.

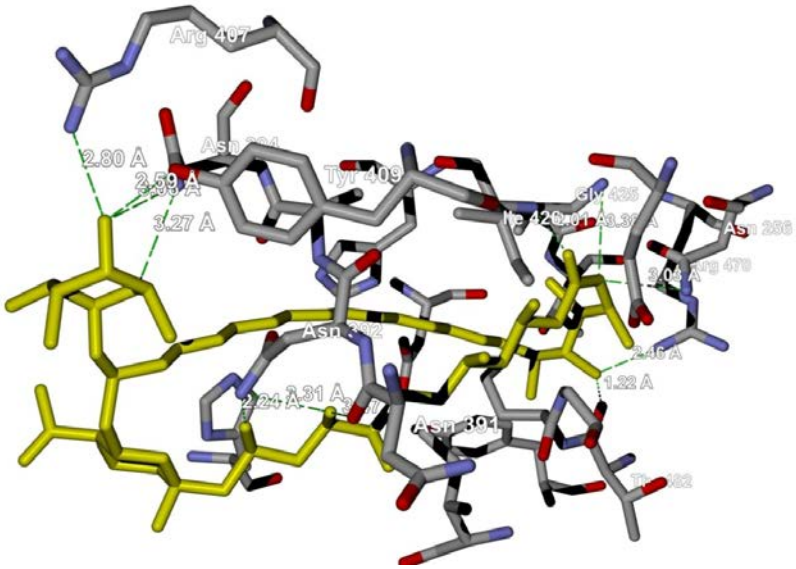

A

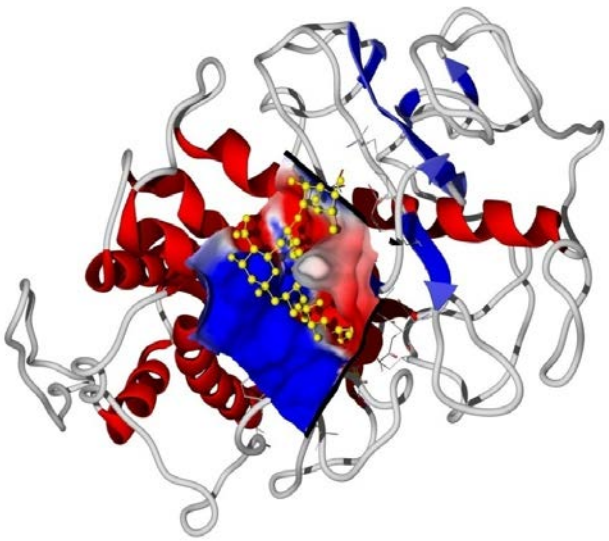

B

Figure S4.28: Visualisation and illustration of **A).** Amphotericin B positioned at the active site of the target Extracellular metalloproteinase mep (PDB ID: 4K90) exhibiting potential modes of interaction (The green dotted lines depict the mode of interaction between the target and the ligand, accompanied by distance annotations, while the yellow-coloured structure represents the ligand itself) **B).** Within the probable active pocket of target.

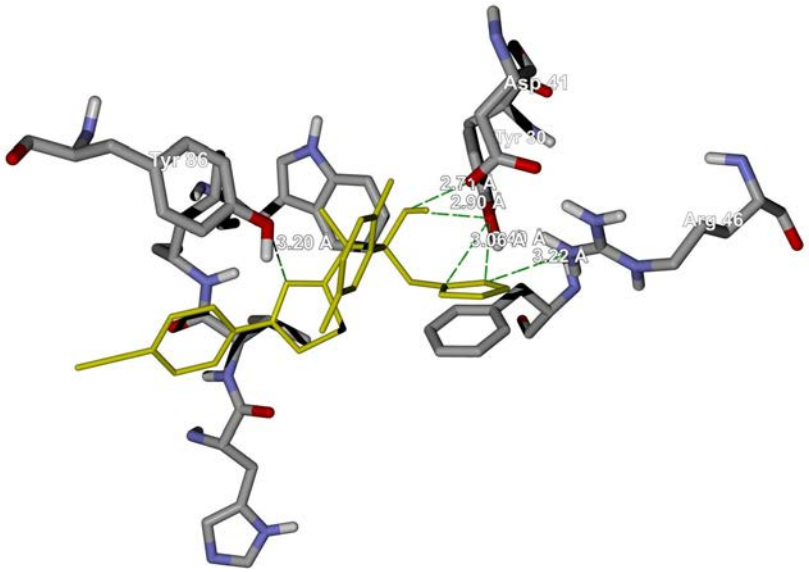

A

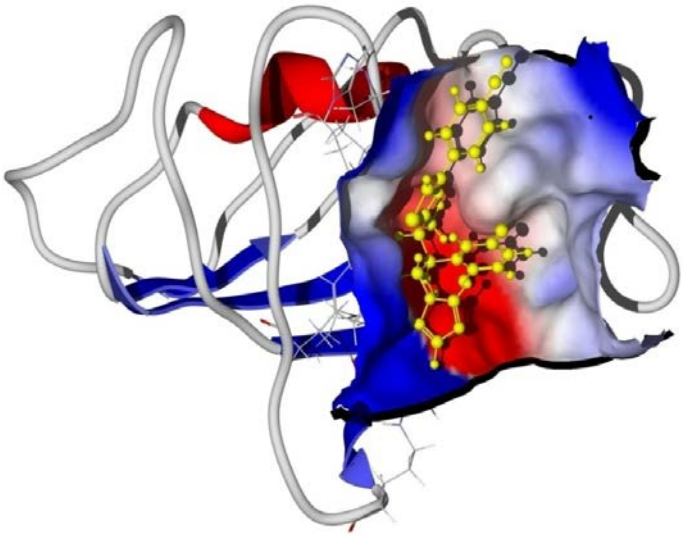

B

Figure S4.30: Visualisation and illustration of **A).** Isavuconazole positioned at the active site of the target Peptidylprolyl isomerase (PDB ID: 6VSI) exhibiting potential modes of interaction (The green dotted lines depict the mode of interaction between the target and the ligand, accompanied by distance annotations, while the yellow-coloured structure represents the ligand itself) **B).** Within the probable active pocket of target.

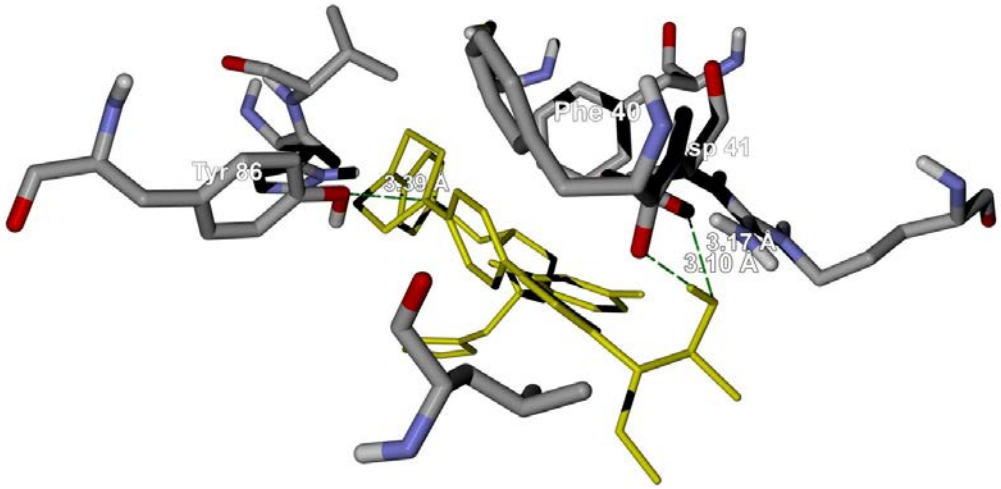

A

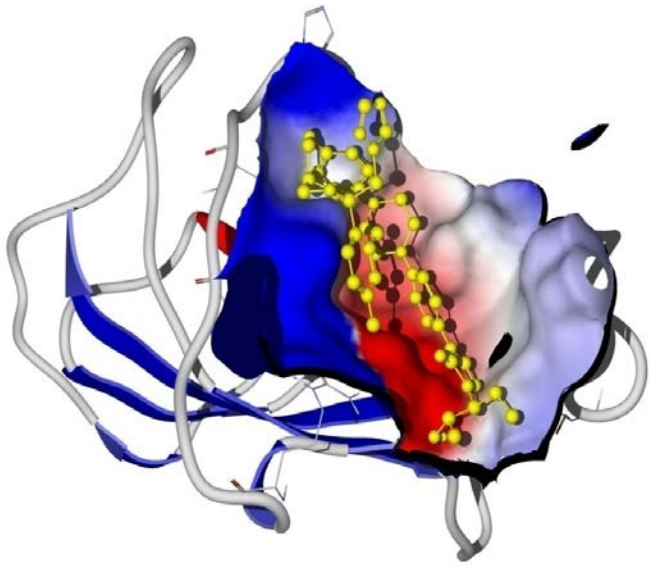

B

Figure S4.31: Visualisation and illustration of **A).** Posaconazole positioned at the active site of the target Peptidylprolyl isomerase (PDB ID: 6VSI) exhibiting potential modes of interaction (The green dotted lines depict the mode of interaction between the target and the ligand, accompanied by distance annotations, while the yellow-coloured structure represents the ligand itself) **B).** Within the probable active pocket of target.

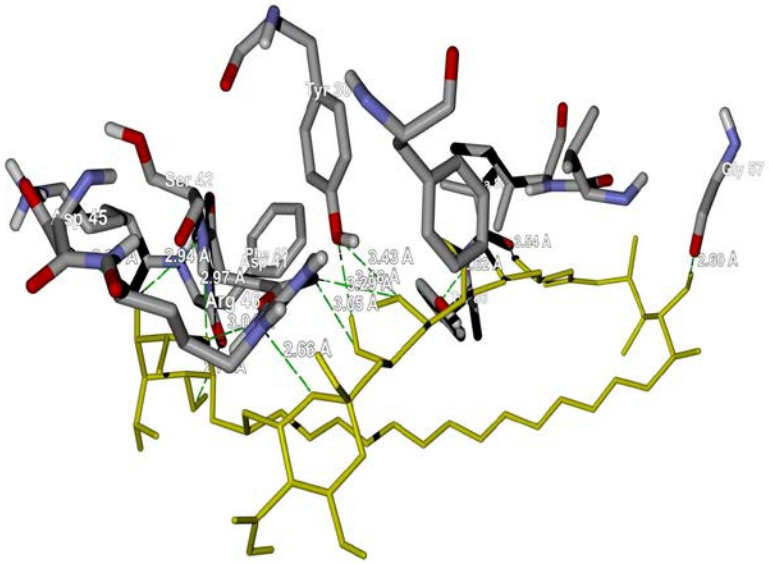

A

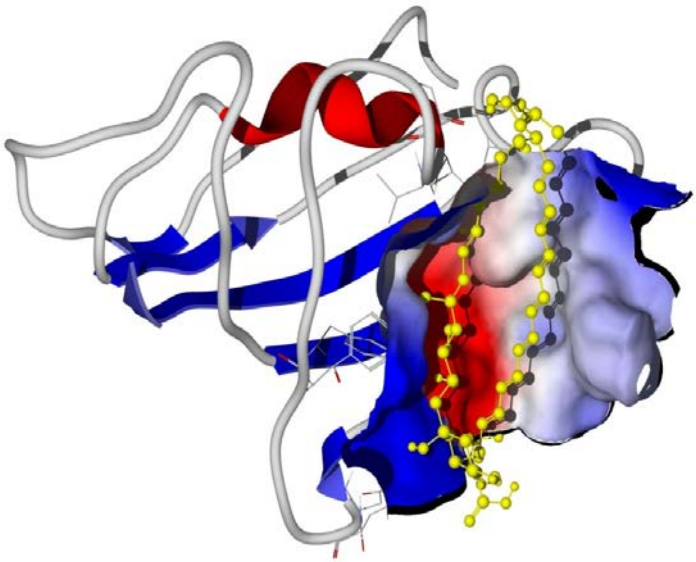

B

Figure S4.32: Visualisation and illustration of **A).** Amphotericin B positioned at the active site of the target Peptidylprolyl isomerase (PDB ID: 6VSI) exhibiting potential modes of interaction (The green dotted lines depict the mode of interaction between the target and the ligand, accompanied by distance annotations, while the yellow-coloured structure represents the ligand itself) **B).** Within the probable active pocket of target

4.3.2. Druglikeness (Physicochemical properties)

Table S4.13: Druglikeness screening of TerrestrolA (**10**) and the standards *via* SwissADME.

COMPOUND	LIPINSKI(RO5)	VEBER	GHOSE	EGAN
Nafamostat	No violations	1 violation: TPSA>140	No violations	1 violation: TPSA>131.6
Arbidol	No violations	No violations	No violations	No violations
Ribavirin	No violations	1 violation: TPSA>140	1 violation: WLOGP<-0.4	1 violation: TPSA>131.6
Favipiravir	No violations	No violations	4 violations: MW<160, WLOGP<-0.4, MR<40, #atoms<20	No violations
Dexamethasone	No violations	No violations	No violations	No violations
Hydroxychloroquine	No violations	No violations	No violations	No violations
Chloroquine	No violations	No violations	No violations	No violations
Isavuconazole	No violations	No violations	No violations	No violations
Posaconazole	2 violations: MW>500, NorO>10	1 violation: Rotors>10	3 violations: MW>480, MR>130, #atoms>70	No violations
Amphotericin.B	3 violations: MW>500, NorO>10, NHorOH>5	1 violation: TPSA>140	3 violations: MW>480, MR>130, #atoms>70	1 violation: TPSA>131.6
Terrestrol A(**10**)	1 violation: H-bond donors > 5	No violations	No violations	No violations

4.3.3. Pharmacokinetics (ADME) and toxicity prediction

4.3.3.1.ADME (pharmacokinetics)

Table S4.14: Pharmacokinetic (ADME) property assessment of Terrestrol A(**10**) and the standards *via* SwissADME and PreADMET

COMPOUNDS	SwissADME	PreADMET

	BBB permeant (Blood Brain Barrier)	**Skin Permeation (log K_p) (cm/s)**	**P-glycoprotein (P-gp) Substrate**	**Caco2 Permeability**	**Human Intestinal absorption (%)**	**MDCK (nm s^{-1})**
Nafamostat	No	-6.98 cm/s	No	21.0164	76.254709	0.928716
Arbidol	No	-6.07 cm/s	No	48.7479	97.257541	0.0210203
Ribavirin	No	-9.10 cm/s	No	1.36443	21.502254	2.22595
Favipiravir	No	-7.66 cm/s	No	17.0652	71.915441	0.633704
Dexamethasone	No	-7.32 cm/s	Yes	20.3458	88.755385	11.4365
Hydroxychloroquine	Yes	-5.81 cm/s	No	46.0839	94.660945	45.1085
Chloroquine	Yes	-4.96 cm/s	No	56.6153	98.056241	0.297955
Isavuconazole	No	-6.46 cm/s	Yes	33.2333	98.277793	0.339009
Posaconazole	No	-7.32 cm/s	Yes	52.1405	97.072369	0.0533242
Amphotericin.B	No	-11.94 cm/s	Yes	14.135	4.681967	0.0453053
Terrestrol A (10)	No	-6.40 cm/s	No	20.2354	71.364574	0.0757768

4.3.3.2. Toxicity prediction.

Table S15: Toxicity profiling of Terrestrol A(**10**) and the standards conducted *via* ProTOX-II

COMPOUNDS	**TOXICITY ENDPOINTS USING ProTox-II**						
	HEPATOTOXICITY	**CARCINO-GENICITY**	**IMMUNO-TOXICITY**	**MUTA-GENICITY**	**CYTO-TOXICITY**	**Predicted ^{1}LD50**	**Predicted Toxicity Class:**
Nafamostat	Active Probability: 0.60	Active Probability: 0.57	Inactive Probability: 0.84	Active Probability: 0.58	Active Probability: 0.63	3050mg/kg	5
Arbidol	Inactive Probability: 0.56	Inactive Probability: 0.60	Inactive Probability: 0.95	Inactive Probability: 0.62	Inactive Probability: 0.58	340mg/kg	4
Ribavirin	Inactive Probability:0.52	Active Probability:0.56	Inactive Probability:0.99	Inactive Probability:0.85	Inactive Probability:0.72	2700mg/kg	5

Favipiravir	Inactive Probability:0.66	Active Probability:0.53	Inactive Probability:0.99	Inactive Probability:0.76	Inactive Probability:0.84	1717mg/kg	4
Dexamethasone	Inactive Probability: 0.99	Inactive Probability: 0.72	Active Probability: 0.99	Inactive Probability: 0.69	Inactive Probability: 0.72	3000mg/kg	5
Hydroxychloroquine	Inactive Probability: 0.94	Inactive Probability: 0.62	Active Probability: 0.99	Active Probability: 0.79	Inactive Probability: 0.72	1240mg/kg	4
Chloroquine	Inactive Probability: 0.90	Inactive Probability: 0.66	Active Probability: 0.99	Active Probability: 0.94	Inactive Probability: 0.93	750mg/kg	4
Isavuconazole	Active Probability:0.75	Inactive Probability:0.65	Inactive Probability:0.62	Inactive Probability:0.65	Inactive Probability:0.62	1000mg/kg	4
Posaconazole	Active Probability: 0.86	Inactive Probability: 0.62	Active Probability: 0.99	Inactive Probability: 0.56	Inactive Probability: 0.75	320mg/kg	4
Amphotericin.B	Inactive Probability: 0.97	Inactive Probability: 0.73	Active Probability: 0.99	Inactive Probability: 0.89	Inactive Probability: 0.83	100mg/kg	3
Terrestrol A(10)	Inactive Probability: 0.80	Inactive Probability: 0.75	Inactive Probability: 0.70	Inactive Probability: 0.66	Inactive Probability: 0.85	900mg/kg	4

4.3.4. Bioactivity prediction

Table S4.16: Bioactivity score prediction of Terrestrol A (**10**) and the standards *via* molinspiration.

COMPOUNDS	**BIOACTIVITY SCORE PARAMETERS**					
	GPCR (G-protein-coupled receptors) ligand	**Ion channel modulator**	**Kinase inhibitor**	**Nuclear receptor ligand**	**Protease inhibitor**	**Enzyme inhibitor**
Nafamostat	0.28	0.14	-0.03	-0.16	0.57	0.19

Arbidol	-0.19	-0.44	-0.39	-0.34	-0.46	-0.07
Ribavirin	0.31	0.21	-0.21	-1.46	-0.20	0.71
Favipiravir	-0.62	-0.44	-0.31	-1.50	-0.91	-0.33
Dexamethasone	0.03	-0.21	-0.81	1.59	0.76	0.78
Hydroxychloroquine	0.35	0.30	0.44	-0.12	0.12	0.15
Chloroquine	0.32	0.32	0.38	-0.19	0.05	0.11
Isavuconazole	0.00	-0.07	0.00	-0.18	-0.07	-0.00
Posaconazole	-0.63	-1.78	-1.40	-1.50	-0.57	-1.20
Amphotericin.B	-3.06	-3.51	-3.54	-3.45	-2.45	-2.95
Terrestrol A(10)	0.07	0.00	0.02	0.19	0.05	0.10

Compounds possessing values >0.00 are most likely to exhibit significant biological activities, while those with values ranging from -0.50 to 0.00 are expected to be moderately active, and values less than -0.50 are assumed to be inert.

4.3.5. PASS (prediction of activity spectra for substances).

Table S17: PASS (Prediction of Activity Spectra for Substances) prediction of Terrestrol A(10) and the standards with respect to SARS-CoV2 (antiviral related activity) *via* PASS Online.

Compounds	**ANTIVRAL Parameters**	[a] **Pa**	[b] **Pi**
Nafamostat	Antiviral (Picornavirus)	0,277	0,268
	Antiviral (Influenza)	0,490	0,024
	Antiviral (Adenovirus)	0,225	0,171
	Antiviral (Herpes)	NIL	NIL
	Antiviral (CMV)	NIL	NIL
	Antiviral	NIL	NIL
	3C-like protease (Human coronavirus) inhibitor	NIL	NIL
Arbidol	Antiviral (Picornavirus)	NIL	NIL
	Antiviral (Influenza)	0,740	0,004
	Antiviral (Adenovirus)	0,304	0,086
	Antiviral (Herpes)	NIL	NIL
	Antiviral (CMV)	NIL	NIL
	Antiviral	NIL	NIL
	3C-like protease (Human coronavirus) inhibitor	NIL	NIL
Ribavirin	Antiviral (Picornavirus)	0,674	0,008
	Antiviral (Influenza)	0,829	0,003

	Antiviral (Adenovirus)	0,324	0,071
	Antiviral (Herpes)	0,495	0,010
	Antiviral (CMV)	NIL	NIL
	Antiviral	0,806	0,004
	3C-like protease (Human coronavirus) inhibitor	NIL	NIL
Favipiravir	Antiviral (Picornavirus)	0,387	0,121
	Antiviral (Influenza)	0,662	0,008
	Antiviral (Adenovirus)	0,274	0,112
	Antiviral (Herpes)	0,199	0,177
	Antiviral (CMV)	0,217	0,139
	Antiviral	0,447	0,010
	3C-like protease (Human coronavirus) inhibitor	0,247	0,081
Dexamethasone	Antiviral (Picornavirus)	NIL	NIL
	Antiviral (Influenza)	NIL	NIL
	Antiviral (Adenovirus)	NIL	NIL
	Antiviral (Herpes)	NIL	NIL
	Antiviral (CMV)	NIL	NIL
	Antiviral	NIL	NIL
	3C-like protease (Human coronavirus) inhibitor	NIL	NIL
Hydroxychloroquine	Antiviral (Picornavirus)	NIL	NIL
	Antiviral (Influenza)	NIL	NIL
	Antiviral (Adenovirus)	NIL	NIL
	Antiviral (Herpes)	NIL	NIL
	Antiviral (CMV)	NIL	NIL
	Antiviral	NIL	NIL
	3C-like protease (Human coronavirus) inhibitor	NIL	NIL
Chloroquine	Antiviral (Picornavirus)	NIL	NIL
	Antiviral (Influenza)	NIL	NIL
	Antiviral (Adenovirus)	NIL	NIL
	Antiviral (Herpes)	NIL	NIL
	Antiviral (CMV)	NIL	NIL
	Antiviral	NIL	NIL
	3C-like protease (Human coronavirus) inhibitor	NIL	NIL
Terrestrol A(10)	Antiviral (Picornavirus)	0,323	0,193
	Antiviral (Influenza)	0,242	0,141
	Antiviral (Adenovirus)	0,243	0,147
	Antiviral (Herpes)	0,330	0,072
	Antiviral (CMV)	0,262	0,061
	Antiviral	0,237	0,068
	3C-like protease (Human coronavirus) inhibitor	0,270	0,050
	Simian immunodeficiency virus proteinase inhibitor	0,356	0,076

[a]Pa : Probability for active compound [b]Pi:Probability for inactive compound). NIL : Not applicable

Table S18: PASS (Prediction of Activity Spectra for Substances) prediction of Terrestrol A(**10**) and the standards with respect to SARS-CoV2 (antifungal related activity) *via* PASS Online

Compounds	**ANTIVRAL Parameters**	**PA**	**PI**
Isavuconazole	Aspergillus nuclease S1 inhibitor	NIL	NIL
	Aspergillopepsin I inhibitor	NIL	NIL
	Aspergillopepsin II inhibitor	NIL	NIL
	Yeast ribonuclease inhibitor	NIL	NIL
	Antifungal	0,738	0,008
	Antifungal enhancer	NIL	NIL
	Antifungal (Pneumocystis)	NIL	NIL
	Lanosterol 14 alpha demethylase inhibitor	0,903	0,001
	Mucorpepsin inhibitor	NIL	NIL
	Rhizopuspepsin inhibitor	NIL	NIL
	ADP-ribosylarginine hydrolase inhibitor	NIL	NIL
Posaconazole	Aspergillus nuclease S1 inhibitor	NIL	NIL
	Aspergillopepsin I inhibitor	NIL	NIL
	Aspergillopepsin II inhibitor	NIL	NIL
	Yeast ribonuclease inhibitor	NIL	NIL
	Antifungal	0,832	0,004
	Antifungal enhancer	NIL	NIL
	Antifungal (Pneumocystis)	NIL	NIL
	Lanosterol 14 alpha demethylase inhibitor	0,729	0,001
	Mucorpepsin inhibitor	0,146	0,138
	Rhizopuspepsin inhibitor	NIL	NIL
	ADP-ribosylarginine hydrolase inhibitor	NIL	NIL
Amphotericin.B	Aspergillus nuclease S1 inhibitor	NIL	NIL
	Aspergillopepsin I inhibitor	NIL	NIL
	Aspergillopepsin II inhibitor	NIL	NIL
	Yeast ribonuclease inhibitor	NIL	
	Antifungal	0,977	0,000
	Antifungal enhancer	0,133	0,012
	Antifungal (Pneumocystis)	NIL	NIL
	Lanosterol 14 alpha demethylase inhibitor	NIL	NIL
	Mucorpepsin inhibitor	NIL	NIL
	Rhizopuspepsin inhibitor	NIL	NIL
	ADP-ribosylarginine hydrolase inhibitor	NIL	NIL
Terrestrol A(10)	Aspergillus nuclease S1 inhibitor	0,387	0,041
	Aspergillopepsin I inhibitor	0,373	0,054
	Aspergillopepsin II inhibitor	0,312	0,031
	Yeast ribonuclease inhibitor	0,195	0,108
	Antifungal	0,357	0,061
	Antifungal enhancer	0,106	0,048
	Antifungal (Pneumocystis)	0,097	0,004
	Lanosterol 14 alpha demethylase inhibitor	0,114	0,089

	Mucorpepsin inhibitor	0,148	0,134
	Rhizopuspepsin inhibitor	0,264	0,027
	ADP-ribosylarginine hydrolase inhibitor	0,221	0,034

[a]Pa : Probability for active compound [b]Pi:Probability for inactive compound). NIL : Not applicable

4.3.6. DFT (Density functional theory)

Table S.19: Optimized structures of Terrestrol A(**10**) and the standards using DFT/B3LYP with a 6-311G (d, p) basis set

COMPOUND	OPTIMIZED STRUCTURE
Terrestrol A(10)	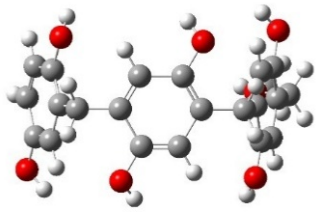
Amphotericin B	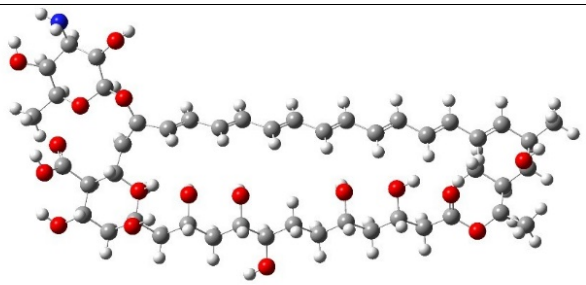
Arbidol	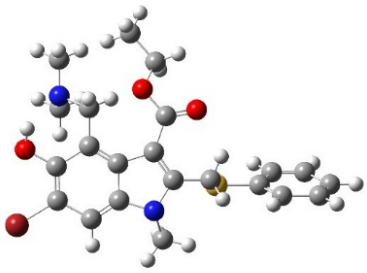

Chloroquine	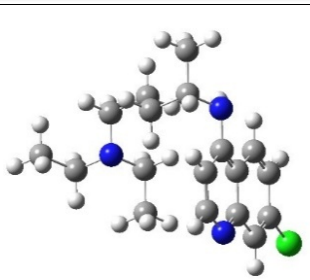
Dexamethasone	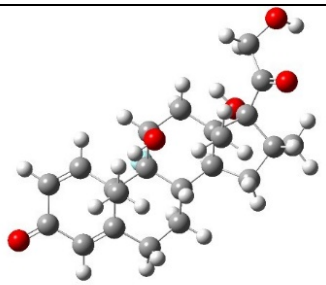
Posaconazole	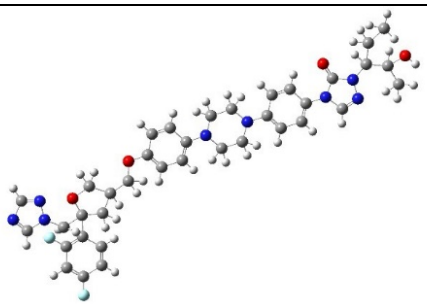
Favipiravir	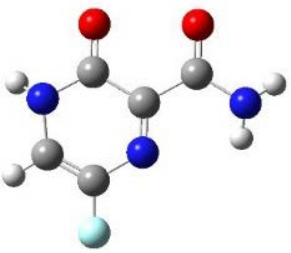
Hydroxychloroquine	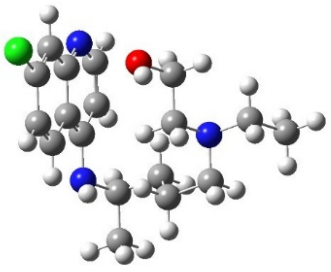

Isavuconazole	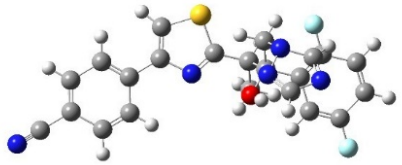
Nafamostat	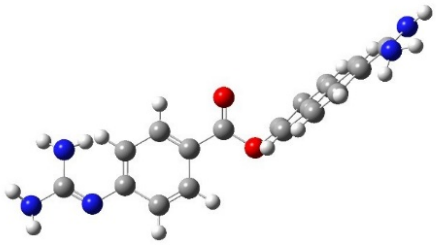
Ribavirin	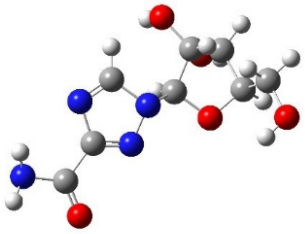

Table S4.20: Calculated global reactivity descriptors of Terrestrol A(**10**) and the standards using DFT/B3LYP with a 6-311G (d, p) basis set

COMPOUNDS	**Dipole moment (debye)**	**Iionization potential (eV)**	**Electron affinity (eV)**	**Hardness (eV)**	**Chemical potential (eV)**	**Electrophilicity (eV)**	**Electron-egativity(eV)**
Terrestrol A(10)	1.372716	0.28215	-0.13685	0.2095	-0.07265	0.000552873	0.07265
Amphotericin B	14.953855	0.2942	-0.11869	0.206445	-0.087755	0.00079491	0.087755
Arbidol	4.961687	0.28732	-0.09246	0.18989	-0.09743	0.000901275	0.09743
Chloroquine	6.683841	0.29223	-0.09187	0.19205	-0.10018	0.00096371	0.10018
Dexamethasone	4.149043	0.29223	-0.09278	0.192505	-0.099725	0.000957238	0.099725

Posaconazole	5.165541	0.15745	-0.0405	0.098975	-0.058475	0.000169214	0.058475
Favipiravir	5.535293	0.34347	-0.038	0.190735	-0.152735	0.002224731	0.152735
Hydroxychloroquine	8.294773	0.29008	-0.09535	0.192715	-0.097365	0.000913464	0.097365
Isavuconazole	7.065805	0.32285	-0.06193	0.19239	-0.13046	0.001637221	0.13046
Nafamostat	7.488310	0.28372	-0.08939	0.186555	-0.097165	0.000880636	0.097165
Ribavirin	8.662803	0.38156	-0.13023	0.255895	-0.125665	0.002020508	0.125665

Table S4.21: Calculated frontier molecular orbitals (FMOs) energy values of the HOMO, LUMO and the resultant HOMO-LUMO energy gap using DFT/B3LYP with a 6-311G (d, p) basis set.

COMPOUNDS	E (LUMO) (eV)	E (HOMO) (eV)	E_{LUMO}-E_{HOMO} (in H)	E_{LUMO}-E_{HOMO} (eV)
Terrestrol A(10)	0.13685	-0.28215	0.419	11.4015766
Amphotericin B	0.11869	-0.2942	0.41289	11.23531495
Arbidol	0.09246	-0.28732	0.37978	10.33434549
Chloroquine	0.09187	-0.29223	0.3841	10.45189874
Dexamethasone	0.09278	-0.29223	0.38501	10.47666111
Posaconazole	0.0405	-0.15745	0.19795	5.38649663
Favipiravir	0.038	-0.34347	0.38147	10.38033276
Hydroxychloroquine	0.09535	-0.29008	0.38543	10.4880899
Isavuconazole	0.06193	-0.32285	0.38478	10.47040249
Nafamostat	0.08939	-0.28372	0.37311	10.15284545
Ribavirin	0.13023	-0.38156	0.51179	13.92652241

Table S4.22: Cartoon illustration and visualisation of the HOMO, LUMO and the resultant HOMO-LUMO energy gap using DFT/B3LYP with a 6-311G (d, p) basis set.

COMPOUNDS	HOMO, LUMO and the resultant HOMO-LUMO band gap

Terrestrol A(10)	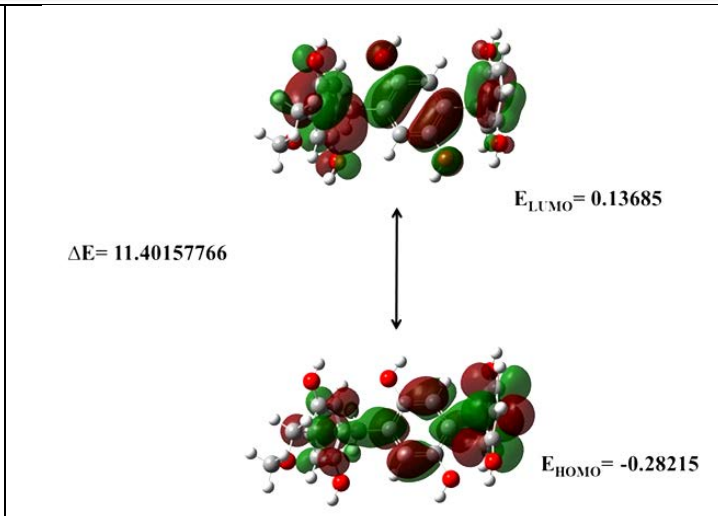
Amphotericin B	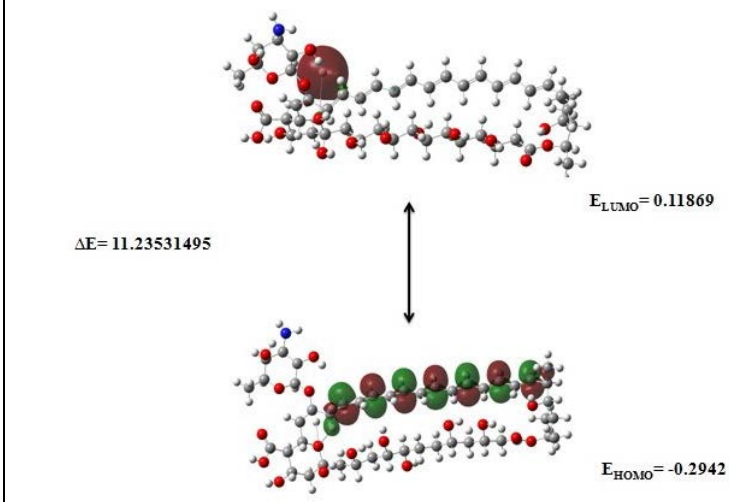
Arbidol	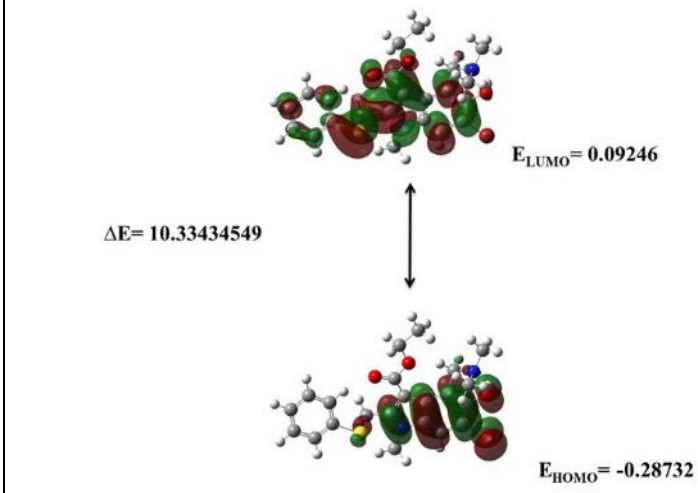

Chloroquine	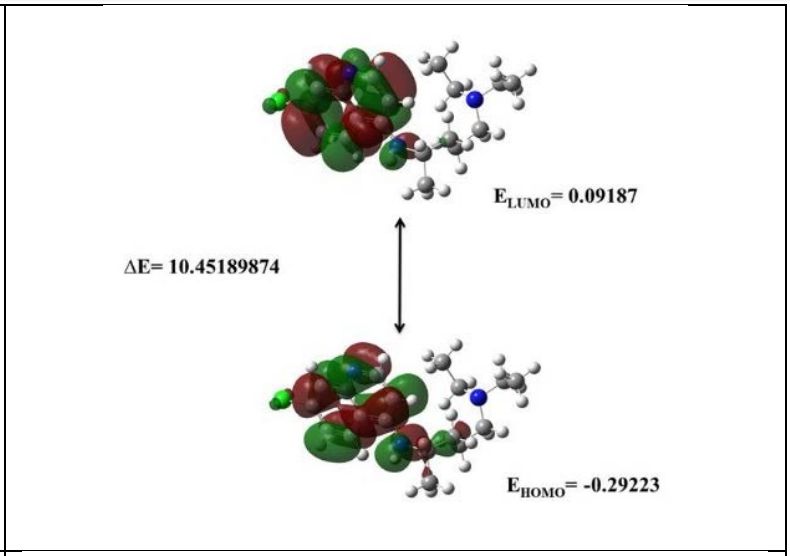
Dexamethasone	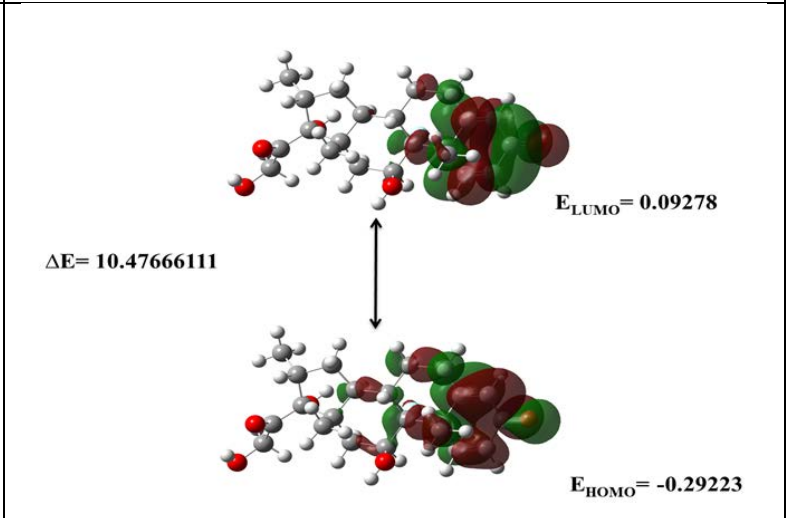
Posaconazole	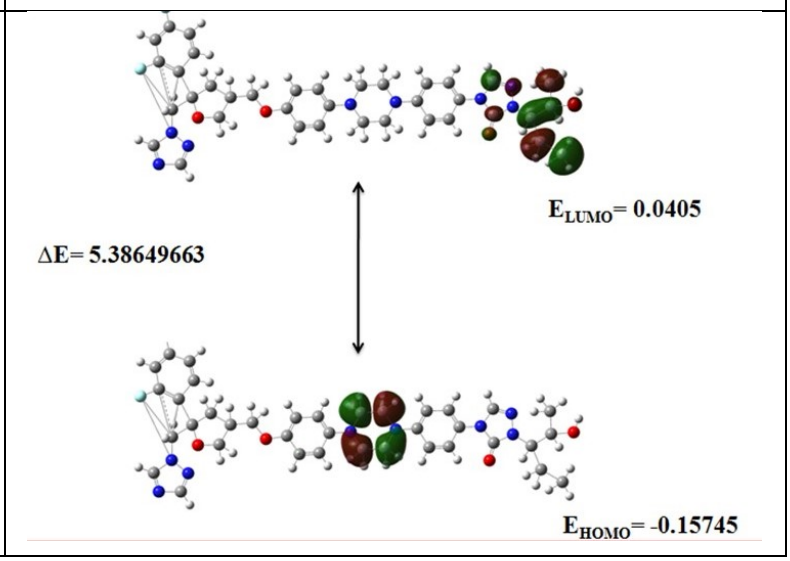

Favipiravir	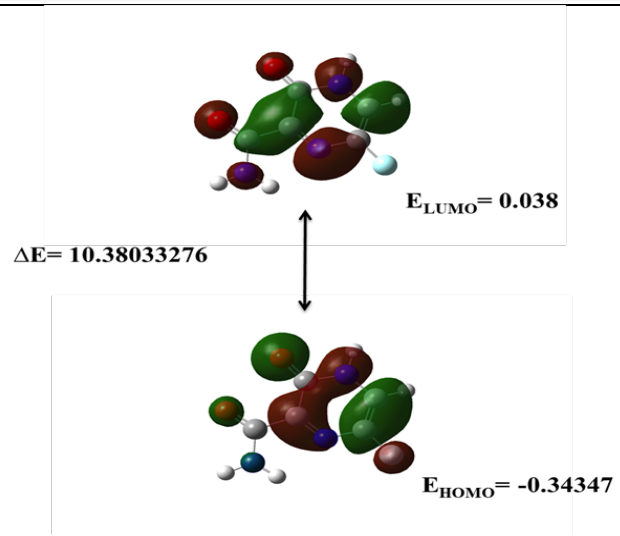
Hydroxychloroquine	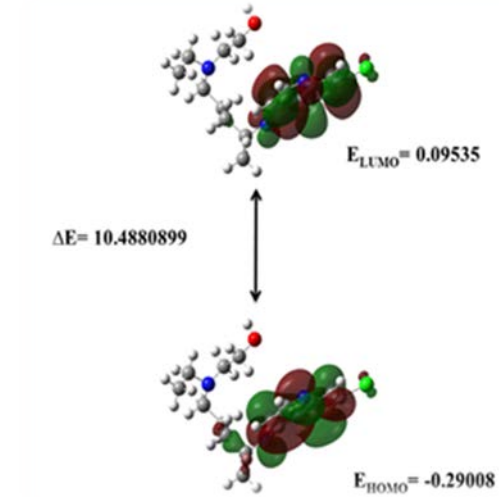
Isavuconazole	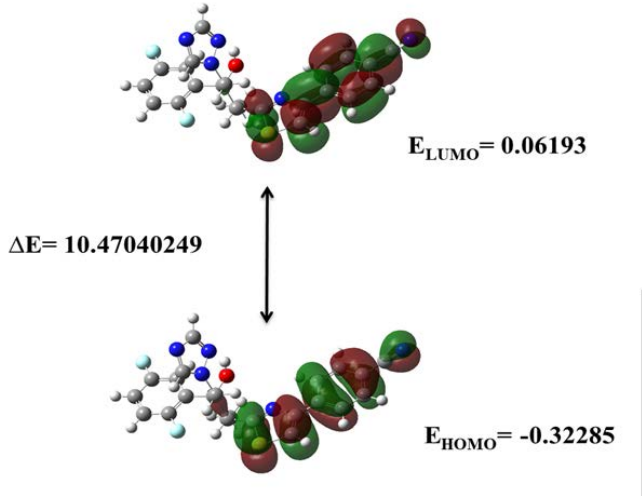

Nafamostat	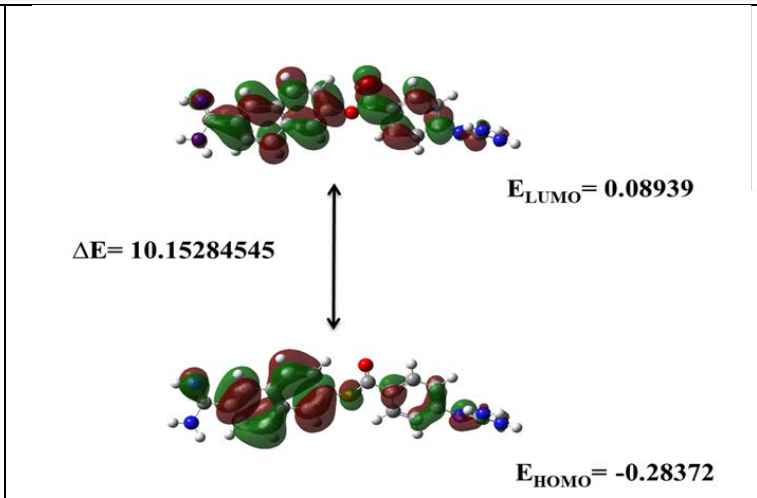
Ribavirin	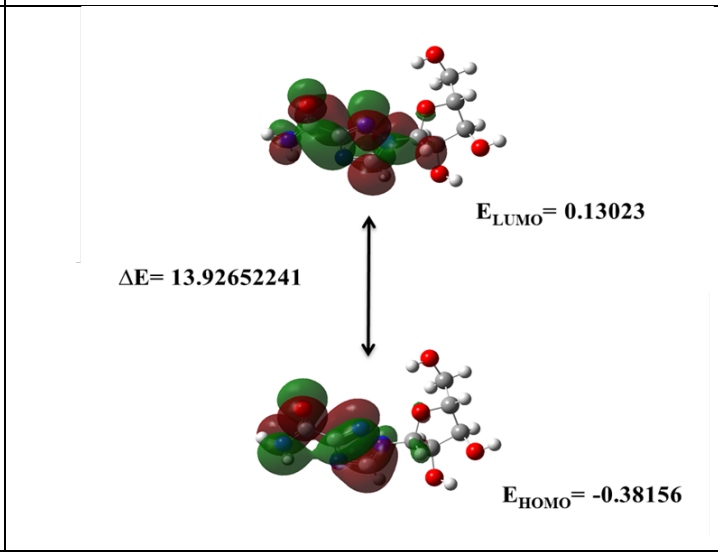

4.3.7. Results and Analysis for MD Simulation.

4.3.7.1.Root mean square deviation (RMSD).

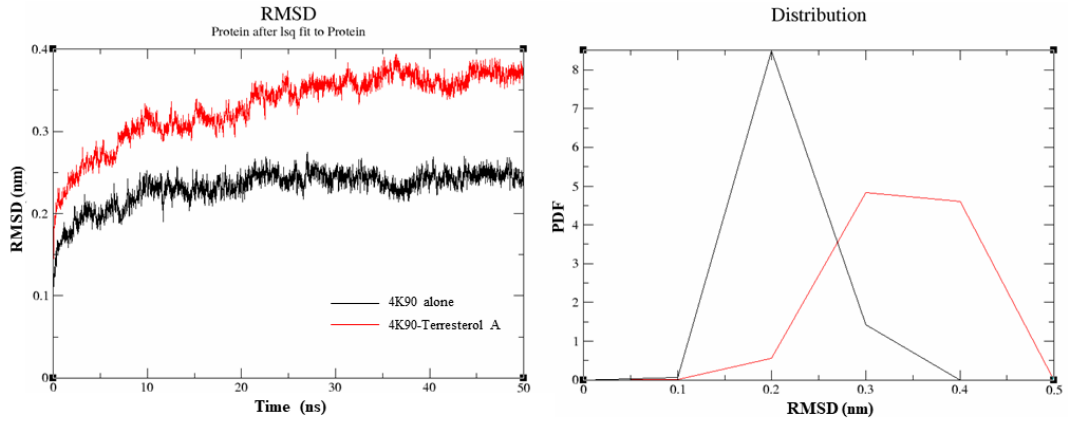

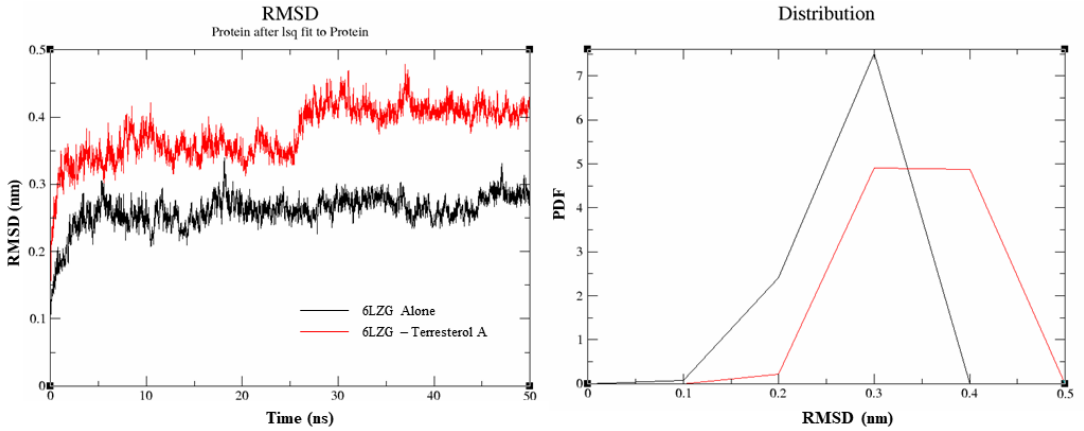

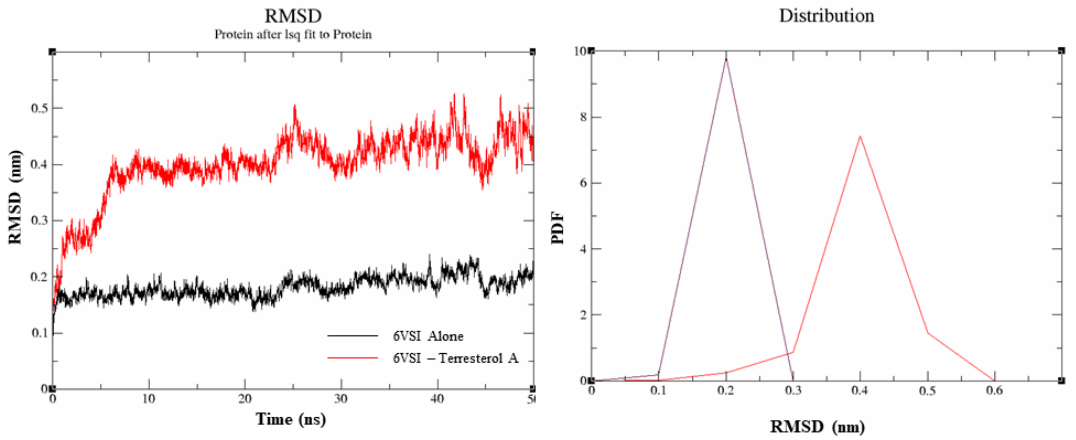

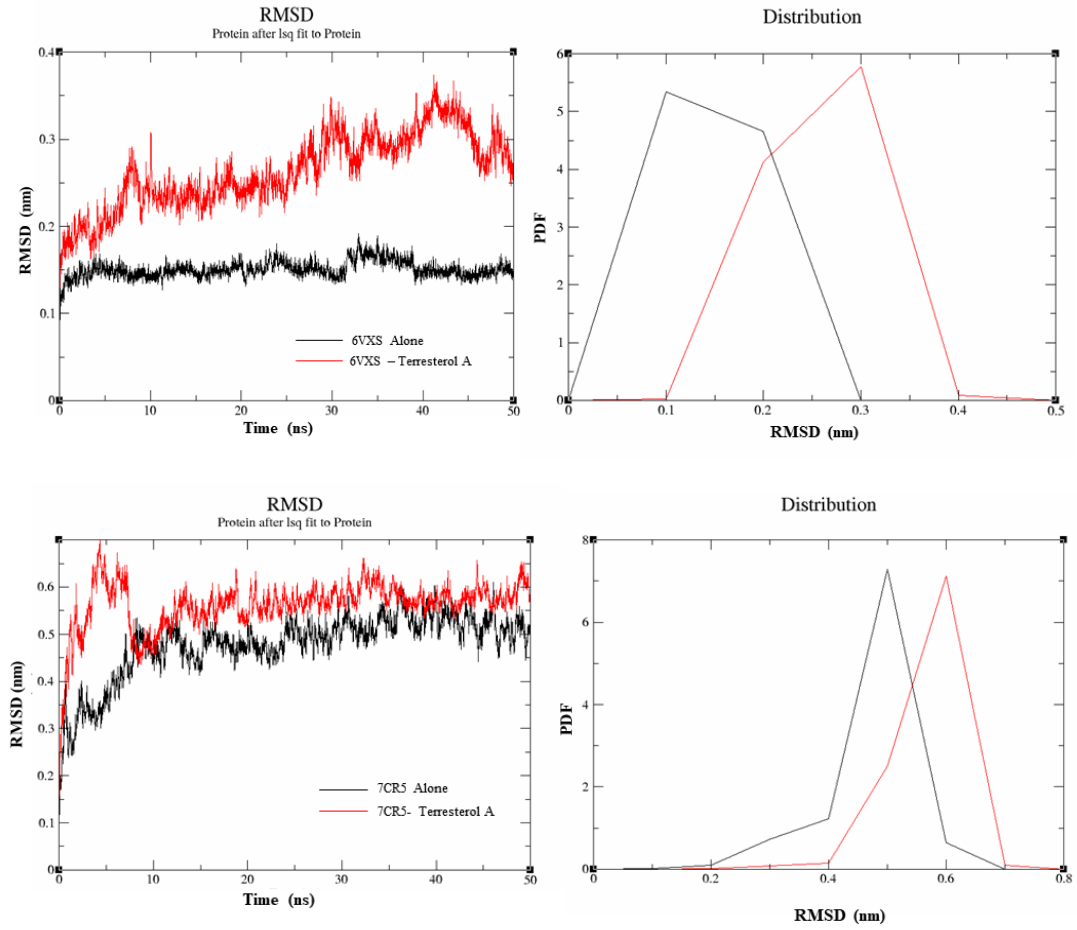

Figure S4.33: RMSD Plots of Terrestrol A(**10**) with PDB IDs 4K90, 6LZG, 6VSI, 6VXS and 7CR5 respectively along with their respective PDF plots.

4.3.7.2.Root mean square fluctuation (RMSF)

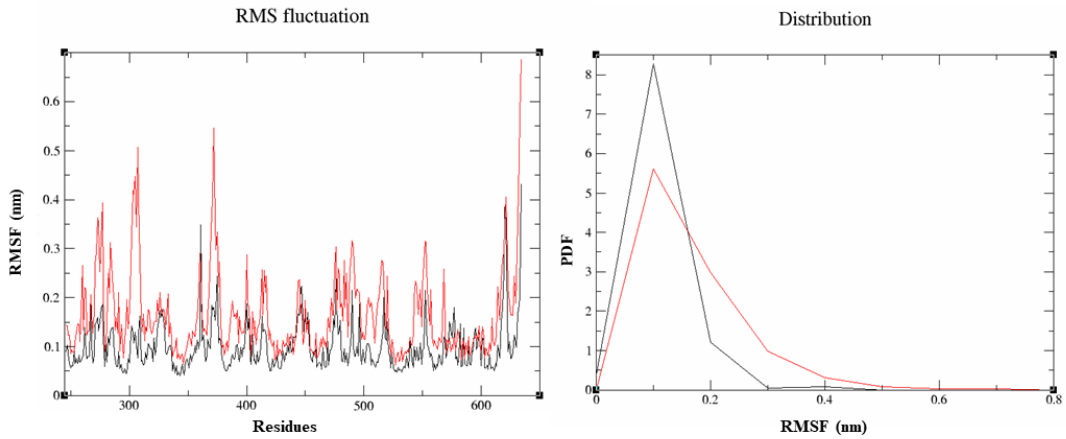

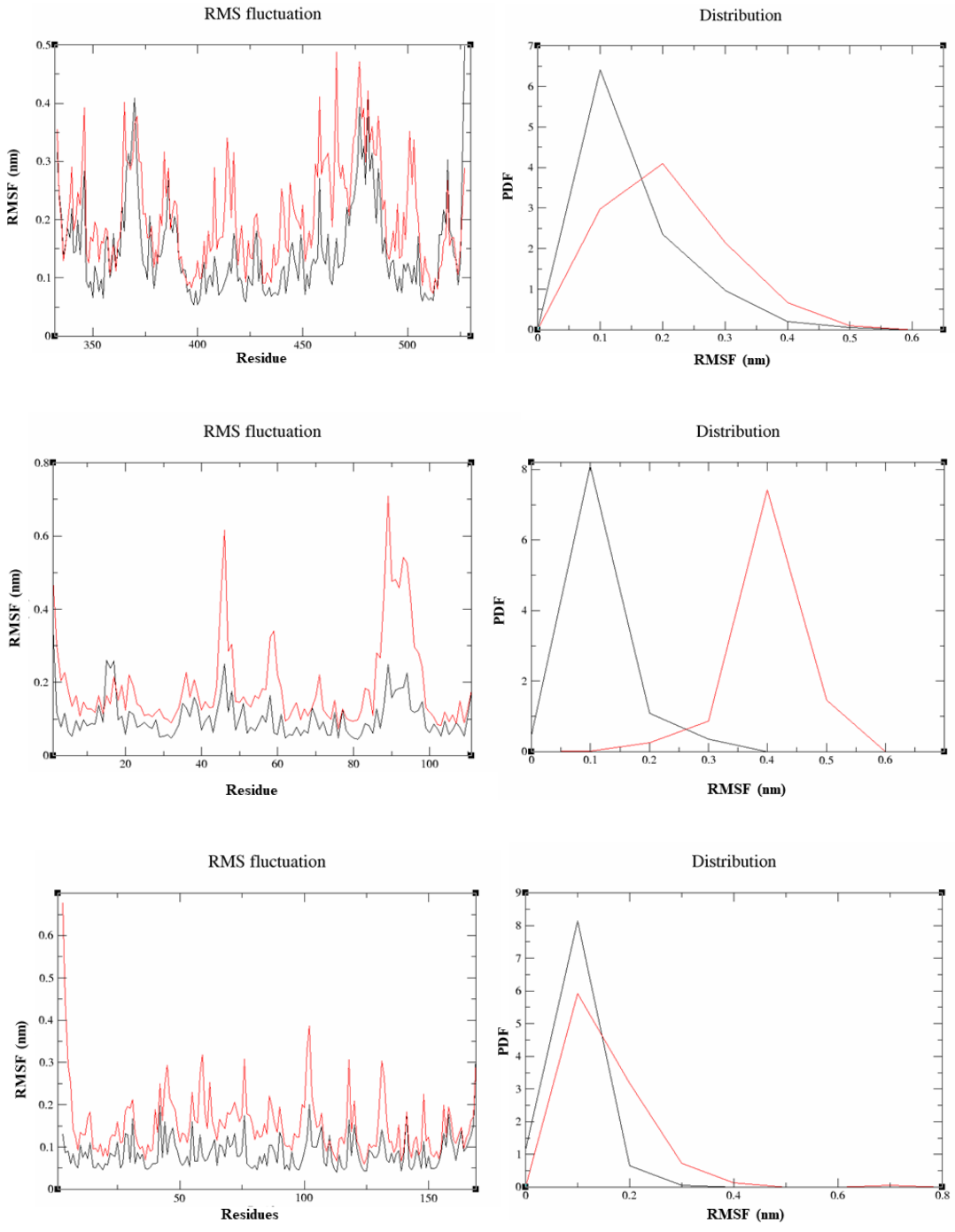
RMS fluctuation
RMSF (nm)
Residue
Distribution
PDF
RMSF (nm)
RMS fluctuation
RMSF (nm)
Residue
Distribution
PDF
RMSF (nm)
RMS fluctuation
RMSF (nm)
Residues
Distribution
PDF
RMSF (nm)

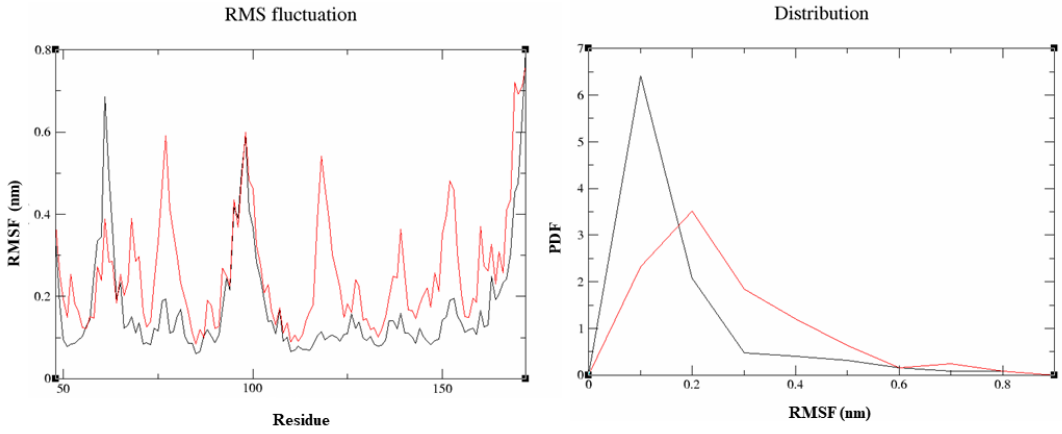

Figure S4.34: RMSF Plots of Terrestrol A(**10**) with with PDB IDs 4K90, 6LZG, 6VSI , 6VXS and 7CR5 respectively along with their respective PDF plots.

4.3.7.3.Radius of gyration (Rg)

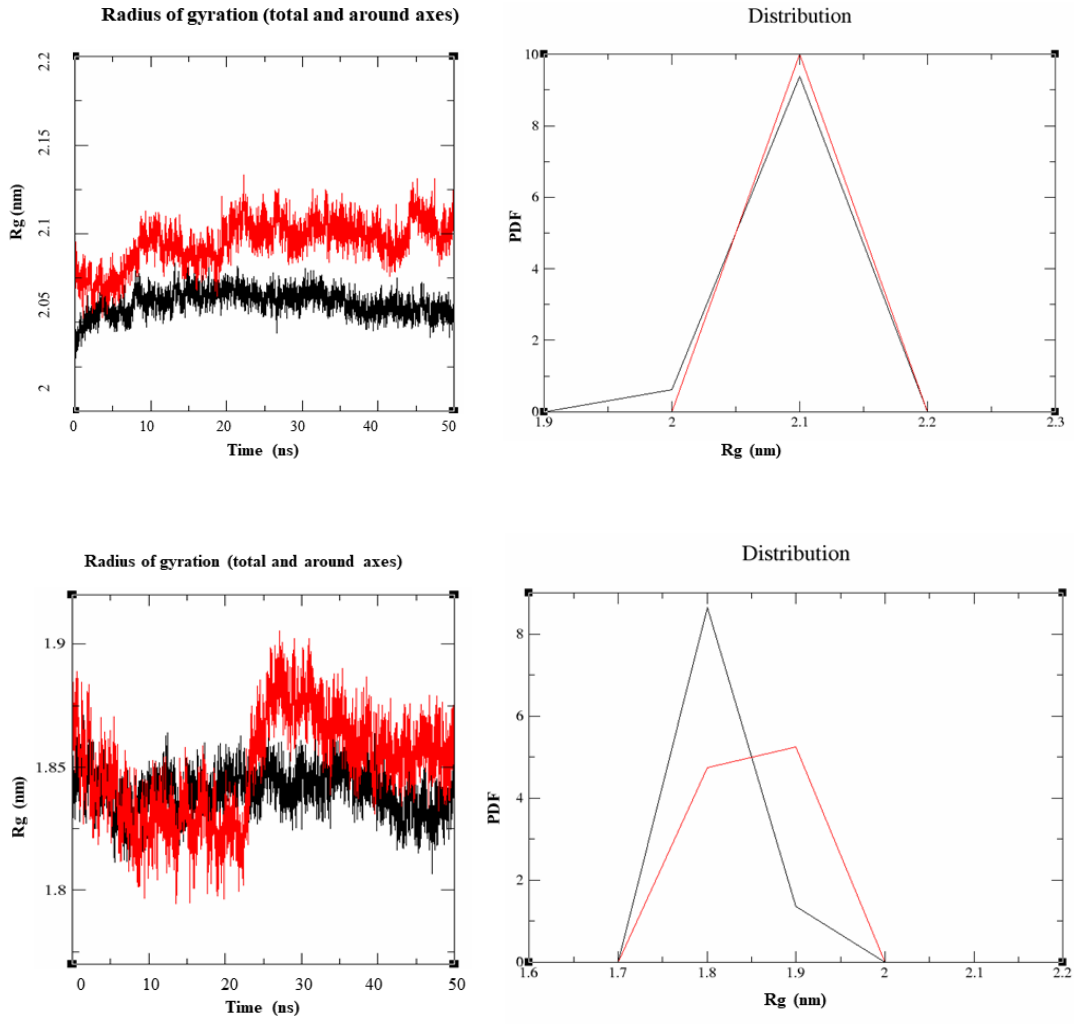

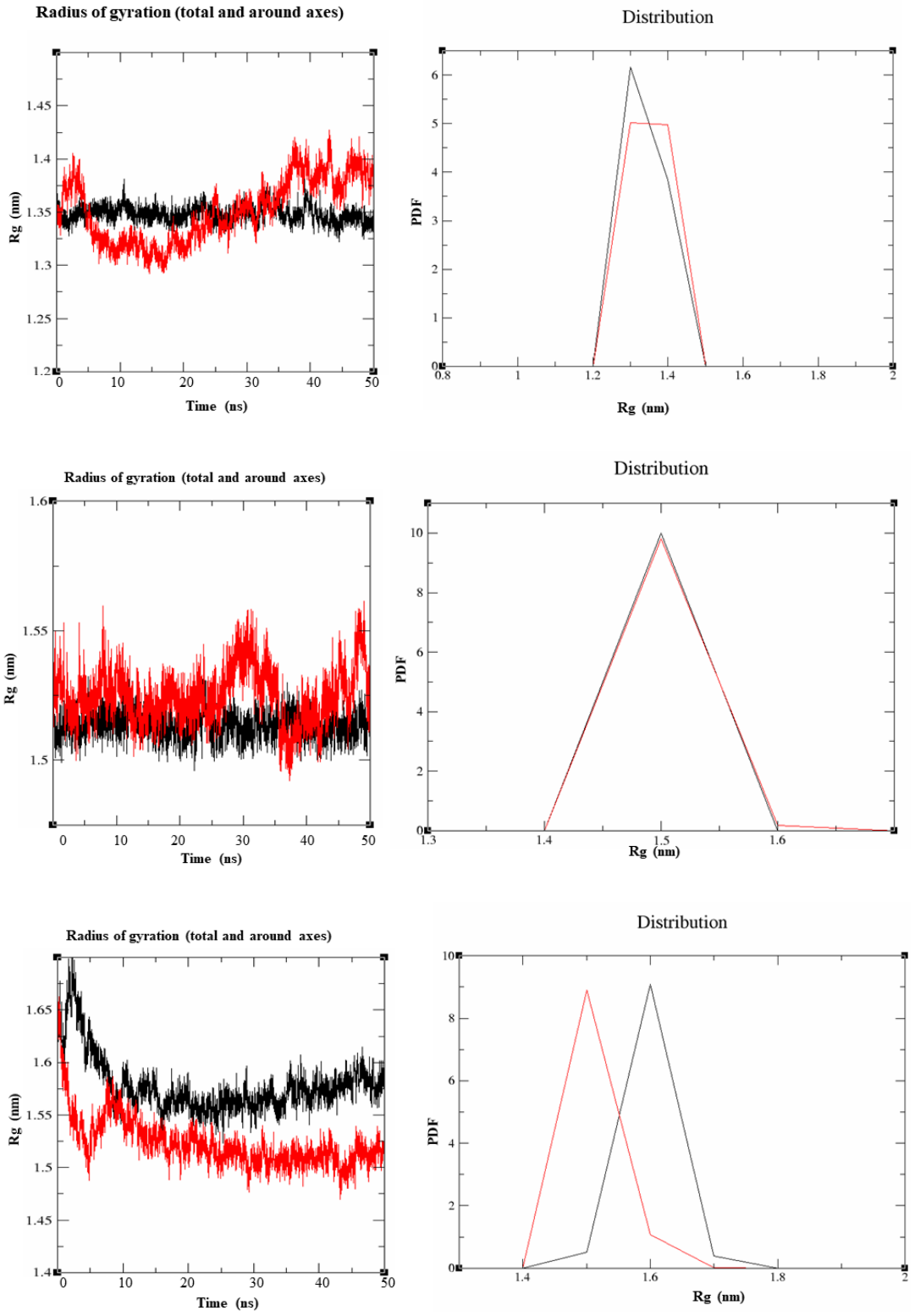

Figure S4.35: Rg Plots of Terrestrol A(**10**) with with PDB IDs 4K90, 6LZG, 6VSI , 6VXS and 7CR5 respectively along with their respective PDF plots.

4.3.7.4. Solvent Accessible Surface Area (SASA)

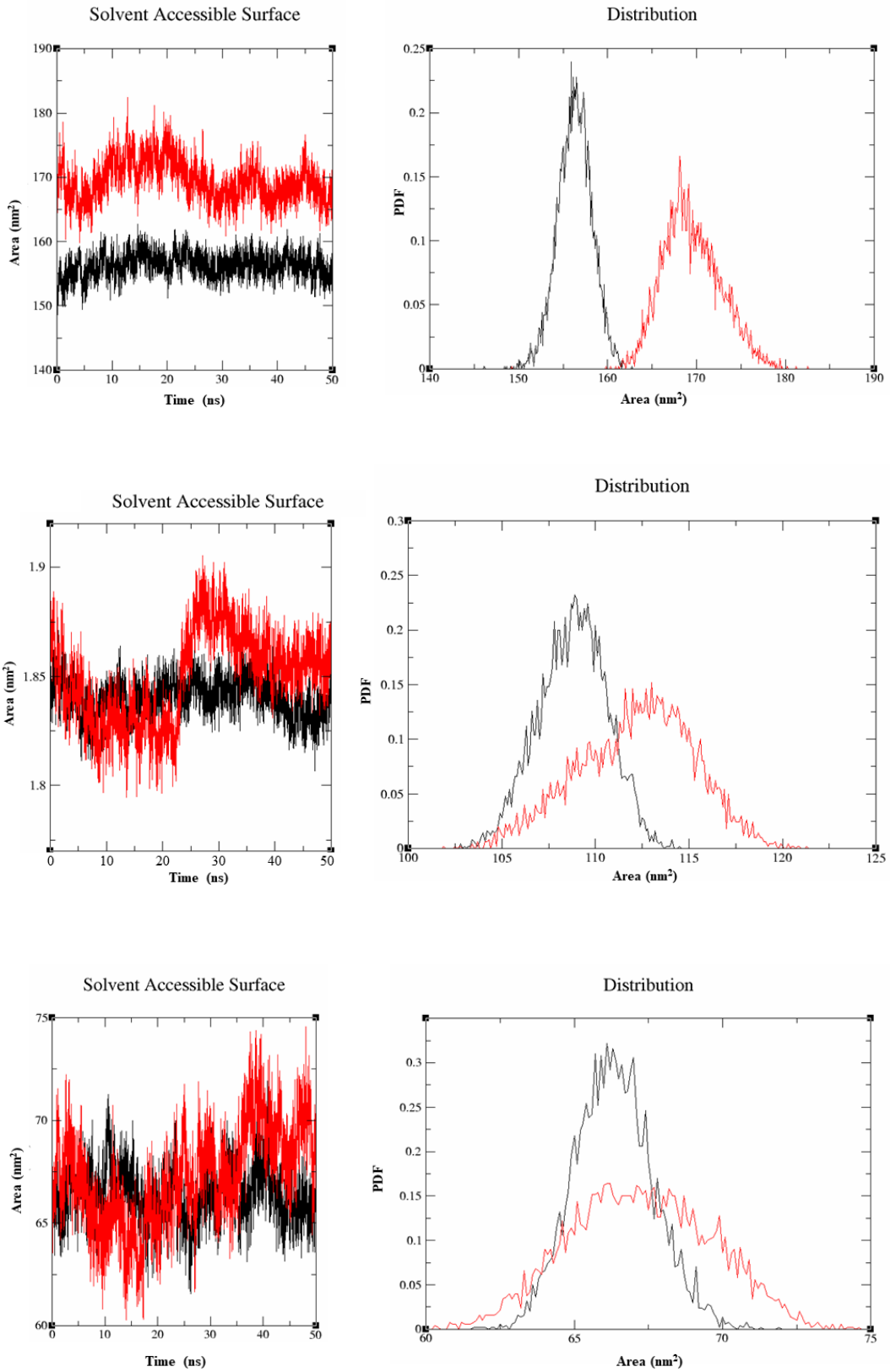

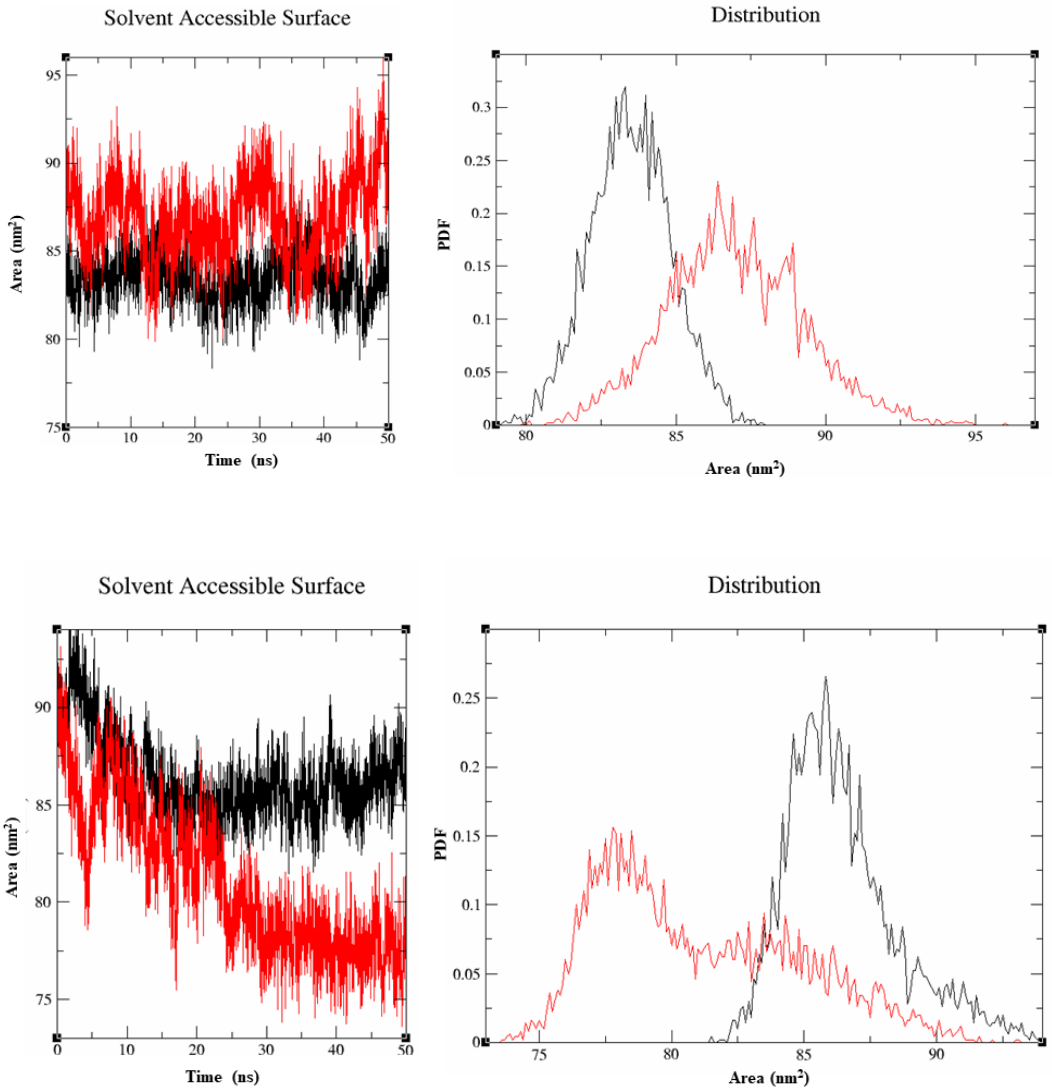

Figure S4.36: SASA Plots of Terrestrol A(**10**) with with PDB IDs 4K90, 6LZG, 6VSI , 6VXS and 7CR5 respectively along with their respective PDF plots.

4.3.7.5. Dynamics of Hydrogen Bonding

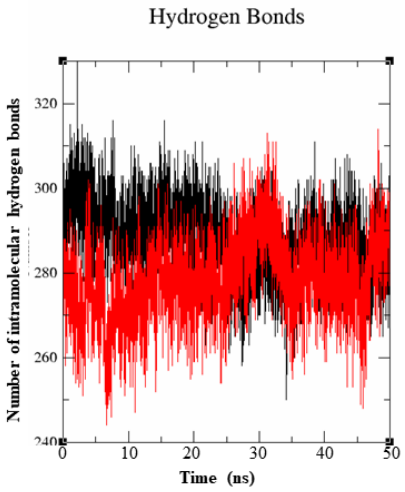
Hydrogen Bonds
Number of intramolecular hydrogen bonds
Time (ns)

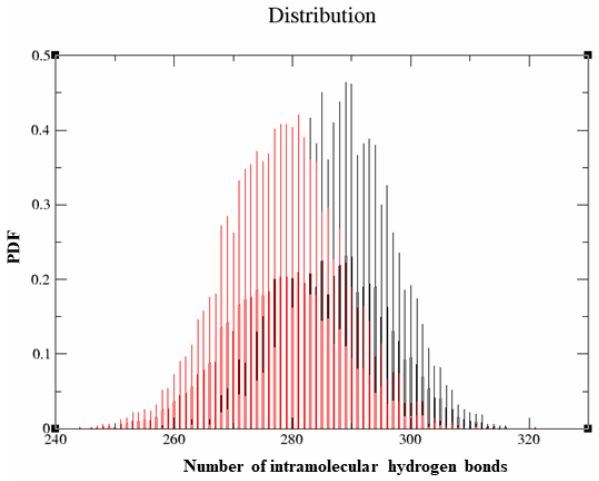
Distribution
PDF
Number of intramolecular hydrogen bonds

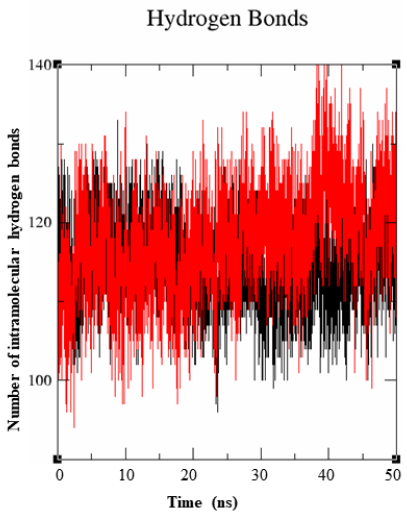
Hydrogen Bonds
Number of intramolecular hydrogen bonds
Time (ns)

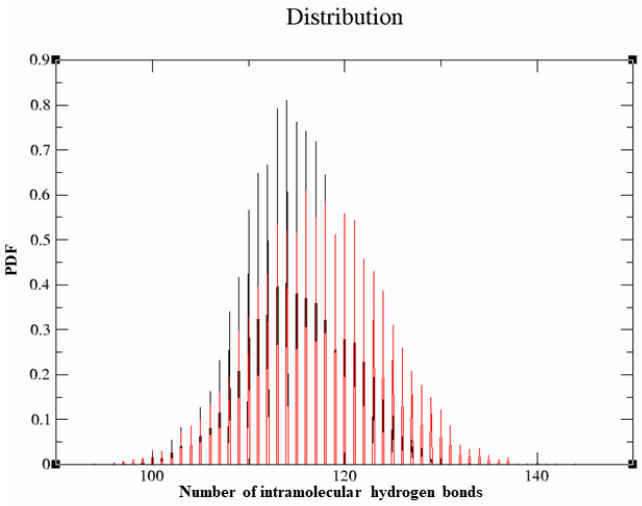
Distribution
PDF
Number of intramolecular hydrogen bonds

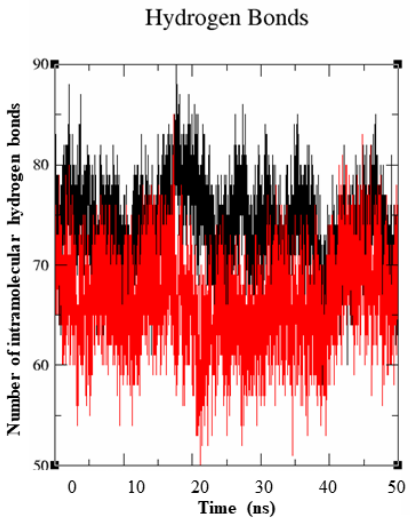
Hydrogen Bonds
Number of intramolecular hydrogen bonds
Time (ns)

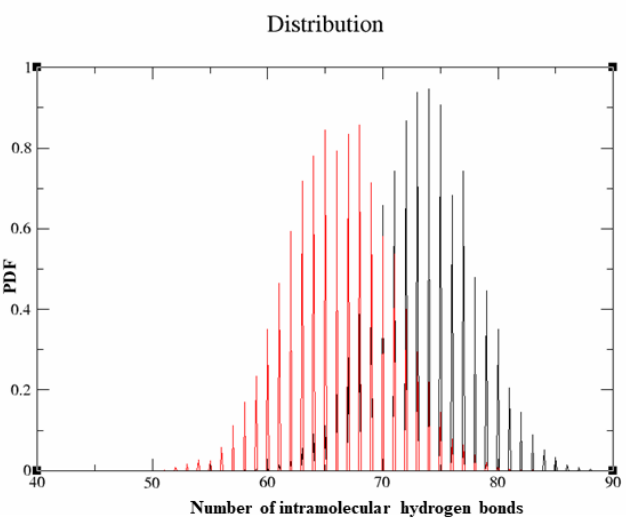
Distribution
PDF
Number of intramolecular hydrogen bonds

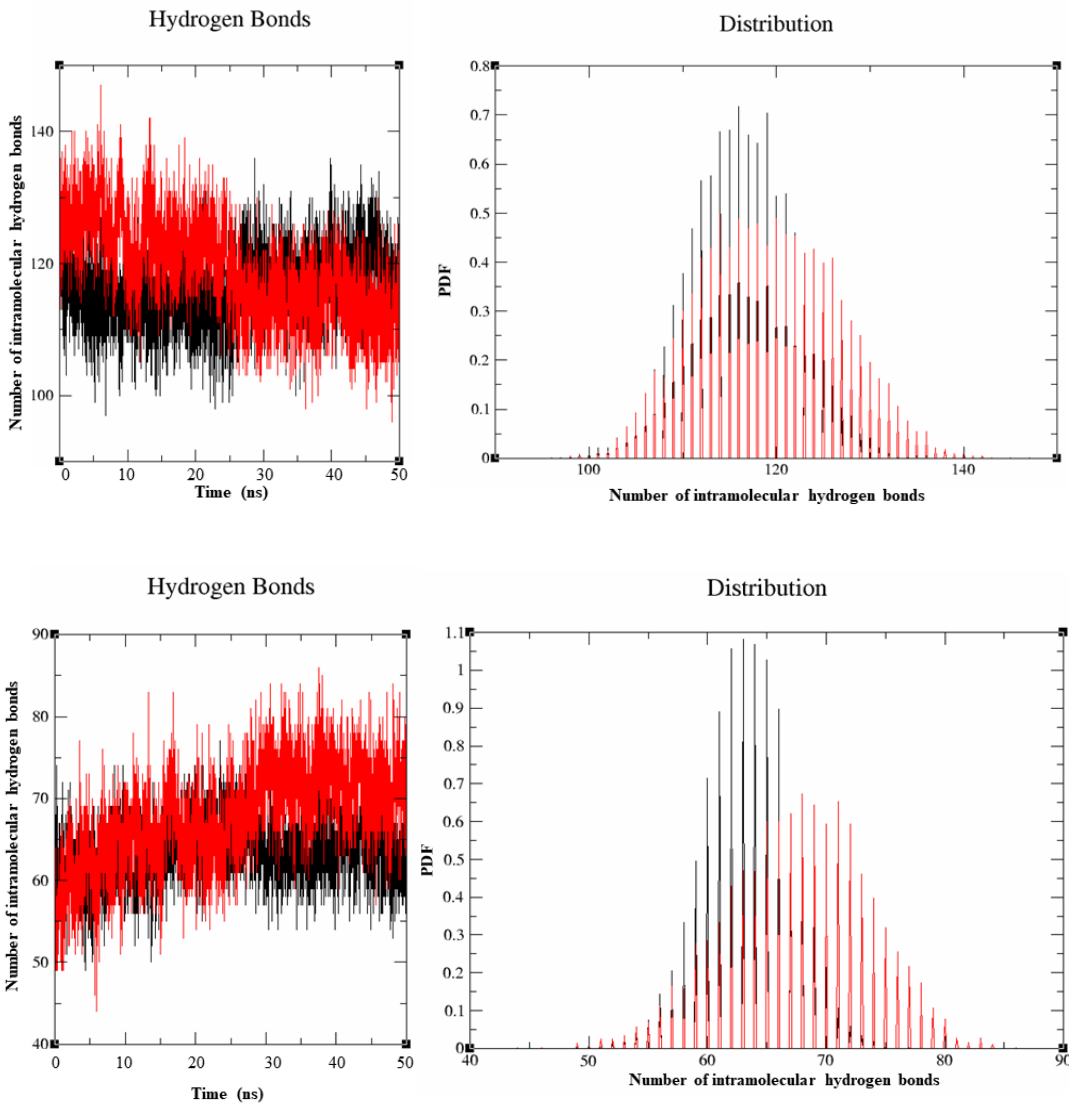

Figure S4.37: Hydrogen Bond Plots of Terrestrol A(**10**) with PDB IDs 4K90, 6LZG, 6VSI , 6VXS and 7CR5 respectively along with their respective PDF plots.

Chapter 5

Resveratrol-Inspired Structure-Guided Computational Profiling of AZD7762 as a Potent and Selective Modulator of LXRα, LXRβ, and FXR: A Targeted Analysis of the Underexplored Pathway in Cancer Therapeutics

This chapter delves into the use of a well-established phenolic compound, resveratrol, as a structural framework to screen for compounds or drugs that can target a relatively underexplored pathway in cancer, namely, the Liver X Receptors (LXRα and LXRβ) and the Farnesoid X Receptor (FXR). An extensive range of computational and quantum mechanical studies were employed to identify the most potent modulators of these receptors.

The text of this chapter has been published as:

- Singha, B., Gogoi, P. P., Longkumer, P., Ahmed, B., Boruah, N., Bezbaruah, B., & Sinha, U. B. (2025). A holistic computational exploration of AZD7762 as a potent selective modulator of LXRα, LXRβ and FXR: An underexplored pathway in cancer therapeutics. *Computers in Biology and Medicine, 194*, 110433.

5.1. Introduction

Cancer continues to represent a major global health burden, remaining one of the foremost causes of mortality. Despite the formidable challenges associated with its management, groundbreaking therapeutic advances are poised to transform treatment paradigms. Building upon established modalities, novel and emerging strategies are rapidly gaining scientific prominence [1-4]. These encompass immunotherapy approaches, including immune checkpoint inhibitors, adoptive T-cell transfer, monoclonal antibodies, therapeutic cancer vaccines, and immune modulators. Nanoparticle-based drug delivery systems are offering precise and targeted therapeutic options. Gene-editing technologies, such as CRISPR, are enabling the modification of oncogenes and tumor suppressor genes to combat cancer more effectively, and emerging receptor-targeted therapies are exploiting cancer-specific vulnerabilities with greater precision and reduced toxicity. Advances in artificial intelligence (AI) are improving the speed, accuracy, and consistency of cancer screening and detection. Simultaneously, computer-aided drug design (CADD) is streamlining the discovery and optimization of novel anticancer agents. Collectively, these developments are transforming the field of cancer research and influencing modern clinical practices. Liver X Receptors (LXRs) comprise two distinct isoforms: LXRα and LXRβ. These are encoded by the NR1H3 and NR1H2 genes, mapped to chromosomal loci 11p11.2 and 19q13.3, respectively [5]. Dysregulation of Liver X receptors (LXRs) significantly impacts cholesterol, lipid metabolism, inflammation and is associated with diseases such as obesity, metabolic dysfunction-associated fatty liver disease (MAFLD), cardiovascular disorders, Type 2 diabetes, osteoporosis, and cancer [6]. Additionally, the Farnesoid X receptor (FXR), also known as NR1H4, is a member of the nuclear receptor superfamily that regulates bile acid homeostasis, lipid metabolism, and inflammation, rendering it a vital therapeutic target for a broad spectrum of diseases [7]. Activation of FXR has demonstrated considerable therapeutic potential in the management of hepatic disorders such as primary biliary cholangitis (PBC) and non-alcoholic fatty liver disease (NAFLD), as well as various malignancies, metabolic dysregulation, and cardiovascular conditions [8]. Modulation of LXRs and FXR

initiate a cascade of cellular processes, with significant anticancer implications through diverse mechanisms as illustrated in **Figure 5.1**.

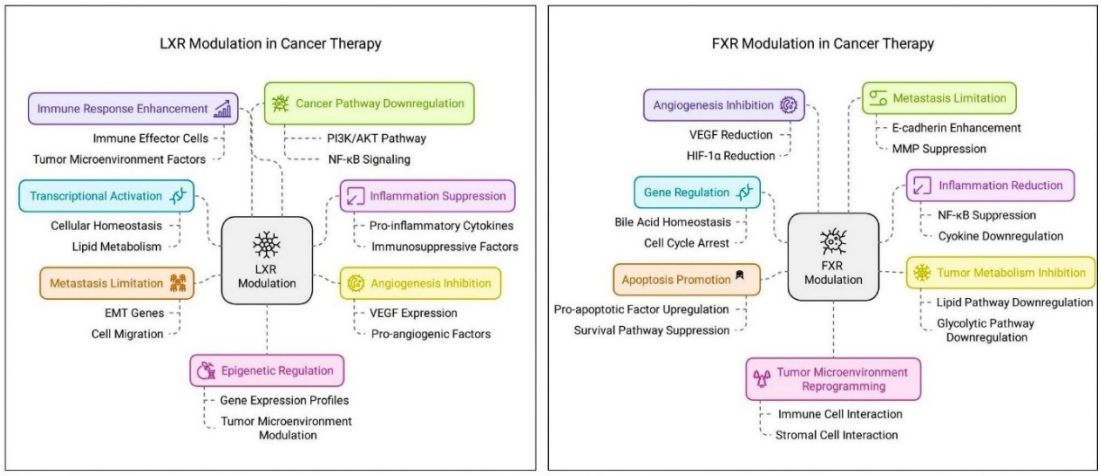

Figure 5.1: Illustration of LXRs and FXR modulation in cancer therapy highlighting key role.

In LXRs, these mechanisms involve the transcriptional activation of target genes essential for maintaining cellular homeostasis, regulating lipid metabolism, and controlling the cell cycle, thereby promoting tumor suppression. LXR activation suppresses inflammation by downregulating pro-inflammatory cytokines, while concurrently inhibiting tumor angiogenesis by reducing the expression of vascular endothelial growth factor (VEGF) and other pro-angiogenic factors. Additionally, these nuclear receptors may restrict metastasis by regulating genes involved in epithelial-mesenchymal transition (EMT) and cell migration, thereby potentially limiting cancer cell dissemination. LXR activation also promotes anti-tumor immune responses through immune modulation, involving the recruitment of immune effector cells or the suppression of immunosuppressive tumor microenvironment factors. Moreover, the downregulation of oncogenic pathways, including PI3K/AKT and NF-κB signaling, impairs cancer cell proliferation and survival. Epigenetic regulation, mediated by the activation of these receptors, may reprogram gene expression profiles in cancer cells, thereby reducing malignancy. Modulating the tumor microenvironment, including alterations in stromal or metabolic interactions, may further aid in limiting tumor growth and progression. These diverse mechanisms

highlight the potential of ligands targeting LXRs as a promising therapeutic strategy to exploit cancer cell vulnerabilities and improve clinical outcomes [9,10]. In FXR, ligand binding activates its function as a ligand-dependent transcription factor, facilitating coactivator recruitment to regulate genes governing bile acid homeostasis, metabolism, and cell cycle arrest. This regulation mitigates inflammation-driven carcinogenesis by inhibiting NF-κB and inflammatory cytokines such as IL-6 and TNF-α, while also suppressing tumor metabolism through the downregulation of lipid and glycolytic pathways. FXR activation promotes apoptosis by upregulating pro-apoptotic factors such as BAX and Caspase-3, while inhibiting survival signaling pathways like PI3K/AKT. Additionally, FXR suppresses angiogenesis by downregulating VEGF and HIF-1α expression, restricts metastasis by upregulating E-cadherin and inhibiting MMPs, reprograms the tumor microenvironment by modulating immune and stromal cell interactions. Epigenetic regulation by FXR may further silence oncogenes and activate tumor suppressor genes, while synergistic crosstalk with nuclear receptors such as LXRs and PPARα enhances its therapeutic efficacy. These diverse mechanisms highlight FXR as a compelling target for cancer therapy [11,12]. **Figure 5.2** shows findings on the modulation of Liver X Receptors (LXRα, LXRβ) and the Farnesoid X Receptor (FXR) in selected preclinical and clinical studies, emphasizing their roles and therapeutic potential in cancer research.

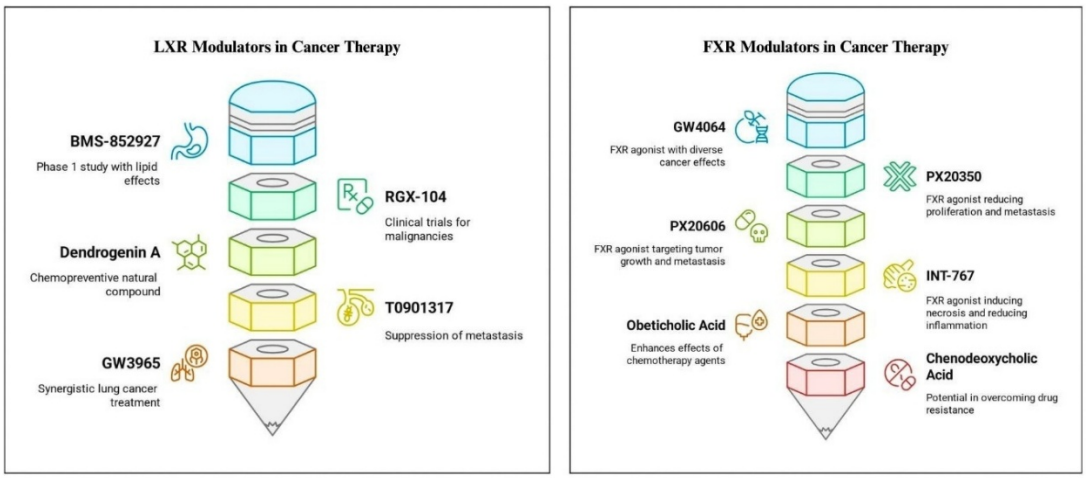

Figure 5.2: Overview of some LXRs and FXR modulators in cancer therapy in select preclinical and clinical studies

In breast cancer, LXRs forms heterodimers with RXRs, thereby regulating tumor growth and metabolic pathways. Agonists such as GW3965 suppress E2F2 expression, thereby limiting proliferation, while T0901317 hinders breast cancer progression and elevates IFN-γ levels, which inversely correlate with tumor growth [13–14]. LXR activation has been linked to reduced proliferation, metastasis, and angiogenesis in lung cancer cells, particularly in non-small cell lung cancer (NSCLC). T0901317 and GW3965 have additionally demonstrated synergistic activity with gefitinib (EGFR-TKI) in gefitinib-resistant NSCLC, suppressing AKT activation and Matrix Metalloproteinase-9 (MMP-9), a promoter of metastasis [15,16]. In hematological malignancies like acute myeloid leukemia (AML) and multiple myeloma (MM), LXR agonists including GW3965 and LXR-623 enhance the expression of cholesterol transporters such as ABCA1, induce apoptosis, and boost immune responses by increasing NK cell cytotoxicity *via* NKG2D ligand upregulation. Dendrogenin A (DDA), a cholesterol-based metabolite, promotes LXRβ-dependent autophagy in AML cells [17,18]. In hepatocellular carcinoma (HCC), LXRα activation suppresses tumor progression by downregulating α-SMA and TGF-β, while upregulating fatty acid synthase (FASN), suppressing tumor growth. Phytoconstituents such as Withaferin A and Bergapten act as LXRα/β agonists, suppressing tumor growth, angiogenesis, and migration by modulating PI3K/AKT pathways [19-21]. LXRs regulate cholesterol accumulation in colorectal cancer (CRC), with reduced expression of LXRα and LXRβ associated with CRC progression. T0901317 and GW3965 suppress proliferation, induce apoptosis, and inhibit the Wnt/β-catenin pathway, which governs CRC cell growth [22,23]. LXR activation has demonstrated potential in pancreatic ductal adenocarcinoma (PDAC), a highly lethal cancer. Agonists like GAC0003A4, GW3965, and T0901317 induce apoptosis and necroptosis by disrupting cholesterol metabolism, while LXR knockdown accelerates cancer progression [24,25]. Structural representations of these selected modulators are shown in **Figure 5.3.** FXR activation in gastric cancer promotes Caudal Type Homeobox 2 (CDX2) expression through its interaction with Small Heterodimer Partner (SHP), essential for inhibiting gastric metaplasia. CDCA treatment increases SHP-CDX2 interaction, while FXR or SHP knockdown negates this effect [26]. In renal cancer,

FXR activation by GW4064 downregulates the oncogene Oct3/4 in normal cells but promotes proliferation in cancer cells [27]. High FXR expression in breast cancer is associated with improved disease-free survival, as GW4064 reduces tumor growth *via* leptin signaling inhibition and SOCS3 induction. FXR agonists like CDCA decrease proliferation in tamoxifen-resistant cells and induce apoptosis in various breast cancer lines [28,29]. In prostate cancer, FXR mitigates androgen signaling by lowering glucuronidation and enhancing PTEN expression, leading to reduced proliferation; however, FXR expression is low in this context [30]. Feroline, a novel FXR modulator, induces conformational changes in FXR, potentially aiding drug design [31]. Guggulsterone serves as an antagonist of FXR in co-activator recruitment assays yet simultaneously enhances bile salt export pump (BSEP) gene transcription.

In colon cancer, FXR inhibits tumor growth by suppressing Src-mediated EGFR activation and enhancing TRAIL-mediated apoptosis. Activation by GW4064 or FXR overexpression further attenuates cellular proliferation by inhibiting EGFR and ERK1/2 signaling pathways [32-34]. In pancreatic cancer, FXR activation promotes tumor progression *via* p38-MAPK and PI3K/AKT pathways, although GW4064 can mitigate this effect [35]. In bone cancer, FXR activation elevates miR-23b-3p, leading to cell cycle arrest and apoptosis in osteosarcoma [36]. In esophageal cancer, FXR inhibits tumor growth by enhancing p27Kip1 and CDX2 expression [37]. In non-small cell lung cancer, FXR knockdown reduces proliferation and induces cell cycle arrest, indicating that high FXR levels suppress tumor growth [38]. In biliary tract cancer, FXR agonists like (OCA) obeticholic acid and GW4064 inhibit proliferation and induce apoptosis in cholangiocarcinoma models, with enhanced effects observed in combination with chemotherapeutics [39-40]. In hepatocellular carcinoma, FXR activation downregulates oncogenes like gankyrin and induces tumor suppressors such as p53 and HNF4α, inhibiting tumor progression. FXR agonists such as INT-767, PX20350, and PX20606 exert anti-tumor effects through bile acid metabolism regulation and apoptosis promotion [41-42]. Structural representations of these selected modulators are shown in **Figure 5.3**. Harnessing adaptive immunity through checkpoint inhibitors has revolutionized cancer treatment. Activation of the Liver-X nuclear receptor (LXR) reduces myeloid-derived suppressor cells (MDSCs), thereby

enhancing cytotoxic T lymphocyte (CTL) responses *via* ApoE-mediated pathways, ultimately amplifying anti-tumor immunity and improving checkpoint inhibitor efficacy. Likewise, the Farnesoid X Receptor (FXR) is pivotal in immune regulation and modulation of the tumor microenvironment (TME). FXR agonists, such as GW4064, enhance PD-L1 expression in colorectal cancer cells, showing synergistic effects when combined with PD-L1 or PD-1 antibodies, leading to tumor regression in preclinical models. These findings highlight the potential of LXR and FXR activation in enhancing immune checkpoint therapies across cancer types [43-44].

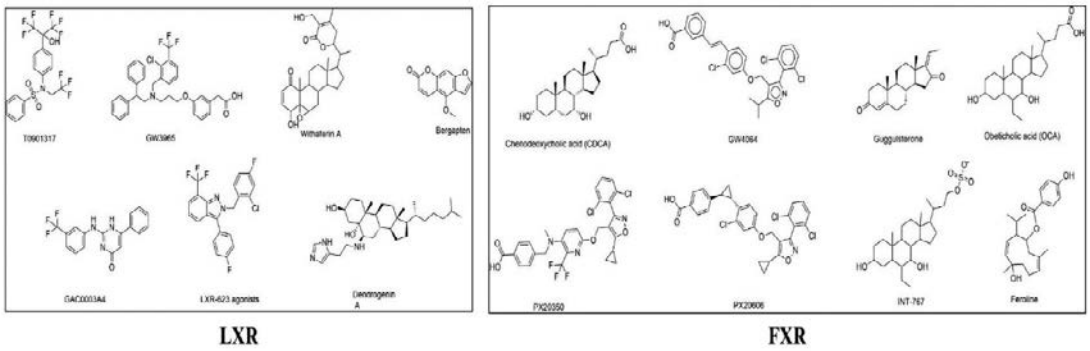

Figure 5.3: Structural representations of selected modulators of LXRs and FXR

Lifestyle and environmental factors may also influence the activity of Liver X Receptors (LXRs) and Farnesoid X Receptors (FXRs), thereby impacting cancer susceptibility. Behaviors such as smoking, alcohol consumption, lack of exercise, and obesity etc can contribute to cancer and its progression [45]. Research has demonstrated that phenolic compounds hold significant potential as anticancer agents by inducing apoptosis, inhibiting proliferation, and targeting angiogenesis, growth, and metastasis. Resveratrol, a polyphenol primarily found in grapes and red wine, possesses antioxidant properties that may guard against cancer, cardiovascular diseases, neurodegeneration and is anticipated to contribute to cancer treatment advancements and therapeutic breakthroughs [46]. Resveratrol modulates lipid metabolism in macrophages by upregulating LXRα, enhancing cholesterol efflux gene expression (e.g., ABCA1, ABCG1) and suppressing lipid uptake genes (e.g., LPL, SR-AII), potentially reducing foam cell formation and atherosclerosis [47]. In HBVX protein transgenic mice, resveratrol (30 mg/kg/day) demonstrated therapeutic effects

on early liver damage, indicating its potential in preventing HBV-related hepatocellular carcinoma [48]. In aged NAFLD rats, it upregulated LXR and FXR, correlating with reduced serum lipids and hepatic apoptosis [49]. As an FXR agonist, resveratrol may alleviate drug-induced cholestasis and induces LXRα expression in macrophages. Combined with exercise, it further enhances LXR and FXR expression, improving lipid metabolism and reducing hepatic apoptosis [50]. Resveratrol also promotes trans-intestinal cholesterol excretion by upregulating duodenal ATP-binding cassette transporters while downregulating NPC1L1, with LXRα serving as a central mediator [51]. Furthermore, it suppresses the expression of lipogenic genes Srebp1-c and PPARγ in HBx transgenic mice, thereby promoting liver regeneration and reducing hepatocarcinogenesis [52]. Key challenges in cancer therapy include tumor heterogeneity, drug resistance, late diagnosis, metastasis, targeting cancer stem cells, insufficient biomarkers, severe side effects, and inefficient drug delivery systems. Thus, new and emerging strategies that target different pathways and mechanisms are necessary. Despite significant progress in biotechnology and our understanding of disease biology, drug development remains complex, costly, and time-consuming, requiring multidisciplinary collaboration [53]. However, advances in 3D molecular modeling, computational tools, and bioinformatics have significantly accelerated drug discovery. Since the development of the first target-based drug, the HIV protease inhibitor Viracept, in 1997 [54], computational approaches have played a crucial role in reducing costs and enhancing efficiency. Emerging technologies such as quantum mechanics-based algorithms, machine learning, and supercomputing are poised to further improve precision and usher in a new era of drug development [55]. Several FDA-approved anticancer drugs, including Crizotinib for lung and esophageal cancers and Axitinib for advanced renal cell carcinoma, have been identified through structure-based drug design [56]. These breakthroughs highlight the significant role of computational tools in accelerating anticancer drug discovery, fueling optimism for their future applications across various diseases. This study investigates the selective modulation of LXRα, LXRβ, and FXR to address current challenges in cancer therapy and lay the groundwork for more effective treatment strategies. By targeting these receptors selectively, the approach aims to improve specificity, reduce off-target

effects, and modulate key pathways involved in cancer progression, making therapies potentially safer and more effective. There is still a shortage of potent modulators that can precisely target these pathways. To address this, a comprehensive computational analysis was conducted, as outlined in **Figure 5.4**. The study focused on identifying and developing selective modulators for LXRα, LXRβ, and FXR using a strong theoretical foundation. Advanced techniques such as molecular docking, molecular dynamics simulations, quantum calculations, binding free energy analysis, pharmacophore mapping and other sophisticated techniques were employed. These findings support the design of targeted therapies with improved precision and efficacy, offering a promising direction for future cancer treatment.

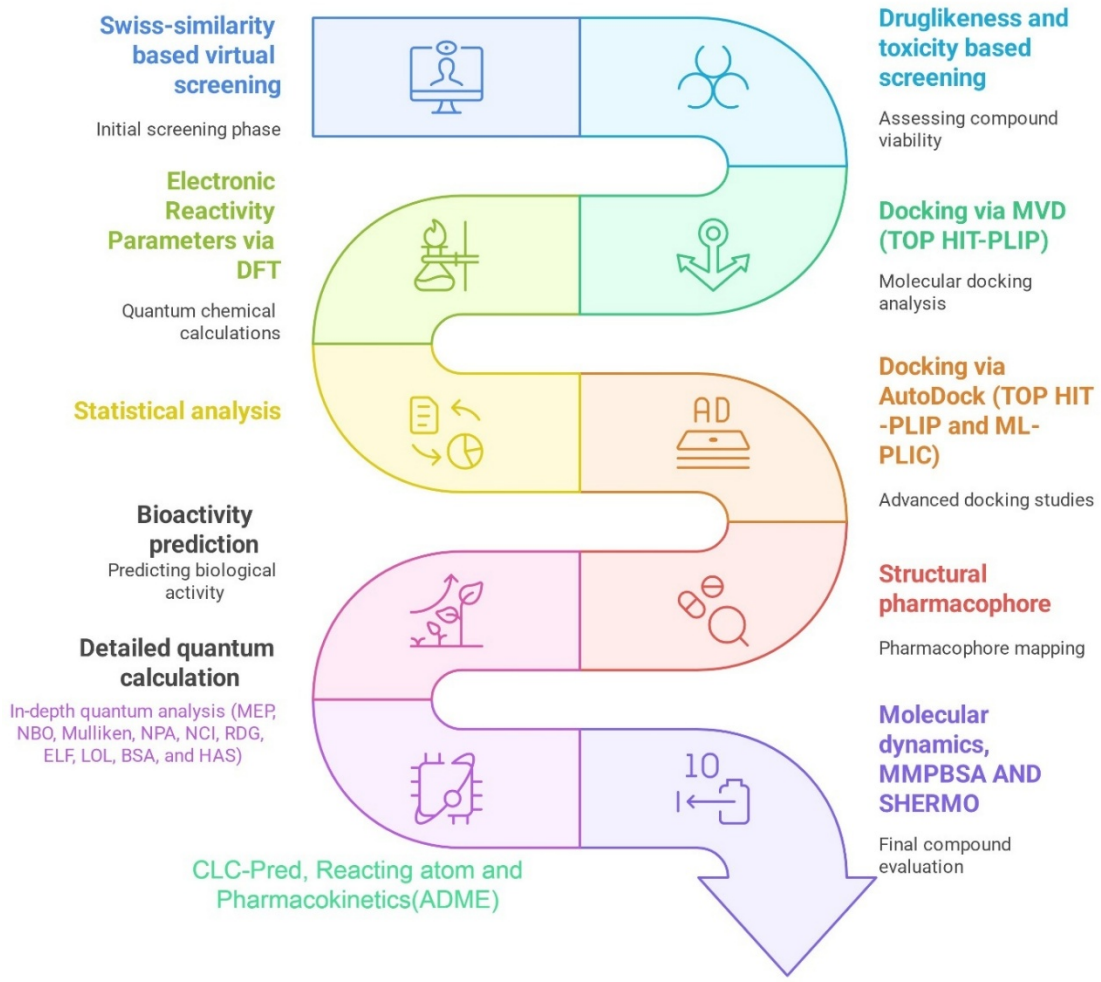

Figure 5.4: Workflow of the comprehensive computational studies conducted.

5.2. Materials and methods

5.2.1. Swiss- similarity based virtual screening

Virtual screening was conducted using the Swiss-Similarity platform (http://www.swisssimilarity.ch/), with resveratrol as the lead scaffold. Canonical SMILES representations, obtained from the NCBI PubChem database (https://pubchem.ncbi.nlm.nih.gov/), was used to represent compound structures. The

screening primarily focused on drugs as the class of compounds, generating three distinct libraries based on molecular similarity: (1) Library 1, derived from DrugBank; (2) Library 2, derived from ChEMBL-approved drugs; and (3) Library 3, comprising ChEMBL drug candidates in clinics. The selection was guided by both 2D and 3D molecular fingerprints to ensure structural alignment with the resveratrol scaffold.

5.2.2. Druglikeness and toxicity-based screening

The initial evaluation of drug-likeness and toxicity profiling represents a critical step in the drug discovery and development pipeline, enabling the elimination of compounds with low therapeutic potential from a broader set of bioactive candidates [57]. Drug-likeness was assessed based on established physicochemical parameters, including Lipinski's Rule of Five, along with Ghose, Veber, Egan, and Muegge criteria, using the SwissADME web server (http://www.swissadme.ch/) [58]. Subsequently, toxicity profiling was carried out *via* the ProTox-II web server (http://tox.charite.de/protox_II), which included predictions of oral toxicity (LD50 in mg/kg), organ-specific toxicities such as hepatotoxicity, and risk assessments for mutagenicity, carcinogenicity, cytotoxicity, and immunotoxicity. SMILES representations were used as input for both platforms to generate predictive outcomes.

5.2.3. Target selection

The targets relevant to Liver X Receptors (LXRα and LXRβ) and Farnesoid X Receptor (FXR) for the present study were obtained from the Research Collaboratory for Structural Bioinformatics (RCSB) Protein Data Bank (PDB) (http://www.rcsb.org/). The specific PDB entries utilized are as follows:

- PDB ID (**1UHL**): Crystal structure of the LXRα-RXRβ ligand-binding domain (LBD) heterodimer [59].
- PDB ID (**1UPV**): Crystal structure of the human Liver X receptor beta (LXRβ) ligand-binding domain in complex with a synthetic agonist [60].
- PDB ID (**5ICK**): A unique binding model of FXR ligand-binding domain (LBD) with feroline [61].

5.2.4. Ligand selection

The compounds that passed both drug-likeness and toxicity screening, including resveratrol, were subjected to molecular docking simulations. To ensure the reliability of the docking protocol, re-docking of native co-crystallized ligands with their corresponding target proteins was performed. These ligands originally resolved within the crystal structures serve as internal references for evaluating docking accuracy. T0901317 (**Figure 5.3**) was identified as a dual co-crystallized ligand for LXRα (PDB ID: 1UHL) and LXRβ (PDB ID: 1UPV), while Feroline was associated with FXR (PDB ID: 5ICK). Additionally, Withaferin A, Bergapten, and Obeticholic Acid were included as reference standards to support comparative pharmacological assessments.

5.2.5. Docking *via* Molegro virtual docker

5.2.5.1. Ligand preparation

The ligands, initially retrieved in SDF format from the PubChem database (https://pubchem.ncbi.nlm.nih.gov), underwent 2D-to-3D conversion using ChemBioDraw Ultra 12.0. Subsequent energy minimization was carried out using the MM2 force field to achieve geometrically optimized conformations. The MM2 force field, specifically designed for small to medium-sized organic compounds, is widely applied in receptor-ligand docking due to its proven reliability in modeling molecular interactions. These preparatory steps are essential for refining ligand structures, thereby improving the accuracy of docking predictions.

5.2.5.2. Docking

Molecular docking was performed using Molegro Virtual Docker 6.0 (MVD) [62], a widely recognized computational tool in medicinal chemistry known for its high predictive accuracy in ligand–receptor interactions. MVD has been extensively validated across diverse protein targets, demonstrating performance comparable to AutoDock4 and AutoDock Vina. Notably, MVD boasts an exceptional success rate of 87.0%, surpassing other well-established docking methodologies, including Glide (81.8%), GOLD (78.2%), Surflex (75.3%), and FlexX2 (57.9%), thereby underscoring

its preeminence in ligand-binding accuracy [63]. Following protein import, the protein preparation wizard is used to remove solvent molecules, cofactors, and irrelevant native ligands. Our docking protocol adhered to standard practices by excluding all water molecules. Shell water molecules (SWs) were excluded from our analysis due to their potential to distort the native architecture of the binding pocket [64]. Their presence can obscure hydrophobic regions and introduce non-physiological hydrogen bonding patterns that are unlikely to persist during actual ligand binding events. They may act as barriers, preventing the drug from directly interacting with the receptor. An effective drug is designed to displace these obstructive waters to enable optimal binding. Thermodynamically, not all SWs contribute to complex stability, many exhibit unfavorable energetic profiles (e.g., high enthalpy and low entropy), making their displacement advantageous upon ligand association [65]. Retained water molecules may fail to adapt to ligand conformations, resulting in unrealistic hydration networks, or biased binding site predictions. Treating the protein as rigid is commonly acceptable in docking studies, as many protein-ligand interactions do not involve significant structural changes. In our study, we employed a semi-flexible docking strategy, wherein, the receptor is typically treated as a rigid body while the ligand retains conformational flexibility. This approach enables the sampling of multiple ligand conformers within the static binding site architecture of the protein. Compared to rigid docking, this method generally provides improved accuracy in predicting ligand binding modes, as it accounts for the dynamic nature of the ligand while maintaining computational efficiency [66]. In one study, a comparative evaluation of semi-flexible and fully flexible docking strategies demonstrated that the increased computational demands of fully flexible docking did not result in a significant enhancement in predictive accuracy [67]. Protein energy minimization may distort the original binding site geometry and assumes that force fields outperform experimental data, which is often not the case. To preserve biological relevance, we retained the original crystallographic coordinates. In contrast, ligand minimization is more appropriate for improving docking accuracy. Additionally, MVD facilitates error correction in protein structures during preparation through features like "Repair and Optimize Residues" and "Optimize Neighborhood," enhancing docking accuracy.

MVD employs an internal cavity-detection algorithm to identify potential ligand-binding sites within the protein structure, typically identifying and ranking five cavities by surface area, with priority given to larger cavities due to their ligand accommodation potential. The identification of binding sites is frequently corroborated by the existence of native co-crystallized ligands within the PDB structure. The native (co-crystallized) ligand was employed as the structural reference to define the binding site for all docking studies, a widely accepted approach in structure-based drug design. This method ensures that ligand docking is performed within a biologically relevant pocket, accurately reflecting the spatial orientation and chemical environment of the true binding site. Moreover, this technique minimizes the risk of identifying artificial binding sites that can result from automated pocket detection algorithms. However, in our case, the binding cavity with the largest volume, identified through cavity detection analysis, was located precisely around the respective ligand in all targets of interest, further validating its relevance and suitability for docking studies. By anchoring the docking grid to those ligands that is experimentally validated to bind within the active site, the study ensures robust and reproducible results that align with physiological relevance. The binding site coordinates of this site, derived from the atomic center of the native ligand, are provided below.

- **PDB ID: 1UHL** (**Chain B**: *Oxysterols receptor LXR-alpha*), Cavity 1 with a volume of 372.736 cubic angstroms (Å^3)**,** center X: 78.25, Y: -1.96, Z: 13.85, within a constraint of a radius of 16 Å.
- **PDB ID: 1UPV** (**Chain A**: *Oxysterols receptor lxr-beta*), Cavity 1 with a volume of 189.952 cubic angstroms (Å^3)**,** centre designated as X: 40.92, Y: -0.75, Z: 15.76, within a constraint of radius 13 Å.
- **PDB ID: 5ICK** (**Chain A**: *Bile acid receptor*), Cavity 1 with a volume of 99.84 cubic angstroms (Å^3)**,** centre designated as X: 26.06, Y: -5.18, Z: 46.50, within a constraint of radius 12 Å.

In this study, docking parameters were carefully set using the MolDock scoring function [GRID], with a grid resolution of 0.30 Å to ensure accurate prediction of

binding affinities. The maximum iteration limit for all specified PDB IDs was set at 1,500, while the maximum population size was designated as 50. Subsequently, 35 independent instantaneous runs were conducted for each ligand to optimize docking precision. The primary scoring parameters included the MolDock score and the Re-rank score. Further analysis was conducted to assess the interactions between the ligands and the receptors [68].

5.2.5.2.1. Scoring functions

The MolDock scoring function in MVD is based on Piecewise Linear Potential (PLP) approach [69]. It evaluates binding interactions through two principal metrics: the MolDock Score and the Re-rank Score, each quantifying interaction energies with differing levels of precision

- **MolDock score**

The docking score, referred to as the E_{score}, encompasses contributions from distinct energetic components [70]. It comprises two primary components: the interaction energy between the ligand and the protein (E_{inter}) and the internal energy of the ligand itself (E_{intra}), as outlined in equation 1.

$$E_{score} = E_{inter} + E_{intra} \quad \ldots(1)$$

As shown in equation 2 below, the interaction energy term (E_{inter}) comprises the cumulative contributions from ligand–protein, ligand–water, and ligand–cofactor interactions

$$E_{inter} = \sum_{i=ligand} \sum_{j=protein} \left[E_{PLP}(r_{ij}) + 332.0 \frac{q_i q_j}{4 r_{ij}^2} \right] \quad \ldots(2)$$

The EPLP scoring term utilizes a piecewise linear potential incorporating two key parameters: one to simulate van der Waals (steric) forces and another, with a steeper

potential, to capture hydrogen bonding interactions. Electrostatic contributions between charged species are modeled using a Coulombic potential, where the dielectric constant varies with interatomic distance as D(r) = 4r. A conversion factor of 332.0 is applied to express the electrostatic energy in kcal/mol. To prevent the attractive electrostatic component from dominating over repulsive core-core interactions, contributions from atom pairs within 2.0 Å are excluded.

E_{intra}, as shown in equation 3, is calculated by summing interaction energies among all non-bonded atomic pairs within the ligand, excluding those separated by two or fewer bonds. This energy encompasses various components, including electronic interactions, hydrogen bonding, steric clashes, sp^2–sp^2 repulsion, torsional strain (both general and ligand-specific), van der Waals forces, soft constraint penalties, and solvation effects.

$$E_{intra} = \sum_{i=ligand} \sum_{j=protein} E_{PLP}(r_{ij}) + \sum_{flexible\ bonds} A[1 - \cos(m.\theta - \theta_0)] + E_{clash} \quad \ldots(3)$$

The torsional energy component is modeled based on the hybridization states of the atoms involved, and when multiple torsional modes are present, their average contribution is considered and θ indicates the angle of torsion between the bonds. Additionally, the clash energy (E_{clash}) addresses steric hindrance between heavy atoms by applying a substantial penalty—1000 units when the interatomic distance is below 2.0 Å, and 10,000 units if a heavy atom lies outside the defined interaction region specified by the spherical grid boundary

- **Re-rank score**

In MVD, the re-rank score serves as an estimate of interaction strength and is not expressed in standard chemical units or based on complex energy components. After

generating one or more potential poses, additional energy terms are computed and combined to yield the re-rank score. This score incorporates terms from the docking function, including sp2-sp2 torsion and Lennard-Jones 12-6 potentials [71]. While more computationally demanding than the primary scoring functions (MOLDOCK and PLANTS), the re-rank score is often more reliable for identifying the optimal pose and evaluating ligand-binding affinity.

5.2.5.3. Protein-Ligand Interaction Profiler (PLIP)

PLIP was employed to analyze the molecular interactions between the ligand and its target [72]. The interaction profile consists of key features and their corresponding quantitative values, which represent the specific interactions occurring within the protein-ligand complex. These features are derived from the ligand's structural properties and the characteristics of the interacting residues at the binding site.

5.2.6. Electronic Reactivity Parameters *via* DFT

Ligands previously subjected to molecular docking using Molegro Virtual Docker (MVD) were subsequently evaluated for their electronic stability and chemical reactivity through Density Functional Theory (DFT) calculations. Molecular geometries were optimized employing the B3LYP functional in the gas phase to ensure optimal results. A 6-311G++(d,p) basis set was utilized, with computational executions facilitated by the Gaussian 16W software package [73]. Molecular visualization and analysis were conducted using GaussView 6.0 [74], enabling accurate interpretation of the optimized structures. The HOMO–LUMO energy gap plays a crucial role in determining the electronic reactivity characteristics of a molecule. Koopmans' theorem offers an alternative approach for estimating the ionization potential (IP) and electron affinity (EA) by utilizing the orbital energies of neutral, optimized molecules. A substantial number of studies has consistently employed Koopmans' approximation as a standard and widely accepted method for estimating global reactivity descriptors, particularly within the framework of Density Functional Theory (DFT) [75,76]. This well-established approach is grounded in theoretical validity and has demonstrated efficacy across diverse chemical systems.

Accordingly, our adoption of Koopmans' approximation is fully aligned with prevailing computational protocols making it dependable. According to this theorem, the ionization potential is approximated by the negative of the energy of the highest occupied molecular orbital (HOMO), while the electron affinity is the negative of the energy of the lowest unoccupied molecular orbital (LUMO) as shown in equation 1 and 2. Utilizing the HOMO and LUMO energies, global chemical reactivity descriptors given below were derived using equation 1-7 along with dipole moment.

The ionization potential (IP)refers to the energy required to remove an electron from a molecule and is related to the E_{HOMO} by the equation 1:

$$IP = -E_{HOMO} \text{ ..... } (1)$$

Electron affinity (EA), on the other hand, is the energy released when an electron is added to a system and is linked to E_{LUMO} through the equation 2:

$$EA = -E_{LUMO} \text{..... } (2)$$

Once the values of IP and EA are known, electronegativity (χ) and global hardness (η) can be determined. Electronegativity represents an atom's or molecule's ability to attract electrons and is calculated using the equation 3:

$$\chi = (IP + EA)/2 \text{……. } (3)$$

Global hardness (η), which measures the resistance of an atom to charge transfer, is given by the following equation 4:

$$\eta = (IP - EA)/2 \text{……. } (4)$$

Chemical softness (S) quantifies the ability of an atom or group of atoms to accept electrons and is calculated as per the equation 5:

$$S = 1/2\ \eta \text{ ……... } (5)$$

Electrophilicity index (ω), which measures a species' tendency to accept electrons, is given by the equation 6 as follows:

$$\omega = \mu^2/2\eta = -\chi^2/2\eta \ldots\ldots\ldots (6)$$

The chemical potential (μ) reflects the likelihood of a chemical reaction. It is given by the equation 7 as follows:

$$\mu = -\chi \ldots\ldots\ldots (7)$$

5.2.7. Statistical analysis

5.2.7.1.Correlation matrix

A correlation matrix was constructed to analyze the relationships between molecular docking scores obtained from Molegro Virtual Docker (MVD) and quantum chemical parameters, including Frontier Molecular Orbital (FMO) energies and global reactivity descriptors obtained from Density Functional Theory (DFT), using Microsoft Excel 2013: Microsoft Corporation (2013). This analytical strategy enables the evaluation of how electronic properties predicted by DFT align with binding energy observed in docking simulations.

5.2.7.2.Principal component analysis

Subsequently, principal component analysis (PCA) was conducted using PAST 4.11 software to identify clusters of compounds sharing similar molecular characteristics and docking scores. PAST version 4.1,1 developed by Hammer Ø., Harper D.A.T., and Ryan P.D. (2001) as part of the Palaeontological Statistics toolkit.

5.2.8. Docking *via* AutoDock

5.2.8.1.Docking

To further validate the molecular docking results obtained from MVD, additional docking simulations were performed using AutoDock 4.2 [77] for the top hit compound alongside resveratrol, native T0901317 (LXRα: 1UHL; LXRβ: 1UPV), native feroline (FXR: 5ICK), withaferin A, bergapten and obeticholic acid, included as benchmark compounds for comparative analysis. This analysis aimed to cross-verify binding affinities and interaction profiles, enhancing confidence in the docking results and identifying highly specific therapeutic candidate. The native co-

crystallized ligand served as a reference to define the binding cavity, analogous to MVD, where the predicted binding site was centered around the native co-crystallized ligand. A grid box was constructed around the native ligand's coordinates, ensuring docking was confined to the experimentally validated site. The binding site axes were then compared to those generated by MVD, revealing close proximity and alignment. The ligands were treated as flexible to explore conformational space, while the protein was kept rigid, as functional binding sites typically exhibit minimal flexibility, making this approach standard in docking studies. The spatial orientation of the target proteins in 3D coordinates was as follows: for 1UHL, coordinates were set at x = 75.783, y = -4.867, z = 15.968; for 1UPV, x = 38.802, y = 0.527, z = 15.276; and for 5ICK, x = 26.558, y = -5.560, z = 47.545. The docking grid, critical for delineating the active binding region, was configured with dimensions of 50 × 50 × 50 grid points for both 1UHL and 1UPV, while for 5ICK, the grid was established at dimensions of 40 × 40 × 40 grid points. The docking procedure employed aligns with standard practices where water molecules are not retained, as their inclusion can misrepresent binding sites by treating them as non-standard residues or ligands. Prior to docking, ligands underwent optimization by assigning Kolmann and Gasteiger [78] partial charges, subsequently saved in the PDBQT format. The grid preparation involved key steps such as macromolecule selection, determination of map types, grid box configuration, and preparation of the grid parameter file. The docking procedure utilized a genetic algorithm with defined parameters from AutoDock 4.2 [79], leading to the formulation of the docking parameter file. Docking simulations were executed using the autogrid4 and autodock4 executable files. The docked protein-ligand complexes were visualized utilizing Biovia DS 2024 [80], with selection criteria predicted on binding affinity and RMSD values thereby elucidating the molecular interactions under investigation.

5.2.9. Protein-Ligand Interaction Profiler (PLIP)

PLIP was also utilized in this case to evaluate the molecular interactions between the ligand and its corresponding target.

5.2.10. Molecular Ligand-Protein Interaction Classifier (ML-PLIC)

Given the growing impact of machine learning in computational drug discovery, a pilot study was conducted on the top hit compound to evaluate its alignment with the results obtained from simulations performed using AutoDock. The ML-PLIC platform [81], which leverages advanced machine learning algorithms to predict and characterize ligand-protein interactions, was employed for this purpose. QuickVina, a variant of AutoDock Vina, was utilized as the default docking engine. To ensure consistency, the binding site coordinates were meticulously aligned with those used in the AutoDock simulations. All other parameters were maintained at their default settings to standardize the docking process and facilitate a meaningful comparison of results between traditional and machine learning-assisted methods.

5.2.11. Structural pharmacophore

To assess common pharmacophoric features, structural pharmacophore mapping was carried out using LigandScout software [82]. Compounds validated *via* AutoDock were selected for further analysis, with pharmacophore models constructed based on the native co-crystallized ligands. The software enabled retrieval of corresponding PDB files, followed by protein refinement to exclude non-essential elements, such as water molecules, while retaining the native ligands. Energy minimization of the ligands was performed using the MMFF94 force field to achieve optimal geometric configurations. The MMFF94 force field is widely used for modeling organic molecules, especially in drug design. Its strong setup, covering van der Waals, electrostatic, and torsional interactions, enables proper conformational energy calculations. Ligands were positioned within their respective active sites, with ligand geometries refined under the same force field. Alignment with native co-crystallized ligands ensured accurate spatial conformation and interaction profiling, facilitating structural pharmacophore generation. This analysis reveals shared structural motifs and key pharmacophoric features, such as hydrogen bond donors/acceptors and hydrophobic interactions etc., facilitating an in-depth evaluation of molecular interactions and guiding compound optimization for therapeutic potential [83].

5.2.12. Bioactivity prediction

The bioactivity scores of compounds validated through AutoDock were evaluated using Molinspiration (https://www.molinspiration.com), which evaluates interactions with various biological target receptors. This analysis provided predictive insights into the compounds' affinity for key drug targets, including GPCR ligands, ion channel modulators, kinase inhibitors, nuclear receptor ligands, protease inhibitors, and enzyme inhibitors. Predictions were performed using input files in SDF or SMILES format, facilitating detailed pharmacological profiling and expediting the identification of promising candidates [84].

5.2.13. Detailed quantum calculation

Quantum mechanical calculations were carried out to investigate the molecular interactions and properties of the selected compounds. Density Functional Theory (DFT) analyses were performed using Gaussian 16, with GaussView employed to enhance visualization of molecular structures and electronic properties, enabling optimization and energy calculations essential for understanding molecular behavior. The top-ranked compound, along with resveratrol, native ligands, and standard references, was included as a benchmark for comparative evaluation. Comprehensive quantum mechanical evaluations were conducted, encompassing molecular electrostatic potential (MEP), natural bond orbital (NBO), Mulliken analysis, Natural Population Analysis (NPA), non-covalent interaction (NCI), reduced density gradient (RDG), electron localization function (ELF), local orbital locator (LOL), Becke surface analysis (BSA), and Hirshfeld surface analysis (HSA). The Multiwfn software package (version 3.8) (http://sobereva.com/multiwfn/) was also employed to enable detailed analysis of electronic distributions and interaction environments within the molecular systems, offering insights into the intermolecular forces influencing the compounds. The incorporation of these computational approaches supported a comprehensive evaluation of the electronic structures, stability, and interaction dynamics of the studied compounds. [85].

5.2.14. CLC-Pred

Cytotoxicity prediction of the aforementioned compounds was evaluated across diverse tumor cell lines *via* CLC-Pred, an advanced *in silico* predictive tool from Way2Drug services (*http://www.way2drug.com/)*. This tool utilizes structure-cell line cytotoxicity relationships (SCCR), derived from specialized training sets based on the PASS (Prediction of Activity Spectra for Substances) software. The algorithm evaluates cytotoxic potential by analyzing structural attributes, providing quantitative estimations of activity probability using Leave-one-out cross-validation of the PASS training set. Two primary metrics are generated: the probability of activity (Pa) and the probability of inactivity (Pi) against specific tumor cell lines. Utilization of the SDF file format in generating the outcomes, delivering comprehensive predictions of cytotoxic potential across diverse tumor lines, offering critical insights into the compound's predicted efficacy in cancer therapy based on its molecular framework [86]. Cytotoxicity predictions for the selected compounds were performed across various tumor cell lines using CLC-Pred, an advanced *in silico* tool provided by Way2Drug services (http://www.way2drug.com/). This platform applies structure–cell line cytotoxicity relationships (SCCR), developed from curated training datasets within the PASS (Prediction of Activity Spectra for Substances) framework. The algorithm assesses cytotoxic potential by examining molecular structure, providing quantitative estimates through Leave-One-Out cross-validation of the PASS training set. Two key metrics are reported: the probability of activity (Pa) and the probability of inactivity (Pi) for specific tumor cell lines. Predictions were generated using the SDF file format, delivering a detailed assessment of cytotoxic potential across multiple tumor types and offering valuable insights into the compound’s anticipated anticancer efficacy based on its structural profile [86].

5.2.15. Reacting atom and Pharmacokinetics (ADME)

Reactive atomic site prediction and ADME profiling were performed for the selected set of compounds. Reacting atom identification, performed using the Way2Drug tool (*http://www.way2drug.com/RA*), predicts essential biotransformation pathways, including aliphatic and aromatic hydroxylation, N- and O-glucuronidation, N-, S-, and C-oxidation, as well as N- and O-dealkylation. Additionally, SwissADME (*http://www.swissadme.ch/*) was employed to assess pharmacokinetic parameters including gastrointestinal absorption, blood-brain barrier permeability, and cytochrome P450 interactions along with prediction of LogP value *via* Molinspiration (*https://www.molinspiration.com*). All analyses were conducted using canonical SMILES format.

5.2.16. Molecular dynamics

5.2.16.1. Molecular dynamics simulation

A 100-ns molecular dynamics (MD) simulation of the protein-ligand complexes (PDB IDs: 1UHL, 1UPV, and 5ICK) bound to the top-ranked compound was conducted utilizing the GROMACS 2021.5 suite. The AMBER 99SB-ILDN force field was applied, offering enhanced accuracy in representing the side chain conformations, particularly for inherently disordered proteins, through refined dihedral angle parameters that improve rotamer [87] at 310 K (37 °C) on a high-performance server equipped with an NVIDIA V100 GPU for enhanced computational efficiency. The force field topology for the ligand was generated using ACPYPE with Gasteiger charges [88]. Each protein-ligand complex was enclosed within a cubic periodic box, maintaining a distance of 7.5 Å from the protein surface. The explicit SPC extended water (SPC/E) model was employed for hydration, with counter-ions added to neutralize the system. SPC/E model, designed to improve its accuracy by incorporating an additional polarization correction, resulting in better representation of water's structural and dynamic properties, particularly its density and diffusion coefficient compared to the original SPC mode. Energy minimization was conducted using the steepest descent algorithm for 50,000 steps. Subsequently, solvent molecules

and counter-ions were equilibrated by restraining the positions of the protein backbones for 500 ps. The system was subjected to an NVT ensemble for 200 ps, where the number of particles (N), volume (V), and temperature (T) were kept constant, followed by an NPT ensemble for 300 ps, maintaining N, pressure (P), and T constant. Temperature regulation at 310 K and pressure at 1 bar was achieved using V-rescale and Berendsen's coupling algorithms, respectively, during position-restrained equilibration. The simulation encompassed a total of 53,418 atoms over 100 ns, allowing free movement of all molecules according to a classical Newtonian leap-frog MD integrator. Isotropic pressure coupling was applied across the x, y, and z components with a time constant τ = 2.0 ps and compressibility of 4.5×10^{-5} bar^{-1}, employing the Parrinello–Rahman barostat to maintain pressure at 1 bar. Electrostatic interactions were treated using the Particle Mesh Ewald (PME) algorithm, with a cutoff of 12 Å for Coulombic and van der Waals forces, and an interpolation order of 4 with grid spacing of 1.6 Å. The integration time step was set to 2 fs, with coordinates stored every 10 ps. Bond lengths were constrained using the LINCS algorithm. All analyses were performed utilizing the tools available in the GROMACS 2021.5 package [89-93]. Plots were generated using GRACE (©1991-1995 Paul J. Turner, Portland; ©1996-2007 Grace Development Team).

5.2.16.2. Calculation of hydrogen bond existences or occupancies

Intermolecular hydrogen bonds between the protein and ligand throughout the simulation were expressed as percentage occurrences or existences or occupancies by counting the numbers of hydrogen bond existing trajectory frames, dividing that number by total number of trajectory frames and then multiplying it by hundred using a perl script obtained from Lemkul Lab (Lemkul, Justin A. “Scripts and Programs.” OSF, 22 Nov. 2018. Web https://osf.io/3wunt). In this analysis, all hydrogen bond occurrences were recorded in an output file, detailing the contributions of key residues involved in these interactions.

5.2.16.3. Binding affinity calculations between the protein and ligand

In order to calculate reliable interaction and solvation energies in complex biological systems, the continuum solvent approach is effectively used [94]. Both long-range polar and short-range non-polar interactions are necessary for valid interpretations on activity of biomolecules to study biochemical systems through classical mechanics [95-96]. Here, binding affinities between the protein and ligand were calculated using the standard Molecular Mechanics Poisson-Boltzmann Surface Area (MMPBSA), considered as a relatively efficient way to predict binding affinities and provides insights into the contributions of different interactions (electrostatic, van der Waals, hydrophobic) to binding affinity [97]. GROMACS version 5.1.2 was compiled to perform MMPBSA calculation using gmmpbsa tool [98]. All energy terms for Van der Walls and electrostatic as MM, polar solvation as PB and non-polar solvent accessible surface energy as SA was calculated for the Protein–ligand interactions. Eventually, all energy terms were represented as the ΔG of binding or free energy of binding between the protein and ligand. The ligand interaction diagrams were generated using Maestro, Schrödinger, LLC, New York, NY, 2021 and 3D graphical images were generated using UCSF Chimera [99].

5.2.17. Shermo online

The thermochemical properties of the top-ranked compound were computed using the Shermo tool [100], based on the output file generated from Gaussian. The analysis excluded vibrational mode contributions. A temperature scan ranging from 100.000 K to 310.000 K, in 10.000 K increments, was performed at a constant pressure of 1.000 atm. Vibrational frequencies were scaled by a factor of 1.0000 for Zero-Point Energy (ZPE), internal energy difference [U(T)-U(0)], entropy [S(T)], and heat capacity (CV). Low-frequency vibrational modes were predicted using the harmonic approximation.

5.3. Results and discussion

5.3.1. Swiss-similarity based virtual screening

A thorough validation was done to identify and eliminate redundant entries from the initial compound libraries, which consisted of 256 compounds. Duplicates were eliminated by cross-referencing inter and intra-library duplicates. Duplicates were identified when a compound appeared in another library, confirming its prior inspection through databases such as PubChem and DrugBank, utilizing canonical SMILES and DrugBank IDs for verification. In Library 1, 177 unique compounds were identified **Table S5.1 (supporting information)**, with similarity scores ranging from 1.0 to 0.057. Library 2 initially contained 27 compounds **Table S5.2 (supporting information),** reduced to 4 distinct entities after eliminating 23 duplicates. Library 3, comprising 52 compounds **Table S5.3 (supporting information)**, was refined to 16 after the removal of 36 redundancies. The final curated dataset, comprising 197 non-redundant compounds, was subjected to downstream analysis.

5.3.2. Druglikeness and toxicity-based screening

Drug-likeness and toxicity assessments are crucial in early-stage drug discovery, minimizing late-stage failures and enhancing therapeutic efficacy. This evaluation was performed on all 197 compounds from the three specified libraries depicted in **Tables S5.4-S5.6 and S5.7-S5.9 (supporting information).**

Drug-likeness Assessment:

- **Library 1:** Out of 177 compounds, 142 met the established drug-likeness criteria.
- **Library 2:** All 4 compounds satisfied the drug-likeness parameters.
- **Library 3:** 11 out of 16 compounds conformed to drug-likeness standards.
- **Cumulative Total:** A total of 157 compounds exhibited favorable drug-likeness attributes, suggesting potential for oral bioavailability.

Toxicity Assessment: Toxicity evaluations were performed on the remaining 157 drug-likeness-compliant compounds.

- **Library 1:** 49 compounds met the toxicity criteria.

- **Library 2:** 1 compound satisfied the toxicity standards.
- **Library 3:** 5 compounds complied with toxicity parameters.
- **Cumulative Total:** A total of 55 compounds were deemed acceptable, ensuring adequate safety profiles.

Following the comprehensive drug-likeness and toxicity screenings, 55 compounds were identified as suitable for further investigation.

5.3.3. Molecular docking *via* Molegro virtual docker

5.3.3.1. Docking score

Molecular docking simulations are essential for identifying highly effective candidates by evaluating their ability to form stable, specific interactions with the target's active site, which reflects their biological activity. Ranking compounds based on docking scores facilitates binder selection, enhancing efficiency and success rates in drug development [101]. Accordingly, a lower docking score signifies a stronger and more favorable binding affinity between a ligand and its target protein. Docking scores aim to correlate with binding free energy, where more negative scores indicate stronger binding. Therefore, a more negative docking score suggests higher affinity [102]. In this study, binding affinities, quantified by MolDock and rerank scores for all ligands, were assessed alongside other parameters detailed in **Tables S5.10-S5.12 (supporting information)**. The analysis conclusively indicated that compound 144 consistently outperformed across all three targets, as evident by its consistently elevated MolDock and rerank scores. Specifically, it achieved MolDock scores of -160.974 kcal/mol, -144.955 kcal/mol, and -147.539 kcal/mol, alongside rerank scores of -127.205, -116.684, and -121.339 for PDB IDs 1UHL, 1UPV, and 5ICK, respectively. The high rerank scores further corroborate its potential biological relevance and stability within the active site. Notably, compound 144 exhibited significantly superior scores relative to resveratrol, native ligands, and the standards as illustrated in the scatter plots presented in **Figure S5.5-S5.7 (supporting information)**. These findings highlight the significant potential of Compound 144 for further investigation into its molecular binding mechanisms and therapeutic efficacy as an anticancer agent, likely through

selective modulation of LXRα, LXRβ, and FXR receptors. Henceforth referred to as C144 (AZD7762) or C144, its 2D structure is depicted in **Figure 5.8**.

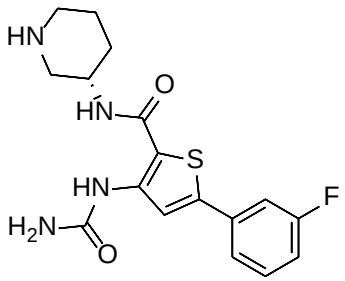

Figure 5.8.: Structure of (C144) AZD776 or 3-(carbamoylamino)-5-(3-fluorophenyl)-N-[(3S)-piperidin-3-yl]thiophene-2-carboxamide

5.3.3.2. Ligand-protein interaction.

Analysis of docking scores reveals that C144 (AZD7762) possesses an exceptionally favorable docking profile. To further substantiate these findings and enhance the mechanistic understanding of its interactions with their respective targets, a comparative framework was applied [103,104]. This methodology assesses the binding interactions of C144 (AZD7762) along with resveratrol, native ligands, and reference standards. The native co-crystallized ligands derived from PDB entries 1UHL, 1UPV, and 5ICK are well-documented for their affinity towards their respective target proteins, thereby serving as benchmarks for evaluating the bioactivity of C144 (AZD7762). C144 (AZD7762) shows strong binding affinity, suggesting higher bioactivity than the native ligands. Reference compounds were used to contextualize and compare its therapeutic potential based on molecular interactions binding interactions. This analysis provides a detailed evaluation of binding modes of the protein-ligand, key residues, interaction distances, energies, and hybridization states, as shown in **Tables S5.13-S5.15 (supporting information)** and illustrated in **Figures 5.9-5.11.**

As illustrated in **Figure 5.9**, C144 (AZD7762) establishes key interactions within the active site of the target protein, specifically engaging with Arg305, Ser264, Thr302, and Met298 *via* hydrogen bonding. These interactions are essential for stabilizing the

ligand within the active site, promoting receptor conformational changes, and triggering downstream biological effects that enhance C144's pharmacological potency. The native T-09019317 (1UHL/1UPV), presumed to be the protein's natural binding partner, interacts with three key residues in the active site, notably Ser264, which is also engaged by C144 (AZD7762). This overlapping interaction is a desirable characteristic in drug discovery, as it significantly increases the likelihood of C144 (AZD7762) exhibiting comparable or superior biological activity relative to the native ligand. Withaferin A interacts with four residues in the active site, including Ser264 and Thr302, while resveratrol with Ser264 further supporting this shared binding pattern with C144 (AZD7762). Notably, Ser264 and Thr302 are identified as key hydrogen bonding hotspots within the receptor's active pocket. The hydroxyl group of Ser264 may have likely contributed in stabilizing the interactions, enhancing ligand-receptor affinity, while the polar side chain of Thr302 may have reinforced these interactions, augmenting ligand stability within the binding site. These characteristics are instrumental in optimizing ligand-receptor interactions, positioning C144 (AZD7762) as a promising candidate for selective and potent anticancer therapeutics through its modulatory effects on LXRα.

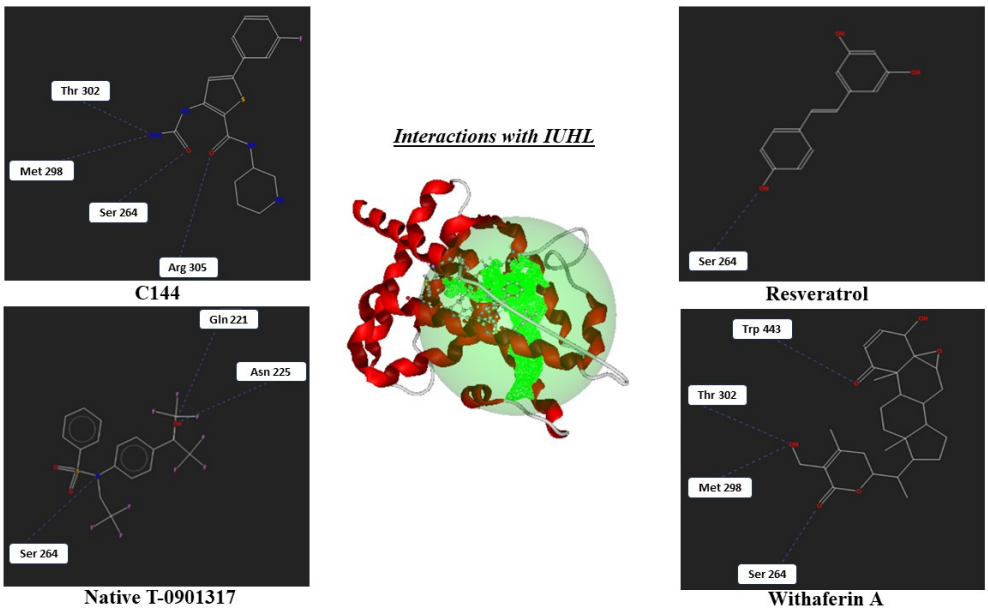

Figure 5.9: Molecular interactions between PDB: 1UHL (active site is depicted as a green, globular envelope) and the ligands. The binding interactions of C144 (top left), Native T-0901317 (bottom left), Resveratrol (top right), and Withaferin A (bottom right) are depicted with the protein 1UHL. Each ligand's interaction is pinpointed to key amino acid residues in the active site.

Figure 5.10 illustrates that Glu315 and Thr316 are the principal residues facilitating the interaction with C144. Glu315, a glutamate residue, likely engages in hydrogen bonding through its negatively charged carboxylate group, thereby enhancing the stabilization of the ligand within the active site. Thr316, a threonine residue, is posited to participate in the interaction likely *via* its hydroxyl-bearing polar side chain, potentially forming additional hydrogen bonds that further contribute to ligand stabilization. Importantly, Thr316 is conserved across C144, Bergapten, and resveratrol, along with other interacting residues, indicating its significant role in stabilizing ligands through hydrogen bonding and positioning it as a critical hotspot for the design of ligands targeting this protein. In contrast, the native T-09019317 (1UHL/1UPV) interacts solely with His435, a residue not engaged by the other ligands. This divergence underscores that C144, while lacking a shared interaction profile with the native T-0901317, attains stability through interactions with other key residues, specifically Glu315 and Thr316. This distinctive interaction pattern positions C144 as a compelling candidate for the development of selective and potent anticancer agents, particularly *via* its modulatory effects on LXRβ.

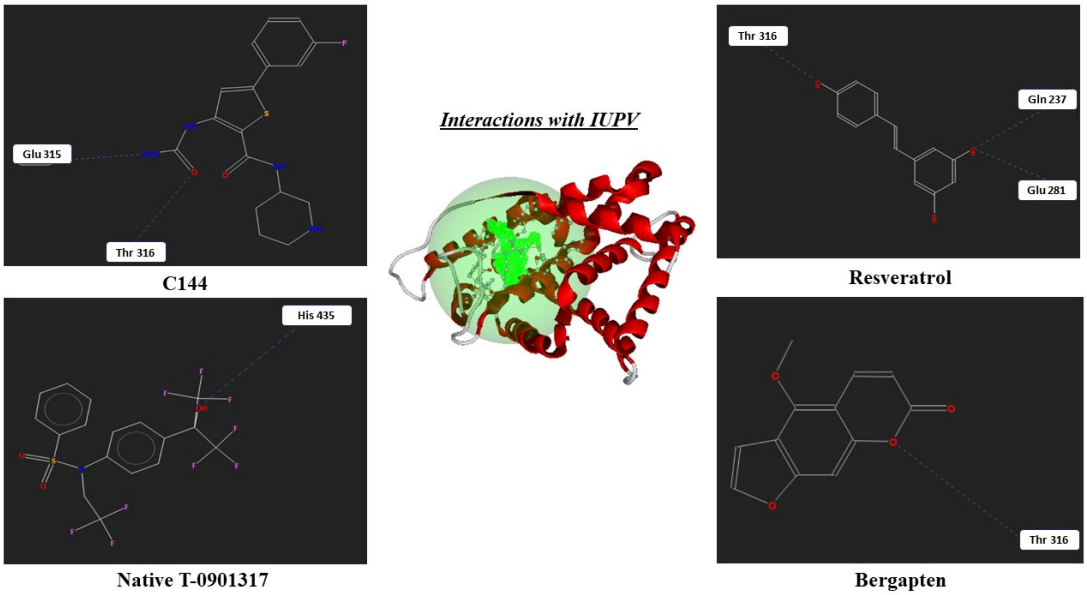

Figure 5.10: Molecular interactions between PDB: 1UPV (active site is depicted as a green, globular envelope) and the ligands. The binding interactions of C144 (top left), Native T-0901317 (bottom left), Resveratrol (top right), and Bergapten (bottom right) are depicted with the protein 1UPV. Each ligand's interaction is pinpointed to key amino acid residues in the active site.

Figure 5.11 illustrates the binding interactions of C144 (AZD7762), the native ligand, resveratrol, and obeticholic acid with the target protein, emphasizing key amino acid residues, notably Tyr369, Ser332, Thr288, and His447. Tyr369 and Ser332 are particularly significant in mediating interactions with C144 (AZD7762). The aromatic polar side chain of Tyr369 may have facilitated hydrogen bonding with the ligand, potentially enhancing C144 (AZD7762)'s stability within the binding pocket. Similarly, Ser332, due to its hydroxyl group, likely participates in hydrogen bonding, playing a critical role in anchoring the ligand. C144 (AZD7762) exhibits pivotal interactions with Ser332 and Tyr369, both of which are also engaged by the native ligand and resveratrol, indicating their essential role in stabilizing ligand-receptor complexes. Notably, Ser332 is the exclusive residue interacting with obeticholic acid, further corroborating its engagement with C144 (AZD7762). The presence of these conserved residues underscores C144 (AZD7762)'s potential as a robust binder,

mirroring the binding efficacy of the native ligand. This similarity suggests that C144 (AZD7762) may exhibit comparable or superior biological activity to the native feroline (5ICK), positioning it as a promising candidate for the development of selective and efficacious anticancer agents through its modulatory effects on the FXR receptor.

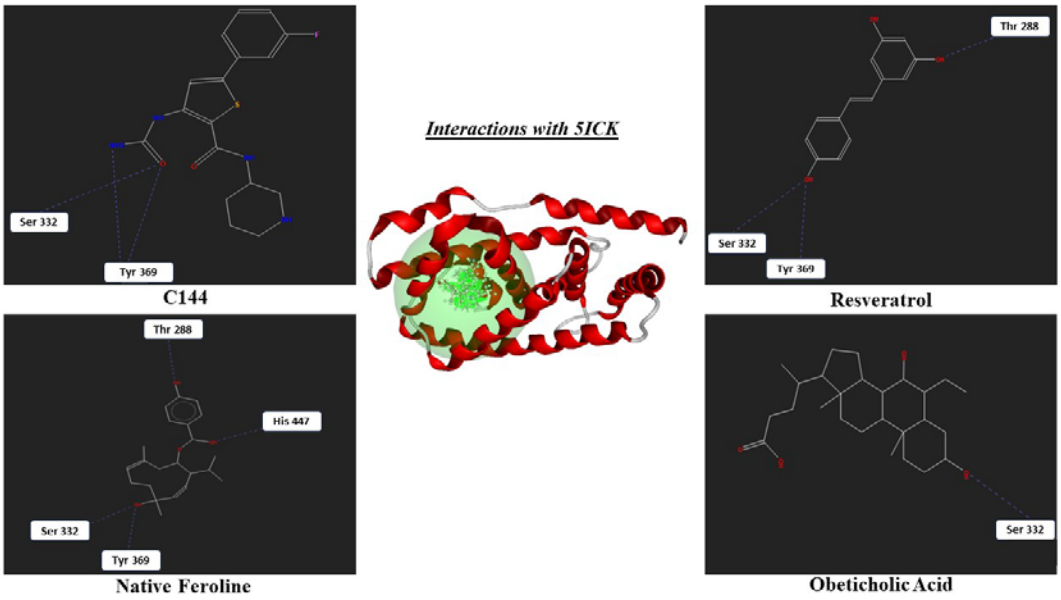

Figure 5.11: Molecular interactions between PDB: 5ICK (active site is depicted as a green, globular envelope) and the ligands. The binding interactions of C144 (top left), Native feroline (bottom left), Resveratrol (top right), and Obeticholic acid (bottom right) are depicted with the protein 5ICK. Each ligand's interaction is pinpointed to key amino acid residues in the active site.

5.3.3.3. Protein-Ligand Interaction Profiler (PLIP)

Following the docking simulation, molecular interaction analysis of the C144 (AZD7762)-target complex was performed using the Protein-Ligand Interaction Profiler (PLIP) as shown in **Figure S5.12** and **Table S5.16 (supporting information)**. The interaction analysis of the C144-1UHL complex highlights common residues that may play key roles in ligand stabilization. Both methods (MVD and PLIP) emphasize the critical hydrogen bonds involving Ser264 and Arg305, which are essential for

ligand binding. PLIP includes hydrophobic interactions with residues like Val263B, Ile268B, Val297B, and Phe271B, along with π-alkyl interactions from Phe271B. A notable distinction in PLIP is the identification of a halogen bond between the ligand's fluorine atom and Gln221B, which is absent in MVD. The interaction analysis of the C144-1UPV complex emphasize the importance of Thr316, which plays a central role in hydrogen bonding and ligand stabilization. MVD focuses on Glu315 and Thr316, with Glu315's negatively charged carboxylate group contributing to stabilization, while PLIP includes hydrophobic interactions with residues like Phe271A, Ile282A, and Ile327A, and also identifies π-alkyl interactions with Phe329A. PLIP additionally reveals an atypical hydrophobic engagement of Glu315A while MVD highlights hydrogen bonding. The PLIP analyses of the C144-5ICK complex highlights common key residues, particularly Tyr369 and Ser332, which are crucial for hydrogen bonding and ligand stabilization in both methods. MVD focuses on the roles of Tyr369 and Ser332 in anchoring C144 (AZD7762), while PLIP adds a broader perspective, identifying significant hydrophobic interactions with residues such as Phe284A, Leu287A, and Ala291A, which contribute to the ligand's stability. PLIP also reveals additional hydrophobic contacts and a unique π-stacking interaction with Trp454A, which MVD does not identify. Both methods emphasize the importance of Tyr369 and Ser332. This profiling provides insights into the interactions that may contribute to the ligand's high binding energy and specificity within the protein's active site.

5.3.4. Electronic Reactivity Parameters *via* DFT

Frontier molecular orbitals, namely HOMO and LUMO, play a central role in governing a compound's reactivity and interaction profile. The energy difference between these orbitals serves as a measure of both reactivity and kinetic stability; a larger gap generally indicates lower reactivity, reduced polarizability, and greater overall stability. [105]. Data presented in **Table S5.17 (supporting information)** and visually depicted in **Figure 5.13** illustrates the following sequence of energy gaps (ΔE) for the compounds examined: Obeticholic acid > native T-09019317 (1UHL/1UPV) > withaferin A > bergapten > native feroline (5ICK) > C144 > resveratrol. C144 has the second lowest HOMO–LUMO gap after Resveratrol, indicating high reactivity

with improved stability. This balance enhances its potential for effective interactions with biological targets. The compound's narrow band gap energy signifies a strong tendency for charge transfer interactions, suggesting increased electronic reactivity. Numerous studies have shown that Density Functional Theory (DFT) effectively predicts the molecular geometries of drug compounds, while global and local reactivity descriptors help clarify their physicochemical properties and interaction profiles [106]. The global reactivity descriptors of the evaluated compounds are analyzed and tabulated in **Table S5.18 (supporting information)**. The LUMO functions as the electron acceptor and is linked to electron affinity (EA), while the HOMO serves as the electron donor, corresponding to ionization potential (IP). Koopmans' theorem, derived from Hartree-Fock theory, suggests that the ionization energy corresponds to the negative value of the HOMO energy, while the electron affinity corresponds to the negative of the LUMO energy. A higher chemical hardness (η) implies greater molecular stability and lower reactivity, whereas increased softness (σ) corresponds to higher chemical reactivity [107,108].

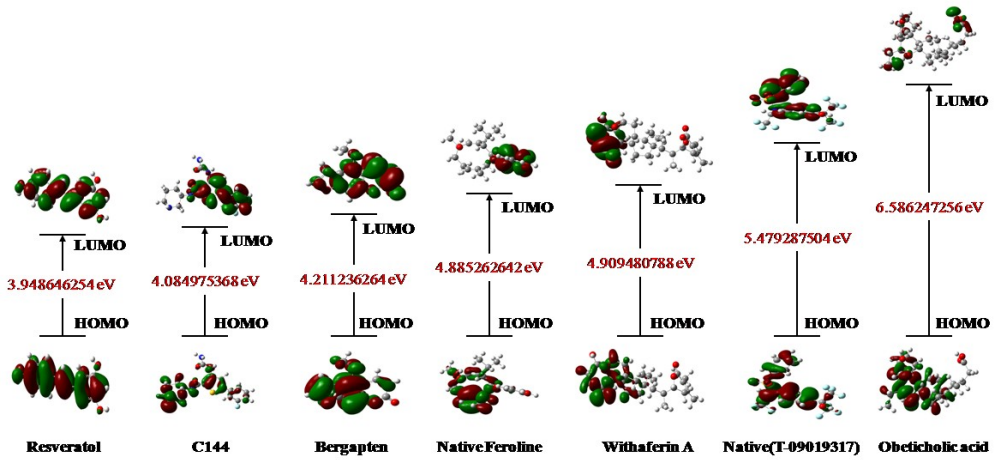

Figure 5.13: HOMO-LUMO energy gap comparisons of Resveratrol, C144, Bergapten, Native Feroline, Withaferin A, Native (T-0901317), and Obeticholic acid derived from DFT calculations.

Chemical Hardness (η): Chemical hardness (η) reflects a molecule's resistance to changes in electron distribution; higher values imply greater stability and lower reactivity [107-108]. C144 exhibits moderate hardness (2.0425 eV), lower than Obeticholic acid and Native T-0901317, indicating higher reactivity. It exhibits close range values with Resveratrol, Native Feroline, Bergapten and Withaferin A, suggesting similar effects to electronic perturbations.

Chemical Softness (S): Softness, the reciprocal of hardness, indicates a molecule's capacity to engage with electron-rich sites, thus promoting nucleophilic interactions [107,108]. C144 exhibits moderate softness (0.2448 eV), higher than Native T-0901317, Obeticholic acid and Bergapten, suggesting better electronic adaptability. However, its softness is lower than that of Resveratrol. This value reflects that C144 possesses adequate reactivity to interact with nucleophilic regions of biological targets.

Chemical Potential (μ): Chemical potential (μ) reflects a molecule's tendency to gain electrons, with lower values indicating higher reactivity [107,108]. C144 has a moderately negative μ, more than Resveratrol and Native Feroline, suggesting it has a slightly higher electron affinity. Native T-0901317 and Withaferin A show comparable μ, thus indicating electron attraction. This suggests C144 is somewhat prone to accepting electrons from electron-rich sites on biological targets.

Electronegativity (χ): Electronegativity (χ) reflects a molecule's ability to attract electrons, influencing the strength and direction of interactions [107,108]. C144 shows a balanced electronegativity, slightly higher than Resveratrol, Native Feroline and Obeticholic acid but lower than the others, suggesting a moderate capacity for polar interactions and better charge distribution control compared to more electronegative molecules. With an electronegativity of 3.9761 eV, C144 exhibits a balanced tendency to attract electron density.

Ionization Potential (IP): Ionization potential represents the energy required to remove the most weakly bound electron from a molecule, typically approximated by the negative of the HOMO energy [107,108]. C144's IP value of 6.0186 eV reflects

moderate electronic stability, indicating it is relatively resistant to oxidation but can still undergo ionization. Compared to other compounds, C144's IP is higher than Resveratrol, and it displays near range values with Native T-0901317, Obeticholic acid and Native Feroline, suggesting a balanced reactivity profile.

Electron Affinity (EA): Electron affinity quantifies a molecule's tendency to accept an electron, typically estimated as the negative of the LUMO energy [107-108]. C144 exhibits a higher EA than Resveratrol, indicating a stronger tendency to accept electrons; it displays close range values with Native T-0901317, Native Feroline and Obeticholic acid, which are more electron-accepting. With an EA of 1.9336 eV, C144 demonstrates a moderate ability to acquire electrons, enhancing its potential to form stable anionic species and interact with nucleophilic sites on biological receptor.

Electrophilicity Index (ω): Electrophilicity quantifies how strongly a molecule tends to attract and accommodate electrons, reflecting its reactivity toward electron-rich species [107,108]. C144 demonstrates a favorable ω value of 0.2050 eV, indicating a stronger electrophilic character. In contrast, native T-0901317, Obeticholic acid, and Bergapten possess lower ω values, reflecting a weaker tendency to accept electrons, whereas Resveratrol shows comparable ω values. The favorable electrophilicity index of C144 highlights its strong affinity for binding with biomolecules, confirming its potential to act as an effective electrophilic agent.

Dipole Moment: The dipole moment (μ) is crucial for predicting molecular stability in polar environments [109]. C144 has a higher dipole moment than Resveratrol and Feroline, indicating greater potential for polar interactions, which could affect solubility and membrane permeability. However, Bergapten and Native T-0901317 have even higher dipole moments, suggesting stronger polar interaction potential. C144's dipole moment of 3.6741 Debye indicates significant polarity, potentially influencing its solubility, bioavailability, and systemic distribution. The HOMO-LUMO gap, chemical potential and chemical hardness (η) seem key parameters, reflecting favorable electronic properties. Nonetheless, all electronic parameters are essential, as they collectively define the compound’s electronic structure, stability, and

reactivity, providing insight into its interaction with biological targets (LXRs and FXR) and supporting its potential as an anticancer agent.

5.3.5. Statistical analysis

5.3.5.1.Correlation matrix

The correlation matrix illustrates the relationships between molecular docking scores (MolDock scores) for the protein–ligand complexes 1UHL, 1UPV, and 5ICK, alongside quantum chemical descriptors derived from Density Functional Theory (DFT), as detailed in **Table S5.19 (supporting information**). A strong positive correlation (0.707) between 1UHL and 1UPV suggests that ligands binding effectively to one complex tend to exhibit similar interactions with the other, indicating comparable binding mechanisms. Moderate correlations with 5ICK (0.406 for 1UHL and 0.477 for 1UPV) imply ligand compatibility, though to a lesser degree. The HOMO–LUMO gap shows a low-to-moderate correlation with docking scores, suggesting limited influence on binding affinity. Electron affinity displays negative correlations for 1UHL and 1UPV, whereas ionization potential presents a weak-to-moderate positive correlation, particularly for 5ICK. Chemical hardness shows moderate alignment with docking scores, indicating that greater ligand stability may be associated with stronger binding, while softness appears to have minimal impact. Overall, while these quantum descriptors offer valuable insights, they are not the primary determinants of binding efficacy.

5.3.5.2.Principal component analysis

The PCA plot illustrates the clustering of compounds based on two principal components (PC1 and PC2) shown in **Fig. S5.14 (supporting information)**. Most data points cluster around the origin, indicating minimal variance in molecular docking scores and quantum chemical descriptors. Notably, Withaferin A and Bergapten are distinctly positioned along PC1, signifying differences in binding affinities. Obeticholic acid and native feroline (5ICK) are located on the negative side of PC2, suggesting unique reactivity profiles. Native T-09019317 (1UHL/1UPV) is positioned positively on PC1. Data point C144 (AZD7762) is located on the far left

along the PC1 axis and appears isolated from the main cluster of points near the center, indicating it has unique properties or characteristics in comparison to other data points. It may also suggest distinct binding or interaction properties. In a pharmacological or biochemical context, this could imply a unique mechanism of action or selective binding affinity, potentially making it an interesting candidate for further study.

5.3.6. AutoDock

5.3.6.1. Docking score

Molecular docking simulations performed using AutoDock 4.2 and analyzed through Biovia Discovery Studio (DS) indicate that *C144 (AZD7762)* demonstrates significantly high binding affinities across the assessed targets, with binding affinity values of -8.23 kcal/mol for 1UHL, -8.20 kcal/mol for 1UPV and -9.17 kcal/mol for 5ICK. Negative docking scores indicate stronger binding and with lower values reflecting higher ligand-target affinity. These affinity values not only indicate a robust interaction but also surpass the binding profiles of all other ligands subjected to comparative analysis, emphasizing its aptitude as a principal candidate. This indicates its potential to elicit anticancer effects *via* the modulation of these receptor activity [110]. Data on binding affinities, root mean square deviation (RMSD) values and interacting amino acid residues for each ligand-target complex are provided in **Tables S5.20-S5.22 (supporting information). Figure 5.15–5.17** illustrate the binding interactions of C144 (AZD7762), resveratrol, and native ligands with target proteins, alongside reference standards Withaferin A (1UHL), Bergapten (1UPV), and Obeticholic acid (5ICK), highlighting interactions and conformational alignments within active sites.

5.3.6.2. Ligand-protein interaction

The target active site in molecular docking refers to the specific ligand-binding region of a protein where a ligand interacts to exert its biological effect. The binding site was initially identified and consistently detected around the native co-crystallized ligand in all cases [111]. The active sites of all targets of interest are well characterized,

making them valuable for molecular docking, drug discovery, and elucidating activation mechanisms. Based on the spatial coordinates, 1UHL contained a total of 18 residues, 1UPV had 23 residues, and 5ICK comprised 20 residues. To further cross-validate these findings, the Protein Data Bank in Europe (PDBe) (*https://www.ebi.ac.uk/pdbe/)* was analyzed to identify specific residues in the vicinity of the native co-crystallized ligand, as well as those directly interacting with it. For 1UHL, 13 residues were identified: Leu331, His421, Phe257, Ile339, Phe326, Leu299, Thr302, Met298, Ser264, Leu260, Glu301, Phe335, and Ala261, of which C144 shared seven. For 1UPV, 19 residues were identified: Phe271, Leu449, Phe268, Trp457, His435, Ile309, Ile353, Leu313, Thr316, Tyr335, Ile327, Leu274, Phe329, Phe340, Phe349, Leu442, Met312, Ala275, and Leu345, with C144 sharing four. For 5ICK, 20 residues were identified: His447, Met328, Ile352, Ile357, Leu287, Met450, His294, Ser332, Tyr369, Met290, Phe329, Met365, Leu465, Ala291, Trp469, Trp454, Leu451, Phe461, Phe284, and Thr288, among which C144 shared nine.

The interaction analysis against the target protein (PDB ID: 1UHL), as illustrated in **Figure 5.15**, reveals that C144 (AZD7762) establishes a multifaceted interaction profile, encompassing conventional hydrogen bonds with PheB:257 and ThrB:302, carbon-hydrogen interactions with ProB:436, halogen bonds with LysB:434, and complex interactions such as π-sigma with LeuB:439, π-sulfur with HisB:421, and π-alkyl interactions with PheB:335, IleB:339, LeuB:299 and AlaB:261. The native T-09019317 (1UHL/1UPV) interacts with multiple residues, notably exhibiting π-alkyl interactions with IleB:339 and LeuB:299, alongside shared interactions with LeuB:439, HisB:421, and PheB:335, irrespective of the binding mechanism. These shared interactions indicate that C144 (AZD7762) occupies a similar spatial region within the active site as the native ligand, suggesting that it mimics the native ligand's binding behavior. Resveratrol, native T-09019317 (1UHL/1UPV), and Withaferin A each exhibit interactions with various amino acid residues within the binding pocket of the target protein. Notably, resveratrol shares a conventional hydrogen bond with C144 (AZD7762) through ThrB:302 and forms similar Pi-alkyl interactions with IleB:339 and LeuB:331, demonstrating a degree of overlap in binding modes. Likewise, Withaferin A, despite differing in overall interaction type, also shares a

residue with C144 (AZD7762) in the form of HisB:421. The significance of these shared interactions within the target's active site underscores a conserved interaction profile among structurally diverse ligands [112]. C144 (AZD7762) engagement with these critical residues indicates it occupies spatial regions analogous to the native T-09019317 (1UHL/1UPV), suggesting its ability to effectively mimic the native ligand's binding behavior. This supports C144's strong binding potential and biological significance, highlighting its promise as a selective and potent anticancer agent through its modulatory action on LXRα.

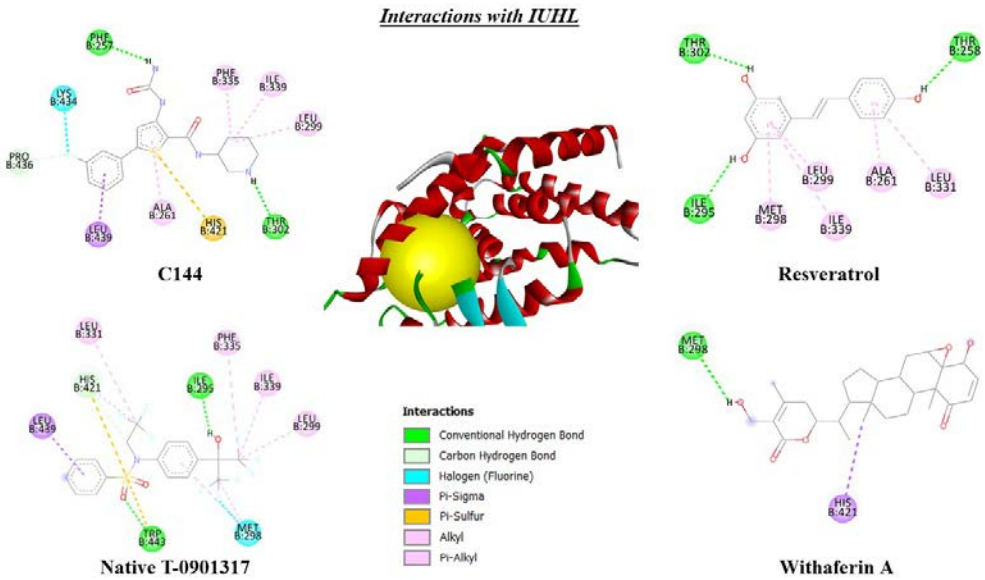

Figure 5.15: This figure illustrates the molecular interactions between the target protein IUHL and the ligands: C144 (top left), Native T-0901317 (bottom left), Resveratrol (top right), and Withaferin A (bottom right). The central image depicts the IUHL protein structure, highlighted with a spherical yellow active site.

The interaction analysis against the target (PDB ID: 1UPV), as illustrated in **Figure 5.16**, reveals that C144 (AZD7762) forms several critical interactions within the active site. It forms a conventional hydrogen bond with ThrA:316, π-π stacking interactions with PheA:340 and PheA:271, and a π-alkyl bond with AlaA:275. The native T-09019317 (1UHL/1UPV) similarly engages with multiple residues, sharing ThrA:316, PheA:271, and AlaA:275 with C144 (AZD7762), irrespective of interaction modality.

These shared interactions indicate that C144 (AZD7762) effectively mimics the native ligand's binding behavior by occupying analogous spatial regions within the active site, thereby enhancing its potential for high binding affinity and biological relevance. Resveratrol interacts with several residues, notably sharing AlaA:275 *via* a π-alkyl bond with C144 (AZD7762) but lacks further overlaps.

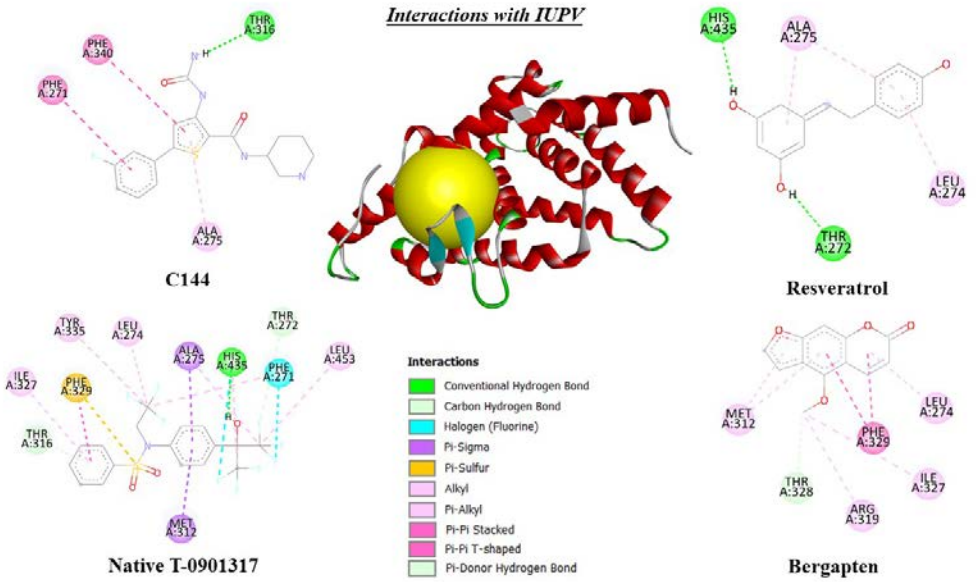

Figure 5.16: This figure illustrates the molecular interactions between the target protein IUPV and the ligands: C144 (top left), Native T-0901317 (bottom left), Resveratrol (top right), and Bergapten (bottom right). The central image depicts the IUPV protein structure, highlighted with a spherical yellow active site.

In contrast, Bergapten binds to different residues with no overlap, indicating divergent interaction patterns. The involvement of key residues such as ThrA:316 and PheA:271 in C144's binding profile highlights its strong affinity and supports its potential to replicate native ligand interactions. This underlines *C144 (AZD7762)* suitability as a lead compound for developing targeted LXRβ modulators in anticancer therapy.

The interaction analysis against the target protein (PDB ID: 5ICK), as depicted in **Figure 5.17**, indicates that C144 (AZD7762) establishes conventional hydrogen bonds with MetA:290, ThrA:288, and SerA:332, alongside carbon-hydrogen interactions with HisA:294 and SerA:332. Additionally, C144 (AZD7762) exhibits alkyl

interactions with TrpA:454, AlaA:291, LeuA:287, LeuA:465, and MetA:328, as well as a π-alkyl interaction with LeuA:287. The native feroline (5ICK) engages multiple residues, sharing critical interactions with C144 (AZD7762) at MetA:328, AlaA:291, LeuA:287, and MetA:290. This spatial overlap suggests that C144 (AZD7762) effectively mimics the binding profile of the native ligand, indicating substantial binding affinity and biological relevance. Resveratrol similarly interacts with multiple residues, notably sharing SerA:332, AlaA:291, and MetA:328 with C144 (AZD7762), reinforcing their binding profile overlap. Obeticholic acid also demonstrates shared interactions with C144 (AZD7762) at LeuA:287, MetA:290, TrpA:454, and AlaA:291. Consequently, *C144 (AZD7762)* aligns within similar spatial regions of the active site, enhancing its potential for strong binding affinity and molecular stability. This positions it as a promising candidate for the development of selective and effective anticancer agents through its modulatory influence on the FXR receptor.

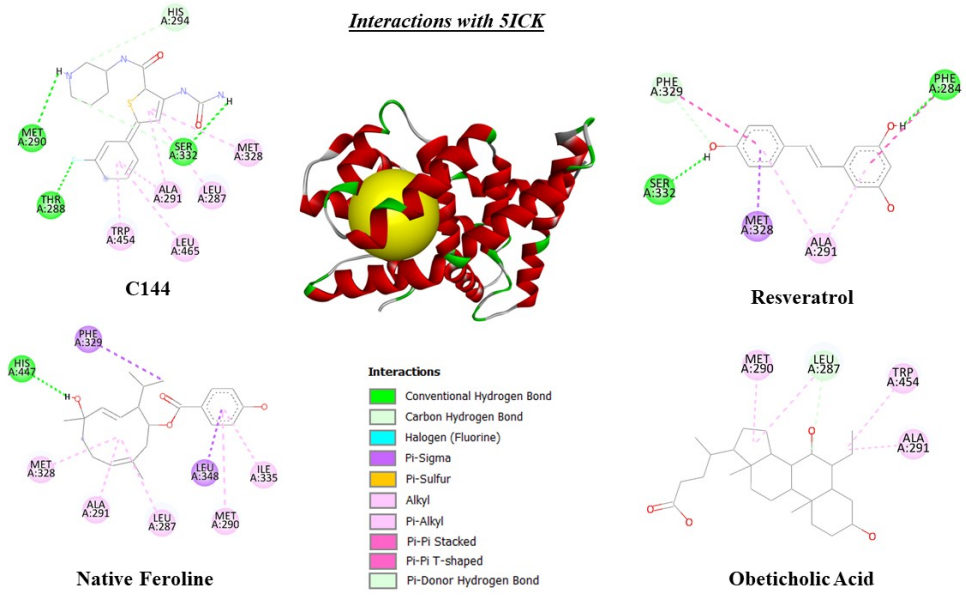

Figure 5.17: This figure illustrates the molecular interactions between the target protein 5ICK and the ligands: C144 (top left), Native feroline (bottom left), Resveratrol (top right), and Obeticholic acid (bottom right). The central image depicts the 1UPV protein structure, highlighted with a spherical yellow active site.

5.3.7. Protein-Ligand Interaction Profiler (PLIP)

Following docking simulations, molecular interaction profiling of the *C144 (AZD7762)*–target complexes was performed using the Protein–Ligand Interaction Profiler (PLIP), as illustrated in **Figure S5.18** and detailed in **Table S23 (supporting information).** The interaction landscape of the C144–1UHL complex provides additional insight into ligand–protein binding, revealing shared stabilizing residues. Both AutoDock and PLIP identify PheB:257 and ThrB:302 as hydrogen bond participants, with PheB:257 consistently involved in both methods. LeuB:299 and PheB:335 participate in hydrophobic interactions in both analyses. PLIP describes them within a hydrophobic pocket, while AutoDock categorizes them as π-alkyl contacts. These results underscore the complementary roles of hydrophobic and hydrogen bonding interactions in stabilizing the ligand.

In the C144–1UPV complex, shared hydrophobic and hydrogen bond-forming residues were similarly identified. Key hydrophobic residues Phe268A, Phe271A, and Phe329A were consistently involved across both analyses, with Phe268A engaging in dual interactions for added stability. Phe340A and Leu345A support a stable hydrophobic environment critical for ligand anchoring. The hydrogen bonding network is reinforced by Ser278A and Thr316A, each forming structurally supportive hydrogen bonds. For the C144–5ICK complex, both methods reveal overlapping hydrophobic and hydrogen bonding contributions to ligand stability. Hydrophobic residues Leu348A, Ile352A, and Trp454A establish π-alkyl interactions, while Trp454A and Trp469A provide additional structural support. Hydrogen bonds with Ser332A and His294A further stabilize the complex, and a halogen bond between the ligand's fluorine and Thr288A enhances overall interaction strength. These findings offer mechanistic insights into the molecular determinants underpinning C144's high binding energy and specificity within the protein's active site.

5.3.8. ML-based protein-ligand interaction capturer (ML-PLIC)

The docking scores and its profile obtained from ML-PLIC (Machine Learning-Protein Ligand Interaction Capturer) is presented **in Table S24 (supporting**

information). Compared with those from AutoDock, reveals strong alignment in predicting the binding affinities of the C144 (AZD7762)-target complexes. For 1UHL, AutoDock reported -8.23 kcal/mol, closely matched by ML-PLIC at -8.90 kcal/mol. For 1UPV, ML-PLIC predicted a score of -9.80 kcal/mol compared to AutoDock's -8.20 kcal/mol. Similarly, for 5ICK, AutoDock yielded -9.17 kcal/mol, nearly identical to ML-PLIC's -9.20 kcal/mol, indicating consistent outcomes across methods. The integration of QuickVina in ML-PLIC appears to maintain algorithmic consistency while leveraging machine learning for refined predictions. The interaction analysis of C144 with 1UHL, 1UPV, and 5ICK are presented **Figure S5.19 (A-C) (supporting information).**

The interaction analysis of the C144-1UHL complex highlights the predominance of hydrophobic contacts, with Phe and Leu exhibiting the highest frequencies (8 occurrences each), indicating their significant role in stabilizing the ligand through non-polar interactions. Tyr and Gln contribute moderately with 2 occurrences each. A single hydrogen bond interaction is identified with Thr, although the reference frequency data suggests it may form up to two hydrogen bonds under certain conditions. While both AutoDock and ML-PLIC show consistency in their identification of key hydrophobic interactions (e.g., Phe and Leu) and hydrogen bonding (primarily with Thr), ML-PLIC offers additional interaction profile by including π-based interactions and halogen bonding.

The interaction analysis of the C144-1UPV complex reveals a balanced contribution of both hydrogen bonding and hydrophobic interactions in ligand stabilization. Key hydrophobic residues include Phe, with a dominant frequency of 8, indicating its critical role in anchoring the ligand through non-polar interactions, while Leu, Ile, and Ala contribute less frequently with 2 occurrences each. Hydrogen bonding interactions involve Ser and Thr, each appearing once in the observed data, though the reference analysis suggests these residues are capable of forming up to two hydrogen bonds. Both AutoDock and ML-PLIC reveal hydrophobic interactions with Phe playing a dominant role in ligand stabilization. While AutoDock focuses more on π-π stacking and π-alkyl interactions, ML-PLIC provides a more interaction profile by including

additional hydrophobic residues (e.g., Leu**,** Ile**,** Ala) and considering the potential for stronger hydrogen bonding under specific conditions. Despite these differences, both methods are consistent in their identification of key residues (Phe and Thr) contributing to the ligand's stability in the active site.

The interaction analysis of the C144-5ICK complex indicates a predominant role of hydrophobic interactions in stabilizing the ligand, with Phe, Leu, and Trp contributing significantly (8, 6, and 4 occurrences, respectively). Additionally, Ala and Met contribute to hydrophobic stabilization, though to a lesser extent (2 occurrences each). The hydrogen bond with Tyr (1 occurrence) is comparatively less frequent, although the reference data suggests that Tyr can form up to two hydrogen bonds, implying that this interaction could be more pronounced under specific conditions. Both AutoDock and ML-PLIC analyses are consistent in their identification of hydrophobic interactions with Phe**,** Leu, and Trp as central contributors to ligand stabilization. Both methods also emphasize the importance of SerA:332 in hydrogen bonding. While AutoDock offers more specific details about alkyl and π-alkyl interactions, ML-PLIC identifies additional hydrophobic residues. The hydrogen bonding observed in both analyses is complementary, with both methods suggesting that stronger interactions could occur under specific conditions.

5.3.9. Structural pharmacophore

Structural pharmacophore mapping of C144 (AZD7762), resveratrol and the selected standards were constructed based on the predefined interactions of the native ligands with their corresponding protein targets (1UHL, 1UPV, and 5ICK), utilizing LigandScout 4.2. These models highlight key structural features associated with biological activity against the specified targets. Comparative analysis of pharmacophoric attributes revealed significant overlap between the test compounds and the native ligands. The identification of these pharmacophoric features offers essential insights into structure-activity relationships (SAR), facilitating the refinement and optimization of these compounds to augment their therapeutic efficacy [113]. The pharmacophore models for each target are depicted in **Figure 5.20-5.22.**

As shown in **Figure 5.20**, C144 (AZD7762) demonstrates significant alignment with the native T-09019317 (1UHL/1UPV) through the engagement of six key residues: LEU299B, ILE295B, ILE339B, THR302B, THR258B, and HIS421B, each contributing to the ligand's binding affinity within the LXRα active site. The pharmacophoric characteristics of C144 (AZD7762) are primarily governed by hydrophobic interactions with LEU299B, ILE295B, and ILE339B, stabilizing the ligand's conformation in the binding pocket. THR302B and THR258B serve as essential hydrogen bond donors, facilitating polar interactions that enhance ligand stability through electrostatic complementarity with electronegative atoms. HIS421B acts as a hydrogen bond acceptor, crucially anchoring both C144 and the native ligand, thereby reinforcing their binding interactions. The pharmacophoric congruence of C144 with Withaferin A and Resveratrol, particularly *via* interactions with HIS421B and THR302B, underscores the structural conservancy of these features. This overlap emphasizes C144's ability to engage key residues THR302B and HIS421B, crucial for ligand stabilization, potentially enabling the fine-tuning of LXRα activity and offering therapeutic strategy in anticancer agent development targeting nuclear receptor pathways.

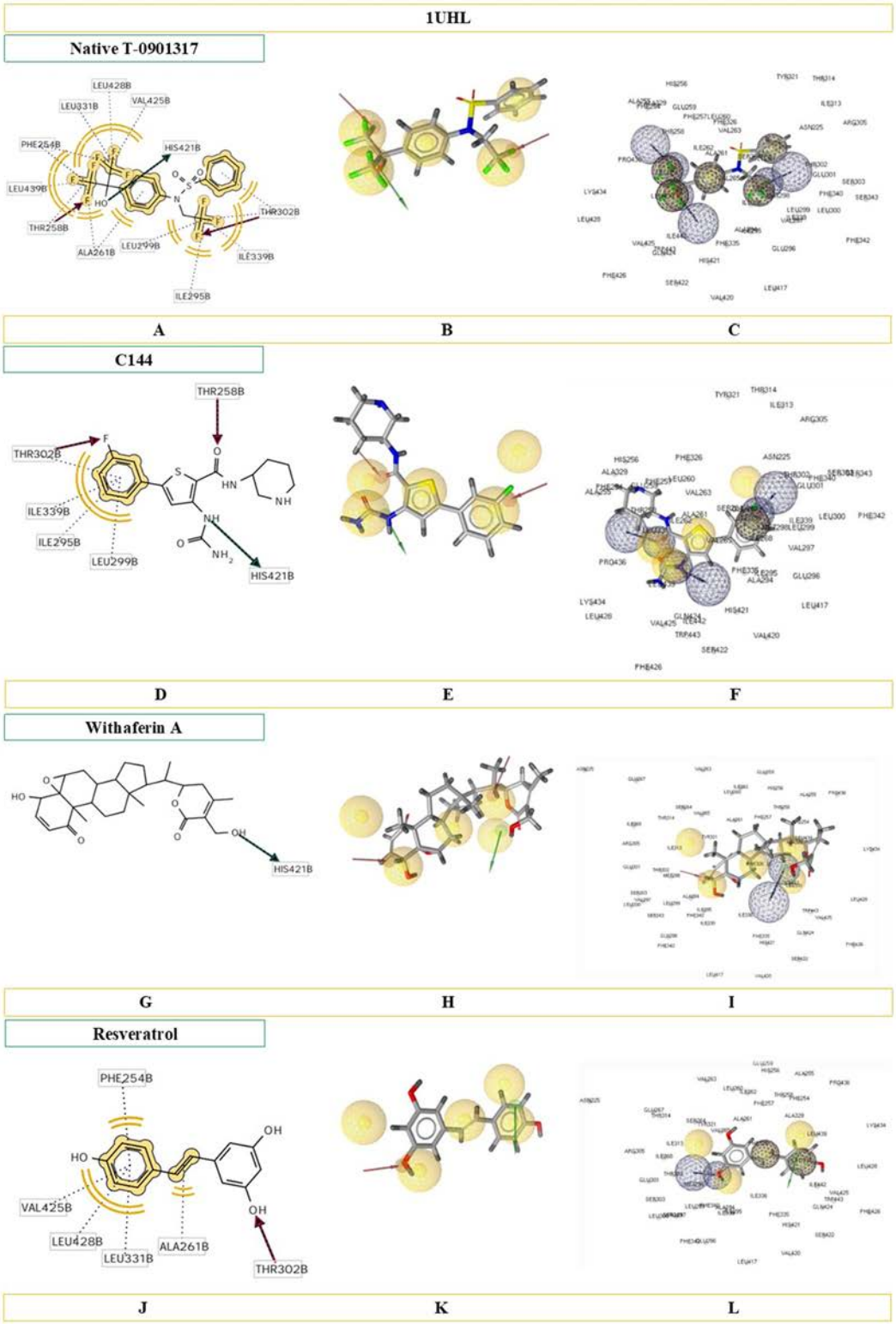
1UHL
Native T-0901317
LEU428B
LEU331B
VAL425B
PHE254B
HIS421B
LEU439B
THR302B
THR258B
ALA261B
LEU299B
ILE339B
ILE295B
A
B
C
C144
THR258B
THR302B
ILE339B
ILE295B
LEU299B
HIS421B
D
E
F
Withaferin A
HIS421B
G
H
I
Resveratrol
PHE254B
VAL425B
LEU428B
LEU331B
ALA261B
THR302B
J
K
L

Figure 5.20: Comparative Binding Analysis of Native T-0901317, Compound C144, Withaferin A, and Resveratrol in the LXR Depict the native T-0901317's pharmacophore features, 3D conformation, and interaction map with the LXR α α Binding Site (PDB ID: 1UHL) Panels **A–C**: binding site. Panels **D–F**: Depict C144's pharmaco phore features, 3D conformation, and interaction network map with the LXR α conformation, and interaction network map with the LXR α binding site. Panels **G–I**: Illustrate Withaferin A's pharmacophore model, 3D binding site. Panels **J–L**: Present Resveratrol's pharmacophore model, 3D conformation, and interaction network map with the LXR α binding site.

As shown in **Figure 5.21**, C144 (AZD7762) establishes three hydrogen bonds and multiple hydrophobic interactions that effectively stabilize its binding within the LXRβ active site. The residues Thr316A and Thr272A serve as hydrogen bond donors, while His435A functions as a hydrogen bond acceptor. Hydrophobic stabilization is facilitated through π-π stacking interactions with Phe340A and Phe271A, complemented by non-polar contacts with Leu274A, Met312A, Ile327A, and Ala275A.

Notably, C144 (AZD7762) shares nine residues with the native T-09019317 (1UHL/1UPV), indicating potential for enhanced pharmacological activity. Both ligands utilize hydrogen bonding from Thr272A, Thr316A, and His435A, with threonine residues acting as donors and His435A as an acceptor. The hydrophobic interactions are reinforced by overlapping residues such as Phe340A, Ile327A, and Met312A, suggesting that C144 (AZD7762) may exhibit comparable or superior binding affinity and efficacy due to its robust pharmacophoric framework.

Bergapten exhibits a complementary pharmacophoric profile, engaging Thr316A, Ala275A, and Met312A, with Thr316A forming a hydrogen bond with the ester oxygen. Resveratrol shares pivotal residues Thr272A, Thr316A, and Ala275A, where both threonine act as hydrogen bond donors, enhancing interactions with hydroxyl groups, while Ala275A contributes hydrophobic stabilization. The interactions delineated between C144 (AZD7762) and LXRβ particularly through hydrogen

bonding and hydrophobic interactions with residues like Thr316A and His435A underscore C144's capability to effectively stabilize its binding conformation within the active site. These pharmacophoric characteristics suggest that C144 (AZD7762) can modulate LXRβ regulatory pathways positioning it as a promising candidate in cancer therapeutics.

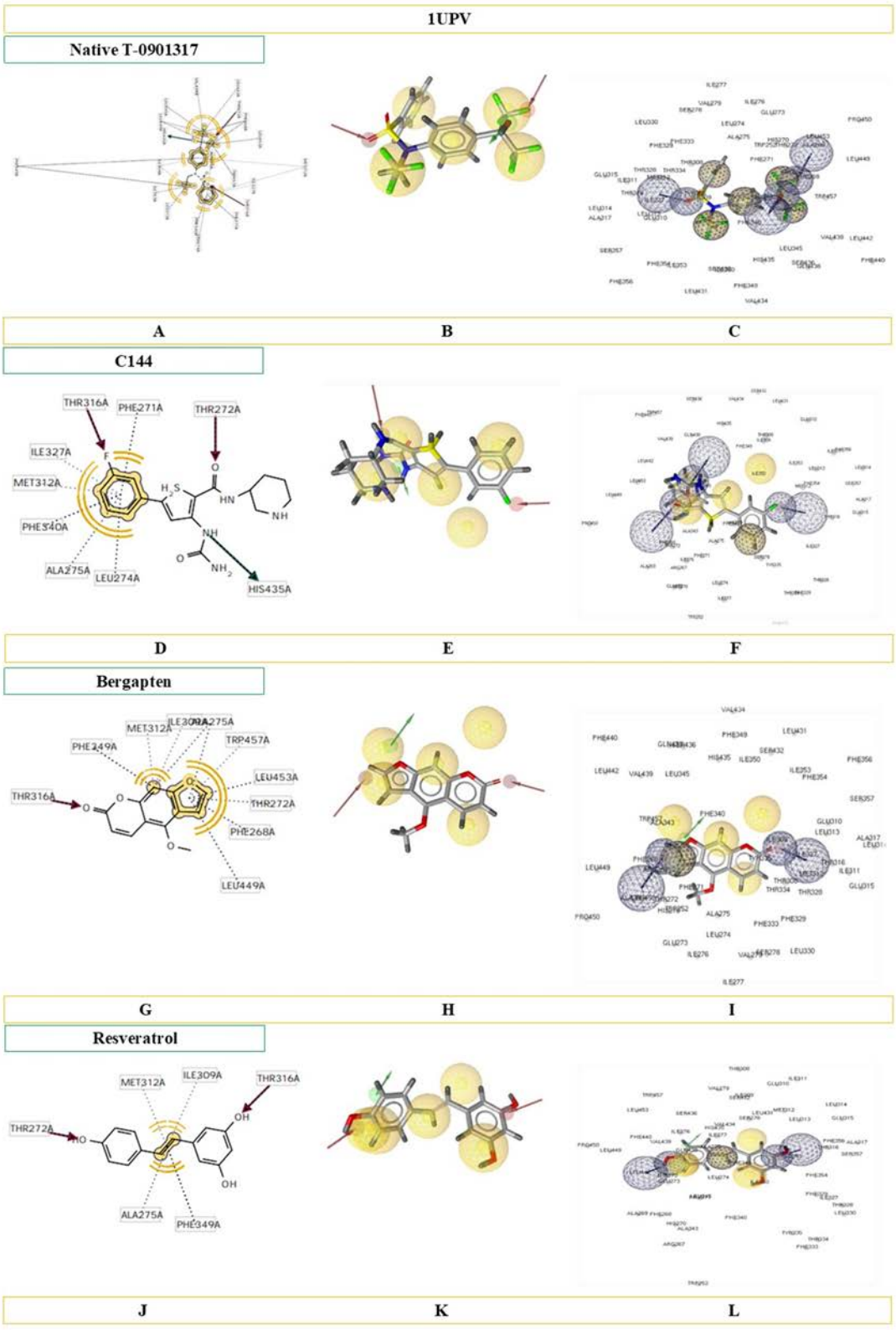
1UPV
Native T-0901317
A
B
C
C144
THR316A
PHE271A
THR272A
ILE327A
MET312A
PHE340A
ALA275A
LEU274A
HIS435A
D
E
F
Bergapten
MET312A
ILE309A
ALA275A
TRP457A
PHE249A
LEU453A
THR316A
THR272A
PHE268A
LEU449A
G
H
I
Resveratrol
MET312A
ILE309A
THR316A
THR272A
ALA275A
PHE349A
J
K
L

Figure 5.21: Comparative Binding Analysis of Native T-0901317, C144, Bergapten and Resveratrol in the LXR native T-0901317's pharmacophore features, 3D conformation, and interaction map with the LXR α α Binding Site (PDB ID: 1UPV) Panels **A–C**: Depict the binding site. Panels **D–F**: Depict C144's pharmacophore features, 3D conformation, and interaction network map with the LXR α interaction network map with the LXR α binding site. Panels **G–I**: Illustrate Bergapten's pharmacophore model, 3D conformation, and binding site. Panels **J–L**: Present Resveratrol's pharmacophore model, 3D conformation, and interaction network map with the LXR α binding site.

As shown in **Figure 22**, C144 (AZD7762) exhibits critical pharmacophoric interactions characterized by hydrogen bonding and hydrophobic forces. The residue SER332A functions as a hydrogen bond donor, enhancing ligand stability. Hydrophobic residues, including PHE329A, ILE357A, ILE352A, MET365A, LEU287A, and TYR369A, contribute to stabilization *via* van der Waals interactions. The conservation of these residues in the native feroline (5ICK) reinforces a similar binding mechanism, indicating that C144 (AZD7762) may possess comparable binding affinities to the native ligand, thus emphasizing its potential as a competitive inhibitor or modulator of FXR activity. In contrast, Obeticholic Acid lacks MET450 and SER332A, suggesting a distinctive binding profile that may adversely affect its binding affinity and stability within the receptor. While MET365A, PHE329A, and ILE357A are conserved with C144 (AZD7762), the absence of the hydrogen bond donor SER332A in Obeticholic Acid implies a weaker interaction relative to C144 (AZD7762). Resveratrol engages hydrophobic residues such as ALA291A, LEU451A, LEU465A, TRP454A, PHE461A, and PHE284A through non-polar contacts to facilitate binding. Its hydroxyl groups interact with THR288A and SER332A, mirroring some functionalities of C144 (AZD7762). The presence of SER332A in both compounds suggests a shared mechanism for ligand stabilization *via* hydrogen bonding. The interaction profile of C144 (AZD7762) with the FXR receptor, marked by hydrogen bonds and extensive hydrophobic interactions, positions it as a potent modulator in therapeutic contexts, particularly concerning cancer. The conservation of key residues such as SER332A, serving as a hydrogen

bond donor, alongside robust hydrophobic stabilization provided by PHE329A and ILE357A, underscores the ligand's capacity to achieve an optimal binding conformation within the receptor's active site. This intricate interaction landscape highlights C144's significance in targeting the FXR receptor, potentially providing a strategic approach for cancer therapeutics.

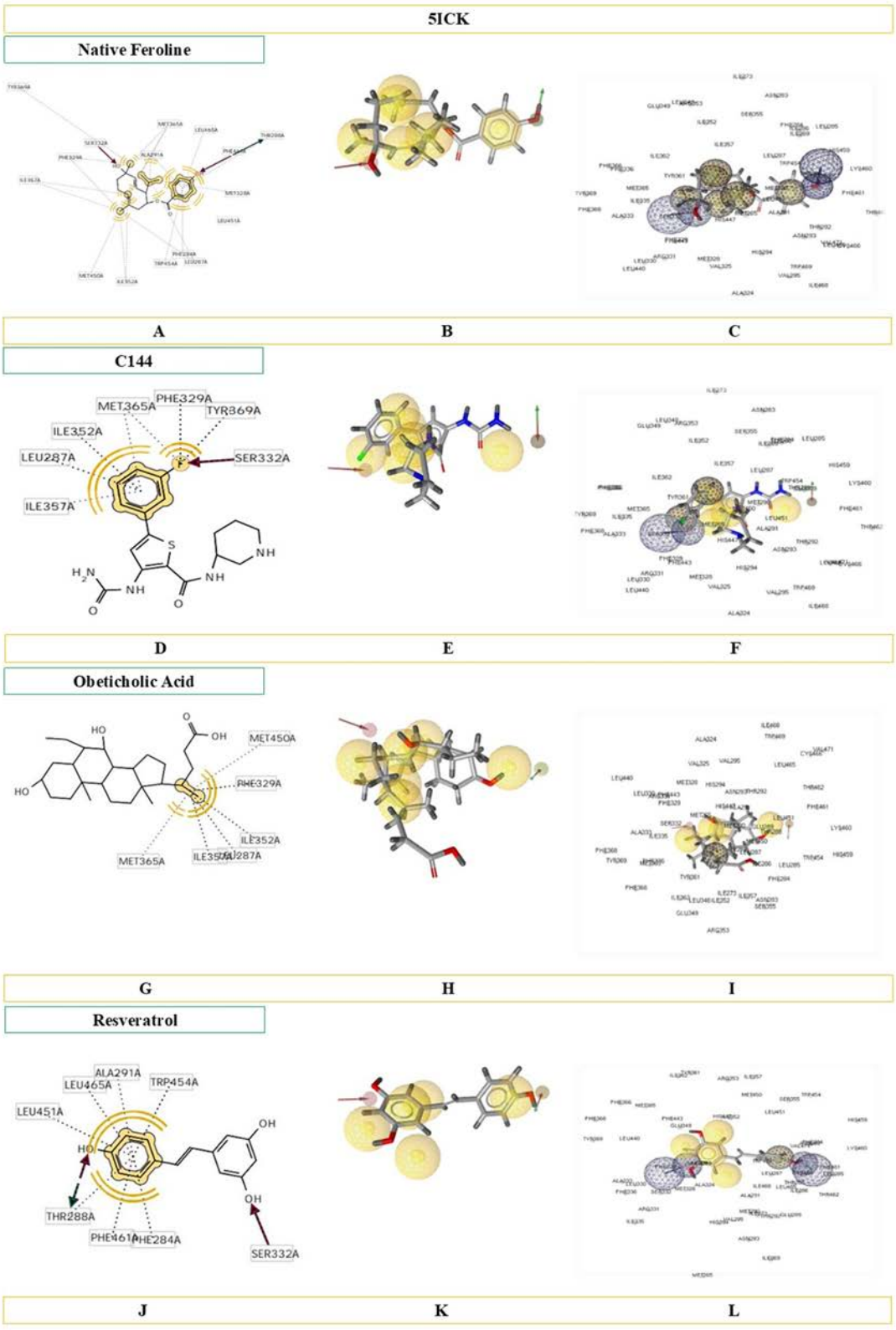
5ICK
Native Feroline
A
B
C
C144
MET365A
PHE329A
TYR869A
ILE352A
LEU287A
SER332A
ILE357A
D
E
F
Obeticholic Acid
MET450A
PHE329A
ILE352A
MET365A
G
H
I
Resveratrol
ALA291A
LEU465A
TRP454A
LEU451A
THR288A
PHE461A
PHE284A
SER332A
J
K
L

Figure 5.22: Comparative Binding Analysis of Native Feroline, C144, Obeticholic acid and Resveratrol in the LXR native feroline pharmacophore features, 3D conformation, and interaction map with the LXR α α Binding Site (PDB ID: 5ICK) Panels **A–C**: Depict the binding site. Panels **D–F**: Depict C144's pharmacophore features, 3D conformation, and interaction network map with the LXR interaction network map with the LXR α α binding site. Panels **G–I**: Illustrate Obeticholic acid pharmacophore model, 3D conformation, and binding site. Panels **J–L**: Present Resveratrol's pharmacophore model, 3D conformation, and interaction network map with the LXR α binding site.

5.3.10. Bioactivity prediction

The bioactivity scores in **Table S5.25 (supporting information)** underscore the potential of C144 (AZD7762) across multiple biological target classes. A GPCR ligand score of 0.16 suggests it may possess notable activity in modulating GPCR pathways, which are essential in regulating cancer cell proliferation, survival, and metastasis. [114]. In contrast, native T-0901317 (1UHL/1UPV) and resveratrol show lower scores of 0.01 and -0.20, respectively. As an ion channel modulator**,** it has moderate activity with a score of -0.15, indicating relevance in cellular homeostasis and cancer regulation, although lower than withaferin A (0.14) [115]. Its kinase inhibitory potential is notable at 0.54, surpassing obeticholic acid (-0.48) and withaferin A (-0.49), positioning it as a promising inhibitor of aberrant kinase activity, a hallmark of many cancers [116]. As a nuclear receptor ligand, scores 0.43, indicating substantial modulation of gene expression related to cancer survival, though slightly lower than native feroline (5ICK, 0.69) and obeticholic acid (0.80) [117]. Furthermore, its protease inhibitor score of 0.30 suggests potential in preventing tumor invasion and metastasis [118]. Despite an enzyme inhibition score of 0.10, C144 (AZD7762) exhibits a balanced and comprehensive bioactivity profile across multiple molecular targets, indicating high pharmacodynamic versatility. This highlights its potential as a potent modulator of LXRα, LXRβ, and FXR signaling pathways, positioning it as a promising candidate for receptor-targeted cancer therapeutics.

5.3.11. Detailed quantum calculation

5.3.11.1. Molecular Electrostatic Potential Analysis

5.3.11.1.1. Analysis of molecular electrostatic potentials (MEPs)

Molecular electrostatic potential (MEP) analysis is a key computational technique commonly employed to investigate intermolecular interactions and the behavior of drug molecules [119]. Graphically, a spatial distribution of MEPs is represented as the chemical activities for a chemical reaction and strong binding on the active locations. MEP is directly connected with the chemical behavior, electronegativity and dipole moment. These plots help visualize molecular polarity by mapping electron densities (ED) [120]. MEP surface plots are visualized using different colors, representing electrostatic potential variations; where red indicates the most -ve potential, blue indicates most +ve potential and green indicates zero potential regions in molecule. MEP increases as in sequence of colors: red, orange, yellow, green and blue on surface mapping/arrays. Here, negative MEP represents the attraction of a proton/light cation in the region of red color due to concentrated ED in the molecule, but the positive MEP represents the repulsion of the proton/cation in the region of blue color due to the atomic nuclei regions as the low concentration of ED in molecule [121].

The MEP analysis of the native T-0901317 (PDB: 1UPV/1UHL) reveals a color gradient from -0.06368 to +0.06368 e^{-2} (-ve to +ve potential). The -ve potential regions, shown in red and yellow, are found near the -O and -N atoms, indicating higher electron density. In contrast, the -H atom attached to oxygen displays a +ve potential (blue), signifying an electron-deficient area. These findings highlight regions likely to engage in nucleophilic and electrophilic interactions depicted in **Figure S5.23 (a-c)** (**supporting information**). MEP analysis of native feroline (5ICK) reveals a color gradient from -0.06789 to +0.06789 e^{-2}. The -ve potential regions, shown in red and yellow, surround the O-H bond in the cyclodeca ring, indicating higher ED. Conversely, the H-atom attached to oxygen in the hydroxybenzoate ring displays a +ve potential (blue), indicating an electron-deficient area depicted in **Figure S5.24 (a-c)** (**supporting information)**. For C144, the MEP analysis reveals a color gradient ranging from-5.943 to +5.943 e^{-2}. The -ve potential regions are primarily found around the -O atoms attached to the nearby thiophene ring, signifying areas of higher ED.

These regions are likely to attract positively charged species, indicating potential sites for nucleophilic interactions. On the other hand, the -H atom bonded to the -N atom shows a +ve potential, depicted in blue, highlighting its electron-deficient nature. This suggests it could be a favorable site for electrophilic interactions. These variations in electrostatic potential help identify key regions of reactivity within the molecule as shown in **Figure 5.25a**.

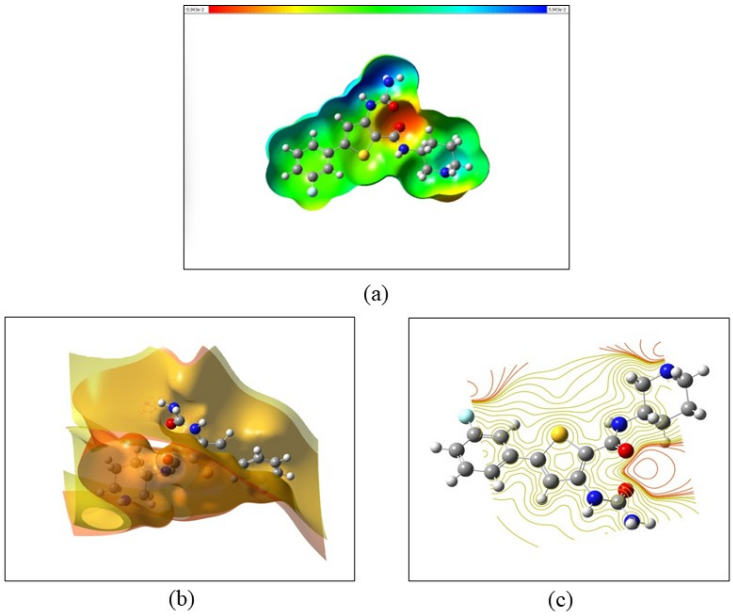

Figure 5.25: a) Molecular electrostatic potentials (MEP) plot of C144, **b**) Contour map plot of ESP isosurface of C144, **c**) Visualization of the ESP array plot for C144.

For bergapten, MEP analysis reveals a potential range from -6.304 × 10^{-2} to +6.304 × 10^{-2} e^{-2}. The -ve potential regions are concentrated around the -O on the furanocoumarin's pyran ring, indicating electron-dense areas favorable for nucleophilic interactions as shown in **Figure. S5.26a** (**supporting information**). In obeticholic acid, the MEP analysis shows a gradient from -5.370 to +5.370 e^{-2}. The -ve potential regions are observed around the -O atom, indicating electron-rich areas, while the -H atom attached to another -O shows +ve potential, suggesting an electron-deficient region as shown in **Figure S5.27a** (**supporting information**). For resveratrol, it reveals a gradient from -6.431 to +6.431 e^{-2}. The analysis shows no regions of negative potential, indicating an absence of areas with higher electron

density as shown in **Figure S5.28a** (**supporting information**). Conversely, the -H atoms bonded to the -O atoms on both benzene rings exhibit a +ve potential (blue), highlighting electron-deficient areas. These observations suggest the regions where the molecule is likely to engage in electrophilic interactions and could be targeted by nucleophiles. In withaferin A, it reveals a gradient from -5.1841 to +5.184 e^{-2}. The -ve potential regions are observed around the O_5 and O_{25} atoms, signifying areas of higher electron density. In contrast, the -H atom (H_{35}) attached to C_1 shows a +ve potential (blue), indicating an electron-deficient region as shown in **Figure S5.29a** (**supporting information**). These variations suggest where the molecule might engage in nucleophilic and electrophilic interactions.

5.3.11.1.2. Analysis of Electrostatic potentials (ESPs)

Electrostatic potential (ESP) analysis is essential for understanding the charge distribution within molecules, as it directly influences their interactions and reactivity [122-123]. The ESP is closely linked to electron density (ED), which reveals the sites for nucleophilic and electrophilic attacks, as well as hydrogen bonding interactions. In ESP plots, -ve potential regions, shown in light red, correspond to areas with high electron density that attract protons, which are typically more reactive to electrophilic attacks [124-125]. On the other hand, +ve potential regions, represented in golden, indicate areas with low electron density, which tend to repel protons, these golden regions are more likely to attract nucleophiles, making them susceptible to nucleophilic attacks. The ESP iso-surface plots, shown in **Figure S5.23b-S5.29b** (**supporting information**) with **Fig. 5.25b** shown above, highlight regions of varying charge distribution [126-128]. The ESP iso-surface plots visualize the 3D distribution of charge, helping to predict molecular behavior, identify reactive sites and determine a compound's reactivity and binding affinity. Additionally, the ESP array plots visualize electronegative regions near molecular rings that may serve as potential sites for chemical attacks. These plots are represented in various colors, as shown in **Figure S5.23c-S5.29c** (**supporting information**), with **Figure 5.25c** displayed above. These diagrams visualize chemically active sites and comparative reactivity at the atomic level. As shown in the figures, the yellow lines indicate electronegative regions near

the atoms of various molecular rings. These regions, regardless of proximity, serve as potential sites for nucleophilic or electrophilic attacks [129]. Understanding this distribution helps predict how the compound interacts with other molecules or ions, providing insight into its chemical behavior and reactivity.

5.3.11.2. Mulliken Charge (MC) analysis

Mulliken charge analysis is an essential method for describing electron density distribution within a molecule, offering insights into chemical reactivity by pinpointing electron-rich and electron-deficient atomic sites. A positive charge on atoms like carbon suggests electrophilic sites, increasing reactivity toward nucleophiles, while negatively charged atoms like oxygen can stabilize positive charges and participate in hydrogen bonding, enabling interactions with other molecules [130,31]. The analysis of the charge distribution in different compounds reveals significant variations illustrated in **Figure S5.30 (supporting information)** where the charge distribution between Carbon and Oxygen atoms are shown for all the compounds. In bergapten, the computed MC density indicates a strong positive charge of 2.295 on the carbon atom, while the oxygen atom carries a moderate negative charge of -0.281. This significant charge separation highlights the carbon's electron deficiency and the oxygen's gain of electron density, resulting in a polarized bond as shown in **Table S5.26 (supporting information).** Such polarization increases bergapten's reactivity, especially in polar environments, where the electron-deficient carbon acts as an electrophilic site and the oxygen can participate in hydrogen bonding and other interactions. This polarization is expected to significantly influence its reactivity, stability, and biological interactions.

In contrast, the MC distribution observed in C144 reveals an uneven electron density distribution between carbon and oxygen. The carbon atom in this compound has a positive charge of 1.416, indicating electron deficiency, while the oxygen atom carries a negative charge of -0.318, suggesting it has acquired additional electron density. This charge separation indicates that C144 possesses polar characteristics, which may influence its interactions with biological targets such as receptors and enzymes. Understanding this charge distribution is essential for predicting the compound's

binding affinity and overall behavior in biological systems, thereby enhancing its potential as a therapeutic agent. In native T-0901317 (1UPV/1UHL), the Mulliken charges show slight positive values for carbon (0.367) and oxygen (0.126) (see Table S24). This indicates a relatively balanced electron density distribution, and a smaller charge separation compared to other compounds. The lower degree of polarization suggests greater stability and potentially lower reactivity than compounds with more pronounced charge differences. Compounds like bergapten and C144 exhibit strong polarization, which increases their reactivity, while native T-0901317 (1UPV/1UHL) shows a more balanced charge distribution, indicating greater stability and lower reactivity.

5.3.11.3. Natural bond orbital (NBO) analysis

NBO analysis offers valuable insights into chemical bonding and electron distribution, particularly within donor–acceptor systems. In therapeutic compounds, it reveals intra-molecular charge transfer (ICT), where charge delocalization enhances conjugation, contributing to the stabilization of molecular complexes. Strong donor-acceptor interactions are quantified through perturbation energy (E^2) values, highlighting the stability of the electronic structure and charge distribution in various molecular systems, offering key insights into their chemical behavior. In the Mulliken charge study, we identified three compounds bergapten, C144 and native T-0901317 (1UPV/1UHL) that exhibited notable charge distribution results, both favorable and unfavorable. Consequently, we focused our NBO analysis on these compounds, as NBO provides more precise and meaningful insights into their electronic interactions. While the MC analysis revealed variations in electron density and molecular polarity, NBO will explore intra-molecular charge transfer (ICT) and donor-acceptor interactions, offering a deeper understanding of their stability, conjugation and overall molecular behaviour [132].

In the NBO analysis, the E^2 values represent the energy associated with donor-acceptor interactions, which reflect the strength of charge transfer between orbitals. In native T-0901317 (1UPV/1UHL) compound, the $\sigma C_{31}–H_{43} \rightarrow \sigma^* C_{30}–H_{42}$ interaction with

an E^2 value of 70.67 kcal/mol indicates a relatively weak donor-acceptor interaction, suggesting limited charge transfer between these orbitals as illustrated in **Table S5.27 (supporting information).** In C144, the $\pi^*C_5–C_6 \rightarrow \sigma^*C_{17}–O_{18}$ interaction with an E^2 value of 98.45 kcal/mol shows a moderate level of charge delocalization, indicating a stronger interaction compared to native T-0901317 (1UPV/1UHL). However, bergapten exhibits a much higher E^2 value of 933.57 kcal/mol for the $\pi^*C_{14}–C15 \rightarrow \sigma^*C_{11}–C_{12}$ interaction, signifying an extensive charge transfer and a highly stable interaction (**Table S5.27**). The higher E^2 value in this compound reflects greater conjugation and more efficient electron sharing between the orbitals, making it significantly more stable than the other two compounds. Herein, NBO analysis highlights the strength of donor-acceptor interactions through E^2 values, revealing the extent of intra-molecular charge transfer (ICT) and stability in therapeutic compounds. Bergapten shows the highest E^2 value, indicating strong conjugation and stability, while C144 and native T-0901317 (1UPV/1UHL) exhibit weaker interactions. These insights provide a deeper understanding of the electronic structure and stability of these molecules.

5.3.11.4. Becke surface analysis (BSA)

The quantitative analysis of molecular surfaces, such as Becke surface analysis reveals that the interaction mechanisms of the complex involve electrostatic as well as hydrogen bonding interactions. The isosurface has a Blue-White-Red (BWR) colour transition, which makes it easy to identify the interaction region by merely observing the colours. The Becke surface quantitative analysis tool is commonly used to identify the active sites of therapeutic agents and to assess the relative intensity of molecular interactions [133]. As shown in **Figure 5.31(a)**, the Becke surface map for the most preferred therapeutic compound i.e., C144 was coloured according to their electron density value (ρ). The Becke surface is represented by points and the presence of red zones corresponds to high electron density regions, which is generated by using Multiwfn and VMD software (https://www.ks.uiuc.edu/Research/vmd/). The redder the colour of the Becke surface map, the higher the electron density. The red zones involve the most interacting atoms within the molecular systems, indicating that the

complex may establish hydrogen bonds. The data range briefly indicates the intensity of molecular interactions based on electron density values. It helps identify and compare the strength of interactions across molecular regions, providing insights into key processes like binding or reactivity. The data range of the active sites between the interacting groups is shown in **Figure 5.31(b)**. In this system, there are several interacting sites (red zones) within the complex i.e., C_{17}-N_{18}, C_8-C_{10}, C_{16}-H_{33} etc. where the relative intensity ranges from 0.192-0.261 a.u. Thus, formation of the red zones represents the sites where the interaction exists within the molecular systems.

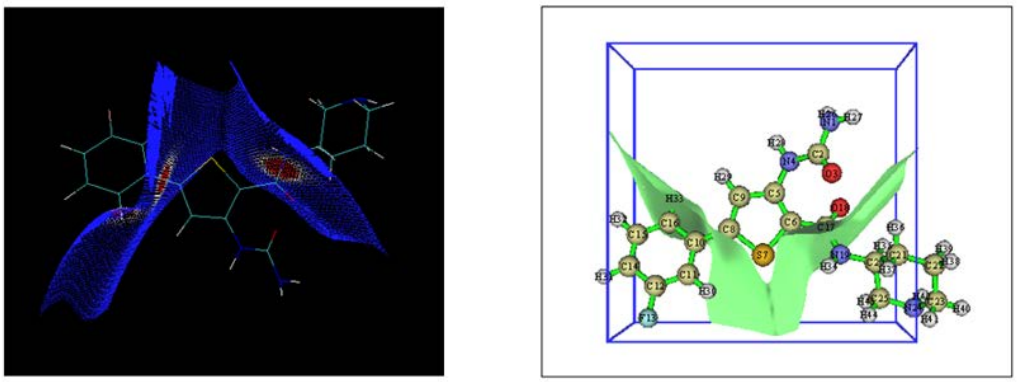

(a) (b)

Figure 5.31(.a-c) Becke surface analysis (BSA) diagrams of the C144 system.

Becke surface analysis, visualized with a Blue-White-Red color gradient, effectively identifies interaction regions in therapeutic compounds based on electron density. Red zones signify high electron density and strong interactions, such as hydrogen bonding. For C144, crucial interaction sites are observed, with relative intensity values ranging from 0.192 to 0.261 a.u., indicating strong molecular interactions and helping to pinpoint active sites critical for binding and reactivity.

5.3.11.5. Hirshfield surface analysis

Hirshfeld surface analysis, enabled by the versatile Multiwfn software, serves as a vital tool for examining non-covalent interactions within molecular crystals. It utilizes electron density contributions from the molecule and its neighboring atoms to

investigate intermolecular forces that govern crystal packing and overall stability. By analyzing parameters like **di** (distance to the nearest atom within the molecule) and **de** (distance to the nearest atom outside), the method provides precise insights into interactions, including hydrogen bonding, van der Waals forces, and π–π stacking. The results of these calculations are often presented in 2D fingerprint plots, color-coded to show surface contact densities. Multiwfn also allows decomposition of the Hirshfeld surface into local contact surfaces for a detailed investigation of specific atom-atom interactions, which is crucial for understanding molecular stability and crystal packing efficiency. These analyses offer valuable insights into the interaction network and driving forces behind crystal formation, making Multiwfn indispensable in crystallography and materials science research [134,135].

The detailed analysis using Multiwfn software to create 2D fingerprint plots within Hirshfeld surface analysis offers a clear understanding of the intermolecular interactions in C144. The holistic plot captures all interactions, while the 2D fingerprint plots highlight specific contact points that play a significant role in the crystal structure. The local contact surface area was found to be 154.229 $Å^2$, covering 100% of the total contact surface, a result consistent with other molecular fragments as shown in **Figure 5.32**. Notably, the 2D fingerprint plot displays a pair of sharp spikes in the lower left corner (i.e., short di and de values), suggesting that C144 functions as both H-acceptor (lower spike, di > de) and H-donor (upper spike, di < de). The yellow, green and purple colors indicate that the points at corresponding region are high, medium and low, respectively. The analysis of intermolecular contacts reveals dominant interactions, including H···H (31.94%), S···H (21.92%), O···H (20.82%), C···C (7.64%), and H···C (18.90%)/C···H (6.26%). These results highlight the key role of hydrogen bonding, sulfur-hydrogen interactions, and carbon-carbon contacts in stabilizing the crystal structure and influencing the properties of complex C144 as illustrated in **Figure 5.33 (a-g)**. The precision of these insights, obtained through Multiwfn, underscores the tool's effectiveness in analyzing intermolecular interactions and their impact on the structure and behavior of molecular systems, contributing valuable knowledge for material science and pharmaceutical research. Multiwfn, though highly versatile and customizable, may not always produce results

that are directly comparable with those from Crystal Explorer (*https://crystalexplorer.net/*), which is specifically optimized for Hirshfeld surface analysis in molecular crystals. This refined analysis emphasizes the importance of non-covalent interactions, offering a deeper understanding of the molecular forces shaping the crystal structure in complex organic systems. Hirshfeld surface analysis using Multiwfn provides precise insights into the non-covalent interactions within molecular crystals, particularly for C144. The 2D fingerprint plots reveal key interactions, including H···H, S···H, and O···H, which contribute to the stability and structure of the crystal. This analysis highlights the role of hydrogen bonding and other intermolecular forces in shaping molecular behavior, offering valuable information for crystallography and materials science research.

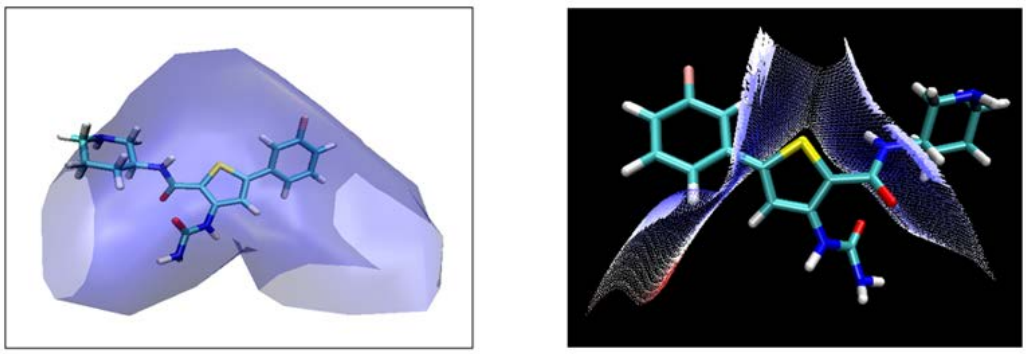

Figure 5.32: The Hirshfeld surface of C144, mapped with *dnorm.*

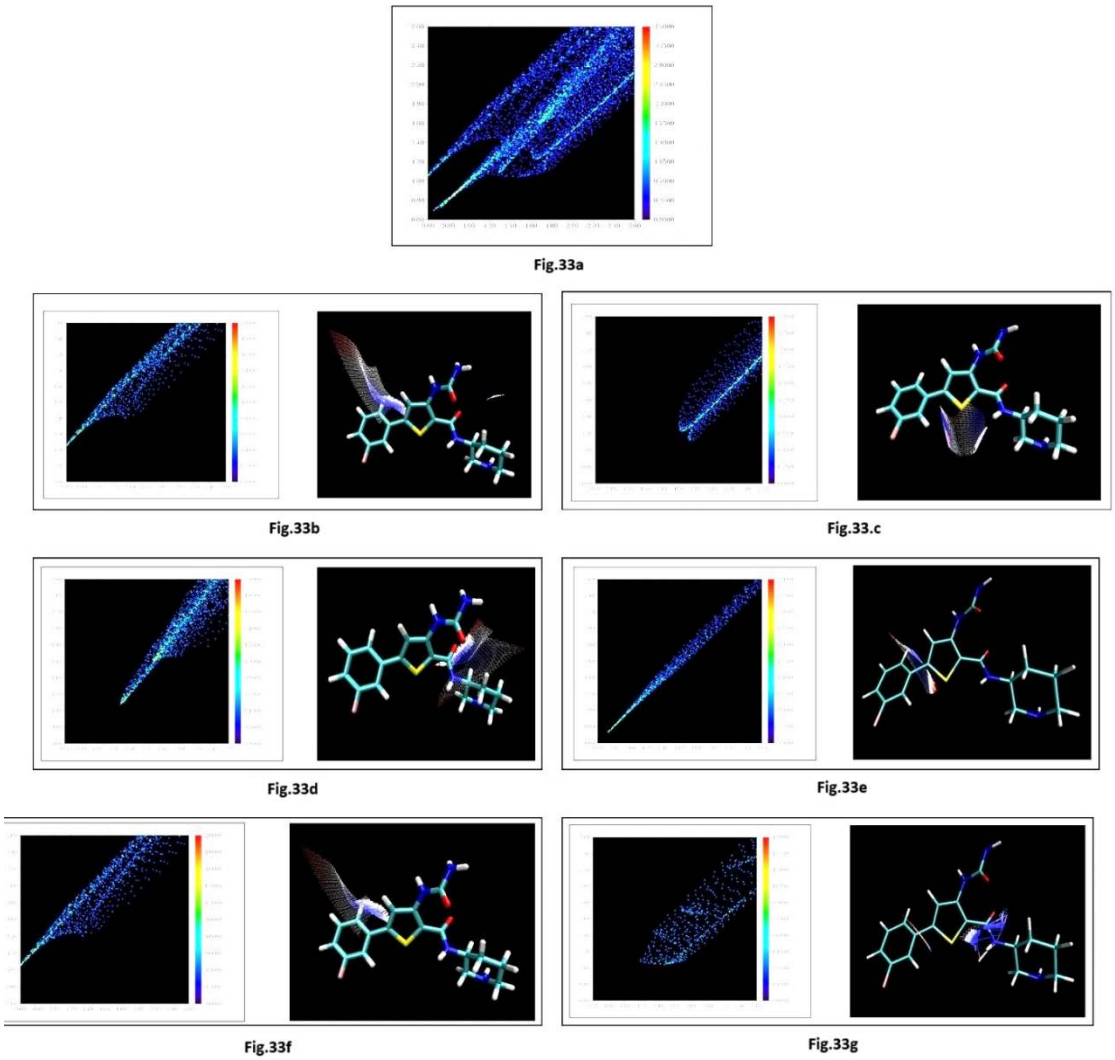

Figure 5.33: The comprehensive 2D fingerprint plot for (a). contributing 100 %, (b). H···H interactions with a 31.94 % contribution, (c). S···H interactions at 21.92 % contribution, (d). O···H interactions at 20.82 % contribution, (e). C···C interactions at 7.64 % contribution (f). H···C interactions 18.90 % contributionand (g). C···H interactions at 6.26 % of C144; X and Y axes correspond to di and de, respectively.

5.3.11.6. Visualizations of non-covalent interaction:

5.3.11.6.1. NCI-RDG analysis

The analysis of non-covalent interactions (NCI) and reduced density gradients (RDG) provides a powerful tool for visually representing interacting regions within complex

systems, aiding in the identification of specific interaction sites. As seen in **Figure 5.34a**, the NCI plots show spikes at low RDG densities which predicts nature of interactions within molecular complexes. The plots of other compound understudy are shown in **Figure S5.34b (supporting information).** The NCI-RDG plot is generated by mapping the reduced density gradient in space, highlighting regions where attractive or repulsive forces occur. It identifies areas of significant interaction within molecules where, the attractive interactions are typically represented by blue regions, indicating regions where electrons are concentrated; while repulsive interactions are denoted by red regions, signifying areas of electron depletion. The plot helps to understand the nature and strength of weak interactions, contributing valuable information to the overall understanding of molecular structures and their behaviour. In this context, green colour indicates weak van der Waals interactions; blue signifies hydrogen bonding and red represents steric interactions. In this analysis, it's observed that van der Waals interactions dominate in the molecular system [136]. For C144 as shown **Figure 5.35a**, it exhibits dominant Van der Waals interactions than other compounds shown in **Fig. S5.35b (supporting information)**. Again, Visual Molecular Dynamics (VMD) analysis is a useful tool in the field of molecular dynamics and computational chemistry. It is extensively used for the visualization, analysis and interpretation of complex systems. VMD allows to explore dynamic processes in biological molecules by providing an interactive 3D representation of molecular structures and their trajectories which reveals weak van der Waals interactions (green patches) within the C144 molecular system. The bluer regions denote stronger attractive interactions, which may result from weaker hydrogen bond interactions. Red patches indicate van der Waals interaction regions, characterized by low electron density. The NCI-RDG and VMD analyses reveal that van der Waals interactions dominate in therapeutic agent C144, as indicated by green patches in the visual plots. The analysis also identifies weaker hydrogen bonding and steric interactions, enhancing the understanding of the molecular interactions and behavior of complex systems [137].

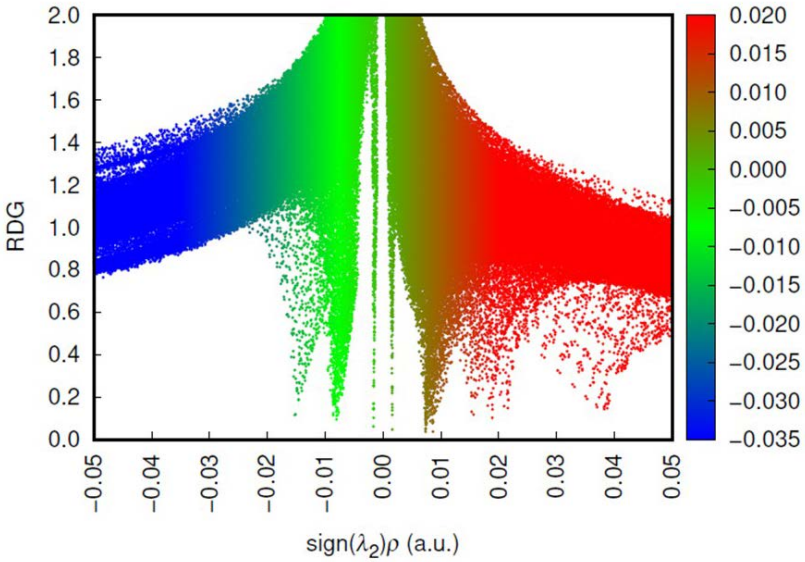

Figure 5.34 (a): Non-covalent Interaction (NCI) plot of C144.

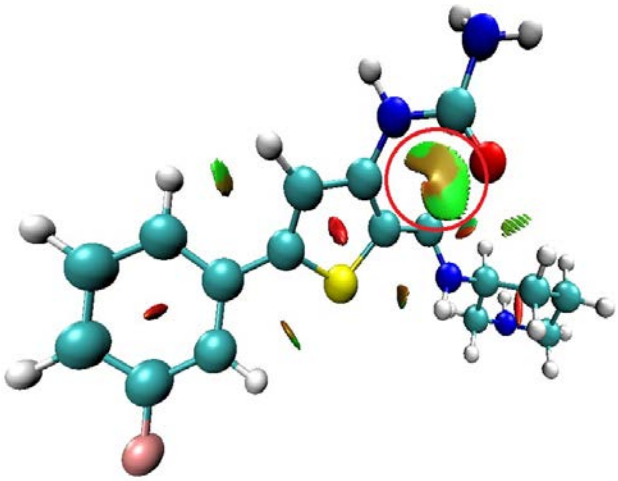

Figure 5.35 (a): Visual molecular dynamics (VMD) model of the C144

5.3.11.6.2. Topology analysis

5.3.11.6.2.1. Electron localization (LOL) and localized orbital locator (ELF) analysis

DFT-based analyses of chemical bonding, including the electron localization function (ELF) and the localized orbital locator (LOL), are important tools for understanding the characteristics of chemical bonds and the distribution of electrons in molecules.

These descriptors rely on topological methods and are built around the concept of the kinetic-energy density (τ), which reflects the reduction in quantum kinetic energy when orbitals are shared, a fundamental driving force behind covalent bonding. ELF is based on the consideration of electron pair density, and it provides insights into the localization of electron pairs within a molecule. On the other hand, LOL recognizes that the gradients of localized orbitals are maximized when these orbitals overlap, helping to identify regions of electron localization and covalent bonding. The topological analysis of electron localization functions (ELF) is used to describe chemical bonds mathematically. The 2D visualization of the ELF isosurfaces for C144 complex reveals significant electronic localization, indicated by red and orange regions. A blue circle marks a depletion zone between the valence and inner electron shells. Topological parameters derived from the Electron Localization Descriptors, as presented in **Figure 5.36,** further elucidate the underlying chemical concepts [138].

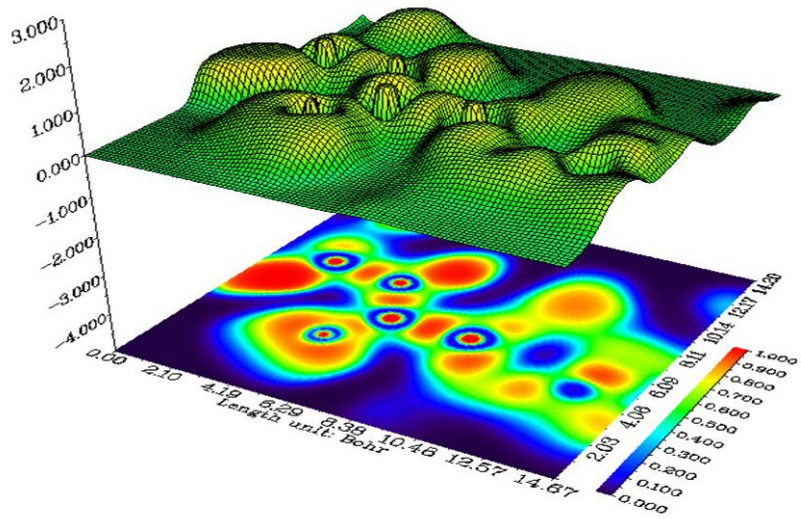

Figure 5.36: Electron localized function (ELF) plot of C144.

5.3.11.7.CLC-Pred

Cytotoxicity predictions are detailed in **Table S5.28 (a-c) (supporting information),** with Pa (probability of activity) and Pi (probability of inactivity) values elucidating its efficacy against various human cancer cell lines. These parameters are instrumental in evaluating the likelihood of cytotoxic activity against specific tumor types [139]. Prediction reveals that C144 demonstrates broad-spectrum anticancer activity with

notable efficacy across a range of tumor types. Lung carcinoma and acute myeloid leukemia (AML) exhibit significant responsiveness, as reflected by high Pa values in cell lines such as DMS-114 (Pa = 0.696, Pi = 0.004) and Kasumi 1 (Pa = 0.678, Pi = 0.003). In breast cancer, represented by MDA-MB-453 (Pa = 0.355) and MDA-MB-231 (Pa = 0.659), the compound shows promising potential for breast adenocarcinoma treatment. Additionally, melanoma (e.g., A2058, Pa = 0.572) and non-small cell lung carcinoma (NSCLC) cell lines (e.g., SK-MES-1, Pa = 0.431) exhibit moderate to high activity, highlighting C144's versatility in targeting solid tumors. Pancreatic carcinoma and leukemia cell lines, such as CFPAC-1 (Pa = 0.598) and MOLT-4 (Pa = 0.351), demonstrate moderate potential, with opportunities for optimization via combination therapies or further refinement. In contrast to C144, native T-0901317 (1UPV/1UHL) shows the highest activity against THP-1 (acute monocytic leukemia, Pa = 0.755), indicating its potent effect on blood-derived cancers, but lower efficacy in solid tumors like Ewing sarcoma and lung carcinoma (Pa = 0.051), suggesting a targeted action on hematological malignancies. Native Feroline (5ICK) demonstrates its strongest activity in lung carcinoma (NCI-H838, Pa = 0.516) and melanoma (SK-MEL-1, Pa = 0.448), with moderate efficacy in leukemia (NALM-6, Pa = 0.379), though its activity is minimal in resistant ovarian adenocarcinoma cell lines (1A9/ptx-10, Pa = 0.036). Bergapten is most effective in leukemia (HL-60, Pa = 0.593) and melanoma (SK-MEL-28, Pa = 0.53), showing moderate activity in glioblastoma (SF-268, Pa = 0.399), but limited effectiveness in pancreatic adenocarcinoma (HPAC, Pa = 0.062) and colorectal carcinoma (SW-60, Pa = 0.014). Obeticholic Acid exhibits promising results in renal carcinoma (UO-31, Pa = 0.634) and melanoma (LOX IMVI, Pa = 0.501), but shows limited activity in hematopoietic malignancies (RWLeu4, Pa = 0.005) and upper aerodigestive tract cancers (FaDu, Pa = 0.068), indicating its potential for targeting renal cancers and melanomas. Resveratrol shows broad-spectrum activity, with the highest efficacy in brain gliomas (Hs 683, Pa = 0.677) and non-small cell lung carcinoma (HOP-18, Pa = 0.526), as well as potential in breast adenocarcinoma (MDA-MB-453, Pa = 0.478) and melanoma, though its lower efficacy in uterine corpus leiomyosarcoma and pancreatic cancer suggests room for refinement. Withaferin A stands out for its strong activity in melanoma (SK-MEL-28,

Pa = 0.924) and breast cancer (MDA-MB-231, Pa = 0.785), showing moderate efficacy in glioma and lung carcinoma, but limited activity in stomach, pancreatic, and ovarian cancers, indicating its more targeted role in skin and breast cancers. Compared to other compounds, C144 shows superior activity in solid tumors and moderate effects in hematologic malignancies. Despite lower efficacy in colon and cervical cancers, its overall profile augmented by modulation of LXRα, LXRβ, and FXR, positions it as a promising candidate for further therapeutic development in cancer.

5.3.11.8. Reacting atom (Biotransformation) and Pharmacokinetics

The metabolic profiles of C144 (AZD7762), native T-0901317 (1UPV/1UHL), native Feroline (5ICK), bergapten, withaferin A and resveratrol reveal distinct patterns in biotransformation pathways as shown in **Table S5.29 (a-c) (supporting information)** [140], highlighting differences in metabolic hotspots and pathways. C144 exhibits strong metabolic reactivity at atom 14 for S-oxidation (ΔP = 0.643) and atom 5 for both N-oxidation (ΔP = 0.478) and N-hydroxylation (ΔP = 0.337), suggesting sulfur and nitrogen-based transformations as key metabolic liabilities. S-oxidation identifies Atom 14 as a key reactive site, indicating its role in sulfur metabolism with potential impacts on biological activity and detoxification. N-glucuronidation, primarily at Atom 25, suggests enhanced solubility and excretion. Aromatic hydroxylation at Atom 19 highlights modifications to the aromatic nucleus that may influence pharmacological properties. N-oxidation and N-hydroxylation at Atoms 5 and 25 indicate susceptibility to oxidative transformations, potentially generating reactive intermediates or metabolites. In contrast, Native T-0901317 (1UPV/1UHL) shows preferential S-oxidation at atom 7 (ΔP = 0.518) and strong N-acetylation and N-hydroxylation reactivity at atom 10 (ΔP = 0.375), indicating a metabolic pattern favoring nitrogen and sulfur modifications. Native Feroline (5ICK) demonstrates high susceptibility to hydroxylation at aliphatic positions, with atom 1 (ΔP = 0.617) ranking highest, whereas epoxidation is predominantly observed at atom 2 (ΔP = 0.654). Bergapten shows limited metabolic vulnerability to hydroxylation but exhibits strong reactivity for O-dealkylation at atom 2 (ΔP = 0.843), marking it as a primary metabolic site. Resveratrol exhibits a broad transformation profile, with atom 1 being the most

reactive site across multiple pathways, including glycination (ΔP = 0.294), aliphatic hydroxylation (ΔP = 0.609), and dehydrogenation (ΔP = 0.565). Similarly, Withaferin A displays significant metabolic activity, with atom 37 (ΔP = 0.497) favored for dehydrogenation and atom 41 (ΔP = 0.436) for C-oxidation. The distinct biotransformation profile of C144 (AZD7762) could potentiate its therapeutic effects by fine-tuning its interaction with key regulatory pathways and enhance its therapeutic efficacy and metabolic resilience.

Subsequently the prediction provided using SwissADME shown in **Table S5.30 (supporting information)** cover several pharmacokinetic properties that are critical for understanding its behavior in a biological system [141]. C144 (AZD7762) demonstrates high gastrointestinal (GI) absorption, suggesting good oral bioavailability, which is advantageous for systemic therapeutic action. However, its inability to permeate the blood-brain barrier (BBB) implies limited use in CNS conditions but may reduce the risk of CNS-related side effects in peripheral treatments. As a P-glycoprotein (P-gp) substrate, C144 (AZD7762) may benefit from reduced toxicity by limiting accumulation in non-target cells but may lower target cell absorption and effectiveness. Its non-inhibitory profile for CYP1A2, CYP2C19, CYP2C9, and CYP3A4 is favorable, reducing the risk of drug-drug interactions with these key enzymes. CYP2D6 inhibition offers potential for optimizing drug interactions but by carefully managing the metabolism of co-administered drugs which can extend drug action. Skin permeability (-6.91 cm/s) may limit transdermal use but reduces unwanted skin absorption. In contrast, native T-0901317 (1UPV/1UHL) and native Feroline (5ICK) show low GI absorption, but the former is a substrate for multiple CYP enzymes, and the latter exhibits a higher skin permeation rate. Bergapten, Resveratrol, and Obeticholic acid all show high GI absorption and varying degrees of BBB permeability, with Resveratrol and Obeticholic acid inhibiting some CYP enzymes. Withaferin A, like C144, has low GI absorption and does not pass the BBB, but its profile is further marked by its inhibition of both CYP2D6 and CYP3A4. In general, C144 (AZD7762) stands out due to its high GI absorption, P-gp interaction, and its selective inhibition of CYP2D6, positioning it differently compared to other compounds that either show broader CYP inhibition or better skin permeation.

Overall, while C144 shows strong potential for systemic oral therapy, the profiles of other compounds suggest greater suitability for topical or CNS-targeted applications based on their absorption and metabolic properties. C144's pharmacokinetic profile presents a compelling case for continued development as an orally administered systemic agent. Additionally, its logP value of 1.97 suggests an ideal level of lipophilicity compared to other compounds. In general, moderately lipophilic compounds (LogP between 2 and 4) tend to be more 'drug-like' due to their balance between membrane permeability and solubility, making them suitable for oral or systemic use with a reduced risk of off-target accumulation and toxicity, positioning C144 (AZD7762) as a promising candidate.

5.3.11.9. Molecular dynamics

5.3.11.9.1. Energy minimization

Energy minimization is a vital preparatory step in molecular dynamics (MD) simulations, intended to eliminate unfavorable atomic interactions and stabilize the system's structure prior to simulation [142]. For the 1UHL–C144, 1UPV–C144, and 5ICK–C144 complexes, energy minimization—incorporating water molecules and ions—was performed using 50,000 steps of the Steepest Descent algorithm. The process was halted once the maximum force acting on any atom was reduced to 200 kJ mol^{-1}. For the 1UHL-C144 complex, the system's potential energy reached a minimum of -1.215×10^6 kJ mol^{-1} at 7,853 steps, while the 1UPV-C144 and 5ICK-C144 complexes achieved minimized potential energies of -8.481×10^5 kJ mol^{-1} at 3,983 steps and -7.198×10^5 kJ mol^{-1} at 3,763 steps, respectively. As shown in **Figure S5.37 (supporting information),** the energy minimization stabilized around 6–7 ns for the 1UHL and 1UPV complexes, and approximately 5–6 ns for the 5ICK complex. This signifies successful convergence of potential energy to the lowest possible values during the minimization process for each system. This process ensures the structural stabilization of the system, facilitating seamless transition into the equilibration and production phases while maintaining a thermodynamically favorable conformation.

5.3.11.9.2. Equilibration

5.3.11.9.2.1. Temperature distribution during NVT equilibration

Following energy minimization, equilibration phases are performed to stabilize the system's temperature and pressure [142]. Proper solvent and ion equilibration around the protein-ligand complex is essential to prevent system instability and ensure robust molecular dynamics at the target simulation temperature. The initial equilibration phase was conducted under a canonical (NVT) ensemble, maintaining constant particle number (N), volume (V), and temperature (T). The duration of NVT equilibration varies based on the system's size and complexity; typically, a period of 50 to 100 picoseconds (ps) is sufficient for solvent equilibration around the protein. However, extended equilibration times, such as 200 ps, may be employed to achieve comprehensive stabilization, particularly in larger or more complex systems. To simulate physiological conditions, the system was equilibrated at 310 K, with minor temperature fluctuations observed throughout the 200 ps equilibration period, as illustrated in **Figure S5.38** (**supporting information**). This approach minimizes unintended structural deviations of the solute during the early equilibration phase, thereby enhancing the accuracy and reliability of the ensuing molecular dynamics simulations.

5.3.11.9.2.2. Pressure distribution during NPT equilibration

In molecular dynamics (MD) simulations, employing an isothermal-isobaric (NPT) ensemble allows the system's volume to fluctuate, thereby maintaining constant pressure and temperature, which closely mimics experimental conditions [142]. After stabilization of the system's temperature during NVT equilibration, pressure and density were further stabilized under an isothermal-isobaric (NPT) ensemble, maintaining constant particles (N), pressure (P), and temperature (T) number, closely simulating experimental conditions. For the 1UHL, 1UPV, and 5ICK systems, pressure was maintained at 1 bar; however, fluctuations were observed at –3.955 ± 95.96 (1UHL) bar, 1.71 ± 124.086 (1UPV) bar, and 0.224 ± 137.285 (5ICK) bar, respectively, throughout the 300 ps equilibration, which could be considered as the

expected behavior of normal distribution of pressure during molecular dynamics, as illustrated in **Figure S5.39 (supporting information).**

5.3.11.9.2.3. Density of the system during NPT equilibration

The average density measured during the 300 ps equilibration was 1003.56 kg/m³ for the 1UHL system, 1011.47 kg/m³ for the 1UPV system, and 1016.80 kg/m³ for the 5ICK system. These values are closely aligned with the experimental density of 1000 kg/m³ and the anticipated density of the SPC/E water model at 1008 kg/m³. The SPC/E model parameters align well with water's experimental properties, and stable density values over time confirm effective equilibration of pressure and density, as illustrated in **Figure S5.40 (supporting information).** This agreement confirms that the SPC/E model accurately reproduces the thermophysical properties of water under standard conditions, thereby validating the equilibration process in these molecular dynamic simulations.

5.3.11.9.3. Outcomes of the molecular dynamic simulation

5.3.11.9.3.1. Root mean square deviation of the protein in the complex

RMSD analysis showed that the 1UHL-C144 complex stabilized after 25 ns, while the 1UPV-C144 and 5ICK-C144 complexes achieved stable conformations after 30 ns, indicating preserved structural integrity without significant conformational alterations occurring beyond this time frame. For the 1UHL-C144 complex, RMSD rose sharply from 0.2 nm to 0.6 nm within 5–6 ns, stabilized near 0.55 nm until 12 ns, then increased to 0.7 nm by 20 ns. After 25 ns, the RMSD remained stable at around 0.68 nm for the duration of the simulation. The 1UPV-C144 complex showed a gradual RMSD rise from 0.2 nm to 0.3 nm over 30 ns, stabilizing at 0.25 nm, indicating minimal conformational changes for the remainder of the simulation. Similarly, the 5ICK-C144 complex exhibited an initial increase from 0.2 nm to 0.3 nm over 25 ns, stabilizing at 0.3 nm from 30 ns until the end of the simulation. The Root Mean Square Deviation (RMSD) analysis of all three are illustrated in **Figure 5.41.**

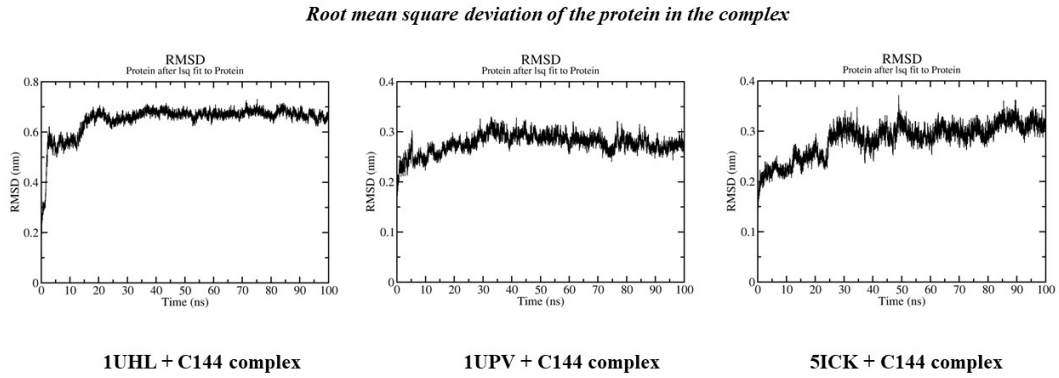

Figure 5.41: Analysis of the simulations from left to right, the RMSD of the protein in the 1UHL–C144 simulation shows consistent stabilization from 25 ns onwards. In the subsequent panels, the RMSD for the 1UPV–C144 simulation stabilizes from 30 ns onwards, which is mirrored in the 5ICK–C144 simulation, where stabilization is also observed from 30 ns onwards.

5.3.11.9.3.2. Root mean square deviation of the ligand in the complex

The conformational dynamics of C144 were assessed by determining its RMSD with respect to the backbone of the 1UHL, 1UPV, and 5ICK proteins. This approach eliminates any global rotational and translational movements of the protein, thereby ensuring that the reported RMSD exclusively represents the positional fluctuations of the ligand relative to the protein structure. For 1UHL, ligand C144 maintained stable RMSD fluctuations below 0.5 nm from 5 ns onwards, indicating a firmly established binding pose. In 1UPV, consistent RMSD values within 0.2–0.3 nm throughout the simulation suggesting minimal alterations in the ligand's binding pose, which appeared securely positioned at the protein's binding site. Similarly, 5ICK showed stable RMSD values, though slight deviations between 70–80 ns hinted at minor ligand repositioning. The Root Mean Square Deviation (RMSD) relative to the backbone structures of the 1UHL, 1UPV, and 5ICK proteins is illustrated in **Figure 5.42.**

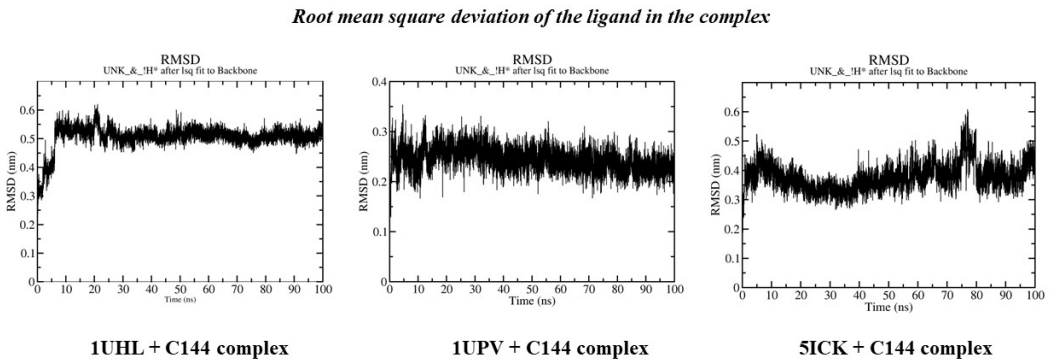

Figure 5.42: The root mean square deviation (RMSD) of the ligand C144 relative to the proteins 1UHL, 1UPV, and 5ICK (from left to right) exhibited a commendable degree of stability throughout the duration of the simulations.

RMSD serves as a critical parameter for differentiating bound states from intermediate and dissociated states. Low ligand RMSD values typically indicate stable bound states, whereas higher RMSD values may suggest ligand dissociation or the presence of metastable states along the dissociation pathway. Protein flexibility and structural adaptability play a significant role in influencing RMSD variations, as proteins with greater conformational plasticity often exhibit higher RMSD shifts upon ligand binding. Additionally, RMSD analysis is inherently time-dependent, demonstrating that stable binding states emerge following an initial phase of structural adjustments [143].

Overall, these observations suggest that the 1UHL protein undergoes more significant conformational changes upon binding with ligand C144 compared to 1UPV and 5ICK. Such variations can be attributed to intrinsic structural differences among the proteins, including flexibility, active site topology, and overall conformational dynamics. Proteins with flexible loop regions or larger active-site cavities often exhibit higher RMSD upon ligand binding, reflecting greater adaptability to accommodate ligands. Additionally, the ligand RMSD remained relatively low across all three complexes, indicating that despite the increased protein flexibility in 1UHL, C144 maintained a stable binding pose. This highlights the significance of accounting for protein

structural features and flexibility when interpreting RMSD data from molecular dynamics simulations.

5.3.11.9.3.3. Root mean square fluctuation of the protein

The root mean square fluctuations (RMSF) of amino acid residues throughout the simulations indicate the localized flexibility of the molecules. For 1UHL, the simulation showed peaks in RMSF exceeding 0.3 nm, with notable contributions to flexibility from residues such as Pro 242 (0.5976 nm), Ala 241 (0.5894 nm), Met 240 (0.5769 nm), Arg 234 (0.5655 nm), Asp 243 (0.5627 nm), Pro 239 (0.4886 nm), Pro 244 (0.4705 nm), Arg 226 (0.4671 nm), Leu 233 (0.4119 nm), Ser 230 (0.3958 nm), Val 235 (0.3949 nm), Ser 246 (0.3897 nm), Phe 426 (0.3866 nm), Arg 232 (0.3832 nm), His 245 (0.3822 nm), Phe 229 (0.3495 nm), Trp 238 (0.3471 nm), Arg 283 (0.3306 nm), Thr 236 (0.324 nm), Asp 231 (0.3188 nm), Arg 401 (0.3187 nm), His 399 (0.3177 nm), Ser 228 (0.3147 nm), Arg 247 (0.3124 nm), Pro 237 (0.3115 nm), Lys 317 (0.3036 nm), Asn 225 (0.3034 nm), and Arg 227 (0.3027 nm). For 1UPV, the simulation displayed localized flexibility with RMSF peaks exceeding 0.26 nm, with significant contributions from residues such as Arg 241 (0.5049 nm), Phe 243 (0.4474 nm), Gln 219 (0.4309 nm), Asp 245 (0.403 nm), Glu 461 (0.3636 nm), Lys 331 (0.3506 nm), Arg 297 (0.3367 nm), Ser 244 (0.3308 nm), Gln 246 (0.3233 nm), Lys 240 (0.3214 nm), Ser 242 (0.3141 nm), Arg 261 (0.2801 nm), and Gln 413 (0.2728 nm). In the case of 5ICK, localized flexibility was evident in RMSF peaks that exceeded 0.2 nm, with contributions from residues such as Glu 425 (0.4028 nm), Ser 342 (0.3966 nm), Gln 428 (0.3662 nm), Asn 426 (0.3127 nm), Pro 427 (0.3105 nm), Arg 264 (0.282 nm), His 344 (0.2708 nm), Gln 423 (0.2752 nm), His 422 (0.2657 nm), Arg 401 (0.2584 nm), Gly 343 (0.2504 nm), Gln 267 (0.2418 nm), Lys 275 (0.2302 nm), His 313 (0.2306 nm), Arg 353 (0.2362 nm), and Pro 424 (0.2337 nm). The Root Mean Square Fluctuations (RMSF) of all three complexes are illustrated in **Fig. S5.43 (supporting information).** The observed RMSF differences among the three complexes are primarily due to variations in structural flexibility, ligand binding-induced conformational changes, amino acid composition, and overall protein

stability. Despite differences in protein flexibility, the ligand remains stably bound in all complexes, reinforcing that C144 exhibits consistent binding behaviour [144].

5.3.11.9.3.4. Radius of Gyration

The radius of gyration (Rg), an indicator of protein compactness, was employed to assess folding behavior in the C144 protein–ligand complexes throughout the molecular dynamic simulations. In the 1UHL complex, the Rg rose sharply to 2.02 nm within 2–3 ns, then gradually declined to 1.87 nm at 20 ns and further to 1.85 nm at 40 ns, stabilizing thereafter between 1.85 and 1.87 nm. The 1UPV complex showed a steady decrease from 1.9 to 1.875 nm within 30 ns, remaining stable at this value until the end of the simulation. or 5ICK, Rg increased to 1.88 nm over 50 ns before stabilizing at 1.84–1.86 nm, indicating initial expansion followed by consistent structural stability for the rest of the simulation. These Rg trends indicate subtle adjustments in protein compactness and overall structural stability throughout the course of the simulations. The Radius of Gyration (Rg) profiles for all three protein-ligand complexes are depicted in **Figure 5.44**. Ligand binding can cause either compaction or expansion depending on the nature of the protein-ligand interactions [145]. The sharp initial increase in Rg for 1UHL indicates that C144 binding initially induced a more open conformation, possibly due to loop movement or active site reorganization before stabilizing at a more compact state. For 5ICK, the delayed increase in Rg suggests a slower structural adaptation process, while 1UPV displayed minimal deviation, implying a stable and rigid binding environment.

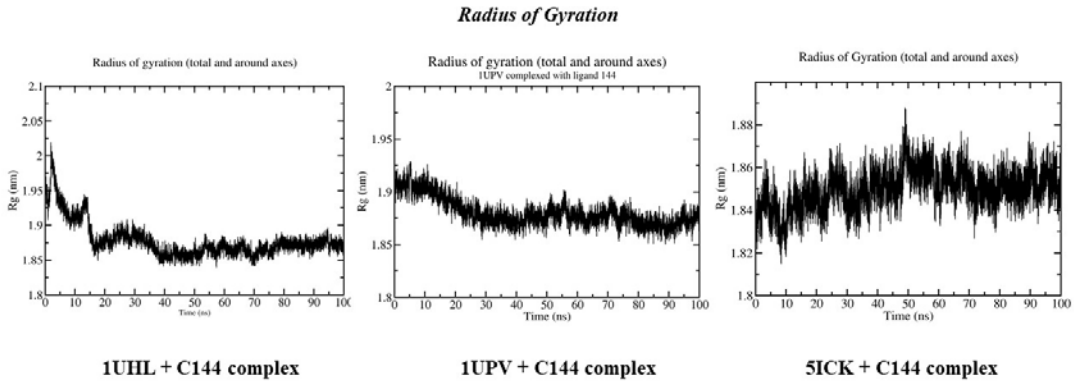

Figure 5.44: The left panel displays the radius of gyration of the protein 1UHL in complex with ligand C144, demonstrating significant stability from 40 ns onwards. The middle panel illustrates the radius of gyration of the protein 1UPV in complex with ligand C144, indicating notable stability from 30 ns onwards. The right panel shows the radius of gyration of the protein 5ICK in complex with ligand C144, reflecting substantial stability from 50 ns onwards.

5.3.11.9.3.5. Hydrogen bonds numbers

Hydrogen bond quantification between the protein targets and ligand C144 during the simulation was conducted using GROMACS' gmxhbond utility. In the 1UHL complex, hydrogen bonds initially ranged from 1 to 2 in the early phases, progressively increasing to 6 as the simulation advanced. From 30 ns onward, a stable formation of 5 to 6 hydrogen bonds between the protein and ligand C144 was consistently maintained until the end. In the 1UPV complex, the overall frequency of hydrogen bonding remained low, with 2 to 3 bonds observed throughout, peaking at 4 by simulation's end. In contrast, the 5ICK complex exhibited transient peaks of 6 hydrogen bonds at 0.87 ns and 97.14 ns but maintained a stable range of 3 to 5 hydrogen bonds for most of the simulation. The number of hydrogen bonds formed between the three protein-ligand complexes is illustrated in **Figure S5.45 (supporting information).** The hydrogen bonding patterns reflect the binding stability of each complex. The differences observed among the 1UHL–C144, 1UPV–C144, and 5ICK–C144 complexes can be attributed to variations in binding pocket architecture, protein flexibility, and the extent of ligand accommodation [146].

5.3.11.9.3.6. Hydrogen bonds existences

The frequency of hydrogen bond interactions throughout the simulation trajectory was quantified utilizing a Perl script, as described in the methodology section. Data for 1UHL, 1UPV, and 5ICK are presented in **Tables S31-S33 (supporting information)** and illustrated in **Fig. S5.46 (supporting information).** 1UHL: A total of 13 hydrogen bond donor (HBD) and acceptor (HBA) pairs were identified at various time points during the simulation. The top five pairs with the highest frequency of interactions are presented. Ligand C144, characterized by its nitrogen atoms, predominantly served as a donor, forming hydrogen bonds with acceptor atoms from neighbouring residues. Notably, Phe 257 contributed to hydrogen bonding with ligand C144 in over 80% of the trajectory frames. Other significant contributors included Glu 301, Met 298, Phe 254, and Thr 258, which accounted for 45.98%, 42.99%, 42.63%, and 29.71% of the total hydrogen bonds observed, respectively. 1UPV: During the simulation, eight hydrogen bond donor-acceptor pairs were identified and ranked based on their occurrence percentage. Ligand C144 acted primarily as a donor due to its nitrogen content. Thr 316 demonstrated active participation in hydrogen bonding with ligand C144, comprising 35.35% of the total trajectory frames, while the other hydrogen bond occurrences were significantly lower, indicating that other non-bonded interactions were prevalent. 5ICK: Throughout the simulation, 60 hydrogen bond donor and acceptor pairs were detected at various timestamps. The frequency of these interactions was calculated using a Perl script, with the top six pairs. Ser 332 was notably engaged in hydrogen bonding with ligand C144 over 57% of the trajectory frames. Additionally, the OE2 atom of Glu 349 and the hydroxyl group of Tyr 369 acted as HBAs for the N3 and N2 atoms of ligand C144, contributing 19.958% and 19.848% to the total hydrogen bonds observed during the simulation, respectively. The hydrogen bonding analysis reveals distinct stability differentials among the 1UHL-C144, 5ICK-C144, and 1UPV-C144 complexes, with 1UHL-C144 demonstrating the most stable interactions, followed by 5ICK-C144, while 1UPV-C144 exhibited the least stability. These disparities stem from inherent differences in binding pocket architecture, conformational dynamics, and protein flexibility, all of

which play a crucial role in governing ligand accommodation and interaction stability [147].

5.3.11.9.3.7. Principal component analysis of 1UHL and ligand C144

Principal component analysis (PCA) was conducted by diagonalizing the non-mass-weighted covariance matrices of backbone atoms from 1UHL, 1UPV, and 5ICK, along with heavy atoms of ligand C144, using GROMACS utilities. Given the link between protein function and conformational dynamics, extracting functionally relevant motions from simulation trajectories presents a significant challenge. To address this, eigenvector analysis *via gmxanaeig* was employed to extract and evaluate collective motions from simulation trajectories. The essential subspace, or "essential dynamics," of a biomolecule, particularly proteins, is defined by the first 10 eigenvectors derived from the covariance matrix, which represent the largest eigenvalues and are commonly referred to as the principal components (PC) of a dataset. Notably, these components capture approximately 70–75% of the cumulative fluctuations in a protein's structure. In line with this concept, the current study identified that the first 30 eigenvectors of the backbone atoms of 1UHL, 1UPV, and 5ICK, as well as ligand C144, exhibited eigenvalues greater than zero, as shown in **Figure S5.47a and b (supporting information)**. Although more than 30 eigenvectors were observed with non-zero eigenvalues, only the first 10 eigenvectors accounted for the most significant correlated motions. Consequently, the first and second eigenvectors of the ligand and respective target proteins were selected as PC1 and PC2, which were projected onto each other to illustrate the collective dynamics, as shown in **Figure S5.47c** and **d** (**supporting information**). The projections of PC1 onto PC2 for ligand C144 and its respective target proteins demonstrate the retention of stable conformations throughout the course of the simulation. For 1UHL, structural stability was evidenced by the convergence and clustering of structures, with a distribution range of –2 nm to 6 nm along PC1 and –4 nm to 5 nm along PC2. Similarly, for 1UPV, the structures were distributed from –2 to 6 nm along PC1 and –2 to 2.5 nm along PC2, while for 5ICK, the distribution spanned from –3 nm to 5 nm along PC1 and –3 nm to 3 nm along PC2 . In the case of ligand C144, the 1UHL complex exhibited a compact range

from –0.2 nm to 0.2 nm along both PC1 and PC2. For 1UPV, ligand C144 was distributed between –0.2 to 0.6 nm along PC1 and –0.4 to 0.4 nm along PC2. Meanwhile, in the 5ICK complex, ligand C144 was observed within a range of –0.6 nm to 0.5 nm along PC1 and –0.4 nm to 0.4 nm along PC2. Furthermore, the projection of the first two eigenvectors (PC1 and PC2) onto one another facilitated the utilization of the GROMACS tool, gmx sham, to construct the Gibbs free energy landscape (FEL) through the Boltzmann inversion of multi-dimensional histograms. For the three protein-ligand complexes (1UHL, 1UPV, and 5ICK in conjunction with ligand C144), a three-column data file containing simulation time in nanoseconds, as well as values for PC1 and PC2, was supplied to the program. This process resulted in the generation of a secondary three-column matrix data file that represented Gibbs free energy (ΔG) for PC1 and PC2 in XpixMap (xpm) format as shown in **Figure 5.47e and f**. The Gibbs free energy landscapes were constructed by configuring the grid count to 64 in all x, y, and z dimensions, establishing an energy level of 64 for both datasets. The matrix data files (xpm) were subsequently transformed into three-dimensional contour plots utilizing the xpm2txt.py add-on utility script alongside the GNU Plot program. The collective or predominant motions of the protein backbone and the heavy atoms of the ligand were reflected in the highest number of structures that accumulated within the energy bin corresponding to ΔG = 0, denoting the Gibbs free energy. At various timestamps between 19 and 53 ns, a total of 102 structures of 1UHL were observed to accumulate within the Gibbs free energy minima as shown in **Figure 5.47e**, while 68 structures of ligand C144 accumulated in the prominent Gibbs free energy minima as shown in **Figure 5.47f**, demonstrating dominant motions from 7.5 ns to 99 ns throughout the simulation. For 1UPV, 69 structures were identified within the Gibbs free energy minima from 26 to 71 ns, whereas ligand C144 exhibited a significant accumulation of 217 structures within the Gibbs free energy minima as shown in, indicating immobilization relative to its initial position. Additionally, from 55 to 98 ns, 35 structures of 5ICK accumulated within the Gibbs free energy minima, while 97 structures of ligand C144 also gathered within this region, reflecting dominant motions from 0.09 ns to 96 ns of the simulation. Overall, the observed broader distribution along the principal components for the 1UHL-C144 complex

suggests enhanced structural flexibility, whereas the confined distributions for the 1UPV-C144 and 5ICK-C144 complexes indicate more restricted conformational dynamics. These disparities can be attributed to inherent differences in protein architecture and the adaptability of their binding pockets, which significantly influence ligand-induced conformational changes [148].

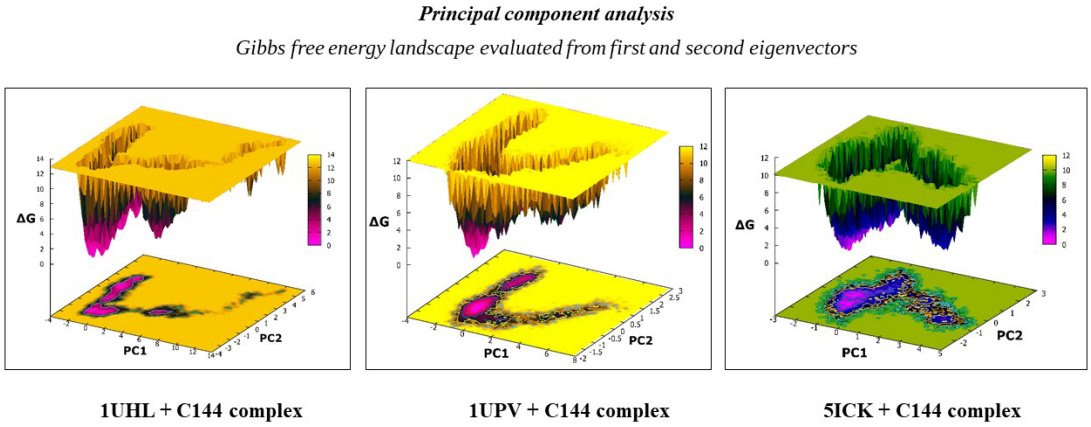

e

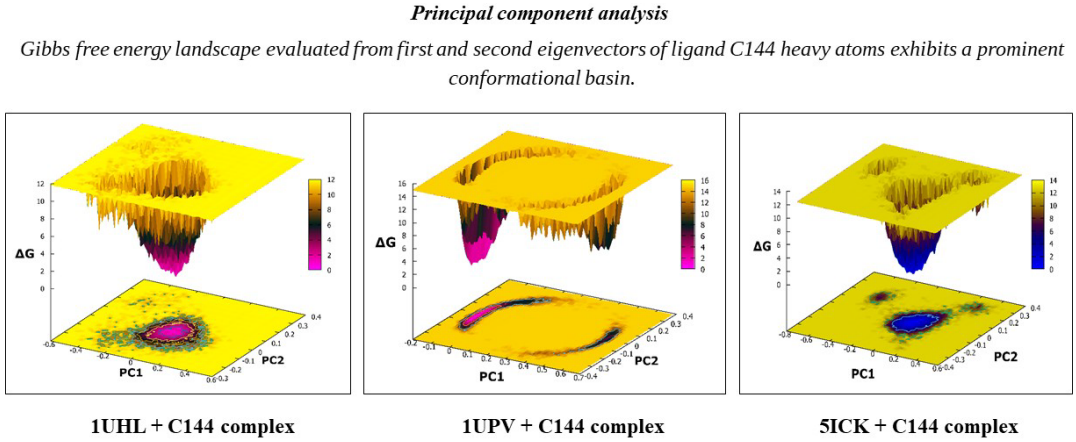

f

Figure 5.47 (e-f): Principal Component Analysis (PCA) of 1UHL, 1UPV, and 5ICK in complex with ligand C144 during the simulations. (**e**) The Gibbs free energy landscape, derived from the first and second eigenvectors of the backbone of 1UHL, 1UPV, and 5ICK, reveals a substantial nonuniform conformational basin. (**f**)

Conversely, the Gibbs free energy landscape derived from the first and second eigenvectors of the heavy atoms of ligand C144 demonstrates a prominent.

5.3.11.9.3.8. MM/PBSA energy calculations

For the 1UHL protein-ligand complex, the ΔG_{MM} energies exhibited initial fluctuations between –450 and –350 kJ mol^{-1} during the first 5 ns, followed by a sharp decline that stabilized around –600 kJ mol^{-1} from 40 ns onward throughout the remainder of the simulation as shown in **Figure 5.48**. The average electrostatic ($\Delta G_{Electrostatic}$) and Van der Waals (ΔG_{VDW}) energies were measured at –348.228 ± 4.614 and –213.68 ± 1.084 kJ mol^{-1} respectively. In the case of 1UPV, the ΔG_{MM} energies demonstrated significant stability and fluctuating between –450 and –350 kJ mol^{-1} until approximately 95 ns after which they dropped sharply to around –530 kJ mol^{-1} by the end of the simulation. The average electrostatic and Van der Waals energies for 1UPV were –189.321 ± 0.68 and –212.331 ± 2.358 kJ mol^{-1} respectively. For the 5ICK protein, the ΔG_{MM} energies initially stabilized at approximately –625 kJ mol^{-1} during the first 30 ns followed by significant fluctuations and ultimately stabilizing around –675 kJ mol^{-1} at the simulation's conclusion. The average electrostatic and Van der Waals energies for 5ICK were –427.562 ± 1.993 and –210.073 ± 0.842 kJ mol^{-1} respectively. The data generated for all Protein-ligand complexes are presented in **Tables S5.31-5.33 (supporting information)**.

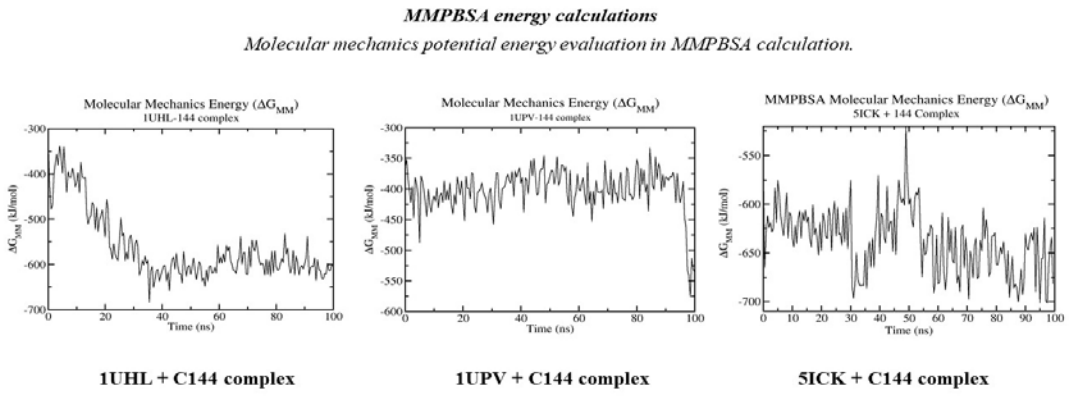

Figure 5.48: Molecular mechanics potential energy evaluation in MMPBSA calculation for all protein-ligand complexes

In the subsequent phase, solvent effects were incorporated into the calculation of Poisson–Boltzmann energy, referred to as polar solvation energy (ΔG_{Polar}) for the interaction between 1UHL and ligand C144. It was noted that ΔG_{Polar} fluctuated between 100 and 200 kJ mol^{-1} during the initial 14-15 ns of the simulation followed by a sudden increase to 300 kJ mol^{-1} and ultimately stabilizing around 350 kJ mol^{-1} for the remainder of the simulation as shown in **Figure S5.49 (supporting information)**. The average ΔG_{Polar} value was maintained at 321.94 ± 4.657 $kJmol^{-1}$. For the 1UPV-ligand C144 complex, ΔG_{Polar} fluctuated from approximately 100 to 250 kJ mol^{-1} until about 95 ns after which it sharply increased to 350 kJ mol^{-1} in the final 5 ns of the simulation. The average ΔG_{Polar} was recorded at 190.058 ± 2.951 kJ mol^{-1}. Regarding the 5ICK ligand C144 complex, ΔG_{Polar} stabilized during the initial 30 ns and subsequently exhibited a steady increase from approximately 250 kJ mol^{-1} to 350 kJ mol^{-1}. The average ΔG_{Polar} for this complex was maintained at 245.451 ± 2.505 $kJmol^{-1}$. The data generated for all Protein-ligand complexes are presented in **Tables S5.34-5.36 (supporting information).** The non-polar energy associated with the interactions between 1UHL-C144, 1UPV-C144 and 5ICK-C144, referred to as ΔG_{Bind} was determined based on the solvent-accessible surface areas of both entities as shown in **Figure S5.50 (supporting information)**. For the 1UHL-C144 complex, ΔG_{Bind} exhibited a gradual decline from approximately –20 to –22.5 kJ mol^{-1} over the initial 20-22 ns. At around 22 ns, a sudden increase to –19 kJ mol^{-1} was observed, followed by consistent fluctuations yielding an average of –20.358 ± 0.061 kJ mol^{-1} for the remainder of the simulation. In the case of 1UPV-C144, ΔG_{Bind} fluctuated erratically between –17 and –22 kJ mol^{-1} throughout the simulation, with an average value of –20.103 ± 0.064 $kJmol^{-1}$. For the 5ICK-C144 complex, ΔG_{Bind} consistently fluctuated between –21 and –18 kJ mol^{-1}, resulting in an average of –20.022 ± 0.05 kJ mol^{-1}.

In conclusion, all energetic components were integrated to derive a comprehensive measure known as the Binding Free Energy (ΔG_{Bind}), which quantifies the interactions

among two or more molecules. For the 1UHL complex, ΔG_{Bind} exhibited a stable trend, fluctuating between approximately –250 and –260 kJ mol^{-1} from around 23 ns until the simulation's conclusion, despite initial instability observed between 10 and 20 ns as shown in **Figure 5.51,** with a running average of –260.32 ± 1.627 kJ $mol^{-}1$. In the case of the 1UPV complex, ΔG_{Bind} remained consistent and stable throughout the simulation, oscillating between –200 and –300 kJ mol^{-1}as shown in Fig. 51 and yielding a running average of –231.697 ± 1.47 kJ mol^{-1}. For the 5ICK complex, ΔG_{Bind} demonstrated significant fluctuations ranging from –360 to –460 kJ mol^{-1} during the simulation, with a running average of –412.201 ± 1.398 kJ mol^{-1}. **Tables S5.31–S5.33 (supporting information)** summarize data for all protein-ligand complexes, including average MMPBSA energies and their standard errors. The calculated free energy of binding ΔG_{Bind} values indicate strong binding affinities: for ligand C144 with 1UHL, ΔG_{Bind} was –260.32 ± 1.627 kJ mol^{-1}; for 1UPV it was –231.697 ± 1.47 kJmol^{-1}; and for 5ICK it was –412.201 ± 1.398 kJ mol^{-1}. These results suggest significant interactions between ligand C144 and the respective targets. Additionally, a refined 2D plot for the 1UHL–C144, 1UPV-C144 and 5ICK-C144 complexes was generated using Maestro (Schrödinger, LLC, New York, NY, 2021), a tool available for academic use. The plot demonstrated that ligand C144 was in close proximity to several hydrophobic and polar amino acid residues, consistently forming hydrogen bonds with HIS 421 in the 1UHL complex, Thr316 in the 1UPV complex, and both SER 332 and HIS 294 in the 5ICK complex, as shown in **Figure 5.52.** The involvement of amino acid residues from 1UHL, 1UPV and 5ICK in all energetic aspects (MM, PB, and SA) during their interaction with ligand C144 was thoroughly examined through MMPBSA analysis, which identified the residues proximal to the ligand along with their corresponding ΔG_{Bind} values as shown in **Figure S5.53 (supporting information)**. This analysis revealed three distinct layers of residue interactions for each protein. In 1UHL, number of residues were identified as **shown in Figure 5.54**. The key polar residues included Thr258, Ser264, and His421, which formed consistent hydrogen bonds along with Gln424. Significant contributions were also made by hydrophobic residues such as Phe254, Ala261, and Leu428. Similarly, in 1UPV many residues were involved as shown in Fig.47. The interactions

encompassed hydrophobic residues like Phe268, Leu274, and Ile311, as well as polar residues, notably Thr316, which established stable hydrogen bonds with the ligand, and the electropositive Arg319. For 5ICK, an array of residues was also involved as shown in Fig. 47. Consistent hydrogen bonding was observed between the ligand and Ser332 and His292, while Thr288 and His447 served as notable polar contributors. Overall, the consistent proximity of C144 underscores its high potential, demonstrating high binding efficiency across these receptor protein environments. Each protein exhibits distinct structural features that influence ligand accommodation and the observed differences in binding free energy across the 1UHL-C144, 1UPV-C144, and 5ICK-C144 complexes arise from variations in binding pocket architecture, electrostatic interactions, solvent effects, and protein flexibility [149].

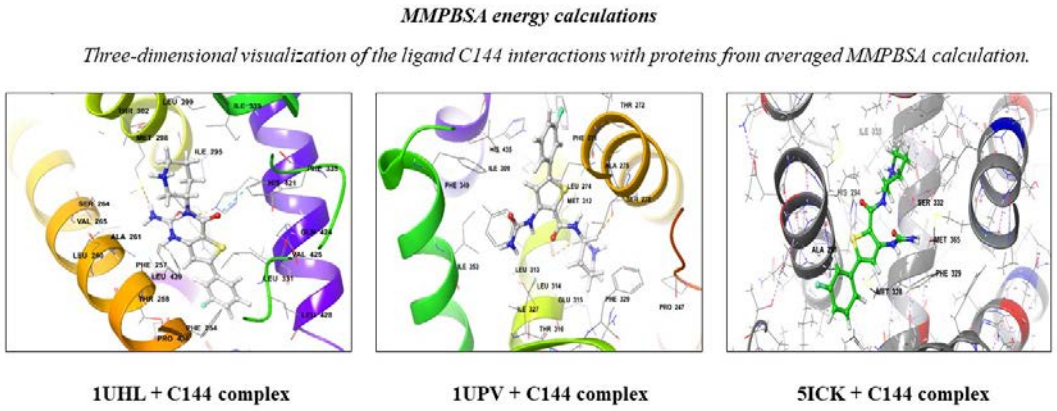

Figure 5.51: Three-dimensional visualization of the ligand C144 interactions with 1UHL, 1UPV and 5ICK from averaged MMPBSA calculation.

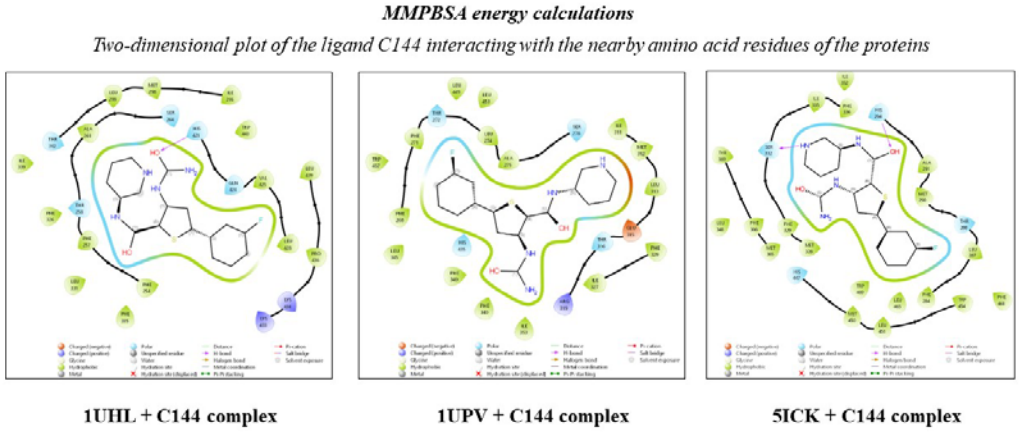

Figure 5.52: Two-dimensional plot of the ligand C144 interacting with the nearby amino acid residues of the protein 1UHL, 1UPV and 5ICK. The complex structure was averaged from MMPBSA calculation.

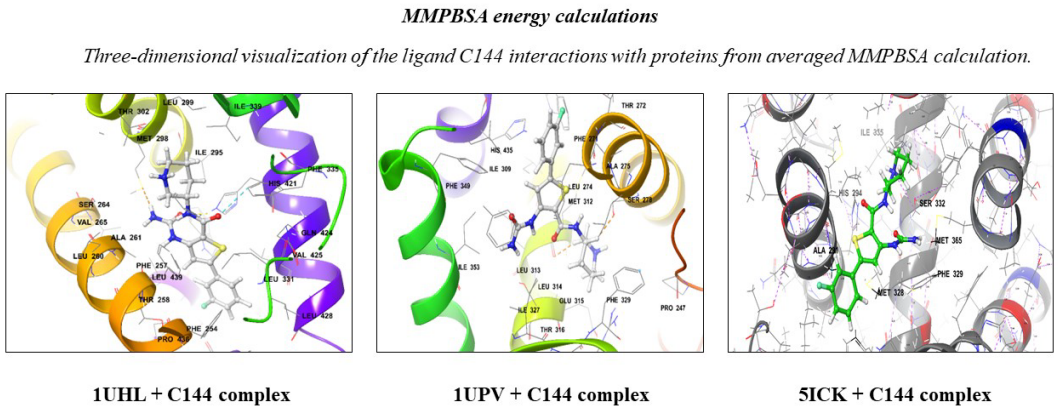

Figure 5.54a: Three-dimensional visualization of the ligand C144 interactions with 1UHL, 1UPV and 5ICK from averaged MMPBSA calculation.

5.3.11.10. Shermo online

This study investigates the thermochemical properties of C144 over a temperature range of 100 K to 310 K at 1 atm, utilizing the Shermo computational tool for analysis [150]. Results indicate that total internal energy (U), enthalpy (H), and Gibbs free energy (G), as presented in **Table S5.37 (supporting information)**, exhibit slight

declines with increasing temperature, signifying enhanced thermodynamic stability at lower temperatures. This is corroborated by the corrected Gibbs free energy (Gcorr), which decreases from 210.62 kcal/mol at 100 K to 180.998 kcal/mol at 310 K. In the low-temperature regime (100 K - 140 K), minimal variations in U, H, and G reflect stable molecular configurations. Conversely, at elevated temperatures (290 K - 310 K), the reduction in Gcorr implies diminished stability. Additionally, as shown in **Table S5.38 (supporting information)**, entropy (S) increases from 105.386 cal/mol/K to 174.360 cal/mol/K, while heat capacities at constant volume (CV) and pressure (CP) rise from 36.339 cal/mol/K and 38.327 cal/mol/K to 92.346 cal/mol/K and 94.333 cal/mol/K, respectively. These trends indicate greater molecular disorder and augmented energy requirements for thermal elevation. The exponential increase in the dimensionless quantity $q(V=0)/N_A$ reflects enhanced molecular dynamics, whereas $q(bot)/N_A$ remains zero, indicating no contribution to energy dynamics. Wherein, '$q(V=0)/N_A$' denotes the heat energy per molecule at constant volume, with **'**q' being the total heat, **'**V=0' indicating no volume change, and 'N_A**'** representing Avogadro's number for conversion to a per-particle scale and '$q(bot)/N_A$' represents the heat energy per molecule at the reference state (denoted as bot, the ground or lowest energy state). The thermodynamic analysis reveals a decline in Gibbs free energy (G) with increasing temperature, indicating reduced stability at elevated thermal conditions. While the compound exhibits relative stability at lower temperatures (approximately 100 K), the progression toward 310 K corresponds with an increase in Gibbs free energy, signifying less favorable thermodynamic states, as illustrated in **Fig. S5.55a** (**supporting information**). The associated graph in **Fig S5.55b (supporting information)** demonstrates a rise in entropy (S), heat capacity at constant volume (Cv), and heat capacity at constant pressure (Cp) with temperature elevation, underscoring increased molecular disorder and enhanced thermal characteristics. The elevated heat capacities indicate the compound's capacity for energy absorption with minimal temperature fluctuation, thereby promoting thermal stability. These findings collectively indicates that favorable thermodynamics at lower temperatures, with increased molecular disorder and energy demands at higher temperatures.

5.4. Conclusion

- Cancer is a leading global health burden, with cases projected to exceed 35 million by 2050—a 77% rise from 2022 necessitating novel, mechanism-driven strategies to improve therapeutic efficacy, mitigate adverse effects, and address tumor heterogeneity.
- Liver X receptors (LXRα and LXRβ) and Farnesoid X receptor (FXR) represent emerging and largely underexplored pathways in cancer research. These nuclear receptors, known for their roles in lipid metabolism, cholesterol homeostasis, and inflammation, have shown promising links to cancer progression, metastasis, and tumor microenvironment regulation. Targeting LXRα, LXRβ, and FXR could pave the way for novel therapeutic strategies, offering unique mechanisms of action distinct from conventional cancer treatments.
- Leveraging resveratrol as a central scaffold, a SwissSimilarity-based virtual screening strategy was applied to identify structurally analogous compounds. Among the screened candidates, C144 (AZD7762) was distinguished as a promising modulator of the intended receptor targets.
- Molecular docking with MVD, AutoDock, and ML-PLIC revealed consistently high binding affinities, validated through cross-platform agreement. Pharmacophore mapping pinpointed key structural features

essential for activity, while predicted stability and reactivity further support the compound's therapeutic potential.

- CLC-pred analysis indicated broad-spectrum anticancer potential across multiple cancer types, with a favorable pharmacokinetic and safety profile.
- Advanced quantum mechanical analysis (MEP, NBO, Mulliken/NPA, NCI, RDG, ELF, LOL, BSA, and HAS) confirmed the compound's strong intermolecular interactions, site-specific reactivity, and target selectivity.
- Molecular dynamics simulations and shermo analyses validated the dynamic stability and thermodynamic feasibility of the C144-receptor complexes.

Taken together, the results support the potential of C144 (AZD-7762) as a promising candidate for cancer therapy through modulation of LXRα, LXRβ, and FXR signaling pathways. Its distinct mode of action may offer novel therapeutic avenues in oncology. Further refinement and experimental validation will be crucial to fully realize its clinical applicability and therapeutic value.

References

1. Christofi, T., Baritaki, S., Falzone, L., Libra, M., &Zaravinos, A. (2019). Current Perspectives in cancer immunotherapy. *Cancers*, *11*(10), 1472. https://doi.org/10.3390/cancers11101472

2. Sufyan, M., Shokat, Z., & Ashfaq, U. A. (2023). Artificial intelligence in cancer diagnosis and therapy: Current status and future perspective. *Computers in Biology and Medicine*, *165*, 107356. https://doi.org/10.1016/j.compbiomed.2023.107356

3. Dahri, M., Abolmaali, S. S., Maleki, R., Najafi, H., Abedanzadeh, M., &Tamaddon, A. M. (2022). Nanoscale aggregation of doxorubicin-short peptide conjugates for enzyme-responsive delivery with various MOF carriers: In-silico steps towards smart cancer chemotherapy. *Computers in Biology and Medicine*, *144*, 105386. https://doi.org/10.1016/j.compbiomed.2022.105386

4. Katti, A., Diaz, B. J., Caragine, C. M., Sanjana, N. E., & Dow, L. E. (2022). CRISPR in cancer biology and therapy. *Nature Reviews. Cancer*, *22*(5), 259–279. https://doi.org/10.1038/s41568-022-00441-w

5. Manickasamy, M. K., Sajeev, A., BharathwajChetty, B., Alqahtani, M. S., Abbas, M., Hegde, M., Aswani, B. S., Shakibaei, M., Sethi, G., &Kunnumakkara, A. B. (2024). Exploring the nexus of nuclear receptors in hematological malignancies.

Cellular and Molecular Life Sciences, *81*(1). https://doi.org/10.1007/s00018-023-05085-z

6. Ramalingam, P. S., Elangovan, S., Mekala, J. R., & Arumugam, S. (2024). Liver X Receptors (LXRs) in cancer-an Eagle's view on molecular insights and therapeutic opportunities. *Frontiers in Cell and Developmental Biology*, *12*. https://doi.org/10.3389/fcell.2024.1386102

7. Chiang, J. Y., & Ferrell, J. M. (2022). Discovery of farnesoid X receptor and its role in bile acid metabolism. *Molecular and Cellular Endocrinology*, *548*, 111618. https://doi.org/10.1016/j.mce.2022.111618

8. Fiorucci, S., Mencarelli, A., Distrutti, E., &Zampella, A. (2012). Farnesoid X receptor: From medicinal chemistry to clinical applications. *Future Medicinal Chemistry*, *4*(7), 877–891. https://doi.org/10.4155/fmc.12.41

9. Lin, C., & Gustafsson, J. (2015). Targeting liver X receptors in cancer therapeutics. *Nature Reviews. Cancer*, *15*(4), 216–224. https://doi.org/10.1038/nrc3912

10. Lo Sasso, G., Bovenga, F., Murzilli, S., Salvatore, L., Di Tullio, G., Martelli, N., D'Orazio, A., Rainaldi, S., Vacca, M., Mangia, A., Palasciano, G., &Moschetta, A. (2013). Liver X receptors inhibit proliferation of human colorectal cancer cells and growth of intestinal tumors in mice. *Gastroenterology*, *144*(7), 1497-1507.e13. https://doi.org/10.1053/j.gastro.2013.02.005

11. Mitra, S., Halder, A. K., Ghosh, N., Mandal, S. C., & Cordeiro, M. N. D. (2023). Multi-model in silico characterization of 3-benzamidobenzoic acid derivatives as partial agonists of Farnesoid X receptor in the management of NAFLD. *Computers in Biology and Medicine*, *157*, 106789. https://doi.org/10.1016/j.compbiomed.2023.106789

12. Nenkov, M., Shi, Y., Ma, Y., Gaßler, N., & Chen, Y. (2023a). Targeting farnesoid X receptor in tumor and the tumor microenvironment: Implication for

therapy. *International Journal of Molecular Sciences*, *25*(1), 6. https://doi.org/10.3390/ijms25010006

13. Nguyen-Vu, T., Vedin, L., Liu, K., Jonsson, P., Lin, J. Z., Candelaria, N. R., Candelaria, L. P., Addanki, S., Williams, C., Gustafsson, J., Steffensen, K. R., & Lin, C. (2013). Liver × receptor ligands disrupt breast cancer cell proliferation through an E2F-mediated mechanism. *Breast Cancer Research*, *15*(3). https://doi.org/10.1186/bcr3443

14. Wang, Q., Sun, L., Yang, X., Ma, X., Li, Q., Chen, Y., Liu, Y., Zhang, D., Li, X., Xiang, R., Wei, Y., Han, J., &Duan, Y. (2016). Activation of liver X receptor inhibits the development of pulmonary carcinomas induced by 3-methylcholanthrene and butylated hydroxytoluene in BALB/c mice. *Scientific Reports*, *6*(1). https://doi.org/10.1038/srep27295

15. Cao, H., Yu, S., Chen, D., Jing, C., Wang, Z., Ma, R., Liu, S., Ni, J., Feng, J., & Wu, J. (2016). Liver X receptor agonist T0901317 reverses resistance of A549 human lung cancer cells to EGFR-TKI treatment. *FEBS Open Bio*, *7*(1), 35–43. https://doi.org/10.1002/2211-5463.12147

16. Wang, Q., Shen, B., Qin, X., Liu, S., & Feng, J. (2019). Akt/mTOR and AMPK signaling pathways are responsible for liver X receptor agonist GW3965-enhanced gefitinib sensitivity in non-small cell lung cancer cell lines. *Translational Cancer Research*, *8*(1), 66–76. https://doi.org/10.21037/tcr.2018.12.34

17. Bilotta, M. T., Abruzzese, M. P., Molfetta, R., Scarno, G., Fionda, C., Zingoni, A., Soriani, A., Garofalo, T., Petrucci, M. T., Ricciardi, M. R., Paolini, R., Santoni, A., &Cippitelli, M. (2019). Activation of liver X receptor up-regulates the expression of the NKG2D ligands MICA and MICB in multiple myeloma through different molecular mechanisms. *The FASEB Journal*, *33*(8), 9489–9504. https://doi.org/10.1096/fj.201900319r

18. Segala, G., David, M., De Medina, P., Poirot, M. C., Serhan, N., Vergez, F., Mougel, A., Saland, E., Carayon, K., Leignadier, J., Caron, N., Voisin, M., Cherier,

J., Ligat, L., Lopez, F., Noguer, E., Rives, A., Payré, B., Saati, T. A., . . . Silvente-Poirot, S. (2017). Dendrogenin A drives LXR to trigger lethal autophagy in cancers. *Nature Communications*, *8*(1). https://doi.org/10.1038/s41467-017-01948-9

19. Hu, C., Liu, D., Zhang, Y., Lou, G., Huang, G., Chen, B., Shen, X., Gao, M., Gong, W., Zhou, P., Dai, S., Zeng, Y., & He, F. (2013). LXRα-mediated downregulation of FOXM1 suppresses the proliferation of hepatocellular carcinoma cells. *Oncogene*, *33*(22), 2888–2897. https://doi.org/10.1038/onc.2013.250

20. Shiragannavar, V. D., Gowda, N. G. S., Puttahanumantharayappa, L. D., Karunakara, S. H., Bhat, S., Prasad, S. K., Kumar, D. P., &Santhekadur, P. K. (2023). The ameliorating effect of withaferin A on high-fat diet-induced non-alcoholic fatty liver disease by acting as an LXR/FXR dual receptor activator. *Frontiers in Pharmacology*, *14*. https://doi.org/10.3389/fphar.2023.1135952

21. Pattanayak, S. P., Bose, P., Sunita, P., Siddique, M. U. M., &Lapenna, A. (2018). Bergapten inhibits liver carcinogenesis by modulating LXR/PI3K/Akt and IDOL/LDLR pathways. *Biomedicine & Pharmacotherapy*, *108*, 297–308. https://doi.org/10.1016/j.biopha.2018.08.145

22. Sharma, B., Gupta, V., Dahiya, D., Kumar, H., Vaiphei, K., & Agnihotri, N. (2019). Clinical relevance of cholesterol homeostasis genes in colorectal cancer. *Biochimica Et Biophysica Acta (BBA) - Molecular and Cell Biology of Lipids*, *1864*(10), 1314–1327. https://doi.org/10.1016/j.bbalip.2019.06.008

23. Uno, S., Endo, K., Jeong, Y., Kawana, K., Miyachi, H., Hashimoto, Y., &Makishima, M. (2008). Suppression of β-catenin signaling by liver X receptor ligands. *Biochemical Pharmacology*, *77*(2), 186–195. https://doi.org/10.1016/j.bcp.2008.10.007

24. Candelaria, N. R., Addanki, S., Zheng, J., Nguyen-Vu, T., Karaboga, H., Dey, P., Gabbi, C., Vedin, L., Liu, K., Wu, W., Jonsson, P. K., Lin, J. Z., Su, F., Bollu, L. R., Hodges, S. E., McElhany, A. L., Issazadeh, M. A., Fisher, W. E., Ittmann,

M. M., . . . Lin, C. (2014). Antiproliferative effects and mechanisms of liver X receptor ligands in pancreatic ductal adenocarcinoma cells. *PLoS ONE*, *9*(9), e106289. https://doi.org/10.1371/journal.pone.0106289

25. Widmann, S., Srivastava, S., & Lin, C. (2023). A novel liver X receptor inverse agonist impairs cholesterol and phospholipid metabolism and induces apoptosis and necroptosis in pancreatic ductal adenocarcinoma cells. *Receptors*, *2*(1), 34–46. https://doi.org/10.3390/receptors2010003

26. Zhou, H., Ni, Z., Li, T., Su, L., Zhang, L., Liu, N., & Shi, Y. (2018). Activation of FXR promotes intestinal metaplasia of gastric cells via SHP-dependent upregulation of the expression of CDX2. *Oncology Letters*. https://doi.org/10.3892/ol.2018.8342

27. Fujino, T., Sugizaki, K., Kato, R., Beppu, M., Murakami, S., Lee, H., Oshima, T., & Hayakawa, M. (2020). Farnesoid X receptor and liver X receptors regulate Oct3/4 expression by multiple feedback regulating system in normal renal-derived cells and renal adenocarcinoma cells. *The Journal of Toxicological Sciences*, *45*(1), 25–35. https://doi.org/10.2131/jts.45.25

28. Giordano, C., Barone, I., Vircillo, V., Panza, S., Malivindi, R., Gelsomino, L., Pellegrino, M., Rago, V., Mauro, L., Lanzino, M., Panno, M. L., Bonofiglio, D., Catalano, S., &Andò, S. (2016). Activated FXR inhibits leptin signaling and counteracts tumor-promoting activities of Cancer-Associated fibroblasts in breast malignancy. *Scientific Reports*, *6*(1). https://doi.org/10.1038/srep21782

29. Giaginis, C., Karandrea, D., Alexandrou, P., Giannopoulou, I., Tsouroufl is, G., Troungos, C., Danas, E., Keramopoulos, A., Patsouris, E., Nakopoulou, L., &Theocharis, S. (2017). High Farnesoid X Receptor (FXR) expression is a strong and independent prognosticator in invasive breast carcinoma. *Neoplasma*, *64*(04), 633–639. https://doi.org/10.4149/neo_2017_420

30. Liu, J., Tong, S., Wang, X., & Qu, L. (2014). Farnesoid X receptor inhibits LNcaP cell proliferation via the upregulation of PTEN. *Experimental and Therapeutic Medicine*, *8*(4), 1209–1212. https://doi.org/10.3892/etm.2014.1894

31. Fang, Y., Hegazy, L., Finck, B. N., &Elgendy, B. (2021). Recent advances in the medicinal chemistry of farnesoid X receptor. *Journal of Medicinal Chemistry*, *64*(24), 17545–17571. https://doi.org/10.1021/acs.jmedchem.1c01017

32. Hotta, M., Sakatani, T., Ishino, K., Wada, R., Kudo, M., Yokoyama, Y., Yamada, T., Yoshida, H., & Naito, Z. (2019). Farnesoid X receptor induces cell death and sensitizes to TRAIL-induced inhibition of growth in colorectal cancer cells through the up-regulation of death receptor 5. *Biochemical and Biophysical Research Communications*, *519*(4), 824–831. https://doi.org/10.1016/j.bbrc.2019.09.033

33. Peng, Z., Raufman, J., &Xie, G. (2012). Src-Mediated Cross-Talk between Farnesoid X and Epidermal Growth Factor Receptors Inhibits Human Intestinal Cell Proliferation and Tumorigenesis. *PLoS ONE*, *7*(10), e48461. https://doi.org/10.1371/journal.pone.0048461

34. De Gottardi, A., Touri, F., Maurer, C. A., Perez, A., Maurhofer, O., Ventre, G., Bentzen, C. L., Niesor, E. J., & Dufour, J. (2004). The bile Acid Nuclear receptor FXR and the Bile Acid Binding Protein IBABP are differently expressed in colon cancer. *Digestive Diseases and Sciences*, *49*(6), 982–989. https://doi.org/10.1023/b:ddas.0000034558.78747.98

35. Lee, J. Y., Lee, K. T., Lee, J. K., Lee, K. H., Jang, K., Heo, J. S., Choi, S. H., Kim, Y., & Rhee, J. C. (2011). Farnesoid X receptor, overexpressed in pancreatic cancer with lymph node metastasis promotes cell migration and invasion. *British Journal of Cancer*, *104*(6), 1027–1037. https://doi.org/10.1038/bjc.2011.37

36. Wu, B., Xing, C., & Tao, J. (2019). Upregulation of microRNA-23b-3p induced by farnesoid X receptor regulates the proliferation and apoptosis of

osteosarcoma cells. *Journal of Orthopaedic Surgery and Research*, *14*(1). https://doi.org/10.1186/s13018-019-1404-6

37. Matsuzaki, J., Suzuki, H., Tsugawa, H., Watanabe, M., Hossain, S., Arai, E., Saito, Y., Sekine, S., Akaike, T., Kanai, Y., Mukaisho, K., Auwerx, J., &Hibi, T. (2013). Bile acids increase levels of MicroRNAs 221 and 222, leading to degradation of CDX2 during esophageal carcinogenesis. *Gastroenterology*, *145*(6), 1300–1311. https://doi.org/10.1053/j.gastro.2013.08.008

38. You, W., Chen, B., Liu, X., Xue, S., Qin, H., & Jiang, H. (2017). Farnesoid X receptor, a novel proto-oncogene in non-small cell lung cancer, promotes tumor growth via directly transactivating CCND1. *Scientific Reports*, *7*(1). https://doi.org/10.1038/s41598-017-00698-4

39. Wang, W., Zhan, M., Li, Q., Chen, W., Chu, H., Huang, Q., Hou, Z., Man, M., & Wang, J. (2016). FXR agonists enhance the sensitivity of biliary tract cancer cells to cisplatin via SHP dependent inhibition of Bcl-xL expression. *Oncotarget*, *7*(23), 34617–34629. https://doi.org/10.18632/oncotarget.8964

40. Di Matteo, S., Nevi, L., Costantini, D., Overi, D., Carpino, G., Safarikia, S., Giulitti, F., Napoletano, C., Manzi, E., De Rose, A. M., Melandro, F., Bragazzi, M., Berloco, P. B., Giuliante, F., Grazi, G., Giorgi, A., Cardinale, V., Adorini, L., Gaudio, E., & Alvaro, D. (2019). The FXR agonist obeticholic acid inhibits the cancerogenic potential of human cholangiocarcinoma. *PLoS ONE*, *14*(1), e0210077. https://doi.org/10.1371/journal.pone.0210077

41. Valanejad, L., Lewis, K., Wright, M., Jiang, Y., D'Souza, A., Karns, R., Sheridan, R., Gupta, A., Bove, K., Witte, D., Geller, J., Tiao, G., Nelson, D. L., Timchenko, L., &Timchenko, N. (2017). FXR-Gankyrin axis is involved in development of pediatric liver cancer. *Carcinogenesis*, *38*(7), 738–747. https://doi.org/10.1093/carcin/bgx050

42. Cariello, M., Peres, C., Zerlotin, R., Porru, E., Sabbà, C., Roda, A., &Moschetta, A. (2017). Long-term administration of nuclear bile acid receptor

FXR agonist prevents spontaneous hepatocarcinogenesis in ABCB4−/− mice. *Scientific Reports*, *7*(1). https://doi.org/10.1038/s41598-017-11549-7

43. Tavazoie, M. F., Pollack, I., Tanqueco, R., Ostendorf, B. N., Reis, B. S., Gonsalves, F. C., Kurth, I., Andreu-Agullo, C., Derbyshire, M. L., Posada, J., Takeda, S., Tafreshian, K. N., Rowinsky, E., Szarek, M., Waltzman, R. J., Mcmillan, E. A., Zhao, C., Mita, M., Mita, A., . . . Tavazoie, S. F. (2018). LXR/APOE activation restricts innate immune suppression in cancer. *Cell*, *172*(4), 825-840.e18. https://doi.org/10.1016/j.cell.2017.12.026

44. Wu, J. N., Chen, J. R., & Chen, J. L. (2020). Role of farnesoid X receptor in the pathogenesis of respiratory diseases. *Canadian respiratory journal*, *2020*(1), 9137251.https://doi.org/10.1155/2020/9137251

45. De Boussac, H., Pommier, A. J., Dufour, J., Trousson, A., Caira, F., Volle, H., Baron, S., &Lobaccaro, A. (2013). LXR, prostate cancer and cholesterol: the Good, the Bad and the Ugly. *American Journal of Cancer Research*, *3*, 1. https://pmc.ncbi.nlm.nih.gov/articles/PMC3555197/

46. Lanka, G., Begum, D., Banerjee, S., Adhikari, N., Yogeeswari, P., & Ghosh, B. (2023). Pharmacophore-based virtual screening, 3D QSAR, Docking, ADMET, and MD simulation studies: An *in silico* perspective for the identification of new potential HDAC3 inhibitors. *Computers in Biology and Medicine*, *166*, 107481. https://doi.org/10.1016/j.compbiomed.2023.107481

47. Sevov, M., Elfineh, L., &Cavelier, L. B. (2006). Resveratrol regulates the expression of LXR-α in human macrophages. *Biochemical and Biophysical Research Communications*, *348*(3), 1047–1054. https://doi.org/10.1016/j.bbrc.2006.07.155

48. Voloshyna, I., Hai, O., Littlefield, M. J., Carsons, S., & Reiss, A. B. (2012). Resveratrol mediates anti-atherogenic effects on cholesterol flux in human macrophages and endothelium via PPARγ and adenosine. *European Journal of Pharmacology*, *698*(1–3), 299–309. https://doi.org/10.1016/j.ejphar.2012.08.024

49. Hajighasem, A., Farzanegi, P., Mazaheri, Z., Naghizadeh, M., & Salehi, G. (2018). Effects of resveratrol, exercises and their combination on Farnesoid X receptor, Liver X receptor and Sirtuin 1 gene expression and apoptosis in the liver of elderly rats with nonalcoholic fatty liver. *PeerJ*, *6*, e5522. https://doi.org/10.7717/peerj.5522

50. Tung, B. T., Rodriguez-Bies, E., Thanh, H. N., Le-Thi-Thu, H., Navas, P., Sanchez, V. M., & López-Lluch, G. (2015). Organ and tissue-dependent effect of resveratrol and exercise on antioxidant defenses of old mice. *Aging Clinical and Experimental Research*, *27*(6), 775–783. https://doi.org/10.1007/s40520-015-0366-8

51. Pang, J., Xu, H., Wang, X., Chen, X., Li, Q., Liu, Q., You, Y., Zhang, H., Xu, Z., Zhao, Y., Zhang, Y., Yang, Y., & Ling, W. (2021). Resveratrol enhances trans-intestinal cholesterol excretion through selective activation of intestinal liver X receptor alpha. *Biochemical Pharmacology*, *186*, 114481. https://doi.org/10.1016/j.bcp.2021.114481

52. Lin, H., Chen, Y., Hsu, W., Yang, C., Kao, C., & Tsai, T. (2012). Resveratrol Helps Recovery from Fatty Liver and Protects against Hepatocellular Carcinoma Induced by Hepatitis B Virus X Protein in a Mouse Model. *Cancer Prevention Research*, *5*(7), 952–962. https://doi.org/10.1158/1940-6207.capr-12-0001

53. Kapetanovic, I. (2006). Computer-aided drug discovery and development (CADDD): In silico-chemico-biological approach. *Chemico-Biological Interactions*, *171*(2), 165–176. https://doi.org/10.1016/j.cbi.2006.12.006

54. Kaldor, S. W., Kalish, V. J., Davies, J. F., Shetty, B. V., Fritz, J. E., Appelt, K., Burgess, J. A., Campanale, K. M., Chirgadze, N. Y., Clawson, D. K., Dressman, B. A., Hatch, S. D., Khalil, D. A., Kosa, M. B., Lubbehusen, P. P., Muesing, M. A., Patick, A. K., Reich, S. H., Su, K. S., & Tatlock, J. H. (1997). Viracept (Nelfinavir mesylate, AG1343): a potent, orally bioavailable inhibitor of HIV-1 protease.

Journal of Medicinal Chemistry, *40*(24), 3979–3985. https://doi.org/10.1021/jm9704098

55. Ginex, T., Vázquez, J., Estarellas, C., &Luque, F. J. (2024). Quantum mechanical-based strategies in drug discovery: Finding the pace to new challenges in drug design. *Current Opinion in Structural Biology*, *87*, 102870. https://doi.org/10.1016/j.sbi.2024.102870

56. Cui, W., Aouidate, A., Wang, S., Yu, Q., Li, Y., & Yuan, S. (2020). Discovering Anti-Cancer drugs via computational methods. *Frontiers in Pharmacology*, *11*. https://doi.org/10.3389/fphar.2020.00733

57. Al-Attar, T., &Madihally, S. V. (2020). Modeling the impact of fluid flow on resveratrol release from electrospunfibers. *Computers in Biology and Medicine, 117*, 103622. https://doi.org/10.1016/j.compbiomed.2020.103622

58. Laskar, Y. B., Mazumder, P. B., & Talukdar, A. D. (2021). Hibiscus sabdariffa anthocyanins are potential modulators of estrogen receptor alpha activity with favourable toxicology: a computational analysis using molecular docking, ADME/Tox prediction, 2D/3D QSAR and molecular dynamics simulation. *Journal of Biomolecular Structure and Dynamics*, *41*(2), 611–633. https://doi.org/10.1080/07391102.2021.2009914

59. Hoerer, S., Schmid, A., Heckel, A., Budzinski, R., & Nar, H. (2003). Crystal Structure of the Human Liver X Receptor β Ligand-binding Domain in Complex with a Synthetic Agonist. *Journal of Molecular Biology*, *334*(5), 853–861. https://doi.org/10.1016/j.jmb.2003.10.033

60. Zheng, W., Lu, Y., Lin, S., Wang, R., Qiu, L., Zhu, Y., Yao, B., Guo, F., Jin, S., Jin, L., & Li, Y. (2017). A Novel Class of Natural FXR Modulators with a Unique Mode of Selective Co-regulator Assembly. *ChemBioChem*, *18*(8), 721–725. https://doi.org/10.1002/cbic.201700059

61. Svensson, S., Östberg, T., Jacobsson, M., Norström, C., Stefansson, K., Hallén, D., Johansson, I. C., Zachrisson, K., Ogg, D., &Jendeberg, L. (2003). Crystal structure of the heterodimeric complex of LXR and RXR ligand-binding domains in a fully agonistic conformation. *The EMBO Journal*, *22*(18), 4625–4633. https://doi.org/10.1093/emboj/cdg456

62. ApS, M. (2008). Molegro Virtual Docker, vol. 2.4. *ApS, Aarhus, Denmark*.

63. Thomsen, R., & Christensen, M. H. (2006). MolDock: a new technique for High-Accuracy Molecular Docking. *Journal of Medicinal Chemistry*, *49*(11), 3315–3321. https://doi.org/10.1021/jm051197e

64. Zsidó, B. Z., Bayarsaikhan, B., Börzsei, R., Szél, V., Mohos, V., & Hetényi, C. (2023). The advances and limitations of the determination and applications of water structure in molecular engineering. *International Journal of Molecular Sciences*, *24*(14), 11784. https://doi.org/10.3390/ijms241411784

65. Geschwindner, S., & Ulander, J. (2019). The current impact of water thermodynamics for small-molecule drug discovery. *Expert Opinion on Drug Discovery*, *14*(12), 1221-1225. https://doi.org/10.1080/17460441.2019.1664468

66. Maden, S. F., Sezer, S., & Acuner, S. E. (2022). Fundamentals of molecular docking and comparative analysis of protein–small-molecule docking approaches. In *Molecular Docking-Recent Advances*. IntechOpenhttps://doi.org/10.5772/intechopen.105815

67. Bouchouireb, Z., Olivier-Jimenez, D., Jaunet-Lahary, T., Thany, S. H., & Le Questel, J. Y. (2024). Navigating the complexities of docking tools with nicotinic receptors and acetylcholine binding proteins in the realm of neonicotinoids. *Ecotoxicology and Environmental Safety*, *281*, 116582. https://doi.org/10.1016/j.ecoenv.2024.116582

68. Singha, B., Arora, B., Karmaker, R., Richa, K., Longkumer, N., Abdulhameed, H. T., Abid, M., & Sinha, U. B. (2024). Evaluating Terrestrol A as an inhibitor

against SARS-COV-2and invasive fungal pathogens: A comprehensive computational analysis. *ChemistrySelect*, *9*(14). https://doi.org/10.1002/slct.202304761

69. Thomsen, R., & Christensen, M.H. (2006). MolDock: a new technique for high-accuracy molecular docking, *Journal of Medicinal Chemistry*, *49*, 3315–3321.https://doi.org/10.1021/jm051197e

70. Alencar, W. L. M., da Silva Arouche, T., Neto, A. F. G., de Castro Ramalho, T., de Carvalho Júnior, R. N., & de Jesus Chaves Neto, A. M. (2022). Interactions of Co, Cu, and non-metal phthalocyanines with external structures of SARS-CoV-2 using docking and molecular dynamics. *Scientific reports*, *12*(1), 3316.https://doi.org/10.1038/s41598-022-07396-w

71. Moraes, F. P., & de Azevedo, W. F. (2012). Targeting imidazoline site on monoamine oxidase B through molecular docking simulations. *Journal of molecular modeling*, *18*, 3877-3886.https://doi.org/10.1007/s00894-012-1390-7

72. Salentin, S., Schreiber, S., Haupt, V. J., Adasme, M. F., & Schroeder, M. (2015). PLIP: fully automated protein–ligand interaction profiler. *Nucleic Acids Research*, *43*(W1), W443–W447. https://doi.org/10.1093/nar/gkv315

73. Dennington, R., Keith, T. A., &Millam, J. (2019). GaussView, Version 6.1. 1, Semichem Inc. *Shawnee Mission. KS*.

74. Frisch, M. J., Trucks, G. W., Schlegel, H. B., Scuseria, G. E., Robb, M. A., Cheeseman, J. R., Scalmani, G., Barone, V., Petersson, G. A., Nakatsuji, H., Li, X., Caricato, M., Marenich, A. V., Bloino, J., Janesko, B. G., Gomperts, R., Mennucci, B., Hratchian, H. P., Ortiz, J. V., . . . Fox, D. J. (2016). Gaussian 16 Revision C. 01, 2016. *Gaussian Inc. Wallingford CT*, *1*, 572.

75. Parr, R. G., Szentpály, L. V., & Liu, S. (1999). Electrophilicity Index. *Journal of the American Chemical Society*, *121*(9), 1922–1924. https://doi.org/10.1021/ja983494x

76. Shankar, R., Senthilkumar, K., &Kolandaivel, P. (2008). Calculation of ionization potential and chemical hardness: A comparative study of different methods. *International Journal of Quantum Chemistry*, *109*(4), 764–771. https://doi.org/10.1002/qua.21883

77. Morris, G. M., Huey, R., Lindstrom, W., Sanner, M. F., Belew, R. K., Goodsell, D. S., & Olson, A. J. (2009). AutoDock4 and AutoDockTools4: Automated docking with selective receptor flexibility. *Journal of Computational Chemistry*, *30*(16), 2785–2791. https://doi.org/10.1002/jcc.21256

78. Tian, L., & Fei-Wu, C. (2012). Comparison of computational methods for atomic charges. *Acta Physico-ChimicaSinica*, *28*(01), 1–18. https://doi.org/10.3866/pku.whxb2012281

79. Dulaimy, A., & Jihad, S. (2016). *Computer-Aided Drug Design Using Hybrid Neural Network and Genetic Algorithm*. Polytechnic University.

80. Biovia, D. S. (2024). *Discovery studio modeling environment* [Software]. Release San Diego.

81. Zhang, X., Shen, C., Wang, T., Deng, Y., Kang, Y., Li, D., Hou, T., & Pan, P. (2023). ML-PLIC: a web platform for characterizing protein–ligand interactions and developing machine learning-based scoring functions. *Briefings in Bioinformatics*, *24*(5). https://doi.org/10.1093/bib/bbad295

82. Wolber, G., & Langer, T. (2004). LigandScout: 3-D Pharmacophores Derived from Protein-Bound Ligands and Their Use as Virtual Screening Filters. *Journal of Chemical Information and Modeling*, *45*(1), 160–169. https://doi.org/10.1021/ci049885e

83. Abro, A., Kulsoom, S., & Riaz, N. (2013). Pharmacophore model generation for microtubule-stabilizing anti-mitotic agents (MSAAs) against ovarian cancer. *Medicinal Chemistry Research*, *22*(9), 4322–4330. https://doi.org/10.1007/s00044-012-0445-8

84. Pradeepkiran, J. A., Sainath, S., &Shrikanya, K. (2021). In silico validation and ADMET analysis for the best lead molecules. In *Elsevier eBooks* (pp. 133–176). https://doi.org/10.1016/b978-0-323-85681-2.00008-2

85. Megrouss, Y., Salem, Y., Mansour, A., Zohra Douaa, B., Sid Ahmed, K., Benaissi, H., ... & Abdelkader, C. (2024). Molecular Structure, Lattice Energy, Hirshfeld Surface and NCI-RDG Analysis, DFT Calculations, and In Silico Molecular Docking of an Imidazole Derivative. *Physical Chemistry Research, 12*(4), 975-990.https://doi.org/10.22036/pcr.2024.448149.2495

86. Baby, K., Maity, S., Mehta, C. H., Nayak, U. Y., Shenoy, G. G., Pai, K. S. R., Harikumar, K. B., & Nayak, Y. (2023). Computational drug repurposing of Akt-1 allosteric inhibitors for non-small cell lung cancer. *Scientific Reports*, *13*(1). https://doi.org/10.1038/s41598-023-35122-7

87. Lindorff-Larsen, K., Piana, S., Palmo, K., Maragakis, P., Klepeis, J. L., Dror, R. O., & Shaw, D. E. (2010). Improved side-chain torsion potentials for the Amber ff99SB protein force field. *Proteins Structure Function and Bioinformatics*, *78*(8), 1950–1958. https://doi.org/10.1002/prot.22711

88. Da Silva, A. W. S., &Vranken, W. F. (2012). ACPYPE - AnteChamberPYthon Parser InterFaCE. *BMC Research Notes*, *5*(1). https://doi.org/10.1186/1756-0500-5-367

89. Berendsen, H., Van Der Spoel, D., & Van Drunen, R. (1995). GROMACS: A message-passing parallel molecular dynamics implementation. *Computer Physics Communications*, *91*(1–3), 43–56. https://doi.org/10.1016/0010-4655(95)00042-e

90. Lindahl, E., Hess, B., & Van Der Spoel, D. (2001). GROMACS 3.0: a package for molecular simulation and trajectory analysis. *Journal of Molecular Modeling*, *7*(8), 306–317. https://doi.org/10.1007/s008940100045

91. Van Der Spoel, D., Lindahl, E., Hess, B., Groenhof, G., Mark, A. E., & Berendsen, H. J. C. (2005). GROMACS: Fast, flexible, and free. *Journal of Computational Chemistry*, *26*(16), 1701–1718. https://doi.org/10.1002/jcc.20291

92. Hess, B., Kutzner, C., Van Der Spoel, D., & Lindahl, E. (2008). GROMACS 4: Algorithms for highly efficient, Load-Balanced, and scalable molecular simulation. *Journal of Chemical Theory and Computation*, *4*(3), 435–447. https://doi.org/10.1021/ct700301q

93. Abraham, M. J., Murtola, T., Schulz, R., Páll, S., Smith, J. C., Hess, B., & Lindahl, E. (2015). GROMACS: High performance molecular simulations through multi-level parallelism from laptops to supercomputers. *SoftwareX*, *1–2*, 19–25. https://doi.org/10.1016/j.softx.2015.06.001

94. Massova, I., &Kollman, P. A. (2000). Combined molecular mechanical and continuum solvent approach (MM-PBSA/GBSA) to predict ligand binding. *Perspectives in Drug Discovery and Design*, *18*(1), 113–135. https://doi.org/10.1023/a:1008763014207

95. Perutz, M. F. (1978). Electrostatic effects in proteins. *Science*, *201*(4362), 1187–1191. https://doi.org/10.1126/science.694508

96. Honig, B., & Nicholls, A. (1995). Classical electrostatics in Biology and Chemistry. *Science*, *268*(5214), 1144–1149. https://doi.org/10.1126/science.7761829

97. Baker, N. A., Sept, D., Joseph, S., Holst, M. J., & McCammon, J. A. (2001). Electrostatics of nanosystems: Application to microtubules and the ribosome. *Proceedings of the National Academy of Sciences*, *98*(18), 10037–10041. https://doi.org/10.1073/pnas.181342398

98. Kumari, R., Kumar, R., & Lynn, A. (2014). g_mmpbsa—A GROMACS Tool for High-Throughput MM-PBSA Calculations. *Journal of Chemical Information and Modeling*, *54*(7), 1951–1962. https://doi.org/10.1021/ci500020m

99. Pettersen, E. F., Goddard, T. D., Huang, C. C., Couch, G. S., Greenblatt, D. M., Meng, E. C., &Ferrin, T. E. (2004). UCSF Chimera—A visualization system

for exploratory research and analysis. *Journal of Computational Chemistry*, *25*(13), 1605–1612. https://doi.org/10.1002/jcc.20084

100. Lu, T., & Chen, Q. (2021). Shermo: A general code for calculating molecular thermochemistry properties. *Computational and Theoretical Chemistry*, *1200*, 113249. https://doi.org/10.1016/j.comptc.2021.113249

101. Naik, S., Puttachari, D., L, V. A., D, U., Shetty, V. P., Prabhu, C., &Deekshit, V. K. (2024). Synthesis and biological evaluation of novel hybrid compounds bearing pyrazine and 1,2,4-triazole analogues as potent antitubercular agents. *RSC Pharmaceutics*, *1*(2), 283–295. https://doi.org/10.1039/d3pm00054k

102. Kallert, E., Fischer, T. R., Schneider, S., Grimm, M., Helm, M., & Kersten, C. (2022). Protein-Based virtual screening tools applied for RNA–Ligand docking identify new binders of the preQ1-Riboswitch. *Journal of Chemical Information and Modeling*, *62*(17), 4134–4148. https://doi.org/10.1021/acs.jcim.2c00751

103. Lee, Y., Basith, S., & Choi, S. (2017). Recent advances in Structure-Based drug design targeting Class A G Protein-Coupled receptors utilizing crystal structures and computational simulations. *Journal of Medicinal Chemistry*, *61*(1), 1–46. https://doi.org/10.1021/acs.jmedchem.6b01453

104. Maden, S. F., Sezer, S., &Acuner, S. E. (2022). Fundamentals of molecular docking and comparative analysis of Protein–Small-Molecule docking approaches. In *Biomedical engineering*. https://doi.org/10.5772/intechopen.105815

105. Chaudhary, M. K., Srivastava, A., Singh, K. K., Tandon, P., & Joshi, B. D. (2020). Computational evaluation on molecular stability, reactivity, and drug potential of frovatriptan from DFT and molecular docking approach. *Computational and Theoretical Chemistry*, *1191*, 113031. https://doi.org/10.1016/j.comptc.2020.113031

106. Matuszek, A. M., & Reynisson, J. (2016). Defining known drug space using DFT. *Molecular informatics*, *35*(2), 46-53.https://doi.org/10.1002/minf.201500105

107. Parr, R.G., & Pearson, R.G. (1983). Absolute hardness: companion parameter to absolute electronegativity. Journal of the American Chemical Society, 105(26), 7512–7516. https://doi.org/10.1021/ja00364a005

108. Bhatia, M. (2024). An overview of conceptual-DFT based insights into global chemical reactivity of volatile sulfur compounds (VSCs). *Computational Toxicology*, *29*, 100295. https://doi.org/10.1016/j.comtox.2023.100295

109. Shiroudi, A., Safaei, Z., Kazeminejad, Z., Repo, E., &Pourshamsian, K. (2020). DFT study on tautomerism and natural bond orbital analysis of 4-substituted 1, 2, 4-triazole and its derivatives: solvation and substituent effects. *Journal of Molecular Modeling*, *26*, 1-11. https://doi.org/10.1007/s00894-020-4316-9

110. Kitchen, D. B., Decornez, H., Furr, J. R., &Bajorath, J. (2004). Docking and scoring in virtual screening for drug discovery: methods and applications. *Nature Reviews Drug Discovery*, *3*(11), 935–949. https://doi.org/10.1038/nrd1549

111. Shode, F. O., Amobonye, A., Pillai, S., Govender, P. P., & Govender, K. K. (2025). Acteoside as a Multi-target Anti-SARS-COV-2 agent: An In-Silico Study. *Topics in Catalysis*. https://doi.org/10.1007/s11244-024-02034-3

112. Yu, H., Ma, S., Li, Y., & Dalby, P. A. (2022). Hot spots-making directed evolution easier. *Biotechnology Advances*, *56*, 107926. https://doi.org/10.1016/j.biotechadv.2022.107926

113. Jack, K. S., Asaruddin, M. R. B., & Bhawani, S. A. (2022). Pharmacophore study, molecular docking and molecular dynamic simulation of virgin coconut oil derivatives as anti-inflammatory agent against COX-2. *Chemical and Biological Technologies in Agriculture*, *9*(1). https://doi.org/10.1186/s40538-022-00340-0

114. Chaudhary, P. K., & Kim, S. (2021). An Insight into GPCR and G-Proteins as Cancer Drivers. *Cells*, *10*(12), 3288. https://doi.org/10.3390/cells10123288

115. Rao, R., Shah, S., Bhattacharya, D., Toukam, D. K., Cáceres, R., Krummel, D. a. P., & Sengupta, S. (2022). Ligand-Gated ion channels as targets for treatment and management of cancers. *Frontiers in Physiology*, *13*. https://doi.org/10.3389/fphys.2022.839437

116. Bouabdallah, S., Al-Maktoum, A., & Amin, A. (2023). Steroidal saponins: naturally occurring compounds as inhibitors of the hallmarks of cancer. *Cancers*, *15*(15), 3900. https://doi.org/10.3390/cancers15153900

117. Lonard, D. M., & O'Malley, B. W. (2012). Nuclear receptor coregulators: modulators of pathology and therapeutic targets. *Nature Reviews Endocrinology*, *8*(10), 598–604. https://doi.org/10.1038/nrendo.2012.100

118. Yang, P., Li, Z., & Li, H. (2016). Potential roles of protease inhibitors in cancer progression. *Asian Pacific Journal of Cancer Prevention*, *16*(18), 8047–8052. https://doi.org/10.7314/apjcp.2015.16.18.8047

119. Scrocco, E., &Tomasi, J. (1978). Electronic Molecular Structure, Reactivity and Intermolecular Forces: An Euristic interpretation by means of Electrostatic Molecular Potentials. In *Advances in quantum chemistry* (pp. 115–193). https://doi.org/10.1016/s0065-3276(08)60236-1

120. Parr, R. G., & Weitao, Y. (1995). Density-Functional theory of atoms and molecules. In *Oxford University Press eBooks*. https://doi.org/10.1093/oso/9780195092769.001.0001

121. Murray, J. S., &Politzer, P. (1998). Electrostatic Potentials: Chemical applications. *Encyclopedia of Computational Chemistry*. https://doi.org/10.1002/0470845015.cca014

122. Özdemir, N., Eren, B., Dinçer, M., &Bekdemir, Y. (2010). Experimental and ab initio computational studies on 4-(1H-benzo[d]imidazol-2-yl)-N,N-

dimethylaniline. *Molecular Physics*, *108*(1), 13–24. https://doi.org/10.1080/00268970903476688

123. Politzer, P., & Murray, J. S. (2002). The fundamental nature and role of the electrostatic potential in atoms and molecules. *Theoretical Chemistry Accounts*, *108*(3), 134–142. https://doi.org/10.1007/s00214-002-0363-9

124. Luque, F. J., López, J. M., & Orozco, M. (2000). Perspective on "Electrostatic interactions of a solute with a continuum. A direct utilization of ab initio molecular potentials for the prevision of solvent effects." *Theoretical Chemistry Accounts*, *103*(3–4), 343–345. https://doi.org/10.1007/s002149900013

125. Okulik, N., &Jubert, A. H. (2004). Theoretical study on the structure and reactive sites of non-steroidal anti-inflammatory drugs. *Journal of Molecular Structure THEOCHEM*, *682*(1–3), 55–62. https://doi.org/10.1016/j.theochem.2004.04.069

126. Chattopadhyay, B., Basu, S., Chakraborty, P., Choudhuri, S. K., Mukherjee, A. K., & Mukherjee, M. (2009). Synthesis, spectroscopic characterization, X-ray powder structure analysis, DFT study and in vitro anticancer activity of N-(2-methoxyphenyl)-3-methoxysalicylaldimine. *Journal of Molecular Structure*, *932*(1–3), 90–96. https://doi.org/10.1016/j.molstruc.2009.05.047

127. Singh, U. C., &Kollman, P. A. (1984). An approach to computing electrostatic charges for molecules. *Journal of Computational Chemistry*, *5*(2), 129–145. https://doi.org/10.1002/jcc.540050204

128. Connolly, M. L. (1983). Solvent-Accessible surfaces of proteins and nucleic acids. *Science*, *221*(4612), 709–713. https://doi.org/10.1126/science.6879170

129. Muthu, S., &Maheswari, J. U. (2012). Quantum mechanical study and spectroscopic (FT-IR, FT-Raman, 13C, 1H, UV) study, first order hyperpolarizability, NBO analysis, HOMO and LUMO analysis of 4-[(4-aminobenzene) sulfonyl] aniline by ab initio HF and density functional method.

Spectrochimica Acta Part a Molecular and Biomolecular Spectroscopy, *92*, 154–163. https://doi.org/10.1016/j.saa.2012.02.056

130. Ahmed, B., Barukial, P., &Bezbaruah, B. (2023). Some halogenated anticancer agents, role of halide (-X) and their interaction mechanism with AT/GC base pairs: A computational study. *Journal of the Indian Chemical Society*, *100*(7), 101027. https://doi.org/10.1016/j.jics.2023.101027

131. Carneiro, S. S., Lima, A. R., Marinho, M. M., &Marinho, E. S. (2016). In silico Study Of The Therapeutic Agent In The Treatment Of Non-Hodgkin's Lymphomas, Peripheral T-Cell Belinostat, A Semi-Empirical Approach. *Imp. J. Interdiscip. Res*, *2*(8), 1645–1648.

132. Steffy, A. D., Dhas, D. A., Joe, I. H., & Balachandran, S. (2023). Theoretical investigations on structural, spectral, NBO, NLO and topology exploration (AIM, ELF, LOL, RDG) of piperazine-2,5-dione oxalic acid monohydrate. *Journal of Molecular Structure*, *1295*, 136653. https://doi.org/10.1016/j.molstruc.2023.136653

133. Lu, T., & Chen, F. (2012). Quantitative analysis of molecular surface based on improved Marching Tetrahedra algorithm. *Journal of Molecular Graphics and Modelling*, *38*, 314–323. https://doi.org/10.1016/j.jmgm.2012.07.004

134. Ahmed, B., Bezbaruah, B., Barukial, P., Singha, B., & Sinha, U. B. (2024). The Some pyridyl moiety based metal complexes (viz., Mn+2, Co+2 and Zn+2) as potential anticancer agents and DNA nucleobase interaction: A DFT Approach. *Indian Journal of Chemistry*, *63*(6). https://doi.org/10.56042/ijc.v63i6.7542

135. Spackman, M. A., &Jayatilaka, D. (2008). Hirshfeld surface analysis. *CrystEngComm*, *11*(1), 19–32. https://doi.org/10.1039/b818330a

136. Lu, T., & Chen, F. (2011). Multiwfn: A multifunctional wavefunction analyzer. *Journal of Computational Chemistry*, *33*(5), 580–592. https://doi.org/10.1002/jcc.22885

137. Silvi, B., &Savin, A. (1994). Classification of chemical bonds based on topological analysis of electron localization functions. *Nature*, *371*(6499), 683–686. https://doi.org/10.1038/371683a0

138. Sheeba, B. Q., Mary, M. S. M., Amalanathan, M., & Job, C. B. (2021). Structural and vibrational spectral investigation on the identification of Non-Linear Optical properties and wave function analyses (electrostatic potential, electron localisation function, localised orbital locator) of 3-Ethoxy Salicilaldehyde. *Molecular Simulation*, *47*(15), 1217–1233. https://doi.org/10.1080/08927022.2021.1962862

139. Gupta, A. K., Tulsyan, S., Bharadwaj, M., & Mehrotra, R. (2019). Systematic Review on Cytotoxic and Anticancer potential of N-Substituted ISatins as novel class of compounds useful in Multidrug-Resistant Cancer therapy: in silico and In vitro analysis. *Topics in Current Chemistry*, *377*(3). https://doi.org/10.1007/s41061-019-0240-9

140. Rudik, A. V., Dmitriev, A. V., Lagunin, A. A., Filimonov, D. A., &Poroikov, V. V. (2016). Prediction of reacting atoms for the major biotransformation reactions of organic xenobiotics. *Journal of Cheminformatics*, *8*(1). https://doi.org/10.1186/s13321-016-0183-x

141. Isyaku, Y., Uzairu, A., &Uba, S. (2020). Computational studies of a series of 2-substituted phenyl-2-oxo-, 2-hydroxyl- and 2-acylloxyethylsulfonamides as potent anti-fungal agents. *Heliyon*, *6*(4), e03724. https://doi.org/10.1016/j.heliyon.2020.e03724

142. Shukla, R., & Tripathi, T. (2020). Molecular Dynamics Simulation of protein and Protein–Ligand complexes. In *Springer eBooks* (pp. 133–161). https://doi.org/10.1007/978-981-15-6815-2_7

143. Kokh, D. B., Doser, B., Richter, S., Ormersbach, F., Cheng, X., & Wade, R. C. (2020). Exploring ligand dissociation from macromolecules: An efficient workflow using random acceleration molecular dynamics and interaction

fingerprint analysis. *The Journal of Chemical Physics, 153(12)*.https://doi.org/10.1063/5.0022433

144. Bagewadi, Z. K., Khan, T. Y., Gangadharappa, B., Kamalapurkar, A., Shamsudeen, S. M., &Yaraguppi, D. A. (2023). Molecular dynamics and simulation analysis against superoxide dismutase (SOD) target of Micrococcus luteus with secondary metabolites from Bacillus licheniformis recognized by genome mining approach. *Saudi Journal of Biological Sciences*, *30*(9), 103753. https://doi.org/10.1016/j.sjbs.2023.103753

145. Dey, J., Mahapatra, S. R., Raj, T. K., Misra, N., &Suar, M. (2023). Identification of potential flavonoid compounds as antibacterial therapeutics against Klebsiella pneumoniae infection using structure-based virtual screening and molecular dynamics simulation. *Molecular Diversity*. https://doi.org/10.1007/s11030-023-10738-z

146. Chen, D., Oezguen, N., Urvil, P., Ferguson, C., Dann, S. M., &Savidge, T. C. (2016). Regulation of protein-ligand binding affinity by hydrogen bond pairing. *Science Advances*, *2*(3). https://doi.org/10.1126/sciadv.1501240

147. Lippert, T., &Rarey, M. (2009). Fast automated placement of polar hydrogen atoms in protein-ligand complexes. *Journal of Cheminformatics*, *1*(1). https://doi.org/10.1186/1758-2946-1-13

148. Moradi, S., Nowroozi, A., Nezhad, M. A., Jalali, P., Khosravi, R., &Shahlaei, M. (2024). A review on description dynamics and conformational changes of proteins using combination of principal component analysis and molecular dynamics simulation. *Computers in Biology and Medicine*, *183*, 109245. https://doi.org/10.1016/j.compbiomed.2024.109245

149. Wang, E., Sun, H., Wang, J., Wang, Z., Liu, H., Zhang, J. Z. H., & Hou, T. (2019). End-Point Binding Free Energy Calculation with MM/PBSA and MM/GBSA: Strategies and Applications in Drug Design. *Chemical Reviews*, *119*(16), 9478–9508. https://doi.org/10.1021/acs.chemrev.9b00055

150. Pushpam, S., Sheelarani, V., Jeyaseelan, S. C., &Benial, A. M. F. (2023). Spectroscopic, Quantum chemical and molecular docking studies on N-(9H-Purin-

6-yl) benzamide: a potent antimalarial agent. *Polycyclic Aromatic Compounds*, *44*(7), 4908–4931. https://doi.org/10.1080/10406638.2023.2259051

151. Zhu, J., Zou, H., Yu, W., Huang, Y., Liu, B., Li, T., Liang, C., & Tao, H. (2019). Checkpoint kinase inhibitor AZD7762 enhance cisplatin-induced apoptosis in osteosarcoma cells. *Cancer Cell International*, *19*(1). https://doi.org/10.1186/s12935-019-0896-9

152. Zabludoff, S. D., Deng, C., Grondine, M. R., Sheehy, A. M., Ashwell, S., Caleb, B. L., Green, S., Haye, H. R., Horn, C. L., Janetka, J. W., Liu, D., Mouchet, E., Ready, S., Rosenthal, J. L., Queva, C., Schwartz, G. K., Taylor, K. J., Tse, A. N., Walker, G. E., & White, A. M. (2008). AZD7762, a novel checkpoint kinase inhibitor, drives checkpoint abrogation and potentiates DNA-targeted therapies. *Molecular Cancer Therapeutics*, *7*(9), 2955–2966. https://doi.org/10.1158/1535-7163.mct-08-0492

153. Babiker, H. M., McBride, A., Cooke, L. S., & Mahadevan, D. (2017). Therapeutic potential of investigational CHK-1 inhibitors for the treatment of solid tumors. *Expert Opinion on Investigational Drugs*, *26*(9), 1063–1072. https://doi.org/10.1080/13543784.2017.1360275

154. Rébé, C., Filomenko, R., Raveneau, M., Chevriaux, A., Ishibashi, M., Lagrost, L., Junien, J. L., Gambert, P., & Masson, D. (2012). Identification of biological markers of liver X receptor (LXR) activation at the cell surface of human monocytes. *PLoS ONE*, *7*(11), e48738. https://doi.org/10.1371/journal.pone.0048738

155. Williams, T. M., Galbán, S., Li, F., Heist, K. A., Galbán, C. J., Lawrence, T. S., Holland, E. C., Thomae, T. L., Chenevert, T. L., Rehemtulla, A., & Ross, B. D. (2013). DW-MRI as a Predictive Biomarker of Radiosensitization of GBM through Targeted Inhibition of Checkpoint Kinases. *Translational Oncology*, *6*(2), 133–142. https://doi.org/10.1593/tlo.13214

156. Rébé, C., Filomenko, R., Raveneau, M., Chevriaux, A., Ishibashi, M., Lagrost, L., Junien, J. L., Gambert, P., & Masson, D. (2012). Identification of biological markers of liver X receptor (LXR) activation at the cell surface of human monocytes. *PLoS ONE*, *7*(11), e48738. https://doi.org/10.1371/journal.pone.0048738

157. Journe, F., Durbecq, V., Chaboteaux, C., Rouas, G., Laurent, G., Nonclercq, D., Sotiriou, C., Body, J., &Larsimont, D. (2008). Association between farnesoid X receptor expression and cell proliferation in estrogen receptor-positive luminal-like breast cancer from postmenopausal patients. *Breast Cancer Research and Treatment*, *115*(3), 523–535. https://doi.org/10.1007/s10549-008-0094-2

SUPPORTING INFORMATION

5.3. Results and discussion

5.3.1. Swiss-similarity based virtual screening

Table S5.1: Screened compounds from library 1

SL. No.	COMPOUNDS	DrugBank ID; Similarity Score; Usual Name; SMILES
1	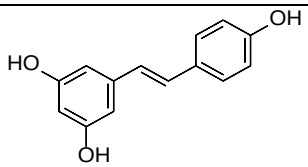	DB02709; 1.000; Resveratrol ; OC1=CC=C(C=CC2=CC(O)=CC(O)=C2)C=C1
2	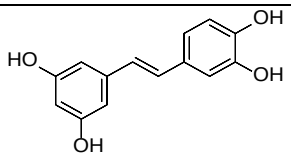	DB08399; 0.998; Piceatannol; OC1=CC(C=CC2=CC=C(O)C(O)=C2)=CC(O)=C1
3	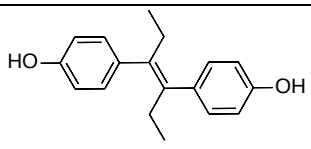	DB00255; 0.939; Diethylstilbestrol; CCC(=C(CC)C1=CC=C(O)C=C1)C1=CC=C(O)C=C1

4	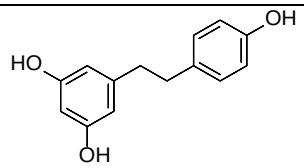	DB08466; 0.908; "5-[2-(4-hydroxyphenyl)ethyl]benzene-1; OC1=CC=C(CCC2=CC(O)=CC(O)=C2)C=C1
5	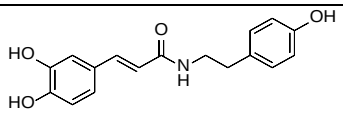	DB08754; 0.874; N-Caffeoyltyramine; OC1=CC=C(CCNC(=O)C=CC2=CC(O)=C(O)C=C2)C=C1
6	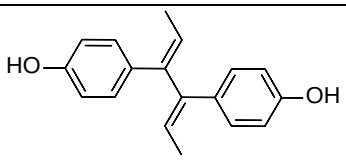	DB00890; 0.865; Dienestrol; CC=C(C(=CC)C1=CC=C(O)C=C1)C1=CC=C(O)C=C1
7	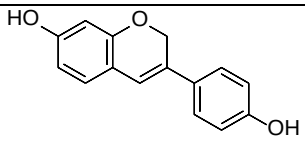	DB04915; 0.854; Idronoxil; OC1=CC=C(C=C1)C1=CC2=C(OC1)C=C(O)C=C2
8	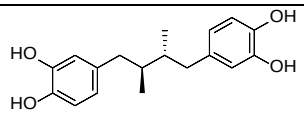	DB00179; 0.785; Masoprocol; C[C@H](CC1=CC(O)=C(O)C=C1)[C@@H](C)CC1=CC=C(O)C(O)=C1
9	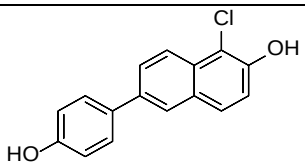	DB07119; 0.718; 1-CHLORO-6-(4-HYDROXYPHENYL)-2-NAPHTHOL; OC1=CC=C(C=C1)C1=CC2=CC=C(O)C(Cl)=C2C=C1
10	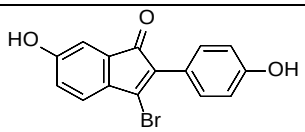	DB07230; 0.716; 3-BROMO-6-HYDROXY-2-(4-HYDROXYPHENYL)-1H-INDEN-1-ONE; OC1=CC=C(C=C1)C1=C(Br)C2=C(C=C(O)C=C2)C1=O
11	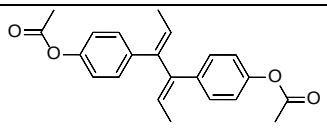	DB14668; 0.696; Dienestrol diacetate; CC=C(C(=CC)C1=CC=C(OC(C)=O)C=C1)C1=CC=C(OC(C)=O)C=C1
12	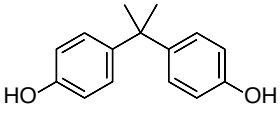	DB06973; 0.679; Bisphenol A; CC(C)(C1=CC=C(O)C=C1)C1=CC=C(O)C=C1

13	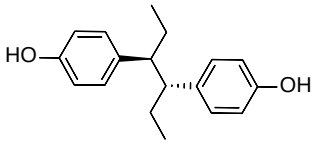	DB07931; 0.586; Hexestrol; CC[C@@H]([C@@H](CC)C1=CC=C(O)C=C1)C1=CC=C(O)C=C1
14	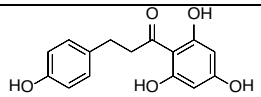	DB07810; 0.585; Phloretin; OC1=CC=C(CCC(=O)C2=C(O)C=C(O)C=C2O)C=C1
15	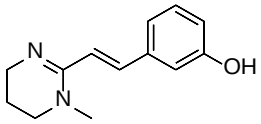	DB13670; 0.572; Oxantel; CN1CCCN=C1C=CC1=CC=CC(O)=C1
16	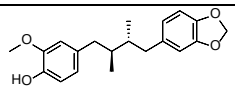	DB14129; 0.551; Macelignan; COC1=CC(C[C@H](C)[C@H](C)CC2=CC3=C(OCO3)C=C2)=CC=C1O
17	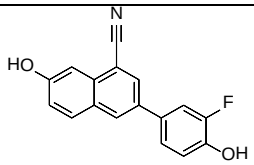	DB06875; 0.541; ERB-196; OC1=CC2=C(C=C(C=C2C=C1)C1=CC=C(O)C(F)=C1)C#N
18	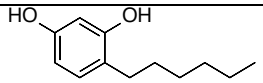	DB11254; 0.530; Hexylresorcinol; CCCCCCC1=CC=C(O)C=C1O
19	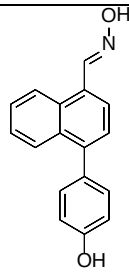	DB07150; 0.528; 4-(4-HYDROXYPHENYL)-1-NAPHTHALDEHYDE OXIME; ON=CC1=C2C=CC=CC2=C(C=C1)C1=CC=C(O)C=C1
20	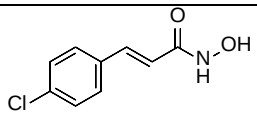	DB07819; 0.519; (2E)-3-(4-CHLOROPHENYL)-N-HYDROXYACRYLAMIDE; ONC(=O)C=CC1=CC=C(Cl)C=C1
21	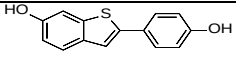	DB08773; 0.518; 2-(4-hydroxyphenyl)benzo[b]thiophen-6-ol; OC1=CC=C(C=C1)C1=CC2=CC=C(O)C=C2S1

22	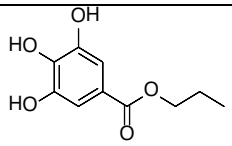	DB12450; 0.515; Propyl Gallate; CCCOC(=O)C1=CC(O)=C(O)C(O)=C1 .
23	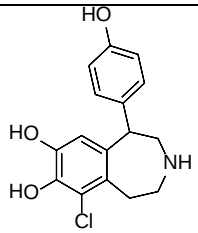	DB00800; 0.500; Fenoldopam; OC1=CC=C(C=C1)C1CNCCC2=C(Cl)C(O)=C(O)C=C12
24	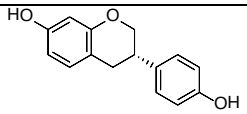	DB11674; 0.499; Equol; OC1=CC=C(C=C1)[C@H]1COC2=C(C1)C=CC(O)=C2
25	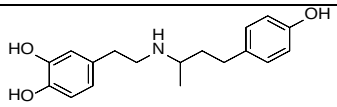	DB00841; 0.452; Dobutamine; CC(CCC1=CC=C(O)C=C1)NCCC1=CC=C(O)C(O)=C1
26	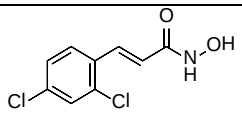	DB07818; 0.449; "(2E)-3-(2; ONC(=O)C=CC1=C(Cl)C=C(Cl)C=C1
27	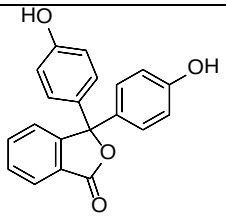	DB04824; 0.417; Phenolphthalein; OC1=CC=C(C=C1)C1(OC(=O)C2=C1C=CC=C2)C1=CC=C(O)C=C1
28	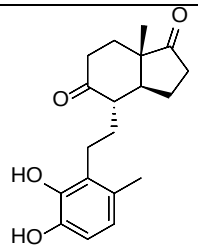	DB08542; 0.416; "3; CC1=CC=C(O)C(O)=C1CC[C@H]1[C@@H]2CCC(=O)[C@@]2(C)CCC1=O
29	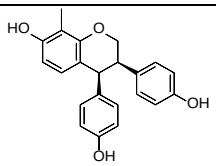	DB13062; 0.415; ME-344; CC1=C(O)C=CC2=C1OC[C@H]([C@H]2C1=CC=C(O)C=C1)C1=CC=C(O)C=C1

30	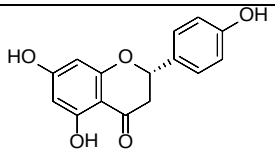	DB03467; 0.401; Naringenin; OC1=CC=C(C=C1)[C@@H]1CC(=O)C2=C(O1)C=C(O)C=C2O
31	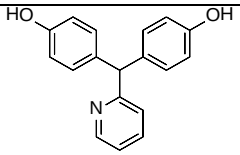	DB14232; 0.400; Deacetylbisacodyl; OC1=CC=C(C=C1)C(C1=CC=C(O)C=C1)C1=CC=CC=N1
32	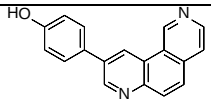	DB03623; 0.394; "9-(4-Hydroxyphenyl)-2; OC1=CC=C(C=C1)C1=CC2=C(C=CC3=C2C=NC=C3)N=C1
33	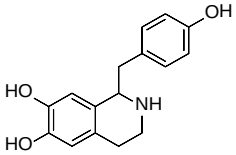	DB12779; 0.390; Higenamine; OC1=CC=C(CC2NCCC3=CC(O)=C(O)C=C23)C=C1
34	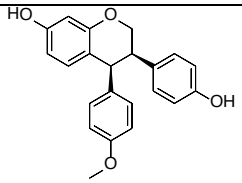	DB06588; 0.384; Triphendiol; COC1=CC=C(C=C1)[C@@H]1[C@@H](COC2=CC(O)=CC=C12)C1=CC=C(O)C=C1
35	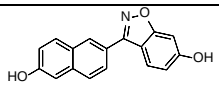	DB07236; 0.367; 3-(6-HYDROXY-NAPHTHALEN-2-YL)-BENZO[D]ISOOXAZOL-6-OL; OC1=CC=C2C(ON=C2C2=CC3=CC=C(O)C=C3C=C2)=C1
36	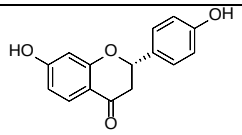	DB03601; 0.366; 5-deoxyflavanone; OC1=CC=C(C=C1)[C@@H]1CC(=O)C2=CC=C(O)C=C2O1
37	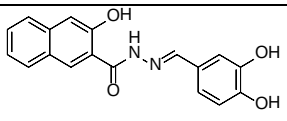	DB15964; 0.364; Dynasore; OC1=CC2=CC=CC=C2C=C1C(=O)NN=CC1=CC(O)=C(O)C=C1
38	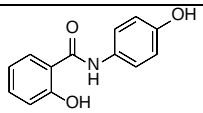	DB16273; 0.362; Osalmid; OC1=CC=C(NC(=O)C2=CC=CC=C2O)C=C1

39	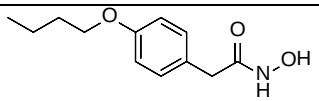	DB13346; 0.344; Bufexamac; CCCCOC1=CC=C(CC(=O)NO)C=C1
40	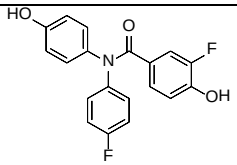	DB14969; 0.342; GTX-758; OC1=CC=C(C=C1)N(C(=O)C1=CC=C(O)C(F)=C1)C1=CC=C(F)C=C1
41	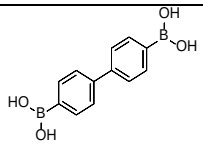	DB02627; 0.334; "4; OB(O)C1=CC=C(C=C1)C1=CC=C(C=C1)B(O)O
42	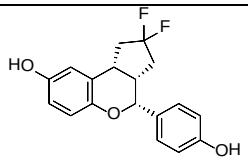	DB07638; 0.327; "(3AS; OC1=CC=C(C=C1)[C@@H]1OC2=C(C=C(O)C=C2)[C@@H]2CC(F)(F)C[C@H]12
43	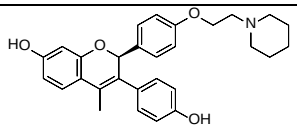	DB16080; 0.315; Acolbifene; CC1=C([C@@H](OC2=C1C=CC(O)=C2)C1=CC=C(OCCN2CCCCC2)C=C1)C1=CC=C(O)C=C1
44	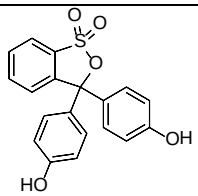	DB13212; 0.312; Phenolsulfonphthalein; OC1=CC=C(C=C1)C1(OS(=O)(=O)C2=CC=CC=C12)C1=CC=C(O)C=C1
45	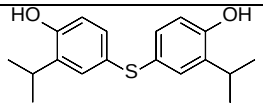	DB02881; 0.307; 4-(4-Hydroxy-3-Isopropylphenylthio)-2-Isopropylphenol; CC(C)C1=CC(SC2=CC=C(O)C(=C2)C(C)C)=CC=C1O
46	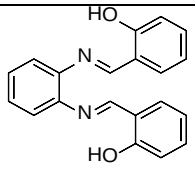	DB04811; 0.303; Salophen iron chelate; OC1=CC=CC=C1C=NC1=CC=CC=C1N=CC1=CC=CC=C1O

47	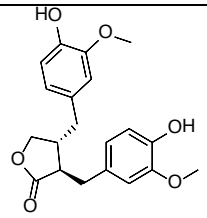	DB04200; 0.299; Matairesinol; COC1=CC(C[C@H]2COC(=O)[C@@H]2CC2=CC=C(O)C(OC)=C2)=CC=C1O
48	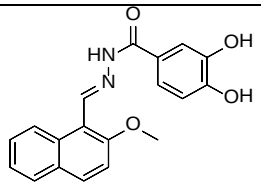	DB08034; 0.297; "(E)-3; COC1=C(C=NNC(=O)C2=CC(O)=C(O)C=C2)C2=CC=CC=C2C=C1
49	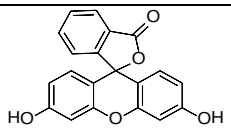	DB00693; 0.295; Fluorescein; OC1=CC2=C(C=C1)C1(OC(=O)C3=C1C=CC=C3)C1=CC=C(O)C=C1O2
50	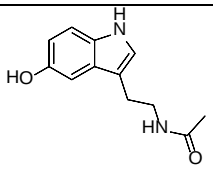	DB04275; 0.291; N-acetylserotonin; CC(=O)NCCC1=CNC2=CC=C(O)C=C12
51	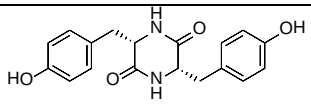	DB08761; 0.287; "(3S; OC1=CC=C(C[C@@H]2NC(=O)[C@H](CC3=CC=C(O)C=C3)NC2=O)C=C1
52	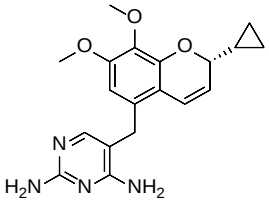	DB08741; 0.287; "5-[[(2R)-2-cyclopropyl-7; COC1=CC(CC2=C(N)N=C(N)N=C2)=C2C=C[C@H](OC2=C1OC)C1CC1
53	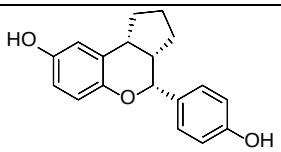	DB07933; 0.283; Erteberel; OC1=CC=C(C=C1)[C@@H]1OC2=CC=C(O)C=C2[C@@H]2CCC[C@H]12
54	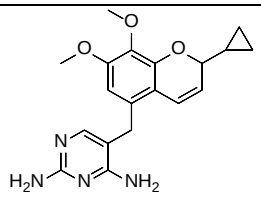	DB06358; 0.277; Iclaprim; COC1=CC(CC2=CN=C(N)N=C2N)=C2C=CC(OC2=C1OC)C1CC1

55	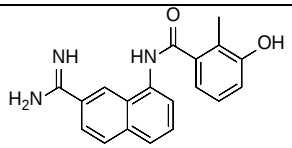	DB07212; 0.273; N-(7-CARBAMIMIDOYL-NAPHTHALEN-1-YL)-3-HYDROXY-2-METHYL-BENZAMIDE; CC1=C(O)C=CC=C1C(=O)NC1=C2C=C(C=CC2=CC=C1)C(N)=N
56	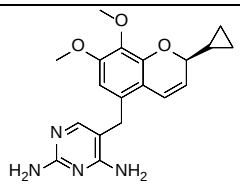	DB07938; 0.271; (S)-iclaprim; COC1=CC(CC2=C(N)N=C(N)N=C2)=C2C=C[C@@H](OC2=C1OC)C1CC1
57	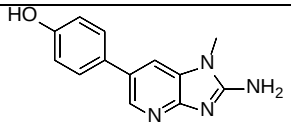	DB06898; 0.267; "4-(2-amino-1-methyl-1H-imidazo[4; CN1C(N)=NC2=NC=C(C=C12)C1=CC=C(O)C=C1
58	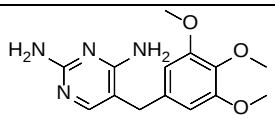	DB00440; 0.259; Trimethoprim; COC1=CC(CC2=C(N)N=C(N)N=C2)=CC(OC)=C1OC
59	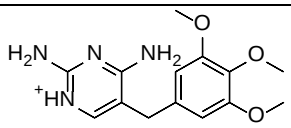	DB03125; 0.257; "2; COC1=CC(CC2=CN=C(N)N=C2N)=CC(OC)=C1OC
60	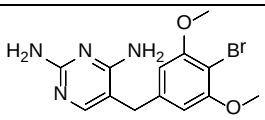	DB13795; 0.251; Brodimoprim; COC1=CC(CC2=CN=C(N)N=C2N)=CC(OC)=C1Br
61	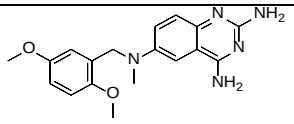	DB02427; 0.240; "2; COC1=CC(CN(C)C2=CC3=C(N)N=C(N)N=C3C=C2)=C(OC)C=C1
62	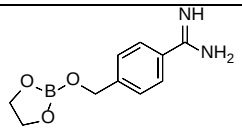	DB04109; 0.236; "[4-(1; NC(=N)C1=CC=C(COB2OCCO2)C=C1
63	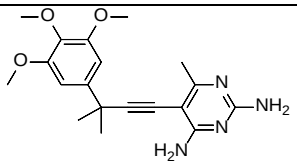	DB07153; 0.233; "6-methyl-5-[3-methyl-3-(3; COC1=CC(=CC(OC)=C1OC)C(C)(C)C#CC1=C(C)N=C(N)N=C1N

64	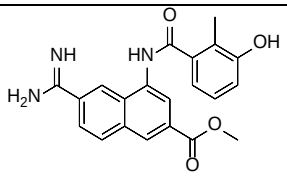	DB07074; 0.232; 6-CARBAMIMIDOYL-4-(3-HYDROXY-2-METHYL-BENZOYLAMINO)-NAPHTHALENE-2-CARBOXYLIC ACID METHYL ESTER; COC(=O)C1=CC2=CC=C(C=C2C(NC(=O)C2=CC=CC(O)=C2C)=C1)C(N)=N
65	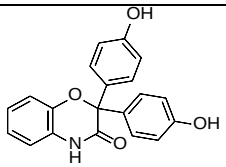	DB09219; 0.231; Bisoxatin; OC1=CC=C(C=C1)C1(OC2=C(NC1=O)C=CC=C2)C1=CC=C(O)C=C1
66	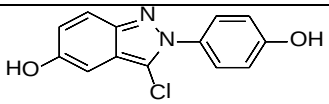	DB07708; 0.231; 3-CHLORO-2-(4-HYDROXYPHENYL)-2H-INDAZOL-5-OL; OC1=CC=C(C=C1)N1N=C2C=CC(O)=CC2=C1Cl
67	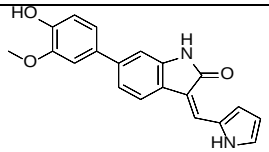	DB07078; 0.228; "(3Z)-6-(4-HYDROXY-3-METHOXYPHENYL)-3-(1H-PYRROL-2-YLMETHYLENE)-1; COC1=C(O)C=CC(=C1)C1=CC2=C(C=C1)C(=CC1=CC=CN1)C(=O)N2
68	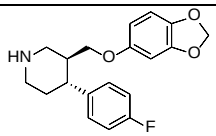	DB00715; 0.227; Paroxetine; FC1=CC=C(C=C1)[C@@H]1CCNC[C@H]1COC1=CC2=C(OCO2)C=C1
69	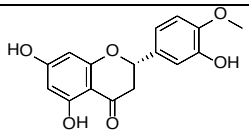	DB01094; 0.219; Hesperetin; COC1=C(O)C=C(C=C1)[C@@H]1CC(=O)C2=C(O1)C=C(O)C=C2O
70	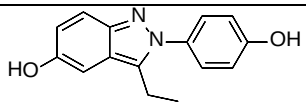	DB07712; 0.218; 3-ETHYL-2-(4-HYDROXYPHENYL)-2H-INDAZOL-5-OL; CCC1=C2C=C(O)C=CC2=NN1C1=CC=C(O)C=C1
71	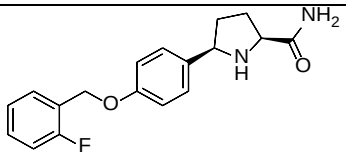	DB11706; 0.218; Raxatrigine; NC(=O)[C@@H]1CC[C@@H](N1)C1=CC=C(OCC2=CC=CC=C2F)C=C1

72	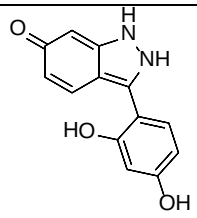	DB08048; 0.216; "4-(6-HYDROXY-1H-INDAZOL-3-YL)BENZENE-1; OC1=CC=C(C2=C3C=CC(=O)C=C3NN2)C(O)=C1
73	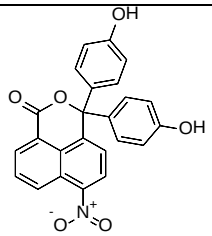	DB08204; 0.213; 3-DIPHENOL-6-NITRO-3H-BENZO[DE]ISOCHROMEN-1-ONE; OC1=CC=C(C=C1)C1(OC(=O)C2=CC=CC3=C(C=CC1=C23)[N+]([O-])=O)C1=CC=C(O)C=C1
74	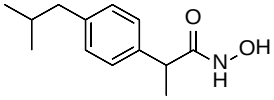	DB08955; 0.205; Ibuproxam; CC(C)CC1=CC=C(C=C1)C(C)C(=O)NO
75	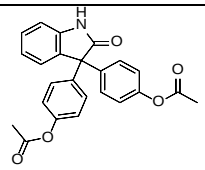	DB14627; 0.202; Oxyphenisatin acetate; CC(=O)OC1=CC=C(C=C1)C1(C(=O)NC2=C1C=CC=C2)C1=CC=C(OC(C)=O)C=C1
76	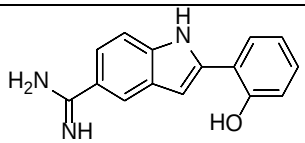	DB02463; 0.201; 2-(2-Hydroxy-Phenyl)-1h-Indole-5-Carboxamidine; NC(=N)C1=CC=C2NC(=CC2=C1)C1=CC=CC=C1O
77	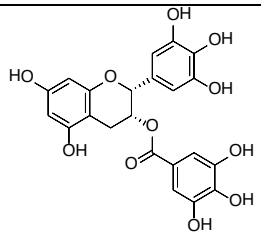	DB12116; 0.199; Epigallocatechin gallate; OC1=CC2=C(C[C@@H](OC(=O)C3=CC(O)=C(O)C(O)=C3)[C@H](O2)C2=CC(O)=C(O)C(O)=C2)C(O)=C1
78	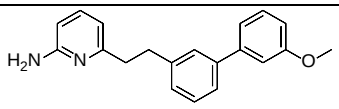	DB07245; 0.197; 6-[2-(3'-METHOXYBIPHENYL-3-YL)ETHYL]PYRIDIN-2-AMINE; COC1=CC=CC(=C1)C1=CC=CC(CCC2=CC=CC(N)=N2)=C1

79	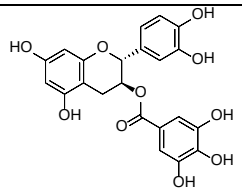	DB16120; 0.193; Epigallo Catechin Gallate; OC1=CC2=C(C[C@H](OC(=O)C3=CC(O)=C(O)C(O)=C3)[C@H](O2)C2=CC(O)=C(O)C=C2)C(O)=C1
80	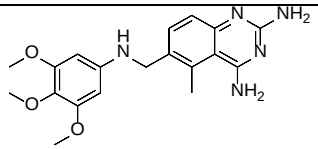	DB01157; 0.191; Trimetrexate; COC1=CC(NCC2=C(C)C3=C(N)N=C(N)N=C3C=C2)=CC(OC)=C1OC
81	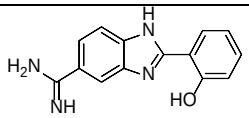	DB02287; 0.191; 2-(2-hydroxy-phenyl)-3H-benzoimidazole-5-carboxamidine; NC(=N)C1=CC=C2NC(=NC2=C1)C1=CC=CC=C1O
82	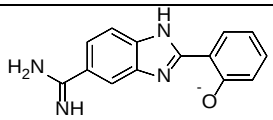	DB03643; 0.191; CRA_1144; NC(=N)C1=CC=C2NC(=NC2=C1)C1=CC=CC=C1O
83	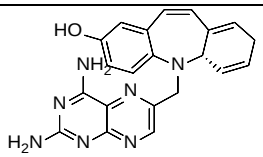	DB08448; 0.188; "(4aS)-5-[(2; NC1=NC2=NC=C(CN3[C@H]4C=CCC=C4C=CC4=CC(O)=CC=C34)N=C2C(N)=N1
84	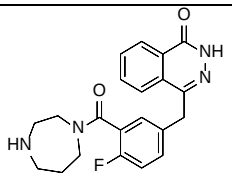	DB08058; 0.188; "4-[3-(1; FC1=CC=C(CC2=NNC(=O)C3=CC=CC=C23)C=C1C(=O)N1CCCNCC1
85	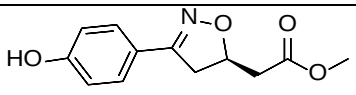	DB07888; 0.188; "3-(4-HYDROXYPHENYL)-4; COC(=O)C[C@H]1CC(=NO1)C1=CC=C(O)C=C1
86	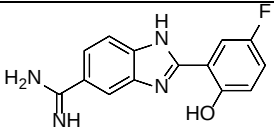	DB02875; 0.184; CRA_1802; NC(=N)C1=CC=C2NC(=NC2=C1)C1=CC(F)=CC=C1O

87	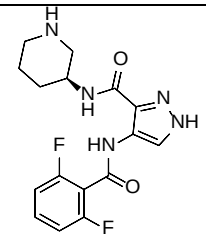	DB08141; 0.184; "4-{[(2; FC1=CC=CC(F)=C1C(=O)NC1=CNN=C1C(=O)N[C@H]1CCCNC1
88	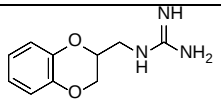	DB13211; 0.182; Guanoxan; NC(=N)NCC1COC2=C(O1)C=CC=C2
89	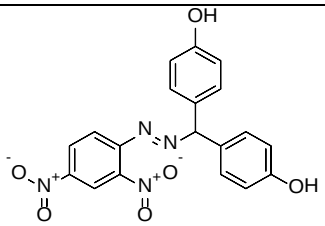	DB05686; 0.182; Sivifene; OC1=CC=C(C=C1)C(N=NC1=CC=C(C=C1[N+]([O-])=O)[N+]([O-])=O)C1=CC=C(O)C=C1
90	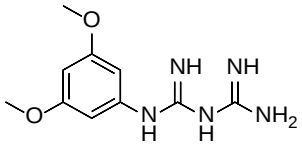	DB08479; 0.182; "N-(3; COC1=CC(OC)=CC(NC(=N)NC(N)=N)=C1
91	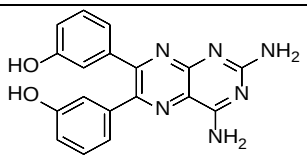	DB05552; 0.181; TG100-115; NC1=NC2=NC(C3=CC(O)=CC=C3)=C(N=C2C(N)=N1)C1=CC=CC(O)=C1
92	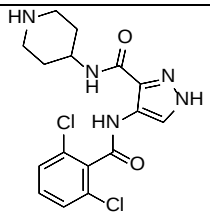	DB08142; 0.178; AT-7519; ClC1=CC=CC(Cl)=C1C(=O)NC1=CNN=C1C(=O)NC1CCNCC1
93	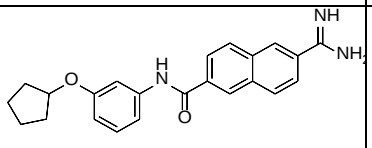	DB07076; 0.176; 6-[(Z)-AMINO(IMINO)METHYL]-N-[3-(CYCLOPENTYLOXY)PHENYL]-2-NAPHTHAMIDE; NC(=N)C1=CC2=CC=C(C=C2C=C1)C(=O)NC1=CC=CC(OC2CCCC2)=C1

94	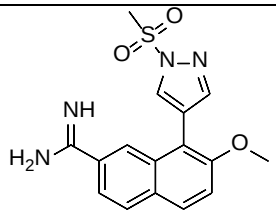	DB03046; 0.175; 7-Methoxy-8-[1-(Methylsulfonyl)-1h-Pyrazol-4-Yl]Naphthalene-2-Carboximidamide; COC1=C(C2=CN(N=C2)S(C)(=O)=O)C2=CC(=CC=C2C=C1)C(N)=N
95	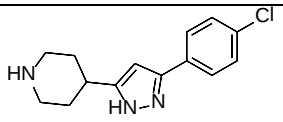	DB08061; 0.173; 4-[3-(4-CHLOROPHENYL)-1H-PYRAZOL-5-YL]PIPERIDINE; ClC1=CC=C(C=C1)C1=NNC(=C1)C1CCNCC1
96	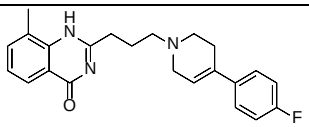	DB03072; 0.171; "2-{3-[4-(4-Fluorophenyl)-3; CC1=C2NC(CCCN3CCC(=CC3)C3=CC=C(F)C=C3)=NC(=O)C2=CC=C1
97	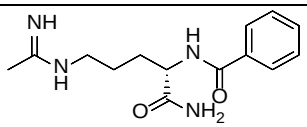	DB07449; 0.166; N-[(1S)-1-(aminocarbonyl)-4-(ethanimidoylamino)butyl]benzamide; CC(=N)NCCC[C@H](NC(=O)C1=CC=CC=C1)C(N)=O
98	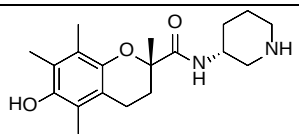	DB16333; 0.164; Sonlicromanol; CC1=C(O)C(C)=C2CC[C@](C)(OC2=C1C)C(=O)N[C@@H]1CCCNC1
99	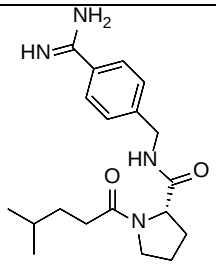	DB06936; 0.163; N-(4-carbamimidoylbenzyl)-1-(4-methylpentanoyl)-L-prolinamide; CC(C)CCC(=O)N1CCC[C@H]1C(=O)NCC1=CC=C(C=C1)C(N)=N
100	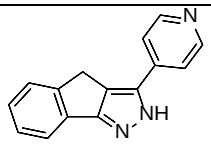	DB03490; 0.162; "3-Pyridin-4-Yl-2; C1C2=C(C=CC=C2)C2=NNC(=C12)C1=CC=NC=C1

101	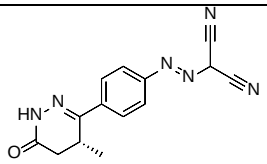	DB00922; 0.162; Levosimendan; C[C@@H]1CC(=O)NN=C1C1=CC=C(C=C1)N=NC(C#N)C#N
102	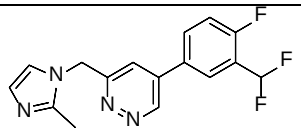	DB05956; 0.161; EVT-101; CC1=NC=CN1CC1=CC(=CN=N1)C1=CC=C(F)C(=C1)C(F)F
103	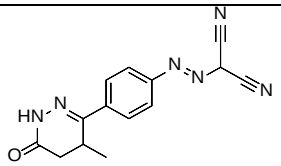	DB12286; 0.158; Simendan; CC1CC(=O)NN=C1C1=CC=C(C=C1)N=NC(C#N)C#N
104	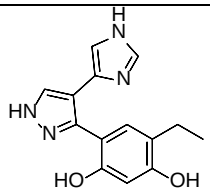	DB03749; 0.158; "4-(1h-Imidazol-4-Yl)-3-(5-Ethyl-2; CCC1=C(O)C=C(O)C(=C1)C1=NNC=C1C1=CNC=N1
105	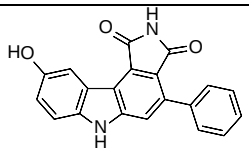	DB04608; 0.155; "9-HYDROXY-4-PHENYL-6H-PYRROLO[3; OC1=CC2=C(NC3=C2C2=C(C(=O)NC2=O)C(=C3)C2=CC=CC=C2)C=C1
106	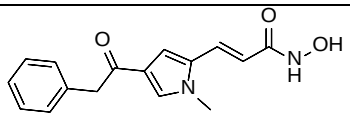	DB07350; 0.154; (2E)-N-hydroxy-3-[1-methyl-4-(phenylacetyl)-1H-pyrrol-2-yl]prop-2-enamide; CN1C=C(C=C1C=CC(=O)NO)C(=O)CC1=CC=CC=C1
107	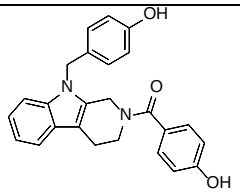	DB04030; 0.153; "1; OC1=CC=C(CN2C3=C(CCN(C3)C(=O)C3=CC=C(O)C=C3)C3=CC=CC=C23)C=C1
108	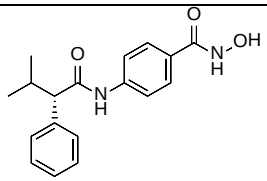	DB12707; 0.153; AR-42; CC(C)[C@H](C(=O)NC1=CC=C(C=C1)C(=O)NO)C1=CC=CC=C1

109	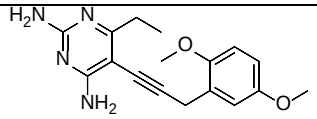	DB08234; 0.152; "5-[3-(2; CCC1=NC(N)=NC(N)=C1C#CCC1=CC(OC)=CC=C1OC
107	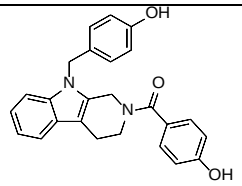	DB04030; 0.153; "1; OC1=CC=C(CN2C3=C(CCN(C3)C(=O)C3=CC=C(O)C=C3)C3=CC=CC=C23)C=C1
111	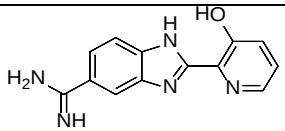	DB03016; 0.144; CRA_1801; NC(=N)C1=CC=C2NC(=NC2=C1)C1=C(O)C=CC=N1
112	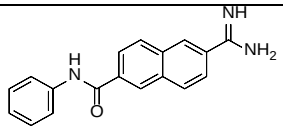	DB01977; 0.142; 6-(N-Phenylcarbamyl)-2-Naphthalenecarboxamidine; NC(=N)C1=CC2=CC=C(C=C2C=C1)C(=O)NC1=CC=CC=C1
113	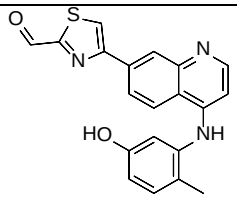	DB07832; 0.142; "4-{4-[(5-hydroxy-2-methylphenyl)amino]quinolin-7-yl}-1; CC1=C(NC2=C3C=CC(=CC3=NC=C2)C2=CSC(C=O)=N2)C=C(O)C=C1
114	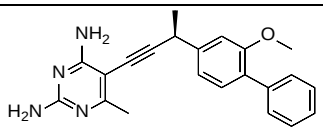	DB06847; 0.142; "5-[(3S)-3-(2-methoxybiphenyl-4-yl)but-1-yn-1-yl]-6-methylpyrimidine-2; COC1=C(C=CC(=C1)[C@H](C)C#CC1=C(C)N=C(N)N=C1N)C1=CC=CC=C1
115	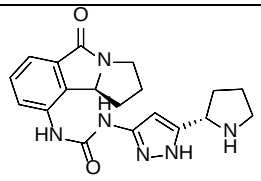	DB06976; 0.141; "1-(5-OXO-2; O=C(NC1=NNC(=C1)[C@@H]1CCCN1)NC1=CC=CC2=C1[C@@H]1CCCN1C2=O
116	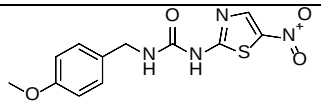	DB01950; 0.140; AR-AO-14418; COC1=CC=C(CNC(=O)NC2=NC=C(S2)[N+]([O-])=O)C=C1
117	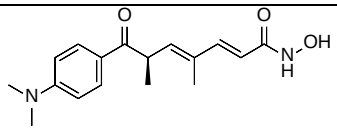	DB04297; 0.138; Trichostatin A; C[C@H](C=C(C)C=CC(=O)NO)C(=O)C1=CC=C(C=C1)N(C)C

118	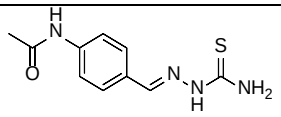	DB12829; 0.138; Amithiozone; CC(=O)NC1=CC=C(C=NNC(N)=S)C=C1
119	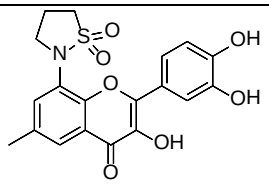	DB07024; 0.138; "2-(3; CC1=CC(N2CCCS2(=O)=O)=C2OC(=C(O)C(=O)C2=C1)C1=CC=C(O)C(O)=C1
120	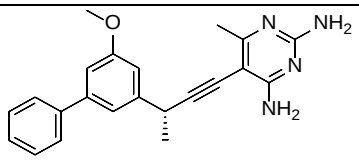	DB07140; 0.137; "5-[(3R)-3-(5-methoxybiphenyl-3-yl)but-1-yn-1-yl]-6-methylpyrimidine-2; COC1=CC(=CC(=C1)[CH](C)C#CC1=C(C)N=C(N)N=C1N)C1=CC=CC=C1
121	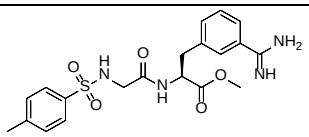	DB01737; 0.133; "Nalpha-(2-Naphthylsulfonylglycyl)-3-Amidino-D; COC(=O)[C@H](CC1=CC=CC(=C1)C(N)=N)NC(=O)CNS(=O)(=O)C1=CC=C(C)C=C1
122	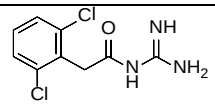	DB01018; 0.133; Guanfacine; NC(=N)NC(=O)CC1=C(Cl)C=CC=C1Cl
123	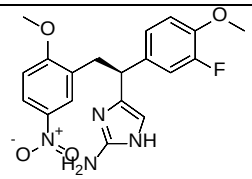	DB07415; 0.133; 4-[(1S)-1-(3-fluoro-4-methoxyphenyl)-2-(2-methoxy-5-nitrophenyl)ethyl]-1H-imidazol-2-amine; COC1=CC=C(C=C1F)[C@H](CC1=CC(=CC=C1OC)[N+]([O-])=O)C1=CNC(N)=N1
124	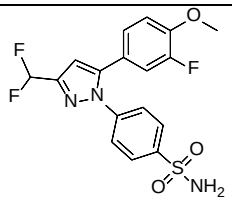	DB11395; 0.131; Deracoxib; COC1=CC=C(C=C1F)C1=CC(=NN1C1=CC=C(C=C1)S(N)(=O)=O)C(F)F
125	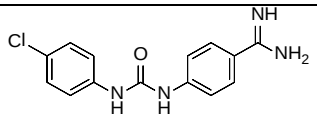	DB04336; 0.130; 1-(4-Amidinophenyl)-3-(4-Chlorophenyl)Urea; NC(=N)C1=CC=C(NC(=O)NC2=CC=C(Cl)C=C2)C=C1

126	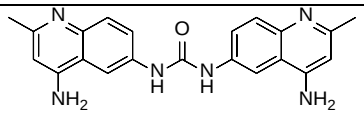	DB04452; 0.128; Aminoquinuride; CC1=CC(N)=C2C=C(NC(=O)NC3=CC=C4N=C(C)C=C(N)C4=C3)C=CC2=N1
127	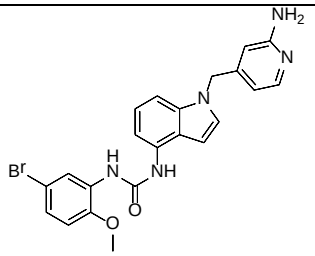	DB12744; 0.128; CGI-1842; COC1=CC=C(Br)C=C1NC(=O)NC1=C2C=CN(CC3=CC=NC(N)=C3)C2=CC=C1
128	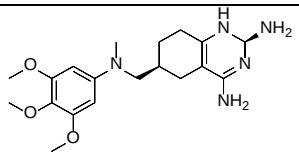	DB08642; 0.128; "(2R; COC1=CC(=CC(OC)=C1OC)N(C)C[C@H]1CCC2=C(C1)C(N)=N[C@H](N)N2
129	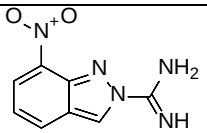	DB03065; 0.127; 7-Nitroindazole-2-Carboxamidine; NC(=N)N1C=C2C=CC=C(C2=N1)[N+]([O-])=O
130	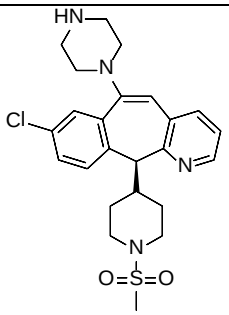	DB07216; 0.127; "(11S)-8-CHLORO-11-[1-(METHYLSULFONYL)PIPERIDIN-4-YL]-6-PIPERAZIN-1-YL-11H-BENZO[5; CS(=O)(=O)N1CCC(CC1)[C@H]1C2=C(C=C(Cl)C=C2)C(=CC2=C1N=CC=C2)N1CCNCC1
131	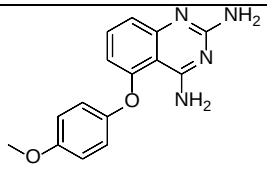	DB02402; 0.127; "5-(4-Methoxyphenoxy)-2; COC1=CC=C(OC2=C3C(N)=NC(N)=NC3=CC=C2)C=C1
132	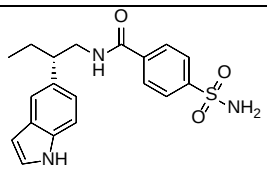	DB03596; 0.127; N-[2-(1h-Indol-5-Yl)-Butyl]-4-Sulfamoyl-Benzamide; CC[C@H](CNC(=O)C1=CC=C(C=C1)S(N)(=O)=O)C1=CC=C2NC=CC2=C1
133	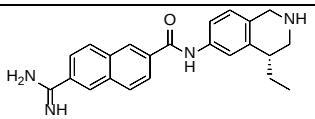	DB02551; 0.124; "6-[N-(4-Ethyl-1; CC[C@H]1CNCC2=C1C=C(NC(=O)C1=CC3=CC=C(C=C3C=C1)C(N)=N)C=C2

134	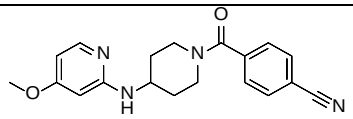	DB07002; 0.122; 4-({4-[(4-methoxypyridin-2-yl)amino]piperidin-1-yl}carbonyl)benzonitrile; COC1=CC=NC(NC2CCN(CC2)C(=O)C2=CC=C(C=C2)C#N)=C1
135	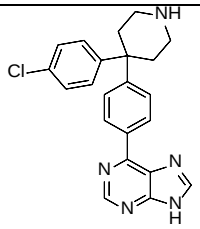	DB07856; 0.120; 6-{4-[4-(4-CHLOROPHENYL)PIPERIDIN-4-YL]PHENYL}-9H-PURINE; ClC1=CC=C(C=C1)C1(CCNCC1)C1=CC=C(C=C1)C1=C2N=CNC2=NC=N1
136	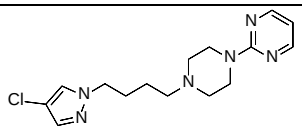	DB04970; 0.117; Lesopitron; ClC1=CN(CCCCN2CCN(CC2)C2=NC=CC=N2)N=C1
137	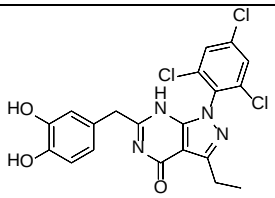	DB07606; 0.115; "6-(3; CCC1=NN(C2=C1C(=O)N=C(CC1=CC(O)=C(O)C=C1)N2)C1=C(Cl)C=C(Cl)C=C1Cl
138	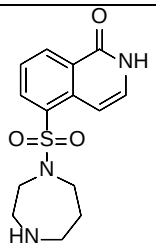	DB04707; 0.114; Hydroxyfasudil; O=C1NC=CC2=C(C=CC=C12)S(=O)(=O)N1CCCNCC1
139	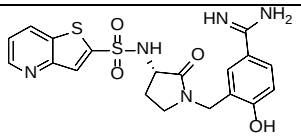	DB02744; 0.113; RPR131247; NC(=N)C1=CC=C(O)C(CN2CC[C@H](NS(=O)(=O)C3=CC4=NC=CC=C4S3)C2=O)=C1
140	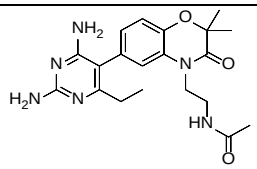	DB07059; 0.112; "N-{2-[6-(2; CCC1=C(C(N)=NC(N)=N1)C1=CC=C2OC(C)(C)C(=O)N(CCNC(C)=O)C2=C1
141	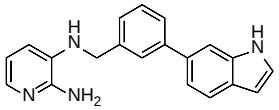	DB07993; 0.110; "N~3~-[3-(1H-INDOL-6-YL)BENZYL]PYRIDINE-2;

		NC1=NC=CC=C1NCC1=CC=CC(=C1)C1=CC=C2C=CNC2=C1
142	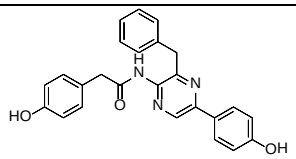	DB04049; 0.110; Coelenteramide; OC1=CC=C(CC(=O)NC2=NC=C(N=C2CC2=CC=CC=C2)C2=CC=C(O)C=C2)C=C1
143	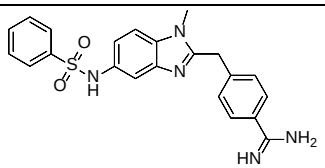	DB07508; 0.110; 4-(5-BENZENESULFONYLAMINO-1-METHYL-1H-BENZOIMIDAZOL-2-YLMETHYL)-BENZAMIDINE; CN1C(CC2=CC=C(C=C2)C(N)=N)=NC2=CC(NS(=O)(=O)C3=CC=CC=C3)=CC=C12
144	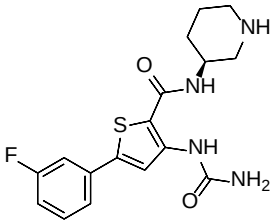	DB12242; 0.110; AZD-7762; NC(=O)NC1=C(SC(=C1)C1=CC(F)=CC=C1)C(=O)N[C@H]1CCCNC1
145	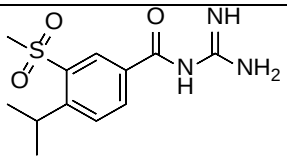	DB06468; 0.110; Cariporide; CC(C)C1=CC=C(C=C1S(C)(=O)=O)C(=O)NC(N)=N
146	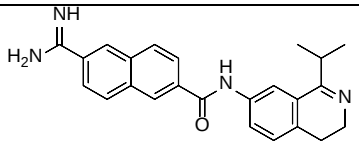	DB02473; 0.108; "6-[N-(1-Isopropyl-3; CC(C)C1=NCCC2=C1C=C(NC(=O)C1=CC3=CC=C(C=C3C=C1)C(N)=N)C=C2
147	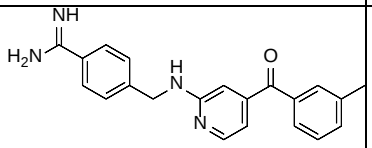	DB07809; 0.106; 4-({[4-(3-METHYLBENZOYL)PYRIDIN-2-YL]AMINO}METHYL)BENZENECARBOXIMIDAMIDE; CC1=CC=CC(=C1)C(=O)C1=CC=NC(NCC2=CC=C(C=C2)C(N)=N)=C1
148	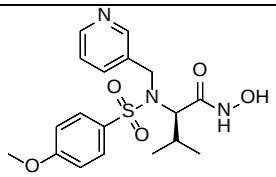	DB07556; 0.102; CGS-27023; COC1=CC=C(C=C1)S(=O)(=O)N(CC1=CC=CN=C1)[C@H](C(C)C)C(=O)NO

149	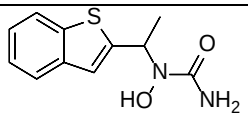	DB00744; 0.100; Zileuton; CC(N(O)C(N)=O)C1=CC2=CC=CC=C2S1
150	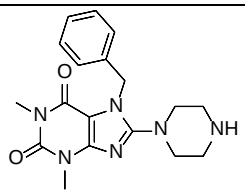	DB08530; 0.099; "7-BENZYL-1; CN1C2=C(N(CC3=CC=CC=C3)C(=N2)N2CCNCC2)C(=O)N(C)C1=O
151	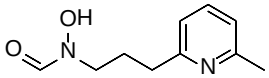	DB08525; 0.099; HYDROXY[3-(6-METHYLPYRIDIN-2-YL)PROPYL]FORMAMIDE; CC1=NC(CCCN(O)C=O)=CC=C1
152	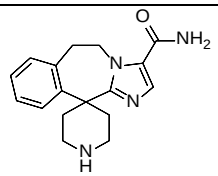	DB05738; 0.099; Vapitadine; NC(=O)C1=CN=C2N1CCC1=C(C=CC=C1)C21CCNCC1
153	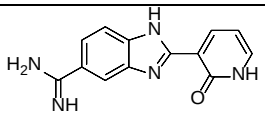	DB04442; 0.099; "Imino[2-(2-oxo-1; NC(=N)C1=CC=C2NC(=NC2=C1)C1=CC=CNC1=O
154	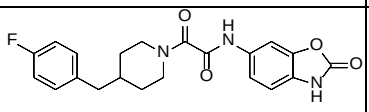	DB12260; 0.094; Radiprodil; FC1=CC=C(CC2CCN(CC2)C(=O)C(=O)NC2=CC=C3NC(=O)OC3=C2)C=C1
155	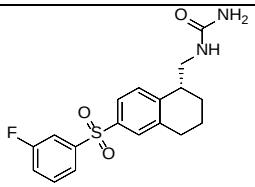	DB16214; 0.091; Landipirdine; NC(=O)NC[C@@H]1CCCC2=CC(=CC=C12)S(=O)(=O)C1=CC(F)=CC=C1
156	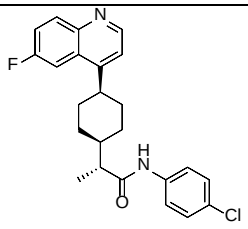	DB14986; 0.091; Linrodostat; C[C@H]([C@H]1CC[C@H](CC1)C1=CC=NC2=CC=C(F)C=C12)C(=O)NC1=CC=C(Cl)C=C1

157	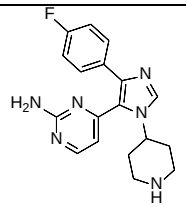	DB04338; 0.090; SB220025; NC1=NC(=CC=N1)C1=C(N=CN1C1CCN CC1)C1=CC=C(F)C=C1
158	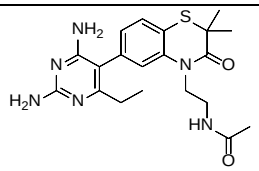	DB06899; 0.090; "N-{2-[6-(2; CCC1=C(C(N)=NC(N)=N1)C1=CC=C2SC (C)(C)C(=O)N(CCNC(C)=O)C2=C1
159	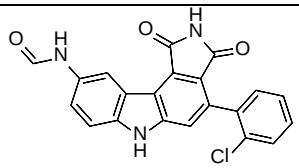	DB07226; 0.090; "N-[4-(2-CHLOROPHENYL)-1; ClC1=CC=CC=C1C1=CC2=C(C3=C(N2)C =CC(NC=O)=C3)C2=C1C(=O)NC2=O
160	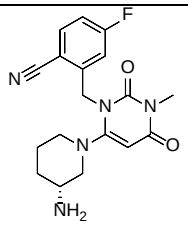	DB15323; 0.085; Trelagliptin; CN1C(=O)C=C(N2CCC[C@@H](N)C2)N(CC2=CC(F)=CC=C2C#N)C1=O
161	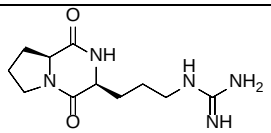	DB04433; 0.084; Verpacamide A; NC(=N)NCCC[C@@H]1NC(=O)[C@@H] 2CCCN2C1=O
162	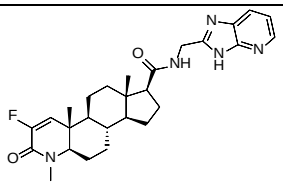	DB16244; 0.082; MK-0773; CN1[C@@H]2CC[C@H]3[C@@H]4CC[C @H](C(=O)NCC5=NC6=CC=CN=C6N5)[C@@]4(C)CC[C@@H]3[C@@]2(C)C=C(F)C1=O
163	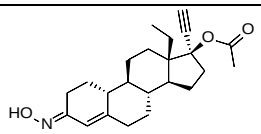	DB00957; 0.081; Norgestimate; CC[C@]12CC[C@H]3[C@@H](CCC4=C C(CC[C@H]34)=NO)[C@@H]1CC[C@@]2(OC(C)=O)C#C
164	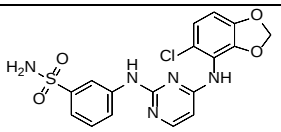	DB07252; 0.081; "3-({4-[(5-chloro-1; NS(=O)(=O)C1=CC(NC2=NC=CC(NC3=C 4OCOC4=CC=C3Cl)=N2)=CC=C1

165	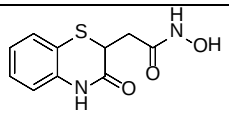	DB02036; 0.080; "2-(3; C1=CC=C2C(=C1)NC(=O)C(S2)CC(=O)NO
166	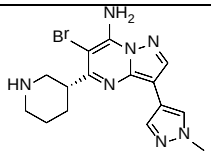	DB11899; 0.079; MK-8776; CN1C=C(C=N1)C1=C2N=C([C@@H]3CCCNC3)C(Br)=C(N)N2N=C1
167	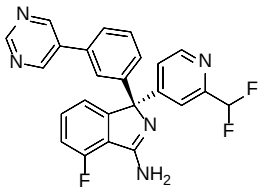	DB12368; 0.079; AZD-3839; NC1=N[C@@](C2=CC=CC(F)=C12)(C1=CC=CC(=C1)C1=CN=CN=C1)C1=CC=NC(=C1)C(F)F
168	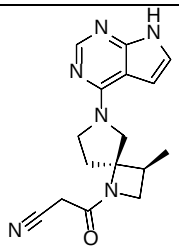	DB16133; 0.077; Delgocitinib; C[C@H]1CN(C(=O)CC#N)[C@]11CCN(C1)C1=C2C=CNC2=NC=N1
169	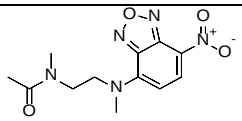	DB08751; 0.073; "N; CN(CCN(C)C1=CC=C(C2=NON=C12)[N+]([O-])=O)C(C)=O
170	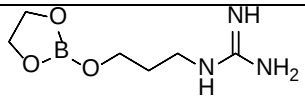	DB03129; 0.072; "Diamino-N-[3-(1; NC(=N)NCCCOB1OCCO1
171	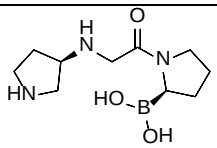	DB11723; 0.069; Dutogliptin; OB(O)[C@@H]1CCCN1C(=O)CN[C@@H]1CCNC1
172	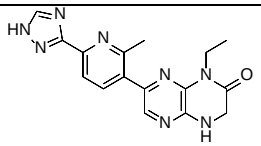	DB12740; 0.065; CC-115; CCN1C(=O)CNC2=C1N=C(C=N2)C1=CC=C(N=C1C)C1=NNC=N1

173	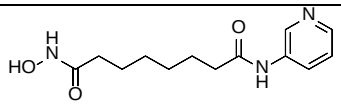	DB12847; 0.061; Pyroxamide; ONC(=O)CCCCCCC(=O)NC1=CN=CC=C1
174	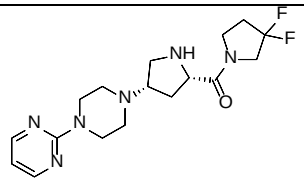	DB08382; 0.059; Gosogliptin; FC1(F)CCN(C1)C(=O)[C@@H]1C[C@@H](CN1)N1CCN(CC1)C1=NC=CC=N1
175	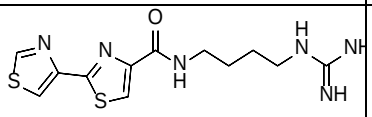	DB07499; 0.057; "N-(4-{[amino(imino)methyl]amino}butyl)-2; NC(=N)NCCCCNC(=O)C1=CSC(=N1)C1=CSC=N1
176	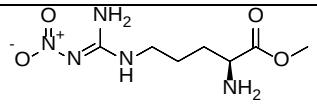	DB12750; 0.057; N-omega-nitro-L-arginine methyl ester; COC(=O)[C@@H](N)CCCNC(N)=N[N+]([O-])=O
177	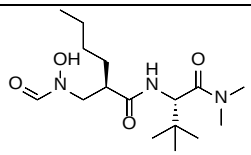	DB04368; 0.057; Bb-3497; CCCC[C@H](CN(O)C=O)C(=O)N[C@H](C(=O)N(C)C)C(C)(C)C

Table S5.2: Screened compounds from library 2

SL. No.	**COMPOUNDS**	**DrugBank ID; Similarity Score; Usual Name; SMILES**	**Remarks (Duplicates)**

1	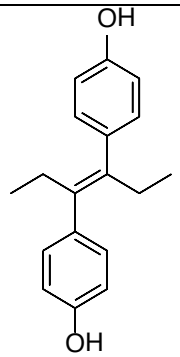	CHEMBL411; 0.939; CC(=C(CC)C1=CC=C(O)C=C1)C1=CC=C(O)C=C1	Library-1 SL.no-3
2	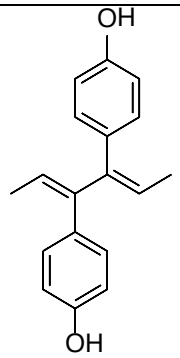	CHEMBL1018; 0.865; CC=C(C(=CC)C1=CC=C(O)C=C1)C1=CC=C(O)C=C1	Library-1 SL.no -6
3	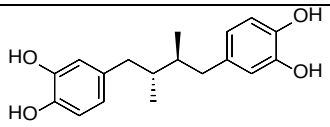	CHEMBL313972; 0.745; C[C@@H](CC1=CC=C(O)C(O)=C1)[C@H](C)CC1=CC=C(O)C(O)=C1	Library-1 SL.no -8
4	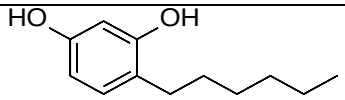	CHEMBL443605; 0.538; CCCCCCC1=CC=C(O)C=C1O	Library-1 SL.no -18
5	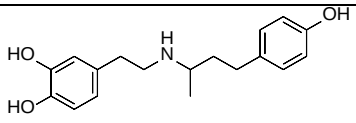	CHEMBL1200418; 0.503; CC(CCC1=CC=C(O)C=C1)NCCC1=CC=C(O)C(O)=C1	Library-1 SL.no -25
6	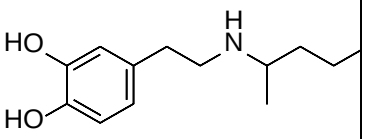	CHEMBL926; 0.503; CC(CCC1=CC=C(O)C=C1)NCCC1=CC=C(O)C(O)=C1	Same as SL.no -5

7	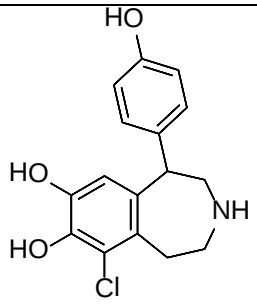	CHEMBL1026; 0.488; OC1=CC=C(C=C1)C1CNCCC2=C1C=C(O)C(O)=C2Cl	Library-1 SL.no-23
8	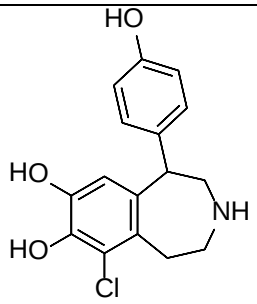	CHEMBL1026; 0.488; OC1=CC=C(C=C1)C1CNCCC2=C1C=C(O)C(O)=C2Cl	Same as SL.no -7
9	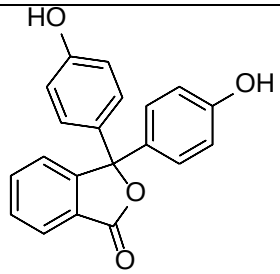	CHEMBL63857; 0.417; OC1=CC=C(C=C1)C1(OC(=O)C2=CC=CC=C12)C1=CC=C(O)C=C1	Library-1 SL.no -27
10	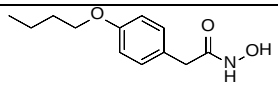	CHEMBL94394; 0.344; CCCCOC1=CC=C(CC(=O)NO)C=C1	Library-1 SL.no -39
11	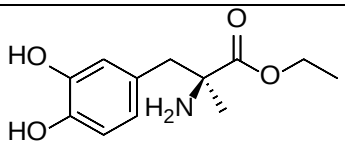	CHEMBL1200432; 0.341; CCOC(=O)[C@@](C)(N)CC1=CC=C(O)C(O)=C1	

12	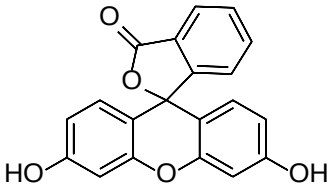	CHEMBL4297067; 0.295; OC1=CC=C2C(OC3=CC(O)=CC=C3C22OC(=O)C3=CC=CC=C23)=C1	Library-1 SL.no -49
13	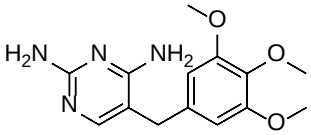	CHEMBL1201080; 0.257; COC1=CC(CC2=CN=C(N)N=C2N)=CC(OC)=C1OC	Library-1 SL.no -58
14	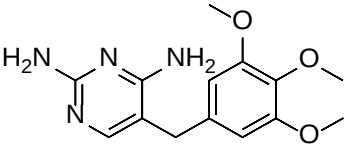	CHEMBL1201080; 0.257; COC1=CC(CC2=CN=C(N)N=C2N)=CC(OC)=C1OC	Same as SL.no -13
15	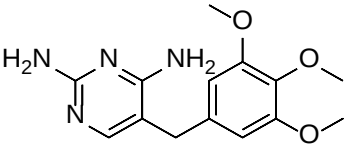	CHEMBL1201080; 0.257; COC1=CC(CC2=CN=C(N)N=C2N)=CC(OC)=C1OC	Same as SL.no -13
16	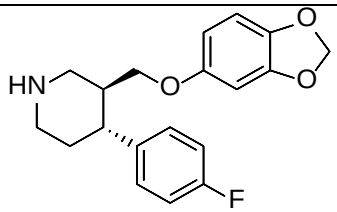	CHEMBL490; 0.227; FC1=CC=C(C=C1)[C@@H]1CCNC[C@H]1COC1=CC=C2OCOC2=C1	Library-1 SL.no -68

17	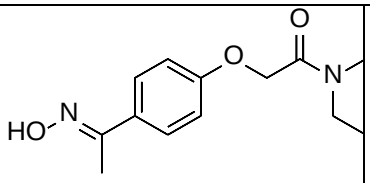	CHEMBL1998966; 0.219; CC(=NO)C1=CC=C(OCC(=O)N2CCCCC2)C=C1	
18	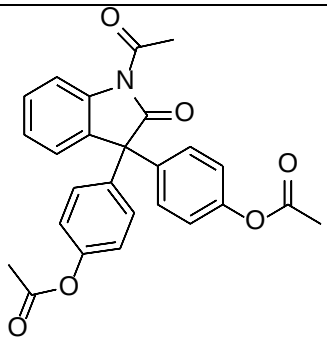	CHEMBL1909288; 0.203; CC(=O)OC1=CC=C(C=C1)C1(C(=O)N(C(C)=O)C2=CC=CC=C12)C1=CC=C(OC(C)=O)C=C1	
19	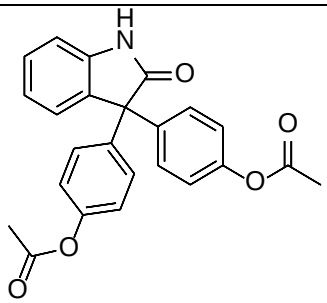	CHEMBL1402684; 0.202; CC(=O)OC1=CC=C(C=C1)C1(C(=O)NC2=CC=CC=C12)C1=CC=C(OC(C)=O)C=C1	Library-1 SL.no -75
20	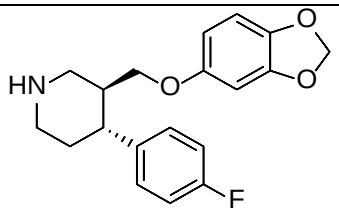	CHEMBL1200609; 0.199; FC1=CC=C(C=C1)[C@@H]1CCNC[C@H]1COC1=CC=C2OCOC2=C1	Same as SL.no -16
21	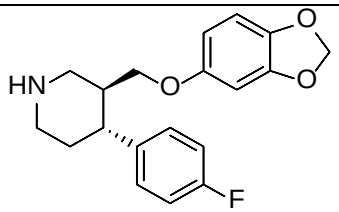	CHEMBL1708; 0.199; FC1=CC=C(C=C1)[C@@H]1CCNC[C@H]1COC1=CC=C2OCOC2=C1 PAROXETINE	Same as SL.no -16

22	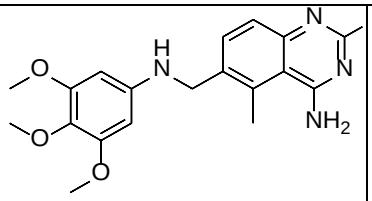	CHEMBL2218878; 0.191; COC1=CC(NCC2=C(C)C3=C(N)N=C(N)N=C3C=C2)=CC(OC)=C1OC	Library-1 SL.no -80
23	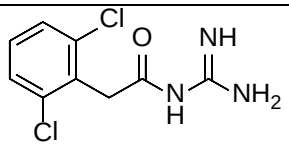	CHEMBL1200494; 0.133; NC(=N)NC(=O)CC1=C(Cl)C=CC=C1Cl	Library-1 SL.no -122
24	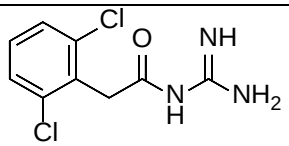	CHEMBL862; 0.133; NC(=N)NC(=O)CC1=C(Cl)C=CC=C1Cl	Same as SL.no -23
25	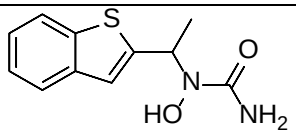	CHEMBL93; 0.100; CC(N(O)C(N)=O)C1=CC2=CC=CC=C2S1	Library-1 SL.no -149
26	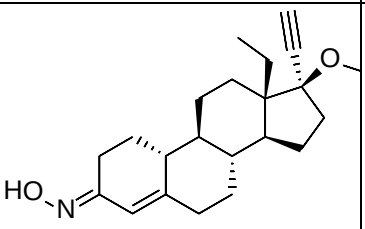	CHEMBL1200934; 0.081; CC[C@]12CC[C@H]3[C@@H](CCC4=CC(CC[C@H]34)=NO)[C@@H]1CC[C@@]2(OC(C)=O)C#C	Library-1 SL.no -163
27	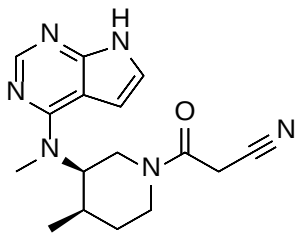	CHEMBL2103743; 0.081; C[C@@H]1CCN(C[C@@H]1N(C)C1=C2C=CNC2=NC=N1)C(=O)CC#N	

Table S5.3: Screened compounds from library 3

SL. No.	**COMPOUNDS**	**DrugBank ID; Similarity Score; Usual Name; SMILES**	**Remarks (Duplicates)**
1	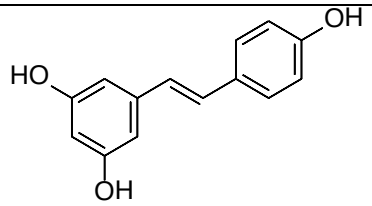	CHEMBL165; 1.000; OC1=CC=C(C=CC2=CC(O)=CC(O)=C2)C=C1	Library-1 SL.no-1
2	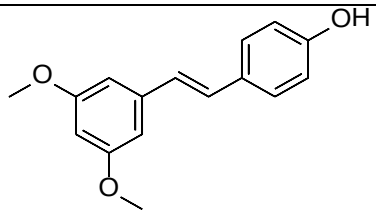	CHEMBL83527; 0.989; COC1=CC(C=CC2=CC=C(O)C=C2)=CC(OC)=C1	
3	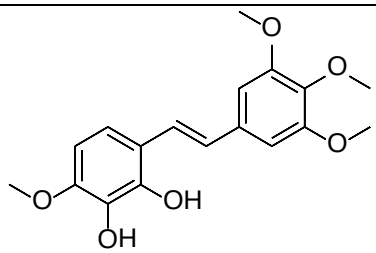	CHEMBL36255; 0.965; COC1=CC=C(C=CC2=CC(OC)=C(OC)C(OC)=C2)C(O)=C1O	
4	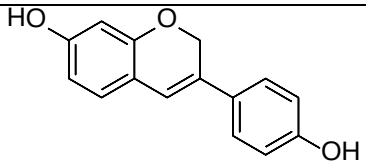	CHEMBL1957038; 0.850; OC1=CC=C(C=C1)C1=CC2=CC=C(O)C=C2OC1	Library-1 SL.no-7
5	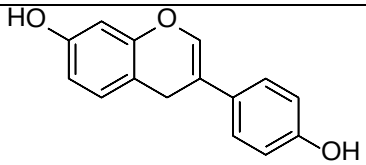	CHEMBL195560; 0.753; OC1=CC=C(C=C1)C1=COC2=CC(O)=CC=C2C1	

6	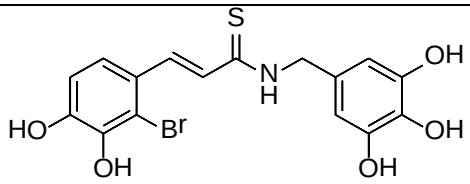	CHEMBL3679680; 0.698; OC1=CC=C(C=CC(=S)NCC2=CC(O)=C(O)C(O)=C2)C(Br)=C1O	
7	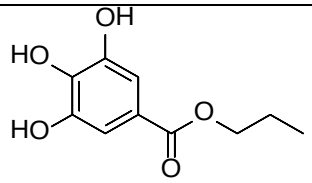	CHEMBL7983; 0.515; CCCOC(=O)C1=CC(O)=C(O)C(O)=C1	Library-1 SL.no-22
8	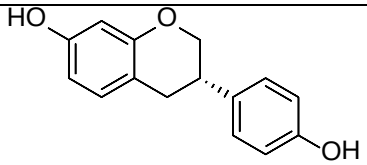	CHEMBL198877; 0.499; OC1=CC=C(C=C1)[C@H]1COC2=CC(O)=CC=C2C1	Library-1 SL.no-24
9	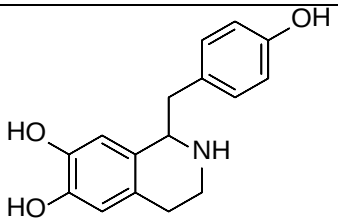	CHEMBL19344; 0.390; OC1=CC=C(CC2NCCC3=CC(O)=C(O)C=C23)C=C1	Library-1 SL.no-33
10	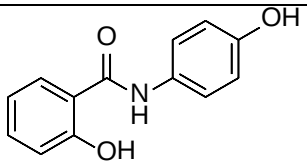	CHEMBL389507; 0.362; OC1=CC=C(NC(=O)C2=CC=CC=C2O)C=C1	Library-1 SL.no-38
11	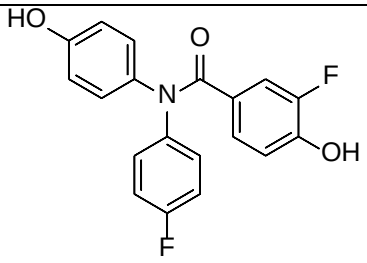	CHEMBL3545017; 0.342; OC1=CC=C(C=C1)N(C(=O)C1=CC=C(O)C(F)=C1)C1=CC=C(F)C=C1	Library-1 SL.no-40
12	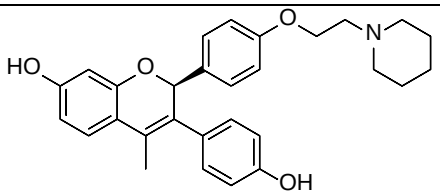	CHEMBL68055; 0.315; CC1=C([C@@H](OC2=CC(O)=CC=C12)C1=CC=C(OCCN2CCCCC2)C=C1)C1=CC=C(O)C=C1	Library-1 SL.no-43

13	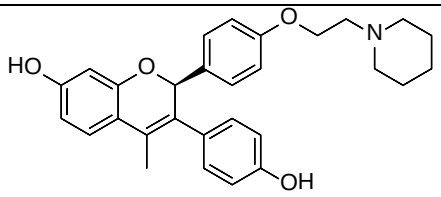	CHEMBL2105965; 0.315; CC1=C([C@@H](OC2=CC(O)=CC=C12)C1=CC=C(OCCN2CCCCC2)C=C1)C1=CC=C(O)C=C1	Same as SL.no -12
14	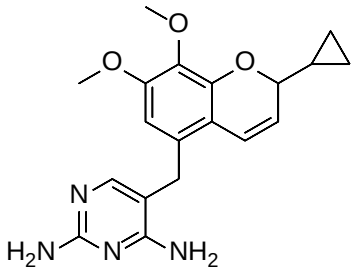	CHEMBL134561; 0.277; COC1=CC(CC2=CN=C(N)N=C2N)=C2C=CC(OC2=C1OC)C1CC1	
15	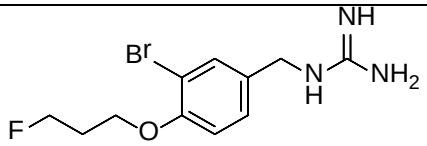	CHEMBL4300856; 0.277; NC(=N)NCC1=CC=C(OCCCF)C(Br)=C1	
16	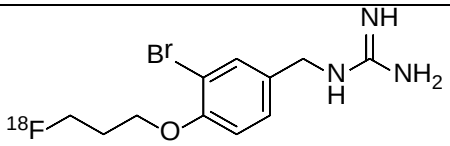	CHEMBL4298157; 0.277; NC(=N)NCC1=CC=C(OCCC[18F])C(Br)=C1	
17	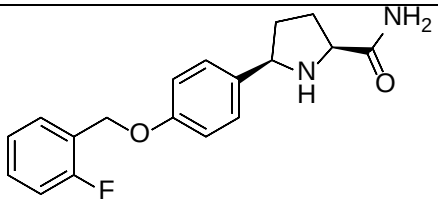	CHEMBL3544913; 0.218; NC(=O)[C@@H]1CC[C@@H](N1)C1=CC=C(OCC2=CC=CC=C2F)C=C1	Library-1 SL.no -71
18		CHEMBL3763743; 0.208; OC1=CC=C(OC2=C(C3=CC=C(O)C=C3S2)C2=CC=C(F)C=C2)C=C1	

	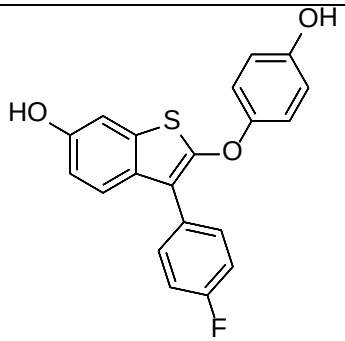		
19	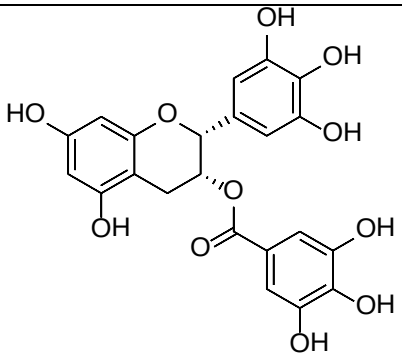	CHEMBL297453; 0.199; OC1=CC(O)=C2C[C@@H](OC(=O)C3=CC(O)=C(O)C(O)=C3)[C@H](OC2=C1)C1=CC(O)=C(O)C(O)=C1	Library-1 SL.no-77
20	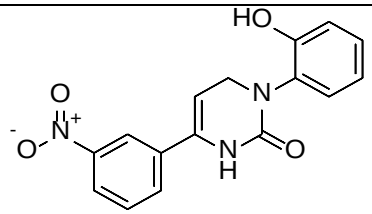	CHEMBL258405; 0.198; OC1=CC=CC=C1N1CC=C(NC1=O)C1=CC=CC(=C1)[N+]([O-])=O	
21	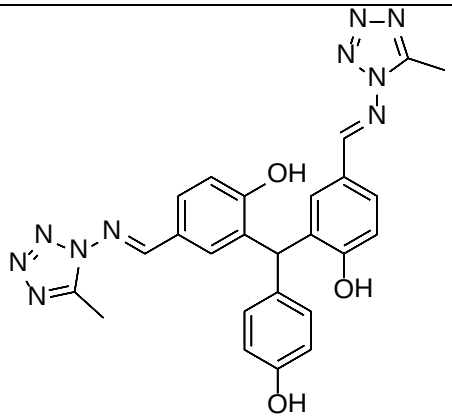	CHEMBL4297402; 0.185; CC1=NN=NN1N=CC1=CC=C(O)C(=C1)C(C1=CC=C(O)C=C1)C1=CC(C=NN2N=NN=C2C)=CC=C1O	

22	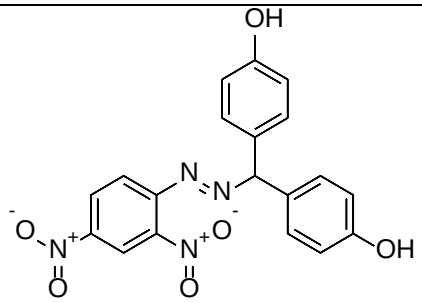	CHEMBL307697; 0.182; OC1=CC=C(C=C1)C(N=NC1=CC=C(C=C1[N+]([O-])=O)[N+]([O-])=O)C1=CC=C(O)C=C1	Library-1 SL.no-89
23	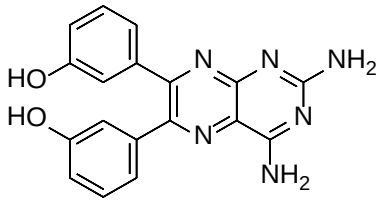	CHEMBL230011; 0.181; NC1=NC2=NC(C3=CC=CC(O)=C3)=C(N=C2C(N)=N1)C1=CC=CC(O)=C1	Library-1 SL.no-91
24	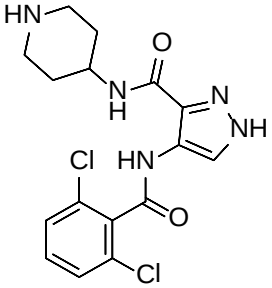	CHEMBL445813; 0.178; ClC1=CC=CC(Cl)=C1C(=O)NC1=CNN=C1C(=O)NC1CCNCC1	Library-1 SL.no-92
25	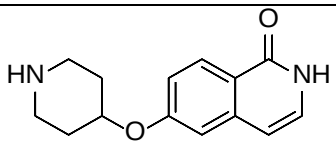	CHEMBL1667969; 0.176; O=C1NC=CC2=CC(OC3CCNCC3)=CC=C12	
26	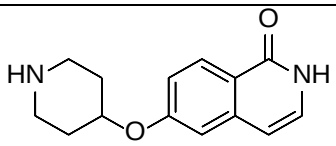	CHEMBL3545341; 0.176; O=C1NC=CC2=CC(OC3CCNCC3)=CC=C12	Same as SL.no-25
27	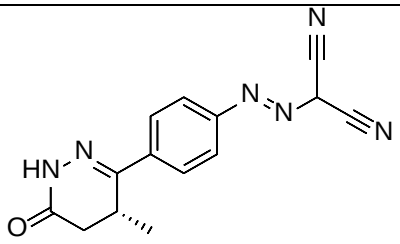	CHEMBL2051955; 0.162; C[C@@H]1CC(=O)NN=C1C1=CC=C(C=C1)N=NC(C#N)C#N	Library-1 SL.no-101

28	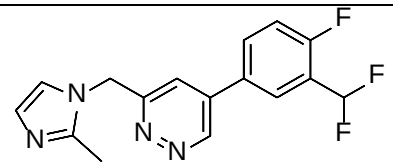	CHEMBL3545349; 0.161; CC1=NC=CN1CC1=CC(=CN=N1)C1=CC=C(F)C(=C1)C(F)F	Library-1 SL.no-102
29	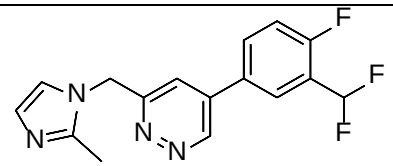	CHEMBL3545350; 0.161; CC1=NC=CN1CC1=CC(=CN=N1)C1=CC=C(F)C(=C1)C(F)F	Same as SL.no-28
30	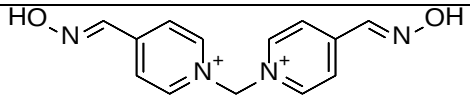	CHEMBL4594415; 0.156; ON=CC1=CC=[N+](C[N+]2=CC=C(C=NO)C=C2)C=C1	
31	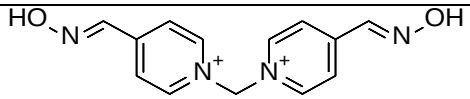	CHEMBL1181952; 0.156; ON=CC1=CC=[N+](C[N+]2=CC=C(C=NO)C=C2)C=C1	Same as SL.no-30
32	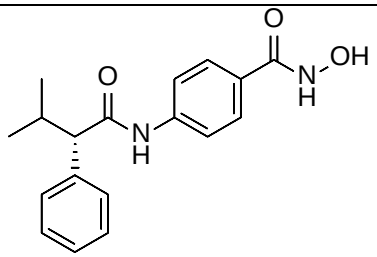	CHEMBL191482; 0.153; CC(C)[C@H](C(=O)NC1=CC=C(C=C1)C(=O)NO)C1=CC=CC=C1	L-1 SL.no-108
33	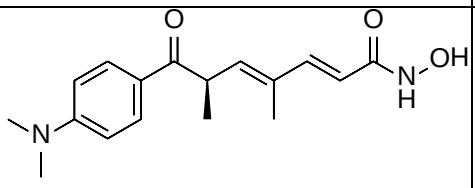	C[C@H](C=C(C)C=CC(=O)NO)C(=O)C1=CC=C(C=C1)N(C)C	Library-1 SL.no-117
34	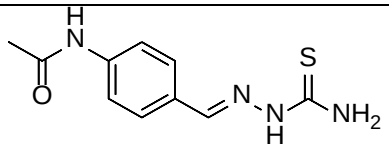	CHEMBL375492; 0.138; CC(=O)NC1=CC=C(C=NNC(N)=S)C=C1	Library-1

			SL.no -118
35	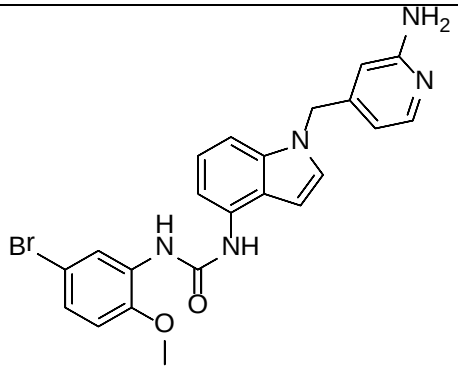	CHEMBL3545155; 0.127; COC1=CC=C(Br)C=C1NC(=O)NC1=C2C=CN(CC3=CC=NC(N)=C3)C2=CC=C1	Library-1 SL.no -127
36	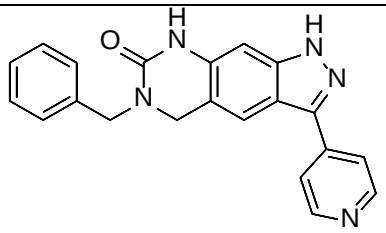	CHEMBL4650284; 0.127; O=C1NC2=C(CN1CC1=CC=CC=C1)C=C1C(NN=C1C1=CC=NC=C1)=C2	
37	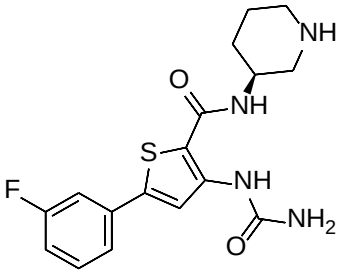	CHEMBL2041933; 0.110; NC(=O)NC1=C(SC(=C1)C1=CC=CC(F)=C1)C(=O)N[C@H]1CCCNC1	Library-1 SL.no -144
38	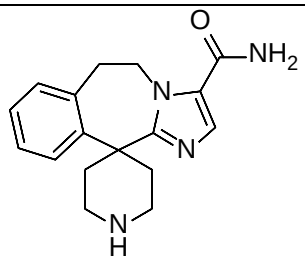	CHEMBL539843; 0.099; NC(=O)C1=CN=C2N1CCC1=CC=CC=C1C21CCNCC1	Library-1 SL.no -152

39	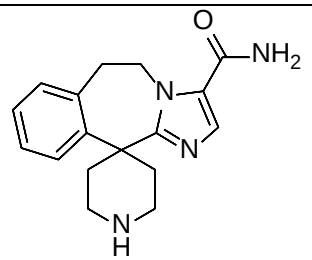 SAME	CHEMBL369075; 0.099; NC(=O)C1=CN=C2N1CCC1=CC=CC=C1C21CCNCC1	Same as SL.no - 38
40	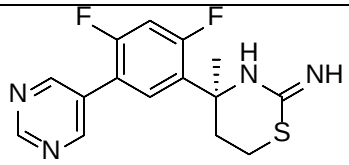	CHEMBL2333941; 0.097; C[C@]1(CCSC(=N)N1)C1=CC(=C(F)C=C1F)C1=CN=CN=C1	
41	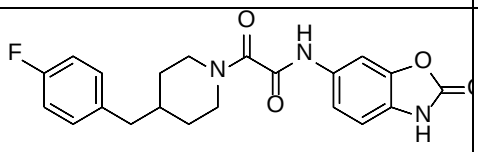	CHEMBL182066; 0.094; FC1=CC=C(CC2CCN(CC2)C(=O)C(=O)NC2=CC=C3NC(=O)OC3=C2)C=C1	Library-1 SL.no -154
42	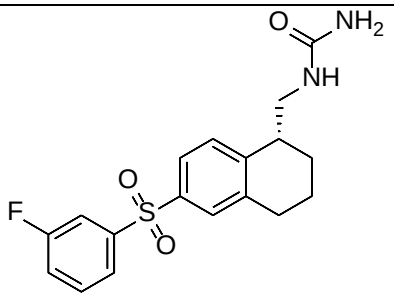	CHEMBL1082508; 0.091; NC(=O)NC[C@@H]1CCCC2=CC(=CC=C12)S(=O)(=O)C1=CC=CC(F)=C1	Library-1 SL.no -155
43	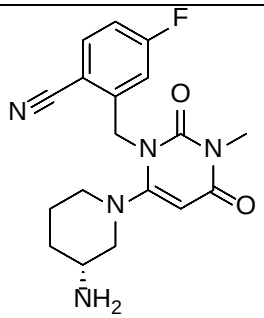	CHEMBL1650443; 0.087; CN1C(=O)C=C(N2CCC[C@@H](N)C2)N(CC2=CC(F)=CC=C2C#N)C1=O	Library-1 SL.no -160

44	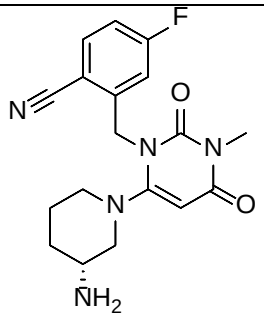	CHEMBL2105754; 0.084; CN1C(=O)C=C(N2CCC[C@@H](N)C2)N(CC2=CC(F)=CC=C2C#N)C1=O	Same as SL.no - 43
45	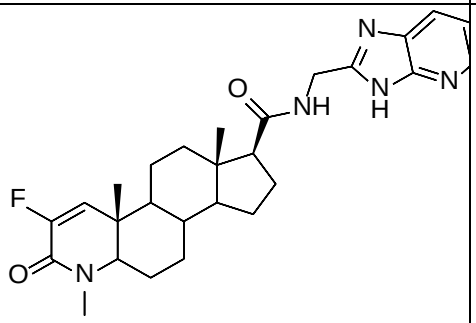	CHEMBL3545333; 0.082; CN1C2CCC3C4CC[C@H](C(=O)NCC5=NC6=CC=CN=C6N5)[C@@]4(C)CCC3[C@@]2(C)C=C(F)C1=O	
46	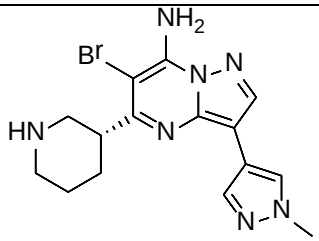	CHEMBL2386889; 0.079; CN1C=C(C=N1)C1=C2N=C([C@@H]3CCCNC3)C(Br)=C(N)N2N=C1	Library-1 C-166
47	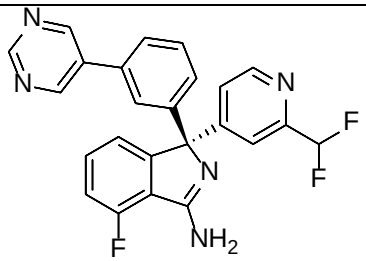	CHEMBL2177913; 0.079; NC1=N[C@@](C2=CC=CC(F)=C12)(C1=CC=CC(=C1)C1=CN=CN=C1)C1=CC=NC(=C1)C(F)F	L-1 SL.no -167
48	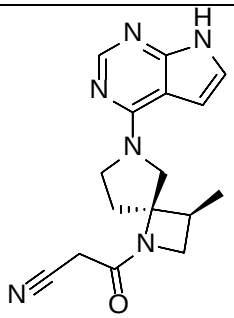	CHEMBL4297507; 0.077; C[C@H]1CN(C(=O)CC#N)[C@]11CCN(C1)C1=C2C=CNC2=NC=N1	Library-1 SL.no -168

49	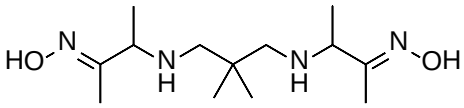	CHEMBL2218892; 0.063; CC(NCC(C)(C)CNC(C)C(C)=NO)C(C)=NO	
50	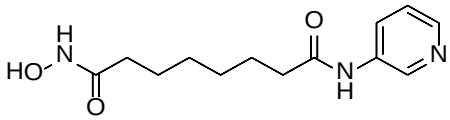	CHEMBL353581; 0.061; ONC(=O)CCCCCCC(=O)NC1=CC=CN=C1	Library-1 SL.no-173
51	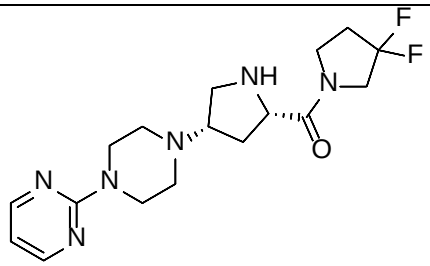	CHEMBL515387; 0.059; FC1(F)CCN(C1)C(=O)[C@@H]1C[C@@H](CN1)N1CCN(CC1)C1=NC=CC=N1	Library-1 SL.no-174
52	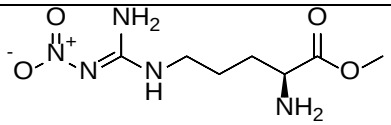	CHEMBL7890; 0.057; COC(=O)[C@@H](N)CCCNC(N)=N[N+]([O-])=O	Library-1 SL.no-176

5.3.2. Druglikeness and toxicity based screening

Table S5.4: Druglikeness screening of compounds from Library 1.

Compound	Lipinski	Ghose	Veber	Egan	Muegge
1	Yes; 0 violation	Yes	Yes	Yes	Yes
2	Yes; 0 violation	Yes	Yes	Yes	Yes
3	Yes; 0 violation	Yes	Yes	Yes	No; 1 violation:

					XLOGP3> 5
4	Yes; 0 violation	Yes	Yes	Yes	Yes
5	Yes; 0 violation	Yes	Yes	Yes	Yes
6	Yes; 0 violation	Yes	Yes	Yes	No; 1 violation: XLOGP3> 5
7	Yes; 0 violation	Yes	Yes	Yes	Yes
8	Yes; 0 violation	Yes	Yes	Yes	Yes
9	Yes; 0 violation	Yes	Yes	Yes	Yes
10	Yes; 0 violation	Yes	Yes	Yes	Yes
11	Yes; 1 violation: MLOGP>4	Yes	Yes	Yes	No; 1 violation: XLOGP3> 5
12	Yes; 0 violation	Yes	Yes	Yes	Yes
13	Yes; 0 violation	Yes	Yes	Yes	No; 1 violation: XLOGP3> 5
14	Yes; 0 violation	Yes	Yes	Yes	Yes
15	Yes; 0 violation	Yes	Yes	Yes	Yes

16	Yes; 0 violation	Yes	Yes	Yes	No; 1 violation: XLOGP3> 5
17	Yes; 0 violation	Yes	Yes	Yes	Yes
18	Yes; 0 violation	Yes	Yes	Yes	No; 1 violation: MW<200
19	Yes; 0 violation	Yes	Yes	Yes	Yes
20	Yes; 0 violation	Yes	Yes	Yes	No; 1 violation: MW<200
21	Yes; 0 violation	Yes	Yes	Yes	Yes
22	Yes; 0 violation	Yes	Yes	Yes	Yes
23	Yes; 0 violation	Yes	Yes	Yes	Yes
24	Yes; 0 violation	Yes	Yes	Yes	Yes
25	Yes; 0 violation	Yes	Yes	Yes	Yes
26	Yes; 0 violation	Yes	Yes	Yes	Yes
27	Yes; 0 violation	Yes	Yes	Yes	Yes
28	Yes; 0 violation	Yes	Yes	Yes	Yes

29	Yes; 0 violation	Yes	Yes	Yes	Yes
30	Yes; 0 violation	Yes	Yes	Yes	Yes
31	Yes; 0 violation	Yes	Yes	Yes	Yes
32	Yes; 0 violation	Yes	Yes	Yes	Yes
33	Yes; 0 violation	Yes	Yes	Yes	Yes
34	Yes; 0 violation	Yes	Yes	Yes	Yes
35	Yes; 0 violation	Yes	Yes	Yes	Yes
36	Yes; 0 violation	Yes	Yes	Yes	Yes
37	Yes; 0 violation	Yes	Yes	Yes	Yes
38	Yes; 0 violation	Yes	Yes	Yes	Yes
39	Yes; 0 violation	Yes	Yes	Yes	Yes
40	Yes; 0 violation	Yes	Yes	Yes	Yes
41	Yes; 0 violation	No; 1 violation: WLOGP<-0.4	Yes	Yes	Yes
42	Yes; 0 violation	Yes	Yes	Yes	Yes

43	Yes; 0 violation	No; 1 violation: MR>130	Yes	Yes	No; 1 violation: XLOGP3>5
44	Yes; 0 violation	Yes	Yes	Yes	Yes
45	Yes; 1 violation: MLOGP>4.15	Yes	Yes	Yes	No; 1 violation: XLOGP3>5
46	Yes; 0 violation	Yes	Yes	Yes	Yes
47	Yes; 0 violation	Yes	Yes	Yes	Yes
48	Yes; 0 violation	Yes	Yes	Yes	Yes
49	Yes; 0 violation	Yes	Yes	Yes	Yes
50	Yes; 0 violation	Yes	Yes	Yes	Yes
51	Yes; 0 violation	Yes	Yes	Yes	Yes
52	Yes; 0 violation	Yes	Yes	Yes	Yes
53	Yes; 0 violation	Yes	Yes	Yes	Yes
54	Yes; 0 violation	Yes	Yes	Yes	Yes
55	Yes; 0 violation	Yes	Yes	Yes	Yes

56	Yes; 0 violation	Yes	Yes	Yes	Yes
57	Yes; 0 violation	Yes	Yes	Yes	Yes
58	Yes; 0 violation	Yes	Yes	Yes	Yes
59	Yes; 0 violation	Yes	Yes	Yes	Yes
60	Yes; 0 violation	Yes	Yes	Yes	Yes
61	Yes; 0 violation	Yes	Yes	Yes	Yes
62	Yes; 0 violation	Yes	Yes	Yes	Yes
63	Yes; 0 violation	Yes	Yes	Yes	Yes
64	Yes; 0 violation	Yes	Yes	Yes	Yes
65	Yes; 0 violation	Yes	Yes	Yes	Yes
66	Yes; 0 violation	Yes	Yes	Yes	Yes
67	Yes; 0 violation	Yes	Yes	Yes	Yes
68	Yes; 0 violation	Yes	Yes	Yes	Yes
69	Yes; 0 violation	Yes	Yes	Yes	Yes
70	Yes; 0 violation	Yes	Yes	Yes	Yes

71	Yes; 0 violation	Yes	Yes	Yes	Yes
72	Yes; 0 violation	Yes	Yes	Yes	Yes
73	Yes; 0 violation	Yes	Yes	Yes	Yes
74	Yes; 0 violation	Yes	Yes	Yes	Yes
75	Yes; 0 violation	Yes	Yes	Yes	Yes
76	Yes; 0 violation	Yes	Yes	Yes	Yes
77	No; 2 violations: NorO>10, NHorOH>5	Yes	No; 1 violation: TPSA>140	No; 1violation: TPSA>131.6	No; 3 violations: TPSA>150, H-acc>10, H-don>5
78	Yes; 0 violation	Yes	Yes	Yes	Yes
79	Yes; 1 violation: NHorOH>5	Yes	No; 1 violation: TPSA>140	No; 1 violation: TPSA>131.6	No; 2 violations: TPSA>150, H-don>5
80	Yes; 0 violation	Yes	Yes	Yes	Yes
81	Yes; 0 violation	Yes	Yes	Yes	Yes

82	Yes; 0 violation	Yes	Yes	Yes	Yes
83	Yes; 0 violation	Yes	Yes	Yes	Yes
84	Yes; 0 violation	Yes	Yes	Yes	Yes
85	Yes; 0 violation	Yes	Yes	Yes	Yes
86	Yes; 0 violation	Yes	Yes	Yes	Yes
87	Yes; 0 violation	Yes	Yes	Yes	Yes
88	Yes; 0 violation	Yes	Yes	Yes	Yes
89	Yes; 0 violation	Yes	No; 1 violation: TPSA>140	No; 1 violation: TPSA>131.6	No; 1 violation: TPSA>150
90	Yes; 0 violation	Yes	Yes	Yes	Yes
91	Yes; 0 violation	Yes	No; 1 violation: TPSA>140	No; 1 violation: TPSA>131.6	Yes
92	Yes; 0 violation	Yes	Yes	Yes	Yes
93	Yes; 0 violation	Yes	Yes	Yes	Yes

94	Yes; 0 violation	Yes	Yes	Yes	Yes
95	Yes; 0 violation	Yes	Yes	Yes	Yes
96	Yes; 1 violation: MLOGP>4.15	Yes	Yes	Yes	Yes
97	Yes; 0 violation	Yes	Yes	Yes	Yes
98	Yes; 0 violation	Yes	Yes	Yes	Yes
99	Yes; 0 violation	Yes	Yes	Yes	Yes
100	Yes; 0 violation	Yes	Yes	Yes	Yes
101	Yes; 0 violation	Yes	Yes	Yes	Yes
102	Yes; 0 violation	Yes	Yes	Yes	Yes
103	Yes; 0 violation	Yes	Yes	Yes	Yes
104	Yes; 0 violation	Yes	Yes	Yes	Yes
105	Yes; 0 violation	Yes	Yes	Yes	Yes
106	Yes; 0 violation	Yes	Yes	Yes	Yes
107	Yes; 0 violation	Yes	Yes	Yes	Yes

108	Yes; 0 violation	Yes	Yes	Yes	Yes
109	Yes; 0 violation	Yes	Yes	Yes	Yes
110	Yes; 0 violation	Yes	Yes	Yes	Yes
111	Yes; 0 violation	Yes	Yes	Yes	Yes
112	Yes; 0 violation	Yes	Yes	Yes	Yes
113	Yes; 0 violation	Yes	Yes	Yes	Yes
114	Yes; 0 violation	Yes	Yes	Yes	Yes
115	Yes; 0 violation	Yes	Yes	Yes	Yes
116	Yes; 0 violation	Yes	Yes	No; 1 violation: TPSA>131.6	Yes
117	Yes; 0 violation	Yes	Yes	Yes	Yes
118	Yes; 0 violation	Yes	Yes	Yes	Yes
119	Yes; 0 violation	Yes	Yes	No; 1 violation: TPSA>131.6	Yes
120	Yes; 0 violation	Yes	Yes	Yes	Yes
121	Yes; 0 violation	Yes	No; 2 violations : Rotors>1	No; 1 violation: TPSA>131.6	No; 1 violation:

			0, TPSA>140		TPSA>150
122	Yes; 0 violation	Yes	Yes	Yes	Yes
123	Yes; 0 violation	Yes	Yes	Yes	Yes
124	Yes; 0 violation	Yes	Yes	Yes	Yes
125	Yes; 0 violation	Yes	Yes	Yes	Yes
126	Yes; 0 violation	Yes	Yes	Yes	Yes
127	Yes; 0 violation	Yes	Yes	Yes	Yes
128	Yes; 0 violation	Yes	Yes	Yes	Yes
129	Yes; 0 violation	Yes	Yes	Yes	Yes
130	Yes; 0 violation	No; 1 violation: MR>130	Yes	Yes	Yes
131	Yes; 0 violation	Yes	Yes	Yes	Yes
132	Yes; 0 violation	Yes	Yes	Yes	Yes
133	Yes; 0 violation	Yes	Yes	Yes	Yes
134	Yes; 0 violation	Yes	Yes	Yes	Yes

135	Yes; 0 violation	Yes	Yes	Yes	Yes
136	Yes; 0 violation	Yes	Yes	Yes	Yes
137	Yes; 0 violation	Yes	Yes	Yes	Yes
138	Yes; 0 violation	Yes	Yes	Yes	Yes
139	Yes; 0 violation	Yes	No; 1 violation: TPSA>140	No; 1 violation: TPSA>131.6	No; 1 violation: TPSA>150
140	Yes; 0 violation	Yes	Yes	No; 1 violation: TPSA>131.6	Yes
141	Yes; 0 violation	Yes	Yes	Yes	Yes
142	Yes; 0 violation	Yes	Yes	Yes	Yes
143	Yes; 0 violation	Yes	Yes	Yes	Yes
144	Yes; 0 violation	Yes	Yes	Yes	Yes
145	Yes; 0 violation	Yes	Yes	Yes	Yes
146	Yes; 0 violation	Yes	Yes	Yes	Yes
147	Yes; 0 violation	Yes	Yes	Yes	Yes
148	Yes; 0 violation	Yes	Yes	Yes	Yes

149	Yes; 0 violation	Yes	Yes	Yes	Yes
150	Yes; 0 violation	Yes	Yes	Yes	Yes
151	Yes; 0 violation	Yes	Yes	Yes	No; 1 violation: MW<200
152	Yes; 0 violation	Yes	Yes	Yes	Yes
153	Yes; 0 violation	Yes	Yes	Yes	Yes
154	Yes; 0 violation	Yes	Yes	Yes	Yes
155	Yes; 0 violation	Yes	Yes	Yes	Yes
156	Yes; 1 violation: MLOGP>4.15	No; 1 violation: WLOGP>5.6	Yes	No; 1 violation: WLOGP>5.88	YesNo; 1 violation: XLOGP3>5
157	Yes; 0 violation	Yes	Yes	Yes	Yes
158	Yes; 0 violation	Yes	No; 1 violation: TPSA>140	No; 1 violation: TPSA>131.6	No; 1 violation: TPSA>150
159	Yes; 0 violation	Yes	Yes	Yes	Yes
160	Yes; 0 violation	Yes	Yes	Yes	Yes
161	Yes; 0 violation	No; 1 violation:	Yes	Yes	Yes

		WLOGP<-0.4			
162	Yes; 0 violation	No; 1 violation: MR>130	Yes	Yes	Yes
163	Yes; 1 violation: MLOGP>4.15	Yes	Yes	Yes	Yes
164	Yes; 0 violation	Yes	Yes	No; 1 violation: TPSA>131.6	Yes
165	Yes; 0 violation	Yes	Yes	Yes	Yes
166	Yes; 0 violation	Yes	Yes	Yes	Yes
167	Yes; 0 violation	Yes	Yes	Yes	Yes
168	Yes; 0 violation	Yes	Yes	Yes	Yes
169	Yes; 0 violation	Yes	Yes	Yes	Yes
170	Yes; 0 violation	No; 1 violation: WLOGP<-0.4	Yes	Yes	No; 1 violation: MW<200
171	Yes; 0 violation	No; 1 violation: WLOGP<-0.4	Yes	Yes	Yes
172	Yes; 0 violation	Yes	Yes	Yes	Yes

173	Yes; 0 violation	Yes	Yes	Yes	Yes
174	Yes; 0 violation	No; 1 violation: WLOGP<-0.4	Yes	Yes	Yes
175	Yes; 0 violation	Yes	No; 1 violation: TPSA>140	No; 1 violation: TPSA>131.6	No; 1 violation: TPSA>150
176	Yes; 0 violation	No; 1 violation: WLOGP<-0.4	No; 1 violation: TPSA>140	No; 1 violation: TPSA>131.6	Yes
177	Yes; 0 violation	Yes	No; 1 violation: Rotors>10	Yes	Yes

Table S5.5: Druglikeness screening of compounds from Library 2.

Compound	Lipinski	Ghose	Veber	Egan	Muegge
11	Yes; 0 violation	Yes	Yes	Yes	Yes
17	Yes; 0 violation	Yes	Yes	Yes	Yes
18	Yes; 0 violation	Yes	Yes	Yes	Yes
27	Yes; 0 violation	Yes	Yes	Yes	Yes

Table S5.6: Druglikeness screening of compounds from Library 3.

Compound	Lipinski	Ghose	Veber	Egan	Muegge
2	Yes; 0 violation	Yes	Yes	Yes	Yes
3	Yes; 0 violation	Yes	Yes	Yes	Yes
5	Yes; 0 violation	Yes	Yes	Yes	Yes
6	Yes; 1 violation: NHorOH>5	Yes	No; 1 violation: TPSA>140	No; 1 violation: TPSA>131.6	No; 1 violation: H-don>5
14	Yes; 0 violation	Yes	Yes	Yes	Yes
15	Yes; 0 violation	Yes	Yes	Yes	Yes
16	Yes; 0 violation	Yes	Yes	Yes	Yes
18	Yes; 0 violation	No; 1 violation: WLOGP>5.6	Yes	No; 1 violation: WLOGP>5.88	No; 1 violation: XLOGP3>5
20	Yes; 0 violation	Yes	Yes	Yes	Yes
21	No; 2 violations: MW>500, NorO>10	No; 2 violations: MW>480, MR>130	No; 1 violation: TPSA>140	No; 1 violation: TPSA>131.6	No; 2 violations: TPSA>150, H-acc>10
25	Yes; 0 violation	Yes	Yes	Yes	Yes
30	Yes; 0 violation	Yes	Yes	Yes	Yes

36	Yes; 0 violation	Yes	Yes	Yes	Yes
40	Yes; 0 violation	Yes	Yes	Yes	Yes
45	Yes; 0 violation	No; 1 violation: MR>130	Yes	Yes	Yes
49	Yes; 0 violation	Yes	Yes	Yes	Yes

Table S5.7: Toxicity screening of druglikeness complied compounds from Library 1

Compound	**PREDICTED LD50 (mg/kg)**	**PREDICTED TOXICITY CLASS**	**HEPATO-TOXICITY**	**CARCINOGENICITY**	**IMMUNO-TOXICITY**	**MUTAGE-NICITY**	**CYTOTO-XICITY**
1	1560	4	Inactive	Inactive	Inactive	Inactive	Inactive
2	2400	5	Inactive	Active	Inactive	Inactive	Inactive
3	3000	5	Inactive	Active	Inactive	Inactive	Inactive
4	2450	5	Inactive	Inactive	Inactive	Inactive	Inactive
5	500	4	Inactive	Inactive	Active	Inactive	Inactive
6	2830	5	Inactive	Inactive	Inactive	Inactive	Inactive

7	500	4	Inactive	Inactive	Inactive	Inactive	Inactive
8	2000	4	Inactive	Inactive	Inactive	Inactive	Inactive
9	4220	5	Inactive	Inactive	Active	Inactive	Inactive
10	1000	4	Active	Active	Inactive	Inactive	Inactive
11	1503	4	Active	Inactive	Inactive	Inactive	Inactive
12	4950	5	Inactive	Inactive	Inactive	Inactive	Inactive
13	1000	4	Inactive	Active	Inactive	Inactive	Inactive
14	500	4	Inactive	Inactive	Inactive	Inactive	Inactive
15	300	3	Inactive	Inactive	Active	Inactive	Inactive
16	2260	5	Inactive	Inactive	Active	Inactive	Inactive
17	4920	5	Inactive	Inactive	Inactive	Inactive	Inactive
18	550	4	Inactive	Inactive	Active	Inactive	Inactive
19	4920	5	Inactive	Inactive	Inactive	Inactive	Inactive
20	1460	4	Active	Active	Inactive	Active	Inactive
21	4000	5	Inactive	Inactive	Inactive	Inactive	Inactive

22	1700	4	Inactive	Inactive	Inactive	Inactive	Inactive
23	185	3	Inactive	Inactive	Inactive	Inactive	Active
24	500	4	Inactive	Inactive	Inactive	Inactive	Inactive
25	1324	4	Inactive	Inactive	Inactive	Inactive	Inactive
26	1460	4	Active	Active	Inactive	Active	Inactive
27	880	4	Inactive	Active	Inactive	Inactive	Inactive
28	4800	5	Inactive	Inactive	Inactive	Inactive	Inactive
29	500	4	Inactive	Inactive	Inactive	Inactive	Inactive
30	2000	4	Inactive	Inactive	Inactive	Inactive	Active
31	8550	6	Inactive	Inactive	Inactive	Inactive	Inactive
32	800	4	Inactive	Inactive	Active	Inactive	Inactive
33	3350	5	Inactive	Inactive	Inactive	Inactive	Inactive
34	500	4	Inactive	Inactive	Inactive	Inactive	Inactive
35	600	4	Active	Active	Inactive	Inactive	Inactive
36	2000	4	Inactive	Active	Inactive	Inactive	Inactive

37	375	4	Active	Active	Active	Active	Inactive
38	1050	4	Active	Active	Inactive	Inactive	Inactive
39	3370	5	Inactive	Inactive	Inactive	Active	Inactive
40	1145	4	Active	Inactive	Inactive	Inactive	Inactive
41	1900	4	Inactive	Inactive	Inactive	Inactive	Inactive
42	5000	5	Inactive	Active	Inactive	Inactive	Inactive
43	5000	5	Inactive	Inactive	Active	Inactive	Inactive
44	50	2	Inactive	Inactive	Inactive	Inactive	Inactive
45	3000	5	Inactive	Inactive	Inactive	Inactive	Inactive
46	500	4	Inactive	Active	Inactive	Active	Inactive
47	1500	4	Inactive	Inactive	Active	Inactive	Inactive
48	375	4	Active	Active	Active	Active	Inactive
49	4738	5	Inactive	Active	Inactive	Inactive	Inactive
50	1000	4	Inactive	Inactive	Inactive	Inactive	Inactive
51	2287	5	Inactive	Inactive	Inactive	Inactive	Inactive

52	1500	4	Active	Active	Active	Active	Inactive
53	5000	5	Inactive	Active	Inactive	Inactive	Inactive
54	1500	4	Active	Active	Active	Active	Inactive
55	1145	4	Active	Active	Active	Active	Inactive
56	1500	4	Active	Active	Active	Active	Inactive
57	500	4	Active	Active	Inactive	Active	Inactive
58	3500	5	Inactive	Active	Active	Inactive	Inactive
59	3500	5	Inactive	Active	Active	Inactive	Inactive
60	1054	4	Inactive	Active	Active	Inactive	Inactive
61	500	4	Inactive	Active	Active	Active	Inactive
62	200	3	Inactive	Inactive	Inactive	Inactive	Inactive
63	3740	5	Inactive	Active	Active	Inactive	Inactive
64	1145	4	Inactive	Active	Active	Active	Inactive
65	7000	6	Active	Active	Inactive	Inactive	Inactive
66	1075	4	Active	Inactive	Inactive	Inactive	Inactive

67	1000	4	Active	Active	Active	Active	Inactive
68	378	4	Inactive	Inactive	Active	Inactive	Inactive
69	2000	4	Inactive	Inactive	Active	Inactive	Inactive
70	1680	4	Inactive	Active	Inactive	Active	Inactive
71	1200	4	Inactive	Inactive	Inactive	Inactive	Inactive
72	500	4	Active	Active	Active	Inactive	Inactive
73	2050	5	Active	Active	Active	Active	Inactive
74	1540	4	Active	Active	Inactive	Active	Inactive
75	4000	5	Active	Active	Inactive	Inactive	Inactive
76	100	3	Active	Active	Active	Inactive	Inactive
77	1000	4	Inactive	Inactive	Inactive	Inactive	Inactive
78	1632	4	Inactive	Active	Inactive	Active	Inactive
79	1000	4	Inactive	Inactive	Inactive	Inactive	Inactive
80	230	3	Inactive	Active	Active	Active	Inactive
81	73	3	Active	Active	Inactive	Active	Inactive

82	73	3	Active	Active	Inactive	Active	Inactive
83	135	3	Inactive	Active	Active	Active	Inactive
84	500	4	Inactive	Inactive	Inactive	Inactive	Inactive
85	1500	4	Inactive	Active	Inactive	Inactive	Inactive
86	32	2	Active	Active	Active	Inactive	Inactive
87	1000	4	Active	Active	Inactive	Inactive	Inactive
88	402	4	Inactive	Inactive	Inactive	Inactive	Inactive
89	1500	4	Active	Active	Inactive	Active	Inactive
90	2066	5	Inactive	Inactive	Inactive	Inactive	Inactive
91	1800	3	Active	Active	Inactive	Active	Inactive
92	500	4	Inactive	Inactive	Inactive	Inactive	Inactive
93	10000	6	Inactive	Active	Inactive	Active	Inactive
94	1000	4	Inactive	Active	Inactive	Inactive	Inactive
95	700	4	Inactive	Inactive	Inactive	Inactive	Inactive
96	616	4	Inactive	Inactive	Inactive	Inactive	Inactive

97	1200	4	Inactive	Inactive	Inactive	Inactive	Inactive
98	1235	4	Inactive	Inactive	Inactive	Inactive	Inactive
99	2290	5	Inactive	Inactive	Inactive	Inactive	Inactive
100	500	4	Active	Inactive	Inactive	Inactive	Inactive
101	507	4	Active	Active	Inactive	Inactive	Inactive
102	2000	4	Inactive	Inactive	Inactive	Inactive	Inactive
103	507	4	Active	Active	Inactive	Inactive	Inactive
104	1000	4	Active	Active	Active	Inactive	Inactive
105	200	3	Active	Active	Inactive	Inactive	Inactive
106	300	3	Active	Active	Inactive	Inactive	Inactive
107	650	4	Inactive	Inactive	Inactive	Inactive	Inactive
108	1600	4	Active	Active	Inactive	Active	Inactive
109	500	4	Inactive	Active	Inactive	Active	Inactive
110	3000	5	Inactive	Inactive	Inactive	Inactive	Inactive
111	495	4	Active	Inactive	Active	Active	Inactive

112	1500	4	Active	Inactive	Inactive	Inactive	Inactive
113	1000	4	Active	Inactive	Active	Active	Inactive
114	500	4	Active	Active	Inactive	Active	Inactive
115	400	4	Inactive	Active	Inactive	Inactive	Inactive
116	1350	4	Inactive	Active	Inactive	Active	Inactive
117	1230	4	Active	Active	Inactive	Active	Inactive
118	950	4	Active	Active	Inactive	Active	Inactive
119	2000	4	Inactive	Inactive	Inactive	Inactive	Inactive
120	800	4	Active	Active	Inactive	Active	Inactive
121	1000	4	Inactive	Inactive	Inactive	Inactive	Inactive
122	15	2	Inactive	Inactive	Inactive	Inactive	Inactive
123	155	3	Active	Active	Inactive	Active	Inactive
124	1400	4	Inactive	Inactive	Inactive	Inactive	Inactive
125	2300	4	Active	Inactive	Inactive	Inactive	Inactive
126	350	4	Active	Inactive	Inactive	Inactive	Inactive

127	3000	5	Inactive	Active	Active	Inactive	Inactive
128	650	4	Inactive	Inactive	Inactive	Inactive	Inactive
129	650	4	Active	Active	Inactive	Active	Inactive
130	1000	4	Inactive	Inactive	Active	Inactive	Inactive
131	500	4	Active	Active	Active	Active	Inactive
132	4000	5	Inactive	Inactive	Inactive	Inactive	Inactive
133	1000	4	Inactive	Inactive	Inactive	Inactive	Inactive
134	1000	4	Inactive	Inactive	Inactive	Inactive	Inactive
135	780	4	Inactive	Inactive	Inactive	Inactive	Inactive
136	374	4	Inactive	Inactive	Active	Inactive	Inactive
137	1000	4	Active	Inactive	Inactive	Inactive	Inactive
138	420	4	Inactive	Inactive	Inactive	Inactive	Inactive
139	5000	5	Inactive	Inactive	Active	Inactive	Inactive
140	400	4	Inactive	Inactive	Active	Inactive	Inactive
141	1000	4	Inactive	Active	Inactive	Inactive	Inactive

142	1000	4	Active	Inactive	Inactive	Inactive	Inactive
143	1000	4	Inactive	Active	Inactive	Inactive	Inactive
144	3000	5	Inactive	Inactive	Inactive	Inactive	Inactive
145	1250	4	Inactive	Inactive	Inactive	Inactive	Inactive
146	1000	4	Inactive	Inactive	Inactive	Inactive	Inactive
147	1000	4	Inactive	Inactive	Inactive	Inactive	Inactive
148	300	3	Active	Inactive	Active	Inactive	Inactive
149	1000	4	Active	Active	Inactive	Active	Inactive
150	660	4	Inactive	Inactive	Inactive	Active	Inactive
151	343	3	Inactive	Active	Inactive	Inactive	Inactive
152	550	4	Inactive	Inactive	Inactive	Inactive	Inactive
153	73	3	Active	Active	Inactive	Inactive	Inactive
154	1500	4	Inactive	Active	Inactive	Inactive	Inactive
155	500	4	Inactive	Inactive	Inactive	Inactive	Inactive
156	200	3	Inactive	Inactive	Inactive	Active	Inactive

157	1150	4	Inactive	Inactive	Active	Inactive	Inactive
158	92	3	Inactive	Inactive	Active	Inactive	Inactive
159	200	3	Active	Active	Inactive	Inactive	Inactive
160	1000	4	Inactive	Inactive	Inactive	Inactive	Inactive
161	1078	4	Inactive	Inactive	Inactive	Inactive	Inactive
162	200	3	Inactive	Inactive	Active	Inactive	Inactive
163	3460	5	Inactive	Inactive	Active	Inactive	Inactive
164	495	4	Active	Inactive	Active	Inactive	Inactive
165	500	4	Inactive	Inactive	Inactive	Active	Inactive
166	300	3	Inactive	Active	Inactive	Inactive	Inactive
167	1000	4	Active	Active	Inactive	Active	Inactive
168	2000	4	Inactive	Inactive	Inactive	Inactive	Inactive
169	99	3	Inactive	Active	Active	Active	Inactive
170	2400	5	Inactive	Inactive	Inactive	Inactive	Inactive
171	1050	4	Inactive	Inactive	Inactive	Inactive	Inactive

172	300	3	Inactive	Active	Active	Inactive	Inactive
173	3500	5	Inactive	Active	Inactive	Active	Active
174	590	4	Inactive	Inactive	Active	Inactive	Inactive
175	300	3	Inactive	Inactive	Inactive	Inactive	Inactive
176	5510	5	Inactive	Active	Inactive	Active	Inactive
177	890	4	Inactive	Inactive	Inactive	Inactive	Inactive

Table S5.8: Toxicity screening of druglikeness complied compounds from Library 2

Compound	**PREDICTED LD50 (mg/kg)**	**PREDICTED TOXICITY CLASS**	**HEPATO-TOXICITY**	**CARCINOGENICITY**	**IMMUNO-TOXICITY**	**MUTAGE-NICITY**	**CYTOTO-XICITY**
11	3370	5	Inactive	Inactive	Inactive	Active	Inactive
17	1000	4	Inactive	Active	Inactive	Inactive	Inactive
18	500	4	Active	Active	Inactive	Inactive	Inactive
27	874	4	Inactive	Inactive	Inactive	Inactive	Inactive

Table S5.9: Toxicity screening of druglikeness complied compounds from Library 3

Compound	PREDICTED LD50 (mg/kg)	PREDICTED TOXICITY CLASS	HEPATO-TOXICITY	CARCINOGENICITY	IMMUNO-TOXICITY	MUTAGE-NICITY	CYTOTO-XICITY
2	1560	4	Inactive	Inactive	Active	Inactive	Inactive
3	1560	4	Inactive	Inactive	Active	Inactive	Inactive
5	500	4	Inactive	Active	Inactive	Inactive	Inactive
14	1500	4	Active	Active	Active	Active	Inactive
15	535	4	Inactive	Inactive	Inactive	Inactive	Inactive
16	535	4	Inactive	Inactive	Inactive	Inactive	Inactive
20	2000	4	Active	Inactive	Inactive	Active	Inactive
25	1000	4	Inactive	Inactive	Inactive	Inactive	Inactive
30	134	3	Inactive	Inactive	Inactive	Inactive	Inactive
36	1000	4	Inactive	Active	Inactive	Inactive	Inactive
40	900	4	Inactive	Inactive	Inactive	Inactive	Inactive

5.3.3. Molecular docking *via* Molegro virtual docker

5.3.3.1. Docking score

Table S5.10: Docking scores of the ligands with PDB ID 1UHL generated *via* MVD

Ligand	MolDock Score	[a]Rerank Score	[b]Interaction	[c]Internal	[d]HBond	[e]LE1	[f]LE3
C144 (144)	-160.974	-127.205	-158.672	-2.30166	-3.34194	-6.43897	-5.0882
135	-139.61	-111.605	-177.63	38.0199	-1.65272	-4.98609	-3.9859
102	-138.248	-111.374	-161.719	23.4709	0	-6.0108	-4.84234
Native T-09019317	-116.864	-109.13	-170.351	53.4866	-2.8415	-3.7698	-3.52033
147	-134.776	-108.412	-158.714	23.9375	-1.01908	-5.18371	-4.1697
132	-132.985	-108.318	-149.199	16.2144	-0.127477	-5.1148	-4.16609
99	-138.312	-107.673	-140.685	2.37327	-2.16772	-5.53247	-4.30693
92	-141.426	-107.018	-126.614	-14.812	-2.567	-5.65703	-4.28071
134	-134.229	-104.288	-154.843	20.6143	-1.47646	-5.36915	-4.17153
97	-125.269	-101.649	-134.073	8.80393	-5.32092	-6.26346	-5.08247
Withaferin A	-115.566	-101.503	-142.058	26.4926	-3.94624	-3.39899	-2.98539
71	-113.202	-100.006	-138.902	25.6993	0	-4.92185	-4.34808
146	-131.989	-99.598	-141.373	9.38413	-4.6004	-4.55133	-3.43441

25	-122.288	-98.9752	-144.286	21.9986	-5.19925	-5.55854	-4.49887
107	-122.595	-97.5936	-144.353	21.7575	-2.80474	-4.0865	-3.25312
155	-121.095	-96.7244	-136.496	15.4007	-2.56229	-4.84379	-3.86897
128	-114.535	-95.1071	-128.797	14.2619	-3.39351	-4.24205	-3.52248
168	-117.177	-93.9205	-119.055	1.87841	-2.51211	-5.09465	-4.0835
95	-108.477	-93.2089	-120.93	12.4532	-0.711729	-6.02647	-5.17827
L-3-15	-114.295	-91.9424	-121.469	7.17397	-3.31866	-6.72324	-5.40837
124	-123.024	-91.9126	-131.695	8.67118	-2.4478	-4.55645	-3.40417
84	-116.041	-90.8763	-134.036	17.995	-2.1993	-4.14433	-3.24558
4	-112.614	-90.8657	-129.982	17.3683	-4.72942	-6.62434	-5.34504
110	-119.485	-90.4621	-116.544	-2.94019	-5.55015	-5.43112	-4.11191
145	-110.548	-90.2753	-112.608	2.05969	-0.288982	-5.81831	-4.75133
L-3-25	-104.393	-89.7017	-126.784	22.3905	-0.829133	-5.79963	-4.98343
133	-118.617	-89.6389	-141.95	23.3328	-1.03182	-4.23632	-3.20139
160	-113.514	-89.585	-121.355	7.84101	-1.61594	-4.36592	-3.44558

L-3-30	-107.137	-88.7016	-121.368	14.2314	-3.05395	-5.63877	-4.66851
50	-114.302	-88.4482	-117.559	3.2575	-2.64392	-7.14385	-5.52801
51	-109.442	-87.4473	-132.738	23.2962	-3.87979	-4.56008	-3.64364
34	-115.521	-87.317	-132.063	16.5424	-2.39154	-4.44311	-3.35834
62	-108.57	-86.8684	-122.168	13.5981	-1.01894	-6.78561	-5.42928
8	-111.768	-86.809	-130.851	19.0824	-2.48223	-5.08038	-3.94586
L-2-27	-104.945	-86.2621	-120.589	15.644	-1.94217	-4.56281	-3.75053
Resveratrol (1)	-103.383	-85.2811	-115.188	11.8053	-1.20027	-6.08135	-5.01654
44	-108.686	-84.5897	-116.832	8.14549	0	-4.34744	-3.38359
14	-102.371	-84.2018	-119.169	16.798	-6.02573	-5.11855	-4.21009
L-3-40	-98.1485	-83.3011	-112.099	13.9504	0	-4.4613	-3.78641
17	-110.169	-82.5835	-131.131	20.9629	0	-5.24612	-3.93255
22	-91.1458	-81.3926	-108.781	17.6355	-4.74389	-6.07638	-5.42617
L-3-16	-97.571	-80.6495	-115.438	17.8673	-0.988921	-5.73947	-4.74409
152	-101.931	-80.2779	-111.308	9.37773	-1.11891	-4.63321	-3.649

98	-94.525	-80.0329	-128.564	34.0386	-1.29422	-3.93854	-3.33471
90	-95.1514	-79.7489	-102.737	7.58579	-4.16028	-5.59714	-4.69111
88	-96.6013	-78.3311	-112.963	16.362	-0.125339	-6.44009	-5.22207
28	-99.4909	-77.2372	-119.849	20.3584	-8.00652	-4.32569	-3.35814
21	-99.5366	-76.0361	-110.546	11.0098	0	-5.85509	-4.47271
138	-85.4033	-75.2701	-107.317	21.9136	-2.53511	-4.06682	-3.58429
7	-91.3221	-74.7925	-111.124	19.8022	0	-5.07345	-4.15514
29	-95.5693	-74.697	-123.328	27.7588	-2.5	-3.67574	-2.87296
31	-96.3177	-73.5336	-121.874	25.556	-2.16596	-4.58656	-3.5016
19	-92.9038	-71.2807	-113.46	20.5567	0	-4.64519	-3.56403
122	-86.9039	-70.2357	-89.9714	3.06756	-2.97228	-5.79359	-4.68238
33	-93.5816	-70.0909	-112.321	18.7396	-2.2683	-4.67908	-3.50455
12	-79.8107	-65.874	-98.8243	19.0136	0	-4.69475	-3.87494
24	-74.0419	-62.4479	-93.9229	19.881	-2.49932	-4.11344	-3.46933

[a]The rerank score is a linear combination of E-inter (steric, Van der Waals, hydrogen bonding, electrostatic) between the ligand and the protein, and E-intra.

(torsion, sp2-sp2, hydrogen bonding, Van der Waals, electrostatic) of the ligand weighted by pre-defined coefficients. [b]The total interaction energy between the pose and the protein (kJ/mol). [c]The internal energy of the pose. [d]Hydrogen bonding energy (kJ/mol). [e]Ligand efficiency 1: MolDock score divided by heavy atoms count. [f]Ligand efficiency 3: Rerank score divided by heavy atoms count.

Table S5.11: Docking scores of the ligands with PDB ID 1UPV generated *via* MVD

Ligand	MolDock Score	[a]Rerank Score	[b]Interaction	[c]Internal	[d]HBond	[e]LE1	[f]LE3
C144 (144)	-144.955	-116.684	-141.525	-3.42979	-1.39555	-5.79821	-4.66736
132	-142.497	-113.934	-156.418	13.9205	-2.5	-5.48066	-4.38206
92	-141.065	-109.216	-124.97	-16.0956	0	-5.64261	-4.36865
147	-131.51	-108.059	-159.758	28.248	-0.326512	-5.05808	-4.15611
99	-127.189	-105.826	-140.038	12.8488	-2.10005	-5.08755	-4.23303
155	-133.34	-105.72	-150.517	17.1768	-2.35949	-5.3336	-4.22879
133	-134.222	-105.039	-157.764	23.5421	-3.87583	-4.79365	-3.75138
146	-132.187	-104.762	-155.792	23.6046	-1.10207	-4.55817	-3.61248
Native T-09019317	-95.5933	-103.088	-149.999	54.4058	-2.46743	-3.08366	-3.32543
134	-120.352	-100.634	-140.892	20.5409	-2.25816	-4.81406	-4.02537
84	-114.034	-99.8864	-145.355	31.3204	-0.710818	-4.07266	-3.56737

124	-138.259	-99.8661	-145.354	7.09538	-2.02007	-5.1207	-3.69874
128	-116.227	-98.5196	-140.086	23.8589	-2.51146	-4.30471	-3.64887
71	-118.712	-97.8268	-145.182	26.4705	-2.72991	-5.16139	-4.25334
51	-119.457	-97.4724	-139.936	20.4789	-5.11229	-4.97737	-4.06135
110	-121.38	-97.4539	-126.466	5.08572	0	-5.51727	-4.42972
102	-116.971	-96.5144	-143.259	26.2873	0	-5.08571	-4.19628
168	-121.947	-96.3579	-123.165	1.21782	0	-5.30206	-4.18948
107	-124.075	-95.873	-144.51	20.4349	-2.60867	-4.13583	-3.19577
160	-119.559	-94.792	-129.871	10.3113	0	-4.59844	-3.64585
L-3-40	-109.431	-94.4819	-125.958	16.5273	-0.218369	-4.97412	-4.29463
97	-117.953	-93.9486	-122.291	4.3382	-1.1718	-5.89763	-4.69743
28	-107.396	-92.3223	-125.687	18.2907	-3.2273	-4.6694	-4.01401
25	-121.913	-90.8479	-139.348	17.4355	-7.5	-5.54149	-4.12945
34	-118.506	-90.0377	-134.704	16.1984	-4.3427	-4.55791	-3.46299
95	-111.35	-89.6247	-123.481	12.1307	-0.431435	-6.18613	-4.97915

L-3-16	-107.889	-88.31	-114.981	7.09209	-0.654456	-6.34643	-5.19471
50	-110.852	-88.2765	-112.837	1.98487	-4.84875	-6.92828	-5.51728
90	-107.51	-86.5308	-110.971	3.46168	-1.00436	-6.3241	-5.09005
145	-106.556	-86.1722	-107.162	0.605682	-4.01785	-5.60822	-4.53538
135	-110.78	-86.1476	-141.36	30.5803	-1.71414	-3.95643	-3.0767
14	-101.221	-86.0606	-119.89	18.6691	-8.98048	-5.06106	-4.30303
Bergapten	-100.426	-83.9567	-108.23	7.80396	-0.393912	-6.27662	-5.24729
8	-107.307	-83.7454	-114.007	6.70002	-4.36095	-4.8776	-3.80661
L-3-25	-103.679	-83.2865	-125.022	21.3437	-2.16197	-5.75993	-4.62703
L-3-30	-99.8105	-82.824	-114.747	14.936	-2.04455	-5.25319	-4.35916
98	-86.2217	-82.5479	-118.645	32.4234	0	-3.59257	-3.4395
62	-100.618	-82.5353	-114.066	13.4484	-1.62689	-6.28862	-5.15845
138	-94.2595	-82.2175	-122.914	28.6543	-0.137019	-4.48855	-3.91512
Resveratrol (1)	-106.979	-82.1886	-117.808	10.8289	-5.64044	-6.29287	-4.83462
L-3-15	-102.003	-82.1011	-108.225	6.22225	-1.11609	-6.00016	-4.82948

152	-95.6287	-79.4362	-104.72	9.09109	0	-4.34676	-3.61074
4	-101.845	-79.3662	-114.954	13.1093	-2.46175	-5.99089	-4.6686
L-2-27	-110.913	-78.8621	-122.528	11.6152	-2.46287	-4.82231	-3.42879
7	-97.5595	-78.0898	-118.781	21.2217	-2.5	-5.41997	-4.33832
122	-95.2559	-76.9909	-99.4078	4.15191	-1.58553	-6.3504	-5.13272
88	-91.1718	-76.4833	-104.212	13.0404	-3.61718	-6.07812	-5.09889
33	-98.2154	-76.0511	-120.88	22.6647	-5.78041	-4.91077	-3.80256
19	-106.696	-75.9067	-125.716	19.0203	-2.5	-5.33479	-3.79534
22	-87.336	-75.1451	-96.1266	8.7906	-4.01122	-5.8224	-5.00968
24	-88.0758	-74.4311	-109.35	21.2741	-1.50341	-4.8931	-4.13506
21	-93.8402	-74.3422	-105.394	11.5543	-2.04421	-5.52001	-4.37307
17	-100.144	-73.352	-122.881	22.7371	-6.70777	-4.76876	-3.49295
31	-108.364	-72.8434	-132.626	24.2628	-1.21848	-5.16017	-3.46873
44	-104.861	-70.7989	-111.243	6.38242	0	-4.19443	-2.83196
29	-103.803	-66.2699	-125.328	21.5253	-5	-3.99241	-2.54884

12	-85.2345	-66.0504	-105.814	20.5799	0	-5.01379	-3.88532

[a]The rerank score is a linear combination of E-inter (steric, Van der Waals, hydrogen bonding, electrostatic) between the ligand and the protein, and E-intra. (torsion, sp2-sp2, hydrogen bonding, Van der Waals, electrostatic) of the ligand weighted by pre-defined coefficients. [b]The total interaction energy between the pose and the protein (kJ/mol). [c]The internal energy of the pose. [d]Hydrogen bonding energy (kJ/mol). [e]Ligand efficiency 1: MolDock score divided by heavy atoms count. [f]Ligand efficiency 3: Rerank score divided by heavy atoms count.

Table S5.12:Docking scores of the ligands with PDB ID 5ICK generated via MVD

Ligand	**MolDock Score**	**[a]Rerank Score**	**[b]Interaction**	**[c]Internal**	**[d]HBond**	**[e]LE1**	**[f]LE3**
C144 (144)	-147.539	-121.339	-148.285	0.745721	-5.94625	-5.90158	-4.85357
99	-143.604	-115.938	-145.936	2.3325	-4.60348	-5.74416	-4.63754
128	-132.48	-108.903	-158.152	25.6726	-2.27066	-4.90666	-4.03343
147	-138.12	-108.613	-164.472	26.3525	-2.34369	-5.3123	-4.17741
132	-133.992	-106.769	-148.536	14.5436	0	-5.15355	-4.10649
28	-122.795	-105.357	-140.045	17.2501	-7.80198	-5.33892	-4.58076

134	-125.048	-105.121	-143.39	18.3425	0	-5.0019	-4.20483
155	-130.566	-103.525	-148.607	18.0412	0	-5.22263	-4.14102
8	-124.921	-103.323	-146.896	21.9754	-9.07877	-5.67822	-4.69649
168	-127.004	-103.065	-129.362	2.35854	0	-5.5219	-4.4811
133	-131.677	-102.635	-157.546	25.869	-3.0903	-4.70274	-3.66554
25	-121.93	-100.502	-142.376	20.4456	-4.17155	-5.54229	-4.56825
92	-143.591	-99.2562	-125.485	-18.1063	-5.04028	-5.74363	-3.97025
Native Feroline	-119.565	-99.1676	-147.914	28.3487	-9.06762	-4.59866	-3.81414
14	-117.158	-96.0592	-134.769	17.6107	-6.07634	-5.85789	-4.80296
84	-110.512	-96.0059	-145.788	35.2754	-2.32055	-3.94687	-3.42878
102	-115.16	-96.0055	-135.492	20.3321	-2.75819	-5.00694	-4.17415

L-3-30	-112.007	-95.141	-128.714	16.7068	-4.65962	-5.89512	-5.00742
97	-115.287	-94.8001	-125.813	10.5258	-2.6091	-5.76434	-4.74
110	-122.787	-94.4343	-124.439	1.6526	0	-5.58121	-4.29247
71	-112.09	-92.09	-129.527	17.4363	-3.18496	-4.87349	-4.00391
135	-116.557	-90.6894	-146.063	29.5053	0	-4.16276	-3.23891
138	-102.11	-89.7036	-128.344	26.2334	-1.57476	-4.8624	-4.2716
L-2-27	-114.979	-88.0541	-131.538	16.5592	0	-4.99907	-3.82844
160	-122.026	-86.1119	-130.551	8.52533	0	-4.69331	-3.312
4	-102.735	-86.0539	-116.097	13.3616	-7.49837	-6.04325	-5.062
7	-101.878	-85.4448	-118.764	16.886	-7.42527	-5.65992	-4.74693
90	-106.982	-85.4393	-109.821	2.83895	-1.37252	-6.29308	-5.02584

Resveratrol (1)	-102.557	-85.3105	-114.472	11.9152	-7.39506	-6.03277	-5.01826
33	-98.0287	-85.192	-120.54	22.5112	-6.87033	-4.90144	-4.2596
L-3-16	-107.135	-85.1429	-113.774	6.6396	-0.537402	-6.30205	-5.0084
145	-105.497	-84.6486	-106.611	1.11444	-3.66457	-5.55248	-4.45519
95	-99.8573	-84.1984	-108.27	8.41248	-3.57368	-5.54763	-4.67769
19	-105.972	-83.9888	-125.811	19.8386	-7.34963	-5.29861	-4.19944
L-3-25	-96.0794	-83.9543	-117.59	21.5108	-1.58404	-5.33775	-4.66413
50	-102.83	-83.6927	-106.057	3.22637	-4.65669	-6.4269	-5.23079
L-3-15	-101.902	-83.6667	-109.188	7.28621	-3.64201	-5.99424	-4.92157
21	-101.781	-83.6585	-110.674	8.89308	-6.85037	-5.98713	-4.92109
17	-107.662	-83.3362	-127.61	19.9473	-7.10026	-5.12678	-3.96839

22	-95.2211	-83.3083	-104.125	8.90414	-5.19074	-6.34807	-5.55389
51	-108.492	-82.2341	-134.803	26.3112	-3.63361	-4.52049	-3.42642
L-3-40	-96.3133	-81.8334	-115.059	18.7454	-0.343858	-4.37788	-3.7197
146	-122.76	-80.0779	-149.932	27.1713	-2.27774	-4.23311	-2.76131
88	-86.9226	-75.5516	-101.923	15.0002	-2.5	-5.79484	-5.03677
62	-87.9295	-74.6378	-101.243	13.3136	-1.78856	-5.49559	-4.66486
152	-94.84	-74.3191	-105.658	10.8177	0	-4.31091	-3.37814
29	-121.343	-73.0909	-139.595	18.252	-5.83202	-4.66704	-2.81119
24	-82.9318	-71.3021	-102.913	19.9815	-1.6873	-4.60732	-3.96123
122	-86.919	-69.2498	-92.6316	5.71261	0	-5.7946	-4.61665
12	-84.5948	-68.3453	-101.398	16.803	-5	-4.97616	-4.02031

34	-121.013	-64.7879	-135.988	14.9752	-5.98628	-4.65435	-2.49184
98	-89.7751	-63.6687	-121.457	31.682	-2.5	-3.74063	-2.65286
107	-117.634	-46.3967	-143.328	25.6938	0	-3.92115	-1.54656
44	-94.8885	-36.686	-99.6321	4.74362	-3.34492	-3.79554	-1.46744
31	-80.8254	-27.9489	-102.606	21.7801	-5	-3.84883	-1.3309
124	-94.1554	-19.7383	-111.759	17.6039	0	-3.48724	-0.73105
Obeticholic acid	-105.236	28.1381	-104.062	-1.17383	-0.430335	-3.50786	0.937937

[a]The rerank score is a linear combination of E-inter (steric, Van der Waals, hydrogen bonding, electrostatic) between the ligand and the protein, and E-intra. (torsion, sp2-sp2, hydrogen bonding, Van der Waals, electrostatic) of the ligand weighted by pre-defined coefficients. [b]The total interaction energy between the pose and the protein (kJ/mol). [c]The internal energy of the pose. [d]Hydrogen bonding energy (kJ/mol). [e]Ligand efficiency 1: MolDock score divided by heavy atoms count. [f]Ligand efficiency 3: Rerank score divided by heavy atoms count.

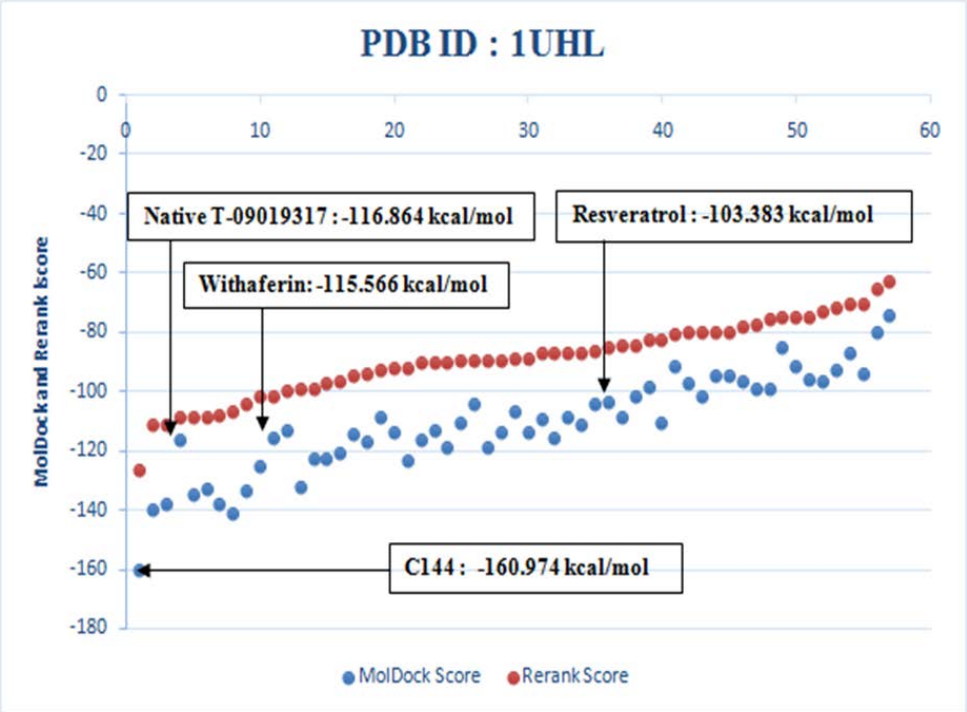

Figure S5.5: Scatter plot showing Docking score of all the compounds understudy with respect to PDB ID: 1UHL

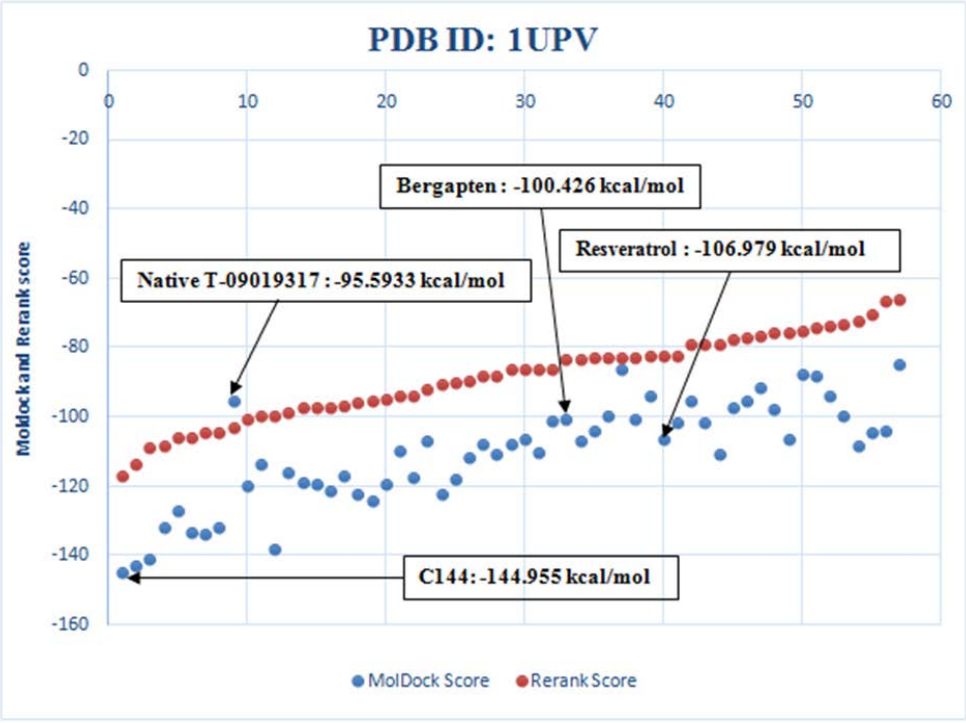

Figure S5.6: Scatter plot showing Docking score of all the compounds understudy with respect to PDB ID: 1UPV

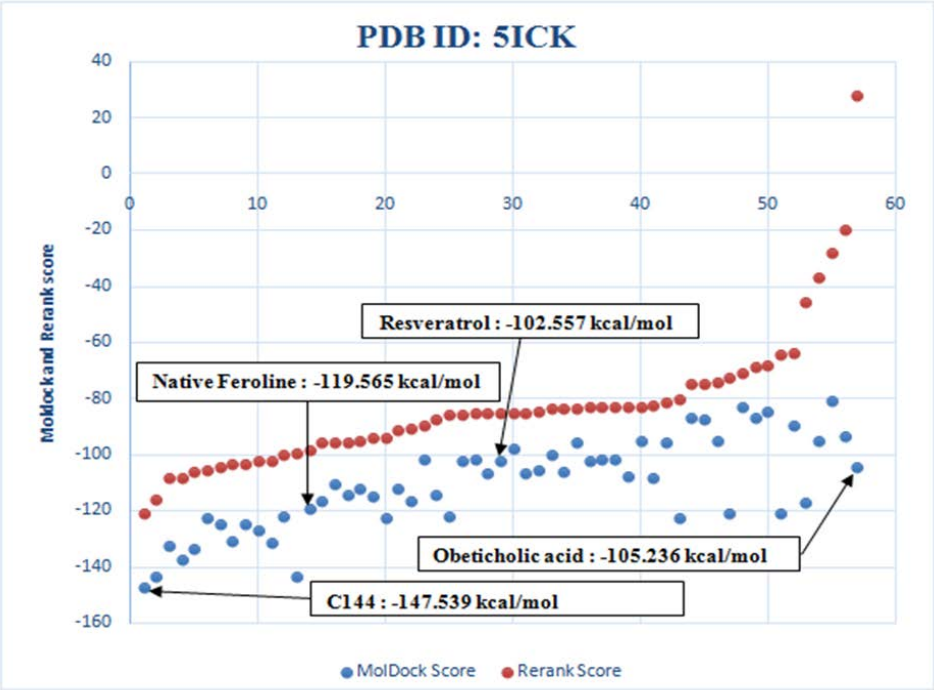

5.3.3.2. Ligand-protein interaction.

Table S5.13: Ligand-protein (1UHL) interaction *via* MVD

Ligand	Interaction (P---L)	Interaction distance	Intercation energy	Hybridization protein	Hybridization ligand
C144 (144)	Arg305 NH1(661)----O(17)	-1.83	2.56 Å	Sp2 Donor	Sp2 Acceptor
	Ser264 OG(334)---O(2)	-2.5	2.77 Å	Sp3 Both	Sp2 Acceptor
	Thr302 OG1(633)---N(O)	-2.5	2.73 Å	Sp3 Both	Sp2 Donor
	Met298 O(598)---N(O)	-2.02	2.54 Å	Sp2 Acceptor	Sp2 Donor

Native T-09019317	Ser264 OG(334)---N(9)	-1.45	3.31 Å	Sp3 Both	Sp2 Acceptor
	Gln221 NE2 (118)---O(26)	-2.5	2.77 Å	Sp2 Donor	Sp3 Both
	Asn225 ND2(150)---O(26)	-2.42	3.11 Å	Sp2 Donor	Sp3 Both
Withaferin A	Met298 O(598)---O(33)	-2.5	2.76 Å	Sp2 Acceptor	Sp3 Both
	THR302 (OG1)---O(33)	-2.5	2.66 Å	Sp3 Both	Sp3 Both
	Ser264 (OG)---O(4)	-1.15	2.44 Å	Sp3 Both	Sp2 Acceptor
	Trp443 (NE1)---O(24)	-0.79	3.31 Å	Sp2 Donor	Sp2 Acceptor
1 Resveratrol (1)	Ser264 (OG)---O(0)	-1.52	3.29 Å	Sp3 Both	Sp3 Both

Table S5.14: Ligand-protein(1UPV) interaction *via* MVD

Ligand	Interaction (P---L)	Interaction distance	Intercation energy	Hybridization protein	Hybridization ligand
C144 (144)	Glu315(O)---N(0)	-2.5	3.06 Å	Sp2 Acceptor	Sp2 Donor
	Thr316(OG1)---O(2)	-2.16	3.17 Å	Sp3 Both	Sp2 Acceptor
Native T-09019317	His435(NE2)---O(26)	-2.5	2.90 Å	Sp2 Acceptor	Sp3 Both
Bergapten	Thr316(OG1)---O(8)	-2.5	2.91 Å	Sp3 Both	Sp3 Acceptor
1 Resveratrol (1)	Thr316(OG1)---O(0)	-2.39	3.12 Å	Sp3 Both	Sp3 Both
	Gln237(NE2)---O(13)	-1.14	3.37 Å	Sp2 Donor	Sp3 Both
	Glu281(O)---O(13)	-2.2	3.16 Å	Sp2 Acceptor	Sp3 Both

Table S5.15:Ligand-protein (5ICK) interaction via MVD

Ligand	Interaction (P---L)	Interaction distance	Intercation energy	Hybridization protein	Hybridization ligand
144 (C144)	Tyr369 (OH)---N(0)	-2.5	3.09 Å	Sp3 Both	Sp2 Donor
	Tyr369 (OH)---O(2)	-2.35	3.13 Å	Sp3 Both	Sp2 Acceptor
	Ser332 (OG)---O(2)	-2.5	3.01 Å	Sp3 Both	Sp2 Acceptor
Native Feroline	Ser332 (OG)---O(24)	-1.56	2.49 Å	Sp3 Both	Sp3 Both
	Tyr369(OH)---O(24)	-2.5	3.06 Å	Sp3 Both	Sp3 Both
	His447 (NE2)---O(13)	-2.5	2.91 Å	Sp2 Acceptor	Sp3 Both
	Thr288(OG1)---O(18)	-2.5	2.81 Å	Sp3 Both	Sp3 Both
Obethicholic acid	Ser332 (OG)---O(29)	-1.38	3.06 Å	Sp3 Both	Sp3 Both
Resveratrol (1)(1)	Thr288(OG1)---O(10)	-2.5	2.67 Å	Sp3 Both	Sp3 Both
	Tyr369(OH)---O(0)	-2.5	3.01 Å	Sp3 Both	Sp3 Both
	Ser332(OG)---O(0)	-2.44	2.59 Å	Sp3 Both	Sp3 Both

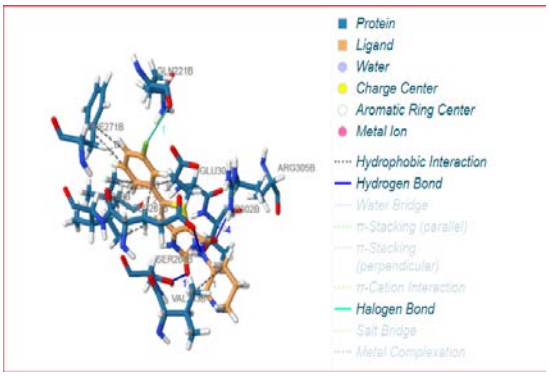

C144-1UHL

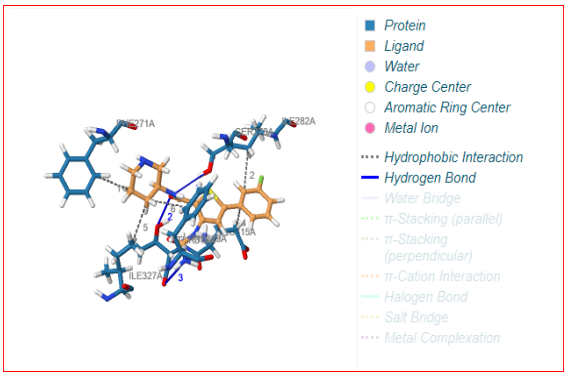

C144-1UPV

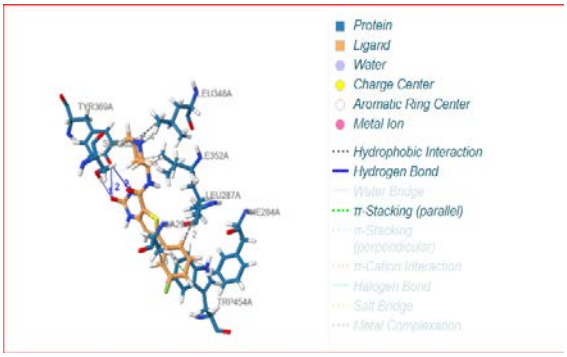

C144-5ICK

T

5.3.3.3. Protein-Ligand Interaction Profiler (PLIP).

Table S5.16: PLIP analysis of compound C144 with respect to 1UHL, 1UPV, and 5ICK (MVD).

C144-1UHL

Hydrophobic Interactions

Index	Residue	AA	Distance	Ligand Atom	Protein Atom
1	263B	VAL	3.45	3586	640
2	267B	GLU	3.81	3576	699
3	268B	ILE	3.22	3581	715
4	268B	ILE	3.53	3574	717

5	271B	PHE	3.93	3580	763
6	271B	PHE	3.24	3579	762
7	297B	VAL	3.28	3581	1183
8	301B	GLU	3.64	3575	1254

Hydrogen Bonds

Index	Residue	AA	Distance H-A	Distance D-A	Donor Angle	Donor Atom	Acceptor Atom
1	264B	SER	1.94	2.77	136.00	656 [O3]	3568 [O2]
2	267B	GLU	3.16	3.75	117.96	3584	703 [O2]
3	302B	THR	2.16	2.73	114.25	3566	1269 [O3]
4	305B	ARG	2.16	2.56	100.66	1322 [Ng+]	3583 [O2]

Halogen Bonds

Index	Residue	AA	Distance	Donor Angle	Acceptor Angle	Donor Atom	Acceptor Atom
1	221B	GLN	3.59	160.38	102.16	3578 [F]	232 [O2]

C144-1UV

Hydrophobic Interactions					
Index	Residue	AA	Distance	Ligand Atom	Protein Atom
1	271A	PHE	3.91	3823	654
2	282A	ILE	3.85	3812	827
3	315A	GLU	3.27	3810	1361
4	315A	GLU	3.09	3811	1362
5	327A	ILE	3.63	3822	1558
6	329A	PHE	3.93	3822	1590

Hydrogen Bonds

Index	Residue	AA	Distance H-A	Distance D-A	Donor Angle	Donor Atom	Acceptor Atom
1	278A	SER	3.10	3.48	103.61	3820	768 [O3]
2	316A	THR	2.35	2.80	104.66	1377 [O3]	3819 [O2]
3	316A	THR	2.89	3.71	138.08	3802	1375 [O2]

C144-5ICK

Hydrophobic Interactions					
Index	Residue	AA	Distance	Ligand Atom	Protein Atom
1	284A	PHE	3.51	3774	670
2	287A	LEU	3.30	3775	724

3	291A	ALA	3.32	3770	789
4	348A	LEU	3.13	3781	1688
5	352A	ILE	3.75	3780	1761

Hydrogen Bonds

Index	Residue	AA	Distance H-A	Distance D-A	Donor Angle	Donor Atom	Acceptor Atom
1	332A	SER	1.98	3.01	174.07	1443 [O3]	3762 [O2]
2	369A	TYR	2.56	3.13	114.08	2033 [O3]	3762 [O2]
3	369A	TYR	2.17	3.09	150.24	3760	2033 [O3]

π-Stacking

Index	Residue	AA	Distance	Angle	Offset	Stacking Type	Ligand Atoms
1	454A	TRP	4.37	25.67	1.82	P	3769, 3770, 3771, 3773, 3774, 3775

5.3.4. Electronic Reactivity Parameters *via* DFT

Table S5.17: The calculated HOMO, LUMO and Δ**E.**

COMPOUND	**HOMO**	**LUMO**	**HOMO-LUMO (in H)**	**$\Delta E = E_{HOMO}$-E_{LUMO} (in eV)**
Resveratrol (1)	-0.2078	-0.06269	0.14511	3.948646254
C144	-0.22118	-0.07106	0.15012	4.084975368

Native T-09019317 (1UHL/1UPV)	-0.26957	-0.06821	0.20136	5.479287504
Native feroline (5ICK)	-0.22955	-0.05002	0.17953	4.885262642
Bergapten	-0.22924	-0.07448	0.15476	4.211236264
Withaferin A	-0.25097	-0.07055	0.18042	4.909480788
Obeticholic acid	-0.25983	-0.01779	0.24204	6.586247256

Table S5.18: The calculated global reactivity descriptors

COMPOUND	HARDNESS (η)	SOFTNESS (S)	CHEMICAL POTENTIAL (μ)	IONIS ATION POTEN TIAL (IP)	ELECTRON AFFINITY (EA)	ELECTRO NEGATIVITY (χ)	ELECTRO PHILICITY (ω)	DIPOLE MOMENT
Resveratrol (1)	1.9743 23127	0.9871616	-3.68 205793	5.654 52892	1.7058 82666	3.6802058	3.6026764	0.712224
C144	2.042 487684	0.2447995	-3.9761 29768	6.01861 7452	1.9336 42084	3.9761298	0.2050602	3.674155

Native T-09019317 (1UHL/ 1UPV)	2.7396 43752	0.1825055	-4.595733346	7.33533 77098	1.856 89594	4.5957333	0.0986093	5.600918
Native feroline (5ICK)	2.4426 31321	0.2046973	-3.803745549	6.2463 7687	1.3611 14228	3.8037455	0.1498765	3.202067
Bergapten	2.1056 18132	0.23746	-4.132323204	6.2379 41336	2.0267 5072	4.1323232	0.1856553	8.005872
Withaferin A	2.4547404	0.2036875	-4.37454664	6.8292451	1.9197 6427	4.3745047	0.129039	4.67931
Obeticholic acid	3.2931236	0.1518315	-3.777214434	7.0703381	0.4840908	3.7772144	0.0830373	3.867124

5.3.5. Statistical analysis

Table S5.19: Correlation Matrix Analyzing the Relationship Between Molecular Docking Scores (MDS) and Electronic Reactivity Descriptors Derived from Density Functional Theory (DFT)

	Moldock score 1UHL	*Moldock score 1UPV*	*Moldock score 5ICK*	*HOMO-LUMO (in eV)*	*ELECTRON AFFINITY (A)*	*IONISATION POTENTIAL (I)*	*HARDNESS (η)*	*SOFTNESS (S)*	*ELECTRONEGATIVITY (χ)*	*ELECTROPHILICITY (ω)*	*CHEMICAL POTENTIAL (μ)*	*DIPOLE MOMENT*
Moldock score	1											

1UHL												
Mold ock score 1UPV	0.707456917	1										
Mold ock score 5ICK	0.405914561	0.477069664	1									
HOMO-LUMO (in eV)	0.236207124	0.262387788	0.161911684	1								
ELECTRON AFFINITY (A)	-0.271314897	-0.211559855	0.001628737422	-0.645665022	1							
IONISATION POTENTIAL (I)	0.023807934	0.118889631	0.224479755	0.618406122	0.200814809	1						
HARDNESS(η)	0.236207124	0.262387788	0.161911684	1	-0.645665022	0.618406122	1					
SOFTNESS (S)	-0.057277087	-0.023705946	-0.001858273636	-0.256387528	0.04454269404	-0.2830739039	-0.256387528	1				
ELECTRONEGAT	-0.1624	-0.062832	-0.153242	-0.029219	0.7822207199	0.767405797	-0.002992	-0.1508	1			

IVITY (χ)	32827	54037		94056			94056	74057				
ELECTROPHILICITY (ω)	-0.032591	0.076541	-5.382E-06	-0.020912	0.07657361	-0.195832535	-0.021205	0.978019875	-0.174663777	1		
CHEMICAL POTENTIAL (μ)	-0.162432827	-0.062854037	0.153242	-0.029256940	0.78722097199	0.76740579797	-0.029256940	-0.150874057	1	-0.17466377	1	
DIPOLE MOMENT	-0.048519058	-0.080537933	0.106779	-0.130596375	0.34864171762	0.19126166835	-0.130596375	-0.184019582	0.34982495922	-0.18951256	0.34982495922	1

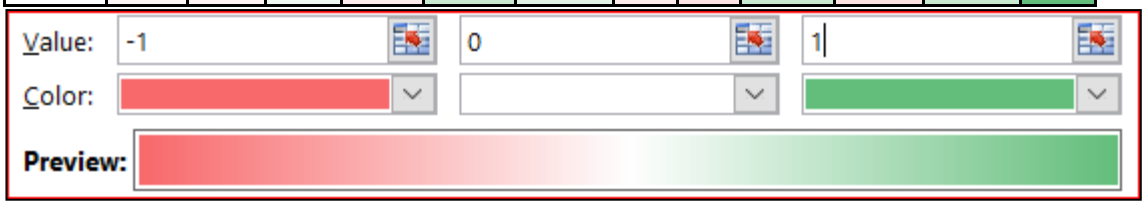

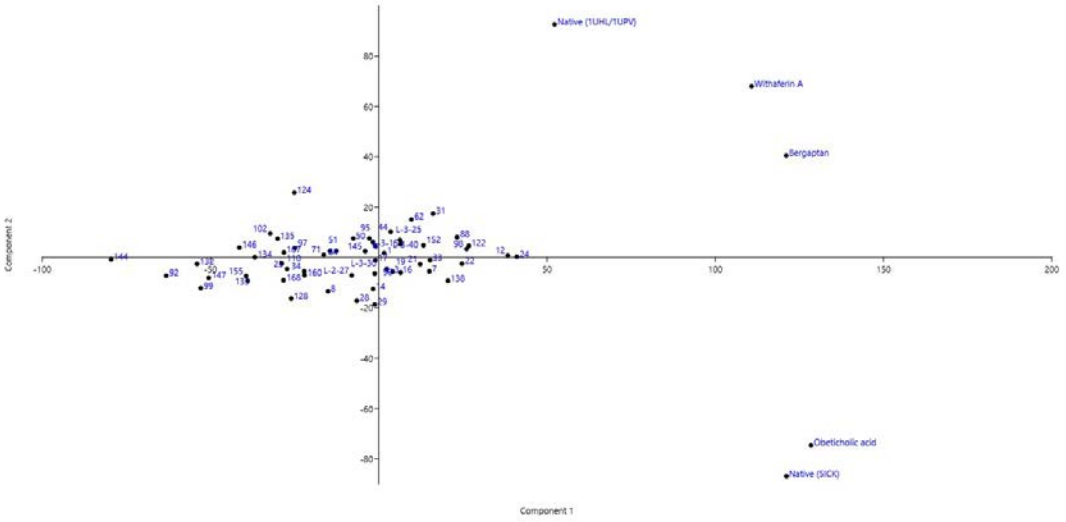

5.3.6. AutoDock

Table S5.20: Docking profile of 1UHL and the ligands *via* autodock

Ligands	Binding Affinity	RMSD	Interacting Residues
C144	-8.23	1.21	PHE B:257, THR B:302, PRO B:436, LYS B:434, LEU B:439, HIS B:421, ALA B:261, PHE B:335, ILE B:339, LEU B:299.
Resveratrol (1)	-6.47	0.32	THR B:302, ILE B:295, THR B:258, MET B:298, LEU B:299, ILE B:339,

			ALA B:261, LEU B:331.
Native T-09019317 (1UHL/1UPV)	-6.82	1.19	ILE B:295, TRP B:443, MET B:298, LEU B:439, HIS B:421, PHE B:335, LEU B:331, ILE B:339, LEU B:299.
Withaferin A	-6.17	0.88	MET B:298, HIS B:421

Table S5.21: Docking profile of 1UPV and the ligands *via* autodock

Ligands	**Binding Affinty**	**RMSD**	**Interacting Residues**
C144	-8.2	0.26	THR A:316, PHE A:340, PHE A:271, ALA A:275.
Resveratrol (1)	-6.88	0.28	HIS A:435, THR A:272, ALA A:275, LEU A:274.
Native T-09019317 (1UHL/1UPV)	-7.17	0.85	HIS A:435, THR A:316, THR A:272, PHE A:271, ALA A:275, MET A:312, PHE

			A:329, ILE A:327, TYR A:335, LEU A:274, LEU A:453.
Bergapten	-6.52	0.06	THR A:328, PHE A:329, MET A:312, LEU A:274, ILE A:327, ARG A:319.

Table S5.22: Docking profile of 5ICK and the ligands *via* autodock

Ligands	**Binding Affinty**	**RMSD**	**Interacting Residues**
C144	-9.17	1.52	MET A:290, THR A:288, SER A:332, HIS A:294, TRP A:454, ALA A:291, LEU A:465, MET A:328, LEU A:287.
Resveratrol (1)	-7.39	0.17	SER A:332, PHE A:284, PHE A:329, MET A:328, ALA A:291.
Native feroline (5ICK)	-7.92	0.24	HIS A:447, PHE A:329, LEU A:348, MET A:328, ALA A:291, ILE A:335,

			MET A:290, LEU A:287.
Obeticholic Acid	-3.84	0.28	LEU A:287, MET A:290, TRP A:454, ALA A:291.

5.3.7. Protein-Ligand Interaction Profiler (PLIP).

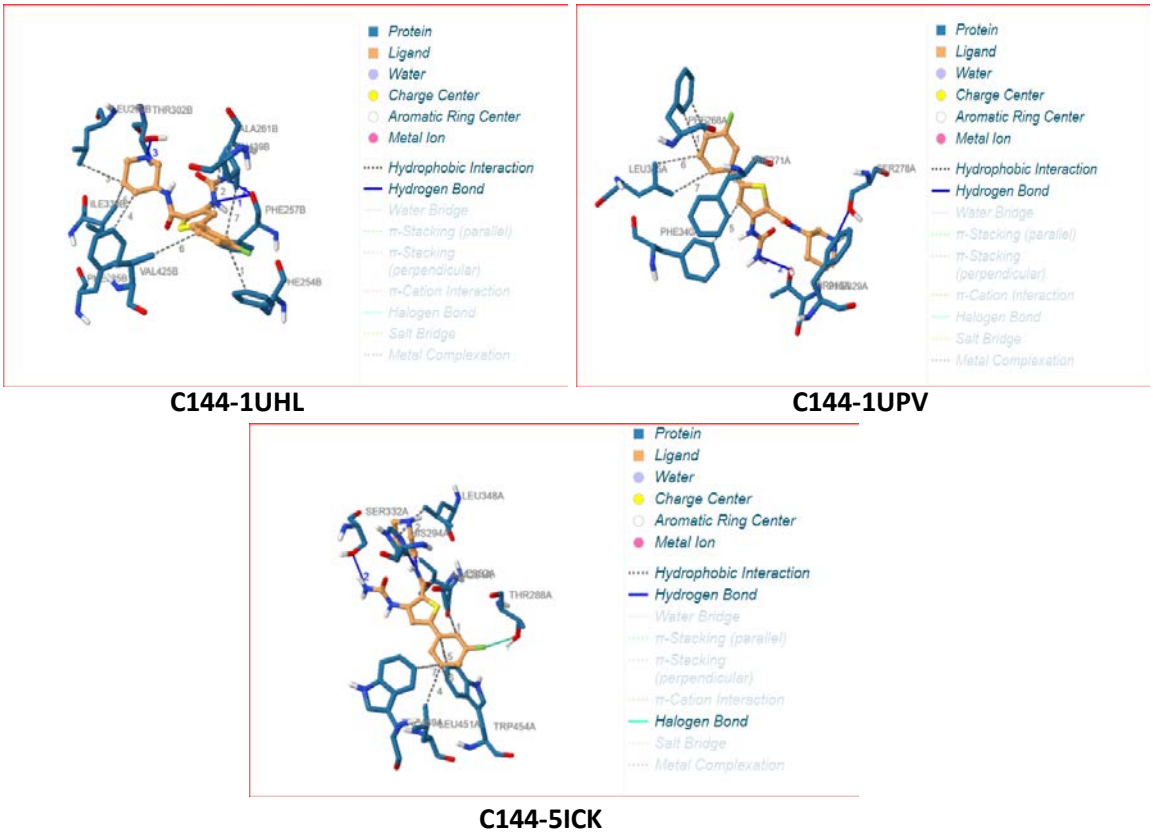

Figure S5.18: PLIP analysis of compound C144-1UHL, C144-1UPV and C144-5ICK complex (AutoDock).

Table S5.23:PLIP analysis of compound C144 with respect to 1UHL, 1UPV, and 5ICK (AutoDock).

C144-1UHL

Hydrophobic Interactions

Index	Residue	AA	Distance	Ligand Atom	Protein Atom
1	254B	PHE	3.70	2200	323
2	261B	ALA	3.63	2187	387
3	299B	LEU	3.65	2194	744
4	335B	PHE	3.29	2193	1079
5	339B	ILE	3.24	2194	1114
6	425B	VAL	3.74	2204	1972
7	439B	LEU	3.52	2200	2112

Hydrogen Bonds

Index	Residue	AA	Distance H-A	Distance D-A	Donor Angle	Donor Atom	Acceptor Atom
1	257B	PHE	2.28	2.74	106.25	2179 [Nam]	346 [O2]
2	257B	PHE	2.15	2.79	119.00	2176 [Nam]	346 [O2]
3	302B	THR	2.21	2.63	101.26	2196 [N3]	770 [O3]

C144-1UPV

Hydrophobic Interactions					
Index	Residue	AA	Distance	Ligand Atom	Protein Atom
1	268A	PHE	3.97	2325	368
2	268A	PHE	3.03	2324	370
3	271A	PHE	3.24	2320	396
4	329A	PHE	3.62	2315	959
5	340A	PHE	3.87	2308	1079
6	345A	LEU	3.65	2325	1129
7	345A	LEU	3.80	2326	1128

Hydrogen Bonds

Index	Residue	AA	Distance H-A	Distance D-A	Donor Angle	Donor Atom	Acceptor Atom
1	278A	SER	2.14	3.06	143.95	2317 [N3]	461 [O3]
2	316A	THR	2.11	2.84	127.72	2297	817 [O3]

C144-5ICK

Hydrophobic Interactions					
Index	Residue	AA	Distance	Ligand Atom	Protein Atom
1	291A	ALA	3.32	2298	483
2	348A	LEU	3.46	2310	1026
3	352A	ILE	3.61	2310	1072
4	451A	LEU	3.46	2303	2060
5	454A	TRP	3.96	2297	2093

6	454A	TRP	3.45	2303	2092
7	469A	TRP	3.91	2303	2251

Hydrogen Bonds

Index	Residue	AA	Distance H-A	Distance D-A	Donor Angle	Protein donor?	Sidechain	Donor Atom	Acceptor Atom
1	294A	HIS	3.23	4.02	135.46			2306	514
2	332A	SER	1.98	2.90	151.16			2285	875 [O3]

Halogen Bonds

Index	Residue	AA	Distance	Donor Angle	Acceptor Angle	Donor Atom	Acceptor Atom
1	288A	THR	2.76	163.38	102.17	2301 [F]	456 [O3]

5.3.8. ML-based protein-ligand interaction capturer (ML-PLIC)

Table S5.24: Docking scores and Interaction profile of C144 with respective targets obtained through ML-PLIP analysis.

SL.NO	PDB ID	LIGAND	SCORE (kcal/mol)
1	1UHL	C144	-8.90
2	1UPV	C144	-9.80
3	5ICK	C144	-9.20

C144-1UHL complex interaction information

Interaction **Toggle Dropdown**	**Residue**	**Residue_ID**	**Residue_Atom**	**Frequency**
hydrogen bond	THR	B	O	1
hydrophobic contacts	PHE	B	C	8
hydrophobic contacts	LEU	B	C	8
hydrophobic contacts	TYR	B	C	2
hydrophobic contacts	GLN	B	C	2

Interaction frequency analysis for reference

Interaction **Toggle Dropdown**	**Residue**	**Residue_ID**	**Residue_Atom**	**Frequency**
hydrogen bond	THR	B	O	2

C144-1UPV complex interaction information

Interaction **Toggle Dropdown**	**Residue**	**Residue_ID**	**Residue_Atom**	**Frequency**
hydrogen bond	SER	A	O	1
hydrogen bond	THR	A	O	1

hydrophobic contacts	PHE	A	C	8
hydrophobic contacts	LEU	A	C	2
hydrophobic contacts	ILE	A	C	2
hydrophobic contacts	ALA	A	C	2

Interaction frequency analysis for reference

Interaction **Toggle Dropdown**	**Residue**	**Residue_ID**	**Residue_Atom**	**Frequency**
hydrogen bond	SER	A	O	2
hydrogen bond	THR	A	O	2

C144-5ICK complex interaction information

Interaction **Toggle Dropdown**	**Residue**	**Residue_ID**	**Residue_Atom**	**Frequency**
hydrogen bond	TYR	A	O	1
hydrophobic contacts	PHE	A	C	8
hydrophobic contacts	LEU	A	C	6
hydrophobic contacts	TRP	A	C	4

hydrophobic contacts	ALA	A	C	2
hydrophobic contacts	MET	A	C	2
Interaction frequency analysis for reference				
Interaction **Toggle Dropdown**	**Residue**	**Residue_ID**	**Residue_Atom**	**Frequency**
hydrogen bond	TYR	A	O	2

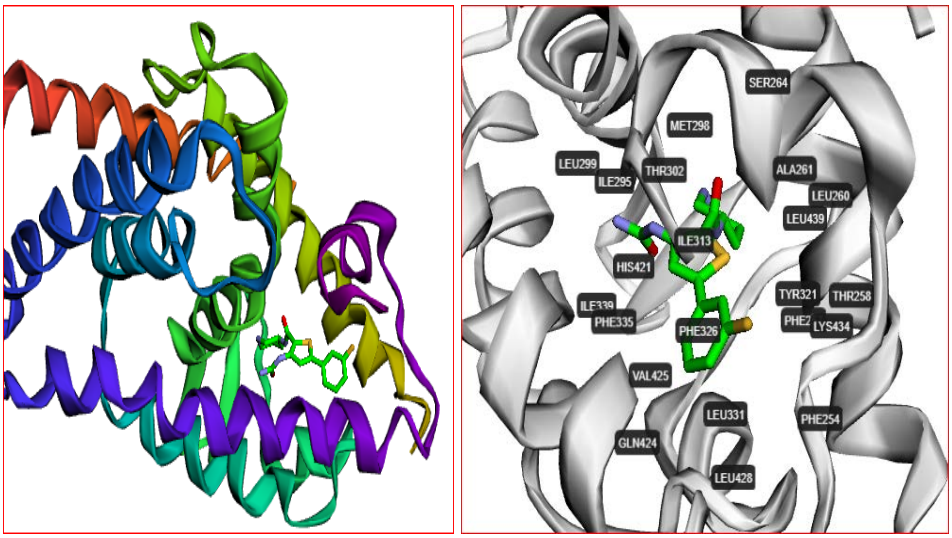

C144-1UHL

A.

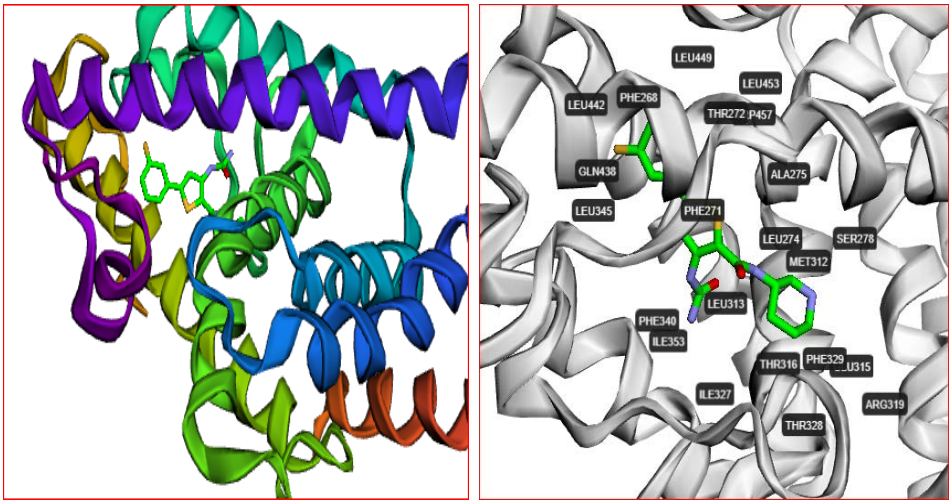

C144-1UPV

B.

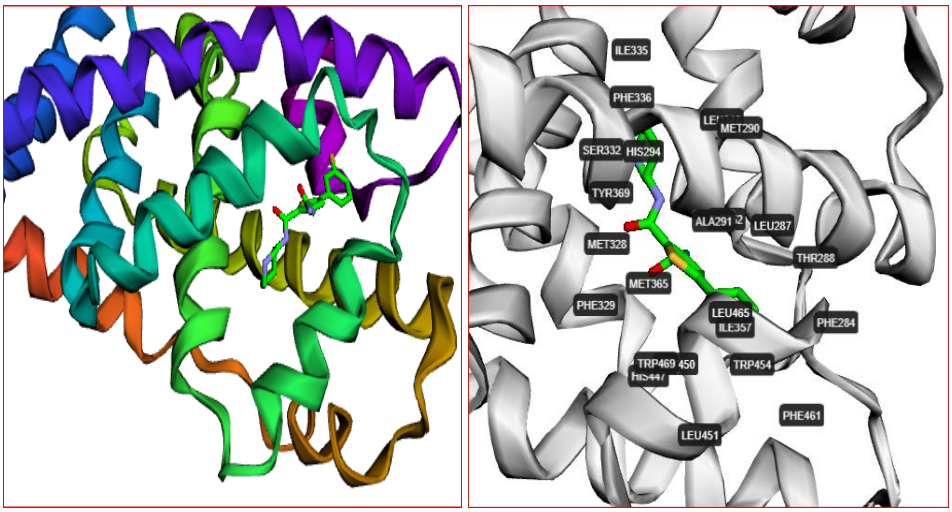

C144-5ICK

C.

Figure S5.19 (a-c): Protein-ligand interactions of C144 with 1UHL, 1UPV, and 5ICK, respectively, as visualized through ML-PLIC.

5.3.10. Bioactivity prediction

Table S5.25: Bioactivity score prediction *via* molinspiration.

COMPOUNDS	BIOACTIVITY SCORE PARAMETERS					
	GPCR (G-protein-coupled receptors) ligand	**Ion channel modulator**	**Kinase inhibitor**	**Nuclear receptor ligand**	**Protease inhibitor**	**Enzyme inhibitor**
C144	0.16	-0.15	0.54	0.43	0.30	0.10
Native T-09019317 (1UHL/1UPV)	0.01	0.02	-0.34	0.28	0.12	0.08
Native feroline (5ick)	0.16	0.05	-0.24	0.69	-0.02	0.28
Bergapten	-0.65	-0.07	-0.98	-1.14	-0.98	-0.27
Obeticholic acid	0.24	0.13	-0.48	0.80	0.20	0.61
Withaferin A	0.07	0.14	-0.49	0.76	0.15	0.94
Resveratrol (1)	-0.20	0.02	-0.20	0.01	-0.41	0.02

Compounds possessing values >0.00 are most likely to exhibit significant biological activities, while those with values ranging from -0.50 to 0.00 are expected to be moderately active, and values less than -0.50 are assumed to be inert.

5.3.11. Detailed quantum calculation

5.3.11.1. Molecular Electrostatic Potential Analysis:

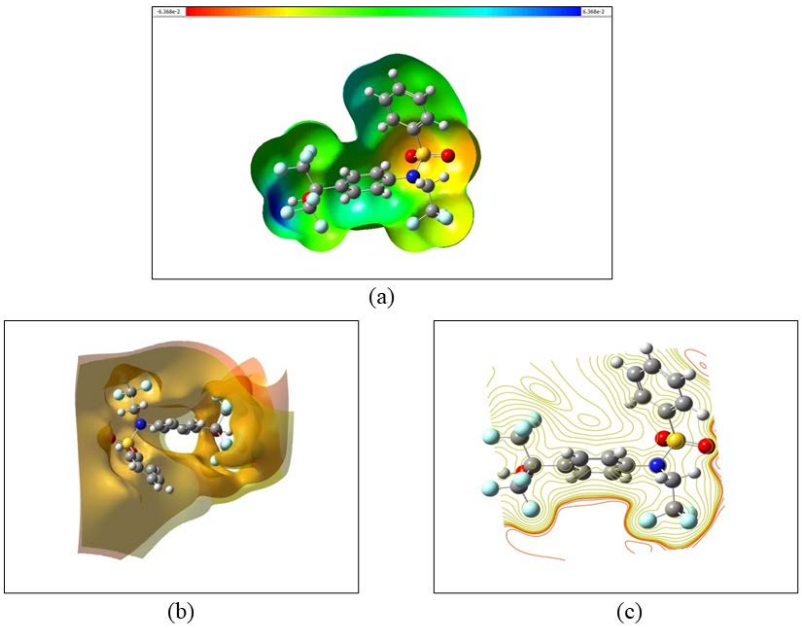

S5

Figure S5.23: a: Molecular electrostatic potentials (MEP) plot of native T-0901317 (1UPV/1UHL), **b:** contour map plot of ESP isosurface of native T-0901317 (1UPV/1UHL), **c:** visualization of the ESP array plot for native T-0901317 (1UPV/1UHL)

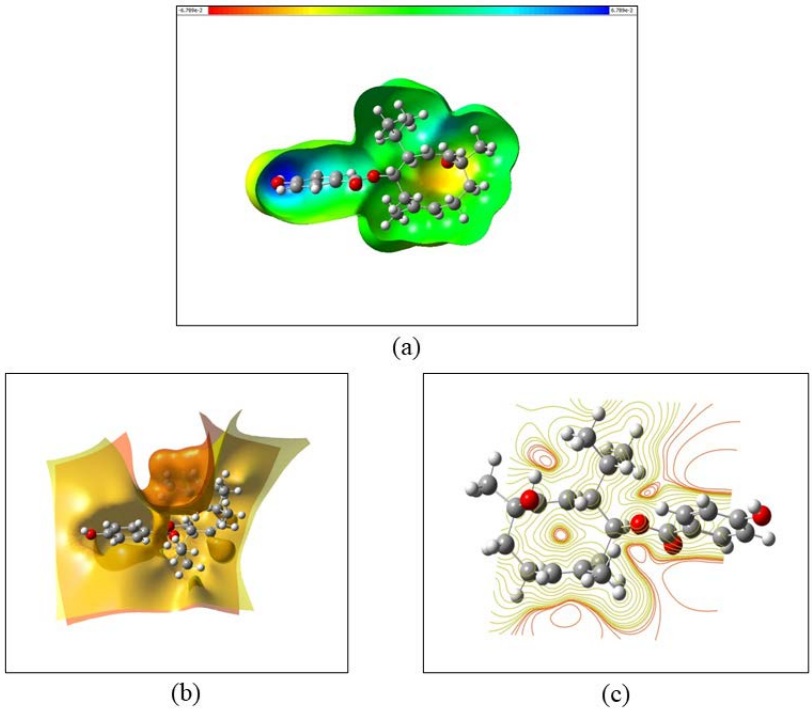

Figure S5.24.a: Molecular electrostatic potentials (MEP) plot of native feroline(5ICK), **b:** contour map plot of ESP isosurface of native Feroline (5ICK), **c:** visualization of the ESP array plot for native feroline (5ICK)

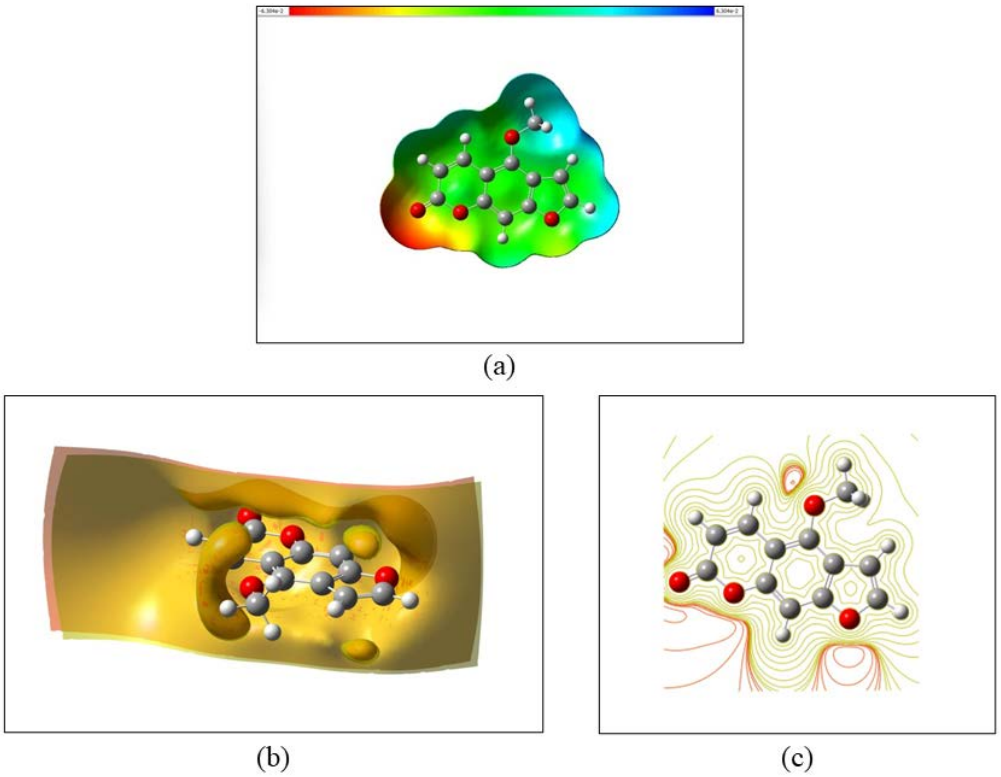

Figure S5.26.a: Molecular electrostatic potentials (MEP) plot of bergapten, **b:** contour map plot of ESP isosurface of bergapten, **c:** visualization of the ESP array plot for bergapten

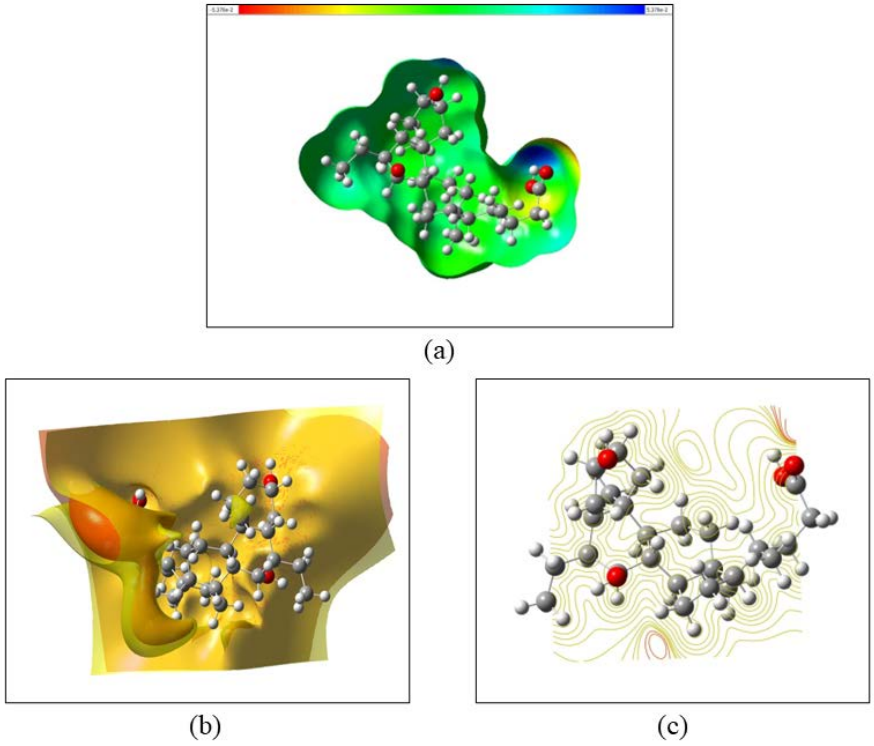

Figure S5.27.a: Molecular electrostatic potentials (MEP) plot of obeticholic acid, **b:** contour map plot of ESP isosurface of obeticholic acid, **c:** visualization of the ESP array plot for obeticholic acid

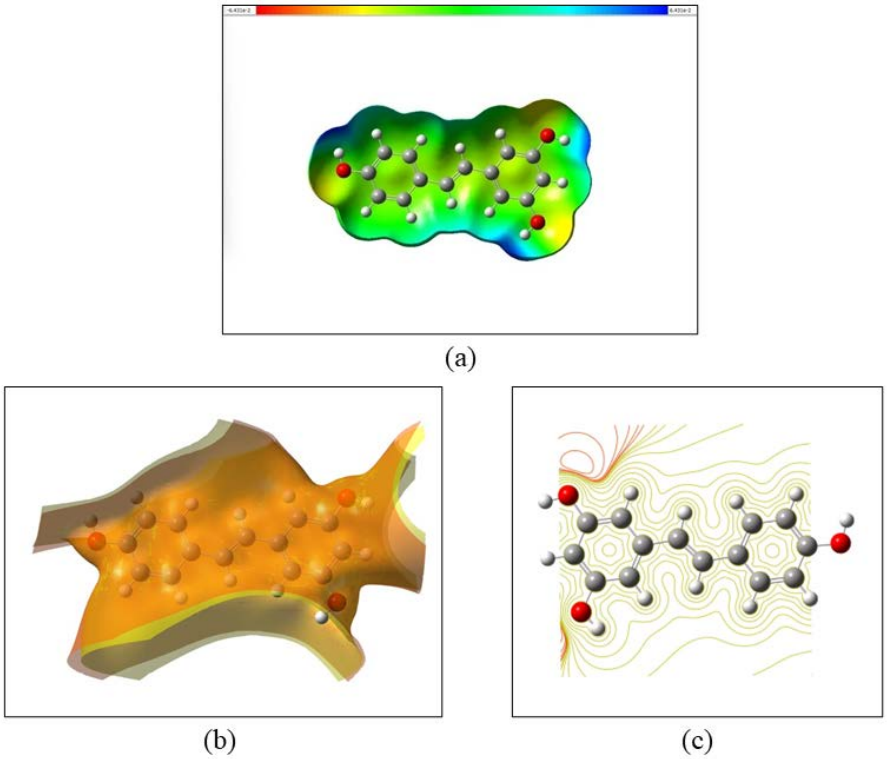

Figure S5.28. a: Molecular electrostatic potentials (MEP) plot of resveratrol, **b:** contour map plot of ESP isosurface of resveratrol, **c:** visualization of the ESP array plot for resveratrol

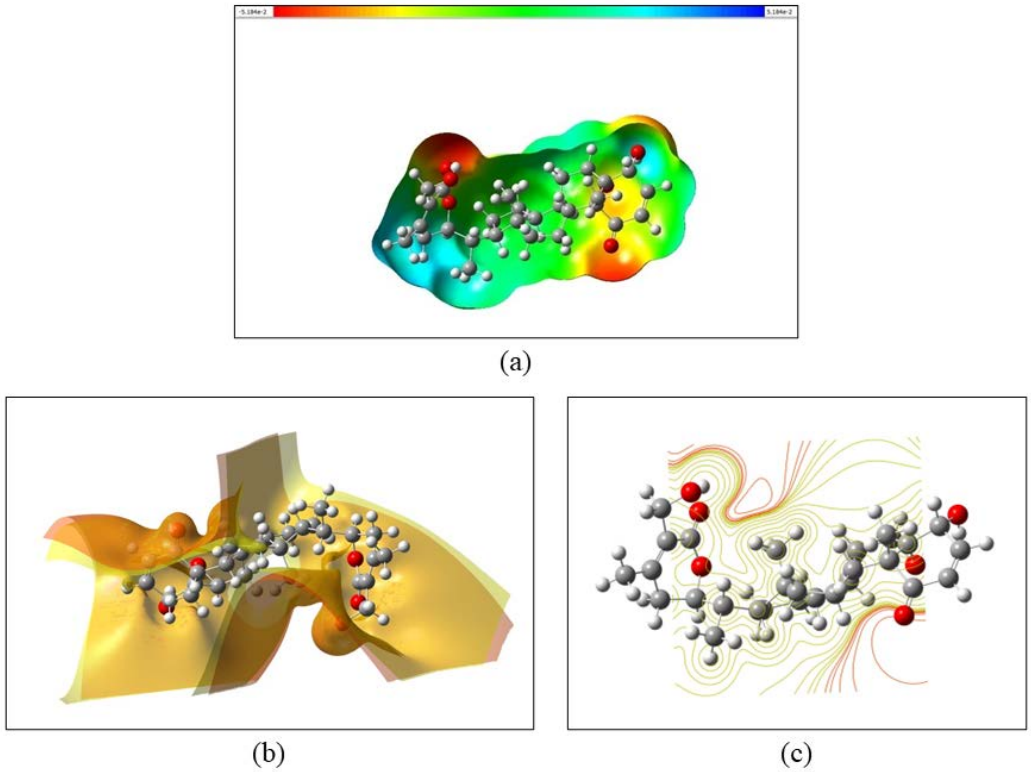

Figure S5.29.a: Molecular electrostatic potentials (MEP) plot of withaferin A, **b:** contour map plot of ESP isosurface of withaferin A, **c:** visualization of the ESP array plot for withaferin A

5.3.11.2. Mulliken Charge and Natural bond orbital (NBO) analysis:

Table S5.26: Computed Mulliken Charge (MC) distribution of the compounds computed by DFT/6-311++g (d,p) basis set

SL No.	Compounds	Atoms	
		C	O
1	Resveratrol (1)	1.242	-0.227
2	Native T-0901317 (1UHL/1UPV)	0.367	0.126
3	Native feroline (5ICK)	0.840	-0.222
4	C144	1.417	-0.319
5	Bergapten	2.295	-0.281
6	Obeticholic acid	0.901	0.192
7	Withaferin A	0.885	-0.230

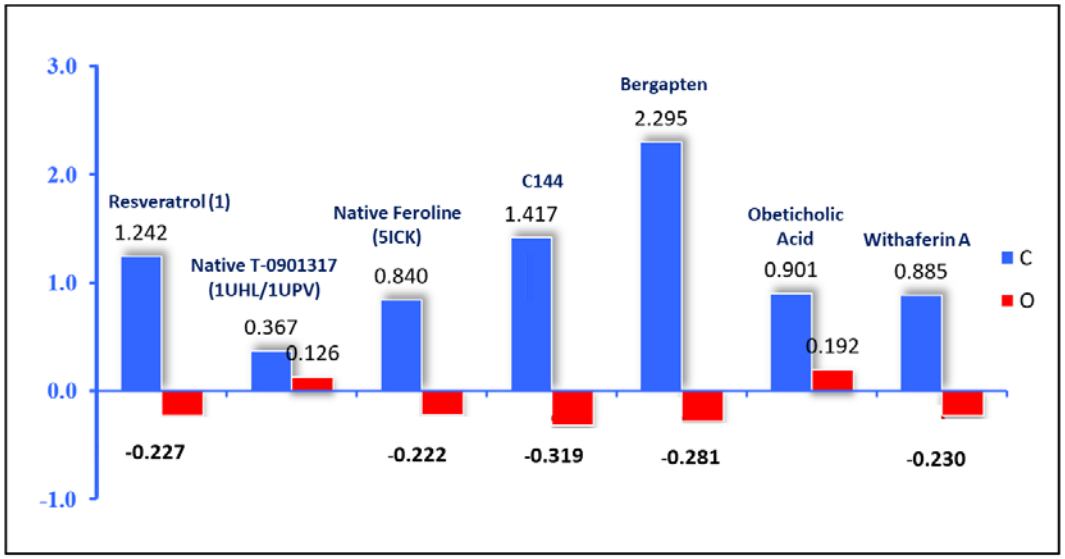

5.3.11.3. Natural bond orbital (NBO) analysis

Table S5.27: Computed NBO analysis for the most prominent therapeutic compounds with E^2 energies

Compounds	Donor NBO (i) → Acceptor NBO (j)	E(2) kcal/mol	E(j)-E(i) a.u.	F(i,j)a.u.
Native T-0901317 (1UPV/1UHL)	$\sigma C_{31} - H_{43} \rightarrow \sigma^* C_{30} - H_{42}$	70.67	4.63	0.511
C144	$\pi^* C_5 - C_6 \rightarrow \sigma^* C_{17} - O_{18}$	98.45	0.02	0.063
BERGAPTEN	$\pi^* C_{14} - C_{15} \rightarrow \sigma^* C_{11} - C_{12}$	933.57	76.97	22.08

5.3.11.6. Visualizations of non-covalent interaction:

5.3.11.6.1. NCI-RDG analysis

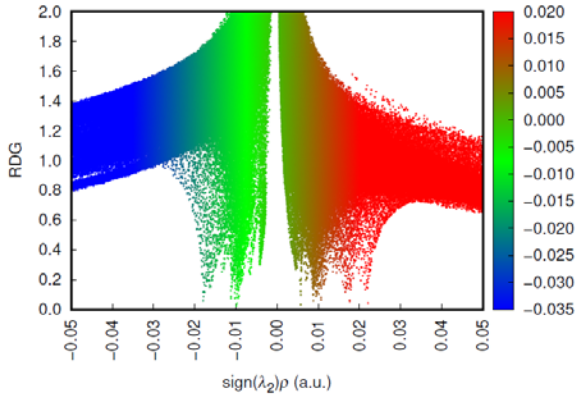

Native T-0901317 (1UPV/1UHL)

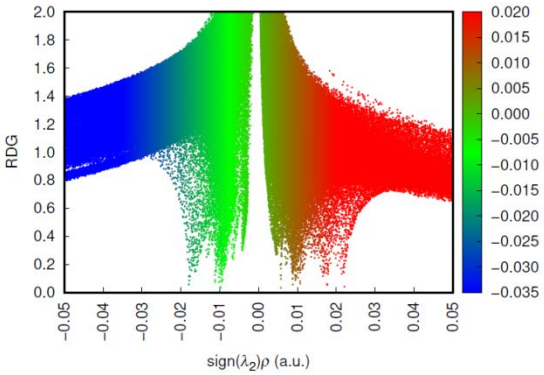

Native feroline (5ICK)

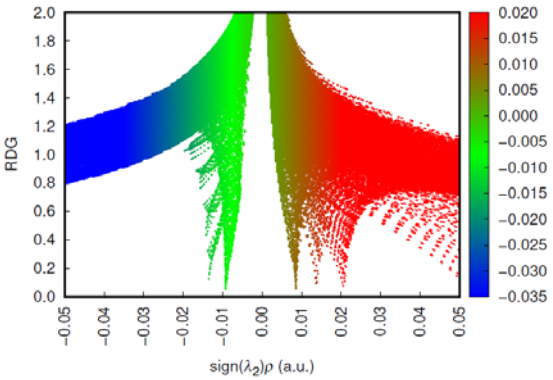

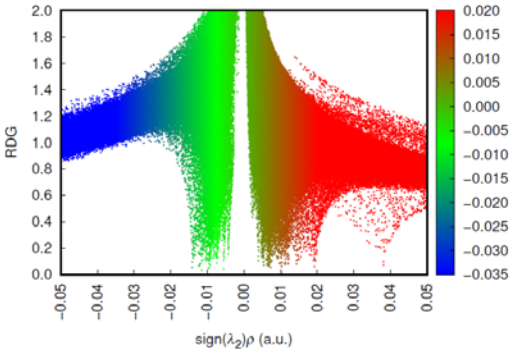

Bergapten Obeticholic acid

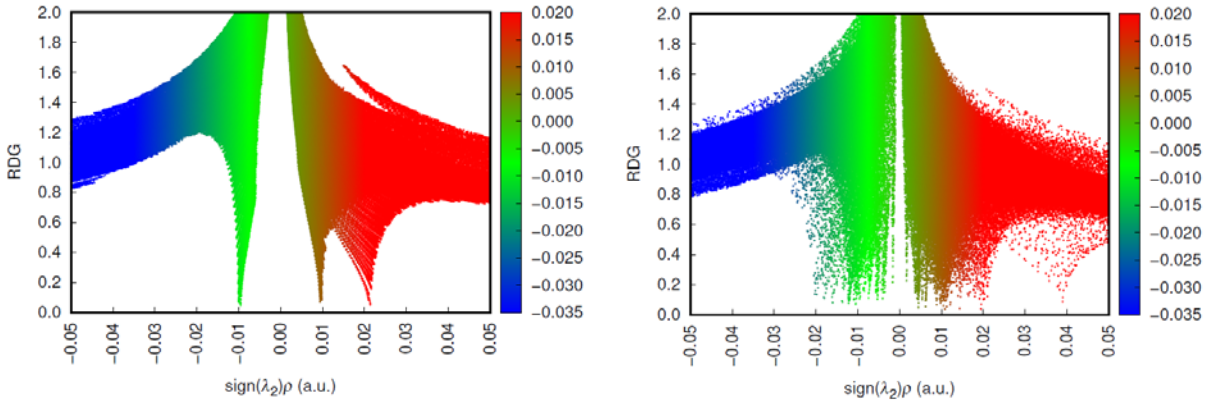

Resveratrol Withaferin A

Figure S5.34b: Non-covalent Interaction (NCI) plot of other compounds understudy.

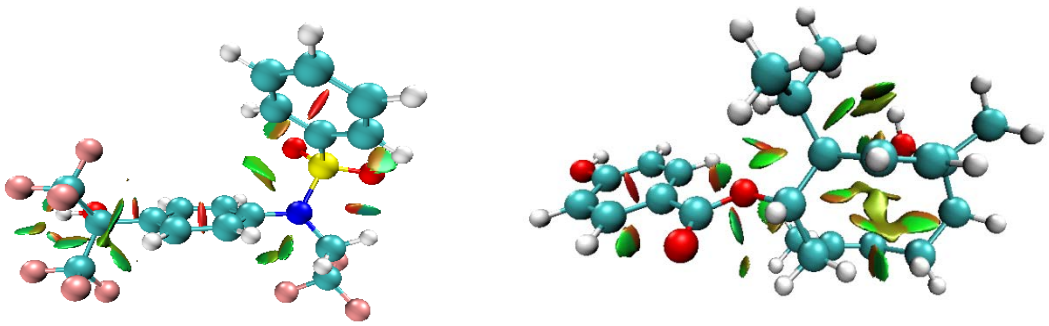

Native T-0901317 (1UPV/1UHL) Native feroline (5ICK)

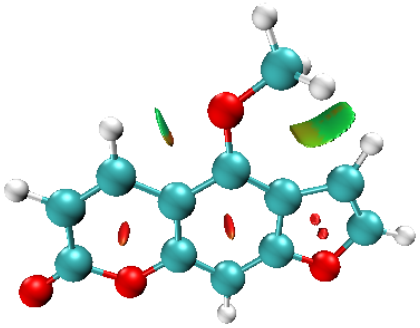

Bergapten

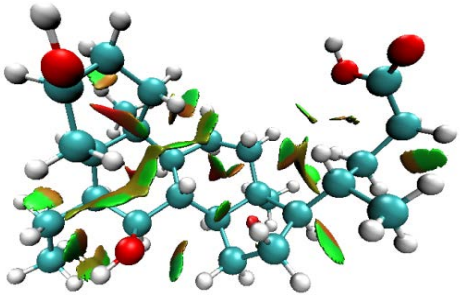

Obeticholic acid

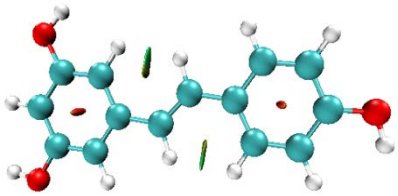

Resveratrol

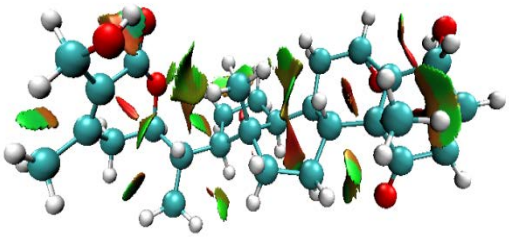

Withaferin A

Figure S5.35b: VMD plots of other compounds under study.

5.3.11.7. CLC-Pred

Table S5.28: CLC-Pred of C144 (AZD7762), Native Ligands, and Reference Standards Across Cell Lines

Pa	Pi	Cell line	Cell line in full name	Tissue	Tumor type
0.696	0.004	DMS-114	Lung carcinoma	Lung	Carcinoma

0.678	0.003	Kasumi 1	Childhood acute myeloid leukemia with maturation	Haematopoietic and lymphoid tissue	Leukemia
0.659	0.003	MDA-MB-453	Breast adenocarcinoma	Breast	Adenocarcinoma
0.628	0.013	MOLT-4	Acute T-lymphoblastic leukemia	Blood	Leukemia
0.598	0.004	CFPAC-1	Pancreatic carcinoma	Pancreas	Carcinoma
0.598	0.013	UACC-257	Melanoma	Skin	Melanoma
0.572	0.005	A2058	Melanoma	Skin	Melanoma
0.549	0.005	U-266	Plasma cell myeloma	Blood	Myeloma
0.541	0.004	YAPC	Pancreatic carcinoma	Pancreas	Carcinoma
0.535	0.005	RKO	Colon carcinoma	Colon	Carcinoma
0.494	0.005	PA-1	Ovarian carcinoma	Ovarium	Carcinoma
0.491	0.004	HuP-T3	Pancreatic adenocarcinoma	Pancreas	Adenocarcinoma

0.486	0.005	HOS	Osteosarcoma	Bone	Sarcoma
0.492	0.013	RPMI-8226	Multiple myeloma	Haematopoietic and lymphoid tissue	Myeloma
0.473	0.005	SK-MES-1	Squamous cell lung carcinoma	Lung	Carcinoma
0.479	0.024	OVCAR-4	Ovarian adenocarcinoma	Ovarium	Adenocarcinoma
0.455	0.004	SJSA-1	Osteosarcoma	Bone	Sarcoma
0.443	0.01	MIA PaCa-2	Pancreatic carcinoma	Pancreas	Carcinoma
0.435	0.006	AGS	Gastric adenocarcinoma	Stomach	Adenocarcinoma
0.431	0.005	T98G	Glioblastoma	Brain	Carcinoma
0.421	0.014	H9	T-lymphoid	Haematopoietic and lymphoid tissue	Leukemia
0.404	0.005	CWR22R	Prostate carcinoma epithelial cell line	Prostate	Carcinoma
0.431	0.033	OVCAR-5	Ovarian adenocarcinoma	Ovarium	Adenocarcinoma

0.415	0.034	HOP-92	Non-small cell lung carcinoma	Lung	Carcinoma
0.378	0.005	5637	Urothelial bladder carcinoma	Urinary tract	Carcinoma
0.375	0.005	C8166	Leukemic T-cells	Blood	Leukemia
0.369	0.005	G-361	Melanoma	Skin	Melanoma
0.401	0.042	NCI-H226	Non-small cell lung carcinoma	Lung	Carcinoma
0.366	0.008	T-24	Bladder carcinoma	Urinary tract	Carcinoma
0.354	0.005	MDA-MB-361	Breast adenocarcinoma	Breast	Adenocarcinoma
0.379	0.042	A498	Renal carcinoma	Kidney	Carcinoma
0.349	0.015	NCI-H1299	Non-small cell lung carcinoma	Lung	Carcinoma
0.372	0.042	UO-31	Renal carcinoma	Kidney	Carcinoma
0.354	0.026	8505C	Thyroid gland undifferentiated (anaplastic) carcinoma	Thyroid	Carcinoma

0.342	0.044	BT-549	Breast ductal carcinoma	Breast	Carcinoma
0.355	0.064	MDA-MB-231	Breast adenocarcinoma	Breast	Adenocarcinoma
0.308	0.017	A-427	Lung carcinoma	Lung	Carcinoma
0.347	0.057	OVCAR-8	Ovarian adenocarcinoma	Ovarium	Adenocarcinoma
0.339	0.059	SK-MEL-2	Melanoma	Skin	Melanoma
0.347	0.067	HCT-116	Colon carcinoma	Colon	Carcinoma
0.294	0.022	HT-1080	Fibrosarcoma	Soft tissue	Sarcoma
0.304	0.059	CCRF-CEM	Childhood T acute lymphoblastic leukemia	Blood	Leukemia
0.248	0.005	THP-1	Acute monocyticleukemia	Blood	Leukemia
0.25	0.02	J82	Bladder carcinoma	Urinary tract	Carcinoma
0.235	0.007	NCI-N87	gastric carcinoma	Stomach	Carcinoma

0.318	0.091	NCI-H23	Non-small cell lung carcinoma	Lung	Carcinoma
0.237	0.012	SW1573	Lung carcinoma	Lung	Carcinoma
0.303	0.079	KM12	Colon adenocarcinoma	Colon	Adenocarcinoma
0.292	0.07	IGROV-1	Ovarian adenocarcinoma	Ovarium	Adenocarcinoma
0.237	0.019	NUGC-3	Gastric carcinoma	Stomach	Carcinoma
0.3	0.089	CAKI-1	Kidney carcinoma	Kidney	Carcinoma
0.293	0.085	786-0	Renal carcinoma	Kidney	Carcinoma
0.282	0.074	M14	Melanoma	Skin	Melanoma
0.206	0.043	A-375	Malignant melanoma	Skin	Melanoma
0.264	0.101	SK-MEL-28	Melanoma	Skin	Melanoma
0.185	0.063	A2780	Ovarian carcinoma	Ovarium	Carcinoma

0.181	0.066	LoVo	Colon adenocarcinoma	Colon	Adenocarcinoma
0.112	0.028	SiHa	Cervical squamous cell carcinoma	Cervix	Carcinoma
0.122	0.044	Huh-7	Hepatocellular carcinoma	Liver	Carcinoma
0.207	0.135	MDA-MB-468	Breast adenocarcinoma	Breast	Adenocarcinoma
0.222	0.161	HT-29	Colon adenocarcinoma	Colon	Adenocarcinoma
0.161	0.112	Ramos	Burkittslymhoma B-cells	Blood	Leukemia
0.196	0.15	SK-OV-3	Ovarian carcinoma	Ovarium	Carcinoma
0.188	0.145	HOP-62	Non-small cell lung carcinoma	Lung	Carcinoma
0.215	0.174	SF-268	Glioblastoma	Brain	Glioblastoma
0.046	0.01	CEM-0	T-cell leukemia	Blood	Leukemia
0.071	0.043	GHOST CXCR4	Osteosarcoma	Bone	Sarcoma

0.074	0.05	Ishikawa	Endometrial adenocarcinoma	Uterus	Adenocarcinoma
0.089	0.07	ASPC1	Pancreatic ductal adenocarcinoma	Pancreas	Adenocarcinoma
0.184	0.165	SN12C	Renal carcinoma	Kidney	Carcinoma
0.177	0.168	UACC-62	Melanoma	Skin	Melanoma
0.19	0.181	PC-3	Prostate carcinoma	Prostate	Carcinoma
Native T-0901317 (1UPV/1UHL)					
Pa	**Pi**	**Cell line**	**Cell line in full name**	**Tissue**	**Tumor type**
0.755	0.002	THP-1	Acute monocytic leukemia	Blood	Leukemia
0.141	0.056	Melanoma cells	Melanoma	Skin	Melanoma
0.141	0.073	HOS-TE85	Osteosarcoma	Bone	Sarcoma
0.078	0.021	SK-ES1	Ewing sarcoma	Bone	Sarcoma
0.21	0.202	MKN-7	Gastric carcinoma	Stomach	Carcinoma

0.051	0.044	LUNG CANCER	NA	NA	NA
Native feroline (5ICK)					
Pa	**Pi**	**Cell line**	**Cell line in full name**	**Tissue**	**Tumor type**
0.516	0.042	NCI-H838	Non-small cell lung cancer. 3 stage	Lung	Carcinoma
0.448	0.056	SK-MEL-1	Metastatic melanoma	Skin	Melanoma
0.379	0.068	NALM-6	Adult B acute lymphoblastic leukemia	Haematopoietic and lymphoid tissue	Leukemia
0.341	0.091	CFPAC-1	Pancreatic carcinoma	Pancreas	Carcinoma
0.384	0.165	DMS-114	Lung carcinoma	Lung	Carcinoma
0.371	0.158	MDA-MB-453	Breast adenocarcinoma	Breast	Adenocarcinoma
0.217	0.013	SHP77	Small cell lung carcinoma	Lung	Carcinoma
0.273	0.074	MKN-7	Gastric carcinoma	Stomach	Carcinoma
0.22	0.053	St-4	Stomach carcinoma	Stomach	Carcinoma
0.266	0.1	CWR22R	Prostate carcinoma epithelial cell line	Prostate	Carcinoma
0.262	0.114	H9	T-lymphoid	Haematopoietic and lymphoid tissue	Leukemia
0.315	0.184	NCI-H187	Small cell lung carcinoma	Lung	Carcinoma

0.335	0.205	YAPC	Pancreatic carcinoma	Pancreas	Carcinoma
0.257	0.129	PC-6	Small cell lung carcinoma	Lung	Carcinoma
0.135	0.014	1A9	Ovarian adenocarcinoma	Ovarium	Adenocarcinoma
0.182	0.065	SW1573	Lung carcinoma	Lung	Carcinoma
0.262	0.151	8505C	Thyroid gland undifferentiated (anaplastic) carcinoma	Thyroid	Carcinoma
0.283	0.18	A2058	Melanoma	Skin	Melanoma
0.277	0.185	T98G	Glioblastoma	Brain	Carcinoma
0.104	0.023	Col2	Colon carcinoma	Colon	Carcinoma
0.101	0.025	Lu1	Lung carcinoma	Lung	Carcinoma
0.174	0.104	Bel-7402	Hepatoma	Liver	Hepatoma
0.267	0.206	PA-1	Ovarian carcinoma	Ovarium	Carcinoma
0.113	0.054	RXF 944	Renal carcinoma	Kidney	Carcinoma
0.057	0.034	L2987	Lung adenocarcinoma	Lung	Adenocarcinoma
0.125	0.113	Caov-3	High grade ovarian serous adenocarcinoma	Ovarium	Adenocarcinoma
0.175	0.166	HL-60	Promyeloblast leukemia	Haematopoietic and lymphoid tissue	Leukemia

0.036	0.027	1A9/ptx-10	Ovarian adenocarcinoma	Ovarium	Adenocarcinoma
0.032	0.03	1A9/ptx-22	Ovarian adenocarcinoma	Ovarium	Adenocarcinoma
Bergapten					
Pa	**Pi**	**Cell line**	**Cell line in full name**	**Tissue**	**Tumor type**
0.593	0.018	HL-60	Promyeloblast leukemia	Haematopoietic and lymphoid tissue	Leukemia
0.53	0.014	SK-MEL-28	Melanoma	Skin	Melanoma
0.491	0.024	NCI-H322M	Non-small cell lung carcinoma	Lung	Carcinoma
0.454	0.005	NALM-6	Adult B acute lymphoblastic leukemia	Haematopoietic and lymphoid tissue	Leukemia
0.453	0.025	T47D	Breast carcinoma	Breast	Carcinoma
0.45	0.028	NCI-H226	Non-small cell lung carcinoma	Lung	Carcinoma
0.416	0.032	Malme-3M	Melanoma	Skin	Melanoma
0.405	0.04	HeLa	Cervical adenocarcinoma	Cervix	Adenocarcinoma
0.399	0.04	SF-268	Glioblastoma	Brain	Glioblastoma
0.375	0.037	M14	Melanoma	Skin	Melanoma
0.358	0.049	SK-MEL-2	Melanoma	Skin	Melanoma

0.355	0.053	SN12C	Renal carcinoma	Kidney	Carcinoma
0.351	0.053	A498	Renal carcinoma	Kidney	Carcinoma
0.38	0.092	MCF7	Breast carcinoma	Breast	Carcinoma
0.352	0.07	NCI-H23	Non-small cell lung carcinoma	Lung	Carcinoma
0.321	0.074	K562	Erythroleukemia	Haematopoietic and lymphoid tissue	Leukemia
0.267	0.022	U-937	Histiocytic lymphoma	Haematopoietic and lymphoid tissue	Lymphoma
0.272	0.029	HT-1080	Fibrosarcoma	Soft tissue	Sarcoma
0.314	0.074	RPMI-8226	Multiple myeloma	Haematopoietic and lymphoid tissue	Myeloma
0.272	0.035	G-361	Melanoma	Skin	Melanoma
0.214	0.012	MeWo	Melanoma	Skin	Melanoma
0.272	0.075	MKN-7	Gastric carcinoma	Stomach	Carcinoma
0.286	0.091	NCI-H522	Non-small cell lung carcinoma	Lung	Carcinoma
0.283	0.094	SR	Adult immunoblastic lymphoma	Haematopoietic and lymphoid tissue	Lymphoma
0.284	0.103	CAKI-1	Kidney carcinoma	Kidney	Carcinoma
0.255	0.096	HCT-15	Colon adenocarcinoma	Colon	Adenocarcinoma

0.203	0.046	BGC-823	Stomach adenocarcinoma	Stomach	Adenocarcinoma
0.225	0.07	Bel-7402	Hepatoma	Liver	Hepatoma
0.236	0.097	SK-MEL-5	Melanoma	Skin	Melanoma
0.2	0.061	A-431	Epidermoid carcinoma	Skin	Carcinoma
0.235	0.103	MDA-MB-468	Breast adenocarcinoma	Breast	Adenocarcinoma
0.246	0.134	KM12	Colon adenocarcinoma	Colon	Adenocarcinoma
0.225	0.125	SK-OV-3	Ovarian carcinoma	Ovarium	Carcinoma
0.219	0.118	NCI-H460	Non-small cell lung carcinoma	Lung	Carcinoma
0.087	0.005	TCC-SUP	Bladder Carcinoma	Urinary tract	Carcinoma
0.119	0.039	COLO 320	Colon adenocarcinoma	Colon	Adenocarcinoma
0.143	0.065	U2OS	Osteosarcoma	Bone	Sarcoma
0.223	0.152	HOP-18	Non-small cell lung carcinoma	Lung	Carcinoma
0.218	0.156	786-0	Renal carcinoma	Kidney	Carcinoma
0.288	0.232	Hs 683	Oligodendroglioma	Brain	Glioma
0.1	0.043	Bcap37	Breast adenocarcinoma	Breast	Adenocarcinoma

0.096	0.065	SQ20B	Head and neck Squamous carcinoma	Head and neck	Carcinoma
0.21	0.181	BT-549	Breast ductal carcinoma	Breast	Carcinoma
0.062	0.045	HPAC	Pancreatic adenocarcinoma	Pancreas	Adenocarcinoma
0.014	0.004	SW-60	Colorectal carcinoma	Colon	Carcinoma
0.27	0.265	NCI-H187	Small cell lung carcinoma	Lung	Carcinoma
Obeticholic acid					
Pa	**Pi**	**Cell line**	**Cell line in full name**	**Tissue**	**Tumor type**
0.634	0.009	UO-31	Renal carcinoma	Kidney	Carcinoma
0.501	0.014	LOX IMVI	Melanoma	Skin	Melanoma
0.504	0.019	786-0	Renal carcinoma	Kidney	Carcinoma
0.447	0.028	HCC 2998	Colon adenocarcinoma	Colon	Adenocarcinoma
0.436	0.019	SF-539	Glioblastoma	Brain	Glioblastoma
0.438	0.025	U-251	Glioma	Brain	Glioma
0.457	0.05	SK-MEL-1	Metastatic melanoma	Skin	Melanoma

0.428	0.025	SN12C	Renal carcinoma	Kidney	Carcinoma
0.42	0.022	EKVX	Non-small cell lung carcinoma	Lung	Carcinoma
0.386	0.013	MKN-7	Gastric carcinoma	Stomach	Carcinoma
0.425	0.107	NCI-H838	Non-small cell lung cancer. 3 stage	Lung	Carcinoma
0.341	0.033	8505C	Thyroid gland undifferentiated (anaplastic) carcinoma	Thyroid	Carcinoma
0.348	0.05	HepG2	Hepatoblastoma	Liver	Hepatoblastoma
0.362	0.08	A2058	Melanoma	Skin	Melanoma
0.327	0.054	IGROV-1	Ovarian adenocarcinoma	Ovarium	Adenocarcinoma
0.343	0.075	NCI-H23	Non-small cell lung carcinoma	Lung	Carcinoma
0.32	0.053	OVCAR-3	Ovarian adenocarcinoma	Ovarium	Adenocarcinoma
0.327	0.061	T98G	Glioblastoma	Brain	Carcinoma
0.314	0.053	H9	T-lymphoid	Haematopoietic and lymphoid tissue	Leukemia
0.268	0.015	ADR5000	Childhood T acute lymphoblastic leukemia	Blood	Leukemia
0.395	0.145	DMS-114	Lung carcinoma	Lung	Carcinoma
0.319	0.071	OVCAR-8	Ovarian adenocarcinoma	Ovarium	Adenocarcinoma

0.318	0.071	SK-MEL-2	Melanoma	Skin	Melanoma
0.26	0.023	BGC-823	Stomach adenocarcinoma	Stomach	Adenocarcinoma
0.275	0.043	Bel-7402	Hepatoma	Liver	Hepatoma
0.244	0.028	St-4	Stomach carcinoma	Stomach	Carcinoma
0.297	0.089	HOP-92	Non-small cell lung carcinoma	Lung	Carcinoma
0.272	0.072	HOP-62	Non-small cell lung carcinoma	Lung	Carcinoma
0.33	0.159	NCI-H187	Small cell lung carcinoma	Lung	Carcinoma
0.233	0.082	Raji	B-lymphoblastic cells	Haematopoietic and lymphoid tissue	Leukemia
0.185	0.039	SHP77	Small cell lung carcinoma	Lung	Carcinoma
0.231	0.087	UACC-62	Melanoma	Skin	Melanoma
0.266	0.169	OVCAR-4	Ovarian adenocarcinoma	Ovarium	Adenocarcinoma
0.091	0.005	Leukemia cells	Leukemia	Blood	Leukemia
0.228	0.152	SF-268	Glioblastoma	Brain	Glioblastoma
0.228	0.157	TK-10	Renal carcinoma	Kidney	Carcinoma
0.194	0.144	M19-MEL	Melanoma	Skin	Melanoma

0.111	0.062	SW480	Colon adenocarcinoma	Colon	Adenocarcinoma
0.219	0.171	NCI-H522	Non-small cell lung carcinoma	Lung	Carcinoma
0.101	0.054	SGC-7901	Gastric carcinoma	Stomach	Carcinoma
0.21	0.168	SK-MEL-28	Melanoma	Skin	Melanoma
0.278	0.242	CFPAC-1	Pancreatic carcinoma	Pancreas	Carcinoma
0.313	0.28	MDA-MB-453	Breast adenocarcinoma	Breast	Adenocarcinoma
0.129	0.097	SMMC-7721	Hepatocellular carcinoma	Liver	Carcinoma
0.18	0.159	HL-60	Promyeloblast leukemia	Haematopoietic and lymphoid tissue	Leukemia
0.073	0.055	1A9	Ovarian adenocarcinoma	Ovarium	Adenocarcinoma
0.202	0.184	HOP-18	Non-small cell lung carcinoma	Lung	Carcinoma
0.068	0.055	FaDu	Hypopharyngeal squamous carcinoma	Upper aerodigestive tract	Carcinoma
0.045	0.033	R2	Prostate Carcinoma	Prostate	Carcinoma
0.055	0.05	NB-4	Acute promyelocytic leukemia	Haematopoietic and lymphoid tissue	Leukemia
0.005	0.002	RWLeu4	Chronic myelogenous leukemia	Blood	Leukemia
0.113	0.111	U-937	Histiocytic lymphoma	Haematopoietic and lymphoid tissue	Lymphoma

0.003	0.002	BEL-7404 TUMOR	NA	NA	NA
Resveratrol					
Pa	**Pi**	**Cell line**	**Cell line in full name**	**Tissue**	**Tumor type**
0.677	0.013	Hs 683	Oligodendroglioma	Brain	Glioma
0.526	0.008	HOP-18	Non-small cell lung carcinoma	Lung	Carcinoma
0.478	0.014	MDA-MB-453	Breast adenocarcinoma	Breast	Adenocarcinoma
0.419	0.002	HNO 97	Oral cavity squamous cell carcinoma	Head and neck	Carcinoma
0.446	0.067	MCF7	Breast carcinoma	Breast	Carcinoma
0.415	0.043	K562	Erythroleukemia	Haematopoietic and lymphoid tissue	Leukemia
0.366	0.003	MeWo	Melanoma	Skin	Melanoma
0.364	0.052	DU-145	Prostate carcinoma	Prostate	Carcinoma
0.344	0.049	NCI-H460	Non-small cell lung carcinoma	Lung	Carcinoma
0.335	0.049	SK-MEL-28	Melanoma	Skin	Melanoma
0.319	0.035	MKN-7	Gastric carcinoma	Stomach	Carcinoma
0.339	0.058	SF-268	Glioblastoma	Brain	Glioblastoma

0.336	0.055	RPMI-8226	Multiple myeloma	Haematopoietic and lymphoid tissue	Myeloma
0.319	0.039	Hs-578T	Invasive ductal breast carcinoma	Breast	Carcinoma
0.318	0.044	RXF 393	Renal carcinoma	Kidney	Carcinoma
0.368	0.103	NCI-H187	Small cell lung carcinoma	Lung	Carcinoma
0.332	0.068	PC-6	Small cell lung carcinoma	Lung	Carcinoma
0.327	0.064	KM12	Colon adenocarcinoma	Colon	Adenocarcinoma
0.28	0.021	Caco-2	Colon adenocarcinoma	Colon	Adenocarcinoma
0.296	0.037	LS174T	Colon adencocarcinoma	Colon	Adenocarcinoma
0.31	0.052	SK-MEL-5	Melanoma	Skin	Melanoma
0.302	0.058	MDA-MB-468	Breast adenocarcinoma	Breast	Adenocarcinoma
0.293	0.053	CWR22R	Prostate carcinoma epithelial cell line	Prostate	Carcinoma
0.31	0.08	SNB-75	Glioblastoma	Nervous system	Glioblastoma
0.304	0.074	NCI-H522	Non-small cell lung carcinoma	Lung	Carcinoma
0.312	0.092	OVCAR-5	Ovarian adenocarcinoma	Ovarium	Adenocarcinoma
0.289	0.072	IGROV-1	Ovarian adenocarcinoma	Ovarium	Adenocarcinoma

0.283	0.067	BT-549	Breast ductal carcinoma	Breast	Carcinoma
0.301	0.086	NCI-H226	Non-small cell lung carcinoma	Lung	Carcinoma
0.297	0.082	786-0	Renal carcinoma	Kidney	Carcinoma
0.276	0.063	NCI-H1299	Non-small cell lung carcinoma	Lung	Carcinoma
0.298	0.088	HOP-92	Non-small cell lung carcinoma	Lung	Carcinoma
0.283	0.074	M14	Melanoma	Skin	Melanoma
0.278	0.07	AGS	Gastric adenocarcinoma	Stomach	Adenocarcinoma
0.227	0.021	MAXF401	Breast carcinoma	Breast	Carcinoma
0.298	0.111	NCI-H322M	Non-small cell lung carcinoma	Lung	Carcinoma
0.268	0.082	U-251	Glioma	Brain	Glioma
0.272	0.088	T47D	Breast carcinoma	Breast	Carcinoma
0.276	0.093	UO-31	Renal carcinoma	Kidney	Carcinoma
0.255	0.076	SF-295	Glioblastoma	Brain	Glioblastoma
0.268	0.096	A498	Renal carcinoma	Kidney	Carcinoma
0.351	0.18	YAPC	Pancreatic carcinoma	Pancreas	Carcinoma

0.297	0.127	OVCAR-4	Ovarian adenocarcinoma	Ovarium	Adenocarcinoma
0.277	0.109	CAKI-1	Kidney carcinoma	Kidney	Carcinoma
0.272	0.105	SR	Adult immunoblastic lymphoma	Haematopoietic and lymphoid tissue	Lymphoma
0.17	0.011	SK-N-SH	Neuroblastoma	Nervous system	Neuroblastoma
0.179	0.023	A2780cisR	Cisplatin-resistant ovarian carcinoma	Ovarium	Carcinoma
0.17	0.015	COLO 320	Colon adenocarcinoma	Colon	Adenocarcinoma
0.335	0.183	NALM-6	Adult B acute lymphoblastic leukemia	Haematopoietic and lymphoid tissue	Leukemia
0.275	0.122	NCI-H23	Non-small cell lung carcinoma	Lung	Carcinoma
0.253	0.103	Malme-3M	Melanoma	Skin	Melanoma
0.147	0.004	CPT30	Nasopharyngeal carcinoma	Head and neck	Carcinoma
0.258	0.119	OVCAR-8	Ovarian adenocarcinoma	Ovarium	Adenocarcinoma
0.249	0.115	MDA-MB-231	Breast adenocarcinoma	Breast	Adenocarcinoma
0.205	0.074	St-4	Stomach carcinoma	Stomach	Carcinoma
0.233	0.103	ACHN	Papillary renal carcinoma	Kidney	Carcinoma
0.136	0.006	MEXF276L	Xenograft melanoma	Skin	Melanoma

0.136	0.006	MEXF989	Xenograft melanoma	Skin	Melanoma
0.136	0.006	PAXF546	Pancreatic carcinoma	Pancreas	Carcinoma
0.25	0.12	TK-10	Renal carcinoma	Kidney	Carcinoma
0.152	0.027	HuT78	T-lymphoma	Haematopoietic and lymphoid tissue	Leukemia
0.15	0.025	CEM/C2	Camptothecin-resistant CEM	Blood	Leukemia
0.161	0.037	MES-SA/DxS	Uterine corpus sarcoma	Uterus	Sarcoma
0.228	0.106	EKVX	Non-small cell lung carcinoma	Lung	Carcinoma
0.212	0.094	LOX IMVI	Melanoma	Skin	Melanoma
0.229	0.111	HCC 2998	Colon adenocarcinoma	Colon	Adenocarcinoma
0.119	0.003	TSGH 9201	Gastric carcinoma	Stomach	Carcinoma
0.155	0.046	LXFL 529	Non-small cell lung carcinoma	Lung	Carcinoma
0.141	0.033	RXF 944	Renal carcinoma	Kidney	Carcinoma
0.116	0.018	Bcap37	Breast adenocarcinoma	Breast	Adenocarcinoma
0.24	0.144	MOLT-4	Acute T-lymphoblastic leukemia	Blood	Leukemia
0.234	0.142	SK-MEL-2	Melanoma	Skin	Melanoma

0.218	0.128	HCT-15	Colon adenocarcinoma	Colon	Adenocarcinoma
0.209	0.121	OVCAR-3	Ovarian adenocarcinoma	Ovarium	Adenocarcinoma
0.098	0.013	UMSCC22B	Hypopharyngeal squamous cell carcinoma	Upper aerodigestive tract	Carcinoma
0.105	0.02	KETR3	Renal carcinoma	Kidney	Carcinoma
0.162	0.08	SHP77	Small cell lung carcinoma	Lung	Carcinoma
0.093	0.011	SISO	Uterine cervical adenocarcinoma	Cervix	Adenocarcinoma
0.122	0.041	MES-SA	Uterine corpus sarcoma	Uterus	Sarcoma
0.11	0.029	DAN-G	Human pancreas adenocarcinoma cell line	Pancreas	Adenocarcinoma
0.095	0.02	Human lung LXF 629L tumor	Lung adenocarcinoma	Lung	Adenocarcinoma
0.201	0.129	HOP-62	Non-small cell lung carcinoma	Lung	Carcinoma
0.083	0.016	SK-ES1	Ewing sarcoma	Bone	Sarcoma
0.164	0.099	Ramos	Burkitts lymhoma B-cells	Blood	Leukemia
0.139	0.075	U2OS	Osteosarcoma	Bone	Sarcoma
0.201	0.138	HL-60	Promyeloblast leukemia	Haematopoietic and lymphoid tissue	Leukemia
0.077	0.014	CEM-SS	Childhood T acute lymphoblastic leukemia	Blood	Leukemia

0.083	0.023	NB-4	Acute promyelocytic leukemia	Haematopoietic and lymphoid tissue	Leukemia
0.198	0.139	M19-MEL	Melanoma	Skin	Melanoma
0.064	0.005	Skut1B	Uterine corpus leiomyosarcoma	Ovarium	Sarcoma
0.194	0.138	UACC-62	Melanoma	Skin	Melanoma
0.084	0.03	Ishikawa	Endometrial adenocarcinoma	Uterus	Adenocarcinoma
0.265	0.212	U-266	Plasma cell myeloma	Blood	Myeloma
0.063	0.011	HA22T	Hepatocellular carcinoma	Liver	Carcinoma
0.163	0.111	SW1573	Lung carcinoma	Lung	Carcinoma
0.134	0.083	DLD-1	Colon adenocarcinoma	Colon	Adenocarcinoma
0.069	0.021	CCRF-HSB-2	Childhood T acute lymphoblastic leukemia	Blood	Leukemia
0.055	0.008	HONE1	Nasopharyngeal carcinoma	Head and neck	Carcinoma
0.117	0.071	NSCLC	Non-small cell lung carcinoma	Lung	Carcinoma
0.056	0.011	UCLA P-3	Lung carcinoma cell line	Lung	Carcinoma
0.064	0.021	UMUC3	Bladder Carcinoma	Urinary tract	Carcinoma
0.107	0.066	SW480	Colon adenocarcinoma	Colon	Adenocarcinoma

0.169	0.128	MIA PaCa-2	Pancreatic carcinoma	Pancreas	Carcinoma
0.156	0.116	PANC-1	Pancreatic carcinoma	Pancreas	Carcinoma
0.076	0.037	FaDu	Hypopharyngeal squamous carcinoma	Upper aerodigestive tract	Carcinoma
0.102	0.063	MKN-45	Gastric adenocarcinoma	Stomach	Adenocarcinoma
0.13	0.096	U-937/GTB	Histiocytic lymphoma	Blood	Lymphoma
0.084	0.051	SK-MEL	Melanoma	Skin	Melanoma
0.189	0.157	SN12C	Renal carcinoma	Kidney	Carcinoma
0.168	0.136	SF-539	Glioblastoma	Brain	Glioblastoma
0.088	0.057	ZR-75-1	Breast carcinoma	Breast	Carcinoma
0.066	0.035	SW1353	Bone chondrosarcoma	Bone	Sarcoma
0.057	0.027	TCC-SUP	Bladder Carcinoma	Urinary tract	Carcinoma
0.07	0.041	NCI-H417	Small cell lung carcinoma	Lung	Carcinoma
0.105	0.076	SNU-638	Gastric carcinoma	Stomach	Carcinoma
0.222	0.194	A549	Lung carcinoma	Lung	Carcinoma
0.055	0.027	OVCAR	Ovarian adenocarcinoma	Ovarium	Adenocarcinoma

0.065	0.04	HPAC	Pancreatic adenocarcinoma	Pancreas	Adenocarcinoma
0.22	0.197	NCI-H295R	Adrenal cortex carcinoma	Adrenal cortex	Carcinoma
0.059	0.036	TSGH	Glioma	Brain	Glioma
0.055	0.033	LUNG CANCER	NA	NA	NA
0.035	0.016	H322	Lung carcinoma	Lung	Carcinoma
0.062	0.044	U-87 MG	Lymphoblastic lymphoma	Blood	Lymphoma
0.114	0.096	LNCaP	Prostate carcinoma	Prostate	Carcinoma
0.03	0.012	KKLS	Gastric adenocarcinoma	Stomach	Adenocarcinoma
0.034	0.017	UACC-903	Malignant melanoma	Skin	Melanoma
0.032	0.016	SNB-7	Glioblastoma	Brain	Glioblastoma
0.092	0.079	SQ20B	Head and neck Squamous carcinoma	Head and neck	Carcinoma
0.117	0.104	BGC-823	Stomach adenocarcinoma	Stomach	Adenocarcinoma
0.103	0.091	BXPC-3	Pancreatic adenocarcinoma	Pancreas	Adenocarcinoma
0.046	0.035	HBL	Melanoma	Skin	Melanoma
0.104	0.093	Huh-7	Hepatocellular carcinoma	Liver	Carcinoma

0.028	0.018	GLC4	NA	NA	NA
0.017	0.011	H2981	Lung carcinoma	Lung	Carcinoma
0.021	0.015	NT2	Embryonal carcinoma	Germ cell. fibroblast	Carcinoma
0.016	0.011	ST-KM-1	Gastric carcinoma	Stomach	Carcinoma
0.012	0.007	SW-60	Colorectal carcinoma	Colon	Carcinoma
0.014	0.011	SPC-A4	Lung Adenocarcinoma	Lung	Adenocarcinoma
0.017	0.015	NCI-H46	Lung carcinoma	Lung	Carcinoma
Withaferin A					
Pa	**Pi**	**Cell line**	**Cell line in full name**	**Tissue**	**Tumor type**
0.924	0.003	SK-MEL-28	Melanoma	Skin	Melanoma
0.785	0.005	MDA-MB-231	Breast adenocarcinoma	Breast	Adenocarcinoma
0.523	0.047	MCF7	Breast carcinoma	Breast	Carcinoma
0.437	0.039	MDA-MB-453	Breast adenocarcinoma	Breast	Adenocarcinoma
0.347	0.046	U-251	Glioma	Brain	Glioma
0.35	0.053	HeLa	Cervical adenocarcinoma	Cervix	Adenocarcinoma

0.285	0.084	H9	T-lymphoid	Haematopoietic and lymphoid tissue	Leukemia
0.278	0.084	T47D	Breast carcinoma	Breast	Carcinoma
0.365	0.171	NCI-H838	Non-small cell lung cancer. 3 stage	Lung	Carcinoma
0.291	0.1	8505C	Thyroid gland undifferentiated (anaplastic) carcinoma	Thyroid	Carcinoma
0.335	0.15	NCI-H187	Small cell lung carcinoma	Lung	Carcinoma
0.356	0.174	SK-MEL-1	Metastatic melanoma	Skin	Melanoma
0.342	0.165	NALM-6	Adult B acute lymphoblastic leukemia	Haematopoietic and lymphoid tissue	Leukemia
0.296	0.131	A549	Lung carcinoma	Lung	Carcinoma
0.301	0.151	A2058	Melanoma	Skin	Melanoma
0.197	0.049	BGC-823	Stomach adenocarcinoma	Stomach	Adenocarcinoma
0.21	0.066	St-4	Stomach carcinoma	Stomach	Carcinoma
0.246	0.117	MKN-7	Gastric carcinoma	Stomach	Carcinoma
0.173	0.056	SHP77	Small cell lung carcinoma	Lung	Carcinoma
0.167	0.065	ADR5000	Childhood T acute lymphoblastic leukemia	Blood	Leukemia
0.104	0.019	Lu1	Lung carcinoma	Lung	Carcinoma

0.102	0.025	Col2	Colon carcinoma	Colon	Carcinoma
0.168	0.104	PANC-1	Pancreatic carcinoma	Pancreas	Carcinoma
0.122	0.066	SK-BR-3	Breast adenocarcinoma	Breast	Adenocarcinoma
0.071	0.058	1A9	Ovarian adenocarcinoma	Ovarium	Adenocarcinoma
0.248	0.244	RKO	Colon carcinoma	Colon	Carcinoma
0.032	0.031	1A9/ptx-22	Ovarian adenocarcinoma	Ovarium	Adenocarcinoma

5.3.11.8. Reacting atom (biotransformation) and Pharmacokinetis

Table S5.29: Prediction of reacting atom (Biotransformation) of C144 (AZD7762), Native Ligands, and Reference Standards.

Compound	**Structure**	**Pa**	**Pi**			
C144	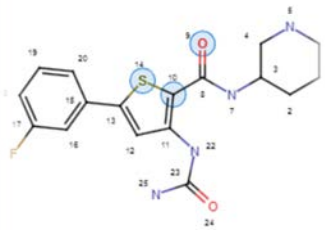	0.401	0.011	S-Oxidation Top-3		
				Atom	Rank	Delta P
				14	1	0.643
				9	2	-0.049
				10	3	-0.108

<table>
<tr>
<td></td>
<td> 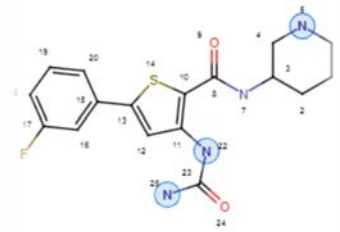 </td>
<td>0.295</td>
<td>0.090</td>
<td>N-Glucuronidation
Top-3<table><tr><th>Atom</th><th>Rank</th><th>Delta P</th></tr><tr><td>25</td><td>1</td><td>0.524</td></tr><tr><td>5</td><td>2</td><td>0.310</td></tr><tr><td>22</td><td>3</td><td>0.177</td></tr></table></td>
</tr>
<tr>
<td></td>
<td> 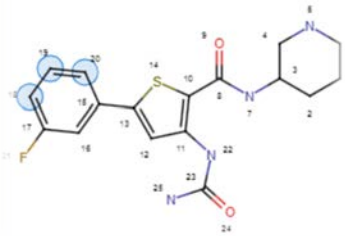 </td>
<td>0.371</td>
<td>0.167</td>
<td>Aromatic Hydroxylation
Top-3<table><tr><th>Atom</th><th>Rank</th><th>Delta P</th></tr><tr><td>19</td><td>1</td><td>0.421</td></tr><tr><td>18</td><td>2</td><td>0.285</td></tr><tr><td>20</td><td>3</td><td>0.079</td></tr></table></td>
</tr>
<tr>
<td></td>
<td></td>
<td>0.264</td>
<td>0.160</td>
<td>N-Oxidation</td>
</tr>
</table>

<table>
<tr><td></td><td> 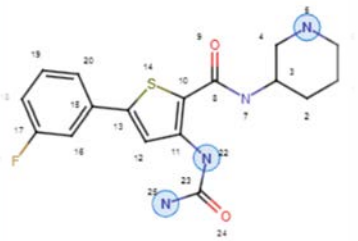 </td><td></td><td></td><td>Top-3<table><tr><th>Atom</th><th>Rank</th><th>Delta P</th></tr><tr><td>5</td><td>1</td><td>0.478</td></tr><tr><td>25</td><td>2</td><td>0.074</td></tr><tr><td>22</td><td>3</td><td>-0.018</td></tr></table></td></tr>
<tr><td></td><td> 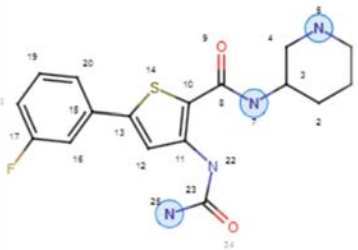 </td><td>0.215</td><td>0.135</td><td>N-Hydroxylation
Top-3<table><tr><th>Atom</th><th>Rank</th><th>Delta P</th></tr><tr><td>5</td><td>1</td><td>0.337</td></tr><tr><td>7</td><td>2</td><td>0.196</td></tr><tr><td>25</td><td>3</td><td>0.135</td></tr></table></td></tr>
<tr><td>Native T-0901317 (1UPV/1UHL)</td><td></td><td>0.385</td><td>0.023</td><td>N-Acetylation
Top-3<table><tr><th>Atom</th><th>Rank</th><th>Delta P</th></tr><tr><td>10</td><td>1</td><td>0.160</td></tr></table></td></tr>
</table>

	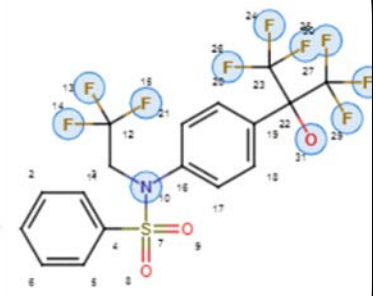			13	2	-0.009
				14	2	-0.009
	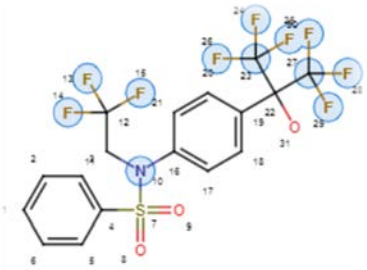	0.274	0.088	N-Hydroxylation Top-3		
				Atom	Rank	Delta P
				10	1	0.375
				13	2	-0.001
				14	2	-0.001

<table>
<tr><td rowspan="4"></td><td></td><td></td><td></td><td colspan="3"></td></tr>
<tr><td> 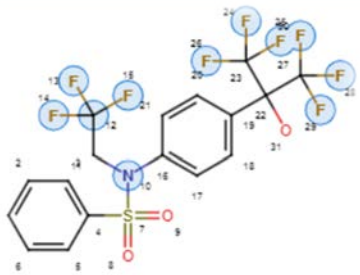 </td><td>0.296</td><td>0.133</td><td colspan="3">N-Oxidation
Top-3</td></tr>
<tr><td colspan="3"><table>
<tr><td>Atom</td><td>Rank</td><td>Delta P</td></tr>
<tr><td>10</td><td>1</td><td>0.200</td></tr>
<tr><td>13</td><td>2</td><td>-0.042</td></tr>
<tr><td>14</td><td>2</td><td>-0.042</td></tr>
</table></td></tr>
<tr><td> 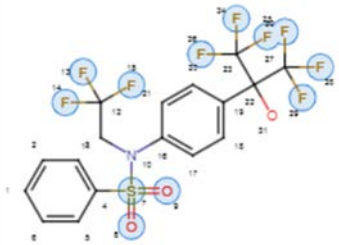 </td><td>0.162</td><td>0.077</td><td colspan="3">S-Oxidation
Top-3</td></tr>
<tr><td colspan="3"><table>
<tr><td>Atom</td><td>Rank</td><td>Delta P</td></tr>
<tr><td>7</td><td>1</td><td>0.518</td></tr>
<tr><td>8</td><td>2</td><td>-0.009</td></tr>
</table></td></tr>
</table>

				9	2	-0.009
	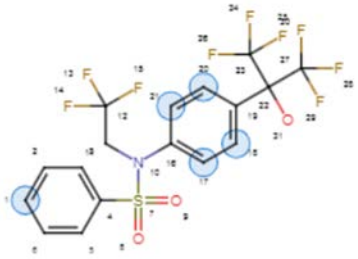	0.173	0.257	Glutathionation Top-3		
				Atom	Rank	Delta P
				18	1	0.384
				20	1	0.384
				17	2	0.286
	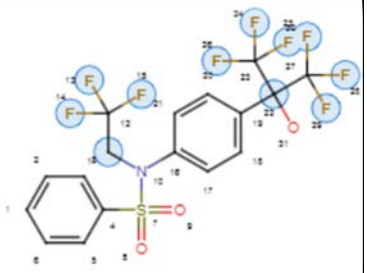	0.273	0.231	C-Oxidation Top-3		
				Atom	Rank	Delta P
				22	1	0.269
				13	2	0.009
				14	2	0.009

<table>
<tr><td></td><td></td><td></td><td></td><td></td></tr>
<tr><td rowspan="3">Native feroline (5ICK)</td><td rowspan="2"> 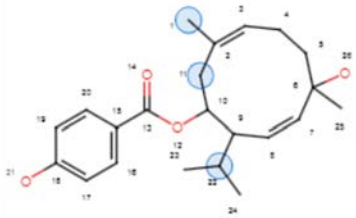 </td><td rowspan="2">0.158</td><td rowspan="2">0.408</td><td>Aliphatic Hydroxylation
Top-3
<table><tr><th>Atom</th><th>Rank</th><th>Delta P</th></tr><tr><td>1</td><td>1</td><td>0.617</td></tr><tr><td>22</td><td>2</td><td>0.560</td></tr><tr><td>11</td><td>3</td><td>0.255</td></tr></table></td></tr>
<tr><td> 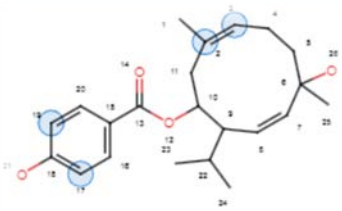 </td><td>Hydrogenation
Top-3
<table><tr><th>Atom</th><th>Rank</th><th>Delta P</th></tr><tr><td>2</td><td>1</td><td>0.454</td></tr><tr><td>3</td><td>2</td><td>0.410</td></tr><tr><td>17</td><td>3</td><td>0.284</td></tr></table></td></tr>
<tr><td></td><td>0.310</td><td>0.097</td><td>Epoxidation
Top-3</td></tr>
</table>

<table>
<tr>
<td></td>
<td> 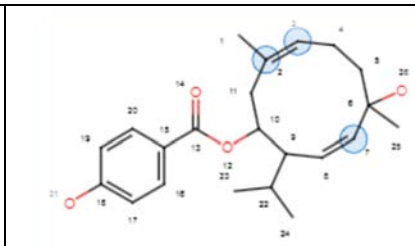 </td>
<td></td>
<td></td>
<td>
<table>
<tr><th>Atom</th><th>Rank</th><th>Delta P</th></tr>
<tr><td>2</td><td>1</td><td>0.654</td></tr>
<tr><td>3</td><td>2</td><td>0.535</td></tr>
<tr><td>7</td><td>3</td><td>0.349</td></tr>
</table>
</td>
</tr>
<tr>
<td></td>
<td> 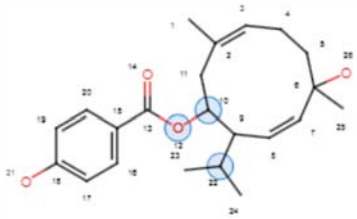 </td>
<td>0.296</td>
<td>0.171</td>
<td>
Dehydrogenation
Top-3
<table>
<tr><th>Atom</th><th>Rank</th><th>Delta P</th></tr>
<tr><td>10</td><td>1</td><td>0.542</td></tr>
<tr><td>22</td><td>2</td><td>0.43</td></tr>
<tr><td>12</td><td>3</td><td>0.419</td></tr>
</table>
</td>
</tr>
</table>

<table>
<tr><td></td><td></td><td></td><td></td><td colspan="3"></td></tr>
<tr><td></td><td> 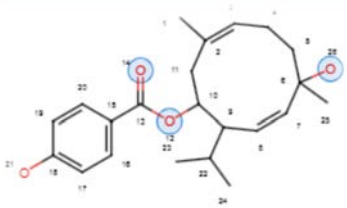 </td><td>0.087</td><td>0.095</td><td colspan="3">Glycination
Top-3</td></tr>
<tr><td></td><td></td><td></td><td></td><td>Atom</td><td>Rank</td><td>Delta P</td></tr>
<tr><td></td><td></td><td></td><td></td><td>14</td><td>1</td><td>0.061</td></tr>
<tr><td></td><td></td><td></td><td></td><td>12</td><td>2</td><td>0.026</td></tr>
<tr><td></td><td></td><td></td><td></td><td>26</td><td>3</td><td>-0.001</td></tr>
<tr><td></td><td></td><td></td><td></td><td colspan="3"></td></tr>
<tr><td>Bergapten</td><td> 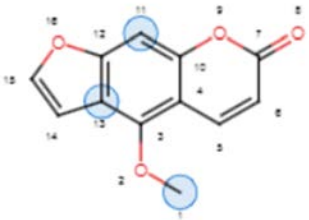 </td><td>0.719</td><td>0.035</td><td colspan="3">Aliphatic Hydroxylation
Top-3</td></tr>
<tr><td></td><td></td><td></td><td></td><td>Atom</td><td>Rank</td><td>Delta P</td></tr>
<tr><td></td><td></td><td></td><td></td><td>11</td><td>1</td><td>-0.111</td></tr>
<tr><td></td><td></td><td></td><td></td><td>13</td><td>2</td><td>-0.161</td></tr>
<tr><td></td><td></td><td></td><td></td><td>1</td><td>3</td><td>-0.290</td></tr>
</table>

<table>
<tr><td rowspan="11"></td><td></td><td></td><td></td><td colspan="3"></td></tr>
<tr><td rowspan="6"> 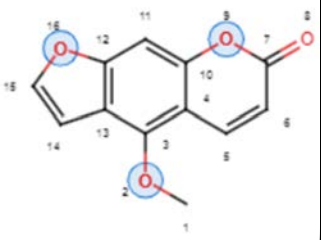 </td><td rowspan="6">0.648</td><td rowspan="6">0.013</td><td colspan="3">O-Dealkylation
Top-3</td></tr>
<tr><td>Atom</td><td>Rank</td><td>Delta P</td></tr>
<tr><td>2</td><td>1</td><td>0.843</td></tr>
<tr><td>16</td><td>2</td><td>-0.047</td></tr>
<tr><td>9</td><td>3</td><td>-0.068</td></tr>
<tr><td colspan="3"></td></tr>
<tr><td rowspan="5"> 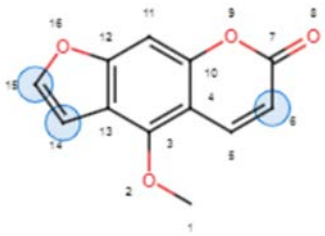 </td><td rowspan="5">0.547</td><td rowspan="5">0.044</td><td colspan="3">Hydrogenation
Top-3</td></tr>
<tr><td>Atom</td><td>Rank</td><td>Delta P</td></tr>
<tr><td>15</td><td>1</td><td>0.595</td></tr>
<tr><td>14</td><td>2</td><td>0.502</td></tr>
<tr><td>6</td><td>3</td><td>0.403</td></tr>
</table>

<table>
<tr><td></td><td></td><td></td><td></td><td></td></tr>
<tr><td></td><td> 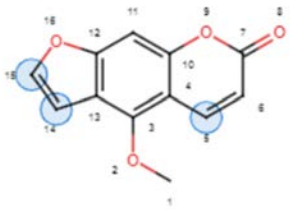 </td><td>0.476</td><td>0.045</td><td>Epoxidation
Top-3<table><tr><th>Atom</th><th>Rank</th><th>Delta P</th></tr><tr><td>14</td><td>1</td><td>0.439</td></tr><tr><td>15</td><td>2</td><td>0.424</td></tr><tr><td>5</td><td>3</td><td>-0.164</td></tr></table></td></tr>
<tr><td></td><td> 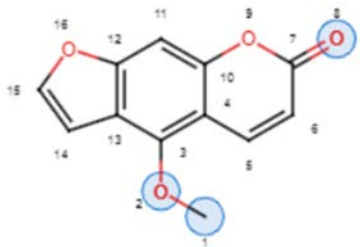 </td><td>0.270</td><td>0.165</td><td>O-Glucuronidation
Top-3<table><tr><th>Atom</th><th>Rank</th><th>Delta P</th></tr><tr><td>2</td><td>1</td><td>-0.045</td></tr></table></td></tr>
</table>

				8	2	-0.069
				1	3	-0.080
Obeticholic acid	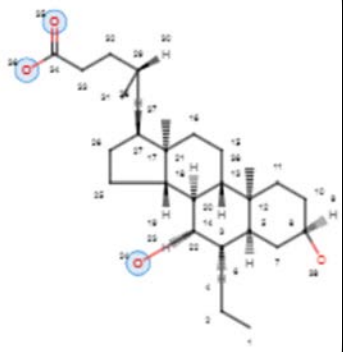	0.726	0.004	Glycination Top-3		
				Atom	Rank	Delta P
				36	1	0.294
				35	2	-0.034
				24	3	-0.140
		0.689	0.044	Aliphatic Hydroxylation Top-3		
				Atom	Rank	Delta P

<table>
<tr><td></td><td> 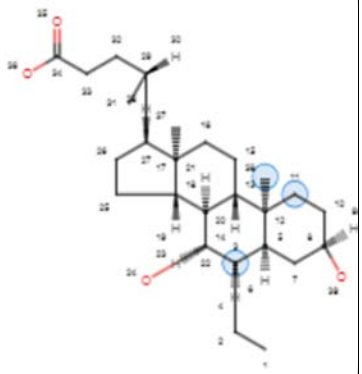 </td><td></td><td></td><td>3</td><td>1</td><td>0.609</td></tr>
<tr><td></td><td></td><td></td><td></td><td>11</td><td>2</td><td>0.317</td></tr>
<tr><td></td><td></td><td></td><td></td><td>38</td><td>3</td><td>0.316</td></tr>
<tr><td></td><td></td><td></td><td></td><td colspan="3"></td></tr>
<tr><td></td><td> 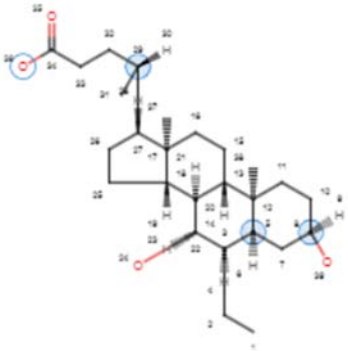 </td><td>0.647</td><td>0.024</td><td colspan="3">Hydrogenation
Top-3</td></tr>
<tr><td></td><td></td><td></td><td></td><td>Atom</td><td>Rank</td><td>Delta P</td></tr>
<tr><td></td><td></td><td></td><td></td><td>8</td><td>1</td><td>0.474</td></tr>
<tr><td></td><td></td><td></td><td></td><td>29</td><td>2</td><td>0.464</td></tr>
<tr><td></td><td></td><td></td><td></td><td>5</td><td>3</td><td>0.434</td></tr>
<tr><td></td><td></td><td></td><td></td><td colspan="3"></td></tr>
<tr><td></td><td></td><td>0.574</td><td>0.032</td><td colspan="3">Dehydrogenation</td></tr>
</table>

<table>
<tr>
<td></td>
<td> 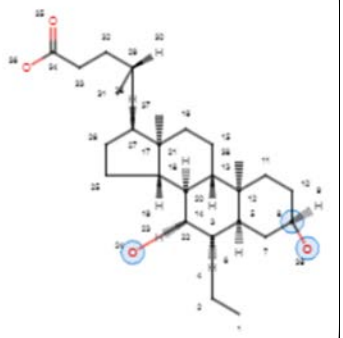 </td>
<td></td>
<td></td>
<td>Top-3
<table><tr><th>Atom</th><th>Rank</th><th>Delta P</th></tr><tr><td>8</td><td>1</td><td>0.565</td></tr><tr><td>39</td><td>2</td><td>0.563</td></tr><tr><td>24</td><td>3</td><td>0.537</td></tr></table></td>
</tr>
<tr>
<td></td>
<td> 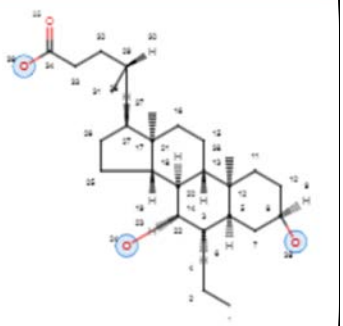 </td>
<td>0.513</td>
<td>0.070</td>
<td>O-Glucuronidation
Top-3
<table><tr><th>Atom</th><th>Rank</th><th>Delta P</th></tr><tr><td>39</td><td>1</td><td>0.360</td></tr><tr><td>36</td><td>2</td><td>0.284</td></tr><tr><td>24</td><td>3</td><td>0.134</td></tr></table></td>
</tr>
<tr>
<td></td>
<td></td>
<td>0.509</td>
<td>0.073</td>
<td>C-Oxidation
Top-3</td>
</tr>
</table>

<table>
<tr><td></td><td> 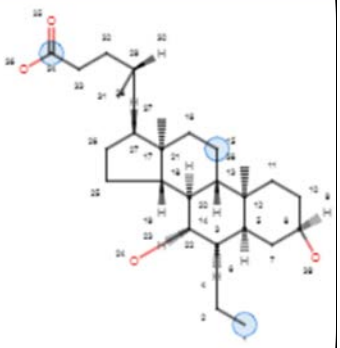 </td><td></td><td></td><td><table>
<tr><td>Atom</td><td>Rank</td><td>Delta P</td></tr>
<tr><td>34</td><td>1</td><td>0.151</td></tr>
<tr><td>1</td><td>2</td><td>0.134</td></tr>
<tr><td>15</td><td>3</td><td>0.089</td></tr>
</table></td></tr>
<tr><td></td><td> 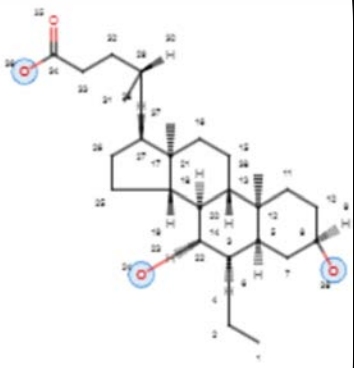 </td><td>0.238</td><td>0.130</td><td>O-Sulfation
Top-3<table>
<tr><td>Atom</td><td>Rank</td><td>Delta P</td></tr>
<tr><td>39</td><td>1</td><td>0.352</td></tr>
<tr><td>24</td><td>2</td><td>0.068</td></tr>
<tr><td>36</td><td>3</td><td>-0.020</td></tr>
</table></td></tr>
<tr><td>Resveratrol</td><td></td><td></td><td></td><td>O-Sulfation</td></tr>
</table>

<table>
<tr>
<td></td>
<td> 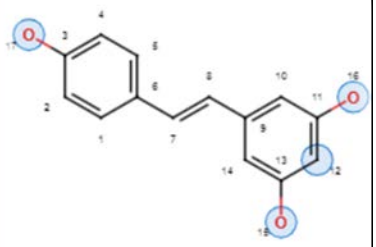 </td>
<td>0.956</td>
<td>0.005</td>
<td>Top-3
<table>
<tr><th>Atom</th><th>Rank</th><th>Delta P</th></tr>
<tr><td>15</td><td>1</td><td>0.877</td></tr>
<tr><td>16</td><td>1</td><td>0.877</td></tr>
<tr><td>17</td><td>2</td><td>0.872</td></tr>
</table>
</td>
</tr>
<tr>
<td></td>
<td> 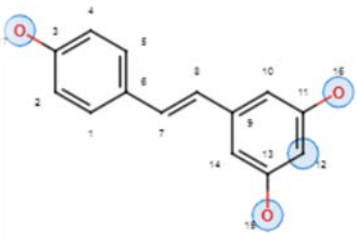 </td>
<td>0.943</td>
<td>0.005</td>
<td>O-Glucuronidation
Top-3
<table>
<tr><th>Atom</th><th>Rank</th><th>Delta P</th></tr>
<tr><td>15</td><td>1</td><td>0.927</td></tr>
<tr><td>16</td><td>1</td><td>0.927</td></tr>
<tr><td>17</td><td>2</td><td>0.920</td></tr>
</table>
</td>
</tr>
<tr>
<td></td>
<td></td>
<td>0.541</td>
<td>0.034</td>
<td>Methylation
Top-3</td>
</tr>
</table>

<table>
<tr><td></td><td> 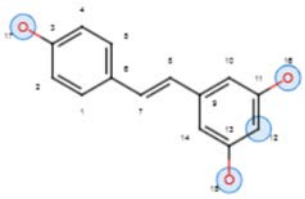 </td><td></td><td></td><td><table>
<tr><th>Atom</th><th>Rank</th><th>Delta P</th></tr>
<tr><td>15</td><td>1</td><td>0.865</td></tr>
<tr><td>16</td><td>1</td><td>0.865</td></tr>
<tr><td>17</td><td>2</td><td>0.804</td></tr>
</table></td></tr>
<tr><td></td><td> 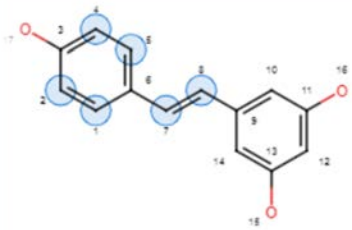 </td><td>0.338</td><td>0.095</td><td>Hydrogenation
Top-3<table>
<tr><th>Atom</th><th>Rank</th><th>Delta P</th></tr>
<tr><td>7</td><td>1</td><td>0.979</td></tr>
<tr><td>8</td><td>1</td><td>0.979</td></tr>
<tr><td>2</td><td>2</td><td>0.502</td></tr>
</table></td></tr>
</table>

<table>
<tr>
<td></td>
<td> 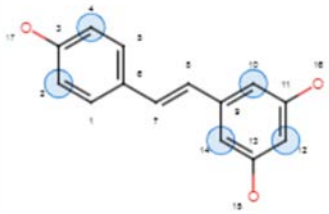 </td>
<td>0.387</td>
<td>0.158</td>
<td colspan="3">Aromatic Hydroxylation
Top-3</td>
</tr>
<tr>
<td></td>
<td></td>
<td></td>
<td></td>
<td>Atom</td>
<td>Rank</td>
<td>Delta P</td>
</tr>
<tr>
<td></td>
<td></td>
<td></td>
<td></td>
<td>12</td>
<td>1</td>
<td>0.8966</td>
</tr>
<tr>
<td></td>
<td></td>
<td></td>
<td></td>
<td>2</td>
<td>2</td>
<td>0.5443</td>
</tr>
<tr>
<td></td>
<td></td>
<td></td>
<td></td>
<td>4</td>
<td>2</td>
<td>0.5443</td>
</tr>
<tr>
<td></td>
<td></td>
<td></td>
<td></td>
<td colspan="3"></td>
</tr>
<tr>
<td></td>
<td> 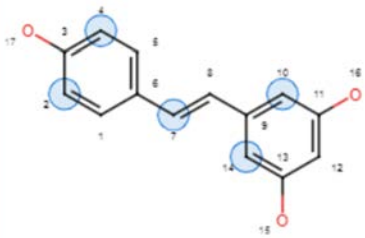 </td>
<td>0.326</td>
<td>0.117</td>
<td colspan="3">Glutathionation
Top-3</td>
</tr>
<tr>
<td></td>
<td></td>
<td></td>
<td></td>
<td>Atom</td>
<td>Rank</td>
<td>Delta P</td>
</tr>
</table>

				2	1	0.7557
				4	1	0.7557
				10	2	0.5579
	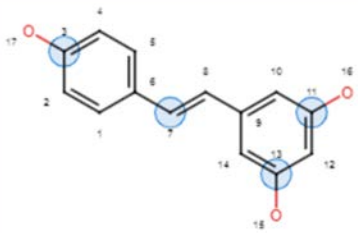	0.297	0.200	C-Oxidation Top-3		
				Atom	Rank	Delta P
				3	1	-0.289
				11	2	-0.345

				13	2	-0.345
	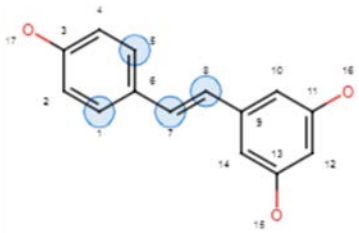	0.2332	0.1422	Epoxidation Top-3		
				Atom	Rank	Delta P
				7	1	0.944
				8	2	0.931
				1	3	0.000
	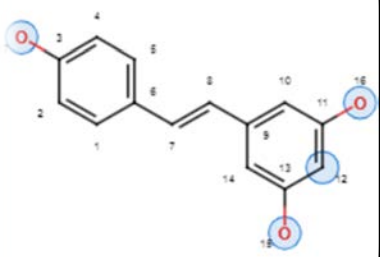	0.1077	0.0699	Glycination Top-3		
				Atom	Rank	Del

						ta P
				15	1	0.073
				16	1	0.073
				17	2	0.064
Withaferin A	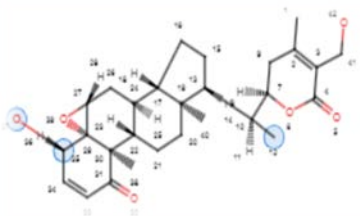	0.464	0.065	Dehydrogenation Top-3		
				Atom	Rank	Delta P
				37	1	0.497

				35	2	0.445
				12	3	0.283
	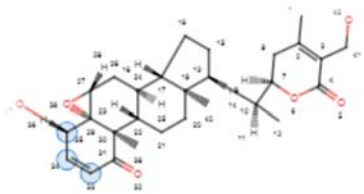	0.351	0.090	Hydrogenation Top-3		
				Atom	Rank	Delta P
				34	1	0.415
				33	2	0.380
				35	3	0.378
	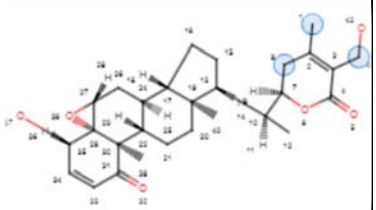	0.337	0.162	C-Oxidation Top-3		
				Atom	Rank	Delta P
				41	1	0.436
				9	2	0.094
				1	3	0.027

	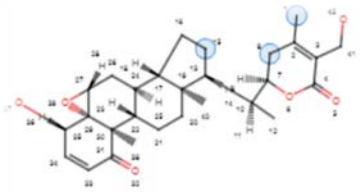	0.344	0.195	Aliphatic Hydroxylation Top-3

Atom	Rank	Delta P
1	1	0.451
9	2	0.432
15	3	0.320

Table S5.30: ADME prediction of C144 (AZD7762), Native Ligands, and Reference Standards *via* SwissADME and molinspiration.

Compounds	GI absorption	BBB permeant	P-gp substrate	CYP 1A2 inhibitor	No CYP 2C19 inhibitor	CYP 2C9 inhibitor	CYP 2D6 inhibitor	CYP 3A4 inhibitor	Log Kp (skin permeation) s.	LogP
C144	High	No	Yes	No	No	No	Yes	No	-6.91 cm/	1.97

Native T-0901317 (1UPV/1UHL)	Low	No	No	No	Yes	Yes	No	Yes	-5.73 cm/s	5.12
Native feroline (5ICK)	High	Yes	No	No	No	No	No	Yes	-5.30 cm/s	5.68
Bergapten	High	Yes	No	Yes	No	No	No	No	-6.25 cm/s	2.28
Obeticholic acid	High	No	Yes	No	No	No	No	No	-6.12 cm/s	5.22
Resveratrol	High	Yes	No	Yes	No	Yes	No	Yes	-5.47 cm/s	2.99
Withaferin A	Low	No	No	No	Yes	Yes	No	Yes	-5.73 cm/s	3.86

5.3.11.9. Molecular dynamics

5.3.11.9.1. Energy minimization

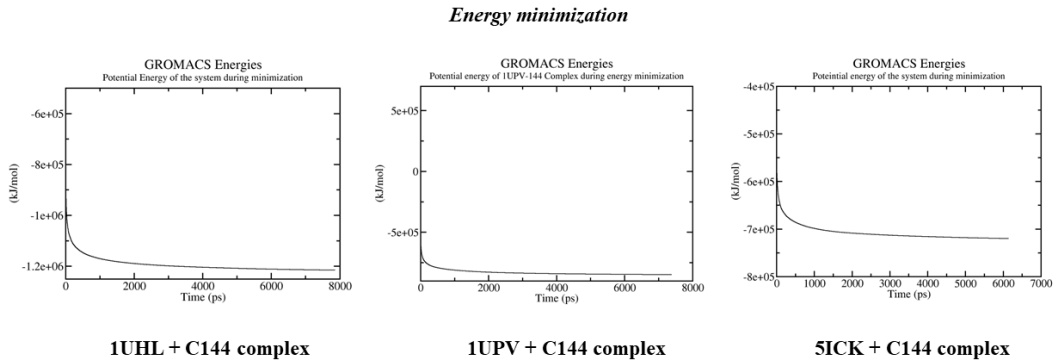

Figure S5.37: Energy minimization of 1UHL-C144, 1UPV-C144 and 5ICK complex system. Convergence occurring at approximately 6–7 ns for the 1UHL and 1UPV complexes, and at 5–6 ns for the 5ICK complex.

5.3.11.9.2. Equilibration

5.3.11.9.2.1 Temperature distribution during NVT equilibration:

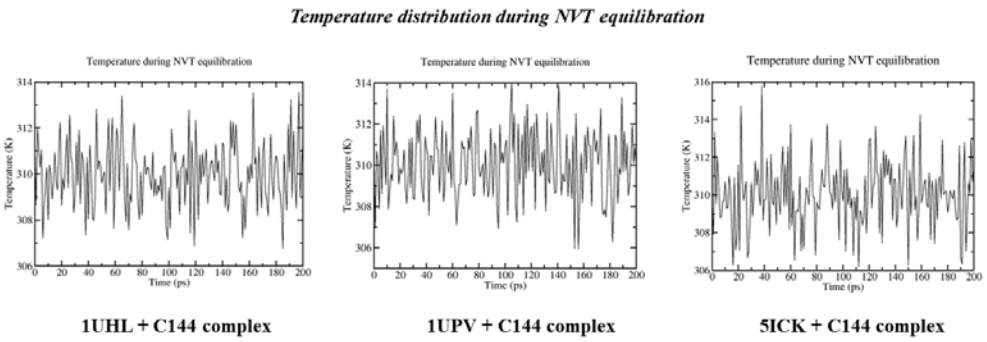

Figure S5.38: The temperature distribution during the NVT equilibration of 1UHL-C144, 1UPV-C144, and 5ICK-C144 complexes exhibited fluctuations around 310 K.

5.3.11.9.2.2. Pressure distribution during NPT equilibration

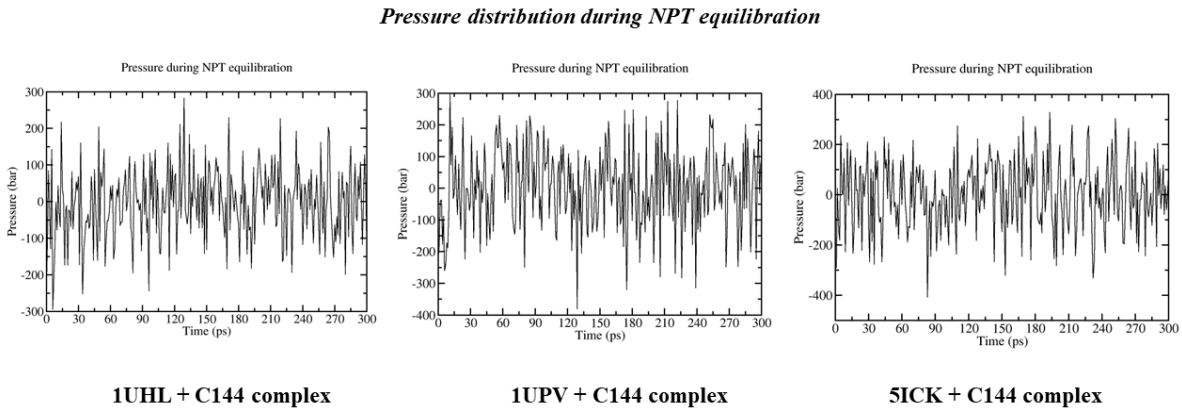

Figure S5.39: The pressure distribution during the NPT equilibration of all three complexes demonstrated substantial fluctuations around the reference value of 1 bar, which is characteristic of the expected behavior in NPT equilibration.

5.3.11.9.3. Density of the system during NPT equilibration

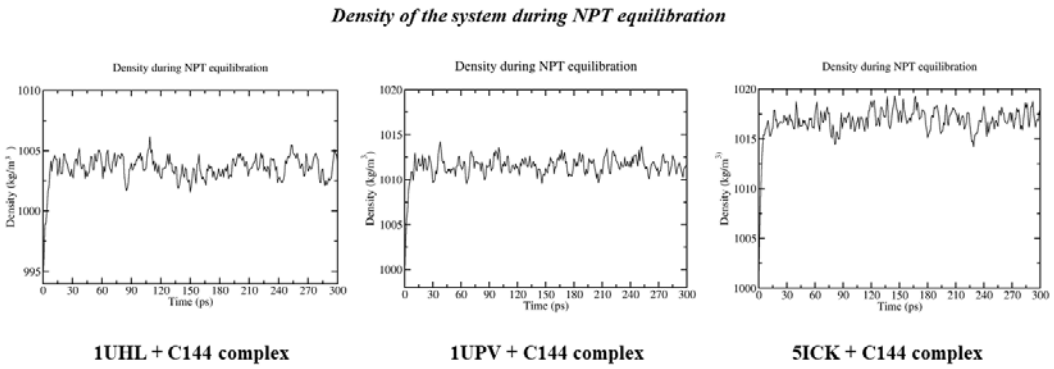

Figure S5.40:During the NPT equilibration of the 1UHL-C144, 1UPV-C144, and 5ICK-C144 complexes, the density values remained highly stable over time.

5.3.11.9.3. Outcomes of the molecular dynamics simulation

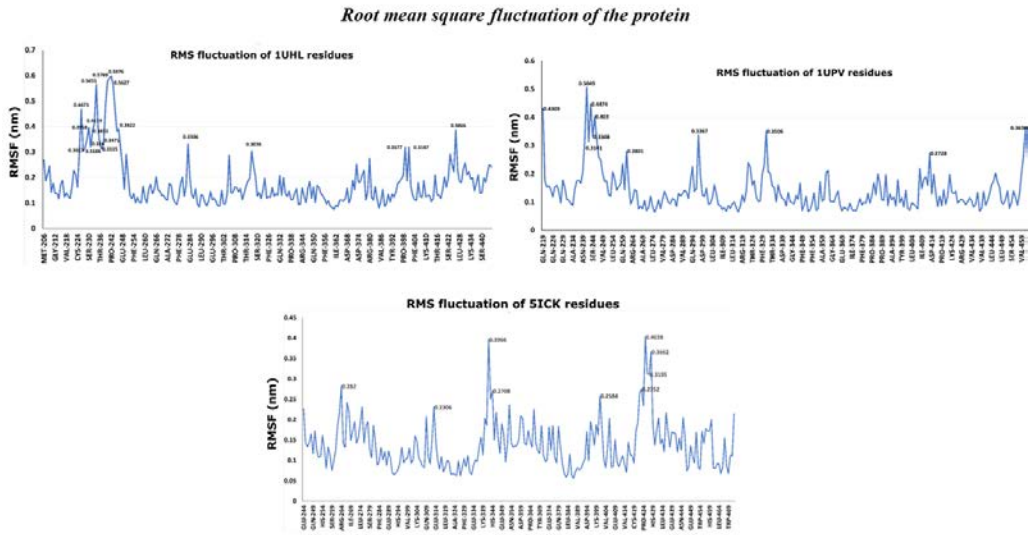

Figure S5.43: The left panel illustrates the residue root mean square fluctuations (RMSF) of the protein 1UHL, highlighting regions of localized flexibility with RMSF values exceeding 0.3 nm during the simulation. The right panel presents the residue RMSF of the protein 1UPV, showcasing localized flexibility in regions with RMSF values greater than 0.26 nm throughout the simulation. The bottom panel displays the residue RMSF of the protein 5ICK, indicating localized flexibility in regions where RMSF values surpass 0.2 nm during the simulation.

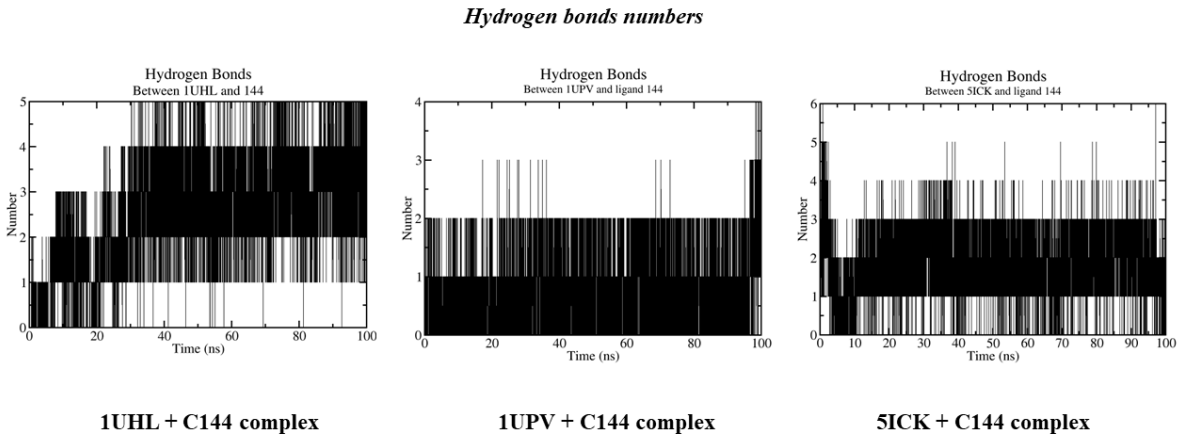

Figure S5.45: The number of hydrogen bonds formed during the simulation for the three complexes is illustrated as follows: **1UHL** (left panel), **1UPV** (middle panel), and **5ICK** (right panel).

Table S5.31: Hydrogen bonding percentage existences between 1UHL and ligand C144 (UNK446)

No	Donor	Donor_atom	Acceptor	Acceptor_atom	% Existence
1	UNK446	N2	PHE257	O	80.752
2	UNK446	N3	GLU301	OE1	45.985
3	UNK446	N3	MET298	O	42.986
4	UNK446	N	PHE254	O	42.626
5	UNK446	N	THR258	N	29.707
6	UNK446	N	PHE257	O	0.46

7	UNK446	N3	LEU260	O	0.42
8	UNK446	N3	SER264	OG	0.35
9	UNK446	N3	GLU301	OE2	0.11
10	HIS421	NE2	UNK446	O1	0.04
11	HIS421	NE2	UNK446	O	0.03
12	UNK446	N	THR258	OG1	0.03
13	UNK446	N1	PHE257	O	0.01

Table S5.32: Hydrogen bonding percentage existences between 1UPV and ligand C144 (UNK462)

No.	Donor	Donor atom	Acceptor	Acceptor atom	% Existence
1	UNK462	N1	THR316	OG1	35.346
2	UNK462	N3	GLU315	OE1	1.47
3	UNK462	N3	GLU281	OE2	1.02
4	THR316	OG1	UNK462	N	0.79
5	UNK462	N1	MET312	O	0.53
6	UNK462	N	MET312	O	0.02
7	UNK462	N3	GLU281	OE1	0.02
8	UNK462	N3	SER278	OG	0.01

Table S5.33: Hydrogen bonding percentage existences between 5ICK and ligand C144 (LIGC144)

No.	Donor	Donor Atom	Acceptor	Acceptor Atom	% Existence
1	LIGC144	N3	SER332	OG	57.134
2	LIGC144	N3	GLU349	OE2	19.958

3	LIGC144	N2	TYR369	OH	19.848
4	HIS294	NE2	LIGC144	O1	12.279
5	TYR369	OH	LIGC144	O	2.46
6	LIGC144	N3	SER332	O	1.75
7	LIGC144	N3	GLU349	OE1	0.23
8	TYR369	OH	LIGC144	N	0.14
9	LIGC144	N3	ILE335	O	0.14
10	LIGC144	N	GLU349	OE2	0.13
11	LIGC144	N1	SER332	OG	0.1
12	LIGC144	N	GLU349	OE1	0.04
13	LIGC144	N	LEU348	O	0.02
14	LIGC144	N	GLU349	N	0.02
15	TYR369	OH	LIGC144	N1	0.01
16	LIGC144	N	ILE362	O	0.01

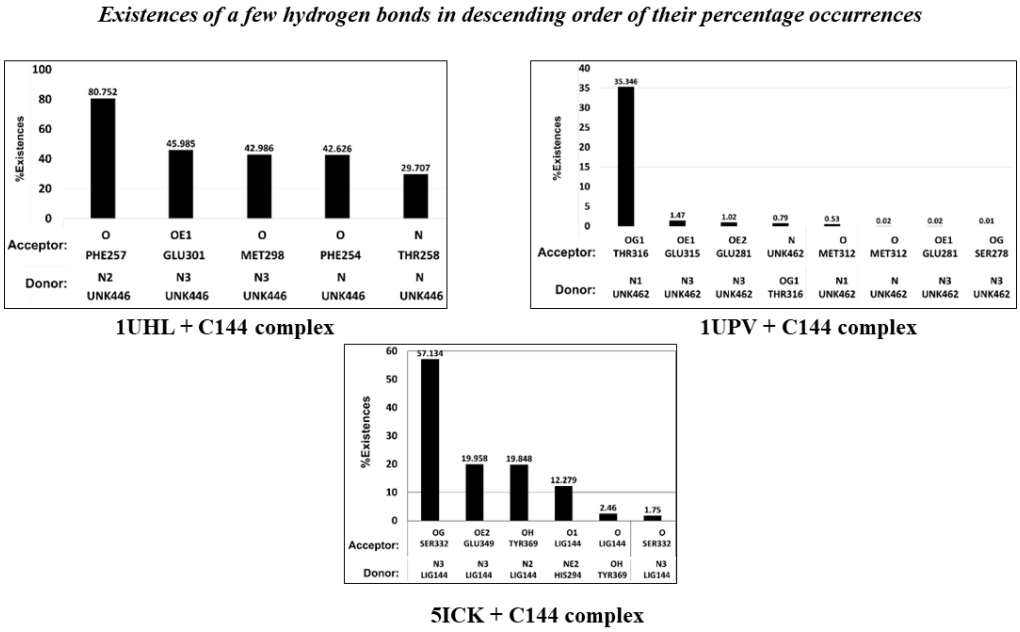

Figure S5.46: To enhance clarity, the most persistent hydrogen bond donors (HBD) and acceptors (HBA) for the 1UHL-C144 (left panel), 1UPV-C144 (right panel), and 5ICK-C144 (bottom panel) complexes are illustrated.

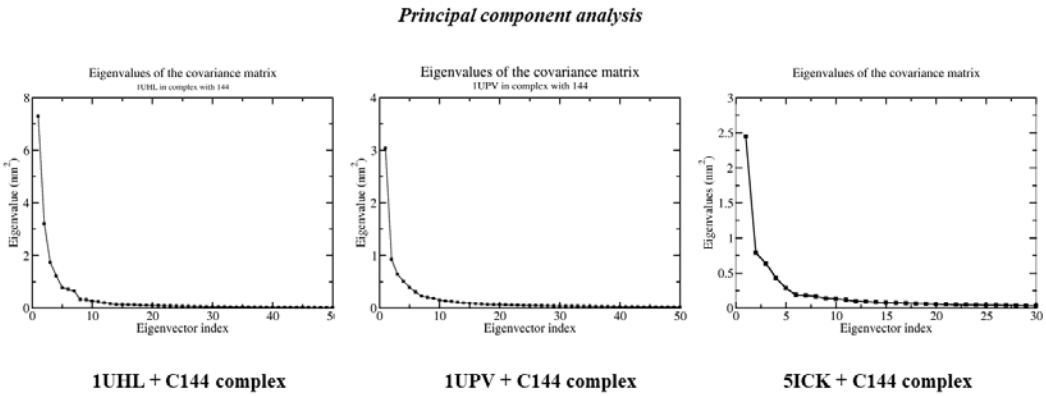

a.

Principal component analysis

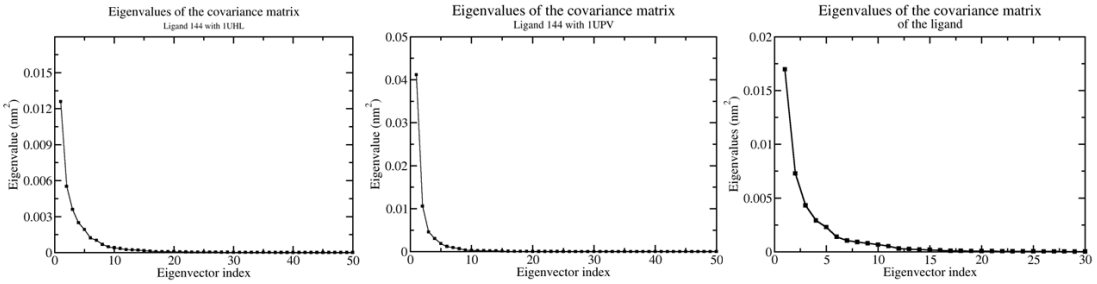

1UHL + C144 complex **1UPV + C144 complex** **5ICK + C144 complex**

b.

Principal component analysis

2D projection of trajectory (proteins)

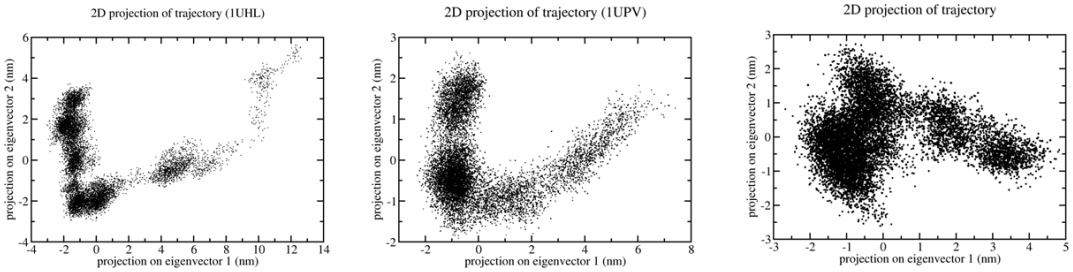

1UHL + C144 complex **1UPV + C144 complex** **5ICK + C144 complex**

c.

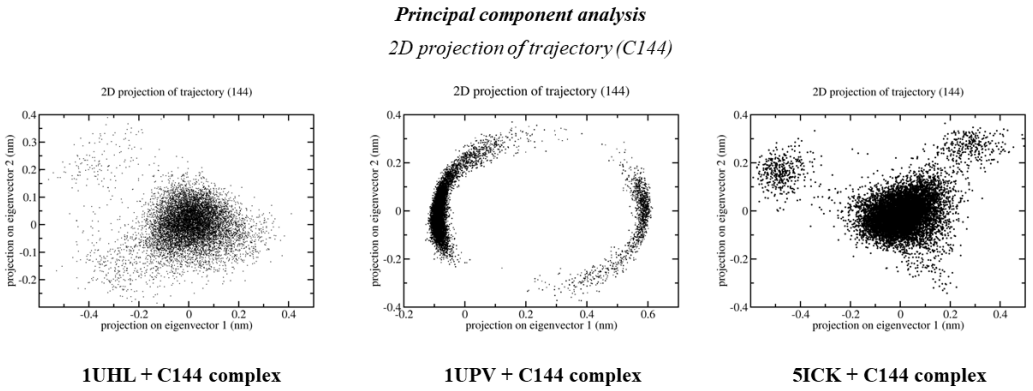

d.

Figure S5.47 (a-d): **Principal Component Analysis (PCA) of 1UHL, 1UPV, and 5ICK in complex with ligand C144 during the simulations.** (**a**) Over 30 eigenvectors derived from the covariance matrix of the backbone of 1UHL, 1UPV, and 5ICK demonstrate values exceeding zero. (**b**) Similarly, more than 30 eigenvectors from the covariance matrix of the heavy atoms of ligand C144 also exhibit values greater than zero. (**c**) The projection of the first principal component (PC1) onto the second principal component (PC2) within the essential subspace allows for the estimation of collective motions of 1UHL, 1UPV, and 5ICK. (**d**) The projection of PC1 onto PC2 within the essential subspace facilitates the assessment of collective motions of ligand C144.

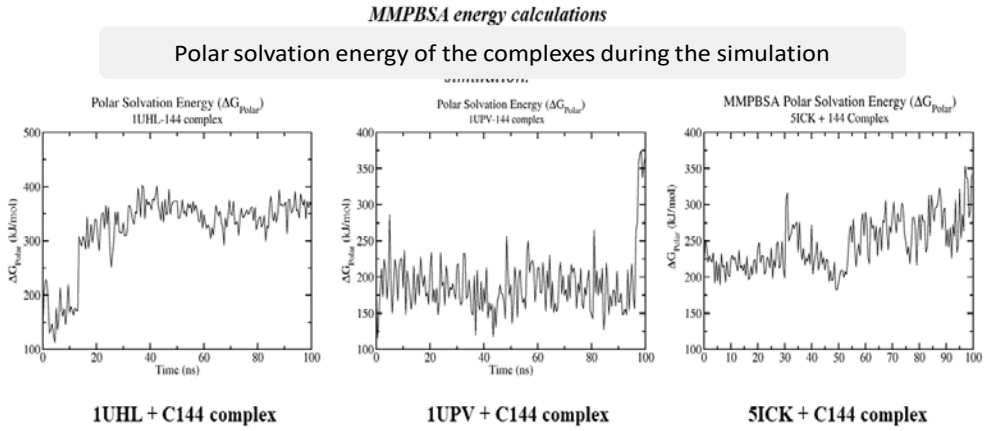

Figure S5.49: Polar solvation energy between 1UHL-C144. 1UPV-C144 and 5ICK-C144 during the simulation.

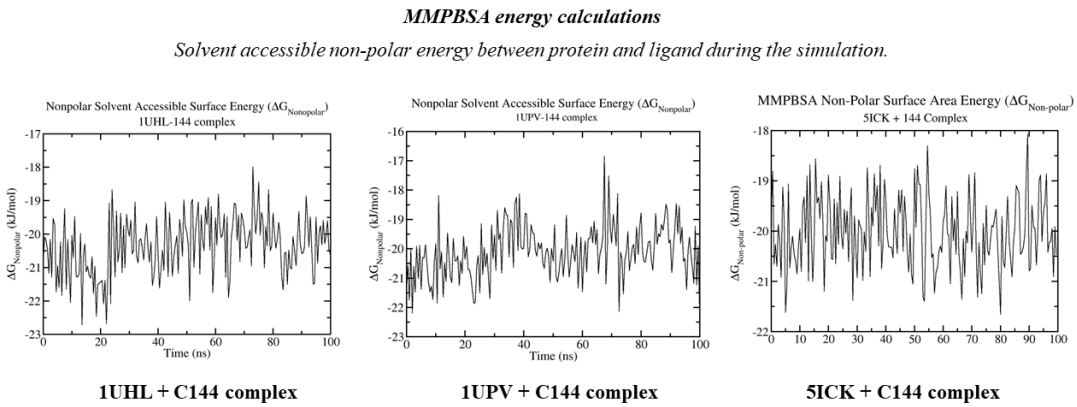

Figure S5.50: Solvent accessible non-polar energy between protein (1UHL, 1UPV and 5ICK) and ligand during the simulation

Table S5.34: Average energetic contributions of the 1UHL–C144complex during the simulation.

Energy terms		**Energies (kJ mol^{-1})**
MM	ΔG_{VDW}	–213.68 ± 1.084
	$\Delta G_{Electrostatic}$	–348.228 ± 4.614
PB	ΔG_{Polar}	321.94 ± 4.657
SA	$\Delta G_{Non\text{-}polar}$	–20.358 ± 0.061
Binding Free Energy	**ΔG_{Bind}**	**–260.32 ± 1.627**

Table S5.35: Average energetic contributions of the 1UPV–C144complex during the simulation.

Energy terms		**Energies (kJ mol^{-1})**
MM	ΔG_{VDW}	–189.321 ± 0.68
	$\Delta G_{Electrostatic}$	–212.331 ± 2.358
PB	ΔG_{Polar}	190.058 ± 2.951
SA	$\Delta G_{Non\text{-}polar}$	–20.103 ± 0.064
Binding Free Energy	**ΔG_{Bind}**	**–231.697 ± 1.47**

Table S5.36: Average energetic contributions of the 5ICK–C144complex during the simulation.

Energy terms		**Energies (kJ mol^{-1})**
MM	ΔG_{VDW}	–210.073 ± 0.842
	$\Delta G_{Electrostatic}$	–427.562 ± 1.993
PB	ΔG_{Polar}	245.451 ± 2.505
SA	$\Delta G_{Non\text{-}polar}$	–20.022 ± 0.05
Binding Free Energy	**ΔG_{Bind}**	**–412.201± 1.398**

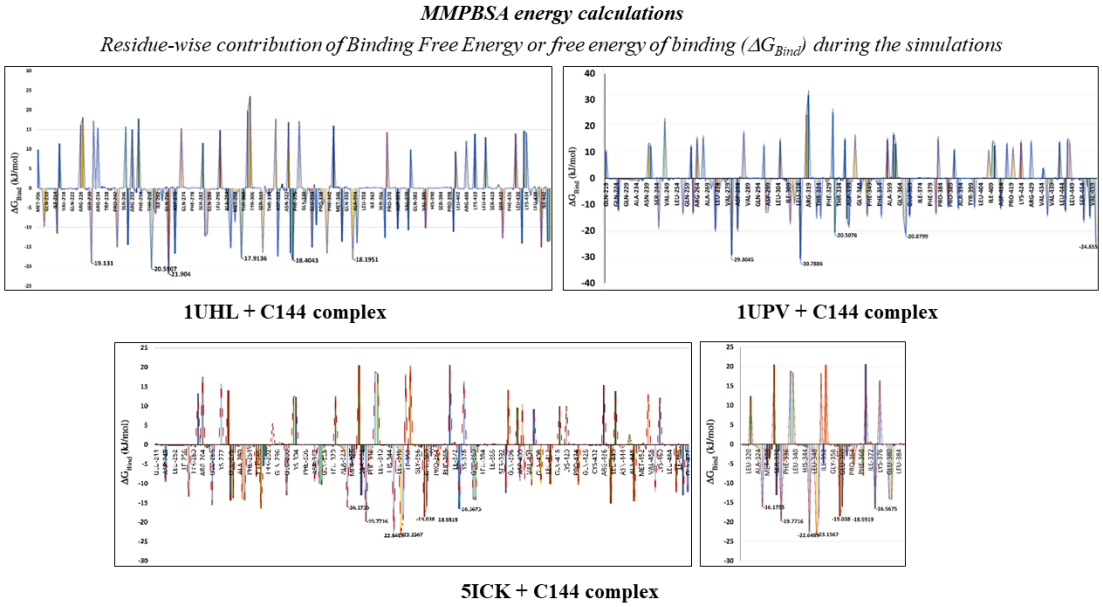

Figure S5.53: Residue-wise contribution of Binding Free Energy or free energy of binding (ΔG_{Bind}) during the simulation of 1UHL–C144, 1UPV–C144 and 5ICK-C144 complexes.

5.3.11.9. Shermo online

Table S5.37: Illustrating the thermodynamic properties of C144 at varying temperatures (100 K to 310 K) under constant pressure (1 atm).

T(K)	P(atm)	Ucorr	Hcorr	Gcorr	U	H	G
100.000	1.000	220.960	221.159	210.620	-1526.764713	-1526.764397	1526.781191
110.000	1.000	221.336	221.555	209.547	-1526.764114	-1526.763765	1526.782900
120.000	1.000	221.738	221.977	208.437	-1526.763473	-1526.763093	1526.784669

130.000	1.000	222.166	222.424	207.291	-1526.762791	-1526.762379	1526.786496
140.000	1.000	222.620	222.899	206.109	-1526.762067	-1526.761624	1526.788379
150.000	1.000	223.101	223.399	204.893	-1526.761301	-1526.760826	1526.790318
160.000	1.000	223.608	223.926	203.642	-1526.760494	-1526.759987	1526.792311
170.000	1.000	224.141	224.479	202.357	-1526.759643	-1526.759105	1526.794358
180.000	1.000	224.701	225.059	201.039	-1526.758751	-1526.758181	1526.796458
190.000	1.000	225.288	225.665	199.689	-1526.757816	-1526.757214	1526.798611
200.000	1.000	225.901	226.299	198.305	-1526.756838	-1526.756205	1526.800816
210.000	1.000	226.542	226.959	196.889	-1526.755818	-1526.755152	1526.803072
220.000	1.000	227.209	227.647	195.441	-1526.754754	-1526.754057	1526.805379
230.000	1.000	227.904	228.361	193.962	-1526.753647	-1526.752919	1526.807738
240.000	1.000	228.626	229.102	192.450	-1526.752497	-1526.751737	1526.810146
250.000	1.000	229.374	229.871	190.907	-1526.751304	-1526.750512	1526.812605

260.000	1.000	230.150	230.667	189.333	-1526.750068	-1526.749244	1526.815114
270.000	1.000	230.953	231.490	187.728	-1526.748788	-1526.747933	1526.817672
280.000	1.000	231.783	232.339	186.092	-1526.747465	-1526.746579	1526.820279
290.000	1.000	232.640	233.216	184.424	-1526.746100	-1526.745182	1526.822936
300.000	1.000	233.523	234.120	182.727	-1526.744692	-1526.743742	1526.825642
310.000	1.000	234.434	235.050	180.998	-1526.743241	-1526.742260	1526.828396

Unit of Ucorr, Hcorr and Gcorr is kcal/mol, unit of U, H and G is a.u. Where, Ucorr, Hcorr, Gcorr: Corrected values of internal energy, enthalpy, and Gibbs free energy, accounting for zero-point and thermal contributions.

Table S5.38: Displaying the thermodynamic properties of Compound 144 at various temperatures (100 K to 310 K) under constant pressure (1 atm).

T(K)	P(atm)	S	CV	CP	$q(V=0)/N_A$	$q(bot)/N_A$
100.000	1.000	105.386	36.339	38.327	3.932252E+017	0.000000E+000
110.000	1.000	109.159	38.909	40.897	1.338381E+018	0.000000E+000
120.000	1.000	112.828	41.501	43.488	4.341139E+018	0.000000E+000
130.000	1.000	116.412	44.110	46.097	1.351931E+019	0.000000E+000
140.000	1.000	119.924	46.732	48.720	4.066260E+019	0.000000E+000

150.000	1.000	123.375	49.368	51.355	1.186818E+020	0.000000E+000
160.000	1.000	126.774	52.014	54.001	3.374407E+020	6.985402E-279
170.000	1.000	130.128	54.670	56.658	9.375967E+020	7.205389E-261
180.000	1.000	133.441	57.337	59.325	2.552652E+021	8.130129E-245
190.000	1.000	136.721	60.014	62.001	6.824868E+021	2.045129E-230
200.000	1.000	139.969	62.701	64.688	1.795346E+022	2.027419E-217
210.000	1.000	143.191	65.396	67.383	4.654359E+022	1.256300E-205
220.000	1.000	146.388	68.098	70.085	1.190799E+023	7.097525E-195
230.000	1.000	149.563	70.806	72.793	3.010323E+023	4.993844E-185
240.000	1.000	152.718	73.518	75.505	7.527390E+023	5.675103E-176
250.000	1.000	155.855	76.230	78.217	1.863530E+024	1.295903E-167
260.000	1.000	158.976	78.940	80.927	4.571343E+024	7.153221E-160
270.000	1.000	162.081	81.645	83.632	1.111933E+025	1.117247E-152
280.000	1.000	165.171	84.341	86.329	2.683594E+025	5.651216E-146
290.000	1.000	168.247	87.026	89.013	6.429856E+025	1.039981E-139
300.000	1.000	171.310	89.695	91.682	1.530197E+026	7.702128E-134
310.000	1.000	174.360	92.346	94.333	3.618637E+026	2.506444E-128

***T(K)**: Temperature in Kelvin, **P(atm)**: Pressure in atmospheres, **S**: Entropy of the system, **CV**: Heat capacity at constant volume, **CP**: Heat capacity at constant pressure, **q**: Total heat energy absorbed or released by the system, **(V=0)**: Volume constant, N_A: Avogadro's number, (bot): the ground or lowest energy state.*

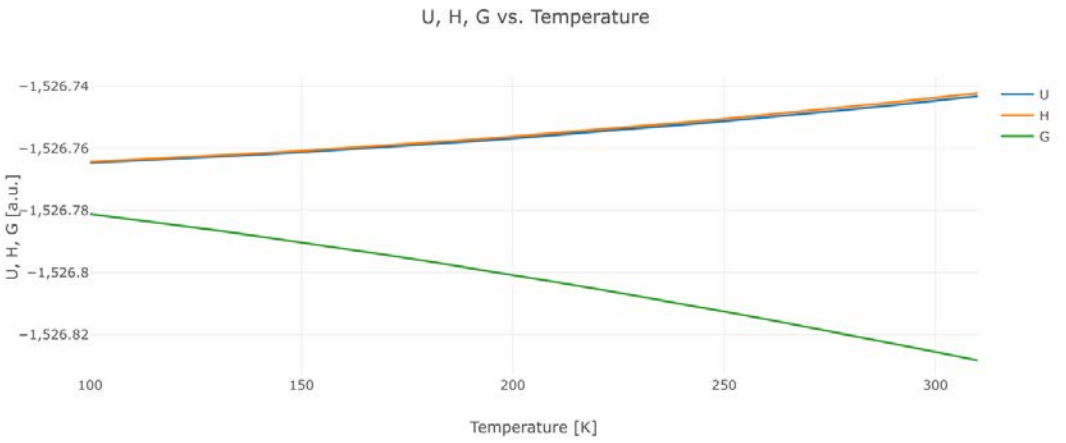

Figure S5.55a: Variation of Internal Energy (U), Enthalpy (H), and Gibbs Free Energy (G) with Temperature.

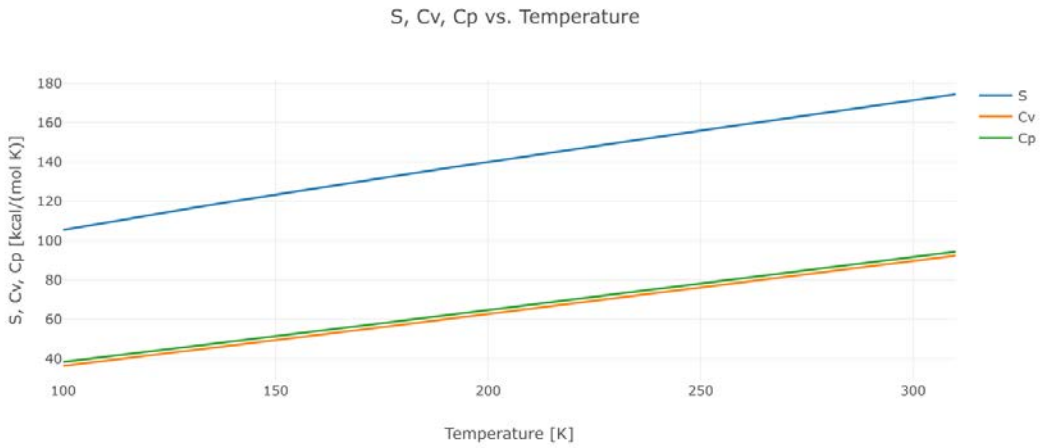

Figure S5.55b: Graph depicting the relationship between entropy (S), heat capacity at constant volume (Cv), and heat capacity at constant pressure (Cp) as functions of temperature, ranging from 100 K to 310 K.

Chapter 6

Integrated Computational, Synthetic and *in vitro* Evaluation of Minimally Explored Laboratory Compounds

Every day, thousands of compounds are synthesized in laboratories and industries, yet many remain unused and set aside. These underutilized molecules represent a valuable untapped resource. By revisiting them with innovative strategies, researchers can explore opportunities for repurposing or re-evaluating their potential. Such an approach not only reduces the need for new syntheses but also conserves energy, reagents, and time, while simultaneously minimizing chemical waste. The present study explores such underutilized compounds, focusing specifically on bromophenols, which are known to possess diverse bioactivities. A thorough computational assessment was carried out against targets related to antibacterial, antifungal, and antioxidant activities, leading to the identification of a top hit compound. This compound was then synthesized using tetrabutylammonium tribromide (TBATB), a recognized green brominating agent in organic synthesis. To further validate its potential, in vitro evaluations were performed against selected microbial strains and antioxidant assays, followed by extensive quantum calculations and additional computational studies.

6.1. Introduction

Every day, thousands of chemical compounds are synthesized across research laboratories and industrial facilities worldwide. While many of these compounds are designed to fulfil specific objectives such as testing a hypothesis, developing a formulation, or targeting a particular biological activity a large number end up shelved, left unused once their immediate purpose is served or if initial results are inconclusive. Over time, these compounds accumulate, representing a significant underutilized resource [1,2]. From a green chemistry perspective, this scenario presents both a challenge and an opportunity. One of the core tenets of green chemistry is the efficient use of resources and the minimization of waste. Allowing potentially valuable compounds to sit unused runs counter to these goals. Instead, by repurposing or re-evaluating these previously synthesized molecules, researchers can reduce the need for new syntheses, thereby saving energy, reagents, and time, and minimizing chemical waste [3,4]. Furthermore, revisiting such compounds with modern computational tools, high-throughput screening, and biological assays can lead to new applications, such as the discovery of new drug leads, the development of catalysts or materials, as well as opportunities for repurposing without the environmental and economic cost of starting from scratch. In this way, the reuse and re-optimization of existing chemical libraries aligns perfectly with the principles of green chemistry promoting sustainability, resource efficiency, and innovation through conservation [5,6].

Scientific Perspective: From a research point of view, many of these "underutilized" compounds may possess unexplored properties. What may have been irrelevant for one project might be highly relevant for another. With advances in cheminformatics, computational docking, and AI-based screening, researchers can now reassess existing compounds for activity against new biological targets, disease models, or industrial applications. Computer-Aided Drug Design (CADD) plays a crucial role in this process by enabling *in silico* evaluation before experimental testing. This reduces the need for redundant synthesis and excessive wet-lab screening, thereby lowering solvent and reagent consumption. By prioritizing the most promising candidates through computational pipelines, CADD aligns seamlessly with the principles of green

chemistry such as waste prevention, energy efficiency, and resource optimization. In this way, digital screening not only enhances scientific productivity but also ensures that the exploration of compound libraries contributes to both sustainable research practices and accelerated innovation. [7]. *Economic Perspective:* Every synthesized compound represents invested resources. Reusing existing molecules minimizes redundancy, reduces R&D costs, and provides affordable alternatives for startups, academic groups, and sectors with limited funding, while lessening reliance on commercial suppliers [8]. *Environmental (Green Chemistry) Perspective*: Discarded compounds translate into wasted reagents, solvents, and energy. Repurposing them not only reduces chemical waste but also supports atom economy and greener practices, directly aligning with the principles of waste prevention, resource efficiency, energy-conscious design, and safer chemistry [9]. *Social Perspective:* In the face of urgent global challenges due to drug resistance and disease mutations, it is both ethical and strategic to extract maximum value from existing compounds. What once seemed irrelevant could emerge as a solution for drug resistance, climate adaptation, or other critical issues, particularly benefiting regions with limited synthetic infrastructure [10].

Our research group has long been engaged in the bromination of various organic compounds, with emphasis on environmentally benign synthetic methodologies. Rather than relying on conventional, hazardous brominating agents, we utilize green brominating reagents known as quaternary ammonium tribromides (QATBs) [11-16]. These reagents are not only safer and more sustainable but also offer high efficiency under mild conditions, aligning with several core principles of green chemistry such as reduced toxicity, atom economy, and minimized waste generation. Over time, this effort has resulted in the synthesis of a collection of brominated compounds, spanning various chemical classes. While some of these compounds have been studied for their biological relevance and other aspects, many remain underexplored, representing an untapped reservoir of potential compounds. Phenolic compounds display a wide spectrum of biological effects, including antioxidant, antimicrobial, anti-inflammatory, anticancer, antidiabetic, cardioprotective, neuroprotective, and hepatoprotective activities, making them highly valuable for therapeutic development

and overall health promotion [17]. Structural diversification through halogenation commonly with fluorine, chlorine, or bromine has become an important strategy in medicinal chemistry, as it can enhance lipophilicity, membrane permeability, and target-binding affinity, ultimately improving potency, bioavailability, and therapeutic efficacy [18]. In this context, halogen bonding has gained increasing attention in drug design, particularly in the transition from hit discovery to lead and candidate optimization, where it plays a critical role in stabilizing drug target interactions. Owing to the reactivity of hydroxyl-substituted aromatic rings, phenolic scaffolds are particularly well suited for such modifications, with chlorination and bromination being the most frequently applied approaches [19]. Bromo-organic compounds hold significant importance in pharmaceuticals and fine chemicals owing to their versatile reactivity and broad applications [20]. Conventional bromination methods, however, rely heavily on hazardous reagents such as liquid bromine, generating toxic waste and consuming large amounts of energy, thereby raising both environmental and safety concerns. In response, greener alternatives have been developed, including in situ bromine generation, N-bromosuccinimide, salt-based reagents, and tribromides [21,22], which not only improve reaction efficiency but also reduce ecological impact. These strategies, when coupled with process intensification and waste minimization, embody the principles of green chemistry and circular economy frameworks [23]. Among them, tribromides such as tetrabutylammonium tribromide (TBATB) have emerged as particularly promising, offering solid, easy-to-handle substitutes for liquid bromine. Their ability to deliver high selectivity and yields and under solvent-free conditions underscores their value as safer, more sustainable brominating agents for modern synthetic applications [24,25]. Using tribromides minimizes pollution, simplifies workup, and avoids the risks and environmental concerns associated with molecular bromine, making the process both safer and environmentally friendly.

Considering this, our current study sought to revisit and repurpose a subset of these previously synthesized but underutilized compounds. Bromophenols have drawn scientific attention due to their broad spectrum of biological activities, including antibacterial, antifungal, antioxidant, anticancer, and anti-inflammatory properties [26-29]. Despite their potential, studies exploring their thorough profiles of these

compounds remains limited. To bridge this gap, we selected a set of brominated phenolic compounds, some of which were previously synthesized using tribromide-based green bromination protocols. We adopted an integrated computational–experimental strategy to explore the bioactivity of the selected compounds. Using molecular docking, pharmacophore mapping, and quantum mechanical calculations, we efficiently screened them against bacterial, fungal, and oxidative stress-related targets. This computational pipeline rapidly highlighted promising hits by evaluating binding energies, structural complementarity, and their mode of interactions, providing a low-waste, sustainable alternative to conventional high-throughput screening. The most promising hit was then synthesized through our green bromination protocol and subjected to *in vitro* testing against representative Gram-positive and Gram-negative bacteria, fungal strains, and antioxidant assays, with established standards (streptomycin, fluconazole, ascorbic acid, Trolox) for comparison. An extensive suite of quantum mechanical (QM) calculations *via* Density Functional Theory (DFT) was also performed. These calculations provided critical insight into the molecular and electronic characteristics of the compound adding to its potential from an electronic standpoint.

6.2. Materials and methods

6.2.1. Molecular docking

6.2.1.1. Target selection

A set of molecular targets were retrieved from the Research Collaboratory for Structural Bioinformatics Protein Data Bank (RCSB PDB), a globally recognized repository of experimentally determined three-dimensional biomolecular structures, accessible at http://www.rcsb.org. The selection encompassed a range of bacterial and fungal pathogens, along with targets involved in oxidative stress mechanisms, thus covering multiple biological pathways of therapeutic interest. The following PDB accession codes were used for the analysis:

- **7DQL** (*Escherichia coli*): *E. coli GyrB ATPase domain in complex with 4-chlorobenzene-1,2-diol.*

- **1JII** (*Staphylococcus aureus*): *Crystal structure of S. aureus TyrRS in complex with SB-219383.*
- **7Y8B** (*Bacillus subtilis*): *Crystal structure of CotA laccase complexed with syringic acid.*
- **7MYL** (*Klebsiella pneumoniae*): *Crystal structure of DfrA1 dihydrofolate reductase in complex with TRIMETHOPRIM.*
- **1M78** (*Candida albicans*): *Candida albicans dihydrofolate reductase complexed with dihydro-nicotinamide-adenine-dinucleotide phosphate (NADPH) and 5-chloryl-2,4,6-quinazolinetriamine (gw1225).*
- **8BHH** (*Fusarium oxysporum*): *The crystal structure of a feruloyl esterase C from Fusarium oxysporum in complex with p-coumaric acid.*
- **4IN4** (antioxidant): *Crystal structure of CPD 15 bound to Keap1 Kelch domain.*
- **4ZZI** (antioxidant): *SIRT1/Activator/Inhibitor Complex.*

6.2.1.2. Compounds under investigation

In this study, thirteen bromophenolic derivatives as presented in **Table S6.1 (supporting information)** were selected, including compounds previously synthesized by our group using green bromination strategies alongside additional analogues. Despite successful synthesis, these molecules have remained underexplored. A systematic evaluation was therefore undertaken to assess their therapeutic relevance, with antibacterial, antifungal, and antioxidant activities benchmarked against established standards streptomycin, fluconazole, ascorbic acid, and Trolox. This approach not only enables a clearer understanding of their mechanisms of action but also positions bromophenolic scaffolds as promising candidates for broader pharmacological investigation. The chemical structures of all compounds were obtained in SDF format from the PubChem database (https://pubchem.ncbi.nlm.nih.gov). The 2D structures were subsequently converted into 3D models using ChemBioDraw Ultra 12.0 and further subjected to energy minimization with the MM2 force field, yielding stable, geometry-optimized conformations suitable for molecular docking analysis.

6.2.1.3. Docking *via* MVD

Molecular docking simulations were carried out using Molegro Virtual Docker (MVD) version 6.0 [30] based on previously established protocols [31]. The initial step involved importing the protein structures into the software, followed by preparation using the built-in wizard, which removed solvent molecules, cofactors, and any non-essential ligands. A semi-flexible docking approach was applied, where the protein receptor was kept rigid, and the ligands were allowed conformational flexibility during binding. MVD's protein preparation toolkit includes functionalities like "*Repair and Optimize Residues*" and "*Optimize Neighborhood*," which help correct structural anomalies and enhance the accuracy of docking predictions. MVD also incorporates an automated cavity detection algorithm that identifies potential binding pockets based on surface geometry. Typically, it highlights and ranks the top five cavities by surface area, prioritizing larger cavities due to their higher likelihood of accommodating ligands effectively. In this study, the active binding site was determined based on the location of the co-crystallized ligand present in the original PDB file, a commonly adopted strategy in structure-based drug design to ensure biological relevance. For each protein-ligand complex, the maximum number of iterations was set to 1,500, and the population size was fixed at 50 with the grid resolution fixed at 0.30 Å. To improve pose accuracy, 30 independent docking runs were executed per ligand. The docking output was evaluated using both the MolDock score and the Re-rank score as key metrics. Finally, the ligand-receptor interactions were analyzed to gain insights into binding efficiency and molecular interactions. The co-ordinates for the binding site, centered on the atomic position of the native ligand, are listed below.

- PDB ID (*7DQL: Chain A*): Cavity 1, possessing an estimated volume of 29.696 Å^3, is spatially centered at coordinates X = 24.75, Y = 20.67, Z = 19.64, and confined within a spherical boundary of 12 Å radius.
- PDB ID (*1JII: Chain A*): Cavity 1, possessing an estimated volume of 296.96 Å^3, is spatially centered at coordinates X: -14.54, Y: 18.58, Z: 85.38, and confined within a spherical boundary of 15 Å radius.

- PDB ID (*7Y8B: Chain B*): Cavity 1, possessing an estimated volume of 115.2 Å³, is spatially centered at coordinates X: 23.14, Y: -47.88, Z: 52.57, and confined within a spherical boundary of 12 Å radius.
- PDB ID (*7MYL: Chain A*): Cavity 1, possessing an estimated volume of 147.968 Å³, is spatially centered at coordinates X: 1.96, Y: 17.93, Z: 33.95, and confined within a spherical boundary of 12 Å radius.
- PDB ID (*1M78: Chain A*): Cavity 1, possessing an estimated volume of 322.56 Å³, is spatially centered at coordinates X: 29.90, Y: -6.36, Z: 7.98, and confined within a spherical boundary of 16 Å radius.
- PDB ID (*8BHH: Chain A*): Cavity 4, possessing an estimated volume of 13.312 Å³, is spatially centered at coordinates X: -23.72, Y: -13.46, Z: -21.22, and confined within a spherical boundary of 12 Å radius.
- PDB ID (*4IN4: Chain A*): Cavity 1, possessing an estimated volume of 316.416 Å³, is spatially centered at coordinates X: 11.05, Y: 3.03, Z: 22.12, and confined within a spherical boundary of 18 Å radius.
- PDB ID (*4ZZI: Chain A*): Cavity 1, possessing an estimated volume of 506.88 Å³, is spatially centered at coordinates X: 7.89, Y: 38.35, Z: -10.71, and confined within a spherical boundary of 15 Å radius.

6.2.1.4. Docking *via* AutoDock

Subsequently molecular docking *via* using AutoDock 4.2 was also executed against all selected targets as per protocols following our previous work [31]. In this phase, docking was restricted to the top-ranked compound, the corresponding standard reference drugs, and the co-crystallized ligands for each target, allowing a direct comparison of binding and interaction patterns. To the binding site coordinates employed were near identical to those used in the MVD simulations, as summarized in **Table S6.2 (supporting information).** Target PDB structures were pre-processed in BIOVIA Discovery Studio by removing water molecules, pre-bound ligands, and non-essential chains, after which polar hydrogens were added to ensure correct geometry. Ligands were prepared by assigning Gasteiger charges, while Kollman charges were added to proteins, and the processed files were converted into the

required macromolecule input formats. The grid box parameters were defined around the active site using the site sphere (SBD) function in Discovery Studio (**Table S6.2**). Docking simulations were executed with the Lamarckian Genetic Algorithm (LGA) under the default parameters of AutoDock 4.2. The resulting protein–ligand complexes were analyzed primarily on the basis of binding free energy and RMSD values, identifying the most stable and favorable interaction patterns.

6.2.2. Pharmacophore mapping

A pharmacophore represents a framework that defines the key molecular features and their spatial arrangement necessary for biological activity. Rather than representing the full chemical structure, it highlights essential elements such as hydrogen bond donors/acceptors, hydrophobic groups, aromatic rings, or charged sites. By abstracting these critical interactions, pharmacophore models serve as powerful tools for identifying, comparing, and designing bioactive molecules in drug discovery [32]. To assess the pharmacophoric features, structural pharmacophore mapping was performed using LigandScout software 4.4.7 [33]. Compounds validated through AutoDock were selected for further analysis, with pharmacophore models built based on the native co-crystallized ligands. The software enabled retrieval of targeted PDBs, followed by refinement steps to remove non-essential elements like water molecules while retaining the co-crystallized ligands. Ligand structures were energy-minimized using the MMFF94 force field to obtain stable conformations. Ligands were then positioned in their respective active sites, with their geometries refined under the same force field and aligned to co-crystallized ligands to ensure accurate spatial orientation and interaction mapping. The resulting pharmacophore highlighted key features such as hydrogen bond donors/acceptors, hydrophobic regions and more thereby facilitating the identification of common interaction patterns. This analysis supports a deeper understanding of molecular interactions and aids in the optimization of lead compounds for therapeutic potential.

6.2.3. Synthesis

6.2.3.1. General chemistry

All chemicals utilized in this study were obtained from Sigma-Aldrich, Merck, and S.D. Fine Chem and were used as received without additional purification. The reactions were carried out in a CATA 2R single-mode microwave reactor (*Catalyst System, Pune, India*). Product characterization was performed using spectroscopic methods, including infrared (IR), nuclear magnetic resonance (NMR), and mass spectrometry. IR spectra were recorded on a PerkinElmer FT-IR spectrometer (Spectrum Two) using KBr pellets. ^{1}H and ^{13}C NMR spectra were recorded using a JEOL-EC 400 MHz spectrometer with DMSO as the solvent. Mass spectra were obtained using an Inkarp mass spectrometer equipped with an APCI source.

6.2.3.2. Synthetic procedure

The reagent tetrabutylammonium tribromide (TBATB), $(C_4H_9)_4N^+Br_3^-$, used for the bromination reaction, was synthesized using a procedure that had already been developed, reported, and analytically validated by our laboratory in earlier works [34-36].

General procedure for the synthesis of 1-bromo-2-naphthol.

In a 50 mL round-bottom flask, an equimolar mixture of TBATB (2 mmol) and 2-naphthol (2 mmol) was prepared. After sealing the flask with a glass stopper, 10 mL of water was introduced, and the contents were stirred thoroughly to obtain a uniform mixture. The resulting reaction mixture was then transferred to a microwave reactor, where it was subjected to controlled irradiation at power setting P-7 (approximately 595 watts). Reaction progress was routinely tracked using thin-layer chromatography (TLC) on silica gel HF254 plates, with an ethyl acetate–hexane mixture (in varying volume ratios) as the mobile phase. Upon completion, the mixture was extracted twice with 10 mL of ethyl acetate, followed by two washes with 5 mL of sodium bicarbonate solution to neutralize any remaining acidic by-products. Purification of the crude product was performed by column chromatography on silica gel, employing an ethyl acetate–hexane eluent system with solvent proportions varied according to the nature of the substrate [37].

6.2.4. *In vitro* antibacterial Studies

The antibacterial potential of the synthesized compound was evaluated *via in vitro* assays against both Gram-negative (*Escherichia coli* and *Klebsiella pneumoniae*) and Gram-positive (*Staphylococcus aureus* and *Bacillus subtilis*) strains. Prior to testing, bacterial cultures were reactivated from stocks by inoculating them into Mueller-Hinton broth and incubating at 37 °C for 24 hours. Antibacterial activity was first assessed using the agar well diffusion method, where inhibition zones around the wells indicated the effectiveness of the compound. To further quantify activity, minimum inhibitory concentrations (MICs) were determined by a two-fold serial dilution method in nutrient broth, with DMSO serving as the solvent and negative control [37-38]. Streptomycin was used as the standard positive control, and the concentration for testing was fixed at 2 mg/mL. All assays were performed in triplicate to ensure reproducibility and reliability of the results. Growth inhibition was evaluated *via* optical density measurements at 600 nm.

6.2.5. *In vitro* antifungal activity

The antifungal activity of the synthesized compound was evaluated *via in vitro* assay against *Fusarium oxysporum* and *Candida albicans*. Antifungal efficacy was initially assessed using the agar well diffusion method, where zones of inhibition were recorded. Subsequently, minimum inhibitory concentrations (MICs) were determined through a two-fold serial dilution assay performed in broth culture [39-40]. Potato dextrose agar (PDA) and potato dextrose broth (PDB) were used as the growth media. Fluconazole served as the standard positive control, while DMSO was employed both as the solvent and negative control. All assays were conducted at a test concentration of 2 mg/mL and performed in triplicate to ensure reliability and reproducibility of results. All experiments were conducted in triplicate to ensure accuracy and reproducibility of the results.

6.2.6. Antioxidant activity

6.2.6.1. 2, 2-diphenyl-1-picryl hydrazyl (DPPH) free radical scavenging assay

The free radical scavenging ability of the synthesized compound was assessed using the DPPH method originally described by Brand-Williams et al. (1995) [41], with

slight procedural adjustments. 1ml of the sample, prepared at concentrations of 5, 10, 15, 20, and 25 µg/mL, was combined with 3 mL of a freshly prepared 0.1 mM DPPH solution in methanol. The mixtures were vortexed and allowed to stand in the dark for 30 min. Absorbance was then recorded at 517 nm using a UV–Vis spectrophotometer. Trolox and ascorbic acid were employed as positive reference standards. All assays were carried out in triplicate, and the results are reported as mean ± standard error.

6.2.6.2. FRAP (Ferric reducing antioxidant power) assay

The reducing potential of the compound was further investigated using the FRAP assay, which measures the ability of antioxidants to convert Fe^{3+} to Fe^{2+} in the presence of 2,4,6-tri-(2-pyridyl)-5-triazine (TPTZ) [42]. FRAP was prepared by combining TPTZ (10 mM), $FeCl_3$ (20 mM), and sodium acetate buffer (300 mM, pH 3.6) in a 10:1:1 proportion. The reagent was freshly prepared and maintained at 37 °C to achieve equilibration before application. For analysis, solutions of the compound (prepared at the same concentrations as in the DPPH assay) were combined with 3 mL of the FRAP reagent and diluted with double-distilled water to a total volume of 4 mL. The prepared samples were kept in the dark at 37 °C for 30 minutes, followed by measurement of absorbance at 593 nm using a UV-Visible spectrophotometer. Trolox and ascorbic acid served as standards. Each experiment was repeated three times, with values expressed as mean ± standard error.

6.2.6.3. Antioxidant Capacity *via* ABTS (2, 2-Azino-(3-ethyl) benzothiazoline)-6-sulfonic acid diammonium salt)

The antioxidant capacity of the compound was also examined through the ABTS radical scavenging assay following a modified procedure of Babbar et al. (2011) [43]. A stock solution of $ABTS^{\bullet+}$ was prepared by reacting 7 mM ABTS with 2.45 mM potassium persulfate, left to stand in the dark at room temperature for 16 h. Before use, ethanol was used to dilute the solution to an absorbance of 3.25 ± 0.02 at 734 nm. For the assay, test solutions of the compound (concentrations identical to those used in DPPH and FRAP) were prepared in methanol and added to 3 mL of the working ABTS solution. Following 30 min of incubation in the dark, absorbance was measured at 734 nm with a UV–Vis spectrophotometer. Trolox and ascorbic acid were used as

positive controls. All determinations were performed in triplicate, and data are presented as mean ± standard error.

6.2.6.4. Quantum Assessment of Antioxidant Reactivity *via* BDE (Bond Dissociation Energy)

Quantum-chemical calculations were performed based on the density functional theory (DFT) at the B3LYP/6–311G++(d,p) level in order to study the association between the antioxidant properties and chemical structures of the studied compounds. Antioxidant activity is closely linked to a molecule's capacity to donate a hydrogen atom and stabilize the resulting radical. The bond dissociation energy (BDE) of phenolic –OH or other reactive bonds is therefore a critical parameter. Compounds with lower BDE values exhibit easier hydrogen release, stronger radical scavenging, and greater antioxidant efficiency. Computational chemistry has emerged as a powerful approach for unraveling structure–activity correlations and exploring the antioxidant behavior of diverse molecular systems. Predicting the dominant antioxidant pathways and their reactivity patterns relies on thermodynamic indicators, among which electron transfer enthalpy (ETE), bond dissociation enthalpy (BDE), proton dissociation enthalpy (PDE), ionization potential (IP), and proton affinity (PA) play central roles [44-47].

6.2.7. Extensive quantum calculations

2.7.1. Frontier Molecular Orbitals (FMOs) and global reactivity descriptors

All computational studies were conducted following Density Functional Theory (DFT) principles using Gaussian 16 software [48], with molecular visualizations and input file preparation performed in GaussView 6.0. Geometry optimization was carried out using the B3LYP functional combined with the 6-311++G(d,p) basis set, and solvent effects were incorporated via the Integral Equation Formalism Polarizable Continuum Model (IEFPCM), with dimethyl sulfoxide (DMSO) as the selected solvent. The 6-311++G(d,p) basis set, being of triple-zeta quality, offers an enhanced representation of molecular electronic structure. The inclusion of diffuse functions (++) and polarization functions (d, p) improves the modeling of electron correlation and spatial distribution of electron density, especially around electronegative atoms

and in lone pair regions. Frontier molecular orbital (FMO) analysis was carried out to assess electronic reactivity behavior, emphasizing the roles of HOMO and LUMO. The distribution of the HOMO reflects a molecule's capacity to release electrons, whereas the spatial orientation of the LUMO highlights its tendency to capture incoming electron density. Together, the HOMO–LUMO framework provides critical insights into charge transfer, chemical stability, and potential reactivity patterns of the studied compounds. To further explore the electronic characteristics, several global reactivity descriptors were calculated, including HOMO energy (E_{HOMO}), LUMO energy (E_{LUMO}), energy gap (ΔE), dipole moment, ionization potential (I), electron affinity (A), electronegativity (χ), chemical potential (μ), electrophilicity index (ω), global hardness (η), and global softness (S). These parameters were derived using standard theoretical expressions (equations 1–7) alongside the computed dipole moment [49].

The ionization potential (IP) denotes the minimum energy required to remove an electron from a molecule. Within frontier molecular orbital theory, it directly corresponds to the E_{HOMO} and is expressed as;

$$IP = -E\ HOMO \ldots\ldots\ldots (1)$$

Conversely, the electron affinity (EA) represents the energy released when an additional electron is accepted by a system, which relates to the energy of the $E_{LUMO,}$ expressed as;

$$EA = -E\ LUMO \ldots\ldots\ldots (2)$$

From these values, other global reactivity descriptors can be derived. Electronegativity (χ), which expresses the inherent tendency of an atom or molecule to draw electrons toward itself, given by;

$$\chi = (IP + EA)/2 \ldots\ldots\ldots (3)$$

The global hardness (η)**,** indicating resistance to charge transfer, is calculated as:

$$\eta = (IP - EA)/2 \ldots\ldots\ldots (4)$$

The reciprocal parameter, chemical softness (S), quantifies the ability of a molecular system to flexibly redistribute or accommodate incoming electron density

$$S = 1/2\ \eta \text{ ……... (5)}$$

The electrophilicity index (ω) serves as a quantitative measure of a molecule's tendency to act as an electron acceptor, defined mathematically as;

$$\omega = \mu\ 2\ /2\eta = -\chi\ 2\ /2\eta \text{ ……. (6)}$$

Lastly, the chemical potential (μ) characterizes the escaping tendency of electrons and governs the direction of charge transfer in chemical processes, expressed as

$$\mu = -\chi \text{……. (7)}$$

2.7.2. Mulliken Charge (MC)

Mulliken population analysis is a standard computational approach used to evaluate the distribution of electron density within molecular systems. It enables the identification of electron-rich and electron-deficient regions, which is vital for predicting chemical reactivity, intramolecular stability and non-covalent interactions. Although Mulliken charges are sensitive to the basis set and orbital overlap, they remain a reliable tool for qualitative assessment of charge polarization and donor–acceptor behavior [50].

2.7.3. Natural Bond Orbital (NBO)

Natural Bond Orbital (NBO) analysis was employed to elucidate the intramolecular electron delocalization and donor–acceptor interactions in BDDE and 1-Bromo-2-naphthol. Second-order perturbation theory was applied to quantify the stabilization energy (E^2) associated with electron donation from occupied (donor) to unoccupied (acceptor) NBOs, offering insight into conjugative and hyperconjugative effects that contribute to the overall electronic stability of each compound [51].

2.7.4. Non-Linear Optics (NLO)

The development of efficient nonlinear optical (NLO) materials remains a fundamental objective in the advancement of modern optoelectronic, photonic, and

telecommunication technologies. Organic molecules, in particular, have gained considerable attention due to their structural diversity, synthetic flexibility, and cost-effective fabrication. Key structural features known to enhance NLO behavior include extended π-conjugation, strong intramolecular charge-transfer (ICT) pathways, and inherent electronic asymmetry. Within this framework, the investigation of bioactive or therapeutically relevant molecules for their NLO potential represents a valuable strategy that merges molecular design with functional applications in advanced materials science [52].

2.7.5. Real-Space Analysis of Non-Covalent Interactions (NCI) and Electron Localization

To gain a comprehensive understanding of the electron distribution, bonding characteristics and weak intermolecular interactions in the studied molecules, we employed two complementary real-space analytical frameworks: the Interaction Region Indicator (IRI) and the Electron Localization Function (ELF). The IRI methodology enables the detection and spatial resolution of non-covalent interactions (NCIs) by analyzing the electron density (ρ), its reduced density gradient (RDG) and the sign of the second eigenvalue (λ_2) of the Hessian matrix of electron density [53]. ELF, in contrast, describes the probability of locating paired electrons in real space, thus revealing the presence and extent of bonding domains, lone pairs and delocalization effects [54].

6.3. Results

6.3.1. Molecular docking

6.3.1.1. Docking *via* MVD

Molecular docking analysis performed using Molegro Virtual Docker (MVD) revealed that compound 6, identified as 1-bromo-2-naphthol (1B2N)**,** consistently exhibited the highest binding energy (Moldock and rerank score) among its derivatives across the selected biological targets. This consistent trend strongly suggests that 1B2N may possess inherent characteristics and physicochemical properties

contributing to its potential as a multi-target inhibitor. It exhibited a Moldock and Re-rank scores of –68.6846 kcal/mol and –58.1503 kcal/mol (7DQL), –79.7955 kcal/mol and –66.9513 kcal/mol (1JII), –55.6935 kcal/mol and –47.4453 kcal/mol (7Y8B), –78.7587 kcal/mol and –65.4974 kcal/mol (7MYL), –71.7551 kcal/mol and –59.6284 kcal/mol (1M78), –78.1558 kcal/mol and –66.8075 kcal/mol (8BHH), –65.1317 kcal/mol and –55.0164 kcal/mol (4IN4), and –77.1461 kcal/mol and –59.2799 kcal/mol (4ZZI) as shown in **Tables S6.3–S6.10 (supporting information)**. Collectively, these results suggest that 1B2N holds significant potential as a lead compound for further structural optimization and experimental validation, particularly in light of its consistent binding efficiency across diverse biological macromolecular target

- *Mode of interaction*

Further investigation into the binding interactions of 1B2N revealed that it engages key active site residues known to be crucial for ligand recognition and activity.

7DQL: The binding mode analysis of 1-bromo-2-naphthol (1B2N) with the target 7DQL as shown in **Figure 6.1,** demonstrates its interactions with residues Val71, Asp73, and Thr165. When compared to the co-crystallized ligand, which interacts with Asp73, Val71, Thr165, and Val167, it becomes evident that 1B2N shares three key residues (Val71, Asp73, Thr165) with the native ligand. Similarly, in comparison with streptomycin, which interacts with Val71, Val43, Thr165, Asp73, Arg76, and Glu50, 1B2N again overlaps with the same residues (Val71, Asp73, Thr165). Such convergence of binding patterns implies that 1B2N may mimic, at least partially, the binding behavior of both the co-crystallized ligand and the clinically validated drug (streptomycin). From a pharmacological perspective, this signifies that 1B2N exhibits binding-site fidelity, meaning it preferentially engages critical residues involved in bioactivity. Consequently, this increases the likelihood that the compound may demonstrate reliable inhibitory activity against the target validating its potential for advancement as a lead candidate in drug development.

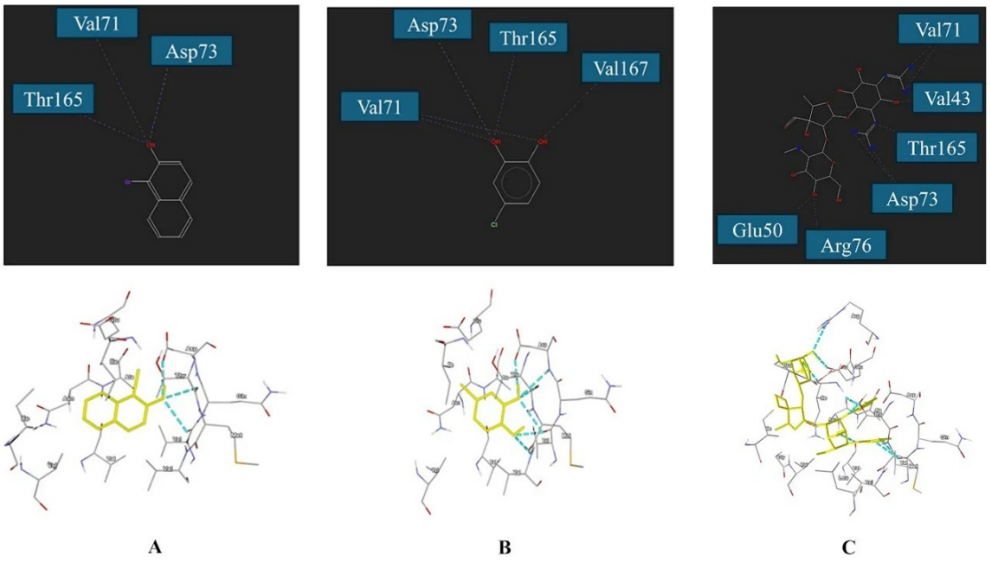

Figure 6.1: Illustration of mode of interaction of A). 1B2N B). Co-crystallized ligand C). Streptomycin with PDB ID 7DQL

1JII: 1-bromo-2-naphthol (1B2N) exhibits interactions with the residues Asp40, Thr75, and Tyr170 as shown in **Figure S6.2 (supporting information)**. When compared with the co-crystallized ligand, which engages a wider network of residues including Asp40, Thr75, Leu70, Gln190, Tyr36, Cys37, Gly38, Gln196, Lys84, Asp80, Arg88, Gln174, and Tyr170**,** it is clear that 1B2N shares three contacts (Asp40, Thr75, Tyr170). Likewise, in comparison with streptomycin, which interacts with Cys37, Gly193, Gly38, Asp195, Gln196, Asp40, Lys84, Arg88, and His50**,** 1B2N again overlaps with Asp40 as a common point of interaction. The ability of 1B2N in interacting with residues engaged by both the co-crystallized ligand and the established antimicrobial agent streptomycin strengthens its profile and although it does not cover the full binding spectrum of either comparator, its selective overlap exhibits its potential as a promising lead compound for further antimicrobial drug development.

7Y8B: 1B2N establishes interactions with Thr415, Arg416, His419, and Gly417 as shown in **Figure S6.3 (supporting information)**. The co-crystallized ligand is bound to the very same residues (Thr415, Arg416, His419, and Gly417), indicating a complete overlap in the interaction pattern. Streptomycin also shares these residues,

specifically Thr415, Gly417, and His419, in addition to several others such as Thr262, Thr260, Thr418, Gly321, Pro226, His497, and Gly323. The consistent overlap of 1B2N with both the co-crystallized ligand and streptomycin at Thr415, Gly417, and His419 underscores its ability to mimic the essential recognition pattern of established binders. This implies that 1B2N is anchoring itself at the critical binding site rather than forming peripheral contacts, thereby enhancing the likelihood of strong inhibitory activity. Such conserved interactions at the sites core residues reinforce its potential bioactivity and suggest that 1B2N may act as a reliable competitor within this binding pocket.

7MYL: 1B2N interacts with Met6, Asn17, Tyr103, and Ser97 as shown in **Figure S6.4 (supporting information)**. The co-crystallized ligand engages with Met6, Ser97, and Glu28, while streptomycin binds to Gly16, Ser116, Glu28, Asn17, Gly18, Gln29, and Pro19. Notably, 1B2N shares Met6 and Ser97 with the co-crystallized ligand, and Asn17 with streptomycin, highlighting its ability to establish conserved interactions with residues crucial for ligand recognition. The overlap with both reference binders indicates that 1B2N not only positions itself effectively within the canonical binding pocket but also engages with residues that contribute to stability and specificity of ligand binding. This dual pattern of common interactions reinforces the potential of 1B2N to act as a competent inhibitor, suggesting that its bioactivity arises from targeting residues fundamental to both natural ligand anchoring and antibiotic activity.

1M78: 1B2N interacts with Arg79, which is also a contact point for the co-crystallized ligand (Arg56, Ser78, Arg79) and for fluconazole (Arg56, Thr58, Gly114, Glu116, Ile117, Arg79, Lys57) as shown in **Figure S6.5 (supporting information)**. The convergence of all three ligands at Arg79 may highlight this residue as a pivotal anchor within the binding pocket for antifungal inhibition. While the co-crystallized ligand also engages Arg56 and Ser78, and fluconazole extends its network across multiple residues, 1B2N's ability to share the highly conserved Arg79 interaction suggests that it binds in a biologically meaningful manner. This commonality implies that Arg79 is a determinant residue for antifungal bioactivity, and 1B2N's alignment with both the

reference ligand and the standard drug reinforces its potential as a candidate for antifungal therapeutic development.

8BHH: 1B2N engages Gln234 and Ser237, matching two of the residues contacted by the co-crystallized ligand **(**Ser237, Gln234, Gly123**)**, whereas streptomycin interacts with **T**yr351, Gly123, and Thr202 as shown in **Figure S6.6 (supporting information)**. The overlap of 1B2N with the co-crystallized ligand with Gln234 and Ser237 indicates favourable binding-site fidelity, suggesting that 1B2N anchors within the hotspot of the pocket through H-bond network (phenolic OH ↔ Ser237 and Gln234). By contrast, streptomycin's contacts point to a broader or partially shifted subsite. Functionally, this means 1B2N likely captures the essential recognition motif of the native binder, supporting its bioactivity as a candidate for antifungal activity.

4IN4: 1B2N interacts with Gly367 and Val606**.** The co-crystallized ligand also engages these two residues, along with Thr560, Val465, and Val418, while ascorbic acid forms contacts with Gly367, Val606, Val465, Val418, and Ile559, and Trolox interacts with Gly367, Val606, and Leu365 as shown in **Figure S6.7 (supporting information)**. The shared binding at Gly367 and Val606 across 1B2N and all reference ligands highlights these residues as critical anchoring points within the binding pocket. This overlap suggests that 1B2N adopts a binding mode consistent with established antioxidants, implying that it can effectively stabilize interactions essential for antioxidant activity. However, unlike ascorbic acid, Trolox, and the co-crystallized ligand, 1B2N does not extend toward the peripheral residues (Val465, Val418, Thr560, Ile559, Leu365), indicating that while it engages the conserved residues, it occupies a more compact binding orientation. This selective interaction profile implies that 1B2N possesses inherent antioxidant potential.

4ZZI: The docking analysis revealed that compound 1B2N interacts predominantly with residues Asp348 and Phe414 within the binding site **Figure S6.8 (supporting information)**. Notably, Asp348 is also a key contact residue for both the co-crystallized ligand and ascorbic acid, suggesting that 1B2N shares a conserved binding mode with established reference molecules. This overlap highlights Asp348 as a crucial interaction hotspot that stabilizes ligand binding and may contribute

significantly to antioxidant activity. While Trolox interacted with a different set of residues (Asp272, Phe273, Tyr280), the conservation of Asp348 in 1B2N's binding profile aligns more closely with ascorbic acid, a well-known antioxidant. The presence of an additional interaction with Phe414 further supports the stable anchoring of 1B2N within the binding cavity. Collectively, these findings suggest that 1B2N may exert antioxidant potential through similar binding mechanisms as classical antioxidants, thereby reinforcing its role as a promising candidate for antioxidant activity.

Specifically, 1B2N was observed to interact with the same amino acid residues as the co-crystallized ligands and standard reference drugs, including streptomycin (antibacterial), fluconazole (antifungal), and ascorbic acid or Trolox (antioxidant), depending on the target as shown in Figure S6.1-S6.8 (**supporting information**). These overlapping interaction patterns suggest that 1B2N may share similar binding mechanisms or pharmacophoric features with known therapeutics. This structural mimicry and high binding affinity suggest that 1-bromo-2-naphthol could serve as a promising multi-target lead compound with potential applications in antibacterial, antifungal, and antioxidant drug development.

6.3.1.2. Docking *via* AutoDock

To gain a deeper mechanistic perspective, **AutoDock 4.2** was employed as a complementary docking platform. This approach provided an additional benchmark to determine whether the interaction patterns of the compound with its respective biological targets are consistent with those of standard reference ligands. Such comparative evaluation enhances the reliability of the predictions and offers greater confidence in the potential bioactivity of the compound.

7DQL: 1B2N emerged as the most potent candidate, showing superior binding affinity and stable interactions with the target as shown in **Table S6.11(supporting information)** and **Figure 6.9.** Its binding energy (–6.56 kcal/mol) was lower than that of the co-crystallized ligand (–4.96 kcal/mol) and streptomycin (–1.7 kcal/mol), indicating a stronger and more favorable interaction. The exceptionally low RMSD value of 0.02 further reflects a precise and stable docking pose, whereas the co-

crystallized ligand (0.38 kcal/mol) and streptomycin (1.12 kcal/mol) displayed less stability. Interaction analysis revealed that 1B2N and the co-crystallized ligand share key binding residues, including Asp73 (conventional hydrogen bond), Val167 (alkyl interaction), and Ala47 and Val43 (pi-alkyl interactions), suggesting a common binding mechanism. 1B2N also shared interactions with streptomycin, such as Met95, Thr165, Asp73, and Val71, albeit through different interaction types. Importantly, 1B2N engaged with a broader range of residues and exhibited more diverse interaction modes, which likely explains its stronger binding energy and enhanced potency compared with both the co-crystallized ligand and streptomycin.

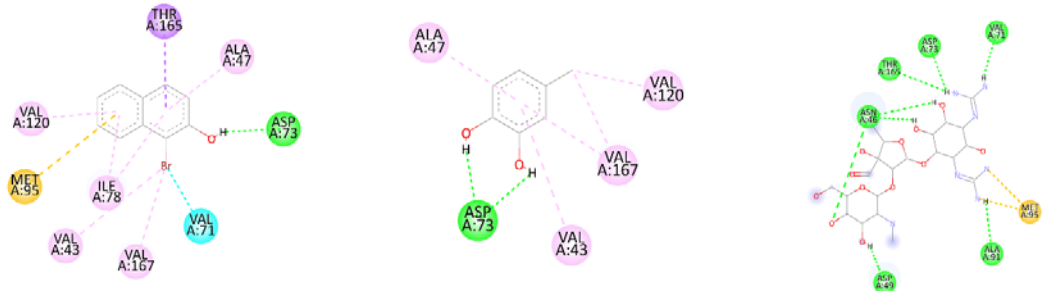

A B C

Figure 6.9: Illustration of mode of interaction of A). 1B2N B). Co-crystallized ligand C). Streptomycin with PDB ID 7DQL

1JII: 1B2N was identified as the most potent candidate, exhibiting the lowest binding energy (–5.93 kcal/mol) compared with the co-crystallized ligand (–5.35 kcal/mol) and streptomycin (–3.69 kcal/mol), indicating stronger and more favorable interactions as shown in **Table S6.12** and **Figure S6.10 (supporting information)**. Its low RMSD value (0.54 Å) further confirms a stable and well-defined docking pose, whereas the co-crystallized ligand (1.68 Å) and streptomycin (1.66 Å) showed less stability. Both 1B2N and the co-crystallized ligand shared key residues, including a conventional hydrogen bond with Asp40 and pi-interactions with Ala39, suggesting a common binding mechanism. By contrast, 1B2N and streptomycin showed no overlapping interactions, implying distinct binding regions or orientations. Although the co-crystallized ligand and streptomycin interacted with more residues overall,

1B2N's unique combination of hydrogen bonding, amide pi-stacking, and pi-alkyl interactions produced a stronger binding affinity and greater stability, underscoring its potential as a superior candidate.

7Y8B: 1B2N emerged as the most potent candidate, exhibiting the lowest binding energy (–5.11 kcal/mol) compared with the co-crystallized ligand (–3.72 kcal/mol) and streptomycin (–2.18 kcal/mol), indicating stronger and more favorable binding as shown in **Table S6.13** and **Figure S6.11 (supporting information)**. Its low RMSD (0.1 Å) further demonstrates a favourable docking pose, in contrast to the less stable orientations of 7Y8B (0.93 Å) and streptomycin (1.82 Å). 1B2N and co-crystallized ligand shared key interactions, including hydrogen bonds with Arg416 and Gly417, as well as alkyl and polar interactions with His419, Pro226, Thr415, and His497, suggesting a common binding mechanism. Additionally, 1B2N and streptomycin both interacted with Gly417, albeit via different bonding modes. Notably, 1B2N established the broadest and most diverse interaction profile, engaging with eight unique residues through four distinct interaction types, including a strong π–π T-shaped interaction with His497. This wider and more versatile interaction network likely underpins its superior binding affinity and remarkable docking stability, highlighting 1B2N as the most promising candidate.

7MYL: 1B2N presents itself as a highly compelling candidate, demonstrating a strong binding affinity and exceptional stability as shown in **Table S6.14** and **Figure S6.12 (supporting information)**. Its binding energy (BE) of -6.7 kcal/mol is highly favorable, significantly stronger than that of Streptomycin (-4.34 kcal/mol), though slightly less than 7MYL CL (-7.59 kcal/mol). Its root-mean-square deviation (RMSD) is 0.02 Å, indicating stable binding pose. This is a critical advantage for a potential drug, as it contrasts sharply with the less stable poses of the co-crystallized ligand (0.5 Å) and Streptomycin (1.68 Å). 1B2N and the co-crystallized ligand anchor themselves in a similar pocket, sharing several critical interactions that define the core binding mode. Both ligands form a conventional hydrogen bond with Glu28 and engage in pi-pi stacking with Phe32. They also share interactions with Met6 and Ala8. This significant overlap suggests that 1B2N effectively occupies the key binding hotspot, while CL builds upon this core with additional, more extensive interactions. In

contrast, 1B2N shares only one interacting residue with Streptomycin, which is Met6. This indicates that 1B2N and Streptomycin utilize largely different binding modes. 1B2N relies on a balanced mix of hydrogen bonding and various pi-interactions (pi-pi and pi-alkyl), whereas Streptomycin primarily uses a broad network of hydrogen bonds. While 7MYL CL shows a marginally lower binding energy, 1B2N stands out for its remarkable balance of strong binding affinity and unparalleled stability. The combination of its potent interactions with residues like Glu28 and Phe32 and its exceptionally low RMSD makes it a prime candidate. This outstanding conformational stability suggests a highly predictable mechanism of action, which is often as crucial as raw binding power in drug development.

1M78: 1B2N emerges as a highly promising candidate, combining strong binding affinity with exceptional conformational stability as shown in **Table S6.15** and **Figure S6.13 (supporting information)**. Its binding energy (–6.7 kcal/mol) is significantly stronger than streptomycin (–4.34 kcal/mol) and only slightly weaker than the co-crystallized ligand (–7.59 kcal/mol). 1B2N with RMSD of 0.02 Å, indicating good binding pose. This contrasts sharply with the less stable orientations of the co-crystallized ligand (0.5 Å) and streptomycin (1.68 Å), highlighting 1B2N's predictable binding behavior an essential trait for drug development. Likethe co-crystallized ligand, 1B2N occupies the same binding pocket, sharing key interactions such as a hydrogen bond with Glu28, π–π stacking with Phe32, and contacts with Met6 and Ala8, suggesting a common binding hotspot. However, while the co-crystallized ligand extends these interactions further, 1B2N achieves a comparable effect through a balanced mix of hydrogen bonding and diverse π-interactions (π–π, π–alkyl). In contrast, its overlap with streptomycin is limited to Met6, reflecting a distinct binding mode. Taken together, 1B2N demonstrates not only potent affinity but also unparalleled docking stability, making it a prime candidate. Its strong yet predictable interaction network underscores a robust mechanism of action, where binding stability may prove as critical as raw binding strength in therapeutic design.

8BHH: 1B2N stands out as the most potent candidate, demonstrating superior binding affinity and stability with the target as shown in **Table S6.16** and **Figure S6.14 (supporting information)**. Its binding energy (–7.84 kcal/mol) is substantially

stronger than both the co-crystallized ligand (–5.81 kcal/mol) and Fluconazole (–5.78 kcal/mol), underscoring its favorable interaction profile. The RMSD of 0.08 Å further highlights its docking pose, contrasting with Fluconazole's less stable orientation (0.75 Å), though comparable to the co-crystallized ligand (0.11 Å). 1B2N and the co-crystallized ligand share a common binding mode, forming a hydrogen bond with Thr202, π–σ interactions with Leu233, and a π–π T-shaped interaction with Tyr351. Similarly, 1B2N overlaps extensively with Fluconazole, engaging residues such as Met124 (π–sulfur), Ala227, Leu233, Ile415 (π–alkyl), Leu414, and Tyr351, indicating that all three ligands target a shared binding pocket. However, 1B2N achieved higher affinity through a uniquely optimized blend of hydrogen bonding, π–sulfur, π–π, and alkyl interactions across seven key residues. This efficient and energetically favorable interaction network not only explains its lower binding energy but also its remarkable stability, firmly establishing 1B2N as the most promising candidate against the 8BHH target.

4IN4: 1B2N demonstrates a balance of strong binding affinity and stability **Table S6.17** and **Figure S6.15 (supporting information)**. Its binding energy (–6.59 kcal/mol) is highly competitive with the reference antioxidant Trolox (–7.07 kcal/mol), while markedly more favorable than Ascorbic Acid (–5.83 kcal/mol) and the co-crystallized ligand (–8.84 kcal/mol). 1B2N achieved low RMSD of 0.02 Å, far superior to Trolox (0.25 Å), Ascorbic Acid (0.9 Å), and the co-crystallized ligand (1.99 Å), indicating stable and predictable binding pose. 1B2N anchors itself in the same active site as Trolox and Ascorbic Acid, sharing similar mode of interactions. Like Trolox, it binds Val465 and Val512, while overlapping even more extensively with Ascorbic Acid through Val418, Val465, Val512, and Val606. Additionally, it interacts with Val418, Val465, and Ala366, which are also contacted by the co-crystallized ligand demonstrating that 1B2N effectively exploits the same pocket but with a more optimized geometry and interaction profile. Its diverse yet efficient interactions within the key binding hotspot support a highly reliable binding mechanism, making 1B2N as potent candidate in terms of drug design.

4ZZI: 1B2N emerges as a compelling candidate with an excellent balance of favorable binding affinity and exceptional stability **Table S6.18** and **Figure S6.16 (supporting**

information). Its binding energy (–5.79 kcal/mol) is comparable to that of the reference antioxidant Trolox (–5.88 kcal/mol), though not as strong as the co-crystallized ligand (–8.38 kcal/mol). However, 1B2N stands out for its remarkable conformational stability, with an RMSD of just 0.07 Å among the lowest observed and on par with Trolox (0.09 Å). This indicates a highly consistent and predictable binding pose. 1B2N binds within the same active site as the top-scoring co-crystallized ligand, sharing critical interactions with residues such as His363, Val412, Phe414, and Ile347. While the co-crystallized ligand engages in a more extensive interaction network, unlike Trolox and Ascorbic Acid, which primarily interact with Lys203 and Asp204, 1B2N occupies a distinct binding interctaions characterized by residues such as His363 and Phe297. This provides valuable insights into the mode of interaction of 1B2N against its respective targets. By identifying both shared and distinct binding residues relative to reference compounds, highlights binding features that may reduce competition with existing ligands or confer selectivity.

6.3.2. Pharmacophore mapping

Pharmacophore mapping was conducted for 1-bromo-2-naphthol (1B2N) to identify and compare the key molecular features shared with the co-crystallized ligands and the respective standard reference compounds across all selected targets. This analysis aimed to uncover whether 1B2N could replicate or mimic critical interaction motifs known to be essential for biological activity. The results clearly indicated that 1B2N closely mimicked several essential pharmacophoric features, particularly hydrogen bond donor and acceptor interactions, which are fundamental to stable and specific binding within the active site. These shared features suggest a high degree of structural and functional similarity between 1B2N and well-established active compounds. As illustrated in Figures S6.17–6.24 **(supporting information)**, these conserved interaction patterns were observed consistently across all target proteins. The overlap in binding features not only validates the docking results but also highlights the strong potential of 1B2N to act as a potent bioactive compound. Its ability to mimic key pharmacophoric elements underscores its promise as a lead molecule for further optimization and development in antimicrobial and antioxidant therapeutic strategies.

7DQL: 1B2N, along with its co-crystallized ligand and streptomycin, demonstrates a range of pharmacophoric features critical for molecular recognition, including hydrogen bond donors and hydrophobic interaction sites. These interactions involve multiple residues within the binding pocket, as illustrated in Figure 6.17. Notably, 1B2N exhibits the potential to emulate these pharmacophoric characteristics, suggesting a conserved mechanistic pathway for ligand binding and activity. Hydrogen bonding interactions play a particularly crucial role in stabilizing the ligand–protein complex. Specifically, residues THR165A, ASP73A, and VAL71A are consistently involved in hydrogen bond formation across all three compounds, indicating a shared mode of interaction. This conservation of key hydrogen-bonding residues suggests that 1B2N can maintain essential intermolecular contacts that are likely important for its biological function. Beyond hydrogen bonding, additional shared features including hydrophobic contacts reinforce the ligand's ability to engage the protein effectively. Such a multifaceted interaction profile not only supports its binding affinity but also provides insight into the mechanistic pathways underlying its potential therapeutic activity.

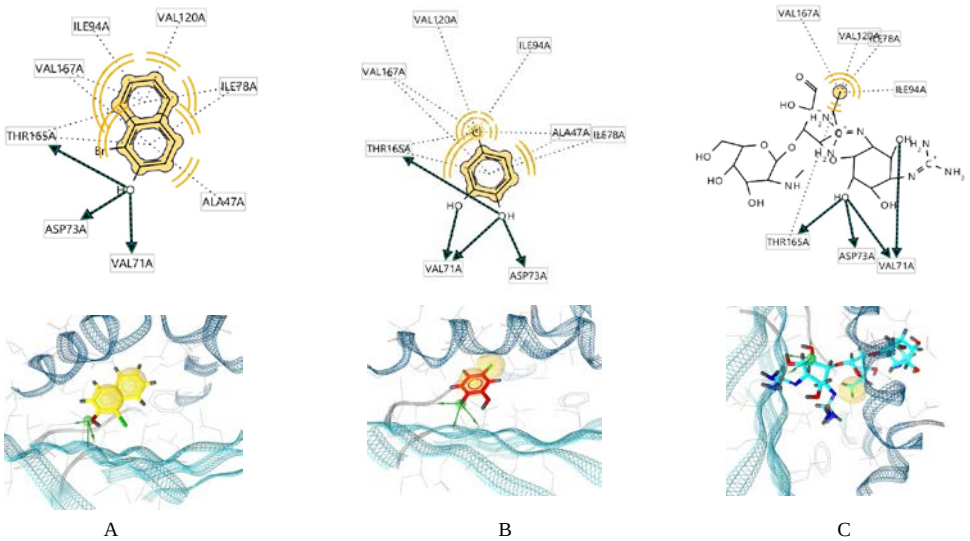

Figure 6.17: 2D and 3D illustrated pharmacophoric features of A). 1B2N B). Co-crystallized ligand C). Streptomycin against PDB ID 7DQL

1JII: Pharmacophore analysis of 1B2N revealed that the pharmacophoric features are mediated through a combination of hydrogen bonding and hydrophobic contacts,

prominently involving the residues TYR36A, LEU70A, and THR75A. The co-crystallized ligand, however, displayed a more extensive binding profile, engaging in both hydrogen-bonding interactions and hydrophobic contacts with a wider array of residues, as illustrated in **Figure S6.18 (supporting information).** Importantly, the interaction pattern of 1B2N shows significant overlap with that of the co-crystallized ligand, particularly through the conserved residues TYR36A, LEU70A, and THR75A, in addition to other contributing residues. This conservation of critical binding interactions suggests that 1B2N not only mimics the binding conformation of the co-crystallized ligand but also demonstrates a comparable mode of molecular recognition, thereby underscoring its potential inhibitory efficacy. By contrast, streptomycin didn't exhibit any residue-level overlap with 1B2N, indicating that its binding is mediated through an entirely distinct interaction framework, which may account for differences in its inhibitory potential and selectivity.

7Y8B: Pharmacophore mapping of the compounds revealed that 1B2N exhibited prominent hydrophobic, hydrogen-bonding, and halogen-bonding features, primarily involving THR415B, ARG416B, and LEU386B. In contrast, the co-crystallized ligand displayed negative ionizable interactions, particularly with ARG416B, which is also shared by 1B2N. This overlap of residues highlights a conserved interaction motif, suggesting that 1B2N closely mimics the binding orientation of the native ligand and therefore possesses significant inhibitory potential and bioactivity as shown in **Figure S6.19 (supporting information).** Furthermore, streptomycin engaged three residues, of which ARG416B and LEU386B overlapped with those of 1B2N and the co-crystallized ligand.

7MYL: The pharmacophore analysis shows that 1B2N is stabilized by a hydrogen bond with ASN17A and hydrophobic contacts with MET6A, ALA8A, PHE32A, and MET51A, reflecting a mixed hydrophobic–polar binding mode as shown in **Figure S6.20 (supporting information).** The co-crystallized ligand, on the other hand, interacts with SER97A, MET6A, and GLU28A, with MET6A being the residue it shares with 1B2N. This overlap suggests that while the co-crystallized ligand adopts a more polar interaction profile, both ligands anchor to the same binding region through MET6A, implying a partially conserved interaction mode and supporting the

potential bioactivity of 1B2N. Streptomycin engages MET6A, SER97A, and GLU28A, thereby sharing MET6A with 1B2N, and also overlapping with the co-crystallized ligand at SER97A and GLU28A. The sharing of MET6A between streptomycin and 1B2N indicates a common stabilizing point within the binding pocket, but the additional polar interactions unique to streptomycin suggest a distinct binding orientation, which may account for differences in inhibitory potential. Overall, the conserved interaction with MET6A across all three ligands highlights it as a critical anchoring residue, while the broader overlap of streptomycin and the co-crystallized ligand suggests that 1B2N only partially mimics the native binding mode.

1M78: For 1B2N, the ligand interacts through hydrophobic contacts with PHE36A, MET25A, ILE33A, ILE112A, THR58A, and NDP193A, indicating that its stabilization is largely driven by nonpolar interactions as shown in **Figure S6.21 (supporting information)**. The co-crystallized ligand forms stronger hydrogen-bonding interactions with ILE9A and GLU32A, while also engaging ILE112A, NDP193A, THR58A, MET25A, PHE36A, and ILE33A, suggesting a mixed polar–hydrophobic binding mode with enhanced stabilization due to its polar contacts. Fluconazole interacts with ILE112A, NDP193A, THR58A, PHE36A, MET25A, and ILE33A, relying primarily on hydrophobic contacts with no explicit polar contribution. Comparing across ligands, 1B2N shares PHE36A, MET25A, ILE33A, ILE112A, THR58A, and NDP193A with the co-crystallized ligand, while fluconazole also shares the same residues, suggesting that both mimic key elements of the native binding environment. However, because the co-crystallized ligand uniquely involves GLU32A and ILE9A through hydrogen bonding, its binding is expected to be stronger and more specific. The residue sharing implies that 1B2N and fluconazole align with the binding pocket in a manner similar to the co-crystallized ligand, but 1B2N's nonpolar emphasis may provide stabilization, whereasfluconazole, despite residue overlap, may lack the polar reinforcement necessary for optimal inhibitory bioactivity.

8BHH: 1B2N establishes a balanced network of hydrogen bonds with SER237A and GLN234A, along with hydrophobic contacts involving TYR351A, LEU233A, ILE415A, ALA227A, PHE349A, and LEU414A, highlighting its stable engagement within the active site as shown in **Figure S.6.22 (supporting information)**.

Importantly, several of these residues are also shared with the co-crystallized ligand (SER237A, GLN234A, TYR351A, LEU233A, ALA227A, LEU414A, ILE415A, and PHE349A) as well as with fluconazole (SER237A, TYR351A, LEU233A, LEU414A, ALA227A, PHE349A, and LEU415A). This overlap suggests that 1B2N closely mimics the binding orientation of both the natural ligand and the clinically used antifungal. While fluconazole extends its interaction network with additional polar contacts at GLY123A and THR202A, the core set of conserved residues shared with 1B2N indicates that the latter is able to anchor itself in a manner highly reminiscent of established binders. Such mimicry implies that 1B2N not only adopts a favorable binding pose but also captures key pharmacophoric interactions essential for bioactivity, underscoring its promise as a potential inhibitor despite its slightly less extensive polar reinforcement compared to fluconazole.

4IN4: 1B2N interacts hydrophobically with ILE461A and PHE478A, reflecting a simple yet stable nonpolar binding orientation as shown in **Figure S.6.23 (supporting information).** These residues are also engaged by both the co-crystallized ligand and trolox, indicating that 1B2N partially mimics the hydrophobic anchoring observed in stronger binders. However, unlike the co-crystallized ligand, which combines this hydrophobic core with hydrogen bonds to SER508A and SER555A and additional contacts with ARG483A and TYR525A, 1B2N lacks polar stabilization. Similarly, while trolox maintains interactions with ILE461A and PHE478A, it also engages in polar hydrogen bonding with ARG483A and SER508A, thereby balancing nonpolar and polar contributions for greater stability. Ascorbic acid, though lacking hydrophobic anchoring, reinforces its binding through hydrogen bonds with ARG483A and SER508A, again highlighting the importance of polar contacts. The fact that 1B2N shares ILE461A and PHE478A with both trolox and the co-crystallized ligand signifies mimicry of the hydrophobic motif essential for binding underscoring its promise as a potential inhibitor.

4ZZI: 1B2N establishes hydrophobic stacking with PHE273A, ILE270A, ILE347A, and ALA262A, along with a hydrogen bond to ASP348A, suggesting a predominantly nonpolar stabilization supported by a key polar anchor as shown in **Figure S.6.24 (supporting information)**. When compared, 1B2N shares PHE273A and ASP348A

with the co-crystallized ligand, indicating partial mimicry of its strong π-stacking and hydrogen-bonding interactions that define optimal binding. With trolox, 1B2N overlaps at PHE273A and ILE347A, reinforcing a similar hydrophobic core, though trolox further enhances stability through an additional hydrogen-bonding network. In contrast, ascorbic acid only engages ASP348A, showing minimal overlap with 1B2N and a weaker, polar-driven binding mode. This pattern suggests that 1B2N reproduces the hydrophobic framework of the co-crystallized ligand and trolox while also conserving the critical hydrogen bond to ASP348A, a feature common across all ligands. Such mimicry implies that 1B2N has the potential to achieve bioactivity by stabilizing within the binding pocket through the same key residues.

6.3.3. Synthesis

TBATB is a bright yellow/orange crystal with melting point 74-76 ℃. Thermogravimetric analysis of TBATB shows good thermal stability up to 174 ℃. The main decomposition occurs at 230 ℃ which is much higher than the temperature at which bromination takes place, thus making it suitable for controlled bromination reactions at elevated temperatures [55]. The bromination product 1-bromo-2-naphthol was obtained after a reaction time of 2 minutes as shown in **scheme 1** with 81% yield. The product was confirmed by analyzing its melting point, Mass spectra, NMR and IR as shown in **Figure S6.25 (supporting information).**

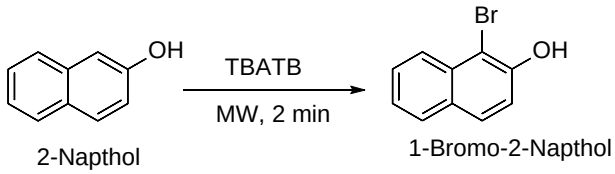

Scheme 1: Bromination of 2-naphthol

6.3.4. Antibacterial activity

The agar well diffusion assay revealed that 1-bromo-2-naphthol (1B2N) exhibits moderate antibacterial activity against both Gram-positive (*Staphylococcus aureus, Bacillus subtilis*) and Gram-negative (*Escherichia coli, Klebsiella pneumoniae*) strains, with zones of inhibition ranging from 15–17 mm as shown in **Figure 6.26 and Table S6.19 (supporting information) and Table 6.20.** While these values are

smaller than those observed for the standard drug streptomycin (30–31 mm), the consistent inhibitory effect across all tested bacteria suggests that 1B2N possesses broad-spectrum antibacterial potential. Its slightly greater effectiveness against *S. aureus* (17 mm) may indicate a stronger affinity for Gram-positive targets, and its activity overall supports its promise as a lead compound for further development in antimicrobial drug design**.**

The MIC values for the compound ranged between 0.0625 mg/mL and 0.125 mg/Ml (Mean ± standard error calculated from triplicate runs) as shown in as shown in **Table 6.21**. In comparison, Streptomycin, used as the standard antibiotic, showed lower MICs across all strains, indicating higher potency. For instance, in B. subtilis, the MIC of the compound was 0.0625 mg/mL, whereas Streptomycin exhibited an MIC of 0.0156 mg/mL, making the standard approximately four times more potent. Similarly, in S. aureus and K. pneumoniae, the compound's MIC was 0.0625 mg/mL compared to Streptomycin’s 0.0312 mg/mL, showing the compound to be about two times less active. The least potency was observed in *E. coli*, where the compound showed an MIC of 0.125 mg/mL, four times higher than the 0.0312 mg/mL MIC of Streptomycin. Although the test compound is less effective than the standard, its consistent inhibitory effect at concentrations below 0.125 mg/mL suggests moderate antibacterial activity, especially in preliminary screening evaluations triplicate .

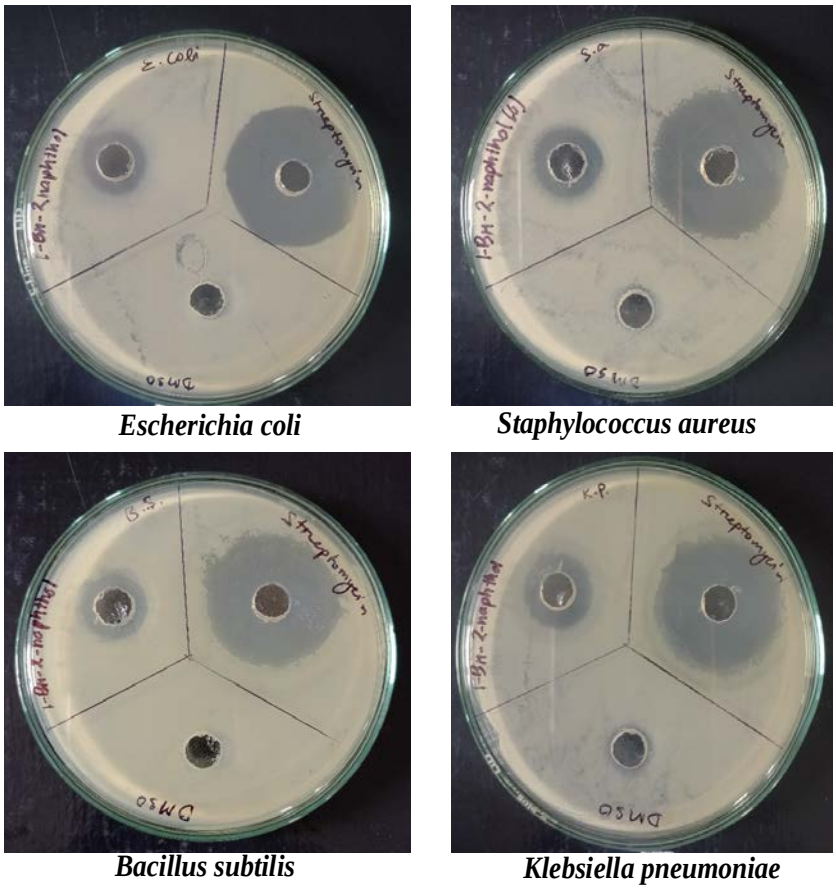

Escherichia coli ***Staphylococcus aureus***

Bacillus subtilis ***Klebsiella pneumoniae***

Figure 6.26: Antibacterial activity of 1-bromo-2-naphthol (1B2N) through well diffusion assay

Table 6.20: Antibacterial activity of 1-bromo-2-naphthol 1B2N via well diffusion assay

Bacterial Strain	**Zone of Inhibition (**1-bromo-2-naphthol**)**	**Zone of Inhibition (Streptomycin)**
Escherichia coli	15 mm	31 mm
Staphylococcus aureus	17 mm	31 mm
Bacillus subtilis	16 mm	30mm
Klebsiella pneumoniae	16 mm	30 mm

Table 6.21: MIC Antibacterial activity of 1-bromo-2-naphthol (1B2N)

Bacterial Strain	MIC (Compound)	MIC (Streptomycin)
Bacillus subtilis	0.0625 mg/ml	0.0156 mg/ml
Staphylococcus aureus	0.0625 mg/ml	0.0312 mg/ml
Escherichia coli	0.125 mg/ml	0.0312 mg/ml
Klebsiella pneumoniae	0.0625 mg/ml	0.0312 mg/ml

6.3.5. Antifungal activity

The antifungal activity assay demonstrated that 1-bromo-2-naphthol exhibits strong inhibitory effects against both Candida albicans and Fusarium oxysporum as shown in **Table 6.22, Figure 6.26 and Table S6.23 (supporting information)**. For Candida albicans, the compound produced a zone of inhibition of 33 mm, which is almost comparable to the standard antifungal agent fluconazole (34 mm). This suggests that 1-bromo-2-naphthol possesses antifungal potency nearly equivalent to a well-established drug, highlighting its potential as a promising antifungal candidate. Similarly, against Fusarium oxysporum, 1-bromo-2-naphthol yielded a zone of inhibition of 29 mm, only slightly lower than that of fluconazole (31 mm). While the activity is marginally less than the standard, the result still indicates a strong inhibitory effect. Taken together, these findings emphasize that 1-bromo-2-naphthol exhibits broad-spectrum antifungal activity with inhibition zones very close to those of fluconazole. Given its relatively simple chemical structure and comparable efficacy, this compound holds significant potential for further investigation as a lead antifungal agent, especially for pathogens like Candida albicans, where its activity is nearly indistinguishable from the standard drug.

Table 6.22: Antifungal activity of 1-bromo-2-naphthol (1B2N)

Bacterial Strain	Zone of Inhibition (1-bromo-2-naphthol)	Zone of Inhibition (Fluconazole)
Candida albicans	33 mm	34 mm
Fusarium oxysporum	29mm	31 mm

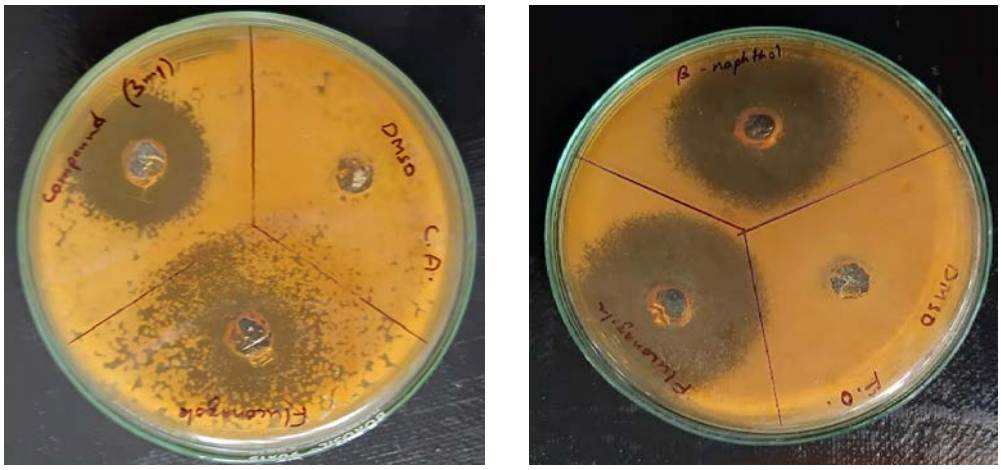

Candida albicans ***Fusarium oxysporum***

Figure 6.26: Antifungal activity of 1-bromo-2-naphthol (1B2N) through well diffusion assay

The antifungal potential of the compound was tested against Fusarium oxysporum and Candida albicans. The MIC values observed were 0.0625 mg/mL and 0.125 mg/Ml (Mean ± standard error calculated from triplicate runs) respectively. Fluconazole, used as the reference antifungal, demonstrated an MIC of 0.0312 mg/mL against F. oxysporum, making it twice as potent as the test compound. However, the compound exhibited significantly higher efficacy against C. albicans, with an MIC of 0.125 mg/mL compared to 1 mg/mL for Fluconazole. This suggests that the compound is approximately eight times more effective than the standard antifungal drug in inhibiting C. albicans. These findings indicate that while the compound shows moderate antifungal activity against F. oxysporum, it possesses strong and promising antifungal properties specifically against C. albicans, warranting further investigation for potential therapeutic applications.

Table 6.24: MIC Antifungal activity of 1-bromo-2-naphthol (1B2N)

Fungal Strain	MIC (Compound)	MIC (Fluconazole)
F. oxysporum	0.0625 mg/ml	0.0312 mg/ml
C. albicans	0.125 mg/ml	1 mg/ml

6.3.6. Antioxidant activity

Various spectrophotometric assays were employed to evaluate the antioxidant potential of 1-bromo-2-naphthol, including DPPH (2,2-diphenyl-1-picrylhydrazyl), ABTS (2,2'-azino-bis(3-ethylbenzothiazoline-6-sulfonic acid)), and FRAP (Ferric Reducing Antioxidant Power) assays. Ascorbic acid and Trolox were employed as reference standards in the study, providing benchmark values for antioxidant activity. By comparing the radical scavenging and reducing capacity of 1-bromo-2-naphthol (1B2N) to these well-established antioxidants, the study aimed to quantify its efficacy and elucidate its potential as a free radical scavenger. These assays collectively offer complementary insights into the compound's ability to neutralize reactive oxygen species and contribute to its overall antioxidant profile.

DPPH: According to DPPH assay, when antioxidants react with DPPH, they donate a hydrogen atom or an electron, reducing DPPH leading to decolorization. The level of decolorization is proportional to the antioxidant's ability to scavenge free radicals [56]. Comparatively the DPPH assay revealed Ascorbic acid as the strongest antiradical, with an IC_{50} of 12.35 μg/mL, while the 1-bromo-2-naphthol demonstrated superior radical scavanging activity than Trolox as shown in **Figure 6.27 and Table 6.25**. 1-bromo-2-naphthol superior DPPH radical scavanging activity over Trolox may be attributed to the antioxidant effects of Ar–OH, mediated through major mechanisms of hydrogen atom transfer (HAT) or single-electron transfer followed by proton transfer (SET-PT) [57,58].

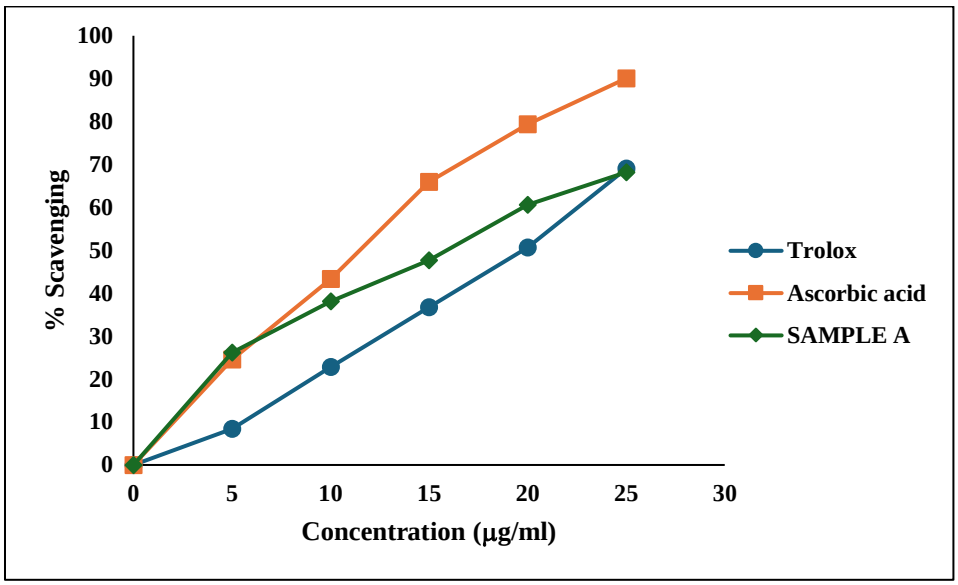

Figure 6.27: Antioxidant activity by DPPH assay

Table 6.25: Antioxidant activity

Compound	DPPH (IC_{50} in µg/ml)	ABTS (IC_{50} in µg/ml)
Trolox	19.25 ± 0.19	11.48± 0.29
Ascorbic Acid	12.35 ± 0.26	30.79± 0.58
Sample A	16.31± 0.26	14.70± 0.15

ABTS: In the ABTS assay, Trolox showed better scavenging activity with IC_{50} of 11.48± 0.29 µg/mL while the 1-bromo-2-naphthol showed superior activity than Ascorbic acid as shown in **Figure 6.28 and Table 6.25**. The results revealed that the standard Trolox is more effective than Ascorbic acid which may be due to the amphiphilic nature (aqueous and lipophilic) of Trolox compared to the hydrophilic nature of ascorbic acid [59,60]. Studies also showed that Trolox forms stable radicals and typically scavenges about 2 molecules of $ABTS^{\bullet+}$, whereas ascorbic acid's oxidized radical is less stable and slower reacting [61] which suffice the better activity of Trolox in the result. 1-bromo-2-naphthol demonstrated activity comparable to Trolox and superior to Ascorbic acid, possibly due to halogenated substituents, which enhance $ABTS^{\bullet+}$ and DPPH• scavenging as studies showed halogenated (F, Cl, Br) substitutions significantly improve $ABTS^{\bullet+}$ and DPPH• scavenging influencing electron/hydrogen donation and radical stability [62].

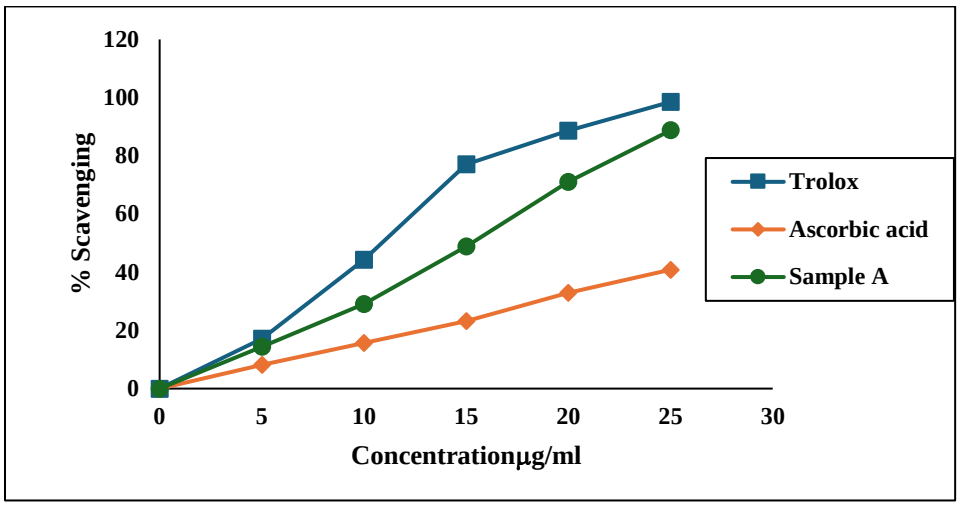

Figure 6.28: Scavenging activity by ABTS assay

FRAP: In FRAP assay, higher absorbance of the test compound indicates better reducing power. (Rakholiya et al., 2015) [63] The potential antioxidant activity of the 1-bromo-2-naphthol revealed by its higher absorbance as compared to the standard Ascorbic acid and Trolox as illustrated in Figure 6.29. This better reducing power of the 1-bromo-2-naphthol maybe attributed to the antioxidant effects of Ar–OH, mediated through single-electron transfer and its halogenated substituent influencing electron transfer as FRAP assay is a SET (Single Electron Transfer) based method [64].

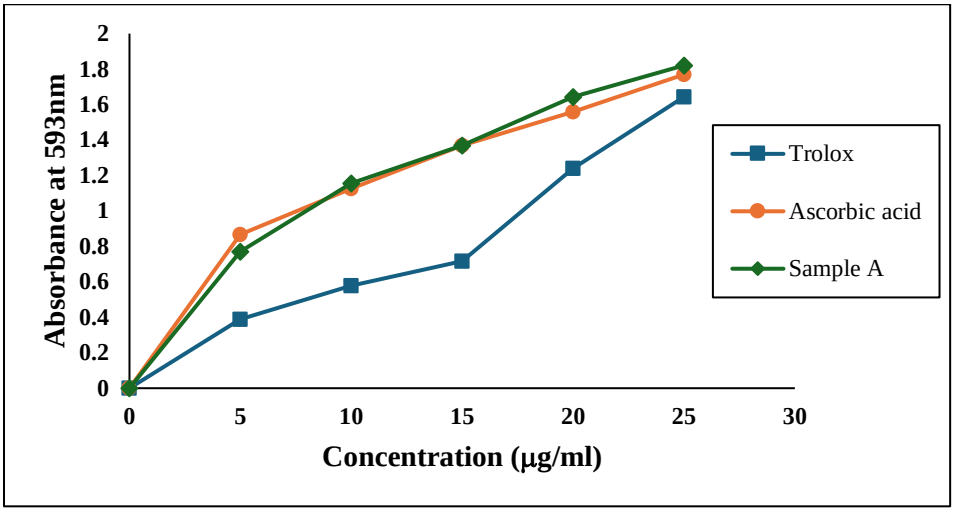

Figure 6.29: Antioxidants activity by Ferric reducing power assay

Bond dissociation energy (BDE): Literature survey suggests that there are three fundamental mechanism which account for the antioxidant properties of phenolic compounds [44-46]. The structures of the investigated compounds is shown in Table 6.26.

(1) hydrogen atom transfer (HAT);

(2) stepwise electron-transfer-proton-transfer (ET-PT); and

(3) sequential proton-loss-electron-transfer (SPLET).

The following three equations outline the mechanism:

$R\bullet + ArOH \rightarrow RH + ArO\bullet$ (1)

$R\bullet + ArOH \rightarrow R^{-} + ArOH^{+}\bullet \rightarrow RH + ArO\bullet$ (2)

$ArOH \rightarrow ArO^{-} + R^{+}ArO^{-} + R\bullet \rightarrow ArO\bullet + R^{-}R^{-} + H^{+} \rightarrow RH$ (3)

HAT mechanism: The antioxidant (ArOH) transfers a hydrogen atom to the free radical (R•) by the homolytic bond breaking of the O–H bond of ArOH to generate a radical (ArO•). The reactivity of the antioxidant is calculated by determining the BDE of the O–H bond, a lower BDE value indicates better antioxidant activity. BDE is calculated by using the following formula:

BDE = H(ArO•) + H(H•) - H(ArOH)

ET-PT mechanism: This mechanism takes places in two steps: (i) the ArOH denotes an electron (e–) to R• and (ii) proton (H^{+}) transfer from the radical cation (ArOH+•) to generate the free radical (ArO•). In the ET-PT mechanism, the IP and PDE are the primary descriptors for examining the scavenging activity. The compounds which exhibit low IP and PDE values are expected to have higher antioxidant activity. IP and PDE are calculated by employing the following formulae:

IP = H(ArOH•+) + H(e-) - H(ArOH)

PDE = H(ArO•) + H(H+) - H(ArOH•+)

SPLET mechanism: Similar to ET-PT, the SPLET mechanism also follows two steps: (i) the ArOH losses a proton (H+) to generate the phenoxide anion (ArO–) and (ii) an electron from ArO– is donated to R• to generate the radical. This mechanistic

pathway involves the PA and ETE of the phenoxide ion as the significant factors in determining the antioxidant activity of the compounds. The IP and PDE are evaluated using the following formulae:

PA = H(ArO-) + H(H+) - H(ArOH)

ETE = H(ArO•) + H(e-) - H(ArO-)

Gaussian16 suite of program was extensively used to perform all the calculations at B3LYP/6-311G++(d,p) level of theory. Vibration frequencies analyses of the optimized structures were computed at the same theoretical level to determine the stationary points on the potential energy surface. All the calculations were performed at DMSO solvent medium to replicate the experimental results.

Table 6.26: Structures of ascorbic acid, Trolox, and 1B2N The numbering 1,2, 3 and 4 indicates the phenolic group where antioxidant activity is studied

Compound	Structure
Ascorbic acid	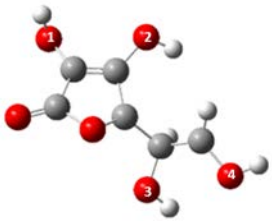
Ascorbic acid 1	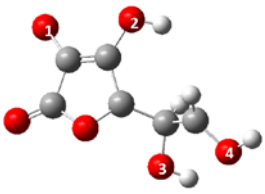
Ascorbic acid 2	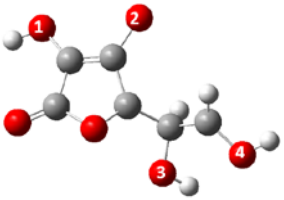

Ascorbic acid 3	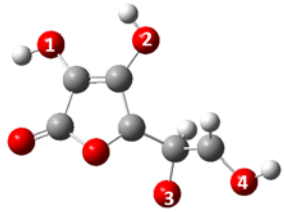
Ascorbic acid 4	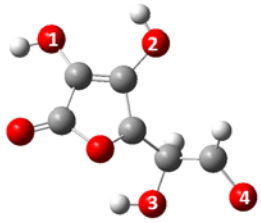
Trolox	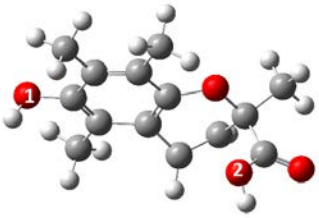
Trolox 1	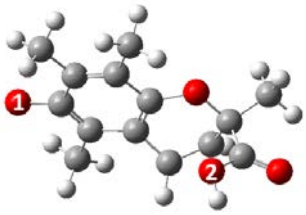
Trolox 2	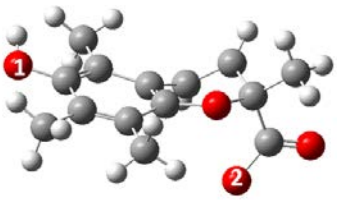
1B2N	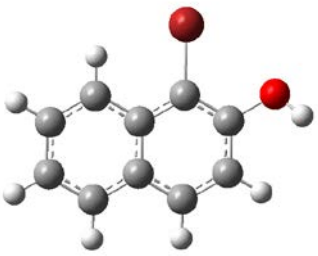

From the BDE values of the studies compounds as Shown in **Table 6.27**, it can be observed that Trolox in position 2 has the lowest BDE, indicating that it has the highest hydrogen donating ability. However, 1-bromo-2-naphthol (1B2N) also has a lower BDE as compared to ascorbic acid in position 2 and Trolox in position 2 suggesting

that your compound also has an excellent potential in hydrogen donation. Furthermore, it can be clearly understood from the IP results that your compound has the best electron donating capability among all the studies compounds. The PDE results indicate that Trolox 2 has the best ability in proton dissociation, followed by ascorbic acid 1. 1B2N also has a very high ability to dissociate a proton, which is comparatively more than ascorbic acid 2. The PA results revealed that the deprotonation of ascorbic acid in position 3 and 4 is the most feasible. 1B2N also has a higher affinity for deprotonation as compared to ascorbic acid in position 1 and 2 as well as Trolox in position 2. The ETE values are significantly lower for 1B2N as compared to ascorbic acid position 2 and 4 and Trolox position 1. An observation of all the computed results indicates that your compound has an excellent potential to act as an antioxidant agent. Furthermore, it can be observed that for 1B2N the PA value is comparatively lower than the BDE and PDE values suggesting that SPLET mechanism might be more dominant in case of1B2N.

Table 6.27: BDE, IP, PDE, PA, and ETE values of different positions of ascorbic acid, Trolox, and 1B2N DMSO solvent medium. All the listed values are in kJ/mol

Compound	BDE	IP	PDE	PA	ETE
Ascorbic acid 1	-29.22	0.46	-29.68	-28.42	-0.80
Ascorbic acid 2	-26.12	0.46	-26.58	-27.99	1.88
Ascorbic acid 3	-28.75	0.46	-29.21	-30.16	1.41
Ascorbic acid 4	-27.88	0.46	-28.34	-30.16	2.28
Trolox 1	-27.06	2.60	-29.66	-30.045	2.97
Trolox 2	-29.39	2.60	-31.99	-28.53	-0.86
1B2N	-27.29	0.35	-27.64	-28.84	1.55

6.3.7. Extensive quantum mechanical calculations

6.3.7.1. Frontier Molecular Orbitals (FMOs) and global reactivity descriptors

Frontier Molecular Orbitals (FMOs) are utilized to identify the most reactive areas in molecular systems and to describe various types of reactions. The HOMO (Highest

Occupied Molecular Orbital) is rich in electrons and tends to donate electrons to vacant orbitals. In contrast, the LUMO (Lowest Unoccupied Molecular Orbital) is deficient in electrons and readily accepts electrons from other occupied orbitals. Thus, the HOMO and LUMO are crucial for interpreting chemical reactivity in terms of nucleophilic or electrophilic attacks [65]. The energy difference between the HOMO and LUMO defines the energy gap (ΔE), which is a key factor in determining the reactivity and stability of a biomolecule, particularly in relation to its lowest electronic excitation. A smaller energy gap allows for easier excitation compared to a larger gap. Consequently, a smaller gap promotes intramolecular charge transfer and contributes to enhanced bioactivity. In contrast, a larger energy gap is associated with greater kinetic stability and lower chemical reactivity [66]. As given in Table S6.28 (supporting information) and depicted in **Figure 6.30,** the HOMO-LUMO energy gap (ΔE) values for the studied compounds ranged from 4.48 eV to 6.18 eV, indicating that the values are relatively close to each other. Our study focused on several key compounds namely compounds 1B2N, four standards (Ascorbic acid, Fluconazole, Streptomycin and Trolox) along with Bis(2,3-dibromo-4,5-dihydroxybenzyl) ether (BDDE), a well-characterized phenolic compound known to exhibit a wide range of biological activities. Incorporating BDDE allowed for a comparative assessment of SAR trends and provided a benchmark for evaluating the quantum chemical calculations with 1B2N. According to the data in Table 1, the energy gaps (ΔE) of the compounds follow this order: Fluconazole > Ascorbic acid > Trolox > BDDE > Streptomycin >1B2N. The largest energy gap (ΔE) was observed for the standard Fluconazole, with a value of 6.186 eV, while the smallest energy gap (ΔE) was found for the compound1B2N, with a value of 4.489 eV. Thus, it has been observed that the energy gap of the compound of interest, 1B2N, was found to be the lowest as compared to the other compounds. These results suggest that the compound 1B2N has low energy gap, which further confirms its potential charge transfer interactions. Therefore, we can infer that the compound 1B2N may exhibit higher reactivity and, consequently, greater pharmacological activity.

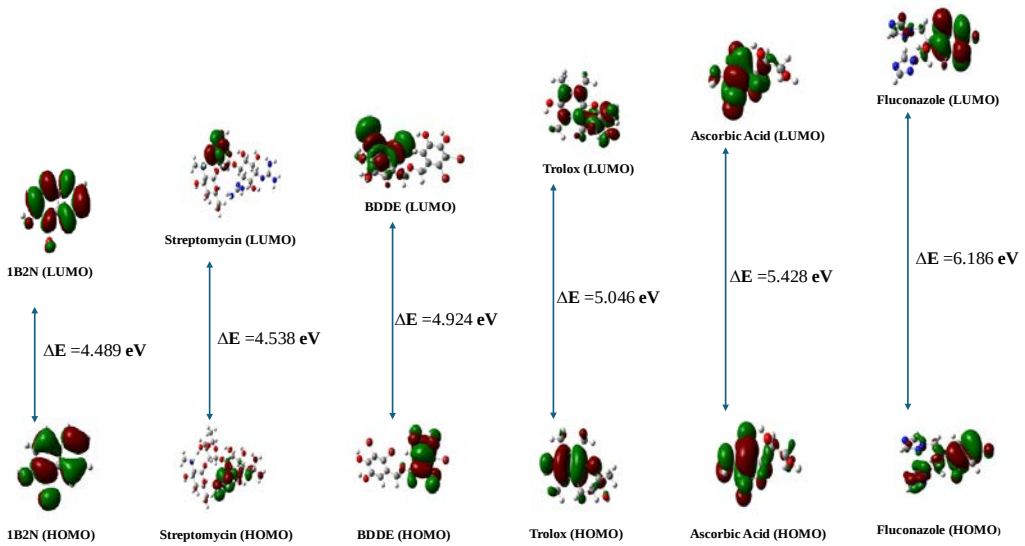

Figure 6.30: Depiction of the frontier molecular orbital (HOMO–LUMO) energy gaps of the investigated compounds

The calculated chemical descriptors for the investigated compounds are presented in **Table 6.29 (supporting information)**. A high ionization energy indicates chemical stability, while a molecule with a high electron affinity is more likely to accept electrons. Fluconazole has the highest ionization potential among the key compounds, with a value of 7.319 eV, while the compound 1B2N has the lowest at 6.160 eV. This suggests that standard fluconazole might be the most chemically stable among the group. Additionally, Streptomycin, one of the standard compounds, exhibited the highest electron affinity at 1.707 eV, followed closely by compound 1B2N at 1.671 eV, indicating that both compounds are highly reactive and can readily accept electrons. The hardness (η) and softness (σ) of a molecule are key descriptors that influence its behavior in chemical reactions. In simple terms, hard molecules resist changes in their electronic distribution during reactions, while soft molecules have low resistance to resist changes in their electronic distribution. Among the key compounds studied, Fluconazole exhibited the highest chemical hardness, with a value of 3.093 eV, while compound 1B2N had the lowest, at 2.244 eV. This suggests that compound 1B2N is likely to be more reactive in charge transfer reactions as it has low resistance to changes in their electron distribution during a reaction.

Electronegativity (χ), which measures an atom's attraction to electrons in a covalent bond, was found to be highest for Fluconazole, with a value of 4.226 eV. Our compound of interest 1B2N , displayed a value of 3.915 eV which justifies that it is a moderate electrophile. Also, the other key compounds exhibited average electronegativity values as well. Chemical Potential (μ) specifies the probability of a chemical reaction. A higher (less negative) μ indicates a greater ease in donating electrons, making the substance an electron donor, while a lower (more negative) μ suggests it more readily accepts electrons, acting as an electron acceptor [67]. From the results, it can be seen that the compound fluconazole has high chemical potential having a value of -4.226 eV showing that it might be a good electron donor. Here, it is also seen that the compound1B2N, exhibited acceptable chemical potential value of -3.915 eV which indicates that it can also act as an electron acceptor. Electrophilicity (ω) predicts the electrophilic nature of a chemical species by measuring its ability to accept electrons. Higher ω values indicate stronger electrophilicity in a molecule [68]. From the data presented in Table 2, our compound of interest 1B2N exhibited high electrophilicity value of 3.415 eV which is better than most of the other studied compounds. Thus, we can justify that the compound1B2N, possesses a lower energy gap and reduced hardness, making it more flexible in accepting electrons due to its higher softness and electrophilicity. The increased softness is advantageous, as soft drugs more easily interact with target enzymes and are recognized as biologically active, with predictable and regulated metabolism. After serving their therapeutic purpose, they transform into non-toxic compounds. These results suggest that compound 1B2N demonstrates good chemical reactivity and can be classified as a soft biomolecule. In conclusion, it can be inferred that compound 1B2N exhibits promising biological properties for use in pharmacological and therapeutic applications.

6.3.7.2.Molecular Electrostatic Potential Analysis

- **Analysis of Molecular Electrostatic Potential (MESP)**

Quantum chemical approaches are highly valuable for pinpointing the reactive regions of drug molecules, with Molecular Electrostatic Potential (MEP) mapping being one of the most informative tools. The MEP reflects the distribution of electronic density within a molecule and provides insights into its reactivity, electrostatic behavior, and

partial charge distribution. As a visualization technique, MEP mapping is widely employed to assess molecular polarity and to distinguish regions of electron-rich and electron-deficient character. When combined with the total electron density surface, these maps help describe the geometry, extent, and charge distribution of potential active sites, thereby highlighting areas most likely to participate in chemical interactions. Typically, the 3D electrostatic potential surface is illustrated using a color gradient: electron-rich regions with negative potential (often linked to electrophilic attack) appear in shades of red to orange, while electron-deficient areas with positive potential (favorable for nucleophilic attack) are depicted in blue. Intermediate or neutral zones are represented in green, with the general potential scale following the trend: red < orange < yellow < green < blue [69]. The MEP analysis of the compound 1B2N reveals a color gradient ranging from - 8.030 e -2 (negative potential) to +8.030 e -2 (positive potential). The negative potential regions, denoted by yellow colors, are observed near the O atom of the hydroxyl group (-OH) of the naphthol ring indicating regions of higher electron density. In contrast, the positive potential regions denoted by blue color are detected near the H atom attached to the O atom depicting electron deficient regions as shown in Figure 6.31A. The analysis also shows zero potential regions around the molecule denoted by green color. These results highlights the regions where the molecule is likely to participate in nucleophilic and electrophilic interactions. For BDDE, the MEP reveals the color gradient ranging from -8.455 e -2 to +8.455 e -2 . Here, the negative potential regions, indicated by yellow colors, are seen near the O atom attached to the hydroxyl group of the benzene ring. The positive potential regions, indicated by blue color, are observed near the H atoms attached to the hydroxyl groups. The regions of zero potential, depicted by green color is also seen in the molecule as shown in Fig. S6.32A (supporting information). In Ascorbic acid, the MEP analysis displays a color gradient ranging from -0.103 e 0 to +0.103 e 0 . The negative potential regions, depicted by yellow color, are primarily found on the O atoms of the lactone ring denoting regions of higher electron density. On the other hand, the positive potential areas indicated by blue color, are seen around the H atoms of the hydroxyl group revealing electron deficient regions around the molecule as shown in Figure S6.33A (supporting information). In the case of Fluconazole, the MEP study displays a color gradient ranging from -8.885 e -2 to +8.885 e -2. The

negative potential regions, denoted by red color, is found near the O atoms of the hydroxyl group whereas the positive potential regions, depicted by blue color, are seen in the H atoms attached to the C atom as shown in Figure S6.34A (supporting information). Areas of zero potential, indicated by green color are also seen in themolecule. The MEP analysis of Trolox depicts a color gradient ranging from -6.948 e -2 to +6.948 e -2. The negative potential regions, denoted by red color is observed near the O atoms attached to C atom of the molecule. In contrast, the positive potential regions, indicated by blue color, are seen near the H atoms of the hydroxyl group. Regions of zero potential, depicted by green color are also seen in the vicinity of the molecule as shown in Figure 6.35A(supporting information).. Lastly, the MEP analysis of Streptomycin shows a color gradient ranging from -7.011 e -2 to +7.011 e -2. The negative potential areas are observed near the O atoms of the hydroxyl groups depicted by red and yellow color. Conversely, the positive areas denoted by blue color are seen near the H atoms of the amine group as shown in Figure S6.36A (supporting information).. The analysis also reveals regions of zero potential, depicted by green color are also seen surrounding the molecule. Thus, the analysis of Molecular Electrostatic Potential (MEP) provides insight into the chemical reactivity and interaction sites of the molecule. Understanding this distribution helps in predicting how the compound will interact with other molecules or ions, aiding in the study of its chemical behavior.

- **Analysis of Electrostatic Potential (ESP)**

Electrostatic potential (ESP) analysis offers an intuitive visualization of the electrostatic potential distribution, molecular size and shape, while also highlighting chemically active sites, atomic reactivity and also aiding in the study of biological recognition [70]. Electrostatic potentials (ESPs) are related to electron density (ED) and help identify regions within a molecule that are susceptible to electrophilic and nucleophilic attacks, as well as potential sites for hydrogen bonding interactions [66]. The negative regions of the Electrostatic Potential Surface (ESP), shown in red, correspond to areas of high electron density and are associated with proton attraction, making them favorable sites for electrophilic attack. Conversely, the positive regions of the ESP, depicted in blue, indicate areas of low electron density and are associated

with proton repulsion, making them more susceptible to nucleophilic attack. The ESP is represented in ascending order of potential using the color gradient: red, orange, yellow, green, and blue. The iso-surface plots of the electrostatic potentials (ESPs) for all the compounds are presented in Figures 6.31B and S6.32B-S6.36b (supporting information). These ESP plots illustrate the charge distribution within each molecule, providing a visual representation of regions with varying electrostatic potential. This information offers valuable insight into how a molecule may interact or react with other molecules. The electron density mapping on the ESP iso-surfaces for all the compounds is illustrated in Figs. 1b- 6b displays the charge distribution across a molecule. The ESP iso surface plots provides insight into the electronic structure, charge distribution and molecular reactivity. The ESP array plots for all the compounds are represented using different colors, as illustrated in the corresponding Figures 6.31C and S6.32C-S6.36C (supporting information). ESP array plots are instrumental in predicting molecular behavior, providing insights into binding affinity, chemical reactivity, and biological recognition processes. These molecular diagrams have been visualized to highlight chemically active sites and the relative reactivity at specific atomic positions. In the regions surrounding atoms within various ring systems of the molecules, yellow-colored contours represent electronegative zones. The density and proximity of these contours whether closely or sparsely distributed indicate potential sites for nucleophilic or electrophilic attacks [71].

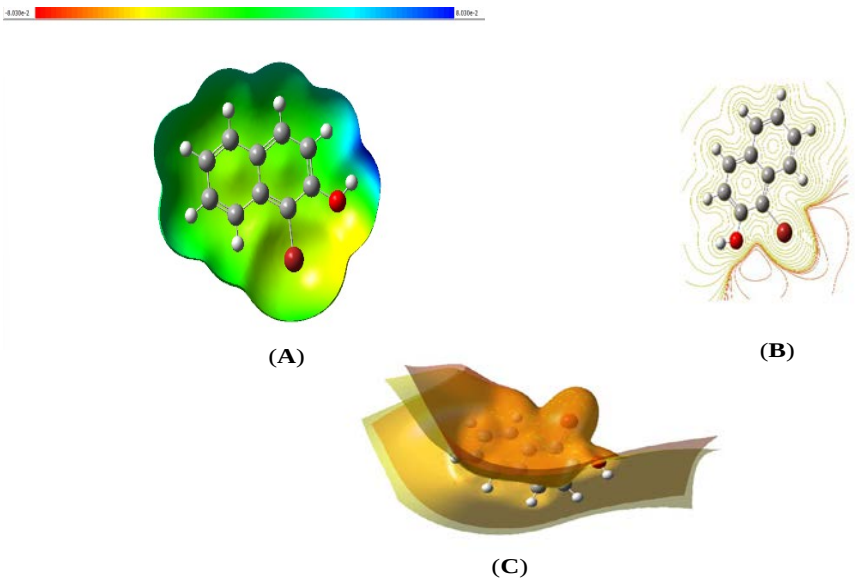

Figure 6.31: A). Molecular electrostatic potentials (MEP) plot of 1B2N, **B).** Contour map plot of ESP isosurface of 1B2N, **C).** Visualization of the ESP array plot for 1B2N

6.3.7.3. Mulliken charge (MC) analysis

In molecular systems composed of hydrogen, carbon, oxygen and halogens, particularly in phenolic and halogenated aromatic frameworks; Mulliken charge (MC) analysis provides critical insights into functionally significant electronic characteristics. Hydrogen atoms typically bear partial positive charges, indicating electron-deficient character. Carbon atoms exhibit variable charges depending on their hybridization and environment, influencing their electrophilic or nucleophilic nature. Oxygen atoms, due to high electronegativity, generally possess significant negative charges and contribute to hydrogen bonding and charge stabilization. Whereas halogen atoms such as bromine also show negative charges, exerting inductive affects that impact molecular polarity and reactivity. In our study, MC analysis was performed on two biologically active compounds viz., BDDE (Bis(2,3-dihydroxy-5-bromobenzyl) ether) and 1-Bromo-2-naphthol, both of which are known for their antioxidant, antimicrobial and antifungal properties. BDDE is a polyphenolic ether derivative comprising multiple -OH and -Br groups, forming a highly conjugated and electronically rich architecture. In contrast, 1B2Nis a fused aromatic system with a

simpler substitution pattern. The key MC values for both compounds are listed in **Table S6.30 (supporting information)**, while the structural and graphical distributions are presented in **Figure 6.37A** and **6.37B** and the MC plot comparisons in **Figure 6.38**. Among the studied carbon atoms, BDDE shows a strongly nucleophilic center at C_3 (-0.89), in contrast to the less negative C_2 in 1B2N (-0.45). Oxygen atoms follow a similar trend, with O_7 in BDDE (-0.31) bearing a more negative charge than O_{12} in the naphthol derivative (-0.25). The –OH containing hydrogen atoms at H_{26} in BDDE (0.32) and H_{19} in 1B2N (0.31) exhibit high positive charges, indicating polarized O–H bonds. For halogen atoms, Br_{11} in 1B2N (-0.15) is slightly more negative than Br_{10} in BDDE (-0.14), although the difference is minor. Significantly, BDDE contains multiple -Br substituents, potentially contributing to cumulative inductive effects on charge distribution.

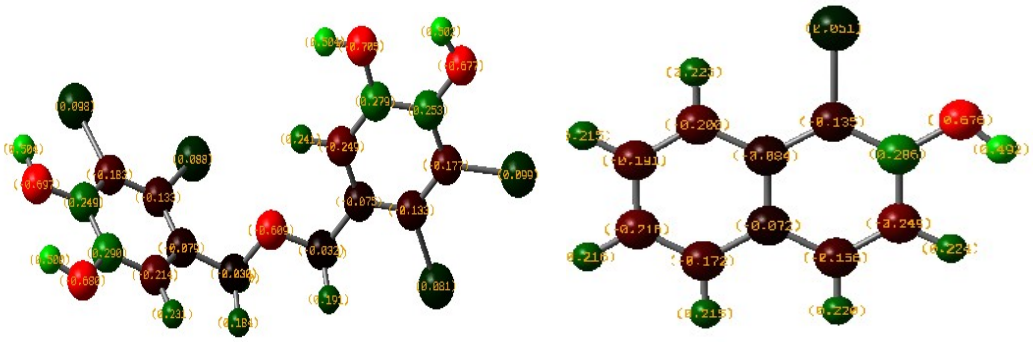

A **B**

Figure 6.37: A) MC distribution mapped on the optimized geometry of 1-Bromo-2-naphthol. Carbon atoms are shown in brown, oxygen in red, hydrogen in light green and bromine in dark green. The numerical values near each atom denote the respective Mulliken charges. Electron-rich regions (-O) are highlighted in red, indicating strong electron localization, while electron-deficient regions (-H) are depicted in green. **B)** MC distribution on the optimized molecular structure of BDDE. Bromine atom (dark green) and hydroxyl groups (red oxygens with adjacent positively charged hydrogens) lead to significant electronic polarization. The highly negative charge on C/O identifies key nucleophilic centers, while positively charged (H) reflects a polar O–H bond. This distribution confirms BDDE's strong charge delocalization and structural suitability for bioactivity.

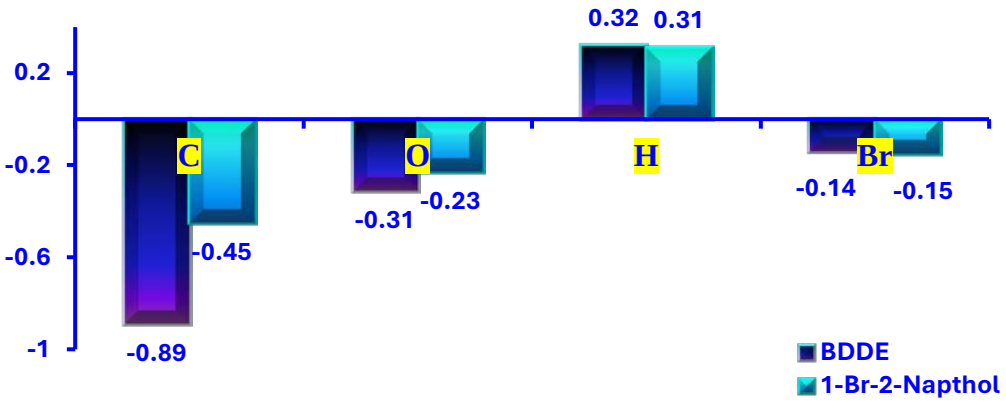

Figure 6.38: Bar plot comparison of Mulliken charges for selected atoms in BDDE and 1-Bromo-2-naphthol. The graph highlights key differences in electron density across C, O, H, and Br atoms in both molecules

Overall, BDDE exhibits a broader and more polarized charge distribution, reflective of its polyphenolic, conjugated and multi-substituted framework. This extensive electronic delocalization aligns with its established biological relevance. In contrast, 1B2N presents a structurally simpler yet electronically competent scaffold, characterized by a stable and localized charge profile. Despite its compact architecture, the molecule retains functionally significant regions of electron density, particularly around the hydroxyl and halogen substituents. These features highlight its potential as a promising candidate for further derivatization aimed at enhancing antioxidant, antimicrobial and antifungal properties. The combination of structural simplicity and meaningful electronic features suggests that 1B2Nmay serve as a valuable lead compound in future medicinal chemistry and molecular design efforts.

6.3.8. Natural Bond Orbital (NBO) analysis

In case of BDDE, the most prominent stabilization interaction corresponds to $\pi(C_4–C_5) \rightarrow \pi^*$ (C2–C3) with an E^2 of 219.17 kcal/mol, signifying a strong $\pi\rightarrow\pi^*$ delocalization within the aromatic framework. This extensive conjugation is further reinforced by lone pair interactions, notably LP_2 on $O_8 \rightarrow \pi^*(C_4–C_5)$ with $E^2 = 29.82$ kcal/mol, reflecting $n\rightarrow\pi^*$ charge transfer. Additionally, a moderate $\sigma(C_{23}–H_{33}) \rightarrow \sigma^*$ $(O_{22}–H_{32})$ interaction with $E^2 = 32.31$ kcal/mol, suggests weak intramolecular hyperconjugation or potential for hydrogen bonding. These interactions highlight the

critical role of oxygen lone pairs and aromatic conjugation in stabilizing the polyphenolic ether structure as depicted in **Figure 6.39A and Table 6.31**. For 1-Bromo-2-naphthol, the dominant interaction arises from $\sigma(O_{12}–H_{19}) \rightarrow \sigma^*$ ($C_{10}–Br_{11}$), exhibiting a remarkably high stabilization energy of 340.47 kcal/mol, indicating pronounced charge delocalization across the O–H and C–Br moieties. A similarly significant $\pi(C_4–C_5) \rightarrow \pi^*$ ($C_2–C_3$) interaction (E^2 = 254.09 kcal/mol) underscores the effectiveness of π-electron delocalization within the fused aromatic ring system. Moreover, LP_2 on $O_{12} \rightarrow \sigma^*$ ($C_{10}–Br_{11}$) contributes an additional stabilization of 199.04 kcal/mol, suggesting lone pair participation in reinforcing halogen-associated interactions, possibly via n→σ* hyperconjugation as listed in **Figure 6.39B and Table 6.31**.

Table 6.31: Second-order perturbation theory analysis of key donor–acceptor NBO interactions in BDDE and 1-Bromo-2-naphthol, showing stabilization energies (E^2, kcal/mol), energy gaps between orbitals (E(j)–E(i)), and Fock matrix elements F(i,j)

Compounds	**Donor NBO (i) → Acceptor NBO (j)**	**E^2 kcal/mol**	**E(j)-E(i) a.u.**	**F(i,j) a.u.**
BDDE	$\pi C_4 – C_5 \rightarrow \pi^* C_2 – C_3$	219.17	0.01	0.076
	$\sigma C_{23} – H_{33} \rightarrow \sigma^* O_{22} – H_{32}$	32.31	2.95	0.278
	$LP_2 O_8 \rightarrow \pi^* C_4 – C_5$	29.82	0.33	0.097
1B2N	$\sigma O_{12} – H_{19} \rightarrow \sigma^* C_{10} – B_{11}$	340.47	3.34	0.958
	$\pi C_4 – C_5 \rightarrow \pi^* C_2 – C_3$	254.09	0.01	0.078
	$LP_2 O_{12} \rightarrow \sigma^* C_{10} – Br_{11}$	199.04	3.24	0.720

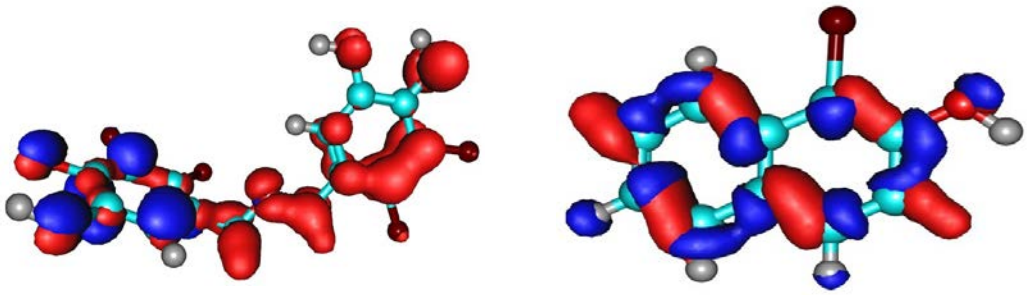

A B

Figure 6.39: NBO interaction plots of **(A)** BDDE and **(B)** 1B2N computed at the B3LYP/6-31G(d,p) level, illustrating key donor–acceptor interactions. BDDE shows prominent π→π *and n→π* delocalizations, while 1B2Nexhibits strong σ→σ* and n→σ* charge transfers involving the phenolic –OH and bromine substituents*

A comparative overview reveals that while BDDE benefits primarily from π→π* and n→π* delocalization, characteristic of extended conjugation and multiple electron-rich substituents, 1B2Ndemonstrates intense σ→σ* and n→σ* interactions, particularly involving the phenolic O–H and adjacent bromine. These findings reflect the diverse electronic stabilization mechanisms inherent to each compound and affirm the role of both halogen substitution and oxygen lone pair delocalization in modulating molecular stability and potential reactivity.

6.3.9. Nonlinear Optical (NLO) Analysis

Herein, the total static dipole moment (μ), the mean polarizability (⟨α⟩) and the first mean hyperpolarizability (⟨β⟩) were computed using the x, y and z components, based on the following equations (1-6):

$$\mu = (\mu_X^2 + \mu_Y^2 + \mu_Z^2)^{1/2} \qquad (1)$$

$$\alpha = \frac{(\alpha_{XX} + \alpha_{YY} + \alpha_{ZZ})}{3} \qquad (2)$$

$$\langle\beta\rangle = (\beta_x^2 + \beta_y^2 + \beta_z^2)^{1/2} \qquad (3)$$

Where,

$$\beta_x = \beta_{xxx} + \beta_{xyy} + \beta_{xzz} \qquad (4)$$

$$\beta_y = \beta_{yyy} + \beta_{xxy} + \beta_{yzz} \quad (5)$$

$$\beta_z = \beta_{zzz} + \beta_{xxz} + \beta_{yyz} \quad (6)$$

In this study, the nonlinear optical responses of two organic molecules BDDE and 1B2N were evaluated using density functional theory (DFT) at the B3LYP/6-311++G(d,p) level of theory. The computed descriptors include the dipole moment (μ), mean polarizability (⟨α⟩), and first-order hyperpolarizability (⟨β⟩). For comparative study, urea, a classical NLO benchmark compound, was employed as a reference due to its well-established theoretical and experimental values. The dipole moment, which reflects the degree of permanent charge separation within a molecule, is an essential parameter influencing both linear and nonlinear optical activity. Among the investigated systems, BDDE exhibited the highest dipole moment (2.90 D), indicating pronounced molecular asymmetry and charge delocalization. In comparison, 1B2N and urea showed similar values of 1.65 D and 1.67 D, respectively, suggesting a more balanced electronic distribution in those systems. The mean polarizability (⟨α⟩) quantifies the extent to which a molecule's electron cloud can be distorted by an external electric field. Here again, BDDE demonstrated superior polarizability (366.94 a.u.), a result attributed to its extended conjugated system and electron-rich framework. 1B2N showed an intermediate value (203.76 a.u.), while urea, with its compact and less conjugated structure, exhibited the lowest polarizability (27.76 a.u.) as shown in **Table 6.32**.

Table 6.32: NLO values of BDDE and 1B2Ncompounds with standard reference Urea

Compound	**Dipole Moment (μ, D)**	**Polarizability (⟨α⟩, a.u)**	**Hyperpolarizability (⟨β⟩, ×10⁻³⁰ esu)**
BDDE	2.90	366.94	1051.07
1B2N	1.65	203.76	1133.86
Urea	1.67	27.76	0.3728

The most significant difference among the three molecules was observed in the first-order hyperpolarizability (⟨β⟩), which is directly associated with second-order NLO effects. 1B2Nexhibited the highest hyperpolarizability (1133.86 × 10^{-30} esu), followed closely by BDDE (1051.07 × 10^{-30} esu). In stark contrast, urea showed a much lower value of 0.3728 × 10^{-30} esu. These findings highlight a dramatic enhancement by more than three orders of magnitude (Table 3) in the NLO response of the studied bioactive molecules compared to the reference compound. The enhanced NLO behavior in BDDE and 1B2N can be attributed to several key structural features: the presence of π-conjugated systems, electron-donating and/or withdrawing substituents, and pronounced molecular asymmetry. These characteristics collectively facilitate efficient intramolecular charge transfer and dynamic polarization, thereby amplifying their nonlinear optical response. Therefore, both BDDE and 1B2Ndemonstrate exceptional NLO performance compared to urea, indicating their potential utility as promising candidates for the design and development of next-generation organic NLO materials. This computational insight underscores the critical influence of electronic structure and molecular topology on optical properties, paving the way for the rational design of high-performance functional materials in the field of nonlinear optics.

6.3.10. Non-covalent Interactions (NCI) studies

Analysis of Non-Covalent Interactions in BDDE using IRI and ELF:

The IRI vs. sign(λ_2)ρ scatter plot of BDDE provides a quantitative fingerprint of the non-covalent interaction topologies embedded in its electron density framework as depicted in **Figure 6.40A**. A prominent concentration of data points in the region where sign(λ_2)ρ < 0 corresponds to attractive interactions, significantly intramolecular hydrogen bonding. These arise in areas where λ_2 is negative, indicating electron accumulation along the interaction pathway, a hallmark of stabilizing donor–acceptor behavior, particularly between proximal hydroxyl groups. A secondary distribution of points near sign (λ_2)ρ ≈ 0 reflects the presence of weak, non-directional dispersive interactions, such as van der Waals (vdW) forces, which are typically observed in low-density, low-gradient regions. These interactions are especially prevalent along the molecule's flexible ether and alkyl chains. The overall distribution pattern affirms

BDDE's multi-modal interaction capacity, underscoring its role as a conformationally adaptable, hydrogen bond–rich system. The corresponding IRI isosurface representation of BDDE (**Figure 6.40B**) provides spatial insight into the localization of these non-covalent interactions. Distinct green-colored isosurfaces enveloping the terminal hydroxyl groups clearly demarcate regions of potential hydrogen bond formation, resulting from lone-pair electron density overlaps with nearby electrophilic hydrogen atoms. These spatial regions correlate well with the attractive interaction zone observed in the scatter plot, reaffirming the molecule's inherent hydrogen-bonding propensity. Additionally, more diffuse green lobes along the ether linkage and alkyl backbone highlight the role of vdW interactions, which contribute to entropic flexibility behavior. The ELF analysis of BDDE further supports the IRI findings by revealing the distribution of electron localization across the molecule (**Figure 6.41**). The 3D ELF isosurface and 2D contour plots highlight regions with ELF values exceeding 0.85, particularly around the O–H and C–O bonds, confirming the presence of strongly localized lone pairs and σ-electrons. These highly localized basins affirm the nucleophilic character of the oxygen atoms and their role as both hydrogen bond donors and acceptors. The nearly spherical ELF basins seen in the contour maps further validate the directional nature of these interactions. Additionally, the presence of moderate ELF values along the alkyl backbone suggests weak nonbonding interactions that, although electronically subtle, may influence packing, flexibility and molecular recognition.

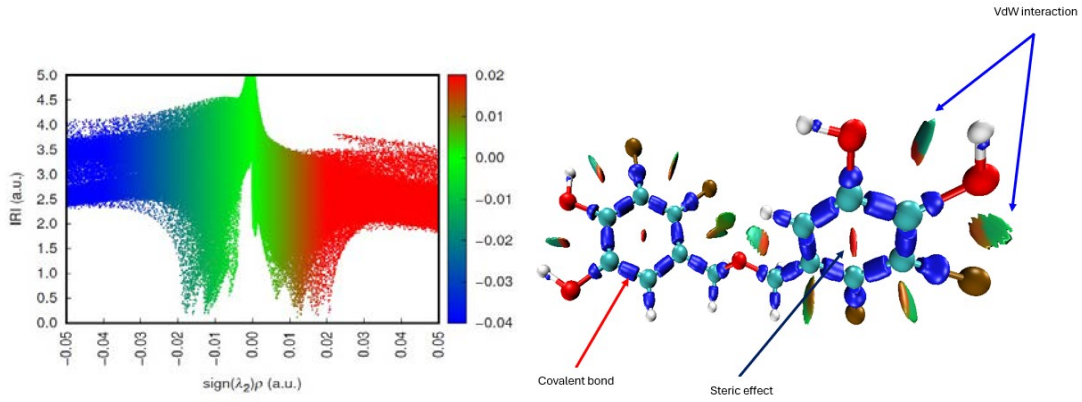

Figure 6.40: A). IRI vs. sign(λ_2)ρ scatter plot of BDDE, **B).** IRI isosurface representation of BDDE

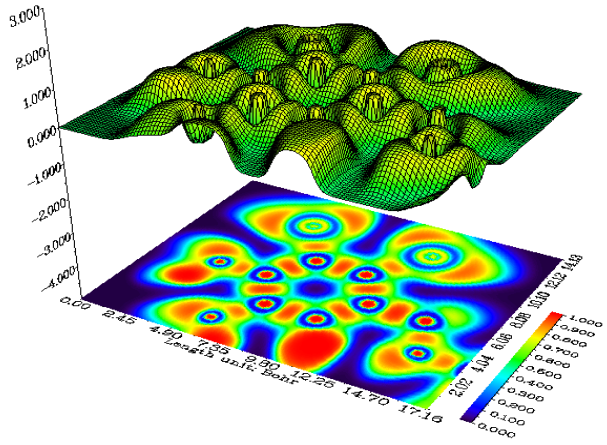

Figure 6.41: 3D isosurface and 2D contour plots of the Electron Localization Function (ELF), illustrating electron pairing distribution in the BDDE.

6.4. Conclusion

- Emphasis must be placed on the vast number of compounds that are synthesized each day yet left unused in laboratories and industries. Rather than allowing these molecules to remain overlooked, they can be regarded as a hidden reservoir of chemical diversity with significant potential. Exploring their utility through modern and innovative approaches provides an opportunity to repurpose or reassess their value. Such efforts not only curb unnecessary synthetic work but also promote sustainability by conserving resources, saving time, and reducing the generation of chemical waste.

- The present study explores a set of selected bromophenols, a total of 13 bromophenols some of which had been previously synthesized in our laboratory, thus using these shelved compounds and repurposing them.
- A comprehensive Molecular docking and pharmacophore mapping studies were performed against antibacterial, antifungal, and antioxidant targets, t undertsanad it poetnaila nd its mode of interctaion
- Among these, **1-bromo-2-naphthol** was identified as the top hit compound.

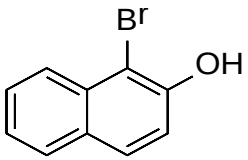

- This compound was then synthesized using **TBATB (a green brominating reagent)**, ensuring a more sustainable synthetic approach.
- To ascertain its activity, *in vitro* assays were carried out against the selected targets. These evaluations revealed favorable biological potential for the compound.
- Further in-depth quantum chemical calculations and additional computational studies were conducted to understand its structural and molecular characteristics.
- Overall, the findings indicated that **1-bromo-2-naphthol exhibits strong potential** and can serve as a promising lead candidate for future in *vivo* and clinical settings.

References

[1] D. T. Richter, "Recycling and reuse in the laboratory," in *The Royal Society of Chemistry eBooks*, 2015, pp. 173–184. doi: 10.1039/9781782622659-00173. Available: https://doi.org/10.1039/9781782622659-00173

[2] B. Sung, K.-M. Park, C. G. Park, Y.-H. Kim, J. Lee, and T.-E. Jin, "What drives researcher preferences for chemical compounds? Evidence from conjoint analysis," *PLoS ONE*, vol. 18, no. 11, p. e0294576, Nov. 2023, doi: 10.1371/journal.pone.0294576. Available: https://doi.org/10.1371/journal.pone.0294576

[3] H. Y. Goh, W. W. C. Wong, and Y. Y. Ong, "A study to reduce chemical waste generated in chemistry teaching laboratories," *Journal of Chemical Education*, vol. 97, no. 1, pp. 87–96, Nov. 2019, doi: 10.1021/acs.jchemed.9b00632. Available: https://doi.org/10.1021/acs.jchemed.9b00632

[4] J. H. Clark, T. J. Farmer, L. Herrero-Davila, and J. Sherwood, "Circular economy design considerations for research and process development in the chemical sciences," *Green Chemistry*, vol. 18, no. 14, pp. 3914–3934, Jan. 2016, doi: 10.1039/c6gc00501b. Available: https://doi.org/10.1039/c6gc00501b

[5] U. Naithani and V. Guleria, "Integrative computational approaches for discovery and evaluation of lead compound for drug design," *Frontiers in Drug Discovery*, vol. 4, Apr. 2024, doi: 10.3389/fddsv.2024.1362456. Available: https://doi.org/10.3389/fddsv.2024.1362456

[6] P. Prabhakaran, S. Bhardwaj, B. Chopra, A. K. Dhingra, and M. Kant, "Chemistry and Technology Innovation to Advance Green and Sustainable Chemistry," *Sustainable Green Catalytic Processes*, pp. 273–300, Sep. 2024, doi: 10.1002/9781394212767.ch12. Available: https://doi.org/10.1002/9781394212767.ch12

[7] L. Pinzi, N. Bisi, and G. Rastelli, "How drug repurposing can advance drug discovery: challenges and opportunities," *Frontiers in Drug Discovery*, vol. 4, Aug.

2024, doi: 10.3389/fddsv.2024.1460100. Available: https://doi.org/10.3389/fddsv.2024.1460100

[8] P. Zhan, B. Yu, and L. Ouyang, "Drug repurposing: An effective strategy to accelerate contemporary drug discovery," *Drug Discovery Today*, vol. 27, no. 7, pp. 1785–1788, Jun. 2022, doi: 10.1016/j.drudis.2022.05.026. Available: https://doi.org/10.1016/j.drudis.2022.05.026

[9] S. Bhar, "Role of drug repurposing in sustainable drug discovery," in *IntechOpen eBooks*, 2023. doi: 10.5772/intechopen.110621. Available: https://doi.org/10.5772/intechopen.110621

[10] A. Recino, M. L. D. Rayner, J. L. Rohn, and O. Della Pasqua, "Therapeutic innovation in drug repurposing: Challenges and opportunities," *Drug Discovery Today*, p. 104390, May 2025, doi: 10.1016/j.drudis.2025.104390. Available: https://doi.org/10.1016/j.drudis.2025.104390

[11] U. Bora, M. K. Chaudhuri, D. Dey, and S. S. Dhar, "Peroxometal-mediated environmentally favorable route to brominating agents and protocols for bromination of organics," *Pure and Applied Chemistry*, vol. 73, no. 1, pp. 93–102, Jan. 2001, doi: 10.1351/pac200173010093. Available: https://doi.org/10.1351/pac200173010093

[12] L. Jamir, B. Alimenla, A. Kumar, D. Sinha, and U. B. Sinha, "Synthesis and reactivity studies of a new reagent, ethyltriphenylphosphonium tribromide," *Synthetic Communications*, vol. 41, no. 1, pp. 147–155, Dec. 2010, doi: 10.1080/00397910903531912. Available: https://doi.org/10.1080/00397910903531912

[13] Kumar, Jamir, Jamir, Sinha, and Sinha, "Cetylpyridinium tribromide-An environmentally benign reagent for organic brominations and acetylations," *Organic Communications*, vol. 4, no. 1, p. 1, 2011.

[14] Bernard, Kumar, Jamir, Sinha, and Sinha, "An Efficient Microwave-Induced Solvent-Free Organic Bromination Using Tetrabutylammonium Tribromide," *Acta Chimica Slovenica*, vol. 56, no. 2, p. 457, 2009.

[15] B. Alimenla, A. Kumar, L. Jamir, D. Sinha, and U. B. Sinha, “Microwave-induced reactions: an alternative route for chemical synthesis,” *Radiation Effects and Defects in Solids*, vol. 161, no. 12, pp. 687–693, Oct. 2006, doi: 10.1080/10420150600907657. Available: https://doi.org/10.1080/10420150600907657

[16] B, K, and Sinha, “Tetrapropylammonium tribromide-an efficient reagent for solvent-free brominations,” *Chem. Sci. Trans*, vol. 3, no. 2, pp. 826–832, 2012.

[17] Kumar, Khan, and Saikia, “The Chemistry inside Spices & Herbs: Research and Development,” in *The Chemistry inside Spices & Herbs: Research and Development: Volume 1*, 2022, pp. 206–236. doi: 10.2174/9789815039566122010 1. Available: https://doi.org/10.2174/9789815039566122010 1

[18] Z. Xu, Z. Yang, Y. Liu, Y. Lu, K. Chen, and W. Zhu, “Halogen Bond: Its Role beyond Drug–Target Binding Affinity for Drug Discovery and Development,” *Journal of Chemical Information and Modeling*, vol. 54, no. 1, pp. 69–78, Dec. 2013, doi: 10.1021/ci400539q. Available: https://doi.org/10.1021/ci400539q

[19] N. E. Kolomiets, “HALOGENATED PHENOLIC COMPOUNDS OF NATURAL ORIGIN CONSTITUTE a RARE MINOR GROUP OF SUBSTANCES (A REVIEW),” *Chemistry of Plant Raw Material*, no. 4, pp. 24–31, Nov. 2024, doi: 10.14258/jcprm.20240413424. Available: https://doi.org/10.14258/jcprm.20240413424

[20] I. Saikia, P. Chakraborty, M. J. Sarma, M. Goswami, and P. Phukan, “Rapid and total bromination of aromatic compounds using TSNBR2 without any catalyst,” *Synthetic Communications*, vol. 45, no. 2, pp. 211–217, Sep. 2014, doi: 10.1080/00397911.2014.956367. Available: https://doi.org/10.1080/00397911.2014.956367

[21] A. Kumar, A. B., L. Jamir, D. Sinha, and U. B. Sinha, “Solvent-free methodologies for organic brominations using quaternary ammonium tribromides,”

Organic Communications, vol. 5, no. 2, pp. 64–69, 2012, Available: https://www.acgpubs.org/doc/202007091118408-OC-1111-221.pdf

[22] R. Karmaker, N. Longkumer, K. Richa, D. Sinha, and U. B. Sinha, "A computational approach to understanding the mechanism of aromatic bromination using quaternary ammonium tribromides," *Journal of the Indian Chemical Society*, vol. 99, no. 8, p. 100574, Jun. 2022, doi: 10.1016/j.jics.2022.100574. Available: https://doi.org/10.1016/j.jics.2022.100574

[23] P. Anastas and N. Eghbali, "Green Chemistry: Principles and practice," *Chemical Society Reviews*, vol. 39, no. 1, pp. 301–312, Nov. 2009, doi: 10.1039/b918763b. Available: https://doi.org/10.1039/b918763b

[24] R. Karmaker, D. Sinha, and U. B. Sinha, "Rationalizing between the efficiency and greenness of solvents – A computational study of their influence on TBATB," *Sustainable Chemistry and Pharmacy*, vol. 20, p. 100387, Feb. 2021, doi: 10.1016/j.scp.2021.100387. Available: https://doi.org/10.1016/j.scp.2021.100387

[25] R. Gopinath, Sk. J. Haque, and B. K. Patel, "Tetrabutylammonium tribromide (TBATB) as an efficient generator of HBR for an efficient chemoselective reagent for acetalization of carbonyl compounds," *The Journal of Organic Chemistry*, vol. 67, no. 16, pp. 5842–5845, Jun. 2002, doi: 10.1021/jo025701o. Available: https://doi.org/10.1021/jo025701o

[26] N. Öztaşkın, R. Kaya, A. Maraş, E. Şahin, İ. Gülcin, and S. Göksu, "Synthesis and characterization of novel bromophenols: Determination of their anticholinergic, antidiabetic and antioxidant activities," *Bioorganic Chemistry*, vol. 87, pp. 91–102, Mar. 2019, doi: 10.1016/j.bioorg.2019.03.010. Available: https://doi.org/10.1016/j.bioorg.2019.03.010

[27] J. Jacobtorweihen and V. Spiegler, "Phylogenetic distribution of bromophenols in marine algae and the generation of a comprehensive bromophenol database," *Phytochemistry Reviews*, vol. 22, no. 3, pp. 505–542, Nov. 2022, doi: 10.1007/s11101-022-09847-8. Available: https://doi.org/10.1007/s11101-022-09847-8

[28] H. Dong, S. Dong, P. E. Hansen, D. Stagos, X. Lin, and M. Liu, "Progress of Bromophenols in Marine Algae from 2011 to 2020: Structure, Bioactivities, and Applications," *Marine Drugs*, vol. 18, no. 8, p. 411, Aug. 2020, doi: 10.3390/md18080411. Available: https://doi.org/10.3390/md18080411

[29] M. Liu, P. E. Hansen, and X. Lin, "Bromophenols in marine algae and their bioactivities," *Marine Drugs*, vol. 9, no. 7, pp. 1273–1292, Jul. 2011, doi: 10.3390/md9071273. Available: https://doi.org/10.3390/md9071273

[30] M. ApS, *Molegro Virtual Docker*, version 2.4, Aarhus, Denmark: CLC bio, 2008.

[31] B. Singha *et al.*, "A holistic computational exploration of AZD7762 as a potent selective modulator of LXRα, LXRβ and FXR: An underexplored pathway in cancer therapeutics," *Computers in Biology and Medicine*, vol. 194, p. 110433, Jun. 2025, doi: 10.1016/j.compbiomed.2025.110433. Available: https://doi.org/10.1016/j.compbiomed.2025.110433

[32] S.-Y. Yang, "Pharmacophore modeling and applications in drug discovery: challenges and recent advances," *Drug Discovery Today*, vol. 15, no. 11–12, pp. 444–450, Apr. 2010, doi: 10.1016/j.drudis.2010.03.013. Available: https://doi.org/10.1016/j.drudis.2010.03.013

[33] G. Wolber and T. Langer, "LigandScout: 3-D Pharmacophores Derived from Protein-Bound Ligands and Their Use as Virtual Screening Filters," *Journal of Chemical Information and Modeling*, vol. 45, no. 1, pp. 160–169, Nov. 2004, doi: 10.1021/ci049885e. Available: https://doi.org/10.1021/ci049885e

[34] B, Sinha, and Sinha, "Studies on quaternary ammonium tribromides and peroxovanadates mediated organic halogenations," PhD Thesis, Nagaland University, 2012. Available: http://hdl.handle.net/10603/388688

[35] Jamir and Sinha, "Synthesis of newer tribromides and studies of some oxidative organic transformations," PhD Thesis, Nagaland University, 2011. Available: http://hdl.handle.net/10603/388689

[36] Kumar and Sinha, "Studies on organic transformation reactions using different quaternary ammonium tribromides," PhD Thesis, Nagaland University, 2010. Available: http://hdl.handle.net/10603/383577

[37] N. Longkumer *et al.*, "Green synthesis of bromo organic molecules and investigations on their antibacterial properties: an experimental and computational approach," *Acta Chimica Slovenica*, vol. 66, no. 2, pp. 276–283, Jun. 2019, doi: 10.17344/acsi.2018.4580. Available: https://doi.org/10.17344/acsi.2018.4580

[38] N. Longkumer, K. Richa, R. Karmaker, B. Singha, and U. B. Sinha, "Experimental and theoretical investigations on the antibacterial activity of some bromoaniline compounds," *Anti-Infective Agents*, vol. 21, no. 3, Jan. 2023, doi: 10.2174/22113525216662301261230 21. Available: https://doi.org/10.2174/2211352521666230126123021

[39] M. Balouiri, M. Sadiki, and S. K. Ibnsouda, "Methods for in vitro evaluating antimicrobial activity: A review," *Journal of Pharmaceutical Analysis*, vol. 6, no. 2, pp. 71–79, Dec. 2015, doi: 10.1016/j.jpha.2015.11.005. Available: https://doi.org/10.1016/j.jpha.2015.11.005

[40] N. Longkumer, K. Richa, R. Karmaker, B. Singha, and U. B. Sinha, "Facile Green Synthesis of Bromoaniline Molecules: An Experimental and Computational Insight into their Antifungal Behaviour," *Asian Journal of Chemistry*, vol. 34, no. 12, pp. 3115–3124, Jan. 2022, doi: 10.14233/ajchem.2022.23994. Available: https://doi.org/10.14233/ajchem.2022.23994

[41] W. Brand-Williams, M. E. Cuvelier, and C. Berset, "Use of a free radical method to evaluate antioxidant activity," *LWT*, vol. 28, no. 1, pp. 25–30, Jan. 1995, doi: 10.1016/s0023-6438(95)80008-5. Available: https://doi.org/10.1016/s0023-6438(95)80008-5

[42] Rakholiya, Kaneria, Nagani, Patel, and Chanda, "Comparative analysis and simultaneous quantification of antioxidant capacity of four terminalia species using various photometric assays," *World J. Pharm. Res*, vol. 4, pp. 1280–1296, 2015, Available: http://www.wjpr.net/dashboard/abstract_id/2535

[43] N. Babbar, H. S. Oberoi, D. S. Uppal, and R. T. Patil, "Total phenolic content and antioxidant capacity of extracts obtained from six important fruit residues," *Food Research International*, vol. 44, no. 1, pp. 391–396, Oct. 2010, doi: 10.1016/j.foodres.2010.10.001. Available: https://doi.org/10.1016/j.foodres.2010.10.001

[44] M. Leopoldini, N. Russo, and M. Toscano, "The molecular basis of working mechanism of natural polyphenolic antioxidants," *Food Chemistry*, vol. 125, no. 2, pp. 288–306, Aug. 2010, doi: 10.1016/j.foodchem.2010.08.012. Available: https://doi.org/10.1016/j.foodchem.2010.08.012

[45] J. S. Wright, E. R. Johnson, and G. A. DiLabio, "Predicting the activity of phenolic antioxidants: theoretical method, analysis of substituent effects, and application to major families of antioxidants," *Journal of the American Chemical Society*, vol. 123, no. 6, pp. 1173–1183, Jan. 2001, doi: 10.1021/ja002455u. Available: https://doi.org/10.1021/ja002455u

[46] K. S. Kumar and R. Kumaresan, "A DFT study on the structural, electronic properties and radical scavenging mechanisms of calycosin, glycitein, pratensein and prunetin," *Computational and Theoretical Chemistry*, vol. 985, pp. 14–22, Jan. 2012, doi: 10.1016/j.comptc.2012.01.028. Available: https://doi.org/10.1016/j.comptc.2012.01.028

[47] N. Nenadis and M. Z. Tsimidou, "Contribution of DFT computed molecular descriptors in the study of radical scavenging activity trend of natural hydroxybenzaldehydes and corresponding acids," *Food Research International*, vol. 48, no. 2, pp. 538–543, May 2012, doi: 10.1016/j.foodres.2012.05.014. Available: https://doi.org/10.1016/j.foodres.2012.05.014

[48] M. J. Frisch, G. W. Trucks, H. B. Schlegel *et al.*, *Gaussian 16*, *Revision C.01*, Gaussian, Inc., Wallingford, CT, USA, 2016

[49] A. Ouaket, A. Chraka, I. Raissouni, M. A. E. Amrani, M. Berrada, and N. Knouzi, "Synthesis, spectroscopic (13C/1H-NMR, FT-IR) investigations, quantum chemical modelling (FMO, MEP, NBO analysis), and antioxidant activity of the bis-benzimidazole molecule," *Journal of Molecular Structure*, vol. 1259, p.

132729, Mar. 2022, doi: 10.1016/j.molstruc.2022.132729. Available: https://doi.org/10.1016/j.molstruc.2022.132729

[50] X. Xiao *et al.*, "Analysis of the structure and Mulliken charges in TM3+-Doped bismuth silicate crystals," *Chemical Physics Impact*, p. 100881, Apr. 2025, doi: 10.1016/j.chphi.2025.100881. Available: https://doi.org/10.1016/j.chphi.2025.100881

[51] S. A. Halim, A. B. El-Meligy, A. M. El-Nahas, and S. H. El-Demerdash, "DFT study, and natural bond orbital (NBO) population analysis of 2-(2-Hydroxyphenyl)-1-azaazulene tautomers and their mercapto analouges," *Scientific Reports*, vol. 14, no. 1, Jan. 2024, doi: 10.1038/s41598-023-50660-w. Available: https://doi.org/10.1038/s41598-023-50660-w

[52] L. H. Abdel-Rahman, A. M. Abu-Dief, H. Moustafa, and A. a. H. Abdel-Mawgoud, "Design and nonlinear optical properties (NLO) using DFT approach of new Cr(III), VO(II), and Ni(II) chelates incorporating tri-dentate imine ligand for DNA interaction, antimicrobial, anticancer activities and molecular docking studies," *Arabian Journal of Chemistry*, vol. 13, no. 1, pp. 649–670, Jul. 2017, doi: 10.1016/j.arabjc.2017.07.007. Available: https://doi.org/10.1016/j.arabjc.2017.07.007

[53] T. Lu and Q. Chen, "Interaction Region Indicator: A simple real space function clearly revealing both chemical bonds and weak interactions**," *Chemistry - Methods*, vol. 1, no. 5, pp. 231–239, May 2021, doi: 10.1002/cmtd.202100007. Available: https://doi.org/10.1002/cmtd.202100007

[54] K. Arulaabaranam, S. Muthu, G. Mani, and A. S. B. Geoffrey, "Speculative assessment, molecular composition, PDOS, topology exploration (ELF, LOL, RDG), ligand-protein interactions, on 5-bromo-3-nitropyridine-2-carbonitrile," *Heliyon*, vol. 7, no. 5, p. e07061, May 2021, doi: 10.1016/j.heliyon.2021.e07061. Available: https://doi.org/10.1016/j.heliyon.2021.e07061

[55] N. Kuotsu, C. Pongen, T. Phucho, and U. Sinha, "Comparative degradation Kinetic studies of Tetrabutyl-ammonium tribromide (TBATB) and Cetyltrimethyl-

ammonium Tribromide(CTMATB) - A route to reactivity Assessment for Solvent-Free Reactions," *Chemical Science Transactions*, Jan. 2015, doi: 10.7598/cst2015.972. Available: https://doi.org/10.7598/cst2015.972

[56] S. Baliyan *et al.*, "Determination of Antioxidants by DPPH Radical Scavenging Activity and Quantitative Phytochemical Analysis of Ficus religiosa," *Molecules*, vol. 27, no. 4, p. 1326, Feb. 2022, doi: 10.3390/molecules27041326. Available: https://doi.org/10.3390/molecules27041326

[57] D. Q. Huong, P. C. Nam, and T. Duong, "Experimental and theoretical insights into free radical capturing activity of 1,5-diaminonaphthalene and 1,5-dihydroxynaphthalene," *Journal of Molecular Structure*, vol. 1285, p. 135537, Apr. 2023, doi: 10.1016/j.molstruc.2023.135537. Available: https://doi.org/10.1016/j.molstruc.2023.135537

[58] İ. Gulcin and S. H. Alwasel, "DPPH radical scavenging assay," *Processes*, vol. 11, no. 8, p. 2248, Jul. 2023, doi: 10.3390/pr11082248. Available: https://doi.org/10.3390/pr11082248

[59] L. Socrier *et al.*, "Nitrone-Trolox conjugate as an inhibitor of lipid oxidation: Towards synergistic antioxidant effects," *Biochimica Et Biophysica Acta (BBA) - Biomembranes*, vol. 1861, no. 8, pp. 1489–1501, Jun. 2019, doi: 10.1016/j.bbamem.2019.06.008. Available: https://doi.org/10.1016/j.bbamem.2019.06.008

[60] A. C. Caritá, B. Fonseca-Santos, J. D. Shultz, B. Michniak-Kohn, M. Chorilli, and G. R. Leonardi, "Vitamin C: One compound, several uses. Advances for delivery, efficiency and stability," *Nanomedicine Nanotechnology Biology and Medicine*, vol. 24, p. 102117, Nov. 2019, doi: 10.1016/j.nano.2019.102117. Available: https://doi.org/10.1016/j.nano.2019.102117

[61] I. R. Ilyasov, V. L. Beloborodov, I. A. Selivanova, and R. P. Terekhov, "ABTS/PP Decolorization Assay of Antioxidant Capacity Reaction Pathways," *International Journal of Molecular Sciences*, vol. 21, no. 3, p. 1131, Feb. 2020, doi: 10.3390/ijms21031131. Available: https://doi.org/10.3390/ijms21031131

[62] M. Erdoğan, L. P. Köse, S. Eşsiz, and İ. Gülçin, "Synthesis and biological evaluation of some 1-naphthol derivatives as antioxidants, acetylcholinesterase, and carbonic anhydrase inhibitors," *Archiv Der Pharmazie*, vol. 354, no. 8, Jun. 2021, doi: 10.1002/ardp.202100113. Available: https://doi.org/10.1002/ardp.202100113

[63] K. Richa, R. Karmaker, T. Ao, N. Longkumer, B. Singha, and U. B. Sinha, "Rationale for antioxidant interaction studies of 4-bromo-1-isothiocyanato-2-methylbenzene – An experimental and computational investigation," *Chemical Physics Letters*, vol. 753, p. 137611, May 2020, doi: 10.1016/j.cplett.2020.137611. Available: https://doi.org/10.1016/j.cplett.2020.137611

[64] N. Liang and D. Kitts, "Antioxidant Property of Coffee Components: Assessment of Methods that Define Mechanisms of Action," *Molecules*, vol. 19, no. 11, pp. 19180–19208, Nov. 2014, doi: 10.3390/molecules191119180. Available: https://doi.org/10.3390/molecules191119180

[65] S. Abu-Melha, "Molecular modeling and antioxidant activity of newly synthesized 3-hydroxy-2-substituted-thiophene derivatives," *Journal of Molecular Structure*, vol. 1250, p. 131821, Oct. 2021, doi: 10.1016/j.molstruc.2021.131821. Available: https://doi.org/10.1016/j.molstruc.2021.131821

[66] J. S. Singh, Mohd. S. Khan, and S. Uddin, "A DFT study of vibrational spectra of 5-chlorouracil with molecular structure, HOMO–LUMO, MEPs/ESPs and thermodynamic properties," *Polymer Bulletin*, vol. 80, no. 3, pp. 3055–3083, Mar. 2022, doi: 10.1007/s00289-022-04181-7. Available: https://doi.org/10.1007/s00289-022-04181-7

[67] N. T. El-Shamy, A. M. Alkaoud, R. K. Hussein, M. A. Ibrahim, A. G. Alhamzani, and M. M. Abou-Krisha, "DFT, ADMET and Molecular Docking Investigations for the Antimicrobial Activity of 6,6′-Diamino-1,1′,3,3′-tetramethyl-5,5′-(4-chlorobenzylidene)bis[pyrimidine-2,4(1H,3H)-dione]," *Molecules*, vol. 27, no. 3, p. 620, Jan. 2022, doi: 10.3390/molecules27030620. Available: https://doi.org/10.3390/molecules27030620

[68] S. K. Alghamdi, F. Abbas, R. K. Hussein, A. G. Alhamzani, and N. T. El-Shamy, "Spectroscopic characterization (IR, UV-Vis), and HOMO-LUMO, MEP, NLO, NBO Analysis and the Antifungal Activity for 4-Bromo-N-(2-nitrophenyl) benzamide; Using DFT Modeling and In silico Molecular Docking," *Journal of Molecular Structure*, vol. 1271, p. 134001, Aug. 2022, doi: 10.1016/j.molstruc.2022.134001. Available: https://doi.org/10.1016/j.molstruc.2022.134001

[69] K. Benbouguerra, N. Chafai, S. Chafaa, Y. I. Touahria, and H. Tlidjane, "New α-Hydrazinophosphonic acid: Synthesis, characterization, DFT study and in silico prediction of its potential inhibition of SARS-CoV-2 main protease," *Journal of Molecular Structure*, vol. 1239, p. 130480, Apr. 2021, doi: 10.1016/j.molstruc.2021.130480. Available: https://doi.org/10.1016/j.molstruc.2021.130480

[70] Y.-M. Chai, H.-B. Zhang, X.-Y. Zhang, and L.-Q. Chai, "X-ray structures, spectroscopic, antimicrobial activity, ESP/HSA and TD/DFT calculations of Bi(III) complex containing imidazole ring," *Journal of Molecular Structure*, vol. 1256, p. 132517, Feb. 2022, doi: 10.1016/j.molstruc.2022.132517. Available: https://doi.org/10.1016/j.molstruc.2022.132517

[71] J. S. Singh, Mohd. S. Khan, and S. Uddin, "Raman and IR spectra and DFT/G-09 molecular analysis with vibrational study and related other parameters of 5-methyluracil," *Indian Journal of Physics*, vol. 97, no. 4, pp. 1037–1053, Nov. 2022, doi: 10.1007/s12648-022-02480-3. Available: https://doi.org/10.1007/s12648-022-02480-3

SUPPORTING INFORMATION

6.2.1.2. Compounds under investigation

Table S6.1: List of compounds under investigation

Compounds	SMILES	Compounds	SMILES
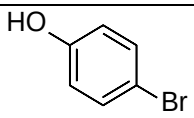 **1**	OC1=CC=C(Br)C=C1	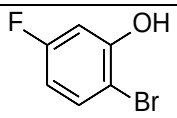 **8**	OC1=C(Br)C=CC(F)=C1
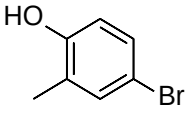 **2**	OC1=C(C)C=C(Br)C=C1	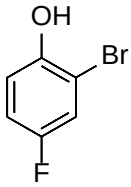 **9**	OC1=C(Br)C=C(F)C=C1
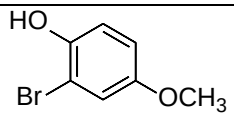 **3**	OC1=C(Br)C=C(OC)C=C1	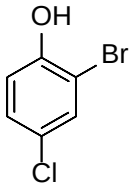 **10**	OC1=C(Br)C=C(Cl)C=C1
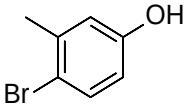 **4**	CC1=C(Br)C=CC(O)=C1	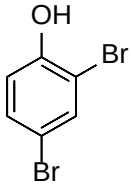 **11**	OC1=C(Br)C=C(Br)C=C1
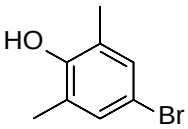 **5**	OC1=C(C)C=C(Br)C=C1C	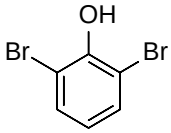 **12**	BrC1=CC=CC(Br)=C1O
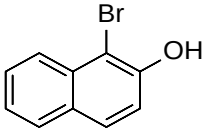 **6**	OC1=C(Br)C2=CC=CC=C2C=C1	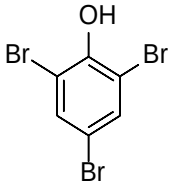 **13**	BrC1=CC(Br)=CC(Br)=C1O
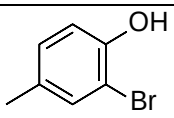 **7**	OC1=C(Br)C=C(C)C=C1		

6.2.1.3. Docking *via* AutoDock

Table S6.2: Grid co-ordinates defining the binding sites of the targets

PDB ID	Grid co-ordinates
7DQL	X=26.158111; Y= 20.283556; Z=19.802889
1JII	X=-11.471621; Y=14.779000; Z=85.397483
7Y8B	X=25.134130; Y=-52.055391; Z=52.042130
7MYL	X=0.691952; Y=16.389905; Z=34.770095
1M78	X=29.574571; Y=-2.551071; Z=1.040643
8BHH	X=-23.942333; Y=-13.608250; Z=-21.224333
4IN4	X=13.808242; Y=7.674879; Z=33.606818
4ZZI	X=8.005200; Y=35.699320; Z=-4.533880

6.3.1.1. Docking *via* MVD

Table S6.3: Docking scores of ligands against PDB ID 7DQL obtained *via* MVD

Ligand	MolDock Score	[a]Rerank Score	[b]Interaction	[c]Internal	[d]HBond	[e]LE1	[f]LE3
Co-crystallized ligand	-67.2718	-59.2671	-76.3669	9.09514	-5.27756	-7.47465	-6.58524
6 (1B2N)	-68.6846	-58.1503	-84.9905	16.3058	-3.30855	-5.72372	-4.84586
5	-64.8773	-56.3429	-76.4148	11.5374	-2.37043	-6.48773	-5.63429
4	-67.1495	-55.5077	-74.591	7.4415	-3.01021	-7.46105	-6.16752
13	-66.0421	-54.0494	-72.8078	6.76569	-2.5	-6.60421	-5.40494
3	-64.3687	-53.504	-73.7961	9.42747	0	-6.43687	-5.3504

12	-62.1985	-52.5478	-70.2717	8.07319	-2.5	-6.91095	-5.83864
2	-62.629	-52.0716	-72.6553	10.0264	-2.39195	-6.95877	-5.78574
7	-61.8492	-52.0508	-70.6298	8.78056	-2.61049	-6.87214	-5.78343
9	-63.4751	-51.5104	-72.1372	8.66203	0	-7.05279	-5.72338
8	-61.82	-50.7652	-70.4776	8.65754	0	-6.86889	-5.64058
10	-61.1737	-50.4446	-69.8805	8.70679	-2.40983	-6.79708	-5.60496
11	-60.7053	-50.1451	-69.5268	8.82149	-2.40568	-6.74503	-5.57168
1	-58.9475	-49.3875	-67.7613	8.81381	-3.00761	-7.36843	-6.17343
Streptomycin	-69.2537	39.5886	-123.598	54.3441	0.270037	-1.73134	0.989715

[a]*The rerank score represents a weighted linear combination of intermolecular interaction energies (steric, van der Waals, hydrogen bonding, electrostatics) between the ligand and protein, along with E-intra (torsional strain, sp^2–sp^2 interactions, hydrogen bonding, van der Waals, and electrostatic forces) within the ligand.*

[b] *Denotes the total interaction energy between the docked ligand conformation (pose) and the target protein, expressed in kJ/mol.*

[c] *Reflects the intramolecular energy of the docked ligand conformation (pose).*

[d] *Hydrogen bond contribution to the interaction energy, in kJ/mol.*

[e] *Ligand efficiency metric 1, calculated as the MolDock score divided by the number of heavy atoms.*

[f] *Ligand efficiency metric 3, calculated by dividing the rerank score by the number of heavy atoms.*

6.3.1.1. Docking *via* MVD

Table S6.4: Docking scores of ligands against PDB ID 1JII obtained *via* MVD

Ligand	MolDock Score	[a]Rerank Score	[b]Interaction	[c]Internal	[d]HBond	[e]LE1	[f]LE3

Streptomycin	-148.164	-119.909	-176.907	28.743	-18.9213	-3.70411	-2.99774
Co-crystallized ligand	-116.547	-115.583	-166.386	49.8387	-13.0491	-4.01887	-3.98562
6 (1B2N)	-79.7955	-66.9513	-96.1017	16.3062	-2.41127	-6.64962	-5.57927
5	-69.1313	-60.2543	-80.6687	11.5374	-1.96179	-6.91313	-6.02543
13	-72.842	-59.9002	-79.6077	6.7657	-2.01079	-7.2842	-5.99002
3	-73.2079	-59.3817	-82.7742	9.56632	-2.90984	-7.32079	-5.93817
4	-68.1183	-55.6874	-75.5597	7.44143	-2.5	-7.5687	-6.18749
2	-63.8272	-53.8854	-73.8536	10.0263	-2.5	-7.09191	-5.98726
8	-66.6458	-53.8801	-75.3033	8.6575	-2.41469	-7.40509	-5.98668
9	-65.4392	-53.1731	-74.1013	8.66207	-0.558292	-7.27103	-5.90812
12	-62.2073	-53.0704	-70.2804	8.07312	0	-6.91192	-5.89671
7	-65.0769	-52.9733	-73.8575	8.78056	-4.21908	-7.23077	-5.88592
10	-64.9739	-52.902	-73.6806	8.70675	-2.5	-7.21932	-5.878
11	-63.0751	-51.5421	-71.8965	8.82139	-2.40288	-7.00835	-5.7269

1	-57.1581	-47.0724	-65.9719	8.81377	-2.36686	-7.14476	-5.88404

6.3.1.1. Docking *via* MVD

Table S6.5: Docking scores of ligands against PDB ID 7Y8B obtained *via* MVD

Ligand	MolDock Score	[a]Rerank Score	[b]Interaction	[c]Internal	[d]HBond	[e]LE1	[f]LE3
Streptomycin	-102.878	-84.6666	-135.388	32.51	-16.343	-2.57195	-2.11667
CL	-67.1586	-58.1128	-78.1144	10.9559	-7.5332	-4.79704	-4.15091
6	-55.6935	-47.4453	-65.7122	10.0187	-5.11121	-4.64113	-3.95377
5	-50.7028	-43.4418	-62.1378	11.4349	-5.27276	-5.07028	-4.34418
3	-51.8065	-42.4713	-60.6787	8.87222	-4.84483	-5.18065	-4.24713
12	-47.4581	-40.4262	-55.5314	8.07321	-5.43263	-5.27313	-4.4918
7	-47.4454	-39.6029	-56.2258	8.78045	-4.85731	-5.27171	-4.40032
2	-46.327	-39.5815	-56.3535	10.0265	-4.96047	-5.14745	-4.39794
13	-50.5974	-39.5309	-60.1584	9.56094	-5.52139	-5.05974	-3.95309
11	-47.4625	-38.8247	-56.284	8.82144	-4.87104	-5.27362	-4.31386
10	-47.5463	-38.8226	-56.2531	8.70679	-4.8715	-5.28292	-4.31363

9	-47.5298	-38.7589	-56.1919	8.66211	-4.87375	-5.28109	-4.30655
8	-47.1612	-38.5653	-55.8188	8.65757	-4.80971	-5.24013	-4.28503
4	-46.5261	-38.3149	-53.9675	7.44145	-5.33076	-5.16956	-4.25721
1	-41.6661	-34.8873	-50.4799	8.81382	-5.16179	-5.20826	-4.36091

6.3.1.1. Docking *via* MVD

Table S6.6: Docking scores of ligands against PDB ID 7MYL obtained *via* MVD

Ligand	MolDock Score	[a]Rerank Score	[b]Interaction	[c]Internal	[d]HBond	[e]LE1	[f]LE3
Co-crystallized ligand	-137.254	-119.821	-157.234	19.9802	-7.62868	-6.53591	-5.70574
6(1B2N)	-78.7587	-65.4974	-95.0647	16.306	-3.08138	-6.56323	-5.45812
Streptomycin	-117.443	-62.5788	-155.528	38.0847	-9.61572	-2.93607	-1.56447
3	-72.3307	-59.7343	-82.2213	9.89055	-3.07594	-7.23307	-5.97343
5	-66.9727	-57.0386	-78.5101	11.5374	0	-6.69727	-5.70386
13	-69.0641	-56.7966	-75.8299	6.76571	0	-6.90641	-5.67966
4	-69.2762	-56.7961	-76.7176	7.44137	-3.11909	-7.69736	-6.31068
8	-70.088	-56.3299	-78.7455	8.65749	-3.09183	-7.78756	-6.25888

7	-66.8227	-55.6437	-75.6033	8.78061	-3.09907	-7.42475	-6.18263
12	-65.3236	-54.908	-73.3968	8.07315	-2.5	-7.25818	-6.10088
9	-67.2674	-54.4891	-75.9295	8.66206	-3.10791	-7.47416	-6.05435
10	-66.2616	-53.8327	-74.9684	8.70676	-3.03123	-7.3624	-5.98141
2	-63.5297	-53.2679	-73.5561	10.0264	-2.77131	-7.05886	-5.91866
11	-64.6058	-52.1077	-73.4273	8.82145	-2.84768	-7.17843	-5.78974
1	-59.1009	-48.7162	-67.9147	8.81375	-3.10969	-7.38762	-6.08952

6.3.1.1. Docking *via* MVD

Table S6.7: Docking scores of ligands against PDB ID 1M78 obtained *via* MVD

Ligand	**MolDock Score**	**[a]Rerank Score**	**[b]Interaction**	**[c]Internal**	**[d]HBond**	**[e]LE1**	**[f]LE3**
Fluconazole	-118.301	-91.5817	-124.446	6.14452	-8.64609	-5.37732	-4.16281
Co-crystallized ligand	-79.8616	-70.2135	-90.7062	10.8446	-5.30794	-5.7044	-5.01525
6(1B2N)	-71.7551	-59.6284	-81.774	10.0189	-1.41096	-5.97959	-4.96904
3	-61.7265	-51.235	-71.0625	9.33607	-3.49504	-6.17265	-5.1235
5	-58.6278	-50.5039	-70.0628	11.435	-2.3126	-5.86278	-5.05039

8	-60.2675	-47.9655	-68.9251	8.65758	-3.13461	-6.69639	-5.3295
13	-60.5325	-47.1621	-70.0935	9.56101	-2.34888	-6.05325	-4.71621
12	-56.2166	-47.0103	-64.2898	8.07316	-2.5	-6.24629	-5.22336
7	-55.8116	-46.5348	-64.5922	8.7806	-2.25474	-6.20129	-5.17054
2	-53.8881	-45.6079	-63.9144	10.0263	-2.22137	-5.98756	-5.06755
9	-56.0216	-45.3592	-64.6837	8.6621	-2.24847	-6.22463	-5.03991
11	-55.7242	-45.1944	-64.5457	8.82147	-2.23302	-6.19158	-5.0216
10	-55.8075	-45.1788	-64.5143	8.70675	-2.25818	-6.20084	-5.01987
4	-59.7551	-44.7751	-67.1966	7.44145	-3.97626	-6.63946	-4.97501
1	-51.4426	-40.062	-60.2564	8.8138	-2.54477	-6.43032	-5.00775

6.3.1.1. Docking *via* MVD

Table S6.8: Docking scores of ligands against PDB ID 8BHH obtained *via* MVD

Ligand	MolDock Score	[a]Rerank Score	[b]Interaction	[c]Internal	[d]HBond	[e]LE1	[f]LE3
Co-crystallized ligand	-88.7963	-76.347	-93.7096	4.91326	-5.16718	-7.39969	-6.36225
Fluconazole	-95.9315	-72.2086	-104.565	8.63314	-9.27188	-4.36052	-3.28221

6(1B2N)	-78.1558	-66.8075	-94.4621	16.3063	-4.25763	-6.51298	-5.5673
3	-71.1255	-59.0045	-81.9499	10.8245	-5.81515	-7.11255	-5.90045
4	-68.4631	-56.8781	-75.9046	7.44142	-4.24166	-7.60702	-6.31979
5	-66.1792	-55.8032	-78.6084	12.4292	-1.10939	-6.61792	-5.58032
2	-62.9262	-54.2297	-72.9526	10.0264	-4.24321	-6.9918	-6.02552
7	-62.6212	-53.5946	-71.4018	8.78056	-2.05558	-6.95792	-5.95495
13	-65.428	-52.7979	-74.512	9.08402	-0.977489	-6.5428	-5.27979
12	-62.0377	-52.7931	-70.1109	8.07315	0	-6.89308	-5.8659
8	-63.2176	-52.738	-71.8751	8.65753	-4.19138	-7.02417	-5.85978
9	-62.9876	-52.3032	-71.6496	8.66198	-2.58968	-6.99862	-5.81147
10	-61.9824	-51.4798	-70.6891	8.70673	-4.53652	-6.88693	-5.71998
11	-61.5008	-51.1883	-70.3222	8.82145	-4.90365	-6.83342	-5.68759
1	-58.7823	-49.829	-67.596	8.81372	-4.28737	-7.34778	-6.22862

6.3.1.1. Docking *via* MVD

Table S6.9: Docking scores of ligands against PDB ID 4in4 obtained *via* MVD

Ligand	MolDock Score	[a]Rerank Score	[b]Interaction	[c]Internal	[d]HBond	[e]LE1	[f]LE3
Co-crystallized ligand	-125.831	-120.974	-165.158	39.3266	-8.76238	-3.81307	-3.66587
Ascorbc acid	-75.7828	-71.4912	-86.0476	10.2648	-19.2639	-6.31523	-5.9576
Trolox	-73.7921	-71.4529	-98.6508	24.8587	-6.56132	-4.09956	-3.9696
6(1B2N)	-65.1317	-55.0164	-81.4376	16.3059	-7.54665	-5.42764	-4.5847
3	-59.5395	-50.2936	-69.4719	9.93243	-7.14109	-5.95395	-5.02936
5	-53.503	-46.9584	-65.0405	11.5375	-6.93261	-5.3503	-4.69584
13	-55.7586	-46.7584	-62.5242	6.76557	-6.60152	-5.57586	-4.67584
2	-51.9675	-44.7424	-61.9939	10.0264	-7.34452	-5.77417	-4.97138
7	-52.3444	-44.5143	-61.1251	8.78064	-5.75173	-5.81605	-4.94604
4	-53.1179	-43.6252	-60.5594	7.44144	-2.82044	-5.90199	-4.84724
10	-52.3967	-43.6188	-61.1035	8.7068	-6.42284	-5.82185	-4.84653
9	-52.6117	-43.5513	-61.2737	8.66205	-5.52777	-5.84574	-4.83903

11	-52.0531	-42.7589	-60.8746	8.82145	-6.37787	-5.78368	-4.75099
12	-48.3324	-42.6397	-56.4056	8.07315	-2.37039	-5.37027	-4.73774
8	-51.6487	-42.1208	-60.3062	8.65757	-3.11745	-5.73874	-4.68008
1	-46.259	-38.8822	-55.0728	8.81382	-2.81476	-5.78237	-4.86027

6.3.1.1. Docking *via* MVD

Table S6.10: Docking scores of ligands against PDB ID 4ZZI obtained *via* MVD

Ligand	**MolDock Score**	**[a]Rerank Score**	**[b]Interaction**	**[c]Internal**	**[d]HBond**	**[e]LE1**	**[f]LE3**
Co-crystallized ligand	-157.82	-131.704	-165.753	7.9332	-8.71709	-6.31278	-5.26815
Ascorbc acid	-86.547	-77.3756	-93.8058	7.25873	-12.6568	-7.21225	-6.44797
Trolox	-75.871	-71.3691	-100.508	24.6372	-3.06724	-4.21505	-3.96495
6(1B2N)	-77.1461	-59.2799	-93.4526	16.3065	-2.19857	-6.42884	-4.94
3	-70.5063	-57.7469	-80.2536	9.74727	-2.5	-7.05063	-5.77469
5	-66.6127	-56.5237	-79.042	12.4293	-2.5	-6.66127	-5.65237
4	-67.3571	-54.6636	-74.7986	7.44144	-2.5	-7.48412	-6.07373
8	-67.8886	-54.5061	-76.5461	8.65752	-3.29333	-7.54318	-6.05623

2	-64.6241	-53.9873	-74.6506	10.0264	-2.90708	-7.18046	-5.99859
7	-64.7377	-53.8349	-73.5184	8.78061	-1.89043	-7.19308	-5.98165
9	-65.9033	-53.6435	-74.5654	8.66206	-1.71111	-7.32259	-5.96039
10	-64.4906	-52.3908	-73.1973	8.70676	-1.72815	-7.16562	-5.8212
13	-66.9808	-52.0261	-76.0648	9.08396	-2.5	-6.69808	-5.20261
11	-64.3896	-51.8688	-73.211	8.82138	-2.87131	-7.1544	-5.7632
12	-60.4842	-51.3475	-68.5574	8.07318	-2.21872	-6.72047	-5.70528
1	-61.1828	-49.529	-69.9966	8.81379	-2.5	-7.64784	-6.19113

6.3.1.1. Docking *via* MVD (IJII)

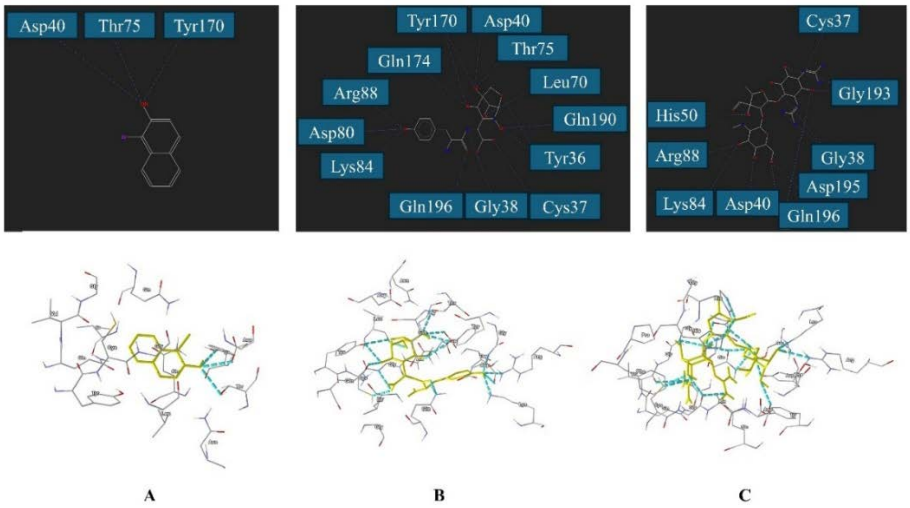

Figure S6.2: Illustration of mode of interaction of A). 1B2N B). Co-crystallized ligand C). Streptomycin with PDB ID 1JII.

6.3.1.1. Docking *via* MVD (7Y8B)

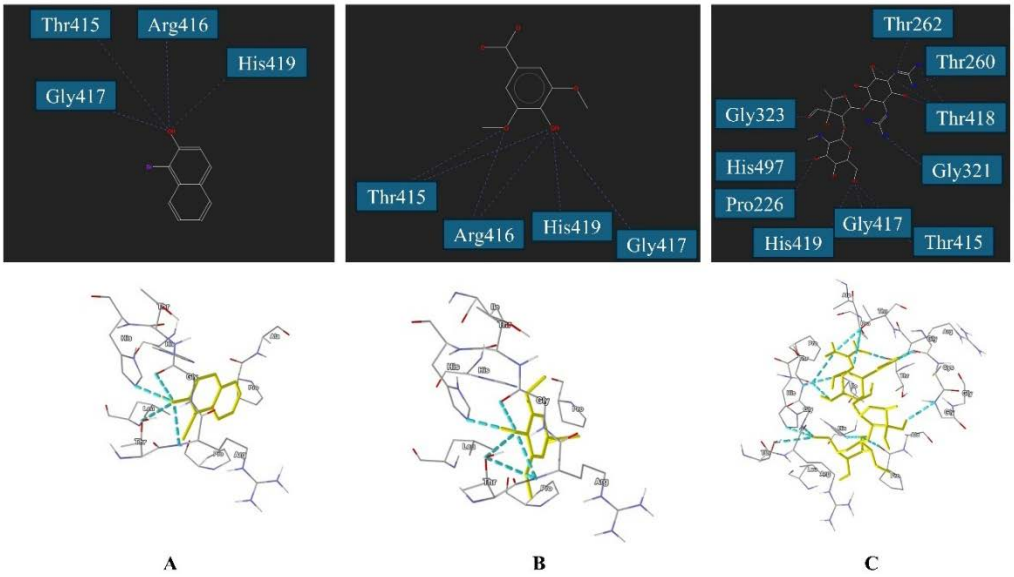

Figure S6.3: Illustration of mode of interaction of A). 1B2N B). Co-crystallized ligand C). Streptomycin with PDB ID 7Y8B.

6.3.1.1. Docking *via* MVD (7MYL)

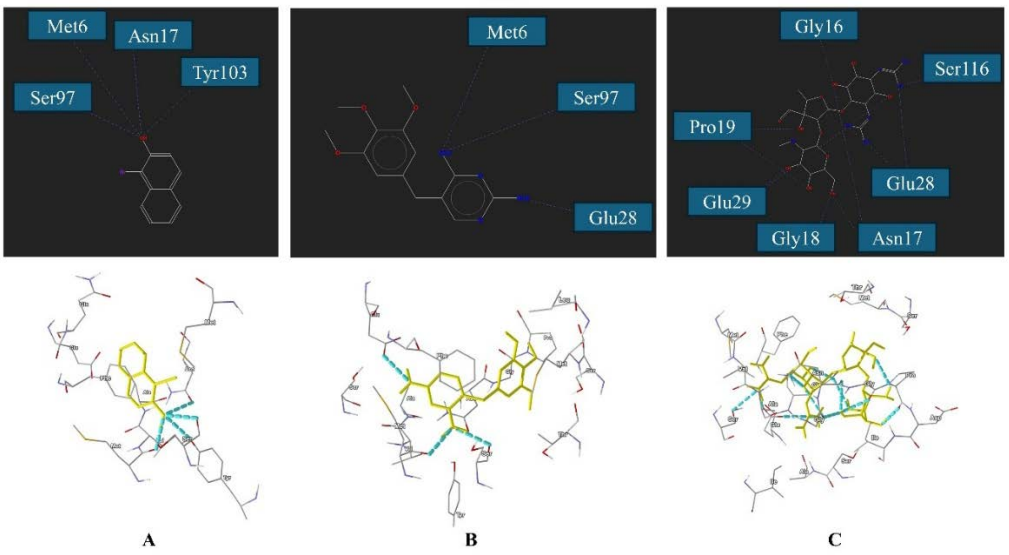

Figure S6.4: Illustration of mode of interaction of A). 1B2N B). Co-crystallized ligand C). Streptomycin with PDB ID 7MYL.

6.3.1.1. Docking *via* MVD (1M78)

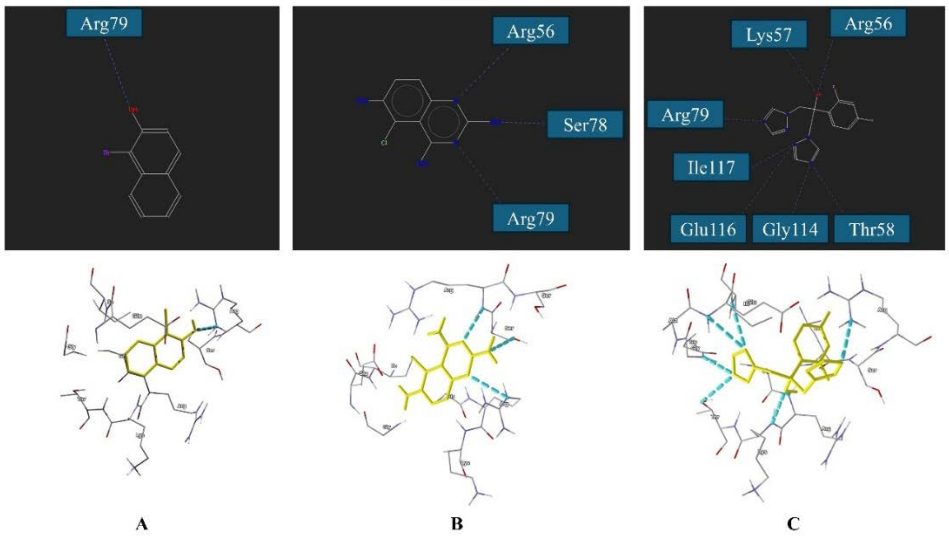

Figure S6.5: Illustration of mode of interaction of A). 1B2N B). Co-crystallized ligand C). Fluconazole with PDB ID 1M78.

6.3.1.1. Docking *via* MVD (8BHH)

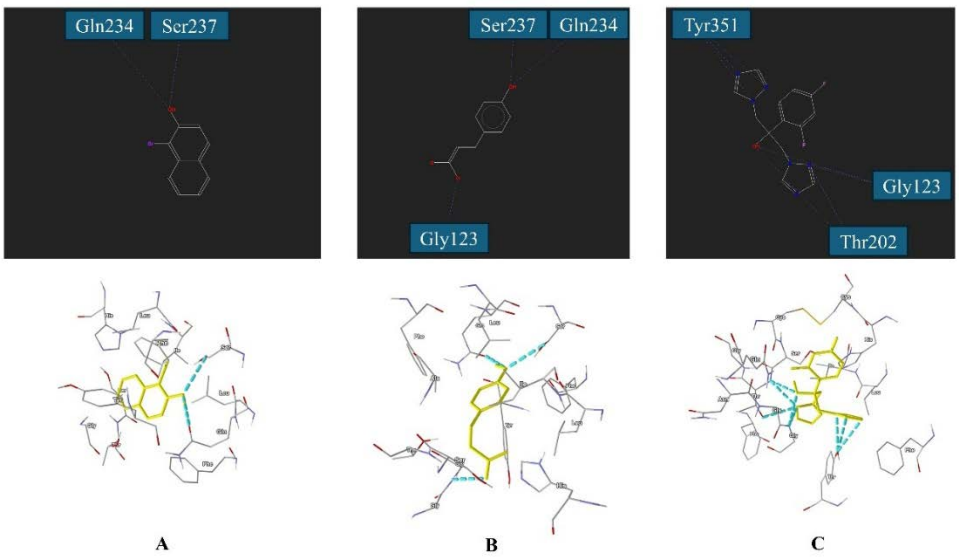

Figure S6.6: Illustration of mode of interaction of A). 1B2N B). Co-crystallized ligand C). Fluconazole with PDB ID 8BHH.

6.3.1.1. Docking *via* MVD (4IN4)

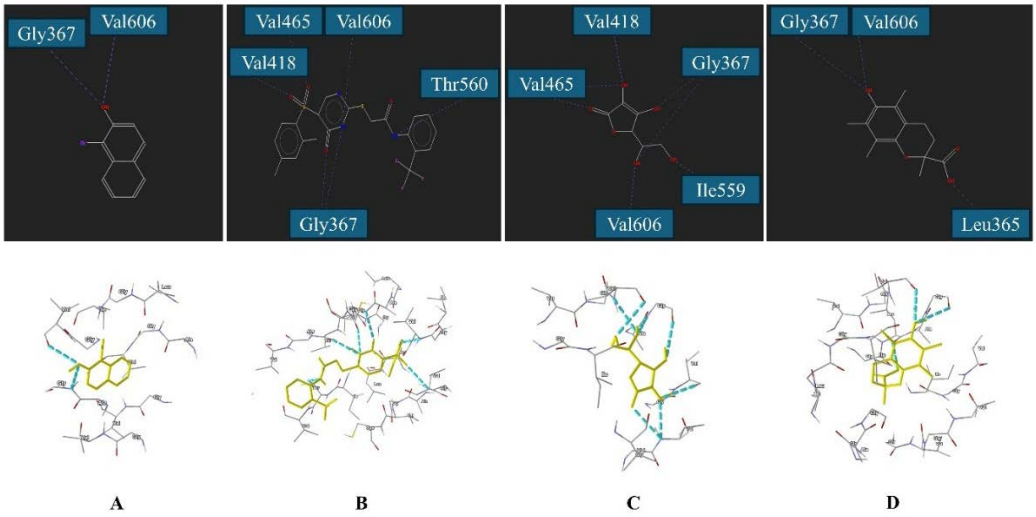

Figure S6.7: Illustration of mode of interaction of A). 1B2N B). Co-crystallized ligand C). Ascorbic acid D). Trolox with PDB ID 4IN4.

6.3.1.1. Docking *via* MVD (4ZZI)

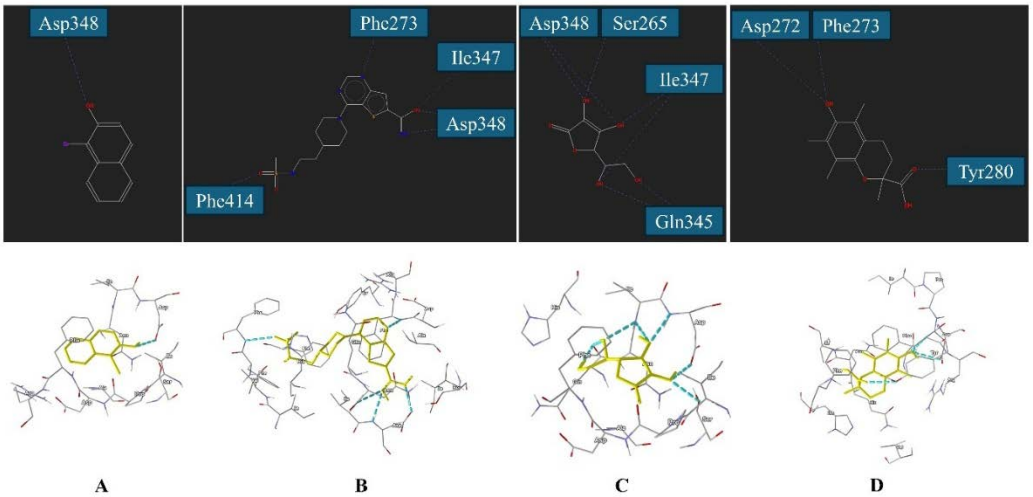

Figure S6.8: Illustration of mode of interaction of A). 1B2N B). Co-crystallized ligand C). Ascorbic acid D). Trolox with PDB ID 4ZZI.

6.3.1.2. Docking *via* AutoDock

Table S6.11: Binding affinities and interaction modes of ligands docked against PDB ID 7DQL

Ligand	BE	RMSD	Type of Interactions	Residues
1B2N	-6.56	0.02	Conventional hydrogen bond	Asp73
			Halogen (Cl, Br, I)	Val71
			Pi-sigma	Thr165
			Pi-sulfur	Met95
			Alkyl	Val43, Val167
			Pi-alkyl	Ile78, Val120, Ala47
7DQL CL	-4.96	0.38	Conventional hydrogen bond	Asp73
			Alkyl	Val167, Val 120
			Pi-alkyl	Ala47, Val43, Val167
Streptomycin	-1.7	1.12	Conventional hydrogen bond	Asp49, Ala91, Val71, Asp73, Thr165, Asn46
			Sulfur-X	Met95

6.3.1.2. Docking *via* AutoDock

Table **S6.12**: Binding affinities and interaction modes of ligands docked against PDB ID 1JII

Ligand	BE	RMSD	Type of Interactions	Residues
6	-5.93	0.54	Conventional hydrogen bond	Asp40
			Amide pi-stacked	Ala39
			Pi-alkyl	Cys37, Leu70
CL	-5.35	1.68	Conventional hydrogen bond	Asp40, Asp195, Arg88, Lys84
			Carbon hydrogen bond	His47
			Pi-sigma	His50
			Pi-alkyl	Ala39

Streptomycin	-3.69	1.66	Conventional hydrogen bond	Arg88, Lys84, Gly38, Gln196, Asp195, Gly193, Pro222
			Carbon hydrogen bond	His50, Gly49

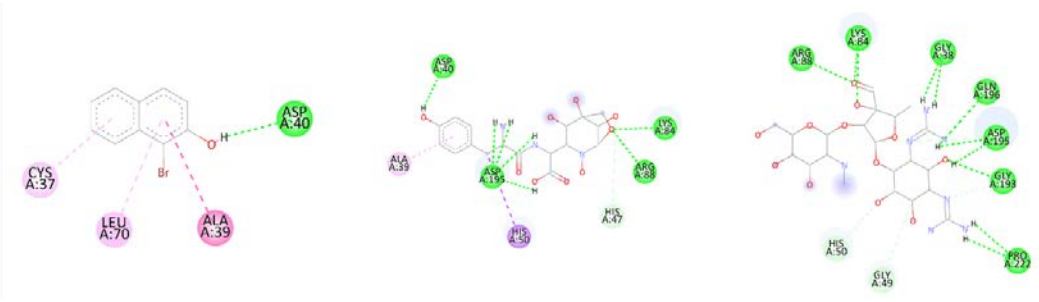

A B C

Figure S6.10: Illustration of mode of interaction of A). 1B2N B). Co-crystallized ligand C). Streptomycin with PDB ID 1JII.

6.3.1.2. Docking *via* AutoDock

Table S6.13: Binding affinities and interaction modes of ligands docked against PDB ID 1JII

Ligand	BE	RMSD	Type of Interactions	Residues
6	-5.11	0.1	Conventional hydrogen bond	Thr415, His419, Arg416, Gly417
			Pi-pi T shaped	His497
			Alkyl	Leu386, Arg416, His419
			Pi-alkyl	Ala227, Pro226
CL	-3.72	0.93	Conventional hydrogen bond	Arg416, Gly417, His497
			Carbon hydrogen bond	Thr415, Thr418
			Alkyl	His419, Pro226, Pro384
			Pi-alkyl	Arg416
Streptomycin			Conventional hydrogen bond	Cys322, Thr262, Thr418, Thr260

	-2.18	1.82	Carbon hydrogen bond	Gly321, Gly417

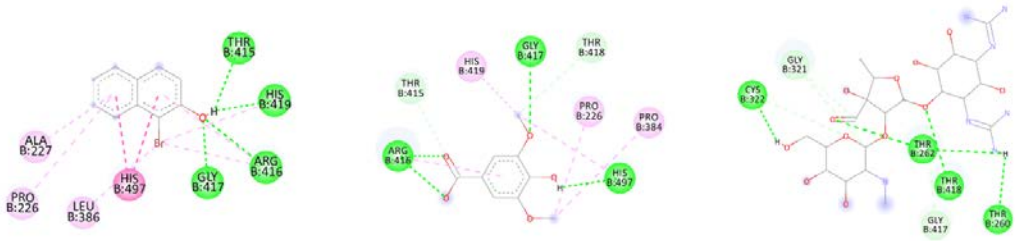

A B C

Figure S6.11: Illustration of mode of interaction of A). 1B2N B). Co-crystallized ligand C). Streptomycin with PDB ID 1JII.

6.3.1.2. Docking *via* AutoDock

Table S6.14: Binding affinities and interaction modes of ligands docked against PDB ID 7MYL

Ligand	BE	RMSD	Type of Interactions	Residues
6	-6.7	0.02	Conventional hydrogen bond	Glu28
			Pi-pi stacked	Phe32
			Pi-alkyl	Met6, Ala8
CL	-7.59	0.5	Conventional hydrogen bond	Met6, Glu28
			Van der waals	Gly18
			Pi-sigma	Met51
			Pi-pi stacked	Val7, Phe32, Asn17
			Amide pi-stacked	Val7, Phe32, Asn17
			Alkyl	Met51
			Pi-alkyl	Ala8
Streptomycin	-4.34	1.68	Conventional hydrogen bond	Met51, Asn17, Ser97, Met6, Gln29
			Carbon hydrogen bond	Ser50, Pro19, Gly18

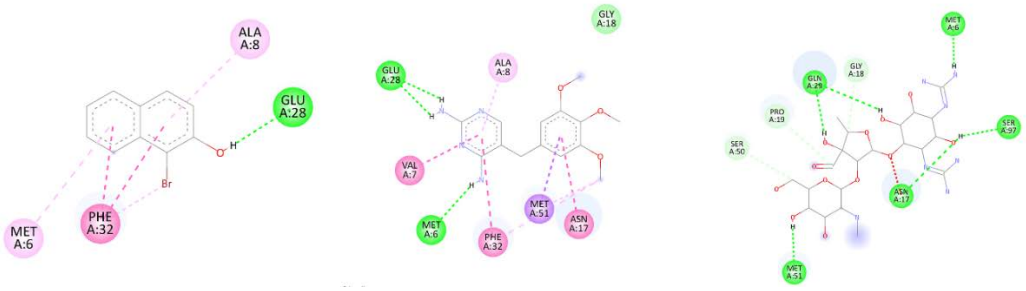

A B C

Figure S6.12: Illustration of mode of interaction of A). 1B2N B). Co-crystallized ligand C). Streptomycin with PDB ID 7MYL.

6.3.1.2. Docking *via* AutoDock

Table S6.15: Binding affinities and interaction modes of ligands docked against PDB ID 1M78

Ligand	BE	RMSD	Type of Interactions	Residues
6	-6.1	0.06	Conventional hydrogen bond	Ala11
			Pi-sigma	Gly113
			Pi-pi T shaped	Tyr118
			Alkyl	Met25
			Pi-alkyl	Val10, Ile19, Met25
CL	-6.03	0.17	Conventional hydrogen bond	Ile112, Ile19, Ala11
			Pi-donor hydrogen bond	Phe36
			Pi-sigma	Met25
			Pi-pi T shaped	Phe36
			Pi-alkyl	Val10
Fluconazole	-5.53	1.47	Conventional hydrogen bond	Ala11, Thr58, Ala115, Gly23
			Carbon hydrogen bond	Tyr118, Ile19, Gly114
			Pi-alkyl	Met25, Val10

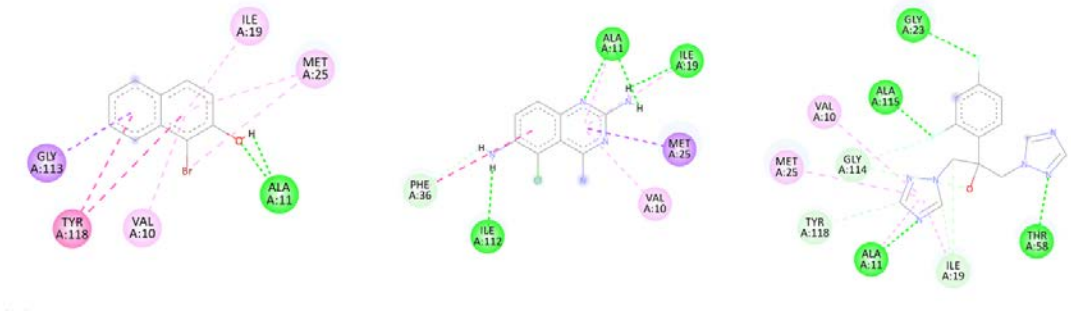

A B C

Figure S6.13: Illustration of mode of interaction of A). 1B2N B). Co-crystallized ligand C). Streptomycin with PDB ID 1M78.

6.3.1.2. Docking *via* AutoDock

Table S6.16: Binding affinities and interaction modes of ligands docked against PDB ID 8BHH

Ligand	BE	RMSD	Type of Interactions	Residues
6	-7.84	0.08	Conventional hydrogen bond	Thr202
			Pi-sigma	Leu233
			Pi-sulfur	Met124
			Pi-pi T-shaped	Tyr351
			Alkyl	Tyr351, Ala227
			Pi-alkyl	Leu414, Ile415
CL	-5.81	0.11	Conventional hydrogen bond	His452, Thr202, Gly123, Gln234
			Carbon hydrogen bond	Ser201
			Pi-sigma	Leu233
			Pi-pi T shaped	Tyr351
Fluconazole	-5.78	0.75	Conventional hydrogen bond	Tyr351, Ser237
			Carbon hydrogen bond	Ser201
			Pi-sigma	Leu414
			Pi-sulfur	Met124
			Pi-pi stacked	Phe230
			Pi-pi T shaped	His452
			Pi-alkyl	Ala227, Leu233, Ile415

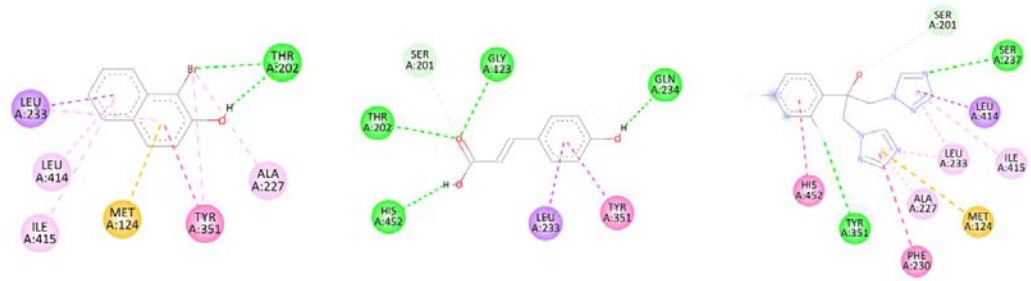

A B C

Figure S6.14: Illustration of mode of interaction of A). 1B2N B). Co-crystallized ligand C). Streptomycin with PDB ID 8BHH.

6.3.1.2. Docking *via* AutoDock

Table S6.17: Binding affinities and interaction modes of ligands docked against PDB ID 4IN4

Ligand	BE	RMSD	Type of Interactions	Residues
6	-6.59	0.02	Conventional hydrogen bond	Val418, Val465
			Alkyl	Val512
			Pi-alkyl	Val606, Val512, Ala366
CL	8.84	1.99	Conventional hydrogen bond	Val604, Gly367, Val418, Val465
			Carbon hydrogen bond	Gly509
			Halogen (Fluorine)	Ile416, Val463, Gly462
			Sulfur-X	Leu557
			Pi-alkyl	Ala556, Arg415, Ala366
Ascorbic Acid	-5.83	0.9	Conventional Hydrogen Bond	Val512, Ile559, Val606, Gly367, Val418, Val465
			Carbon-hydrogen bond	Gly605
Trolox	-7.07	0.25	Conventional hydrogen bond	Val512, Val465, Val604

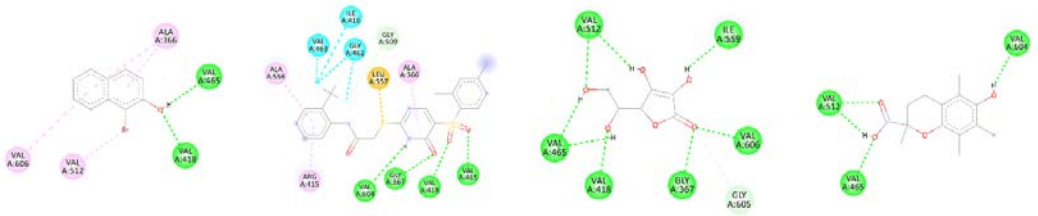

A B C

Figure S6.15: Illustration of mode of interaction of A). 1B2N B). Co-crystallized ligand C). Streptomycin with PDB ID 4IN4.

6.3.1.2. Docking *via* AutoDock

Table S6.18: Binding affinities and interaction modes of ligands docked against PDB ID 4ZZI

Ligand	**BE**	**RMSD**	**Type of Interactions**	**Residues**
6	-5.79	0.07	Conventional hydrogen bond	Val412
			Pi-pi stacked	His363, Phe297
			Pi-alkyl	Ile347, Phe414
CL	-8.38	0.57	Conventional hydrogen bond	Phe273, His363, Arg274
			Carbon hydrogen bond	Gln345, Val412
			Pi-cation	Arg274
			Pi-sigma	Phe414
			Pi-sulfur	Tyr280
			Pi-pi stacked	Phe273
			Alkyl	Ile347, His363
			Pi-alkyl	Ala262
Ascorbic Acid	-3.14	0.69	Conventional Hydrogen Bond	Lys203, Asp204, Lys444, Arg446
			Carbon-hydrogen bond	Val445

Trolox	-5.88	0.09	Conventional hydrogen bond	Lys203, Asp204
			Pi-alkyl	Arg274

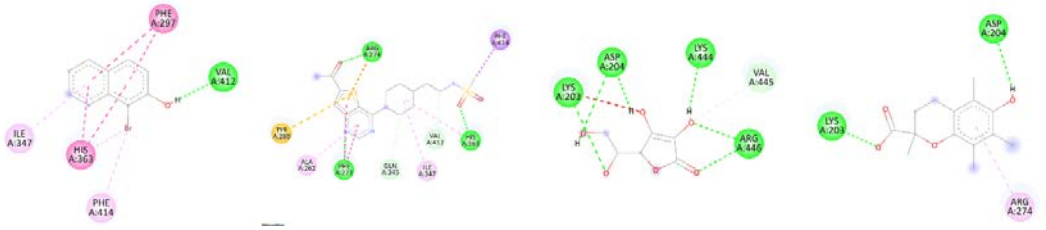

A B C

Figure S6.16: Illustration of mode of interaction of A). 1B2N B). Co-crystallized ligand C). Streptomycin with PDB ID 4ZZI

6.3.2. Pharmacophore mapping

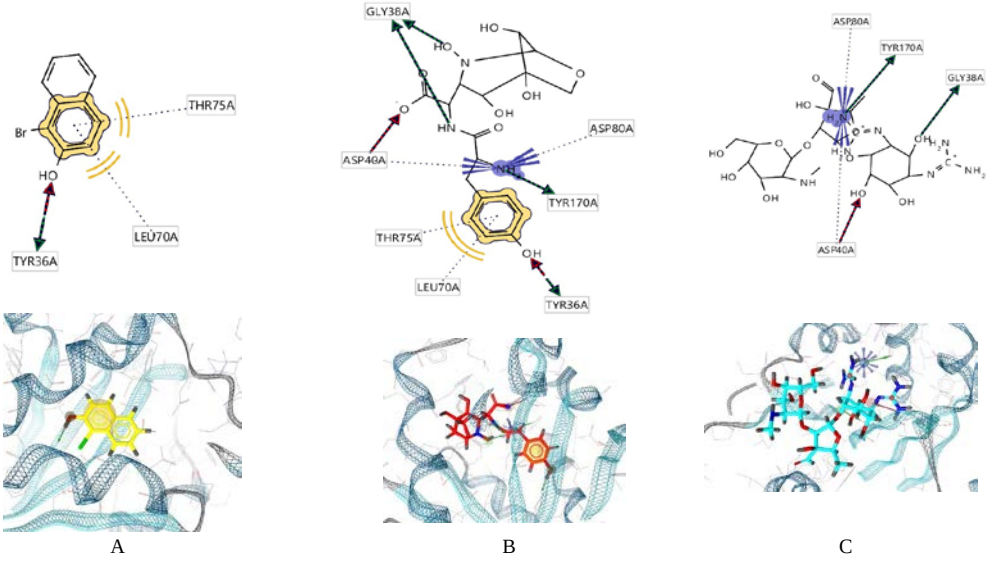

A B C

Figure S6.18: 2D and 3D illustrated pharmacophoric features of A. 1B2N B. CL C. Streptomycin against PDB ID 1JII

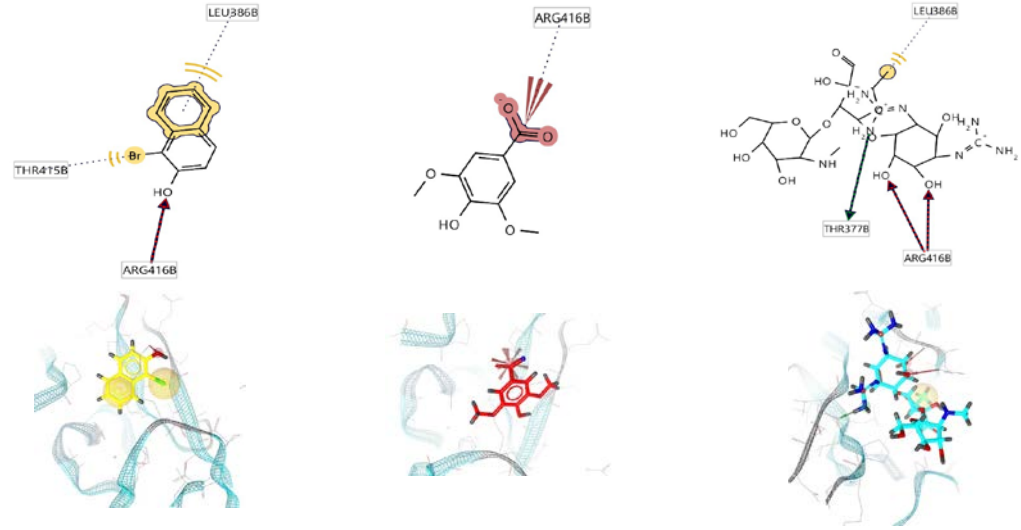

Figure S6.19: 2D and 3D illustrated pharmacophoric features of A. 1B2N B. CL C. Streptomycin against PDB ID 7Y8B

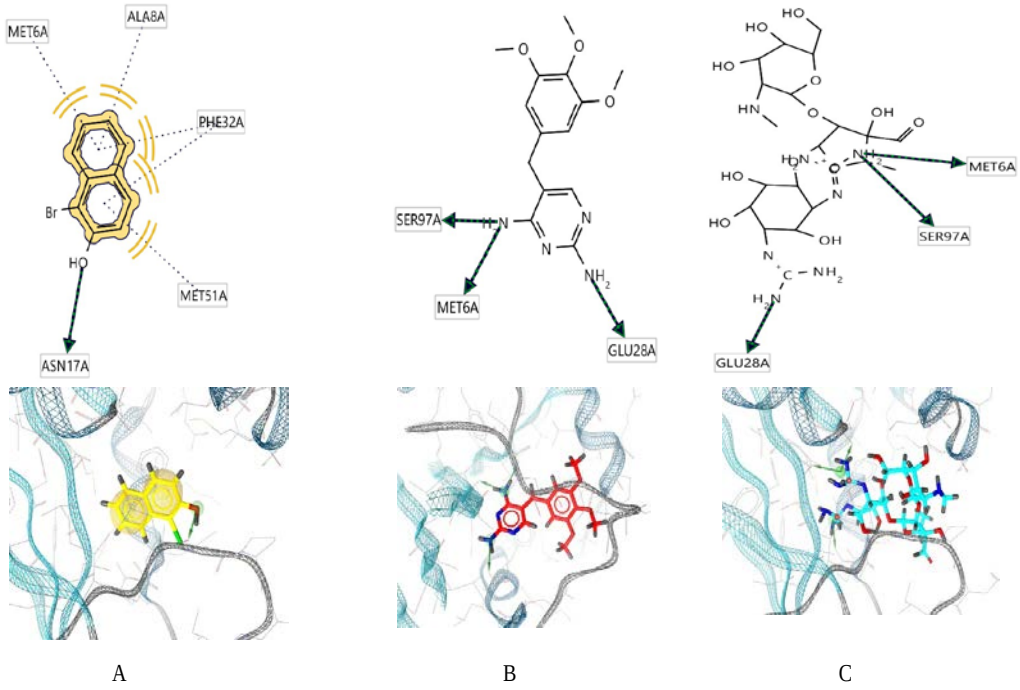

Figure S6.20: 2D and 3D illustrated pharmacophoric features of A. 1B2N B. CL C. Streptomycin against PDB ID 7MYL

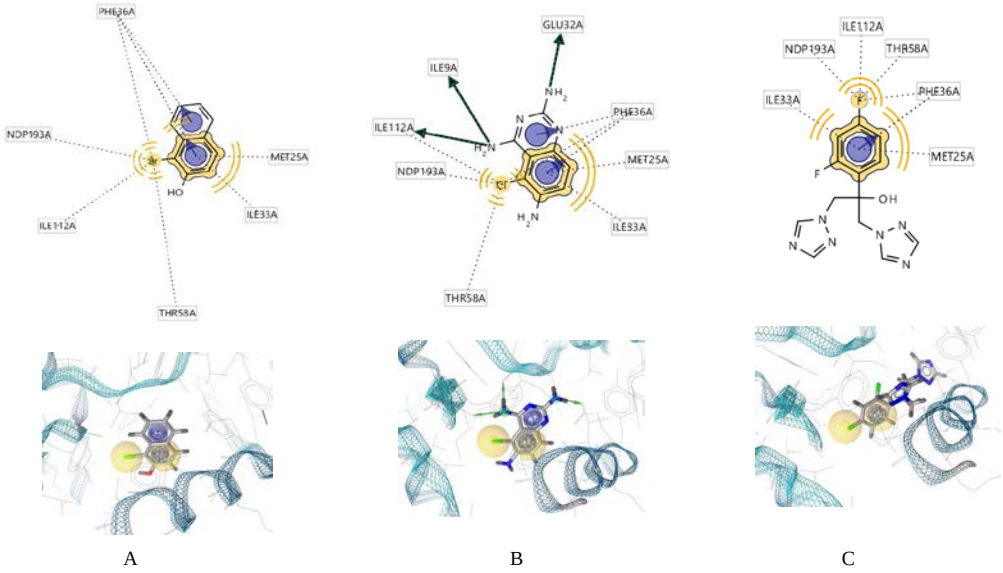

Figure S6.21: 2D and 3D illustrated pharmacophoric features of A. 1B2N B. CL C. Fluconazole against PDB ID 1M78

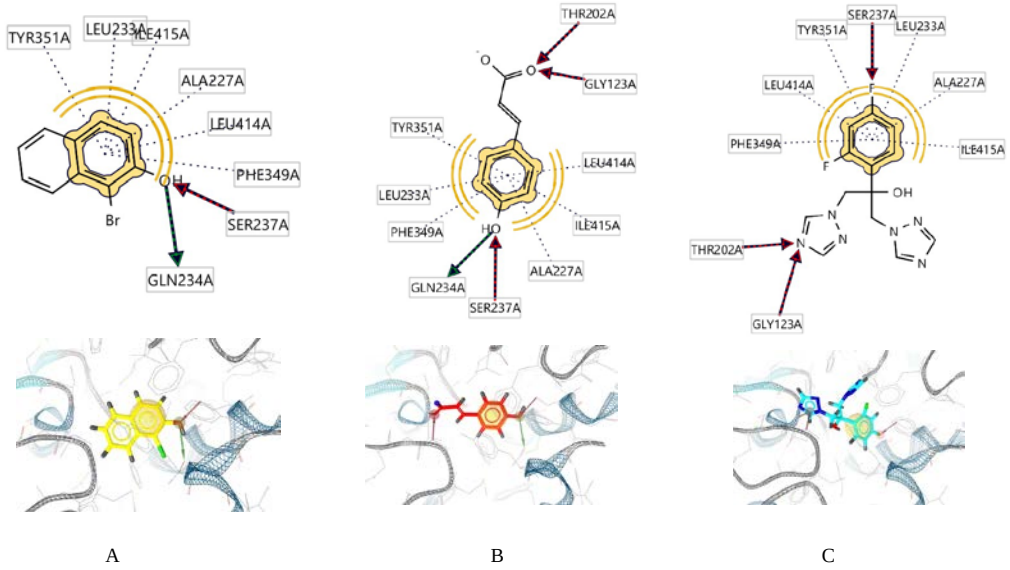

Figure S6.22: 2D and 3D illustrated pharmacophoric features of A. 1B2N B. CL C. Fluconazole against PDB ID 8BHH

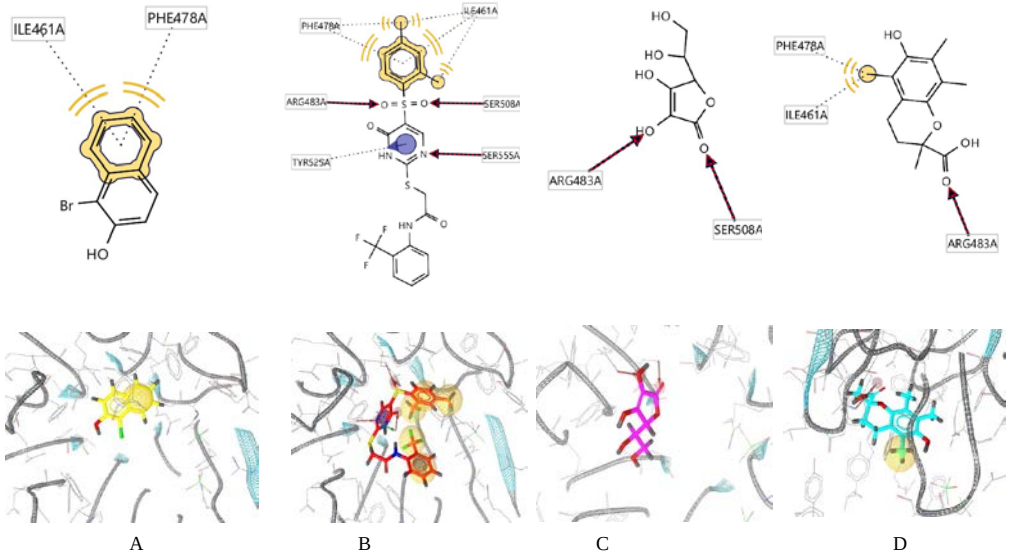

Figure S.6.23: 2D and 3D illustrated pharmacophoric features of A. 1B2N B. CL D. ASCORBIC ACID E. TROLOX against PDB ID 4IN4

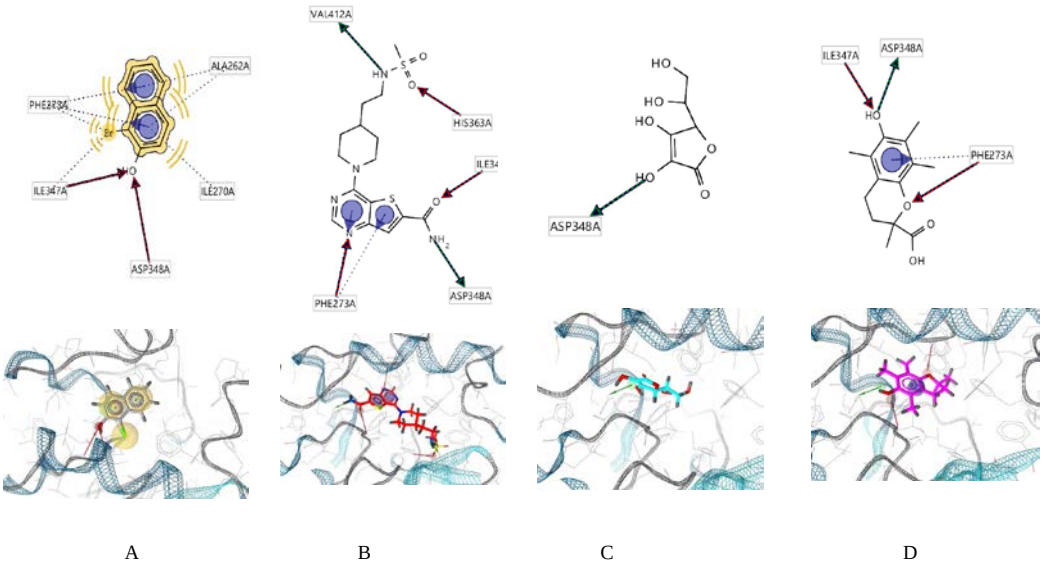

Figure S.6.24: 2D and 3D illustrated pharmacophoric features of A. 1B2N B. CL D. ASCORBIC ACID E. TROLOX against PDB ID 4ZZI

6.3.3. Synthesis

SPECTRAL DATAS

1-bromo-2-naphthol:

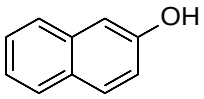

M.P. 77-80 °C; **^{1}H NMR** (400 MHz, DMSO) δ 10.56 (s, 1H), 8.02 (d, *J* = 8.5 Hz, 11H), 7.83 (d, *J* = 8.2 Hz, 8H), 7.81 (d, 8H), 7.55 (t, *J* = 7.4 Hz, 12H), 7.36 (d, *J* = 7.4 Hz, 8H). **^{13}C NMR** (101 MHz, DMSO) δ 152.68, 132.99, 129.12, 128.89, 128.45, 127.96, 125.01, 123.66, 118.56, 104.57, 39.52. **IR** (KBr, cm^{-1}): 3276, 1896, 1632, 1500-1434, 1348-1305, 1237-1146,

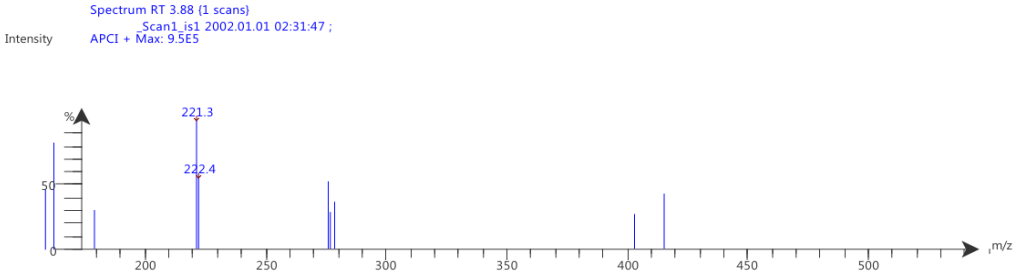

A. MASS

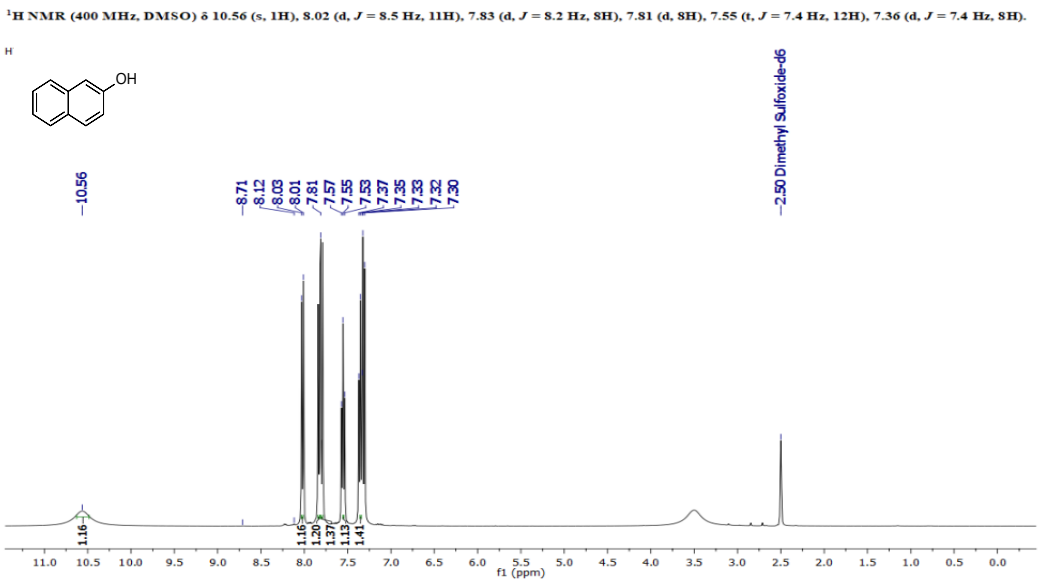

B. ^{1H} NMR

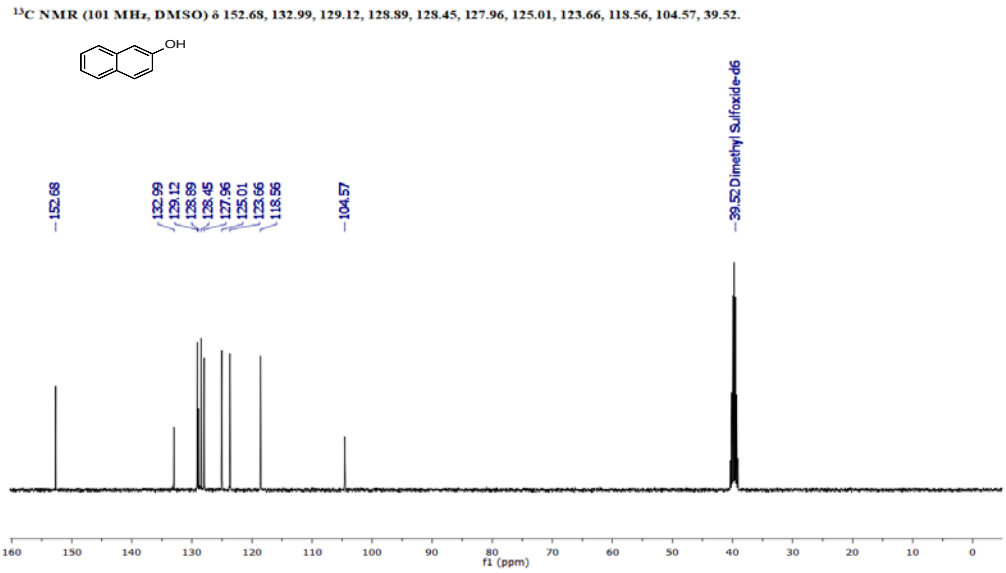

C. ^{13}C NMR

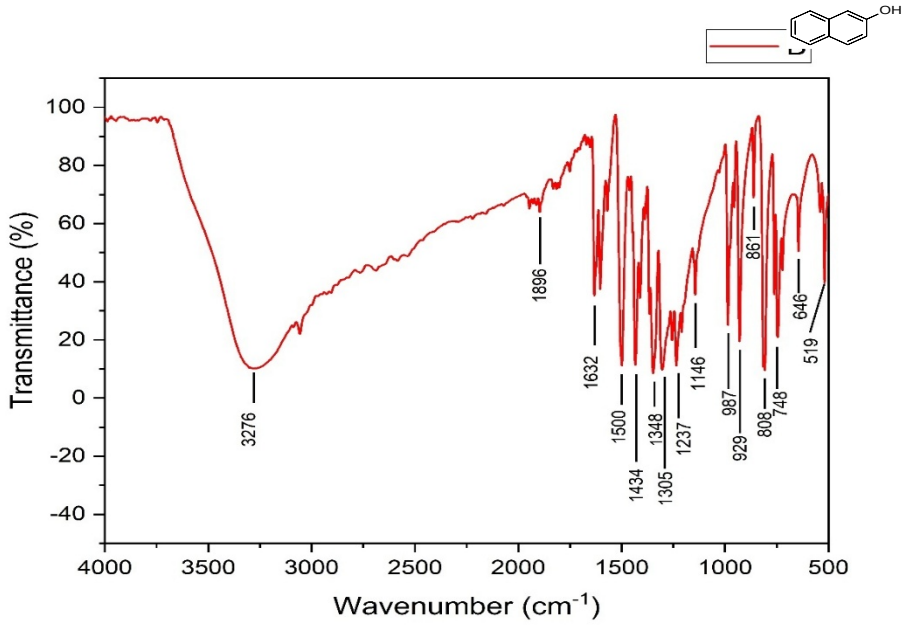

IR (ATR, vmax, cm^{-1}) for 1-bromo-2-naphthol: 3276 (br, νO–H, phenolic, H-bonded), 1896 (aromatic overtone/combination band, naphthalene), 1632 (νC=C, aryl), 1500, 1434 (ring skeletal ν), 1348, 1305 (δin-plane O–H, phenol), 1237, 1146 (νC–O, Ar–O of phenol), 987, 929, 861, 807, 748 (γC–H out-of-plane; pattern consistent with 1,2-disubstituted naphthalene), 646, 519 (νC–Br, aryl bromide).

D. IR

Figure S6.25: Spectral data's A). Mass B). 1HNMR C). 13C NMR and D). IR of 1B2N.

6.3.4. Antibacterial activity

Table S6.19: Antibacterial activity of 1-bromo-2-naphthol (1B2N) through well diffusion assay

E.coli	**1-BROMO-2-NAPHTHOL**	**STREPTOMYCIN**
	14mm	31mm
	11mm	30mm
S.aureus	**1-BROMO-2-NAPHTHOL**	**STREPTOMYCIN**
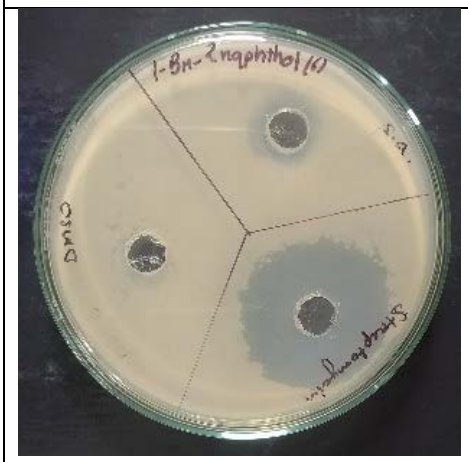	15mm	30mm
	15mm	31mm

B.Subtilis	**1-BROMO-2-NAPHTHOL**	**STREPTOMYCIN**
	14mm	30mm
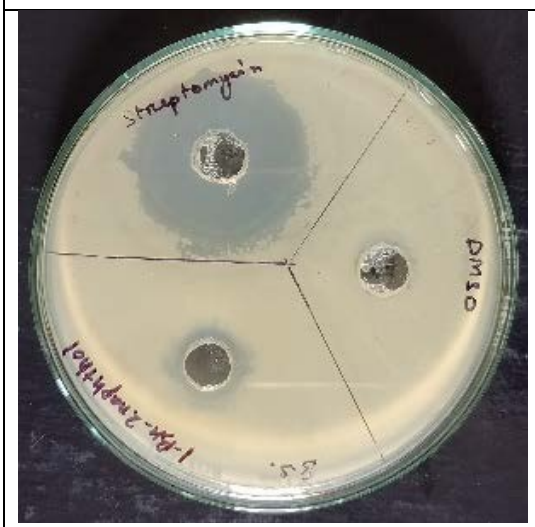	14mm	31mm

K.pneumoniae	**1-BROMO-2-NAPHTHOL**	**STREPTOMYCIN**
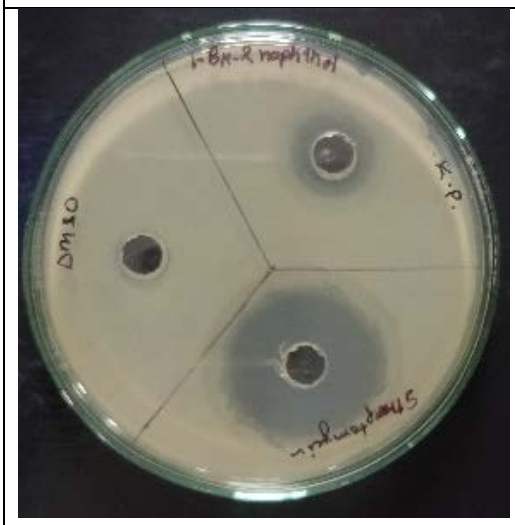	16mm	30mm
	15mm	29mm

6.3.5. Antifungal activity

Table S6.23: Antifungal activity of 1-bromo-2-naphthol (1B2N) through well diffusion assay

F.oxysporum	**1-BROMO-2-NAPHTHOL**	**Fluconazole**

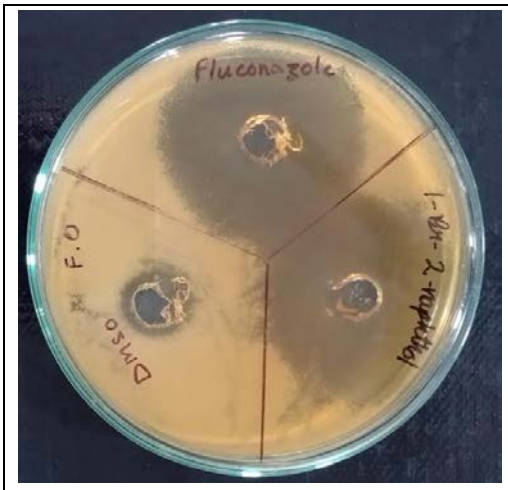	35mm	36mm
	36mm	36mm
C.albicans	**1-BROMO-2-NAPHTHOL**	**Fluconazole**

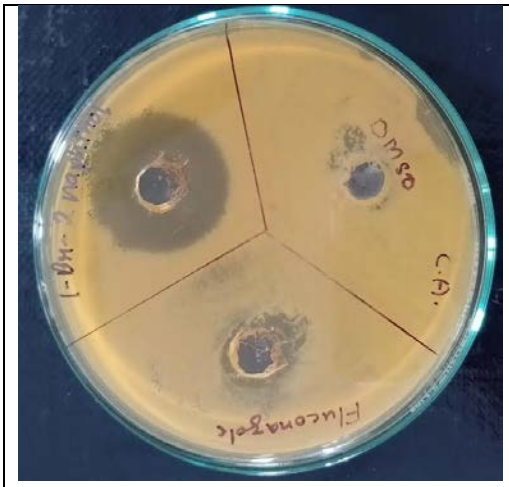	27mm	15mm
	26mm	14mm

Table S6.28: The calculated HOMO, LUMO and Energy gap

COMPOUND	HOMO	LUMO	HOMO-LUMO (in H)	$\Delta E = E_{HOMO}-E_{LUMO}$ (in eV)
1B2N	-0.22638	-0.06141	0.16497	4.489064658
BDDE	-0.23379	-0.05282	0.18097	4.924447058
Ascorbic acid	-0.2459	-0.04641	0.19949	5.428402186
Fluconazole	-0.26899	-0.04163	0.22736	6.186783904
Streptomycin	-0.22953	-0.06275	0.16678	4.538317292
Trolox	-0.20783	-0.02239	0.18544	5.046082016

Table S6.29: The calculated quantum chemical parameters

Compound	Ionization potential (I)	Electron affinity (A)	Hardness (η)	Softness (S)	Electro negativity (χ)	Chemical Potential (μ)	Electro Philicity (ω)	Dipole moment (D)
1 Bromo 2 naphthol	6.160116732	1.671052074	2.24453232	1.12226616 5	3.915584403	-3.915584403	3.41536653 7	4.202757
BDDE	6.361753206	1.437306148	2.46222352 9	1.23111176 5	3.899529677	-3.899529677	3.08792673	7.375685
Ascorbic acid	6.69128326	1.262881074	2.71420109 3	1.35710054 7	3.977082167	-3.977082167	2.91378236 6	6.969958
Fluconazole	7.319594486	1.132810582	3.09339195 2	1.54669597 6	4.226202534	-4.226202534	2.88692608 9	8.177292
Streptomycin	6.245832642	1.70751535	2.26915864 6	1.13457932 3	3.976673996	-3.976673996	3.48453734 1	5.222013
Trolox	5.655345262	0.609263246	2.52304100 8	1.26152050 4	3.132304254	-3.132304254	1.94434611	5.402514

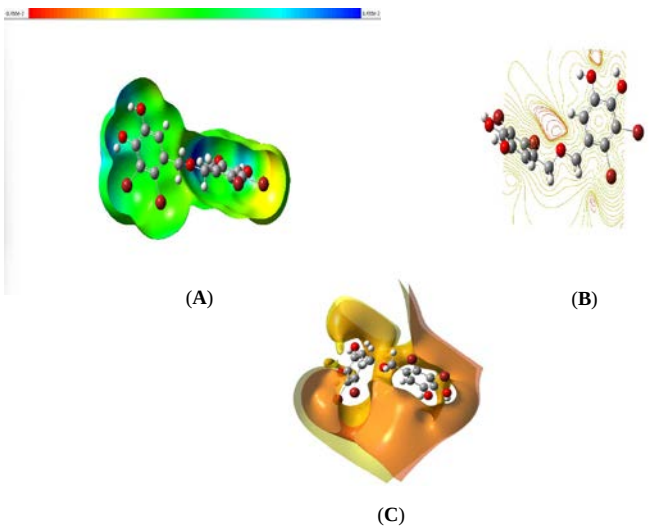

Figure S6.32: **A)**. Molecular electrostatic potentials (MEP) plot of BDDE, **B)**. Contour map plot of ESP isosurface of BDDE, **C)** Visualization of the ESP array plot for BDDE

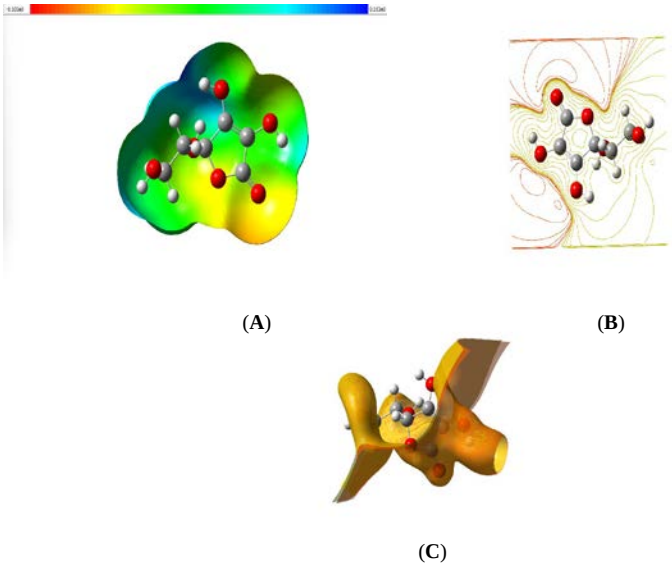

Figure 6.33: **A)**. Molecular electrostatic potentials (MEP) plot of Ascorbic acid, **B).** Contour map plot of ESP isosurface of Ascorbic acid, **C).** Visualization of the ESP array plot for Ascorbic acid

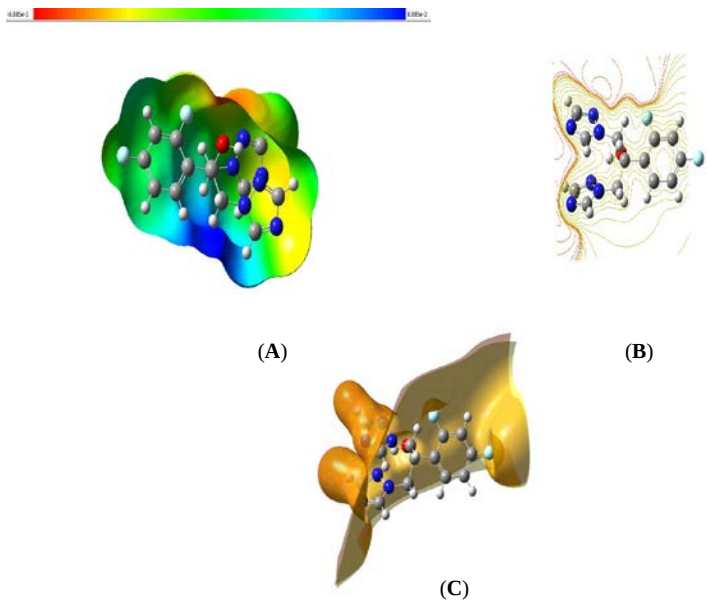

Figure S6.34: **A)**. Molecular electrostatic potentials (MEP) plot of Fluconazole, **B).** contour map plot of ESP isosurface of Fluconazole, **C).** visualization of the ESP array plot for Fluconazole

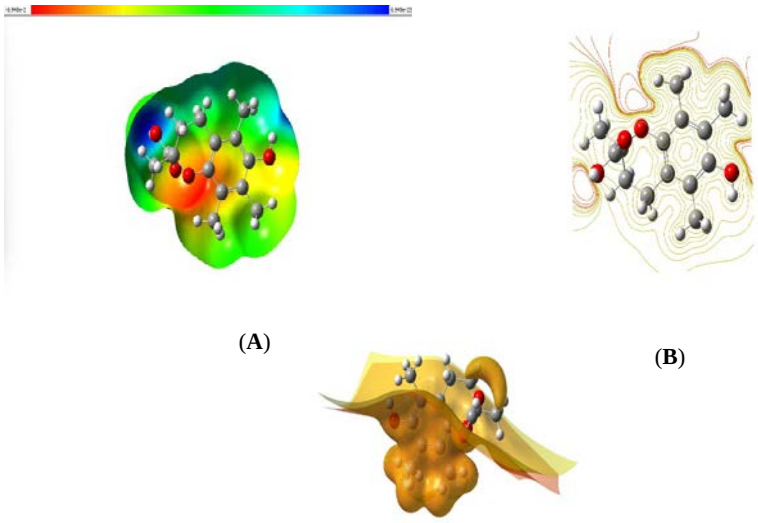

(**A**) (**B**)

(**C**)

Figure 6.35: **A).** Molecular electrostatic potentials (MEP) plot of Trolox, **B).** Contour map plot of ESP isosurface of Trolox, **C).** Visualization of the ESP array plot for Trolox

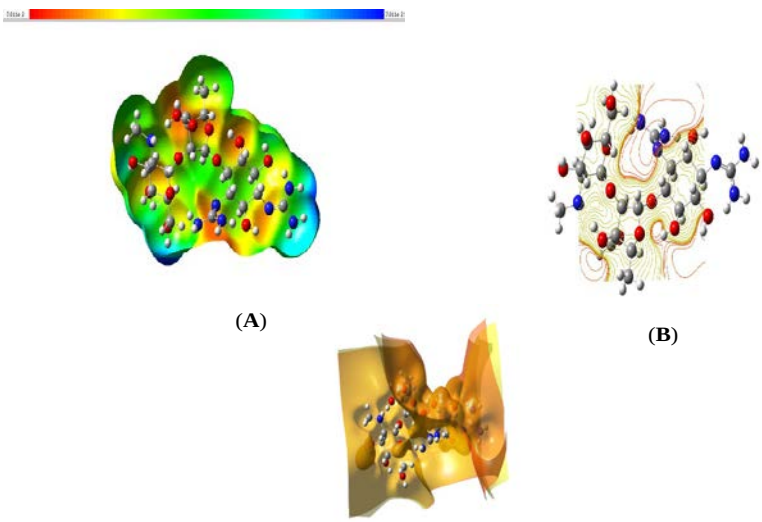

(**A**) (**B**)

(**C**)

Figure S6.36: **A).** Molecular electrostatic potentials (MEP) plot of Streptomycin, **B).** Contour map plot of ESP isosurface of Streptomycin, **C).** Visualization of the ESP array plot for Streptomycin

Table S6.30: Computed Mulliken Charge distribution of some agents computed by DFT/B3LYP basis set

SL NO.	Atoms	Compounds	
		BDDE	**1-Bromo-2-naphthol**
1	C	-0.89	-0.45
2	O	-0.31	-0.23
3	H	0.32	0.31
4	Br	-0.14	-0.15

Appendix

Appendix 1 *Plagiarism Report*

NAGALAND UNIVERSITY
Plagiarism Self Declaration Certificate

Name of Scholar	Basanta Singha	
Registration Number	PhD/CHE/00282 of 31/08/2019	
Title of PhD Thesis	*In-silico* design, synthesis and pharmaceutical assessment of some phenolic compounds	
Name & Institutional Address of the Supervisor/Co-Supervisor	Prof. Upasana Bora Sinha Department of Chemistry Nagaland University Lumami, 798627	
Name of the Department and School	Department of Chemistry, School of Sciences	
Date of submission	28/08/2025	
Date of plagiarism check	28/08/2025	
Name of the software used	iThenticate	
Percentage of similarity detected by the software	**Core Areas**	3 %
	Non-Core areas	NA

I hereby declare/certify that the Ph.D. Thesis submitted by me is complete in all respect, as per the guidelines of the UGC/NU for this purpose. I also certify that the Thesis (soft copy and print version) has been checked for plagiarism using **iThenticate** similarity check software. Copy of the Report generated by the software is also enclosed.

BASANTA SINGHA
(Name & Signature of the Scholar)

Place: Nagaland university, Lumami.
Date: 29/1/2026

(UPASANA BORA SINHA)
Name & Signature of the Supervisor: Dr. Upasana Bora Sinha
with seal Professor
Department of Chemistry
Nagaland University
Lumami - 798627

(Name &Signature of the Co-Supervisor (if any):
with seal

(Name & Signature of the Head):
with seal

विभागाध्यक्ष / Head
रसायन विज्ञान विभाग / Department of Chemistry
नागालैण्ड विश्वविद्यालय / Nagaland University
लुमामी / Lumami-798627

Thesis Basanta singha ..pdf

Nagaland University

Document Details

Submission ID
trn:oid:::3117:547901357

Submission Date
Jan 21, 2026, 2:22 PM GMT+5:30

Download Date
Jan 21, 2026, 2:51 PM GMT+5:30

File Name
Thesis Basanta singha ..pdf

File Size
23.2 MB

724 Pages

161,602 Words

844,761 Characters

3% Overall Similarity

The combined total of all matches, including overlapping sources, for each database.

Filtered from the Report

- Bibliography
- Quoted Text
- Cited Text
- Small Matches (less than 10 words)
- Crossref database
- Crossref posted content database

Match Groups

260 Not Cited or Quoted 3%
Matches with neither in-text citation nor quotation marks

0 Missing Quotations 0%
Matches that are still very similar to source material

0 Missing Citation 0%
Matches that have quotation marks, but no in-text citation

0 Cited and Quoted 0%
Matches with in-text citation present, but no quotation marks

Top Sources

3% Internet sources
1% Publications
0% Submitted works (Student Papers)

Integrity Flags

1 Integrity Flag for Review

Replaced Characters
992 suspect characters on 269 pages
Letters are swapped with similar characters from another alphabet.

Our system's algorithms look deeply at a document for any inconsistencies that would set it apart from a normal submission. If we notice something strange, we flag it for you to review.

A Flag is not necessarily an indicator of a problem. However, we'd recommend you focus your attention there for further review.

PERSONAL DETAILS

Name:	Basanta Singha
Date of birth:	7/02/1994
Address of correspondence:	Department of Chemistry, Nagaland University, Lumami Campus:798627 Zunheboto, Nagaland
Email Address:	basansingha1994@gmail.com
Fellowship:	UGC non-NET fellowship NU/RDC/NNF-126/ 2021-3509
Areas of research interest:	❖ Computational chemistry, ❖ *In-silico*, ❖ Bioinformatics, ❖ Organic synthesis, ❖ Microbiology.

1. **Singha, B.**, Gogoi, P. P., Longkumer, P., Ahmed, B., Boruah, N., Bezbaruah, B., & Sinha, U. B. (2025). A holistic computational exploration of AZD7762 as a potent selective modulator of LXRα, LXRβ and FXR: An underexplored pathway in cancer therapeutics. *Computers in Biology and Medicine*, *194*, 110433.
2. **Singha, B.**, Arora, B., Karmaker, R., Richa, K., Longkumer, N., Thaer Abdulhameed, H., ... & Bora Sinha, U. (2024). Evaluating Terrestrol A as an Inhibitor Against SARS-CoV-2and Invasive Fungal Pathogens: A Comprehensive Computational Analysis. *ChemistrySelect*, *9*(14), e202304761.
3. **Singha, B.**, Gogoi, P. P., Longkumer, P., Boruah, N., & Sinha, U. B. (2024). Evaluation of Some Designed Halogenated Variants of Gentisyl Alcohol: Molecular Docking, DFT, Druglikeness, and ADMET Studies for Assessing Biological Properties. *Journal of Applicable Chemistry*, *13*(2), 98-113.
4. Gogoi, P. P., **Singha, B**., Longkumer, P., Boruah, N., & Sinha, U. B. (2025). Multistep In Silico Pipeline for Targeting FimH Adhesin with Chalcones as Anti-Adhesion Therapeutics. *Current Biotechnology*.
5. Gogoi, P. P., Pucho, M., Jamir, P., Boruah, N., **Singha, B**., Longkumer, P., ... & Sinha, U. B. (2025). Chalcones as Emerging Antibacterial Scaffolds: A Mini Review. *Mini-Reviews in Medicinal Chemistry*.
6. Richa, K., Karmaker, R., Ao, T., Longkumer, N., **Singha, B.**, & Sinha, U. B. (2020). Rationale for antioxidant interaction studies of 4-bromo-1-isothiocyanato-2-methylbenzene–An experimental and computational investigation. *Chemical Physics Letters*, *753*, 137611.
7. Longkumer, N., Richa, K., Karmaker, R., **Singha, B.**, & Sinha, U. B. (2023). Experimental and Theoretical Investigations on the Antibacterial Activity of Some Bromoaniline Compounds. *Anti-Infective Agents*, *21*(3), 12-25.
8. Sharma, S., Umdor, R. S., Longchar, I. T., **Singha, B.**, Ezung, S. L., Bhomick, P. C., & Sinha, D. (2025). Highly efficient photocatalytic degradation of

organic pollutants using novel carbon integrated ZrO2-ZnO nanocomposites: kinetics, molecular docking, DFT simulation and real wastewater application. *Journal of Molecular Liquids*, 128260.

9. Ahmed, B., Bezbaruah, B., Barukial, P., **Singha, B.**, & Sinha, U. B. (2024). The Some pyridyl moiety-based metal complexes (viz., Mn+ 2, Co+ 2 and Zn+ 2) as potential anticancer agents and DNA nucleobase interaction: A DFT Approach: Some pyridyl moiety-based metal complexes (viz., Mn+ 2, Co+ 2 and Zn+ 2) as potential anticancer agents. *Indian Journal of Chemistry (IJC)*, *63*(6), 543-556.
10. Barukial, P., Ahmed, B., **Singha, B.**, Chetia, P., Das, N. K., Thakur, S., ... & Bezbaruah, B. (2024). Some Co (II)-Schiff base complexes as promising anticancer agents: A DFT and molecular docking study. *Indian Journal of Biochemistry and Biophysics (IJBB)*, *61*(6), 354-370.
11. Longkumer, N., Richa, K., Karmaker, R., Kuotsu, V., Supong, A., Jamir, L., ... & Sinha, U. B. (2019). Green synthesis of bromo organic molecules and investigations on their antibacterial properties: An experimental and computational approach. *Acta Chim. Slov*, *66*(2), 276-283.
12. Gogoi, P. P., Boruah, N., **Singha, B.**, Longkumer, P., & Sinha, U. B (2025). In-Silico Evaluation of Chalcone Derivatives as Potent Antifungal Agents Targeting N-Myristoyltransferase. *Journal of Applicable Chemistry*, *14*(3), 633-651.
13. Longkumer, P., **Singha, B.**, Gogoi, P. P., Boruah, N., & Sinha, U. B (2025). Antioxidant Strategy *via* Dual Targeting of SIRT2 and Keap1: A Computational Study of Isothiocyanate Derivatives. *Journal of Applicable Chemistry*, *14*(3), 612-624.
14. Longkumer, N., Richa, K., Karmaker, R., **Singha, B**., Ahmed, B., Longkumer, P., Gogoi, P. P., Boruah, N., Barman, R., Bezbaruah, B., & Sinha, U. B. (2025). Integrated approach: Synthesis, *in vitro* evaluation and computational analysis of bromoanilines as potential antioxidants. Asian Journal of Chemistry, *37(9).*

1. Ein rechnergestütztes System zur Bewertung des Potenzials von halogenierten Gentisylalkoholderivaten als pharmazeutische Wirkstoffe **Basanta Singha**, Nichan Boruah, Partha Pratim Gogoi, Penlisola Longkumer, Upasana Bora Sinha (Published on 27th June, 2024) (German Patent)

2. Halogenated Gentsiyl Alcohol Derivatives for Multi-target Pharmacological Profiling, Indian Patent Application No. 202531050810 A, filed May 27, 2025, published June 6, 2025. Inventors: **Basanta Singha**, Penilosa Longkumer, Nichan Boruah, Partha Pratim Gogoi, Benzir Ahmed, Bijpul Bezbaruah, Konda Mani Saravanan, Upasana Bora Sinha, Giridharan Bupesh. Assignee: Nagaland University.

3. A process for synthesizing 4-bromo-2-methylphenylisothiocyanate for wound healing Nichan Boruah, Bendangtula Walling, **Basanta Singha**, Penlisola Longkumer, Partha Pratim Gogoi, Sudharsan Parthasarathy, Kikoleho Richa, Giridharan Bhupesh, Upasana Bora Sinha. (Published on 14th March 2025) (Indian Patent)

4. Bezeichnung: Ein System zur umweltfreundlichen und schnellen Synthese von Bromographen (BG) unter Verwendung eines umweltfreundlicheren Bromierreagenz. IPC: C01B 32/184. Inhaber/Inhaberin: Kumar, Suraj, Zunheboto, Nagaland, IN; Rangappa, Dinesh, Chikkaballapur, Karnataka, IN; **Singha, Basanta**, Zunheboto, Nagaland, IN; Sinha, Dipak, Zunheboto, Nagaland, IN; Sinha, Upasana Bora, Zunheboto, Nagaland, IN; Supong, Aola, Tuensang, Nagaland, IN.

PAPERS PRESENTED IN CONFERENCE/SYMPOSIUM/WORKSHOP/CONCLAVE/SEMINAR

1. Presented a paper entitled "Computational evaluation of terrestrol a as inhibitor against sarscov-2 and invasive fungal pathogens (aspergillus fumigatus and candida auris): in-silico screening, molecular docking, dynamics and density functional theory study" in the SJU 1st International Conference on Multidisciplinary Research & Innovation (ICMRI-2023) organized by Internal Quality Assurance Cell (IQAC), St. Joseph University, Chumoukedima, Nagaland on 09th & 10th November, 2023.
2. Presented on **Nagaland University Research Conclave 2024**, organised by the NEP and IQAC Cell, in coordination with NURSF (Lumami) held on 3rd and 4th December 2024. **(Paper title: Molecualr dokcing and mlecular dynamics in drug discovery and design,Basanta singha**, Upasana Bora Sinha**)**
3. Participated in the "Oral" category with a presentation titled "Integrative Computational Analysis in Identifying High-Affinity Modulator of LXRα, LXRβ and FXR: An Underexplored Paradigm in Cancer Therapeutics" at the International Conference on Chemistry in Multidisciplinary Research (ICCMR-2025), organized by the Department of Chemistry, Nagaland University, Lumami held from 25th to 27th March 2025.

Computers in Biology and Medicine 194 (2025) 110433

Contents lists available at ScienceDirect

Computers in Biology and Medicine

journal homepage: www.elsevier.com/locate/compbiomed

A holistic computational exploration of AZD7762 as a potent selective modulator of LXRα, LXRβ and FXR: An underexplored pathway in cancer therapeutics

Basanta Singha [a], Partha Pratim Gogoi [a,1], Penlisola Longkumer [a,1], Benzir Ahmed [b,2], Nichan Boruah [a,2], Bipul Bezbaruah [b], Upasana Bora Sinha [a,*]

[a] Department of Chemistry, Nagaland University, Lumami, 798627, Nagaland, India
[b] Department of Applied Sciences, Gauhati University, Jalukbari, 781014, Guwahati, Assam, India

ARTICLE INFO

Keywords:
Liver X receptors (LXRα/β)
Farnesoid X receptor (FXR)
Cancer
AZD7762
Molecular docking
Molecular dynamics
Quantum mechanical calculation

ABSTRACT

Cancer remains one of the leading causes of global mortality, necessitating novel therapeutic strategies. Liver X Receptors (LXRα and LXRβ) and the Farnesoid X Receptor (FXR) are nuclear receptors that regulate lipid and cholesterol homeostasis, bile acid metabolism, inflammation, and immune response pathways intricately linked to cellular dysregulation in oncogenesis. Despite their therapeutic potential, these receptors remain underexplored targets in cancer research. This study implements an extensive suite of computational strategies to identify and evaluate potential modulators of LXRα/β and FXR, through virtual screening using resveratrol as the lead scaffold, followed by drug-likeness evaluation and toxicity profiling. Molecular docking (MVD, AutoDock and ML-PLIC) identified C144 (AZD7762), a well-established CHK1 kinase inhibitor, as the top-ranked ligand, demonstrating superior binding affinity and conformational stability *via* convergent interaction mechanisms. Additionally, reactivity descriptors derived from density functional theory (DFT) and frontier molecular orbital (FMO) analyses further substantiated its favorable electronic properties and chemical stability. Structural pharmacophore mapping using LigandScout confirmed pharmacophoric alignment with receptor active sites, while bioactivity profiles predicted high efficacy. Extensive quantum mechanical analyses (MEP, NBO, Mulliken/NPA, NCI, RDG, ELF, LOL, BSA, HAS) revealed favorable electronic characteristics, stability, charge distribution, and interaction potential. CLC-Pred, biotransformation (RA), pharmacokinetic profiling, molecular dynamics simulations, MM/PBSA and Shermo-based thermodynamic predictions further validated its biostability and systemic compatibility. These findings position C144 (AZD7762) as a promising anticancer candidate targeting LXRα, LXRβ, and FXR pathways. Further optimization and validation through *in vitro* and *in vivo* studies are essential for advancing these findings toward clinical application.

1. Introduction

Cancer continues to represent a major global health burden, remaining one of the foremost causes of mortality. Despite the formidable challenges associated with its management, groundbreaking therapeutic advances are poised to transform treatment paradigms. Building upon established modalities, novel and emerging strategies are rapidly gaining scientific prominence [1–4]. These encompass immunotherapy approaches, including immune checkpoint inhibitors, adoptive T-cell transfer, monoclonal antibodies, therapeutic cancer vaccines, and immune modulators. Nanoparticle-based drug delivery systems are offering precise and targeted therapeutic options. Gene-editing technologies, such as CRISPR, are enabling the modification of oncogenes and tumor suppressor genes to combat cancer more effectively, and emerging receptor-targeted therapies are exploiting cancer-specific vulnerabilities with greater precision and reduced toxicity. Advances in artificial intelligence (AI) are improving the speed, accuracy, and consistency of cancer screening and detection.

* Corresponding author.
E-mail address: upasanabsinha@gmail.com (U.B. Sinha).
[1] (2nd author).
[2] (3rd author).

https://doi.org/10.1016/j.compbiomed.2025.110433
Received 3 November 2024; Received in revised form 17 May 2025; Accepted 20 May 2025
Available online 4 June 2025
0010-4825/© 2025 Elsevier Ltd. All rights are reserved, including those for text and data mining, AI training, and similar technologies.

View publication stats

ChemistrySelect

Research Article
doi.org/10.1002/slct.202304761

Chemistry Europe
European Chemical Societies Publishing

www.chemistryselect.org

Evaluating Terrestrol A as an Inhibitor Against SARS-CoV-2and Invasive Fungal Pathogens: A Comprehensive Computational Analysis

Basanta Singha,[a] Bhoomika Arora,[b] Rituparna Karmaker,[a] Kikoleho Richa,[c] Naruti Longkumer,[a] Haider Thaer Abdulhameed,[b] Mohammad Abid,*[b] and Upasana Bora Sinha*[a]

The highly contagious SARS-CoV-2 virus, which initiated the COVID-19 pandemic, has resulted in a significant loss of life worldwide. While vaccines and therapeutics have helped mitigate the impact of SARS-CoV-2, worries still persist regarding the emergence of Variants of Concern (VOCs). Additionally, the immunosuppressive effects of SARS-CoV-2 and steroid treatments increase susceptibility to complex fungal co–infections (e.g., *aspergillosis* and *candidiasis*), complicating treatment and escalating mortality rates. These circumstances highlight the urgent need for novel therapeutics. Thus, this study explores gentisyl alcohol and its derivatives as inhibitors of SARS-CoV-2 and fungal pathogens (*Aspergillus fumigatus* and *Candida auris*) *via in-silico* methodologies. Initial multi–targeted docking simulations revealed that Terrestrol A(**10**) exhibited highly promising results, displaying the most favourable MolDock-scores against all targets of interest, particularly against PDB ID 4K90 and 7CR5. The subsequent assessment of Terrestrol A(**10**) for their druglikeness, ADME, toxicity profiling, bioactivity, and PASS prediction also yielded highly favourable results. Structural dynamics analysis revealed stable yet slightly unfolding complexes, affirming their integrity. DFT studies also demonstrated favourable reactivity of Terrestrol A(**10**). This investigation identifies Terrestrol A(**10**) as a highly promising inhibitor against SARS-CoV-2 and fungal pathogens, laying the groundwork for *in vitro* and *in vivo* validation of its efficacy and clinical utility.

Introduction

Wuhan, the capital of Hubei Province in central China, was the scene of a sudden outbreak of severe pneumonia cases in late December 2019, causing a global health alarm.[1] After further research, it was found that this outbreak was caused by the severe acute respiratory syndrome coronavirus 2 (SARS-CoV-2). Despite severe containment efforts, the virus quickly spread globally, leading the World Health Organisation (WHO) to declare it a pandemic in March 2020. Countless lives were lost worldwide as a result of this catastrophe.[2–3] The global scientific community and researchers worldwide made substantial efforts to advance the development of vaccines and enhance antiviral medications, which resulted in saving innumerable lives.[4] However, the emergence of multiple variants of concern is an alarming trend of COVID-19 reinfection, whereby individuals are getting infected by distinct variants of SARS-CoV-2 despite possessing prior immunity.[5] These instances of reinfection have even been documented in vaccinated individuals, emphasising their continued susceptibility to severe consequences.[6] Furthermore,SARS-CoV-2 infection weakens the immune system, creating a favourable environment for various pathogens to cause severe health complications. Patients with SARS-CoV-2 infection have been reported to develop fungal diseases such as *mucormycosis*, COVID-19-associated invasive pulmonary *aspergillosis* (CAPA), invasive *candidiasis*,etc. Fungal infections that occurred with COVID-19 heightened the pathogenicity and virulence of the infection, leading to additional challenges in treatment.[7]

Amidst the extensive repercussions induced by the COVID-19 pandemic, a concurrent outbreak emerged during the subsequent surge of COVID-19 in the summer of 2021. Multiple reports documented COVID-19 patients experiencing invasive fungal infections, including *invasive pulmonary, aspergillosis*, *candidemia*, and *mucormycosis*.[8–10] There are substantial difficulties in diagnosing, managing, and treating these fungal infections, which can lead to complications and higher rates of mortality. The exact mechanisms underlying the association between SARS-CoV-2 and fungal infections are not yet fully understood. However, it is believed that factors such as dysregulated immune responses, prolonged hospitalisation, utilisation of immunosuppressive therapies, and disruption of the normal microbiota due to COVID-19 and its treatments contribute to the development of a conducive environment for

[a] *B. Singha, R. Karmaker, N. Longkumer, U. Bora Sinha*
Department of Chemistry, Nagaland University, Lumami-798627, Nagaland, India
Tel: +91-9436006754
E-mail: upasanabsinha@gmail.com

[b] *B. Arora, H. Thaer Abdulhameed, M. Abid*
Medicinal Chemistry Laboratory, Department of Biosciences, Jamia Millia Islamia, Jamia Nagar, New Delhi 110025, India
E-mail: mabid@jmi.ac.in

[c] *K. Richa*
Department of Biotechnology, St. Joseph University, Chumoukedima-797115, Nagaland, India.

Supporting information for this article is available on the WWW under https://doi.org/10.1002/slct.202304761

© 2024 Wiley-VCH GmbH

Available online at **www.joac.info**

ISSN: 2278-1862

Journal of Applicable Chemistry

2024, 13 (2): 98-113

(International Peer Reviewed Journal)

Evaluation of Some Designed Halogenated Variants of Gentisyl Alcohol: Molecular Docking, DFT, Druglikeness, and ADMET Studies for Assessing Biological Properties

Basanta Singha, Partha Pratim Gogoi , Penlisola Longkumer, Nichan Boruah and Upasana Bora Sinha*

Department of Chemistry, Nagaland University, Lumami-798627, Nagaland, **INDIA**

Email: upasanabsinha@gmail.com

Accepted on 20th February, 2024

ABSTRACT

Antimicrobial resistance (AMR) poses a significant threat, complicating infection treatment and increasing the risks of severe illness. Concurrently, inflammation, prevalent in health issues like cardiovascular diseases, cancer, and diabetes, necessitates more effective therapeutic strategies. This dual challenge of AMR (Anti-microbial resistance) and inflammation underscores the critical need for novel and effective therapeutic. Incorporating halogen atom can profoundly alter a molecule's properties and may influence its bioactivity, metabolism, and pharmacokinetic profile. This study thus aims to design variants of gentisyl alcohol by incorporating bromine, fluorine, chlorine, and iodine atoms, evaluating their potential as antibacterial, anti-tubercular, antiviral, anti-parasitic, and anti-inflammatory agents via computational means. Employing molecular docking and Density Functional Theory (DFT), we assessed binding affinity, reactivity, and stability, alongside drug-likeness, pharmacokinetics, and toxicity. Compounds 7F, 4F, 7Br, 1F, and 7I exhibited superior and highest docking scores compared to gentisyl alcohol and native ligands against the target of interest with respect to PDB ID 7DQL, 3O4M, 4YRE, 7NNY, and 7OFS. Similarly DFT analysis revealed lower HOMO-LUMO energy gaps, suggesting enhanced and better stability and reactivity. These compounds met druglikeness criteria, demonstrated favorable ADME/T properties, and exhibited no signs of toxicity, indicating promise for drug development. Their high gastrointestinal absorption, moderate skin permeability, and absence of P-glycoprotein substrate activity further support their potential as lead compounds. In conclusion, compounds 7F, 4F, 7Br, 1F, and 7I shows potential in possessing broad-spectrum bioactivity and thus warrants further exploration and optimization for therapeutic applications.

Graphical Abstract:

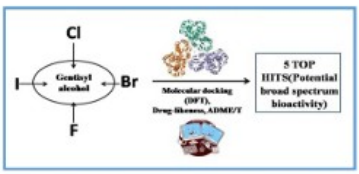

Gentisyl Alcohol: Halogenated Variant's Molecular Docking, DFT, Druglikeness, and ADMET Assessment

Send Orders for Reprints to reprints@benthamscience.net

Current Biotechnology, XXXX, *XX*, 1-34

RESEARCH ARTICLE

Multistep *In Silico* Pipeline for Targeting FimH Adhesin with Chalcones as Anti-Adhesion Therapeutics

Partha Pratim Gogoi[1], Basanta Singha[1], Penlisola Longkumer[1], Nichan Boruah[1] and Upasana Bora Sinha[1,*]

[1]*Department of Chemistry, Nagaland University, Lumami, 798627, Nagaland, India*

ARTICLE HISTORY

Received: June 19, 2025
Revised: September 05, 2025
Accepted: September 16, 2025

DOI: 10.2174/0122115301417613251020102808

Abstract: ***Introduction*:** FimH, a bacterial adhesin on *Uropathogenic Escherichia coli* (UPEC), facilitates host cell attachment and initiates Urinary Tract Infections (UTIs). With rising antibiotic resistance, alternative therapeutics targeting bacterial adhesion are urgently needed. This study investigates chalcone derivatives as potential anti-adhesive agents against FimH, aiming to inhibit bacterial colonization and reduce virulence through an *in silico* approach.

***Methods*:** A total of 200 chalcone derivatives were subjected to *in silico* toxicity screening using ProTox-II, followed by molecular docking using MVD 6.0 and AutoDock Vina against FimH (PDB IDs: 5AAP and 4XO8). The most promising compounds underwent structural pharmacophore modeling in LigandScout, pharmacokinetic profiling *via* SwissADME and PreADMET, and further validation through molecular dynamics simulations and MMPBSA free energy calculations.

***Results*:** Chalcones 103, 122, and 137 showed strong binding affinities, with highly negative MolDock scores surpassing native ligands. Key residues such as Gln133, Asp47, and Phe1 were identified as essential for hydrogen bonding. Pharmacokinetic profiles revealed high gastrointestinal absorption, BBB permeability, and compliance with major drug-likeness filters. RMSF analysis indicated 4XO8's structural rigidity, while MMPBSA confirmed strong binding energies, particularly for the 4XO8-137 complex.

***Discussion*:** These findings suggest chalcone derivatives, especially Chalcone 137, demonstrate promising anti-adhesive properties, structural stability, and favourable pharmacokinetics, making them viable candidates for further drug development.

***Conclusion*:** Chalcones 103, 122, and 137, particularly the 4XO8-137 complex, exhibit strong therapeutic potential as non-antibiotic anti-adhesion agents against UTI-causing *E. coli*, warranting further experimental validation *in vitro* and *in vivo*.

Keywords: Urinary Tract Infections (UTI), Uropathogenic *Escherichia Coli* (UPEC), *in silico*, molecular docking, DFT and ESP studies, molecular dynamics studies.

1. INTRODUCTION

FimH is a key protein component of type 1 pili, filamentous structures made up of pilin subunits present on the surface of uropathogenic *E. coli* (UPEC), a primary causative agent of urinary Tract Infections (UTIs) [1]. FimH contains two main domains: the lectin domain, responsible for binding to carbohydrate moieties such as mannosylated proteins and glycolipids on host cells, and the pilin domain, which anchors it to the pilus structure [2]. FimH-mediated adhesion triggers downstream processes, including host cell signalling, cytoskeletal rearrangement, gene expression modulation, and in some cases, bacterial invasion and colonisation [3, 4]. Its receptor-binding specificity is influenced by factors such as receptor density and the nature of the carbohydrate moiety, particularly mannose and glucose. Due to its central role in bacterial attachment and pathogenesis, FimH has emerged as a promising target for anti-adhesion therapeutic development.

Anti-adhesion therapy targeting FimH aims to block bacterial colonisation by inhibiting its interaction with host cell receptors. This approach can suppress biofilm formation and reduce virulence factor expression [5, 6]. Given FimH's conservation across various bacterial strains, such therapies have broad-spectrum potential and reduce the likelihood of antibiotic resistance by targeting adhesion rather than bacterial viability [7].

Chalcones, a class of aromatic ketones and key intermediates in the biosynthesis of flavonoids and isoflavonoids, exhibit diverse biological activities. These include antibacterial, antiviral, antifungal, anticancer, anti-inflammatory, and anti-

*Address correspondence to this author at the Department of Chemistry, Nagaland University, Lumami, 798627, Nagaland, India;
E-mail: upasanabsinha@gmail.com

2211-5501/XX $65.00+.00 © XXXX Bentham Science Publishers

Send Orders for Reprints to reprints@benthamscience.net

Mini-Reviews in Medicinal Chemistry, 2025, *25*, 1517-1538

REVIEW ARTICLE

Chalcones as Emerging Antibacterial Scaffolds: A Mini Review

Partha Pratim Gogoi[1], Mhasilhoutuo Pucho[1], Pangerkokba Jamir[1], Nichan Boruah[1], Basanta Singha[1], Penlisola Longkumer[1], Beware Dkhar[1], Ilavanalangki Lytan[1] and Upasana Bora Sinha[1,*]

[1]*Department of Chemistry, Nagaland University, Lumami, Zunheboto, 798627, India*

ARTICLE HISTORY

Received: June 15, 2025
Revised: August 14, 2025
Accepted: August 18, 2025

DOI: 10.2174/0113895754349872509181622 46

Abstract: The mounting threat of antimicrobial resistance has intensified the global search for novel antibacterial agents, and chalcones - the aromatic ketones characterized by an α, β-unsaturated carbonyl system has emerged as promising scaffolds against the threat of antimicrobial resistance. This review presents a detailed exploration of chalcones as potent antibacterial agents, emphasizing their structural versatility, mechanisms of action, and therapeutic potential. With a modular backbone that supports diverse substitutions and heterocyclic extensions, chalcones can be easily synthesized and chemically optimized to target a broad spectrum of bacterial pathogens, including multidrug-resistant strains such as MRSA and VRE. Mechanistically, chalcones exert antibacterial effects through multiple pathways, like disrupting bacterial membranes, inhibiting cell wall biosynthesis, interfering with DNA replication *via* DNA gyrase and topoisomerase IV, and suppressing protein synthesis. Their amphipathic nature and ability to bind critical bacterial enzymes offer an advantage in circumventing classical resistance mechanisms. Structure-activity relationships and computational studies have further elucidated the influence of electron-donating and electron-withdrawing groups, positional isomerism, and heterocyclic integration on antibacterial potency. A review of recent literature underlines the efficacy of chalcone derivatives against Gram-positive and Gram-negative strains, with many compounds demonstrating promising activity, such as compound 85 with MIC 3.4 nM against Ciprofloxacin with MIC 4.7 nM. The review also highlights advancements in green synthesis, QSAR modeling, and molecular docking, which collectively facilitate the rational design of next-generation chalcone-based antibacterials. Altogether, chalcones represent a structurally simple yet biologically robust class of compounds, offering significant promise as adaptable and effective agents in the evolving landscape of antimicrobial therapy.

Keywords: Chalcone derivatives, synthetic approach, antibacterial activity, antimicrobial resistance, QSAR, enzymes.

1. INTRODUCTION

The emergence of antimicrobial resistance presents a serious threat to global public health [1], requiring the discovery and development of new classes of antimicrobial agents [2, 3]. According to the World Health Organization, there are high proportions of antibiotic resistance in bacteria that cause common infections (*e.g.*, urinary tract infections, pneumonia, and bloodstream infections) in all regions of the world [4]. Hence, there is an urgent medical need to develop new and effective antibacterial agents to counteract the threat of antimicrobial resistance to available drugs.

Chalcones are aromatic ketones that form the central core for a variety of biologically active compounds (Fig. **1**). They are classified as a subclass of flavonoids. They are characterized by the presence of two aromatic rings (A and B) linked by a three-carbon α, β-unsaturated carbonyl system [5].

*Address correspondence to this author at the Department of Chemistry, Nagaland University, Lumami, Zunheboto, 798627, India; E-mail: upasanabsinha@gmail.com

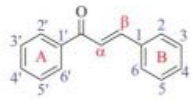

Fig. (1). General structure of chalcone.

The unique structural features of chalcones are not only distinctive but also play a vital role in determining their pharmacological effects, particularly their antibacterial properties. In our study, chalcones with specific substitutions showed significantly enhanced antibacterial activity against both Gram-positive and Gram-negative bacteria, underscoring the importance of their chemical structure in mediating biological effects [6]. Chalcones are typically synthesized through Claisen–Schmidt condensation, where an aromatic aldehyde reacts with an aromatic ketone in an alkaline medium. The defining feature of chalcones is the α, β-unsaturated

1875-5607/25 $65.00+.00

© 2025 Bentham Science Publishers

Mini-Reviews in Medicinal Chemistry

Chemical Physics Letters 753 (2020) 137611

Contents lists available at ScienceDirect

Chemical Physics Letters

journal homepage: www.elsevier.com/locate/cplett

Research paper

Rationale for antioxidant interaction studies of 4-bromo-1-isothiocyanato-2-methylbenzene – An experimental and computational investigation

Kikoleho Richa[a,b], Rituparna Karmaker[a], Toshinungla Ao[c], Naruti Longkumer[a], Basanta Singha[a], Upasana Bora Sinha[a,*]

[a] Department of Chemistry, Nagaland University, Lumami 798627, Nagaland, India
[b] Bioinformatics Facility Centre, Nagaland University, Lumami 798627, Nagaland, India
[c] Department of Botany, Nagaland University, Lumami 798627, Nagaland, India

HIGHLIGHTS

- 4-Bromo-1-isothiocyanato-2-methylbenzene was studied for its antioxidant property.
- DPPH and FRAP revealed its promising antioxidant activity.
- Mechanism of antioxidant activity reveals SET using BDE analysis.
- Interactions observed with Myeloperoxidase through molecular docking studies.

ARTICLE INFO

Keywords:
4-Bromo-1-isothiocyanato-2-methylbenzene
Antioxidant
DFT
Molecular docking

ABSTRACT

Possessing multiple pharmaceutical activities make drug-like compounds more attractive. Therefore, if an anticancer compound can also halt progression of ovarian cancer cells through diminution of radicals, it would be important because reactive oxygen species produced in response to chemotherapeutics is a major complication in cancer treatment. Accordingly, the antioxidant activity of 4-bromo-1-isothiocyanato-2-methylbenzene, which we had recently reported for its activity against ovarian cancer, was investigated. DFT was employed to understand its mode of action and docking simulations were incorporated to evaluate possible interactions with myeloperoxidase. An assessment of the antioxidant potential of this anticancer compound is now presented.

1. Introduction

Small molecules have found significance as new-age pharmaceutical compounds as they can be inexpensive, have relatively basic storage or quality control requirements, and usually have simple manufacturing processes [1,2]. It has been observed that small molecules are still leading in new drug approvals and there is an ongoing search for compounds that have notable pharmaceutical activity [3]. In this connection, in one of our recent works, we reported the possibility that small isothiocyanate molecules synthesized by simple green methodologies can pose as promising candidates for their application as anticancer agents [4]. The studies revealed that 4-bromo-1-isothiocyanato-2-methylbenzene (NC6) has better cytotoxic effects as compared to its counterparts, showed 5-folds lower transcript expression levels of Spindlin1, and induced caspases 3 and 7 expressions as assessed by qRT-PCR in ovarian cancer cells. Furthermore, flow cytometric assay showed the cell cycle arrest at G1/S phase of cell cycle. However, it was realized that the pharmaceutical potential of this anticancer compound would improve if it is shown to possess antioxidant properties as well. This is because unstable reactive oxygen species (ROS) produced in response to chemotherapeutics is a major complication in ovarian cancer treatment, because ROS accumulation in ovarian cancer progression leads to the chemoresistance and tumorigenicity of human ovarian cancer cells [5]. Therefore it was considered important to further study NC6 to assess its antioxidant property.

In fact synthesis of new compounds having antioxidant activity for the prevention of radical induced impairments is of great current importance. This is because though reactive oxygen species (ROS) produced during oxidation play a vital role in metabolic pathways, unfortunately however these free radicals react readily with other molecules to attain stability [6–8]. Therefore, when ROS levels exceed

* Corresponding author.
E-mail address: upasanabsinha@gmail.com (U.B. Sinha).

https://doi.org/10.1016/j.cplett.2020.137611
Received 19 February 2020; Received in revised form 21 April 2020; Accepted 16 May 2020
Available online 18 May 2020
0009-2614/ © 2020 Elsevier B.V. All rights reserved.

Send Orders for Reprints to reprints@benthamscience.net

Anti-Infective Agents, **XXXX**, *XX*, **1-14**

RESEARCH ARTICLE

Experimental and Theoretical Investigations on the Antibacterial Activity of Some Bromoaniline Compounds

Naruti Longkumer[1], Kikoleho Richa[2], Rituparna Karmaker[1], Basanta Singha[1] and Upasana Bora Sinha[1*]

[1]*Department of Chemistry, Nagaland University, Lumami, 798627, Nagaland, India;* [2]*Department of Biotechnology, St. Joseph University, Chumoukedima, 797115, Nagaland, India*

ARTICLE HISTORY

Received: August 12, 2022
Revised: October 26, 2022
Accepted: November 30, 2022

DOI:
10.2174/2211352521666230126123021

Abstract: ***Background*:** Test substrates are routinely used in laboratories to test the efficacy of various reactions, and while many substrates have found success as test substrates, not much is known about their potential intrinsic properties. On that note, some bromoaniline compounds were synthesized and repurposed by studying their antibacterial activity.

***Methods*:** The *in-vitro* antibacterial tests were done against *S. aureus, K. pneumoniae, B. subtilis,* and *E. coli.* Tests were carried out to understand the mode of action of the compounds where changes in permeability and integrity of cell membrane resulting in the leakage of UV absorbing materials were observed. Computational studies were performed by employing density functional theory (DFT) in the Gaussian09 software for determining the reactivity of the studied compounds. Molecular docking studies were executed to define the interaction of the synthesized compounds with microbial target proteins, Dihydrofolate reductase (PDB ID: 3SRW) and DNA gyrase subunit B (PDB ID: 1KZN).

***Results*:** The compound's response to the mode of action tests showed alteration in the membrane permeability and its antimicrobial effectiveness at different pH contributed it to being a potential antibiotic. The results of DFT studies revealed that the molecular descriptors indicate better reactivity of compound **8b** which is in agreement with the experiments performed. Molecular docking studies revealed that interactions of the compounds at the active sites of target proteins depict that the compounds are likely to bind to the protein enhancing their potential as antibacterial agents.

***Conclusions*:** This work concludes that simple molecules synthesized effortlessly through a simple and environmentally benign pathway, can pose as a good therapeutic agent

Keywords: Bromination, Antibacterial, Mode of action, DFT, Molecular docking, microbial target proteins.

1. INTRODUCTION

The endless process of synthesis in research laboratories contributes to the generation of chemical wastes and its effect on the environment has been of great concern and discussion for the past few decades [1]. Many academic institutions have created or are continuously working to create a safer environment, including research safety [2]. Practicing greener synthetic protocol is one way of minimising chemical waste. The chemical transformations generate a lot of generic products which are not tested for their intrinsic activities. In a way, they go on to become waste when in fact they could have some useful properties. Our group has been working on the development of synthetic protocols for bromo organic compounds and over time a number of different compounds have been synthesised. Acknowledging the significance of green chemistry as well as halogenated aromatic compounds in synthetic chemistry [3, 4], this work presents an environmentally benign synthesis of bromoanilines. In order to maximize the environmental benignness of the synthetic protocol, water was used as a solvent, cetyltrimethylammonium tribromide (CTMATB) as the brominating reagent, and the reaction was carried out in a microwave reactor [5]. Taking the work further, the synthesized bromoanilines were then tested for antimicrobial behaviour and initial results showed some compounds to have promising activity, and this paper reports the results of those studies.

Small molecules have been the mainstay of pharmaceutical compounds as they usually involve simple methodology, can be low-cost, and have comparatively easy storage or quality control requirements. In terms of new medicine approvals, small compounds continue to lead and there is a continuous search for pharmacologically active compounds [5, 6]. The substantial use of conventional antibiotics has led to resistance in micro-organisms [7] resulting in major public health concerns [8]. Therefore, the

*Address correspondence to this author at the Department of Chemistry, Nagaland University, Lumami, 798627, Nagaland, India;
Tel: +91-9436006754; Email: upasanabsinha@gmail.com

 © XX Bentham Science Publishers

Journal of Molecular Liquids 436 (2025) 128260

Contents lists available at ScienceDirect

Journal of Molecular Liquids

journal homepage: www.elsevier.com/locate/molliq

Highly efficient photocatalytic degradation of organic pollutants using novel carbon integrated ZrO_2-ZnO nanocomposites: kinetics, molecular docking, DFT simulation and real wastewater application

Shisak Sharma [a], Raplang Steven Umdor [a], Imotila T. Longchar [a], Basanta Singha [a], Soremo L. Ezung [a], Parimal C. Bhomick [b], Dipak Sinha [a,*]

[a] Department of Chemistry, Nagaland University, Lumami, 798627, Nagaland, India
[b] Bristol Composites Institute, Queen's Building, University of Bristol, Bristol BS8 1TR, UK

ARTICLE INFO

Keywords:
Nanocomposite
Photocatalysis
4-nitrophenol
Kinetics
UV irradiation

ABSTRACT

Photocatalysis serves as a promising alternative approach for the treatment of wastewater contaminated with organic pollutants. The method is advantageous owing to its ability for complete mineralization of toxic compounds, degradation of chemically stable pollutants and wide application. Herein, we report the synthesis of a CCAC/ZrO_2-ZnO nanocomposite *via* a hydrothermal method by anchoring ZrO_2-ZnO onto activated carbon derived from *Croton caudatus* biomass for 4-nitrophenol (4-NP) degradation. The nanocomposite was thoroughly characterized using advanced analytical techniques, including XRD, FT-IR, SEM/TEM with SAED and EDS, PL spectroscopy, BET surface area analysis, and XPS. Photocatalytic activity was evaluated through the 4-NP degradation under UV light, achieving an impressive 98.2 % degradation with a catalyst dosage of 0.07 g/L, initial concentration of 40 ppm, irradiation time of 80 min and pH 6. The degradation intermediates and pathway were identified using LC-MS analysis. The nanocomposite exhibited good recyclability, retaining 78.5 % efficiency after multiple cycles and achieved a notable 87.86 % degradation efficiency in real wastewater. Density Functional Theory (DFT) calculations were performed to investigate the chemical reactivity and formation mechanism of the prepared nanocomposite. The results indicated a significant enhancement in its reactivity, which contributed to improve the efficacy in the degradation of 4-NP. Subsequently, the molecular docking studies targeting DNA gyrase and DHFR revealed favorable binding energies (MolDock), providing a valuable theoretical framework for future *in vitro* and *in vivo* experimental validation. These findings may significantly aid in the rational design and development of next-generation antibacterial agents designed at combating the growing threat of antibiotic-resistant pathogens such as *Escherichia coli (E. coli)* and *Staphylococcus aureus (S. aureus)*.

1. Introduction

Nitrophenols are anthropogenic, inhibitory, and biorefractory organic molecules. They have been extensively applied in chemical industry for insecticides, medicines, and dyes [1,2]. 4- nitrophenol (4-NP) is a phenolic molecule that contains two functional groups on its benzene ring; nitro (NO_2) and hydroxyl (OH). European Economic Union and US Environmental Protection Agency considers 4-NP among priority contaminants due to its potential to negatively impact aquatic life, animals, and human beings at low amounts with the maximum allowable limit of 1 ppm [3]. The exposure of 4-NP also leads to a spectrum of acute and chronic health effects including gastrointestinal complication, respiratory tract problems, injury to organs like kidneys and liver, skin and eye irritant, and cardiovascular system problem. It may also lead to hypersalivation, suppression of hunger, breakdown of protein, and interference with the central nervous and circulatory systems [4,5]. In

Abbreviations: AOPs, Advanced Oxidation Processes; AC, Activated carbon; NP, Nitrophenol; DFT, Density functional theory; CCAC, *Croton caudatus* activated carbon; DHFR, Dihydrofolate reductase; TDS, Total dissolved solids; EC, Electrical conductivity; TH, Total hardness; BOD, Biological oxygen demand; TOC, Total organic carbon; MQW, Ultrapure Milli-Q water; MVD, Molegro virtual docker.

* Corresponding author.
E-mail address: dipaksinha@gmail.com (D. Sinha).

https://doi.org/10.1016/j.molliq.2025.128260
Received 15 April 2025; Received in revised form 9 July 2025; Accepted 30 July 2025
Available online 5 August 2025
0167-7322/© 2025 Elsevier B.V. All rights are reserved, including those for text and data mining, AI training, and similar technologies.

Indian Journal of Chemistry
Vol. 63, June 2024, pp. 543-556
DOI: 10.56042/ijc.v63i6.7542

Some pyridyl moiety based metal complexes (*viz*., Mn^{+2}, Co^{+2} and Zn^{+2}) as potential anticancer agents and DNA nucleobase interaction: A DFT approach

Benzir Ahmed[a], Pratyashee Barukial[a], Basanta Singha[b], Upasana Bora Sinha[b] & Bipul Bezbaruah*[a]

[a] Department of Applied Sciences, Gauhati University, Guwahati 781 014, Assam, India

[b] Department of Chemistry, Nagaland University, Lumami 798 627, Nagaland, India

E-mail: bipulbezbaruah@gmail.com

Received 25 December 2023; accepted (revised) 24 May 2024

Many experimental evidences reveal that a new set of complexes involving transition metals (*viz*., Mn^{+2}, Co^{+2} and Zn^{+2}) with pyridyl moiety ligands are being investigated as potential anticancer agents due to their intense ability to follow intercalation mechanisms with DNA nucleobases. Although, the interaction mechanism between anticancer agent-DNA nucleobase itself is quite complicated to understand by using conventional techniques; but some computational methods may still be very helpful for analyzing the proper binding mode of interaction. Hence, exploring the favoured interaction sites within an anticancer agent and finding its donor-acceptor ability is really a challenging task. Moreover, for any drug-DNA receptor complex; there must be few changes in their electron charge density, structure of the molecule, chemical reactivity parameters, *etc*. DFT is one of the best known and most affordable methods for investigating such exploration in metal complexed anticancer agents. Herein, we have described an attempt to investigate the interaction mechanism of some pyridyl moiety based Mn^{+2}, Co^{+2} and Zn^{+2} metal complexes as potential intercalating anticancer agents by using computational techniques.

Keywords: Pyridyl moiety, Anticancer agent, DFT, DNA, Metal complex

Novel transition metals-based anticancer agents have gained significant interest in recent years, as metal ions directly coordinate with the ligands *via* donor atoms such as -O, -N and -S in a precise 3D structure, which may allow the molecule be able to recognize, design and potentially interact with the specific receptors[1-4]. Hence, the effectiveness of metal-based anticancer agents depends on their chemical structures and donor-acceptor behaviour as interacting ligands. Some of the transition metal complexes show effective pharmacological behaviours *i.e*., antibacterial, antifungal, anticonvulsant, antidiabetic, anti-inflammatory, antioxidant and antiproliferative/ antitumor activities[5-8]. Specially, metallic compounds other than *cis*-platin have long been a target of interest for researchers, as they are said to be the most effective and best known anticancer metallodrugs[9,10]. Due to their potential antiproliferative action, higher thermodynamic stability in aqueous phase and flexibility to change their oxidation states to the biological target sites, the development of physiologically active metallodrugs with endogenous metal ions has drawn a lot of interest[11-13]. However, *in vivo* interaction mechanism of such metal complexes within the possible target sites, *viz*., proteins and nucleic acids is still poorly known; *e.g*., some of the bio-active transition metal complexes containing an antibacterial drug flumequine reveal that they directly interact with nucleobases and serum albumin[14-19]. The pyridyl moiety or N-based pyridyl ligands with transition metals have recently been extensively studied as potential anticancer agents; *e.g*., Pd, Ru, Rh, Cu, La, *etc*. metal complexes with pyridine, imidazole along with 1,10-phenanthroline ligands; and their derivatives are showing promising antitumor properties in regard to drug design research[20]. Again, metal complexes comprising pyridyl or polypyridyl ligands are largely dependent on the nature, geometry and overall arrangement of the coordinated ligand. In particular, due to their electron-deficient nature, N-based heterocyclic rings are excellent π-electron acceptors to form a favourable donor-acceptor complex, which results in smooth intercalation of such aromatic rings into DNA base pairs[21-23]. Additionally, a typical tridantate ligand, di(picolyl) amine (DPA) can form stable complexes with transition metal ions by strongly coordinating with their metal cations and using two pyridine nitrogens

Indian Journal of Biochemistry & Biophysics
Vol. 61, June 2024, pp. 354-370
DOI: 10.56042/ijbb.v61i6.8609

Some Co(II)-Schiff base complexes as promising anticancer agents: A DFT and molecular docking study

Pratyashee Barukial[1], Benzir Ahmed[1], Basanta Singha[2], Pankaj Chetia[3], Nipu Kumar Das[4], Samir Thakur[1], Upasana Bora Sinha[2] & Bipul Bezbaruah[1]*

[1]Department of Applied Sciences, Gauhati University, Guwahati-781 014, Assam, India

[2]Department of Chemistry, Nagaland University, Lumami-798 627, Nagaland, India

[3]Department of Life Sciences, Dibrugarh University, Dibrugarh -786 004, Assam, India

[4]Department of Chemical Engineering, Indian Institute of Technology, Guwahati-781 039, Assam, India

Received 07 February 2024; *revised 29 February 2024*

Non-covalent interactions have long been an emerging area of research in anticancer drug-DNA binding investigations since *in vivo* biomolecules are the primary target sites for all types of drug molecules. This study delves into the interaction of five promising Co(II)-Schiff base complexes (M_1-M_5) with DNA nucleobases, employing a multi-pronged approach to unveil their anticancer activity and interaction mechanisms. Density functional theory (DFT) provided a deep dive into the complexes' electronic structures, shedding light on how they interact with DNA nucleobases, their stability within these interactions, and the overall geometry involved. Further insights were gleaned from analysing frontier molecular orbitals (FMOs), molecular electrostatic potential (MEP), and non-covalent interactions (NCI) to investigate other important aspects of Co(II)-Schiff base complexes with the receptor AT/GC base pairs. Moreover, molecular docking simulations predicted the preferred binding sites and orientations of these complexes with B-DNA dodecamer, offering a realistic picture of their interactions with DNA in a larger context. Further, we also carried out Absorption, Distribution, Metabolism, Excretion, and Toxicity (ADMET) studies to analyse the pharmacokinetic and physicochemical properties of the Co(II)-Schiff base complexes. DFT study suggest that the Complex M_1 exhibits a strong affinity for both AT and GC base pairs, as indicated by its high negative interaction energy values of -18.55 kcal/mol for AT and -23.42 kcal/mol for GC.

Keywords: ADMET, AT/GC, DNA nucleobases, NCI, RDG

Metal complexes offer promising avenues for developing new anticancer agents. Researchers are constantly designing new "metallodrugs" with improved potency and reduced toxicity[1]. Metals like Ru, Pd, Rh, and Pt, *etc.*, when combined with the right donor ligands, can create versatile therapeutic agents with applications beyond pharmacology, such as in nanoscience, catalysis, molecular modelling, analysis of electronic and magnetic properties, *etc*[2,3]. These efforts are aided by the use of bioactive Schiff base derivatives, known for their excellent solubility as well as the capacity to form stable complexes with various metals, making them valuable tools in medicinal chemistry research[4]. Past literature reveals that Schiff base complexes with variable oxidation states of metal ions, *e.g.*, Zn^{+n}, Cu^{+n}, Ni^{+n}, Co^{+n}, Fe^{+n}, Mn^{+n}, and V^{+n} in their structural backbone, have a great impact on the interacting sites of any biologically active receptor[5]. Some reported metal complexes with Schiff base ligands *viz.*, N -(2-hydroxy-1- naphthylidene)-4-chloroaniline, N -(2-hydroxybenzylidene)-2,3- dimethylaniline, 2-hydroxy naphthaldehyde, PDH [N-(1-phenyl-2-hydroxy-2-phenylethylidine)-2′-hydroxy phenyl imine], HHP (N-(2-hydroxybenzylidine)-2′-hydroxy phenyl imine), N-(salicylidene)-2-hydroxyaniline, coumarin-thiazole, 2-methoxyethylamine derivatives, *etc.* show potential antibacterial, antituberculosis, anticancer and antitumour activity[5-9]. DNA's unique structure, specifically its nucleobases, makes it a prime target for new cancer therapies[10]. Metal complexes, particularly those containing cobalt, show potential in selectively interacting with DNA nucleobases, potentially disrupting the growth of cancer cells. Cobalt's unique properties, including its ability to change oxidation states (redox properties) and adapt its bonding (flexible valency), make it ideal for designing effective anticancer agents with minimal impact on healthy cells[11,12].

*Correspondence:
Phone: +91-9854634789 (Mob)
E-mail: bipulbezbaruah@gmail.com

Asian Journal of Chemistry; Vol. 34, No. 12 (2022), 3115-3124
ASIAN JOURNAL OF CHEMISTRY
https://doi.org/10.14233/ajchem.2022.23994

Facile Green Synthesis of Bromoaniline Molecules: An Experimental and Computational Insight into their Antifungal Behaviour

NARUTI LONGKUMER[1], KIKOLEHO RICHA[2], RITUPARNA KARMAKER[1], BASANTA SINGHA[1] and UPASANA BORA SINHA[1,*]

[1]Department of Chemistry, Nagaland University, Lumami-798627, India
[2]Department of Biotechnology, St. Joseph University, Chumoukedima-797115, India

*Corresponding author: E-mail: upasanabsinha@gmail.com

Received: 12 July 2022; *Accepted*: 8 September 2022; *Published online*: 25 November 2022; AJC-21035

Through the bromination of organic substrates using cetyltrimethylammonium tribromide (CTMATB), a series of bromoanilines have been synthesized using a greener synthetic process. The synthesized bromoanilines were optimized by testing for antifungal activity against *Fusarium oxysporum*, *Penicillium italicum*, *Candida albicans* and *Aspergillus niger*. The ADMET profiling was studied to determine the drug likeliness of the compounds. *In silico* studies were done to understand the ligand-protein interaction of the compounds with a target protein. Density functional theory (DFT) studies have been carried out in order to study the reactivity of the compounds through their bandgap energy to supplement and validate the antifungal property of the synthesized compounds.

Keywords: Bromo compounds, Antifungal, Density functional theory, Molecular docking, ADMET.

INTRODUCTION

Bromination of aromatic compounds is a widely performed organic reaction due to the importance of bromoorganics in many organic synthesis procedures like oxidation [1-4], cyclization [5-7], co-halogenation [8-12], substitution [13-16], catalysis [17-20], *etc*. Bromo derivatives also finds use in the manufacturing of pharmaceuticals, intermediates for agrochemicals and other new materials [21,22]. Because of these important applications of bromo derivatives over the years, several methodologies have been developed for bromination reactions [23-27]. For these types of transformation reactions, small organic molecules are used as test substrates and while these test substrates serves the purpose in proving the success of the bromination methodologies, it has been observed that their intrinsic properties are not studied and their utility of these test compounds is not explored. On that note, bromoanilies albeit routinely synthesized for various studies [28-30] especially for use in different organic transformations [24,27,31-34], not much information is available on studies done to assess the potential biological activities. Previous work has reported the antibacterial activity of a few bromoaniline [35] and therefore this present work is aimed to look into their antifungal activity.

The use of elemental bromine poses threat to the environment as well as to the researchers and therefore, it has become important to use a substitute for molecular bromine [36,37]. Quaternary ammonium tribromides (QATBs) gained attention in the past decades as versatile alternatives for bromine and one such QATB known for its efficacy is cetyltrimethylammonium tribromide (CTMATB) [38-40]. While adopting green synthetic protocols, the identification and use of solvent is important. Water has been considered as a greener solvent for organic transformations because of its non-toxic, non-corrosive, high vapour pressure and non-flammable nature [41]. In this context, an environmentally benign method for bromination involving the use of CTMATB and water as solvent under microwave irradiation has been reported by us earlier [35]. In present work, a series of bromoanilines have been synthesized using the said methodology.

Bromoorganic compounds have also been reported to have various biological properties like antimicrobial [35,42,43], antioxidant [42,44,45], anticancer [46-48], analgesic [49], antitubercular [42] and cytotoxic [50] activities. Small molecules have found significance in the field of pharmaceutical chemistry as they are usually easy to synthesize, low cost and are able to affect the function of various proteins, enzyme, or

This is an open access journal, and articles are distributed under the terms of the Attribution 4.0 International (CC BY 4.0) License. This license lets others distribute, remix, tweak, and build upon your work, even commercially, as long as they credit the author for the original creation. You must give appropriate credit, provide a link to the license, and indicate if changes were made.

Available online at **www.joac.info**

ISSN: 2278-1862

Journal of Applicable Chemistry

2025, 14 (3): 633-651

(International Peer Reviewed Journal)

In-Silico Evaluation of Chalcone Derivatives as Potent Antifungal Agents Targeting N-Myristoyltransferase

Partha Pratim Gogoi, Nichan Boruah, Basanta Singha, Penlisola Longkumer and Upasana Bora Sinha*

Department of Chemistry, Nagaland University, Lumami, Nagaland – 798627, **INDIA.**

Email: upasanabsinha@gmail.com

Accepted on 20th May, 2025

ABSTRACT

The escalating global threat posed by antifungal resistance demands novel and effective therapeutic strategies, particularly for immunocompromised populations. In response, this study systematically evaluated the therapeutic potential of chalcone derivatives as antifungal agents through comprehensive computational methodologies. Chalcones, characterized by their versatile α, β-unsaturated carbonyl framework, have garnered attention due to their structural flexibility, low toxicity, and diverse antifungal mechanisms. A library of 200 structurally varied chalcone derivatives underwent rigorous computational screening, including toxicity assessment via ProTox-III, molecular docking analyses, pharmacophore modeling, and pharmacokinetic (ADME) evaluations. Molecular docking studies against Candida albicans N-myristoyltransferase (NMT) revealed notably higher binding affinities for several chalcones—particularly Chalcone 96, Chalcone 90, and Chalcone 87—compared to conventional antifungal standards Fluconazole and Voriconazole. These interactions primarily involved critical residues like Tyr 225 and Cys 393, mediated via hydrogen bonds, π–π stacking, and hydrophobic interactions. Complementary pharmacophore modeling underscored structural alignment and similar interaction patterns between chalcones and established antifungal drugs. ADME profiling confirmed favorable oral bioavailability, gastrointestinal absorption, and blood-brain barrier permeability for these chalcone derivatives, notably highlighting Chalcone 96 with superior pharmacokinetic characteristics and minimal drug interaction risks. Toxicity assessments supported their robust safety profiles. Overall, this integrative computational approach positions chalcone derivatives, particularly Chalcone 96, as highly promising antifungal candidates, warranting future in-vitro and in-vivo validations to address the critical need for new antifungal therapies amidst rising resistance challenges.

Graphical abstract:

Chalcone Derivatives as Antifungal Agents.

Available online at **www.joac.info**

ISSN: 2278-1862

Journal of Applicable Chemistry

2025, 14 (3): 612-624

(International Peer Reviewed Journal)

Antioxidant Strategy *via* Dual Targeting of SIRT2 and Keap1: A Computational Study of Isothiocyanate Derivatives

Penlisola Longkumer, Basanta Singha, Partha Pratim Gogoi, Nichan Boruah and Upasana Bora Sinha*

Department of Chemistry, Nagaland University, Lumami, Nagaland-798627, **INDIA**

Email: upasanabsinha@gmail.com

Accepted on 20th May, 2025

ABSTRACT

Oxidative stress, driven by excess reactive oxygen species (ROS), plays a central role in the Oxidative stress, driven by excess reactive oxygen species (ROS), plays a central role in the pathogenesis of various chronic diseases, including cancer, neurodegeneration, and metabolic disorders. Antioxidants counteract ROS, thereby offering protective effects at the cellular level. Among natural antioxidant sources, isothiocyanates are bioactive compounds found in cruciferous vegetables have attracted considerable attention due to their ability to modulate redox signaling pathways and activate cellular defense mechanisms. This study provides a computational evaluation of selected isothiocyanate derivatives to assess their potential as antioxidant agents. Molecular docking was conducted against key antioxidant-related proteins, SIRT2 (PDB ID: 5D7Q) and Keap1 (PDB ID: 5FZJ), identifying ITC-3 and ITC-6 as top-performing ligands with superior binding energy compared to the reference compound phenethyl isothiocyanate (PEITC). Protein–ligand interaction profiling (PLIP) confirmed key stabilizing interactions, including hydrogen bonding and hydrophobic contacts, particularly with residues such as Arg97, Thr262 (SIRT2), and Arg415 (Keap1). Density functional theory (DFT) analysis revealed lower HOMO–LUMO energy gaps for ITC-6 (4.34 eV) and ITC-3 (4.60 eV), indicating greater molecular reactivity than PEITC (5.93 eV). The combined results suggest that ITC-3 and ITC-6 exhibit dual-target antioxidant potential through efficient interaction with Keap1 and SIRT2, positioning them as promising candidates for future therapeutic development aimed at mitigating oxidative stress-related diseases.

Graphical abstract:

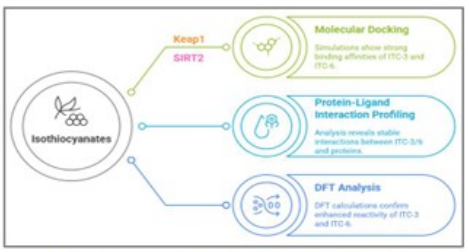

Unveiling the Antioxidant Potential of Isothiocyanates

Asian Journal of Chemistry

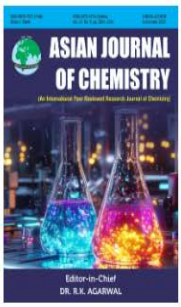

Issue

Vol. 37 No. 9 (2025): Vol 37 Issue 9, 2025

Issue Published : 30 August 2025

Copyright (c) 2025 Naruti Longkumer, Kikoleho Richa, Rituparna Karmaker, Basanta Singha, Benzir Ahmed, Penlisola Longkumer, Partha Pratim Gogoi, Nichan Boruah, Rituraj Barman, Bipul Bezbaruah, Upasana Bora Sinha Upasana

This work is licensed under a Creative Commons Attribution 4.0 International License.

Integrated Approach: Synthesis, in vitro Evaluation and Computational Analysis of Bromoanilines as Potential Antioxidants

https://doi.org/10.14233/ajchem.2025.34158

Naruti Longkumer
Department of Chemistry, Nagaland University, Lumami-798627, India; Department of Chemistry, St. John College, Dimapur-797112, India
https://orcid.org/0000-0002-8905-0674

Kikoleho Richa
Department of Biotechnology, St. Joseph University, Chumoukedima-797115, India
https://orcid.org/0000-0002-2272-7548

Rituparna Karmaker
Department of Chemistry, Nagaland University, Lumami-798627, India; Department of Chemistry, St. John College, Dimapur-797112, India
https://orcid.org/0000-0002-0210-700X

Basanta Singha
Department of Chemistry, Nagaland University, Lumami-798627, India
https://orcid.org/0000-0003-4545-8587

Benzir Ahmed
Department of Applied Sciences, Gauhati University, Guwahati-781014, India
https://orcid.org/0000-0002-3221-3030

Penlisola Longkumer
Department of Chemistry, Nagaland University, Lumami-798627, India
https://orcid.org/0009-0008-4726-1132

Partha Pratim Gogoi
Department of Chemistry, Nagaland University, Lumami-798627, India
https://orcid.org/0009-0009-9155-1265

Nichan Boruah
Department of Chemistry, Nagaland University, Lumami-798627, India
https://orcid.org/0009-0008-9605-9061

Rituraj Barman
Department of Applied Sciences, Gauhati University, Guwahati-781014, India
https://orcid.org/0009-0008-9589-5084

Bipul Bezbaruah
Department of Applied Sciences, Gauhati University, Guwahati-781014, India
https://orcid.org/0000-0003-1534-7405

Upasana Bora Sinha
Department of Chemistry, Nagaland University, Lumami-798627, India
https://orcid.org/0000-0002-8598-5173

Bundesrepublik Deutschland

Urkunde

über die Eintragung des
Gebrauchsmusters Nr. 20 2024 103 106

Bezeichnung:
Ein rechnergestütztes System zur Bewertung des Potenzials von halogenierten Gentisylalkoholderivaten als pharmazeutische Wirkstoffe

IPC:
G16C 20/50

Inhaber/Inhaberin:
Basanta, Singha, Zunheboto, Nagaland, IN
Boruah, Nichan, Zunheboto, Nagaland, IN
Gogoi, Partha Pratim, Zunheboto, Nagaland, IN
Longkumer, Penlisola, Zunheboto, Nagaland, IN
NAGALAND UNIVERSITY, Zunheboto, Nagaland, IN
Sinha, Upasana Bora, Zunheboto, Nagaland, IN

Tag der Anmeldung:
11.06.2024

Tag der Eintragung:
27.06.2024

Die Präsidentin des Deutschen Patent- und Markenamts

Eva Schewior

Eva Schewior

München, 27.06.2024

Die Voraussetzungen der Schutzfähigkeit werden bei der Eintragung eines Gebrauchsmusters nicht geprüft.
Den aktuellen Rechtsstand und Schutzumfang entnehmen Sie bitte dem DPMAregister unter www.dpma.de.

(12) PATENT APPLICATION PUBLICATION
(19) INDIA
(22) Date of filing of Application :27/05/2025

(21) Application No.202531050810 A
(43) Publication Date : 06/06/2025

(54) Title of the invention : Halogenated Gentisyl Alcohol Derivatives for Multi-target Pharmacological Profiling

(51) International classification :G16B0015000000, G16C0010000000, G16B0015300000, G16B0020000000, G16B0015200000
(86) International Application No :NA
Filing Date :NA
(87) International Publication No : NA
(61) Patent of Addition to Application Number :NA
Filing Date :NA
(62) Divisional to Application Number :NA
Filing Date :NA

(71)**Name of Applicant :**
1)Nagaland University
Address of Applicant :Nagaland University, Lumami Headquarters, Zunheboto district -India-798627 Zunheboto ---------- ----------
Name of Applicant : NA
Address of Applicant : NA
(72)**Name of Inventor :**
1)Basanta Singha
Address of Applicant :Department of Chemistry, Nagaland University, Lumami-798627, Nagaland, INDIA Zunheboto ---------- ----------
2)Penlisola Longkumer
Address of Applicant :Department of Chemistry, Nagaland University, Lumami-798627, Nagaland, INDIA Zunheboto ---------- ----------
3)Nichan Boruah
Address of Applicant :Department of Chemistry, Nagaland University, Lumami-798627, Nagaland, INDIA Zunheboto ---------- ----------
4)Partha Pratim Gogoi
Address of Applicant :Department of Chemistry, Nagaland University, Lumami-798627, Nagaland, INDIA Zunheboto ---------- ----------
5)Benzir Ahmed
Address of Applicant :Department of Applied Sciences, Gauhati University, Jalukbari-781014, Guwahati, Assam Guwahati ---------- ----------
6)Bipul Bezbaruah
Address of Applicant :Department of Applied Sciences, Gauhati University, Jalukbari-781014, Guwahati, Assam Guwahati ---------- ----------
7)Konda Mani Saravanan
Address of Applicant :Department of Biotechnology, Bharat Institute of Higher Education and Research. Chennai, Tamil Nadu, INDIA- 600073 chennai ---------- ----------
8)Upasana Bora Sinha
Address of Applicant :Department of Chemistry, Nagaland University, Lumami-798627, Nagaland, INDIA Zunheboto ---------- ----------
9)Giridharan Bupesh
Address of Applicant :Department of Forest Science, Nagaland University, Lumami-798627, Nagaland, INDIA Zunheboto ---------- ----------

(57) Abstract :
The present invention relates to a fluorinated analogues 1F, 4F, and 7F, which exhibited favorable structural and computational profiles, suggesting potential as antiprotozoal, anti-inflammatory, and antibacterial agents. Molecular dynamics analyses (RMSD, RMSF, Rg, H-bonding, MM/PBSA) confirmed their stability, minimal conformational drift, and optimal binding energetics. The compounds exhibited conserved interactions with active-site residues shared with co-crystallized ligands and GA, signifying robust structural compatibility. Quantum chemical analyses (Mulliken, NBO, NLO, MEP, ESP, LOL, ELF, NCI) highlighted their favorable electronic properties and non-covalent interactions. Bioactivity score predictions indicated strong bioactive potential, while PASS exhibiting high probability of activity against relevant targets, further supporting their therapeutic significance. Structurally, all three compounds showed stable, near-planar conformations with minor distortions around fluorine and oxygen atoms.

No. of Pages : 28 No. of Claims : 6

(12) PATENT APPLICATION PUBLICATION
(19) INDIA
(22) Date of filing of Application :27/11/2024

(21) Application No.202431092998 A
(43) Publication Date : 14/03/2025

(54) Title of the invention : A PROCESS FOR SYNTHESIZING 4-BROMO-2-METHYLPHENYLISOTHIOCYANATE FOR WOUND HEALING

(51) International classification :A61P17/02, C07C265/12
(86) International Application No :NA
Filing Date :NA
(87) International Publication No : NA
(61) Patent of Addition to Application Number :NA
Filing Date :NA
(62) Divisional to Application Number :NA
Filing Date :NA

(71)**Name of Applicant :**
1)Nichan Borush
Address of Applicant :Department Of Chemistry, Nagaland University, Lumami, Zunheboto, Nagaland-798627, India Zunheboto ---------- ----------
2)Bendangtula Walling
3)Basanta Singha
4)Penlisola Longkumer
5)Partha Pratim Gogoi
6)Mr. Sudharsan Parthasarathy
7)Dr. Kikoleho Richa
8)Dr. Giridharan Bupesh
9)Prof. Upasana Bora Sinha
Name of Applicant : NA
Address of Applicant : NA
(72)**Name of Inventor :**
1)Nichan Borush
Address of Applicant :Department Of Chemistry, Nagaland University, Lumami, Zunheboto, Nagaland-798627, India Zunheboto ---------- ----------
2)Bendangtula Walling
Address of Applicant :Department Of Environmental Science, Nagaland University, Lumami, Zunheboto, Nagaland-798627, India Zunheboto ---------- ----------
3)Basanta Singha
Address of Applicant :Department Of Chemistry, Nagaland University, Lumami, Zunheboto, Nagaland-798627, India Zunheboto ---------- ----------
4)Penlisola Longkumer
Address of Applicant :Department Of Chemistry, Nagaland University, Lumami, Zunheboto, Nagaland-798627, India Zunheboto ---------- ----------
5)Partha Pratim Gogoi
Address of Applicant :Department Of Chemistry, Nagaland University, Lumami, Zunheboto, Nagaland-798627, India Zunheboto ---------- ----------
6)Mr. Sudharsan Parthasarathy
Address of Applicant :Department Of Forestry, Nagaland University, Lumami, Zunheboto, Nagaland-798627, India Zunheboto ---------- ----------
7)Dr. Kikoleho Richa
Address of Applicant :St. Joseph University, Virgin Town, Ikishe Model Village, Chimoukedima, Nagaland- 797 115, India Chimukedima ---------- ----------
8)Dr. Giridharan Bupesh
Address of Applicant :Department Of Forestry, Nagaland University, Lumami, Zunheboto, Nagaland-798627, India Zunheboto ---------- ----------
9)Prof. Upasana Bora Sinha
Address of Applicant :Department Of Chemistry, Nagaland University, Lumami, Zunheboto, Nagaland-798627, India Zunheboto ---------- ----------

(57) Abstract :
The composition and process for synthesizing 4-bromo-2-methylphenylisothiocyanate, comprising: mixing 5-15 mmol of aniline and 25-35 mmol of triethylamine in an ice-cooled mixture; adding 15-25 mmol of carbon disulfide dropwise to the mixture to form a dithiocarbamate salt; stirring for 2 hours to allow precipitation of the dithiocarbamate salt; drying the resultant dithiocarbamate salt in a vacuum desiccator; forming an ice-cold suspension of 2-4 mmol dithiocarbamate salt in a biphasic solvent system of 5-10 mL of ethyl acetate and 5-10 mL of water; adding 4-8 mmol of sodium bicarbonate and a mixture of 2-4 mmol of hydrogen peroxide and 4-8 mmol of potassium bromide to the suspension; stirring the suspension for 15-20 minutes to complete desulfurization and precipitation of sulfur; separating the organic layer, drying it over anhydrous sodium sulfate, and concentrating it under reduced pressure; and purifying the product using a short column of silica gel chromatography to obtain 4-bromo-2-methylphenylisothiocyanate.

No. of Pages : 19 No. of Claims : 10

Bundesrepublik Deutschland

Urkunde

über die Eintragung des
Gebrauchsmusters Nr. 20 2024 101 833

Bezeichnung:
Ein System zur umweltfreundlichen und schnellen Synthese von Bromographen (BG) unter Verwendung eines umweltfreundlicheren Bromierreagenz

IPC:
C01B 32/184

Inhaber/Inhaberin:
Kumar, Suraj, Zunheboto, Nagaland, IN
Rangappa, Dinesh, Chikkaballapur, Karnataka, IN
Singha, Basanta, Zunheboto, Nagaland, IN
Sinha, Dipak, Zunheboto, Nagaland, IN
Sinha, Upasana Bora, Zunheboto, Nagaland, IN
Supong, Aola, Tuensang, Nagaland, IN

Tag der Anmeldung:
13.04.2024

Tag der Eintragung:
22.04.2024

Die Präsidentin des Deutschen Patent- und Markenamts

Eva Schewior

Eva Schewior

München, 22.04.2024

Die Voraussetzungen der Schutzfähigkeit werden bei der Eintragung eines Gebrauchsmusters nicht geprüft.
Den aktuellen Rechtsstand und Schutzumfang entnehmen Sie bitte dem DPMAregister unter www.dpma.de.